

IMPLEMENTATION AND EVALUATION OF OPTICAL AND STYLUS BASED
PROFILING TECHNIQUES FOR SURFACE METROLOGY

by

Kumar Arumugam

A dissertation submitted to the faculty of
The University of North Carolina at Charlotte
in partial fulfillment of the requirements
for the degree of Doctor of Philosophy in
Mechanical Engineering

Charlotte

2021

Approved by:

Dr. Stuart Smith

Dr. Jimmie Miller

Dr. Tsinghua Her

Dr. Joshua Tarbutton

Dr. Xingde Dai

©2021
Kumar Arumugam
ALL RIGHTS RESERVED

ABSTRACT

KUMAR ARUMUGAM. Implementation and Evaluation of Optical and Stylus Based Profiling Techniques for Surface Metrology. (Under the direction of Dr. STUART SMITH)

A unifying theme of this thesis is the implementation and characterization of point probes for surface metrology. The implementations include two optical non-contact profiling methods; fiber-based Fabry-Perot interferometry, and confocal microscopy. And a stylus profilometer is metrologically characterized to evaluate its suitability in measuring form of optically smooth surfaces.

Fiber-based Fabry-Perot interferometers are typically used to measure displacement in confined spaces. Even though this technique is suitable for measuring surface texture, literature describing its implementation and limitations in its use as a surface profiler are scarce. Therefore, this work attempts to understand the issues with experimental implementation of this technique and the limitations of using a bare fiber probe tip for surface profiling. As outcomes of this part of the research, experimental setup is built and the feasibility in surface height measurements is validated by measuring two sinusoidal reference surfaces with heights of 1 μm and 1.5 μm and wavelengths of 100 μm and 50 μm , respectively.

The second part of this thesis is to implement a flexure-based oscillation of an objective lens stack used for confocal microscopy to determine a localized surface height. Current practices include the oscillation of the surface sample, oscillation of the casing that houses the objective lens stack, and MEMS (micro-electromechanical systems) based scanners. The first two approaches limit the achievable bandwidth of oscillation due to the

mass of the objects being oscillated, and the latter approach is expensive. Using a flexure mechanism to oscillate the optical lens elements has the potential to increase the bandwidth of oscillation and therefore surface scanning speeds. Since the spot size produced by the objective lens determines the spatial resolution of the measurement, spot size is measured for 40X and 60X commercial objective lenses illuminated by laser and mLED (micro-Light Emitting Diode) light sources. A sinusoidal reference sample is designed and manufactured, which is later measured using a confocal microscope prototype built using a 60X objective lens. A flexure to house the lens stack to provide a surface height scanning range of 10 μm is also designed and fabricated.

The third part of this thesis involves characterizing a stylus-based contact profiler for measuring areal form of freeform optics. Typically, for non-contact point probes, the optical axis must be orthogonal to the curvature of the part being measured (probe normal) to reduce errors in the measurement. Additional carriages are required to generate a probe normal scanning path. For many freeform optics, interferometric surface measurement techniques such as Fizeau interferometry requires generating a reference surface for each design prescription. Since the stylus profilers do not have these disadvantages, a commercial stylus profiler (Mahr LD260) is characterized by measuring reference objects such as optical flats, prisms, and spheres. The measurement results are compared with the measurements of these reference objects using a Fizeau interferometer. As a result, the vertical error of the X scanning carriage, side loading on the stylus probe due to the surface slope of the part being measured, and other carriage errors are estimated. A geometrical model of the system including the errors in the motion of carriages is developed, and a Monte Carlo simulation is performed to evaluate the uncertainty in the areal form

measurements. The simulation resulted in a measurement uncertainty of less than 200 nm PV for a 100 mm measurement aperture.

ACKNOWLEDGEMENTS

I would like to thank my parents Shanthi and Arumugam, and my PhD advisor Dr. Stuart Smith. The former for being adamant on providing me the best education possible, and the latter for teaching me science and engineering from a fundamental level that enabled me to possess the required skills and knowledge as an engineer. I would also like to thank the Graduate Assistant Support Program (GASP) at UNC Charlotte, and the Center for Precision Metrology (CPM) for their financial support. Guidance and assistance from the CPM faculty and staff: Dr. Chris Evans, Dr. Jimmie Miller, Dr. Tsinghua Her, Greg Caskey, Brian Dutterer, Geoffrey Heacock, Scott Williams and Jennifer Chastain is much appreciated. Special thanks to Dr. Todd Noste for sharing his expertise on using Fizeau interferometry, analysis of measurement data, and machine tool metrology, Dr. Jeffery Thousand for getting me up to speed on programming and other hands-on activities when I joined the Instrument Development Group, Dr. Joshua Tarbutton , and Dr. Alex Blum for being part of the team from UNC Charlotte that participated in the student challenges held at the annual conference organized by the American Society of Precision Engineering, and Jacob Cole for the hour long lunches and beer discussions.

TABLE OF CONTENTS

LIST OF TABLES.....	xvi
LIST OF FIGURES.....	xvii
LIST OF ABBREVIATIONS.....	xxxv
1. INTRODUCTION	1
1.1 Importance of surface texture and measurement techniques	1
1.2 Overview of the studies undertaken in this thesis.....	2
2. FIBER-BASED FABRY-PEROT INTERFEROMETRIC PROFILER	4
2.1 Background	4
2.2 Motivations for the study	5
2.3 Literature review - fiber-based interferometry for displacement measurements	6
2.3.1 History.....	6
2.3.2 Theoretical	7
2.3.3 Implementations and signal processing techniques	8
2.3.4 Probe tip.....	10
2.4 Working principle	12
2.4.1 Simulation	18
2.5 Experimental setup.....	23

2.5.1 Source	23
2.5.2 Fiber optics.....	23
2.5.3 Signal processing	27
2.5.4 Stage mechanisms	27
2.6 Experimental results.....	30
2.6.1 Laser frequency modulation and signal processing parameters	30
2.6.2 Alignment of tilt of the surface	35
2.6.3 Sample surface measurements	37
2.6.4 Spot size enhancement using Gradient Refractive Index lens	43
2.7 Design studies for producing stress induced modulation of laser sources...	45
2.7.1 Stress induced modulation of laser frequency using a microchip laser.....	45
2.7.2 Background and literature on mechanical stress control of optical materials for laser source modulation	46
2.7.3 Experiments to modulate the laser frequency by compressing the Vanadate-KTP crystal pair.....	50
2.7.4 Multiple longitudinal modes (wavelengths) in a microchip laser.....	61
2.7.5 Modulation of the phase of the light source by compressing an optical flat	64
2.8 Future work	76
2.8.1 Laser diode coupled to the fiber using a self-aligning bearing	76

2.8.2 Rubidium clock source	76
2.9 Conclusions.....	78
3. OBJECTIVE LENS OSCILLATED MONOCHROMATIC CONFOCAL MICROSCOPE	81
3.1 Background of the development of confocal microscopy	81
3.2 Motivations for the study	81
3.3 Working principle	83
3.4 Literature review	85
3.4.1 Review articles.....	85
3.4.2 Improvements in axial response sensitivity	85
3.4.3 Scanning techniques.....	86
3.4.4 Other studies	87
3.5 Theoretical model for the sensitivity of the confocal FWHM to the focal length of the detector lens	88
3.6 Experiments	91
3.6.1 First prototype using a diode laser source, 40X objective lens, and two pinholes	91
3.6.2 Second prototype using a red mLED source and 60X objective lenses.....	96
3.6.3 Third prototype using a red diode laser, and 60X objective lenses ..	101

3.6.4 Fourth prototype using a red diode laser with a pin hole, and 60X and 20X objective lenses	106
3.6.5 Oscillation of the objective lens using a piezo actuated flexure mechanism	110
3.6.6 Sinusoidal reference surface	116
3.7 Conclusions and future work	119
4. CHARACTERIZATION OF A STYLUS PROFILER FOR AREAL FORM MEASUREMENTS	121
4.1 Background	121
4.2 Motivations for the study	122
4.3 Literature review	124
4.3.1 Stylus geometry and dynamics	124
4.3.2 Comparison studies of stylus and optical profilers	125
4.3.3 Form measurement techniques in Fizeau interferometry.....	127
4.3.4 Kinematic support of flats.....	128
4.3.5 Freeform surfaces.....	128
4.3.6 Error modeling and task specific uncertainty	130
4.4 Experimental facility.....	131
4.5 Areal profiling approaches.....	131
4.5.1 Merits and limitations of the stripes approach.....	133

4.5.2	Merits and limitations of the spokes approach	135
4.5.3	Zernike polynomial fit to stripes and spokes	135
4.5.4	Time taken for stripes and spokes.....	137
4.6	Geometrical model.....	138
4.6.1	Simplified geometrical models for stripes and spokes methods of measurements.....	143
4.6.2	Vector containing the X carriage errors and probe displacement terms.....	143
4.7	Flat surface measurements for profiler performance evaluation	148
4.7.1	Interferometric measurements of reference optical flats	148
4.7.2	Static electrical noise and thermal drift	151
4.7.3	Effects of pressure variation in the air supply to the carriages	154
4.7.4	Vertical error in the profiles measured in the middle 130 mm travel in x axis.....	157
4.7.5	Vertical error in the profiles measured in the full x axis travel	159
4.7.6	Dynamic thermal drift.....	171
4.7.7	Validation of force feedback control	175
4.7.8	Areal surface measurements of a flat over an 85 mm aperture.....	177
4.8	Prism measurements	192
4.8.1	Experimental assembly and alignment	194

4.8.2 Arcuate correction of reported X carriage values due to the pivoting stylus	196
4.8.3 Filtering for stylus morphology	198
4.8.4 Vertical error measured on the inclined surfaces of the prism	198
4.8.5 Varying slope profile on the prism and its comparison with a profile on an optical flat.....	202
4.8.6 Estimation of inclined surface angles of the prism.....	204
4.8.7 Estimation of angles using profiles at each Y location.....	205
4.8.8 Summary of estimated inclination angle.....	207
4.9 Spherical cap measurements	210
4.9.1 Silicon nitride sphere	210
4.9.2 Borosilicate concave mirrors	233
4.10 Uncertainty evaluation using Monte Carlo simulation	246
4.10.1 Monte Carlo – stripes	246
4.10.2 Monte Carlo – spokes.....	252
4.11 Future work.....	255
4.12 Conclusion- considerations to use the machine and process the measurement data	261
5. References.....	263
5.1 Surface metrology	263

5.2	Fiber-based Fabry-Perot interferometric profiler.....	263
5.2.1	Stress induced frequency and phase modulation of light source	264
5.3	Objective lens oscillated monochromatic confocal microscope	266
5.4	Characterization of a stylus profiler for areal form measurements.....	267
Appendix A.....		269
A.1	Frequency modulation of the laser by oscillating the grating	270
A.2	Scanning stage used in fiber Fabry-Perot interferometry	272
A.3	Rod flexure based tilt aligner used in fiber Fabry-Perot profiler	281
A.4.	Specifications of a 808 nm laser pump diode	286
A.5.	A prototype compressing a microchip laser crystal pair for frequency modulation.....	287
A.6.	Design of flexure based crystal compressor	289
A.7.	Spectrum of some of the commercially available lasers	293
Appendix B		297
B.1	Procedure followed to build the first prototype	298
B.2	Spot size estimation of various light sources focused by 40X and 60X objective lenses	305
B.3	Procedure followed to build the second prototype	311
B.4	An earlier prototype of pinhole alignment mechanism	312

B.5 Procedure followed to build the third prototype with and without the tip-tilt aligner	313
B.6 Stylus profilometer measurement result of sinusoidal refence sample	316
B.7 Disc coupling flexure for oscillating the objective lens stack.....	318
B.8 Flexure-based tilt aligner and a translation stage for surface scanning.....	320
B.9 LabVIEW program to detect peak intensity from the confocal probe and to control the flexure-based scanning stage.....	331
Appendix C	338
C.1. Manufacturer specification of carriages and equipment used with the profilometer	339
C.1.1 Manufacturer specification of the <i>Y</i> carriage	339
C.1.2 Manufacturer specification of the rotary (<i>C</i>) carriage.....	341
C.1.3 Manufacturer specification of the indicator used for centering the parts	343
C.2. Interferometric measurements of reference objects and data processing....	344
C.2.1 Six inch diameter Fused Silica flat.....	344
C.2.2 Four inch diameter Fused Silica flat	356
C.2.3 Three inch diameter Fused Silica flat.....	358
C.2.4 Four inch diamter Zerodur optical flat	358
C.2.5 Three inch diamater Zerodur optical flat.....	373
C.2.6 Aluminum coated glass bar	374

C.2.7 Silicon Carbide coated hollow Aluminum bar	380
C.2.8 Right-angled prisms	384
C.2.9 Measurement of concave mirrors and calibration of the transmission sphere	388
C.2.10 Measurement of concave mirrors	398
C.3 Calibration of temperature sensors used with the profilometer system	408
C.4 Hertzian analysis of a Zerodur flat supported on a 3-point kinematic mount	410
C.5 Hertzian analysis of a Silicon Nitride sphere supported on a kinematic 3 point mount.....	412

LIST OF TABLES

Table 1: Specifications of two commercially available fiber-based coherence scanning interferometers	5
Table 2: Summary of the computed angle of inclination surfaces and the pyramid angle	209
Table 3: Zernike coefficients of values greater than 4 nm for concave mirror 1.....	235
Table 4: Uncertainty of X and Y carriage errors input to the Monte Carlo simulation.	249
Table 5: Uncertainty of rotary carriage errors input to the Monte Carlo simulation.	253
Table 6: Positions of x and y in measurements to estimate the induced wavefront error in interferogram.....	393
Table 7: Values of the Zernike fit to the measurements at 0° and 120° orientations and their differences	404

LIST OF FIGURES

Figure 1: Schematic of the fiber Fabry-Perot interferometer.....	13
Figure 2: Harmonics and the phase quadrature.....	16
Figure 3: Simulation showing the procedure to obtain the quadrature signal to compute the displacement of a target.	19
Figure 4: Phase unwrapping to calculate the displacement	22
Figure 5: Schematic of the experimental facility showing the equipment with their model number	24
Figure 6: Circuit to amplify and DC offset the sinusoidal signal provided to the piezo actuator oscillating the grating and thereby modulating the frequency of the laser source.....	25
Figure 7: Equipment to control the current to the laser source, frequency modulate the laser source, and to isolate the returning light from destabilizing the source.....	26
Figure 8: Fiber Fabry-Perot interferometric profiler experimental facility	29
Figure 9: Fringes due to the displacement of a copper mirror towards the fiber.....	31
Figure 10: Plot of modulation signal (black) fed to the high voltage amplifier and the photo detector output (blue).....	33
Figure 11: Tilt aligner – design and performance.....	36
Figure 12: Measurement of the Rubert 531 sample.....	38
Figure 13: Measurement of the Rubert 528 sample.....	40
Figure 14: Measurement of a ground cylinder.....	42
Figure 15: Beam divergence at the fiber output and the GRIN lens.....	44
Figure 16: Microchip laser components	49
Figure 17 Earlier prototypes of the crystal compressor	51

Figure 18: Picture of the 808 nm laser diode mount which controls the current and temperature of the diode using the controller units shown on the left top	52
Figure 19: Result of frequency modulation using the clamp assembly	55
Figure 20: Schematic of the flexure - based crystal compressor	56
Figure 21: Dimensions of the notch hinge flexure used to calculate the stress exerted on the crystal pair. The strain gage is located on the top surface of the link C, in line with the notch joint.	57
Figure 22: Result of frequency modulation using the flexure gripper.....	58
Figure 23: Circuit diagram for strain gage sensing and the calculated stress	59
Figure 24: Wavelength spectrum of the microchip laser	62
Figure 25: Polarization based Homodyne interferometer	63
Figure 26: Fringes produced in a Polarization based Homodyne interferometer	65
Figure 27: Schematic showing phase modulation	66
Figure 28: Cutting an optical flat using a grinding wheel	69
Figure 29: Fabrication of piezo plates by dicing using a diamond wheel	70
Figure 30: Experimental setup and results of applying stress on an optical flat.....	71
Figure 31: Experimental setup applying stress on top and bottom of an optical flat.....	73
Figure 32: Experimental setup using a stiff clamping assembly	74
Figure 33: Experimental setup using a piezo stack to compress an optical flat	75
Figure 34: Laser diode coupled to the single mode fiber using a self-aligning bearing	77
Figure 35: Wiring diagram of Rubidium clock with DB-9 connector.....	78
Figure 36: Schematic and a measurement concept of surface profiling using a confocal microscope.	84

Figure 37: Ray diagram showing the sensitivity of the axial response to the focal length of the lens used at the detector end	89
Figure 38: First prototype of the confocal probe assembly	92
Figure 39: First fabricated prototype of the confocal microscope	93
Figure 40: Experimental setup to measure the axial response of the probe.....	94
Figure 41: Intensity peaks observed by the probe for a single period of sinusoidal translation of the copper mirror towards the probe using a flexure stage.....	95
Figure 42: Schematic of a collimated beam converged by a lens indicating the spot size and the depth of focus.....	96
Figure 43: Ray diagrams of a light source focused by a lens element.....	99
Figure 44: Second prototype using a red mLED source and its axial response.....	100
Figure 45: Third prototype using a 30 mW red laser	102
Figure 46: Tip-tilt aligner for the laser source, and the pinhole alignment mechanism	103
Figure 47: Experiment to measure the working distance and axial response of the probe.	105
Figure 48: Intensity recorded when the copper mirror is moved until it contacts the spring-loaded object lens	105
Figure 49: Intensity recorded by the photodetector when a copper mirror is moved towards or away from the objective lens to determine the FWHM of the probe representing its axial response	106
Figure 50: Ray diagram of the assembly using an adjustable focusing lens, a pinhole, and a collimating lens to collimate the beam to reach the objective lens.....	106
Figure 51: Fourth prototype using a 30 mW red laser with a pinhole	107
Figure 52: Fabricated fourth prototype	108

Figure 53: Axial response when a copper mirror is translated towards the 60X objective lens at the object side	109
Figure 54: Fabrication of the flexure based oscillator for the objective lens.....	111
Figure 55: Experimental setup to observe the frequency response function of the flexure-based oscillator.....	112
Figure 56: Left: Input sinusoidal signal to the piezo actuator and the recorded displacement from the capacitance probe plotted as a function of time for frequencies of 2, 20, 50, 100, 120, 150, 160, 200 Hz, Right: Lissajous curves.	114
Figure 57: Testing the prototype using the flexure oscillated object lens head for axial response	115
Figure 58: Sinusoidal reference sample	117
Figure 59: Stylus profiler (Mahr LD260) measuring the sinusoidal reference sample	117
Figure 60: A profile measured on the sinusoidal reference sample using a stylus profiler with the inset showing left half of the profile.	118
Figure 61: Profilometer system.....	132
Figure 62: Areal profiling approaches simulated on a 200 mm diameter flat specimen.	133
Figure 63: Simulation showing the use of tie lines to compensate for the linear thermal drift..	134
Figure 64: Comparison between Zernike fitting for the simulated measurements using stipes and spokes approaches of profiling	136
Figure 65: Schematic showing the half length of a profile according to the chord lengths in a circular area.....	137

Figure 66: Schematic showing the components of the profilometer system, and the locations of the X, Y, and C carriages and the stylus that brings the center of the probe ball to reference coordinate, O_F .	139
Figure 67: Translation and rotation of carriages during the measurement	139
Figure 68: Symbols representing the errors in the motion of the carriages used in the profilometer system.	142
Figure 69: Schematics showing the motion of stylus with respect to the errors in the motion of X carriage.	145
Figure 70: Schematic of (a) perfect flat measured by the stylus (b) concave surface measured by the stylus	146
Figure 71: Simulation of the effect of vertical error of the X carriage on the resulted measurement	147
Figure 72: Interferometric measurements of the reference optical flats	149
Figure 73: Experiment measuring the drift in the system and the temperature variation of the components in the system	152
Figure 74: Drift, and the temperature of (a) air, and surfaces of (b) kinematic plate, (c) rotary carriage, and (d) Y carriage plotted as a function of time.	153
Figure 75: Thermal expansion coefficients of the material, and the height of the components in the profilometer system	155
Figure 76: Measurement to observe the air pressure variation in the air bearing stages and its effect on the motion of the stylus.	156
Figure 77: Plots showing the results of profiling in air and on an optical flat.	158

Figure 78: Schematic (a) of a measurement of an ideal optical flat showing the X carriage error (b)	
Reported measurement in air containing the correction curve	158
Figure 79: Measurement of a Straight edge made of Nitralloy	159
Figure 80: Piece-wise measurement of a Zerodur flat	160
Figure 81 Experimental assembly used in the piecewise measurement of the Zerodur flat.....	162
Figure 82: Results of the profiles measured in piecewise manner.....	165
Figure 83: Standard deviation of the profiles measured in piecewise manner	166
Figure 84: Procedure to stitch the overlapping profiles measured in piecewise manner.....	168
Figure 85: Comparison of the vertical error estimated using the stitched piecewise measurements of Zerodur flat to the Straightedge measurement	169
Figure 86: Comparison of the measured vertical error to the calibration curve of the profilometer	170
Figure 87: Experimental results of a Fused Silica flat measurement to determine the dynamic thermal drift of the profiler	172
Figure 88: Drift of the repeatedly measured profiles	173
Figure 89: Results of twenty repeated profiles of the Fused silica optical flat.....	174
Figure 90: Repeatability assessment for z height relocation and stability	176
Figure 91: Results of the areal surface measurement of the Zerodur optical flat	178
Figure 92: Using a tie line to correct for the Y carriage vertical straightness and vertical squareness errors, and the thermal drift in the measurements by stripes approach	180
Figure 93: Using a tie line to correct for the Y carriage roll, vertical straightness and vertical squareness errors, and the thermal drift in the measurements by stripes approach	181
Figure 94: Repeated areal measurements of the Zerodur flat using stripes approach	183

Figure 95: Estimation of vertical straightness of <i>Y</i> carriage using the repeated areal stripes measurements of the Zerodur flat and its correction	184
Figure 96: Correcting for vertical error of the <i>X</i> carriage in the areal measurements of the Zerodur flat.	185
Figure 97: Correcting for vertical error of the <i>X</i> carriage and vertical straightness of the <i>Y</i> carriage in the areal measurement of Zerodur flat	186
Figure 98: Zerodur flat measured using the spokes approach	188
Figure 99: Slope and offset removed from each profile and their 5 th order polynomial fit.....	189
Figure 100: Results of the 5 th order polynomial fit to the eight spokes profiles made on the flat	190
Figure 101: Estimation of tilt and axial errors of the <i>C</i> rotary carriage.....	191
Figure 102: Results of the angle of inclination of the prism measured using a Multi-surface tester.	192
Figure 103: Interferometric measurements of the prism surfaces	193
Figure 104: Mounting and orienting the prism in the profilometer	195
Figure 105: Measurement results of profiling the prism	197
Figure 106: Plot showing the difference in the data spacing of <i>x</i> values reported (in orange) when the stylus travel on ramp and off ramp of the prism.	198
Figure 107: Raw and morphology filtered results of the measurement of the prism.....	199
Figure 108: Profiles measured on a prism by stepping in <i>x</i> axis. Top row: Orientation of the prism during measurements; middle row: average of ten profiles made at five <i>y</i> locations using the profiler; bottom row: line subtracted from each profile and plotted as profilograms	201

Figure 109: Schematic of (a) top and front view of the prism mounted on the polymer platform and its dimensions and (b) prism rotated to 51° azimuthally to profile along a linearly varying surface slope.	202
Figure 110: Comparison between the profiles measured on a prism and the profile measured on a Zerodur flat	203
Figure 111: Procedure to estimate the ramp angles of the surfaces of the prism	204
Figure 112: Estimation of the inclination angles of the prism surfaces.....	206
Figure 113: Schematic showing the (a) Yaw of the <i>Y</i> carriage (top view of prism) and (b) Pitch of the <i>Y</i> carriage (side view of prism) during the step over to make profiles on the prism.	207
Figure 114: Ramp angles estimated by fitting a plane to the profiles made on a prism.....	208
Figure 115: Schematic diagrams showing (a) the degrees of freedom of the stylus, (b) desired profile and possible profiles due to side loading, (c) the measured datapoints on the sphere	211
Figure 116: Experimental setup and the measurement procedure to measure a Silicon nitride sphere	212
Figure 117: Estimation of <i>Y</i> carriage squareness and the calculated radial residue in the measurement of a Silicon nitride sphere	214
Figure 118: Estimation of <i>Y</i> carriage squareness using the measurement of a Silicon nitride sphere in three azimuth orientations.....	216
Figure 119: Radial residues calculated from the measurements of the Silicon nitride sphere in three azimuth orientations.....	218
Figure 120: Example illustration of sign convention for the estimated horizontal squareness values.	219

Figure 121: Estimation of <i>Y</i> carriage squareness using the measurement of the Silicon nitride sphere in three azimuth orientations on four different days	220
Figure 122: Radial residue of individual profiles of the measured spherical cap of the Silicon nitride sphere.....	222
Figure 123: Radial residue of a meridian profile on the Silicon nitride sphere indicating the need for recalibrating the stylus	223
Figure 124: Using a tie line to correct for the <i>Y</i> carriage vertical squareness, and vertical straightness errors, and thermal drift	225
Figure 125: Using a tie line to correct for the <i>Y</i> carriage vertical squareness and vertical straightness errors, and thermal drift by iteratively translating the tie line along y axis	226
Figure 126: Schematic showing the expected offset of the sphere due to the tilt of the rotary carriage.....	227
Figure 127: Results of the Silicon nitride sphere measured using the spokes approach	229
Figure 128: Radial residue estimated in the spokes approach of profiling.....	230
Figure 129: Radial residue calculated from the spokes measurements made on the Silicon nitride sphere on four different days	231
Figure 130: Results of the spokes measurement over four days.....	232
Figure 131: Interferometric measurement of the concave reference surfaces	234
Figure 132: Zernike polynomial fit to the interferometric measurements of the concave reference surfaces	236
Figure 133: Profilometer measurement of concave mirrors 1 and 2	237
Figure 134: Estimation of squareness of the <i>Y</i> carriage from the profilometer measurements of the concave surfaces	239

Figure 135: Profilometer measurement of Concave mirror 1 using the stripe approach.....	241
Figure 136: Profilometer measurement of Concave mirror 2 using the stripes approach.	241
Figure 137: Flowchart showing the procedure to use the raw measurement data of a concave mirror and correct for the carriage errors.	242
Figure 138: Profilometer measurement of the Concave mirror 1 using the spokes approach	244
Figure 139: Profilometer measurement of the Concave mirror 2 using the spokes approach	244
Figure 140: Comparison of the profilograms of the concave mirror measurements with the interferograms from PSI	245
Figure 141: <i>X</i> carriage errors	247
Figure 142: <i>Y</i> carriage errors.....	248
Figure 143: Monte Carlo simulation of a flat surface, and a concave surface measured using the stripes approach	251
Figure 144: Monte Carlo simulation of a flat surface, and a concave surface measured using the spokes approach	254
Figure 145: Schematics of the motion errors of the <i>X</i> carriage	255
Figure 146: Machine tool metrology methods to estimate the <i>Y</i> carriage motion errors (straightness, roll, and pitch).....	257
Figure 147: Machine tool metrology methods to estimate the <i>Y</i> carriage motion errors (positioning error, and yaw)	258
Figure 148: Machine tool metrology methods to estimate the <i>C</i> carriage motion errors	259
Figure 149: Machine tool metrology method to estimate the <i>C</i> carriage positioning error.....	260
Figure 150: Solid model of the laser frequency modulator	270
Figure 151: Frequency modulation characteristics of the laser	271

Figure 152: x axis scanning stage used in the Fiber interferometric profiler studies	274
Figure 153: Components used in controlling the scanning stage: myRIO microprocessor, OPA549 current amplifier to provide current to the coils, Interpolator for converting the sinusoidal encoder signal to square waves.....	275
Figure 154: Amplifier box providing three current outputs phase shifted by 120° with its signal inputs from myRIO's 12-bit DAC's on connector C.....	276
Figure 155: Circuits to actuate the x axis scanning stage	277
Figure 156: Layout of the interpolator board to convert the $20\text{ }\mu\text{m}$ sinusoidal signal from the linear encoder into a 314 nm periodic square waves, and the counter board to count the number of periods of the square waves generated	278
Figure 157: Feedback control of the stage	279
Figure 158: LabVIEW program with a timed loop to execute a PID controller, to initialize and read the counter board outputting the number of interpolated square waves during the motion of the stage	280
Figure 159: A rod flexure mechanism used to remove the tilt of the sample surface measured using the Fiber Fabry-Perot interferometric profiler	281
Figure 160: Schematic showing the flexure rod inserted to the platform.....	283
Figure 161: Specifications of the 808 nm infrared laser pump diode used in the experiments to frequency modulate a Vanadate-KTP microchip laser by applying stress	286
Figure 162: Prototype to compress the Vanadate-KTP crystal pair	287
Figure 163: Experiment to observe the frequency modulation of the laser output.....	288
Figure 164: Design of the notch hinge flexure to compress the crystal pair	290
Figure 165: Spectrum of Thorlabs CPS532 green laser.....	293

Figure 166: Spectrum of Ebay green laser.....	294
Figure 167 Spectrum of Sparkfun green laser	295
Figure 168: Spectrum of Quarton Inc. red laser	296
Figure 169: Lapping the beam splitter cube and drilling pinholes in a copper sheet	298
Figure 170: Fabrication of the first prototype.....	299
Figure 171: Alignment of the pinhole with respect to the focused spot at the detector end of the confocal probe.....	300
Figure 172: Fabricated prototype;.....	301
Figure 173: Circuit diagram of the photodetector amplifier.....	302
Figure 174: Ethernet connector breakout board used to power the laser, power and read the photodetector circuit using the myRIO.....	303
Figure 175: Intensity peaks measured using the first prototype	304
Figure 176: Experimental facility to estimate the spot size of the converging beam from an objective lens.....	306
Figure 177: Erf function fit to the measurement results	308
Figure 178: Some of the light source - objective lens combinations used in the experiments ...	309
Figure 179: Spot size estimates of various objective lens- light source combinations.....	310
Figure 180: Build of the second prototype that uses a Red mLED.....	311
Figure 181: An earlier prototype of the pinhole alignment mechanism using a bellow flexure	312
Figure 182: Solid model of the fabricated prototype that uses a focus adjustable red laser, a collimating lens, and a pinhole alignment mechanism	313
Figure 183: Building procedure of a prototype that do not use a tip-tilt aligner	314
Figure 184: Building procedure of a prototype that uses a tip-tilt aligner	315

Figure 185: Zoomed in results of the stylus profilometer measurement of the sinusoidal reference sample	317
Figure 186: Schematic of a disc coupling flexure [Smith, 2000]	318
Figure 187: Flexure-based tilt aligner to align the surface sample normal to the confocal probe.	320
Figure 188: Voice coil actuated flexure based stage with a linear encoder feedback to scan surface samples.....	321
Figure 189: Flexure-based x axis scanning stage used with the confocal microscope	322
Figure 190: Characteristics of the voice coil actuator, BEI, Kimco magnetics division	323
Figure 191: Photograph of the circuit boxes used with the stage	324
Figure 192: (a) Fabricated PCB for the 6 channel DAC (b) necessary modification to get one of the channel to work	325
Figure 193: circuit diagram of (a) AD420 DAC (b) the buffer amplifier converting 0 to 5 V input to a ± 10 V output.....	326
Figure 194: Layout of the PCB for a 6 channel DAC.....	327
Figure 195: Amplifier circuit for the encoder signals.....	328
Figure 196: Pin diagram and the color of wires used with the encoder signal conditioner unit.	329
Figure 197: PID Control architecture for the stage.....	330
Figure 198: (a) LabVIEW Project explorer window containing the programs to find the intensity peaks detected by the confocal probe, actuate the piezo oscillating the objective lens, and PID controller for the x axis scanning stage (b) FPGA program	331
Figure 199: LabVIEW program to control the flexure stage using a PID controller	332
Figure 200: Sub VI's used in the LabVIEW program to control the flexure stage	334

Figure 201: Ellipse2circle.vi providing the parameters to convert the elliptical Lissajous to a normalized circular quadrature.	335
Figure 202: LabVIEW program to detect the intensity peak signal from the confocal probe and relate the peak location to the proportional piezo input voltage	336
Figure 203: Front panel of the LabVIEW program	337
Figure 204: Manufacturer's specification of the Y carriage used in the Profilometer system.	340
Figure 205: Manufacturer's specification of the Rotary carriage, C used in the Profilometer system.	342
Figure 206: Experimental setup to measure the 6 in. flat	345
Figure 207: Interferometric measurement results of the flat	347
Figure 208: Stitched profile from both the measurements to obtain the nominal profile of the flat along the Y axis, whose profile height is 15 nm PV	348
Figure 209: (a), (b) Recorded interferograms of top and bottom half of the flat (c), (d) planes fit to the interferograms (e), (f) planes subtracted from the interferograms shown in (a), (b).	349
Figure 210: Tilt in the measured data removed by (a) subtracting a line vs. (b) rotating the data.	349
Figure 211: Schematic showing the length of the data after subtracting a line is almost as same as the length of the surface measured.....	350
Figure 212: Procedure to stitch the interferograms of the flat	351
Figure 213: Simulation showing the stitching error	352
Figure 214: Stitching the interferograms by tilting one interferogram with respect to the other after aligning them in xy plane using the fiducials placed on the measurement surface.....	353

Figure 215: Intersecting region of the interferograms of top and bottom half of the optical flat.	354
Figure 216: Intersecting region of the interferograms	354
Figure 217: Stitched interferograms	355
Figure 218: Comparison of the stitched data with the data stitched using the .exe file provided by Zygo	355
Figure 219: Measurement result of the 4 in. Fused Silica flat;	357
Figure 220: Frequency tuning settings used in the measurement using an MST.	357
Figure 221: Measurement results of 3 in. Fused Silica optical flat; (a) on MST (b) on PSI (c) difference in the 36 term Zernike polynomials fit to the interferograms.....	358
Figure 222: Experimental procedure during the measurement of the flat using a PSI	359
Figure 223: Interferogram of a PSI measurement of 4 in. Zerodur flat.	361
Figure 224: Interferometric measurement results of the 4 in. Zerodur flat when its back surface coated with a blue coating.....	361
Figure 225: PSI interferograms of the Zerodur flat, whose back surface is coated with wintergreen oil and a black card attached to it.....	363
Figure 226: Three flat test - experimental setup	363
Figure 227: Measurement results of the three flat test.....	364
Figure 228: Profiles of the flats along its Y axis obtained from a 3-flat test.	365
Figure 229: Plastic fiducial with adhesive backing	365
Figure 230: Interferometric measurement profile of the Zerodur flat compared with the profiles of the transmission flat obtained from the three flat test.....	367
Figure 231: Nominal profile of the Zerodur flat along the fiducials	367

Figure 232: Difference in the interferogram of 1 st and 5 th measurement in the 3-flat tests using transmission and object flats	368
Figure 233: Five continuous measurements with TF _m and RF, and planes fit to the measurements.	368
Figure 234: (a) Mean of 5 continuous measurements with TF _m and RF (b) standard deviation of the measurements.....	369
Figure 235: Interferometric measurement of the 4 in. Zerodur flat using the MST	370
Figure 236: Experimental setup to measure the 4 in. Zerodur flat using a vertically oriented PSI	371
Figure 237: Measurement result of the 4 in. Zerodur flat measured using a vertically oriented PSI	372
Figure 238: Measurement result of a 3 in. Zerodur flat using the PSI.....	373
Figure 239: Experimental set up to measure an Aluminum coated rectangular bar using the PSI by following a ‘skip flat’ technique	374
Figure 240: Experimental results of the skip flat test performed on the rectangular bar.....	376
Figure 241: Skip flat measurement results of the remeasurement	377
Figure 242: Interferometer measurement of the middle 100 mm portion of the bar	378
Figure 243: interferograms from the CSI measurements of two locations of the bar showing surface height of about 50 nm PV, and less than 4 nm RMS.....	379
Figure 244: Skip flat test of a Silicon Carbide coated Aluminum hollow bar.....	380
Figure 245: Measurement results of the SiC bar	380
Figure 246: Measurement result of SiC bar when it is facing straight towards the transmission flat used in the interferometer.....	381

Figure 247: SiC bar measured on the stylus profilometer (Marsurf LD260)	382
Figure 248 Profiles on the SiC bar from the (a) interferometer measurement, (b) Profilometer measurement.	383
Figure 249: (a) Interferogram of the SiC bar measured using the CSI (b) A profile taken across the surface.	383
Figure 250: Schematics showing the identification marks on (a) Prism ‘E’ and (b) Prism ‘F’..	384
Figure 251: Schematic of the experimental setup of the interferometer measuring the prism ...	385
Figure 252: Photograph of the experimental setup measuring the prism	386
Figure 253: Experimental result of prism ‘E’; Top: on-ramp surface Bottom: off-ramp surface	386
Figure 254: Experimental result of prism ‘F’; Top: on-ramp surface Bottom: off-ramp surface	387
Figure 255: Experimental setup using a Silicon nitride ball to estimate the form of the transmission sphere using the PSI.....	389
Figure 256: Induced tilt due to the x and y translation of the ball and the resulted coma terms.	390
Figure 257: Induced tilt due to y translation of the ball and the resulted vertical astigmatism. .	391
Figure 258: Induced tilt due to the x and y translation of the ball and the resulted oblique astigmatism.	391
Figure 259: Induced defocus due to the z translation of the ball and the resulted oblique primary spherical error.	392
Figure 260: Induced defocus due to the z translation of the ball and the resulted oblique secondary spherical error.	392
Figure 261: Wavefront errors in the interferograms due to the tilt induced during the offset of the ball in x and y axis.....	394

Figure 262: Averages of 64 interferograms in order of four measurements showing the reduction in the RMS and PVr values calculated.	395
Figure 263: Rigid body terms removed from the interferograms used to estimate the form of transmission sphere.....	396
Figure 264: Estimated form of the transmission sphere.	397
Figure 265: Experimental setup to measure the concave reference surface using the PSI.....	399
Figure 266: Measurement area of the concave surface with respect to the transmission sphere area	400
Figure 267: PSI Measurement results of the concave surfaces.....	402
Figure 268: Interferograms of the concave mirrors captured by rotating in steps of 90° clockwise	403
Figure 269: Relatable Zernike polynomials of a surface measured in orthogonal orientations .	404
Figure 270: Measurement results of the concave mirror 1 measured at four angular orientations	406
Figure 271: Extraction of the rotationally variant and invariant form of the concave surface ...	407
Figure 272: Calibration of the temperature sensors used during the measurment of the drift of the profilometer.....	408
Figure 273: After calibration, temperature sensors are attached to the surfaces of the equipment used in the profilometer system.	409
Figure 274: Schematic of a Zerodur flat sitting on a Stainless steel sphere	410
Figure 275: Schematic showing a Silicon nitride sphere in contact with a stainless steel spheres and the normal force on their surfaces	412

LIST OF ABBREVIATIONS

AFM – Atomic Force Microscopy

ASPE - American Society for Precision Engineering

APC- Angle Polished Connector

CMM – Coordinate Measuring Machine

FFT- Fourier Frequency Transform

FP - Fabry-Perot

FPGA – Field Programmable Gate Array

FWHM - Full Width Half Maximum

GRIN - Gradient Refractive INdex

IR – Infra-Red

NA – Numerical Aperture

LVDT- Linear Variable Differential Transformer

MST - Multi-Surface Tester

PSI - Phase Shifting Interferometer

PTB - Physikalisch-Technische Bundesanstalt (National metrology institute, Germany)

WD - Working Distance

1. INTRODUCTION

1.1 Importance of surface texture and measurement techniques

Mechanical objects such as ball bearings, slideways, diesel injectors, and optical elements such as spherical, aspherical, and freeform lenses and mirrors play a major role in the construction and the operation of precision devices. These devices form the basis of many technological achievements in the last century including combustion engine, stereo lithography, large optical telescopes, LIGO observatory, etc. For many precision manufactured components, form and finish of their functional surfaces must be measured quantitatively to assure performance. The requirements for mechanical surfaces might include mating and smooth motion in an assembly, reduced wear, high fatigue strength, load capability, and thermal emissivity. For optical surfaces, the requirements might be to limit scattering and/or wavefront errors of reflective or transmissive surfaces used in applications including lithography and telescopes. As the length and area of the measured surface increases, the surface deviations are classified into roughness, waviness, and form [Peklenik (1968), ISO 4287 (1997)].

Techniques to quantitatively measure surface texture include both contact and non-contact methods. Stylus profilometry and Atomic Force Microscopy (AFM) are commonly used contact methods (it is noted that AFM's can also operate in non-contact mode). Two of the non-contact optical methods predominantly used in commercial devices nowadays are confocal microscopy, and Coherence Scanning Interferometry (CSI). These techniques, and a handful other of optical methods to measure surface deviation, are discussed in Hocken et al. (2005), Williamson (2016), and Wang et al. (2017), Arumugam et al. (2019). Recently, an experimental comparison of five

different contact and non-contact techniques for roughness measurements has been performed by Hagemeyer (2019).

1.2 Overview of the studies undertaken in this thesis

In this dissertation, two non-contact profiling techniques and a contact based stylus profilometer are studied and discussed in Chapters 2 to 4. These studies are briefly discussed below

1. An external cavity fiber Fabry-Perot interferometer that uses a frequency modulated laser source (Infrared, IR 1150 nm). In this method, the phase of the light in the cavity formed by the face of the fiber and the surface being measured changes as a function of surface deviation.
2. A monochromatic (Red, 650 nm) confocal microscope that oscillates an objective lens along its optical axis, where the focus point of the light projected on the surface serves as a means of replicating the surface deviation. While there is nothing new about the technique itself, a novel flexure based oscillation is implemented on a commercially available 60X objective lens used in the microscope.
3. A contact-based stylus profiler is metrologically characterized [Leach et al., 2021] to determine its feasibility to measure areal form of large optical and mechanical surfaces of up to 200 mm aperture and a sagitta of 14 mm. The error sources in these measurements include: the motion of the carriages used to traverse the stylus over the part, interaction of the stylus travelling on surfaces with varying slope (say a sphere), thermal errors, and environmental contributions.

A common approach in the discussions in each chapter is composed in the following order:

1. A brief introduction of the measurement technique and the motivations for our studies
2. Review of literature related to the technique
3. A detailed explanation of the working principle
4. Experimental setup used in the studies
5. Results from the experiments and their analysis
6. Future work

Relevant details that could not be included in these sections are included in the appendices.

Data analysis files of all the results are included in a flash drive attached to the back cover, and folders are named according to the section number the results are discussed.

2. FIBER-BASED FABRY-PEROT INTERFEROMETRIC PROFILER

2.1 Background

While conventional probing techniques such as stylus profilometry, confocal microscopy, and coherence scanning interferometry are suitable for measuring surfaces that are exposed, they are not suitable for measuring confined spaces such as the inner race of a ball bearing, fir tree root of a turbine blade, or inside a gun barrel. The aforementioned conventional optical techniques are not feasible due to the line of sight requirement of these methods and also may be precluded by the size of the optical elements utilized, such as objective lens heads. For a mechanical stylus profiler, the stylus probe tip and the lever arm is sometimes too large (few millimeters) to access the areas of interest. In principle, fiber optics can be used to guide the light to access these areas, after which the variants of well-established optical probing techniques could be implemented, two of these are discussed below.

Fiber-based coherence scanning interferometry using low coherence light sources [Dufour, (2006), Liu (2015)] has been implemented in commercially available instruments such as Novacam™, and Fionec™. The performance specification for these products are listed in Table 1. Recently, the company Micro-Epsilon used this technique for measuring absolute distances of up to 2 mm (working distance, WD = 19 mm), and thin film thickness down to 50 μm (WD = 45 mm). A related work can also be found in Bosbach (2002).

Other fiber-based measuring techniques include fiber optic confocal microscopy which was popularly researched in the decade of the 1990's, but at the time of writing this dissertation, no commercially available product could be found from an internet search. Another technique is fiber

reflectometry [Nan Nan, 2005] that does not provide a graphical representation of the surface profile but provides parameters representing the surface texture, such as Roughness average (Ra).

Table 1: Specifications of two commercially available fiber-based coherence scanning interferometers

product	light source	working distance	amplitude range	amplitude resolution	lateral resolution
Novacam's Microcam	IR (1310 nm)	0.5 mm to 100 mm	7 mm	0.5 μm	2.2 μm to 23 μm
Fionec's SMF-1, SMF-2	Red	100 μm , 1 mm	80 μm , 1 mm	N/A	N/A

2.2 Motivations for the study

A displacement measuring technique, fiber-based Fabry-Perot interferometry which traditionally found its applications in Atomic Force Microscopy, has been recently commercialized by Attocube (IDS3010). Even though this technique is suitable for measuring surface texture, literature describing its implementation and limitations when used as a surface profiler is scarce, except for one technical note with insufficient technical detail on Attocube's website [Hirschman, 2018]. Understanding the nuances of implementing this technique for surface profiling such as signal processing, types of light source (wavelengths, intensity, coherence) and fiber, coupling of reflected light back into the fiber for practical engineering surfaces is the primary goal of this study. Without creating a working setup, it is not possible to develop mathematical models to optimize the design and predict performance limitations such as working distance, height range, local slope of surfaces, surface topography, height resolution and the reflectivity of surface being

measured. An advantage with the frequency modulated fiber Fabry-Perot is the ease of recreating the surface profile using the established phase unwrapping techniques.

2.3 Literature review - fiber-based interferometry for displacement measurements

A short review of the research articles that discuss the early implementations and theory involving fiber-based interferometry are given below. This review is limited to fiber interferometry for displacement measurements and its use for localized surface measurements, a subject that has not received extensive attention in the peer reviewed literature. Section 2.7 presents studies of stress induced modulation of the laser source frequency that is an important sub development that would enable higher bandwidth measurement using fiber Fabry-Perot interferometry. A literature review of stress induced modulation is included in section 2.7.2.

2.3.1 History

This section discusses some of the early implementations of fiber-based interferometry for displacement measurements mainly in the field of Atomic Force Microscopy.

Fiber-optic interferometer for remote sub angstrom vibration measurement [Drake and Leiner, 1983]

One of the first known use of fiber optics for interferometry was for observing the motion of the ear drum of a live house cricket, when it is stimulated by a loudspeaker. They used a spectrum analyzer to perform Fourier Frequency Transform (FFT) of the photo-detector response near a quadrature point and observed that the highest amplitudes in the frequency spectrum corresponds to the chirp frequency of the cricket's ear, which occurs at 6 kHz and 12 kHz .

Force microscope using a fiber-optic displacement sensor [Rugar et al, 1988]

A fiber FP interferometer was applied in AFM to measure the amplitude variation of the resonating tungsten wire that interacts with the sample surface. A couple of design highlights are: (a) strain is induced on the fiber to create birefringence that in turn causes the fiber to act as a quarter waveplate, (b) to reduce air glass interference a drop of oil is used in the interface of a cover slip and the entry face of the fiber. A sensitivity of $1.7 \times 10^{-5} \text{ nm} \cdot \sqrt{\text{Hz}}$ is observed for oscillations of 2 kHz, and a drift of $0.3 \text{ nm} \cdot \text{min}^{-1}$ is reported.

Improved fiber optic interferometer for Atomic Force Microscopy [Rugar et al, 1989]

Two photodetectors were used at two of the four ends of a 2 x 2 fiber coupler. One photodetector acts as a reference and the other monitors the motion of an AFM cantilever measuring a sample surface. To avoid stray reflections into the fiber, the fiber ends at the photodetectors are cleaved to a non-orthogonal angle and immersed in index matching liquid before reaching the photodetectors. 10 pm noise is observed at a 1 kHz bandwidth with a fiber-reflector spacing of 1 μm .

2.3.2 Theoretical

This section reviews and expands upon the work of Wilkinson and Pratt who provided an *analytical model for low finesse, external cavity, fiber Fabry–Perot interferometers including multiple reflections and angular misalignment [Wilkinson, and Pratt, 2011]*

In the theoretical models for the interferometer used for Atomic Force Microscopy, some only consider the single reflection from the object coupled back into the fiber. Intensity variation, I due to the phase change during the displacement, z is approximated as sinusoidal fringes of a same amplitude, and at the quadrature point is given as

$$I = I_0 \frac{4n_a \pi z}{\lambda_0}$$

where I_0 is the amplitude of the fringes, n_a is the refractive index of air, and λ_0 is the wavelength of light in vacuum. Also see equation (2) on page 14. Since this approximation does not hold true for the objects with high reflectivity, r_m that approaches 1, multiple reflections in between the cavity must be, and are, considered in the model of Wilkinson and Pratt reproduced in equation (1). They also experimentally demonstrated the goodness of fit of their mathematical model considering up to five reflections in the cavity.

Precise phase theory for accuracy improvement in a fiber probe interferometer for nanometric sensing, taking into account fiber coupling, [Yoshino, 2020]

Detailed theoretical expressions for fiber coupling induced phase shift during the following conditions are presented.

- (i) Gaussian beam laterally offset from the fiber's core,
- (ii) direct coupling of light reflected from the plane mirror with and without angular misalignment, and
- (iii) focused coupling of light using a convex lens.

However, as of writing this dissertation, no experimental evaluation of these models are published.

2.3.3 Implementations and signal processing techniques

This section discusses different implementations of fiber-based interferometry and techniques used to determine the forward or reverse direction of displacement of the target surface.

Fiber Fabry-Perot interferometers, [Yoshino and Ohno 1981]

To determine the change in the direction of motion of the target surface, a two-mode fiber, two pinholes and a photodetector were used. For every period of the displacement fringes two peaks of different heights are observed at the photodetector. Depending on the order of the appearance of these peaks, it is possible to determine the change in direction of the target. This short paper does not contain enough detail to understand the operation in detail or to evaluate performance as a displacement measuring device.

Thermal tuning of a fiber-optic interferometer for maximum sensitivity [Bruland et al., 1999]

Sensitivity of the fiber FP interferometer is improved by thermally tuning the wavelength of the laser. The significant contribution of this paper is that, to avoid stray reflections in the internal cavity (between the faces of the fiber at different ends) causing interference, all fiber lengths were different by more than the coherence length of the laser, in the order of one millimeter. A noise floor of $1.6 \text{ pm} / \sqrt{\text{Hz}}$ is achieved.

Highly compact fiber Fabry-Perot interferometer: A new instrument design [Nowakowski et al., 2016]

Nowakowski et al. (2016) used a frequency modulated laser source (1550 nm) and utilized the fiber Fabry-Perot technique to measure displacement of objects with up to 5° angular misalignment. They used FPGAs (Field Programmable Gate Array) in the place of lock-in amplifiers to demodulate the intensity measured by the photodetector to obtain the first and second harmonic signal to form a quadrature signal (quadrature signals are very popular in linear encoder scale signal processing) and to calculate the displacement of the object. Instead of using the complete model derived by Pratt and Wilkinson and Pratt, empirical corrections were performed

to reduce the periodic error to a single nanometer level using a look up table obtained using a ramp sweep of the cavity. A PID controller was used to keep the intensity of the first and second harmonics equal by controlling the modulation width of the laser wavelength.

Measurement of distance changes using a fibre-coupled common-path interferometer with mechanical path length modulation [Schulz and Lehmann, 2013]

It is noted that this paper does not consider external Fabry-Perot cavity reflections but oscillates the probe end of the fiber coupler in a 2 x 1 configuration causing sinusoidal fringes. The displacement or surface deviations of the object cause an additional change in phase on top of these sinusoidal fringes, which is extracted using discrete Fourier transform or Hilbert transform methods. A GRIN (Gradient Refractive Index) lens with 0.45 NA (Numerical Aperture) is used at the probe end of the fiber to improve the spatial resolution. Samples with rectangular grooves (1 μm depth, 100 μm width), and sinusoids (200 nm PV, 8 μm pitch) were profiled.

2.3.4 Probe tip

This section discusses recent implementation of GRIN lenses at the probe tip to improve the visibility (or contrast) of displacement fringes.

Fringe Visibility Enhanced Extrinsic Fabry–Perot Interferometer Using a Graded Index Fiber Collimator [Zhang et al., 2010]

Improvements in fringe visibility in using a gradient index fiber to produce a collimated light is reported and compared with a regular fiber from which the emergent light beam diverges. At the cavity length of 0.5 mm, visibility of GRIN lens collimated fringes is 0.8 in comparison with the visibility of 0.2 using a single mode fiber. In this gradient index fiber, the refractive index of the core decreases along its radial direction causing the light to travel in a quasi-sinusoidal path

(‘pitch’), and the fiber tip is cleaved at a quarter of the pitch causing the light to be collimated. A ray matrix mathematical model is given for the waist size of the beam coming out from the gradient index fiber as a function of the distance to the reflecting target. Recently, Reisen et al. reported a tenfold improvement in fringe visibility using a GRIN lens in the paper titled *Lensed GRIN Fiber-Optic Fabry-Perot Interferometers* [2020].

Long-Range Interferometric Displacement Sensing with Tapered Optical Fiber Tips [Hernández et al, 2015]

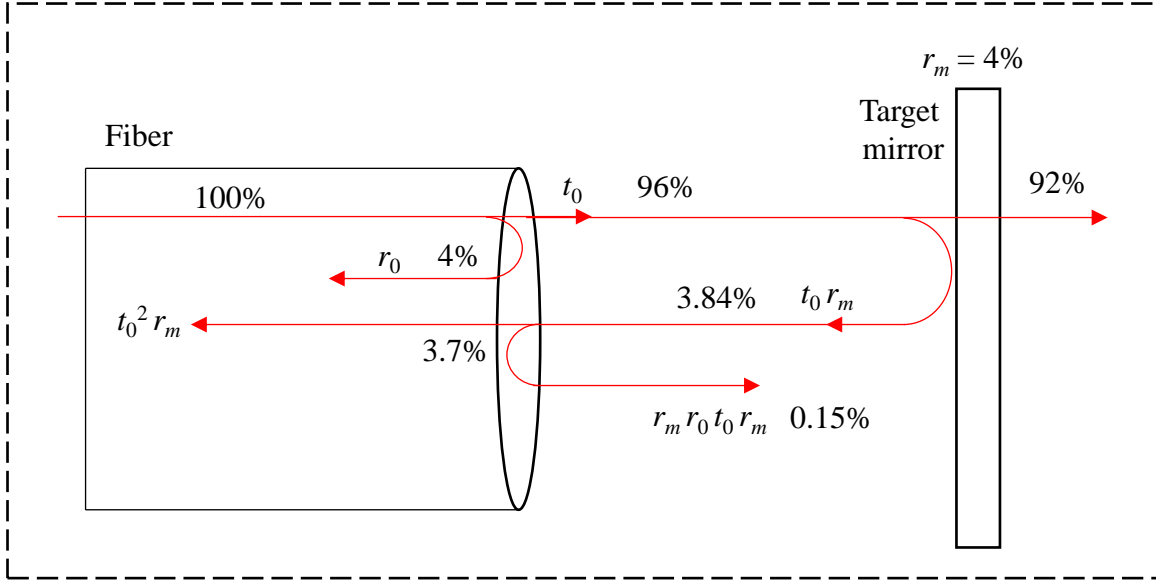
In this paper divergence of the light emanating from the fiber tip is reduced by tapering down the core and cladding of a single mode fiber to achieve displacement measurements with a range of 80 mm.

2.4 Working principle

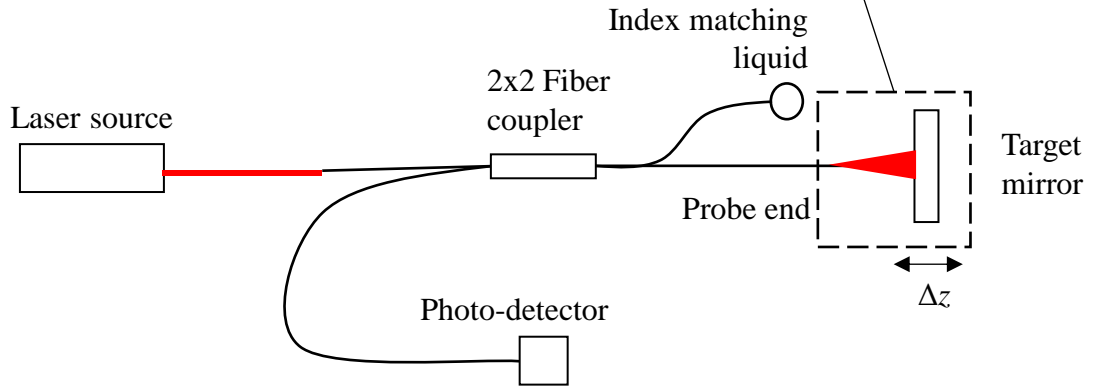
Figure 1 (a) shows a schematic of the core of the fiber made of glass with reflectivity (reflected intensity), $I_r = 4\%$. The light is coupled into the fiber with a coupling coefficient, C . Approximately 4% of the light reflects from the end face of the fiber and goes back into it, and 96% of the remaining light transmits out of the fiber's core (transmissivity, $I_t = 96\%$) and approaches the target surface. The space between the fiber's face and the target is called a 'Fabry-Perot cavity'. If the target mirror is also made of glass with reflectivity of $r_m = 4\%$, 4% of the 96% light (i.e., 3.84%) reflects from it and approaches the face of the fiber and 96% of 96% (i.e., 92%) light transmits through the mirror. 96% of the 3.84% light approaching the fiber (i.e., 3.7%) couples into it, and the remaining 4% (i.e., 0.15%) reflects from it. Technically, this process continues infinitely, but practically, within a few of reflections the amount of reflected light is drastically reduced. The intensity of the light as a function of the number of roundtrips, n of reflections and transmissions, is given by

$$I = r^2 = \left(r_0 C_{n=0} + \frac{t_0^2}{r_0} \sum_{n=1}^{\infty} (r_m r_0)^n C_n e^{-i\pi} \right)^2 \quad (1)$$

where, r is the reflectivity, $r_0 = \sqrt{I_r}$ and $t_0 = \sqrt{I_t}$ are the reflection and transmission coefficients of the face of the glass fiber, C_n is the fraction of the light coupled back into the fiber, and n is the number of times the light reflects from the mirror. A detailed expression for the coupling coefficient (C) considering the angular misalignment of the target mirror and Gouy phase shift is given in Wilkinson and Pratt (2011).



(a)



(b)

Figure 1: Schematic of the fiber Fabry-Perot interferometer; (a) reflections in the cavity formed by the face of the fiber and the target surface, with the percentage numbers representing reflected and transmitted intensities, (b) a simple fiber Fabry-Perot interferometer construction.

A simple construction of a fiber Fabry-Perot interferometer is shown in Figure 1 (b), where a laser source coupled into a 2 x 2 fiber coupler gets split into two fibers. One of the fibers transmits light to the probe end where the target is situated, and the other end is immersed into a refractive index matching liquid to avoid stray reflection at the fiber-air interface from coupling back into the fiber. The refractive index liquid is typically housed in black container, allowing the light to transmit through the liquid and to get absorbed by the black surface. If a 2 x 1 fiber coupler is used, the refractive index liquid is not necessary. At the probe end, the light diverges out and gets reflected from the target and couples back into the fiber with some of this reflected light also reflecting from the end face of the fiber back into the cavity. One component of the light reflected back into the cavity reaches the photodetector monitoring the intensity of the light, and the other returns to the laser source potentially causing the laser to destabilize. If an Angle Polished fiber ferrule Connector (APC) is used at the light source end, the light returning to the laser could be reduced.

Any motion of the target surface normal to the light beam causes a phase shift of the light waves and creates constructive and destructive interference. This interference is recorded by the photodetector as a sinusoidal intensity variation. For cavity separations significantly greater than the Rayleigh length, the change in cavity length (Δz) is related to the change in phase as,

$$\Delta\phi = \frac{4\pi\Delta z}{\lambda_0} \quad (2)$$

where, λ_0 is the wavelength of the light source in vacuum. While it is possible to use this signal to calculate the displacement of the mirror, the change in the direction of motion cannot be directly distinguished. One way of distinguishing the direction is to use a quadrature signal comprising the phase and a similar sinusoidal signal with a 90° phase shift. In this case, quadrature

is achieved by modulating the frequency of the laser source, and this technique is referred to as Frequency Modulated Continuous Wave interferometry [Zheng, 2006]

When the frequency of the laser source is sinusoidally modulated, multiple sidebands, referred to as ‘harmonics’, are produced as shown in Figure 2(a). During the change in the cavity length due to the motion of the target surface, the amplitudes of these harmonics change. The intensity of the frequency modulated source is given by,

$$I = I_0 \sin(\omega_0 t + \Delta\omega \sin \omega_m t)$$

where, I_0 and $\omega_0 = 2\pi f_0$ are the intensity and fundamental frequency of the unmodulated light source, $\Delta\omega$ and $\omega_m = 2\pi f_m$ are the amplitude and the frequency of the modulation.

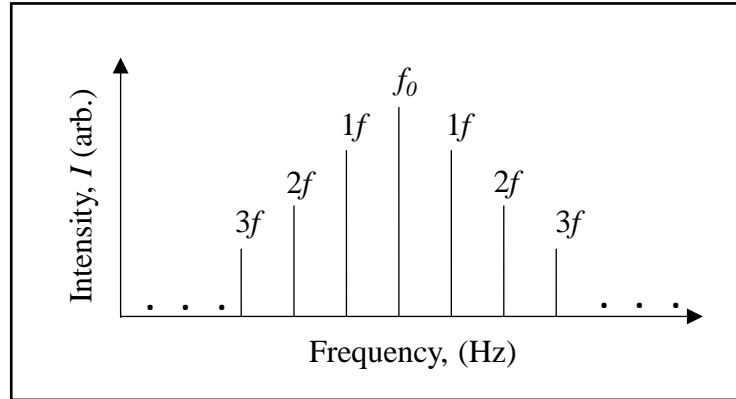
In the frequency domain, one could consider the amplitude of the modulation ($\Delta\omega$) as the amount by which the fundamental frequency of the light moves right or left. Consequently, it is also referred to as modulation depth or modulation width.

When this frequency modulated beam enters the fiber-mirror cavity, the reflection from the face of the fiber and the reflection from the mirror interferes to produce a signal measured by the photodetector shown in Figure 1(b) is given by,

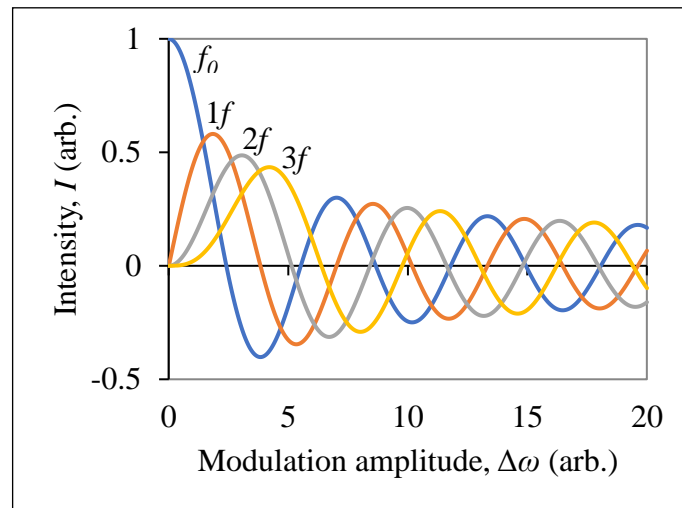
$$I = I_{fiber} + I_{mirror} + 2\sqrt{I_{fiber}I_{mirror}} \sin((\Delta\omega \sin \omega_m t) + \phi)$$

where, I_{fiber} and I_{mirror} are the intensities of the light reflected from the face of the fiber and the target mirror that are interfering. ϕ is the constant phase shift due to the initial length of the cavity.

(a)



(b)



(c)

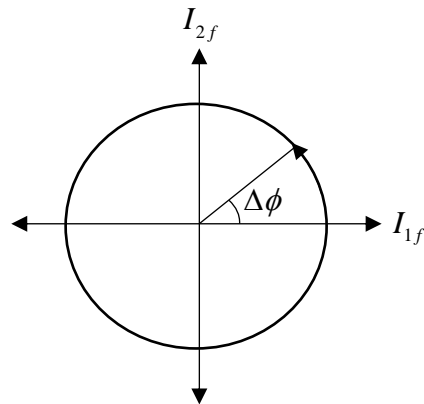


Figure 2: Harmonics and the phase quadrature; (a) Harmonics generated during the sinusoidal modulation of the laser source (b) intensity of these harmonics as a function of the amplitude of the laser frequency modulation (b) quadrature produced during the motion of the target mirror.

It is noted that since the bandwidth of the photodetectors are typically only a few MHz, therefore, they cannot measure the intensity of the fundamental frequency of light source (f_0) in hundreds of terahertz. The intensity measured by the photodetector containing the harmonics is expressed using the Jacobi-Anger expansion as

$$I = I_{fiber} + I_{mirror} + 2\sqrt{I_{fiber}I_{mirror}} \left[\begin{aligned} &\left(J_0(\Delta\omega) + 2\sum_{n=1}^{\infty} J_{2n}(\Delta\omega) \cos(2n\omega_m t) \right) \sin(\phi) + \\ &\left(2\sum_{n=1}^{\infty} J_{2n-1}(\Delta\omega) \sin((2n-1)\omega_m t) \right) \cos(\phi) \end{aligned} \right]$$

Where, J_0 is the intensity of the fundamental frequency, J_{2n} and J_{2n-1} are the intensity of the even and odd harmonics of the signal.

The signal from the photodetector, with the frequency modulated sinusoidal electrical source as the reference, is connected to the lock-in amplifier. When the mirror is displaced, it adds the phase of the light in the cavity ($\Delta\phi$). The ‘demodulated’ output from the lock-in provides the intensity of the first odd and even harmonics given by,

$$\begin{aligned} I_{1f} &= J_1(\Delta\omega) \cos(\Delta\phi) \\ I_{2f} &= J_2(\Delta\omega) \sin(\Delta\phi) \end{aligned}$$

When these two intensities are plotted in orthogonal axis as a function of displacement of the target, it forms a quadrature as shown in Figure 2(c). The phase change during the motion of the target is given by,

$$\Delta\phi = \tan^{-1} \left(\frac{I_{1f}}{I_{2f}} \right) \quad (3)$$

from which the amount of displacement can be calculated as,

$$\Delta z = \frac{\lambda_0}{2} \left(\frac{\Delta \phi}{360} + n_{rot} \right) \quad (4)$$

where, n_{rot} is the number of rotations of the quadrature for a given displacement.

Any change in the direction of motion of the target will be represented by the change in the direction of the rotation of circle, indicated using an arrow in Figure 2(c).

2.4.1 Simulation

A procedure to obtain the quadrature signal for a sinusoidal displacement of the target surface of amplitude $1 \mu\text{m}$ in one second is described in this section, see Figure 3(a). For this simulation, multiple Fabry-Perot reflections in the cavity are ignored and only the displacement fringes monitored by the photodetector during the change in cavity length, Δz , are considered. For a light source of a single fundamental frequency, ω_0 , the fringes observed by the photodetector are shown in Figure 3(a), and can be computed from the equation

$$I = I_0 (1 + \sin \omega_0 \tau)$$

$$\tau = \frac{2\Delta z}{c}, \quad [\text{Arablu, 2018}],$$

where, τ is the time taken by the light to travel the change in cavity back and forth, and c is the speed of light in vacuum. Whereas, if the frequency of the source is modulated as shown in Figure 3(b), the fringes observed by the photodetector become

$$I = I_0 (1 + \sin(\omega_0 + \Delta\omega \sin \omega_m t) \tau)$$

where, $\Delta\omega$ and ω_m are the modulation amplitude and the frequency at which the frequency of the laser (ω_0) is modulated, see Figure 3(b). The change in frequency ($\Delta\omega$) is related to the change in wavelength of light ($\Delta\lambda$) from its fundamental wavelength ($\lambda_0 = 1050 \text{ nm}$) as,

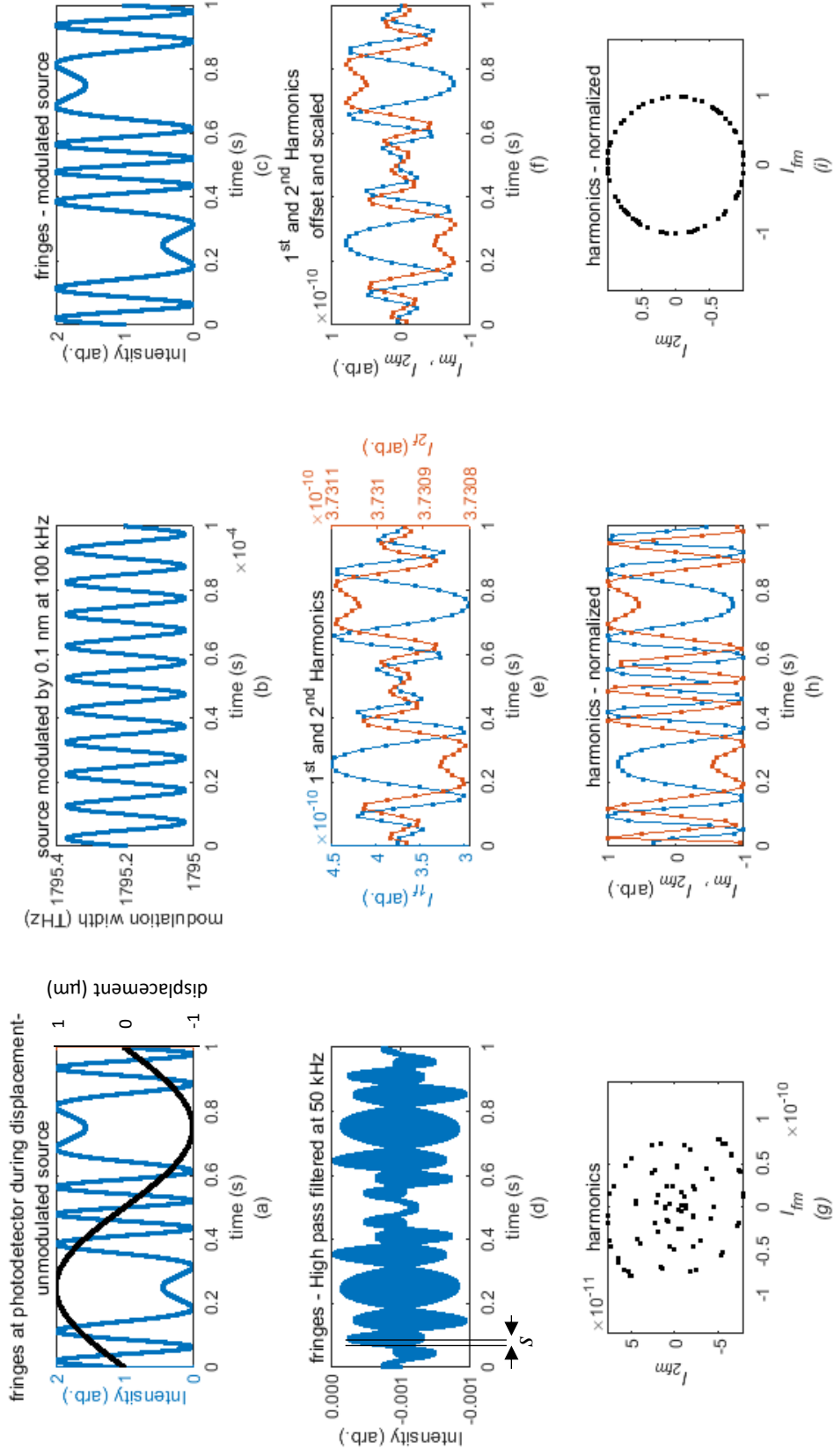


Figure 3: Simulation showing the procedure to obtain the quadrature signal to compute the displacement of a target.

$$\Delta\omega = c \frac{\Delta\lambda}{\lambda_0^2}$$

or

$$\frac{\Delta\omega}{\omega_0} = \frac{\Delta\lambda}{\lambda_0} \quad (5)$$

A source wavelength modulation of $\Delta\lambda = 0.1$ nm, at a frequency $\omega_m = 100$ kHz is shown in Figure 3(b), and the fringes observed during the change in cavity length are shown in Figure 3(c). This signal is high pass filtered at a cutoff frequency that is half the modulation frequency $f_{cutoff} = \frac{f_m}{2} = 50$ kHz and is shown in Figure 3(d). The high pass filter executed in discrete time, t is given by

$$I_{filt,t} = \frac{\alpha}{(1+\alpha)}(I_t - I_{t-1}) + I_{filt,t-1}$$

where, the filtering parameter, $\alpha = \frac{1}{2\pi f_{cutoff} \Delta t}$ with the data spacing in time is given by Δt . As shown in Figure 3(a), 1 μ m amplitude sinusoidal travel of the target covers approximately 4 μ m back and forth in total, for which there are approximately eight fringes (sinusoidal periods plotted in blue) given by,

$$n_{fringes} = \frac{4z_0}{\lambda_0/2}$$

The time it takes for a single fringe is about 0.1 seconds. Since it is optimal to have at least ten datapoints per fringe, the high pass filtered signal shown in Figure 3(d) is split into segments, s of 0.01 seconds, $I_{filt,s}$. Fourier coefficients calculated at each segment, s are given by

$$\begin{aligned}
a_{1,s} &= \frac{2}{N} \sum_1^N I_{filt,s}(t) \cos(\omega_m t) dt \\
b_{1,s} &= \frac{2}{N} \sum_1^N I_{filt,s}(t) \sin(2\omega_m t) dt \\
a_{2,s} &= \frac{2}{N} \sum_1^N I_{filt,s}(t) \cos(\omega_m t) dt \\
b_{2,s} &= \frac{2}{N} \sum_1^N I_{filt,s}(t) \sin(2\omega_m t) dt
\end{aligned}$$

where N is the number of datapoints at each segment. From the Fourier coefficients, the amplitudes of the first and second harmonics shown in Figure 2(a) at each segment is calculated as,

$$\begin{aligned}
{}^oI_{1f} &= \sqrt{(1+a_{1,s})^2 + (1+b_{1,s})^2} \\
{}^oI_{2f} &= \sqrt{(1+a_{2,s})^2 + (1+b_{2,s})^2}
\end{aligned}$$

and is plotted in Figure 3(e). The addition of 1 to the Fourier coefficients before squaring them is done to retain the symmetry of the high-pass filtered signal about its intensity axis. It is noted that the harmonic signals have an offset value of 1.414213562, which is removed by subtracting their mean, i.e., ${}^1I_{1f} = ({}^oI_{1f} - \overline{{}^oI_{1f}})$, and ${}^1I_{2f} = ({}^oI_{2f} - \overline{{}^oI_{2f}})$.

Then, the second harmonic signal was scaled with respect to the first harmonic using the factor below in parenthesis,

$${}^{scaled}I_{2f} = {}^1I_{2f} \left(\frac{\max({}^1I_{1f}) - \min({}^1I_{1f})}{\max({}^1I_{2f}) - \min({}^1I_{2f})} \right),$$

and plotted in Figure 3(f). When the first and second harmonics are plotted against one another, the Lissajous signal spirals in and out as shown in Figure 3(g). Therefore, the harmonics are normalized by using the formula,

$$I_{1f} = \frac{{}^1I_{1f}}{\sqrt{{}^1I_{1f}^2 + {}^{scaled}I_{2f}^2}}$$

$$I_{2f} = \frac{{}^{scaled}I_{2f}}{\sqrt{{}^1I_{1f}^2 + {}^{scaled}I_{2f}^2}}$$

to obtain the quadrature signal, and these two intensities are plotted in Figure 3(h and i) as a function of displacement and when plotted against each other. The phase change during the displacement is calculated using equation (3), and is plotted in Figure 4(a). The phase is unwrapped, and the displacement calculated using equation (4) is shown Figure 4(b), which should ideally look like the displacement shown in Figure 3(a). This discrepancy between these two figures is due to the fact that in the zoomed view of harmonics from Figure 3(h) shown in in Figure 4(c), first harmonic all of a sudden starts to lag behind the second harmonic at about 0.5 seconds closer to the zero crossing of the unwrapped displacement. Practically, this phase lag typically happens only when the direction of motion of the target changes, and this issue is possibly caused by the lack of time resolution in the simulation.

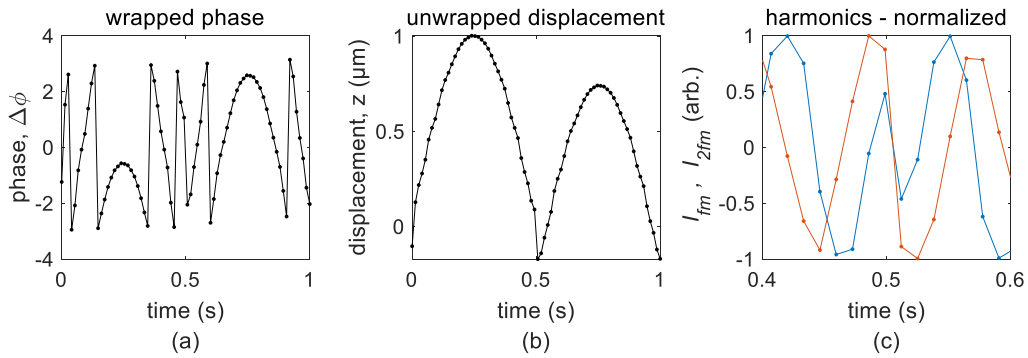


Figure 4: Phase unwrapping to calculate the displacement; (a) Wrapped phase due the displacement of the target (b) unwrapped displacement (c) harmonics causing the discrepancy in the calculated displacement.

2.5 Experimental setup

2.5.1 Source

Figure 5 shows the experimental setup that uses an infrared 1050 nm source chosen because the light of a “longer” wavelength scatters less compared to the sources in the visible regime. The frequency of the laser source is modulated by rotating a grating in a Littman configuration using a piezoelectric actuator. A schematic diagram and the specifications of the frequency modulation module are given in Appendix A.1. This actuator modulation of the frequency is driven using a voltage amplifier with a sinusoidal input provided by a Lock-in amplifier. The make and model of all the components used in the experiments are found in the referred figures. The amplitude and the offset of this input signal is adjusted using the circuit shown in Figure 6. The current controller used to operate the laser source is shown in Figure 7.

2.5.2 Fiber optics

The frequency modulated source is coupled to a 2 x 2 fiber splitter through a fiber isolator. At the splitter, the light splits into two and one of the ends reach a refractive index matching liquid in a black container which was additively manufactured using Formlabs Photopolymer black resin. The light from the fiber transmits through the liquid and is absorbed by the black surface of the container therefore avoiding the back reflection from the face of the fiber. This setup is not necessary if one uses a 2 x 1 fiber splitter. The other end from the splitter henceforth referred to as ‘probe end’ reaches the surface whose profile is to be measured.

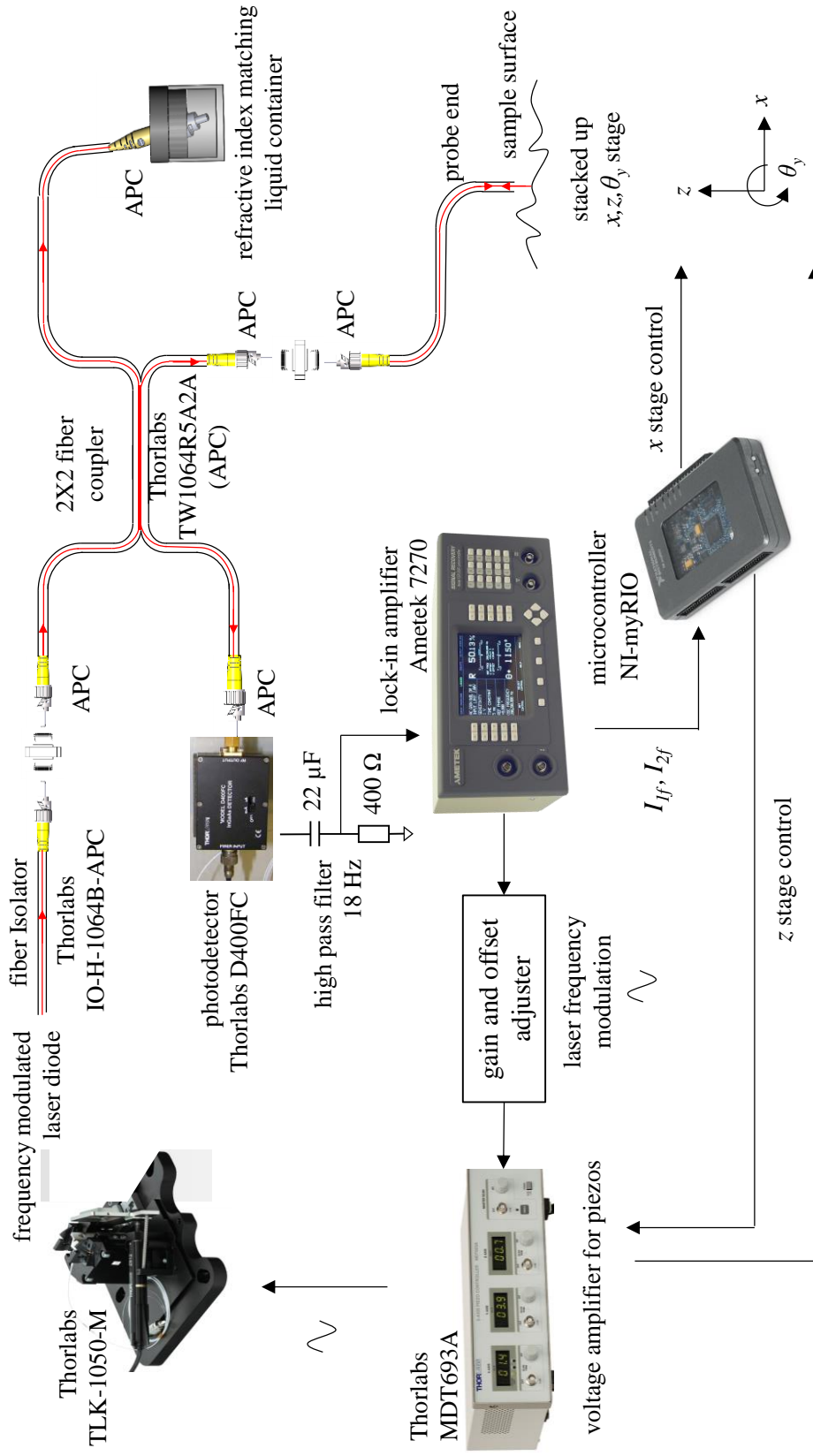
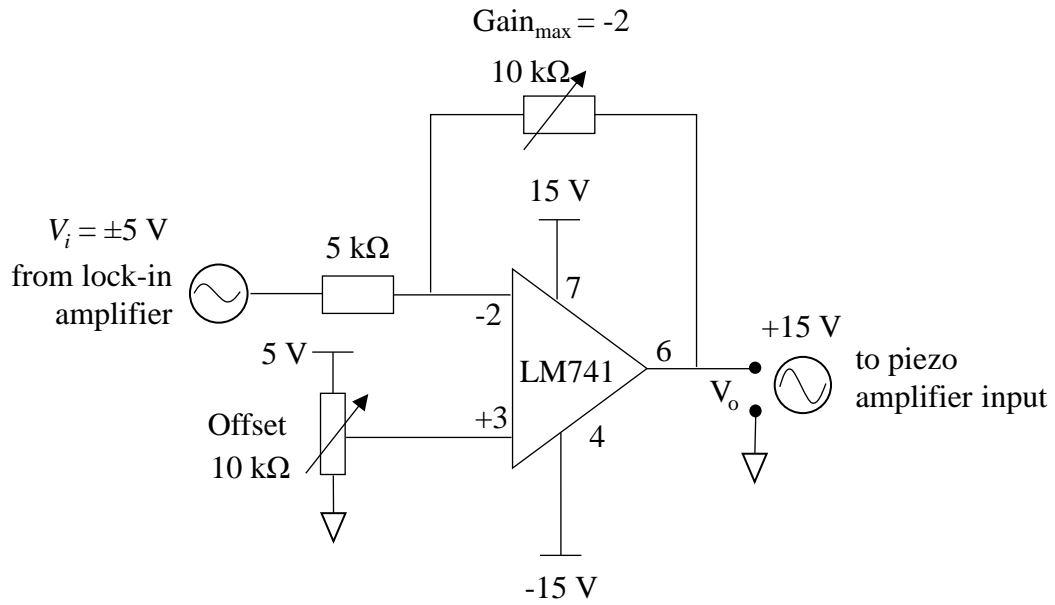


Figure 5: Schematic of the experimental setup showing the equipment with their model number.



Knobs to adjust gain and offset of the sinusoidal input to the piezo amplifier

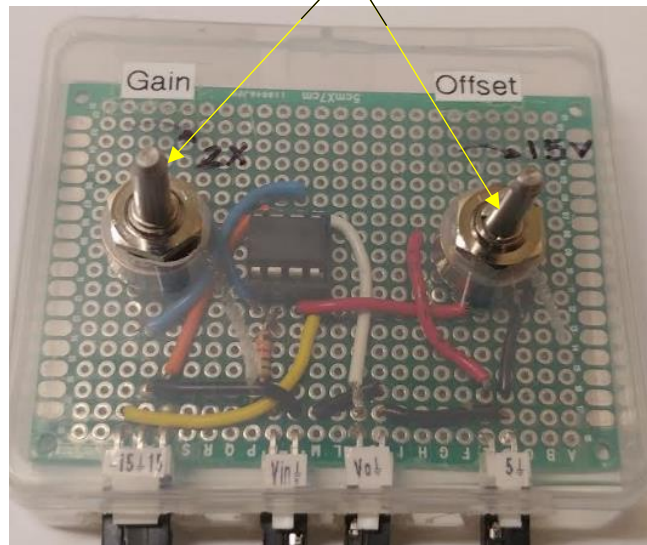


Figure 6: Circuit to amplify and DC offset the sinusoidal signal provided to the piezo actuator oscillating the grating and thereby modulating the frequency of the laser source.

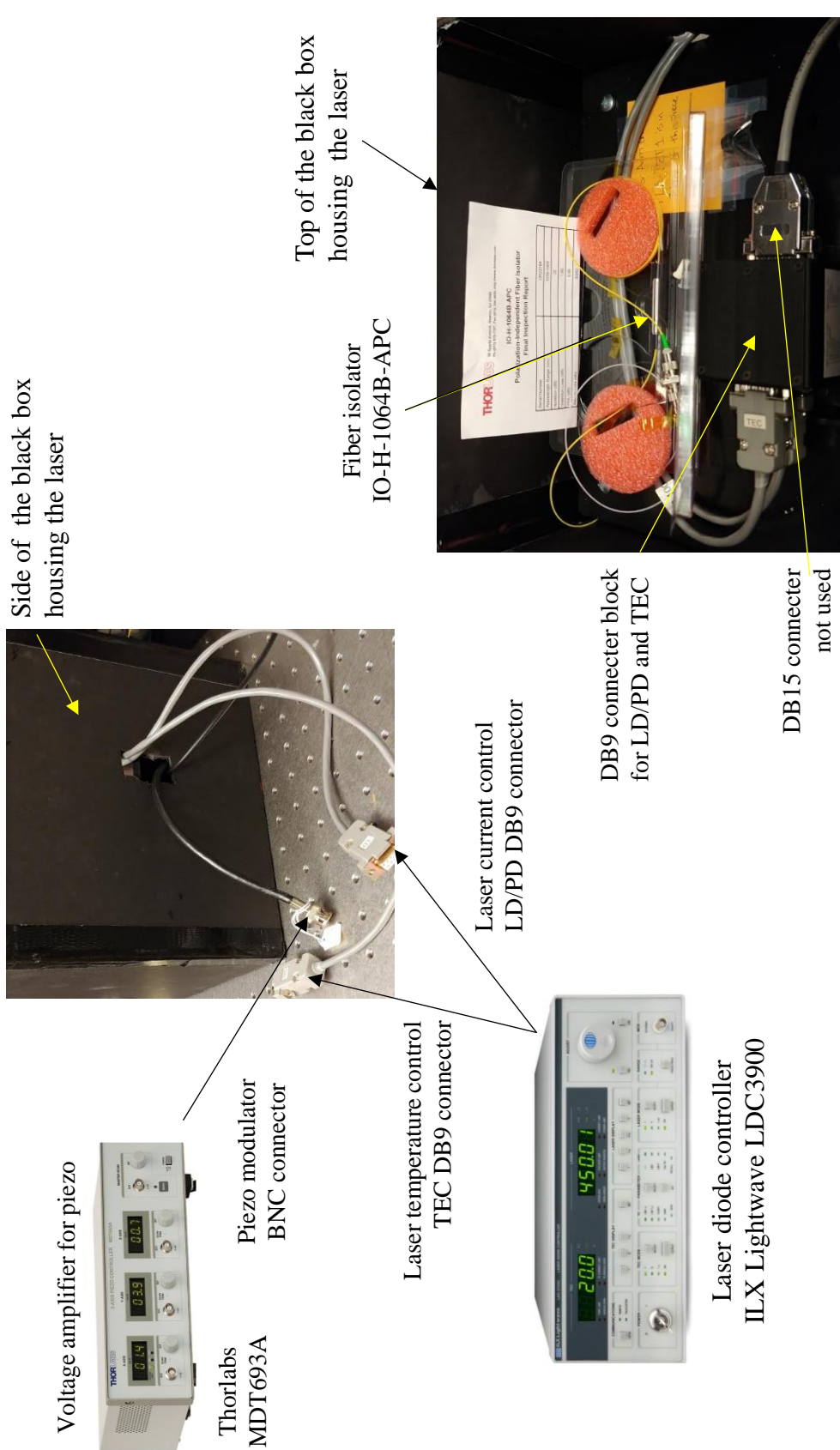


Figure 7: Equipment to control the current to the laser source, frequency modulate the laser source, and to isolate the returning light from destabilizing the source.

The reflected light from the surface after undergoing Fabry-Perot reflections, described in section 2.4, enters back into the probe end and splits into two again. Half of the back reflected beam reaches the photodetector used for signal processing, and the other leads back to the source where the isolator shown in Figure 7 restricts the light from reaching the laser source consequently avoiding its destabilization.

2.5.3 Signal processing

The output from the photodetector is connected to a Lock-in amplifier through a high pass filter to discard the DC offset and slow drifts in the signal under 18 Hz cutoff frequency. The DC offset is removed so that the Lock-in amplifier input is not overloaded because the signal from the photodetector is about $6 V_{PV}$, whereas the Lock-in amplifier is limited to $2 V_{PV}$ for an AC gain of 0 dB. The Lock-in amplifier demodulates the signal to produce first and second harmonics representing the change in phase (fringes) due to the displacement or surface deviation of the sample. These harmonics provide the quadrature signal described in section 2.4, Figure 2(c).

2.5.4 Stage mechanisms

There are three stage mechanisms utilized to displace and align the surface with respect to the probe tip, these being;

1. Horizontal translation (henceforth referred to as scanning) of the sample surface in x axis is achieved by a linear motor driven exact constraint flexure stage with a 10 mm travel. Details of its mechanical design, actuation and sensing circuits and LabVIEW control program are provided in Appendix A.2.
2. Vertical displacement of the sample surface in z axis is achieved by a piezo driven over constraint monolithic flexure made of Aluminum (Elastic modulus, $E = 70$ GPa)

providing a travel of 20 μm . Four flexure leafs of length, $l = 10$ mm, width, $b = 10$ mm, and thickness, $t = 1$ mm provides a stiffness of

$$k = \frac{48EI}{l^3} = \frac{4Ebt^3}{l^3} = 2800 \text{ kN} \cdot \text{m}^{-1}$$

3. Tilt of the sample surface along x direction provided by a rod flexure actuated using two fine screws. Details of the design of this mechanism are also provided in Appendix A.3.

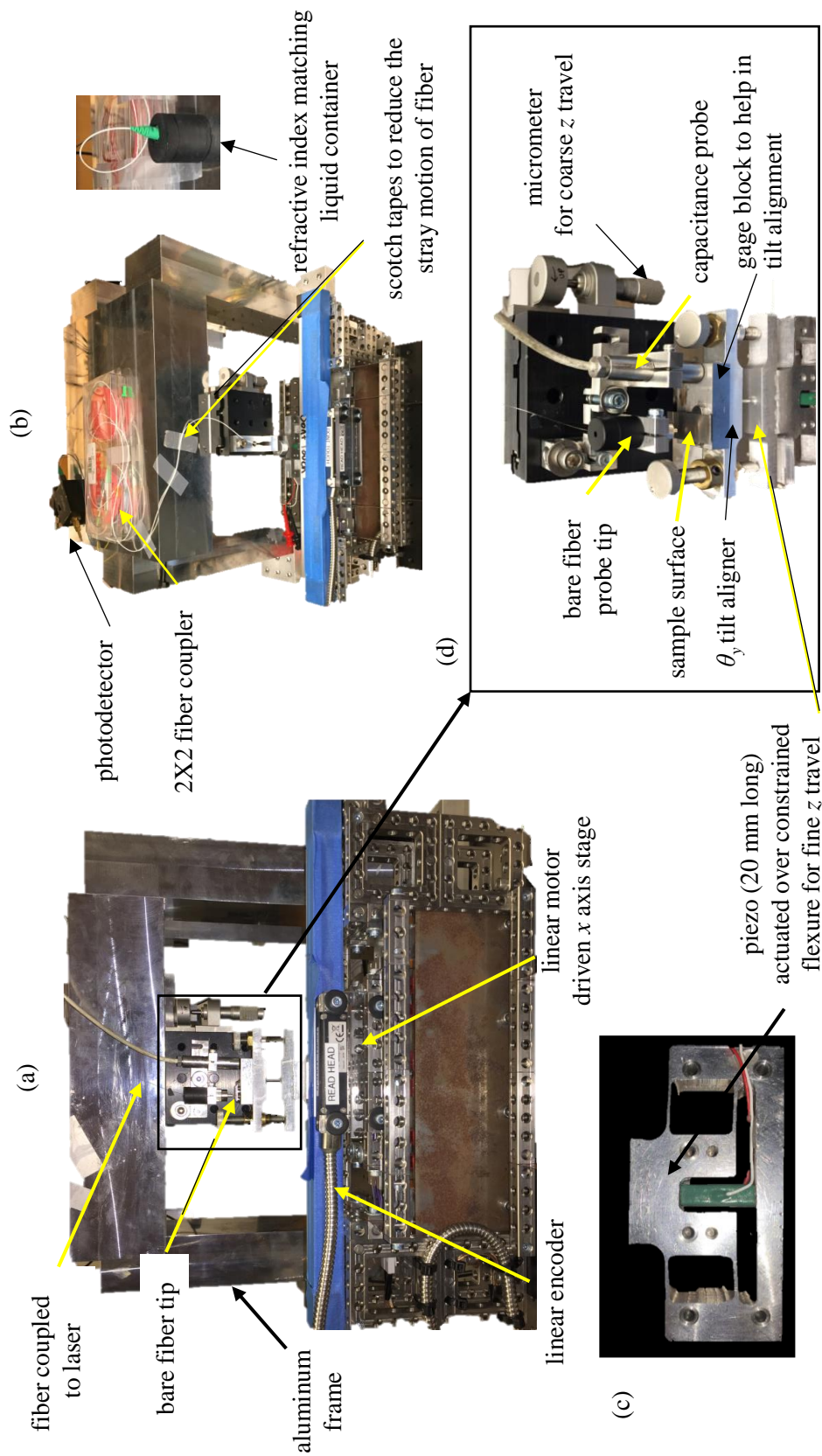


Figure 8: Fiber Fabry-Perot interferometric profiler experimental facility; (a) Top view showing the fiber coupler and the refractive index matching liquid container (c) flexure to translate the sample towards the probe tip (d) inset showing the rod flexure mechanism and a capacitance probe used to adjust the tilt of the sample.

2.6 Experimental results

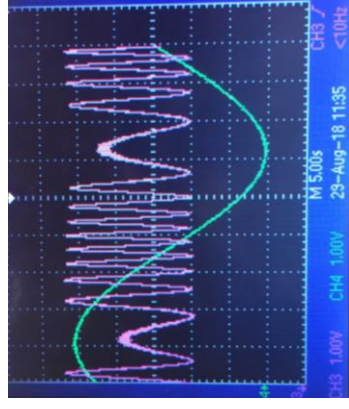
2.6.1 Laser frequency modulation and signal processing parameters

To determine the optimal frequency modulation parameters for the laser diode, Figure 9(a) shows a copper mirror surface that was placed on the platform and translated vertically in z axis towards the face of the fiber using the over-constrained flexure shown in Figure 8(c). It is noted that the frequency of the laser source is not modulated during the travel. The displacement fringes observed during this motion are shown in Figure 9(b), and there are nine of them, indicating a travel of about $4.5\text{ }\mu\text{m}$, see equation (4). For a piezoelectric actuator stack of length 20 mm , it is expected to expand to about 0.1% of its length for a 150 V input, which is $20\text{ }\mu\text{m}$, and this was verified by using a capacitance probe. The green curve in Figure 9(b) shows the sinusoidal input voltage of 5 V_{PV} and this is amplified by 15 resulting in 65 V_{PV} applied to the actuator. For this voltage input, the actuator is expected to travel $8.5\text{ }\mu\text{m}$. Therefore, it is not clear why only $4.5\text{ }\mu\text{m}$ worth of fringes were observed, and this discrepancy was only noticed about two years later during the writing of this dissertation. Since it takes 25 seconds to travel from the peak to valley of the sinusoid shown in Figure 9(b), and assuming that the fringes represent the true displacement of the mirror ($4.5\text{ }\mu\text{m}$) the velocity of travel is estimated to be $0.18\text{ }\mu\text{m}\cdot\text{s}^{-1}$.

Figure 9(b) shows the fringes during the vertical travel of the mirror at $0.18\text{ }\mu\text{m}\cdot\text{s}^{-1}$ when the frequency of the laser was modulated at about 600 Hz with a voltage to the actuator

$$\Delta\lambda = 75 \text{ V}_{\text{PV}} (< 44 \text{ pm}), f_m = 600 \text{ Hz},$$

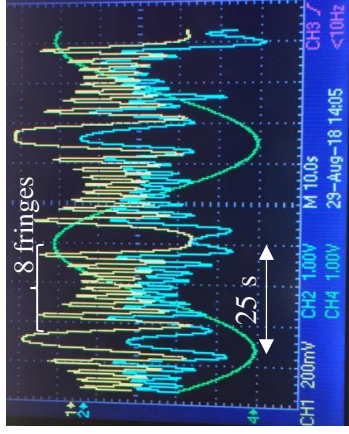
$$v_z = 0.18 \text{ } \mu\text{m.s}^{-1}$$



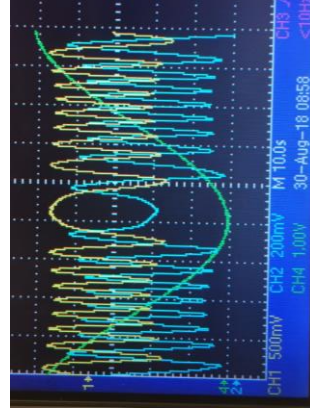
(b)

$$\Delta\lambda = 90 \text{ V}_{\text{PV}} (< 54 \text{ pm}), \text{offset} = 60 \text{ V},$$

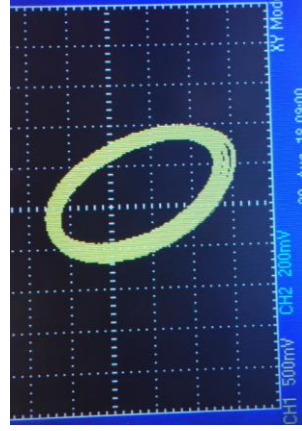
$$f_m = 400 \text{ Hz}, v_z = 0.1 \text{ } \mu\text{m.s}^{-1}$$



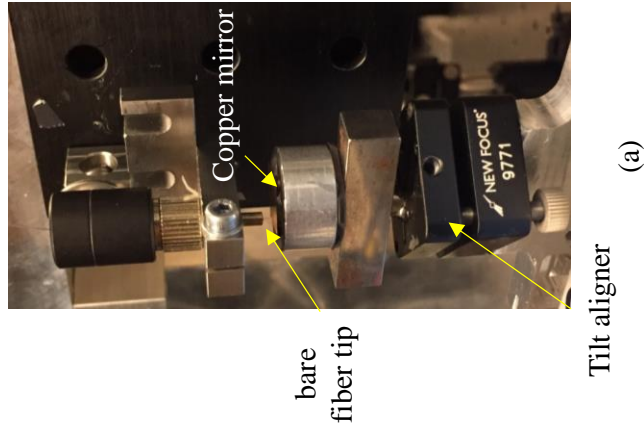
(c)



(d)



(e)



(a)

Figure 9: Fringes due to the displacement of a copper mirror towards the fiber; (a) Picture of the copper mirror target used to establish the optimal operating conditions of frequency modulation and travel velocity and Lock-in sampling period (b) Fringes - unmodulated source (c) Harmonics - source modulated at 600 Hz (d) f Harmonics - source modulated at 400 Hz, travel velocity of target is 0.1 $\mu\text{m.s}^{-1}$ (e) Lissajous of the harmonics

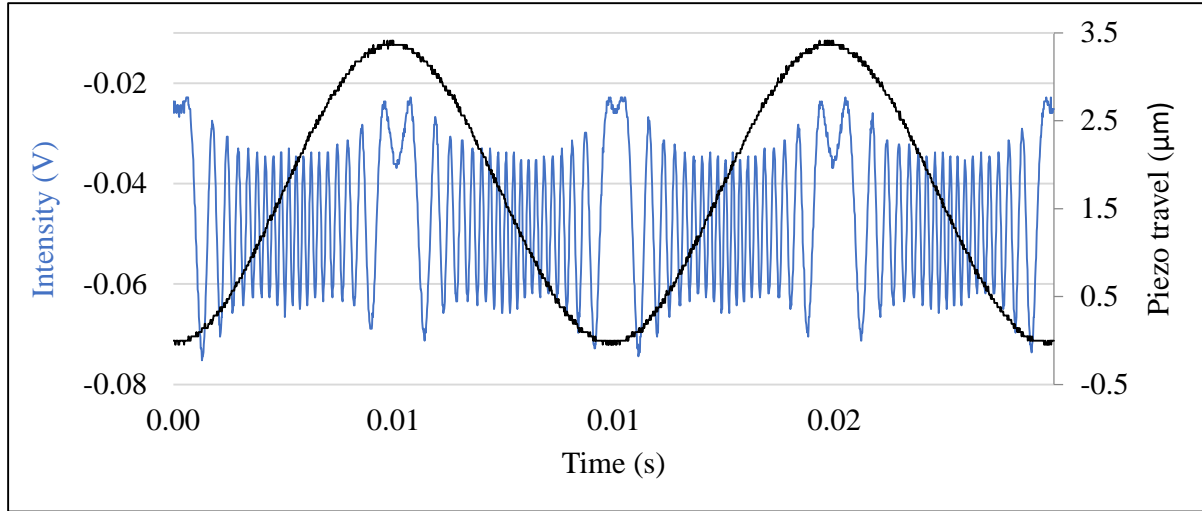
(TLK-PZT1) modulating the grating mirror being 75 V_{PV} (not shown in the plots. Also, see Appendix A.1 for the schematic diagram indicating the location of the actuator modulating the grating). Wavelength modulation is given by,

$$\begin{aligned}\Delta\lambda &= S_1 \cdot S_2 \cdot V_{in} \\ S_1 &= \frac{\Delta\lambda}{\Delta x} \\ S_2 &= \frac{\Delta x}{\Delta V_{in}}\end{aligned}$$

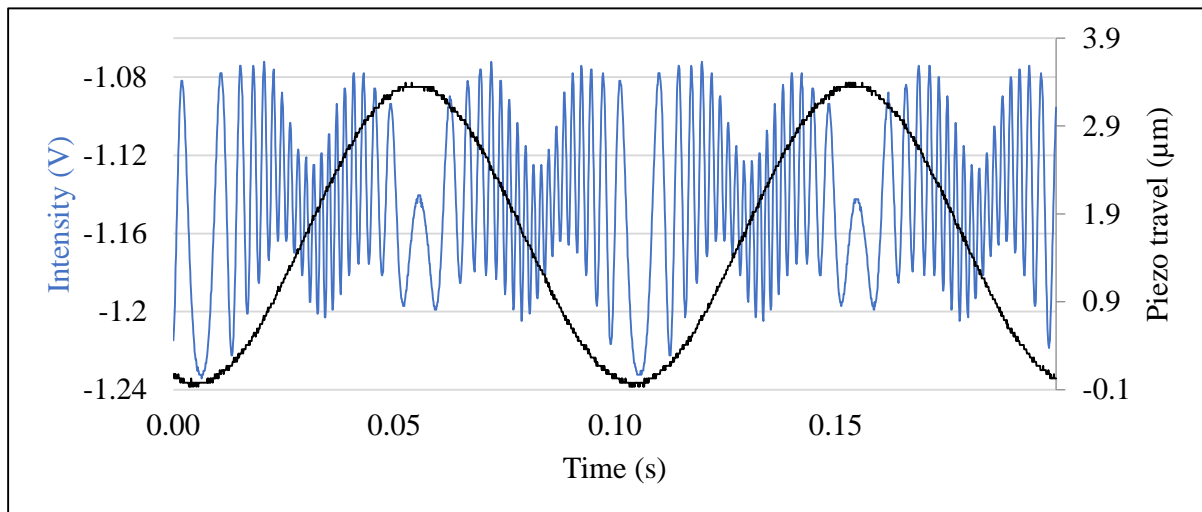
From experimental measurements and manufacturer's specification, $S_1 = 10 \text{ pm} \cdot \mu\text{m}^{-1}$, and $S_2 = 9.1/150 \text{ } \mu\text{m} \cdot \text{V}^{-1}$ (Appendix A.1). For piezo input voltage $V_{in}=75 \text{ V}_{PV}$, from the above equation, the wavelength modulation can be $\Delta\lambda = 44 \text{ pm}$ for the experiments in this section. It is noted that the oscillation frequency of 600 Hz is beyond the 250 Hz bandwidth of the piezo amplifier, causing the gain of the output voltage to reduce at the higher frequency. Because of this fact, the modulation width of the frequency would be less than 44 pm. To experimentally estimate the depth of modulation, a Michelson interferometer was setup with a path length difference of 13 inches ($\Delta x = 0.33 \text{ m}$) and the cube corners on both the arms were fixed to the optical table. For this configuration, when the frequency of the source is modulated, the number of fringes (m) observed by the photodetector are used to estimate the amount of frequency (wavelength) modulation, $\Delta\lambda$. A similar experimental procedure is explained in detail in section 2.7.3 (a).

$$\Delta\lambda = \frac{m\lambda_0^2}{4\Delta x} \quad (6)$$

Figure 10(a and b) show the fringes observed when a sinusoidal input is provided to the piezo modulating the grating. It is observed that there are about 18 fringes observed for a piezo travel



(a)



(b)

Figure 10: Plot of modulation signal (black) fed to the high voltage amplifier and the photo detector output (blue); (a) fringes observed in the photodetector with a pinhole in front of the detector during the modulation of frequency at 100 Hz (b) for a photodetector without pinhole showing a change in contrast of the fringes during modulation.

of $3.5 \mu\text{m}$ at a 100 Hz frequency. For the sensitivity S_1 , this would correspond to the wavelength modulation of $\Delta\lambda = 35 \text{ pm}$. However, using equation (6) the modulated wavelength is estimated to be $\Delta\lambda = 15 \text{ pm}$. It is noted that during this experiment, a pinhole placed in front of the photodetector helped to maintain a same contrast of the fringes. Without the pinhole, the contrast of the fringes vary during the modulation as shown in Figure 10(b).

Under these conditions of frequency modulation, the first and second harmonic outputs from the lock-in amplifier are shown in yellow and blue respectively in Figure 9(b), and it is seen that the amplitude of the “harmonic fringes” varies. If the amplitude and the frequency of modulation is increased any further (say, 700 Hz), the resonances of the grating modulation unit produce an audible noise, therefore for operator’s convenience it was decided not to operate at this high frequency and also due to the limited bandwidth of the piezo amplifier (250 Hz for a $1.6 \mu\text{F}$ piezo load).

Therefore, the amplitude and the frequency of modulation were selected so that no resonance noise is heard, and also to maintain a constant amplitude of the intensity of the harmonics as shown in Figure 9(c). The travel velocity of the copper mirror, and the sampling time period, τ_c of the Lock-in amplifier were also optimized. The optimal operating conditions are:

1. For frequency modulation, $f_m = 400 \text{ Hz}$, $\Delta\lambda = 90 \text{ V}$ ($< 54 \text{ pm}$), with a voltage offset to the piezo being 60 V.
2. Optimal travel velocity is about $v_z = 0.1 \mu\text{m} \cdot \text{s}^{-1}$, and

3. As shown in Figure 9(c), for the 8 fringes produced in 25 seconds of travel, it takes about 3 seconds per fringe. A sampling time-period of 0.5 s set in the Lock-in amplifier enables 6 datapoints per fringe.

2.6.2 Alignment of tilt of the surface

Now that the optimal frequency modulation parameters are known, before profiling the surface deviations of the sample, it is desirable to keep the working distance the same when the surface is being scanned in x axis. There are two source of variation in the working distance, tilt of the sample surface and profile variations. To remove the first of these variations, a tilt aligner shown in Figure 8(d) and Figure 11(a) was designed and implemented. This mechanism uses a rod flexure of length, $l = 10$ mm and diameter, $d = 1.6$ mm. A detailed description of the design is given in Appendix A.3.

Figure 8 (d) shows a gage block placed on the platform of the flexure adjacent to the sample and translated in the x axis back and forth for about 0.5 mm using the linear motor stage. During this travel, the surface of the gage block was sensed by a capacitance probe which is positioned adjacent to the fiber probe tip. Any vertical deviation in z during the scanning in x direction is measured by the capacitance probe. By adjusting two fine screws on the sides of the rod flexure, tilt of the platform could be adjusted to within 0.2 mrad ($\Delta z / x = 200 \text{ nm} \cdot \text{mm}^{-1}$).

It is noted that this flexure was designed only to remove the tilt along x -axis, because the tilt in the y -axis, i.e., perpendicular to the scan direction, does not contribute significant deviations in the probe direction, the z -axis. Also, this single axis tilt aligner can only pivot about the θ_y direction. This single axis adjustment simplifies tilt removal by avoiding coupled motion in other

axes which is a problem with the more widely used two axis tip-tilt aligners, like the one shown in Figure 11(a) (NewFocus 9771).

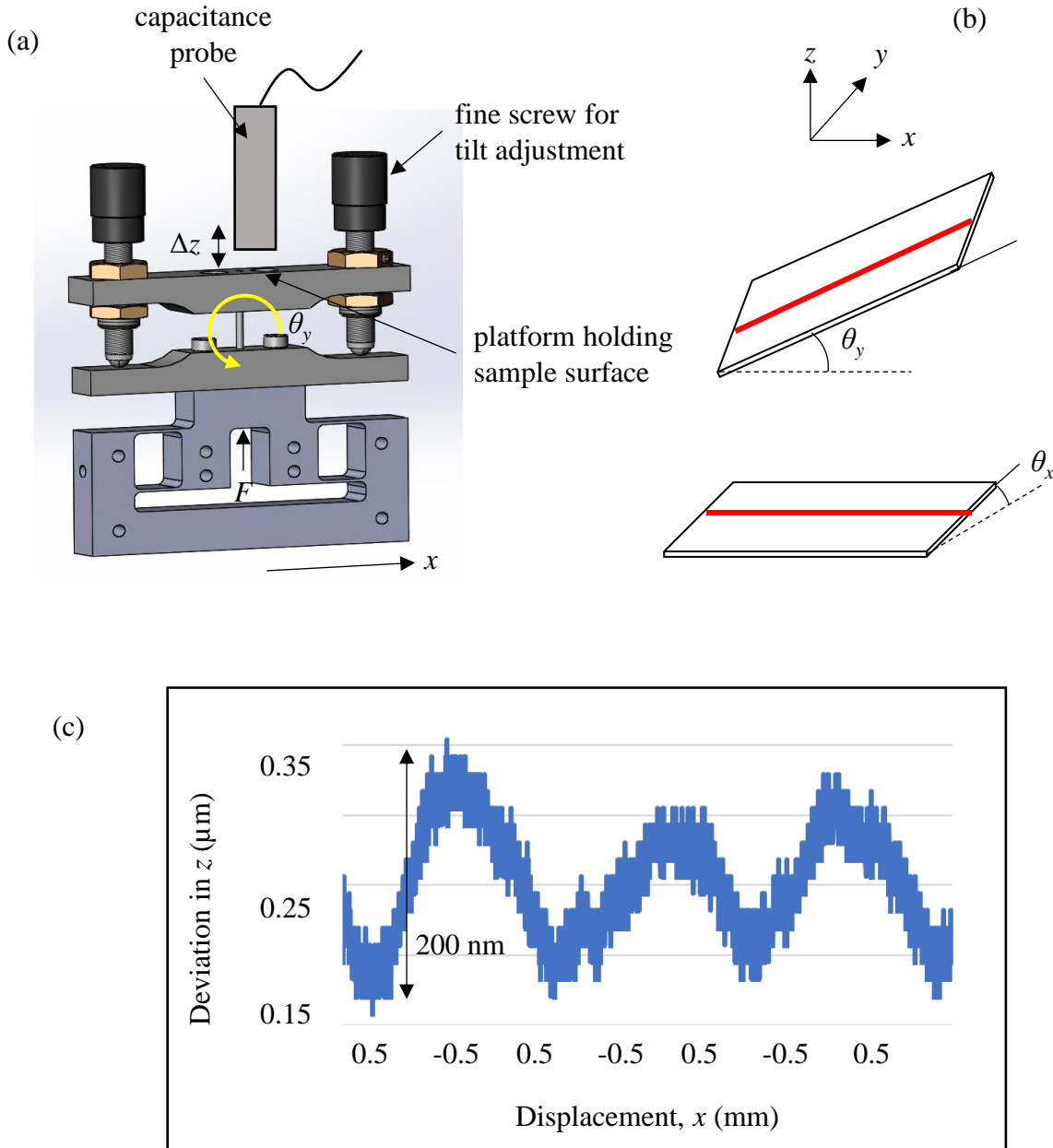


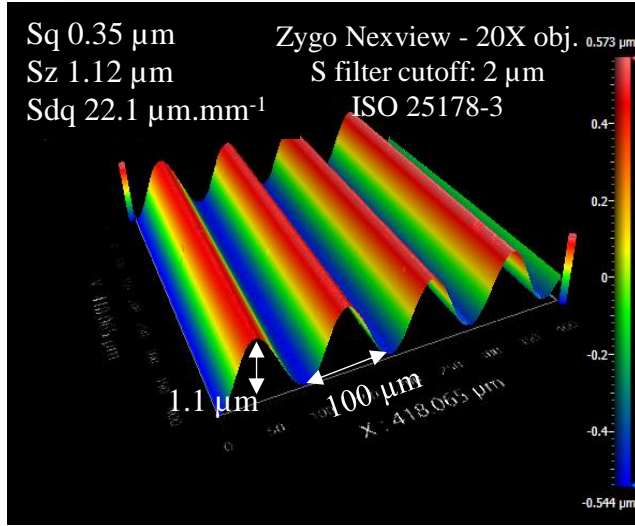
Figure 11: Tilt aligner – design and performance; (a) Solid model of the tilt alignment mechanism constructed using a rod flexure and actuated mechanically using two fine threaded screws (b) Schematic showing the tilted sample surface and the tilt removed surface with the red line representing the expected line of profile using the fiber interferometer (c) Measurement result of the capacitance probe showing the tilt reduced to about 0.2 mrad..

2.6.3 Sample surface measurements

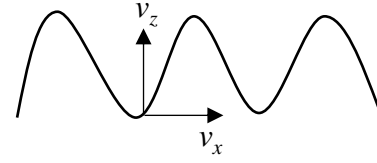
2.6.3.1 Sinusoidal surface: 1 μm PV, 100 μm wavelength

To evaluate the performance of the fiber Fabry-Perot interferometric profiler, a sinusoidal sample surface (Rubert 531) with a height of 1.1 μm PV and a 100 μm spatial wavelength is used. The surface was measured using a Coherence Scanning Interferometer (CSI) and an appropriate filtering was performed [ISO25178-3] and is shown in Figure 12(a). Since the slope of the surface is about 22 $\mu\text{m}\cdot\text{mm}^{-1}$, from the optimal velocity established in section 2.6.1 for a vertical displacement, $v_s = 0.1 \mu\text{m}\cdot\text{s}^{-1}$, the optimal scanning velocity in x axis is estimated to be, $v_x = 4.5 \text{ m}\cdot\text{s}^{-1}$ see Figure 12(b).

Shown in Figure 12(c) is the measurement of the surface (in orange) when it is scanned back and forth in the x -axis for a translation of 250 μm , with one direction of the ramp taking 40 seconds. It is noted that this scanning velocity is a little faster than the estimated optimal velocity. The measurement result is comparable to the estimates of height and wavelength from the CSI measurements, and the downward and upward trend in the profile measured back and forth is due to a small tilt of the surface that is not removed in the post processing.



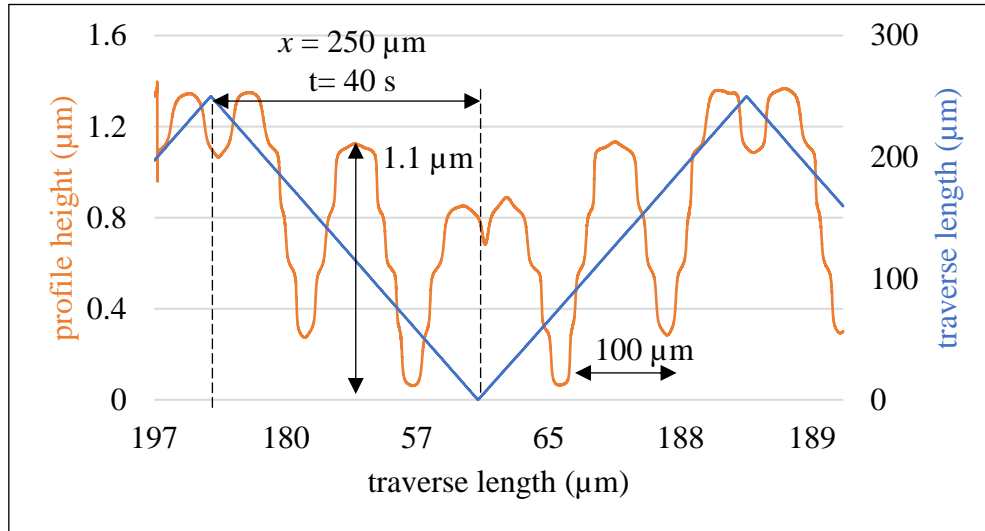
(a)



$$v_z = \frac{dz}{dx} v_x$$

$$v_x = \frac{1}{Sdq} \cdot v_z = \frac{1}{22.1} \cdot 0.1 = 4.5 \mu\text{m} \cdot \text{s}^{-1}$$

(b)



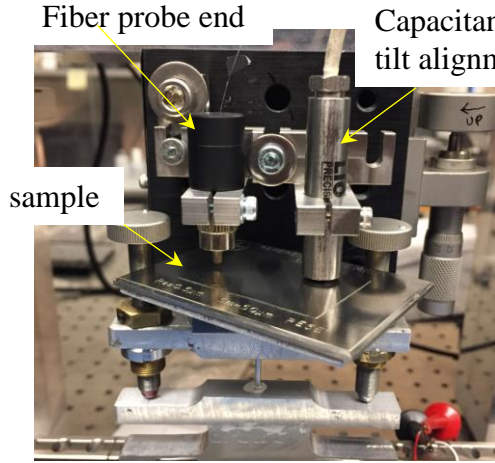
(c)

Figure 12: Measurement of the Rubert 531 sample; (a) measured using a Coherence Scanning Interferometer (CSI) with a 20X objective lens covering about $0.4 \times 0.4 \text{ mm}^2$ area, (b) calculation showing the optimal velocity of travel for a given slope of the surface and (c) measurement profile of the surface using the fiber-Fabry-Perot profiler developed in our work showing the estimates of height and wavelength of the surface comparable to the CSI measurements.

2.6.3.2 Sinusoidal surface: 1.5 μm PV, 50 μm wavelength

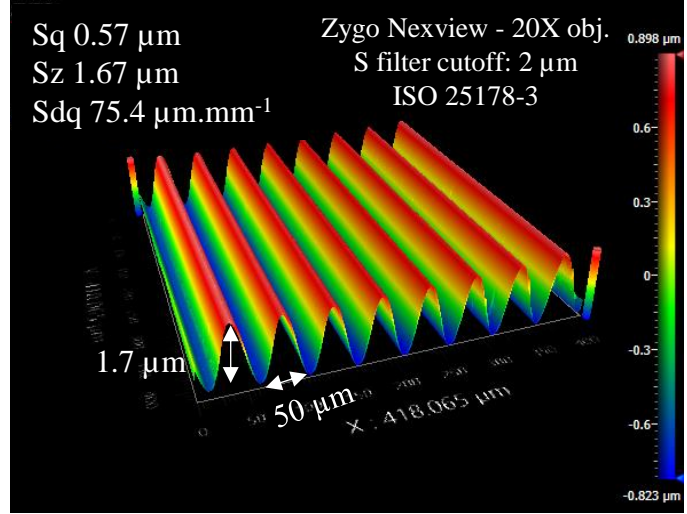
A second sample Rubert 528 that is also a sinusoidal surface having a spatial wavelength of 50 μm that is half of the earlier sample Rubert 521 see Figure 13(a). CSI measurement of the sample surface, and the optimal scanning velocity are shown in Figure 13(b). The measurement result of the fiber Fabry-Perot profiler shown in Figure 13(c) captures the wavelength of the surface comparable to the CSI measurement, but the estimated sinusoidal amplitudes were about one-third of the CSI measurement. Also seen are the horn-like structures at the peak of the sinusoids possibly indicating:

1. spot size of the laser from the fiber illuminating the surface is probably larger than the wavelength of the sinusoids, see Figure 15(a)
2. diffraction caused at the edges of the peak, or any error in unwrapping the phase to calculate the profile height.

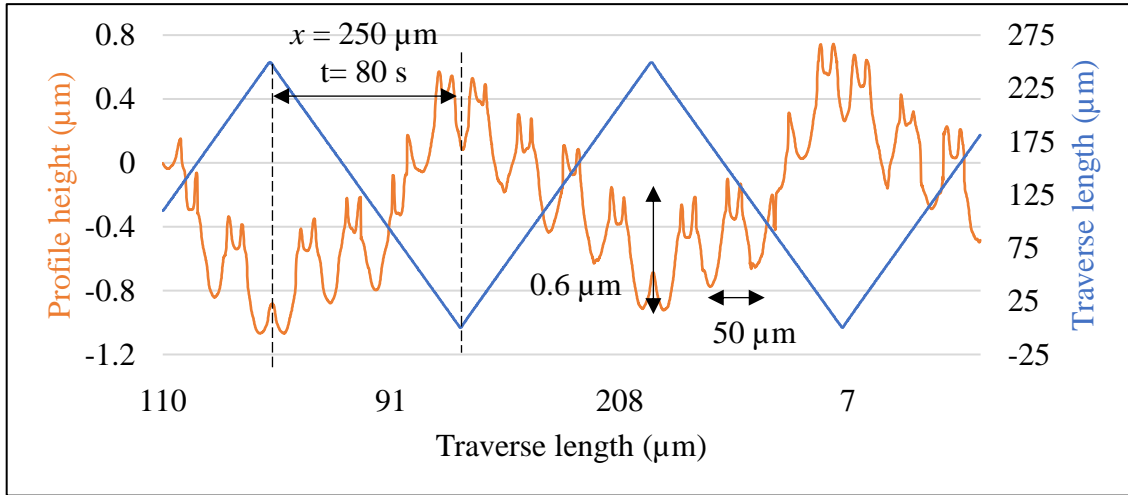


(a)

$$v_x = \frac{1}{Sdq} \cdot v_z = 1.3 \mu\text{m} \cdot \text{s}^{-1}$$



(b)



(c)

Figure 13: Measurement of the Rubert 528 sample; (a) measured using a Coherence Scanning Interferometer (CSI) with a 20X obj. lens covering $0.4 \times 0.4 \text{ mm}^2$ area (b) profile of the surface measured back and forth using the fiber-Fabry-Perot profiler for a traverse length of $250 \mu\text{m}$.

2.6.3.3 Ground surface

To validate the performance of the profiler on a manufactured surface, a ground cylinder shown in Figure 14(a) was used. CSI measurement of the surface and a profile from the measurement is shown in Figure 14(b) and (c) respectively. Repeated back and forth scans of the surface using the fiber profiler measured amplitudes of 2 μm . But it is not guaranteed that this profile was made on the same area as the CSI measurement. Experiments comparing the measurements using the profiler and the CSI at a localized region is part of the future work. Values of both Roughness average, (Ra) and Root mean square (Rq) computed using the equation below for the first forward scan in x shown with a black box in Figure 14(c) is 0.35 μm and 0.44 μm respectively.

$$\text{Ra} = \frac{|(z_1 - \bar{z})| + |(z_2 - \bar{z})| + \dots + |(z_n - \bar{z})|}{n}$$
$$\text{Rq} = \sqrt{\frac{(z_1 - \bar{z})^2 + (z_2 - \bar{z})^2 + \dots + (z_n - \bar{z})^2}{n}}$$

where,

z are the measured values of height,

\bar{z} is the average of measured heights, and

n is the number of datapoints.

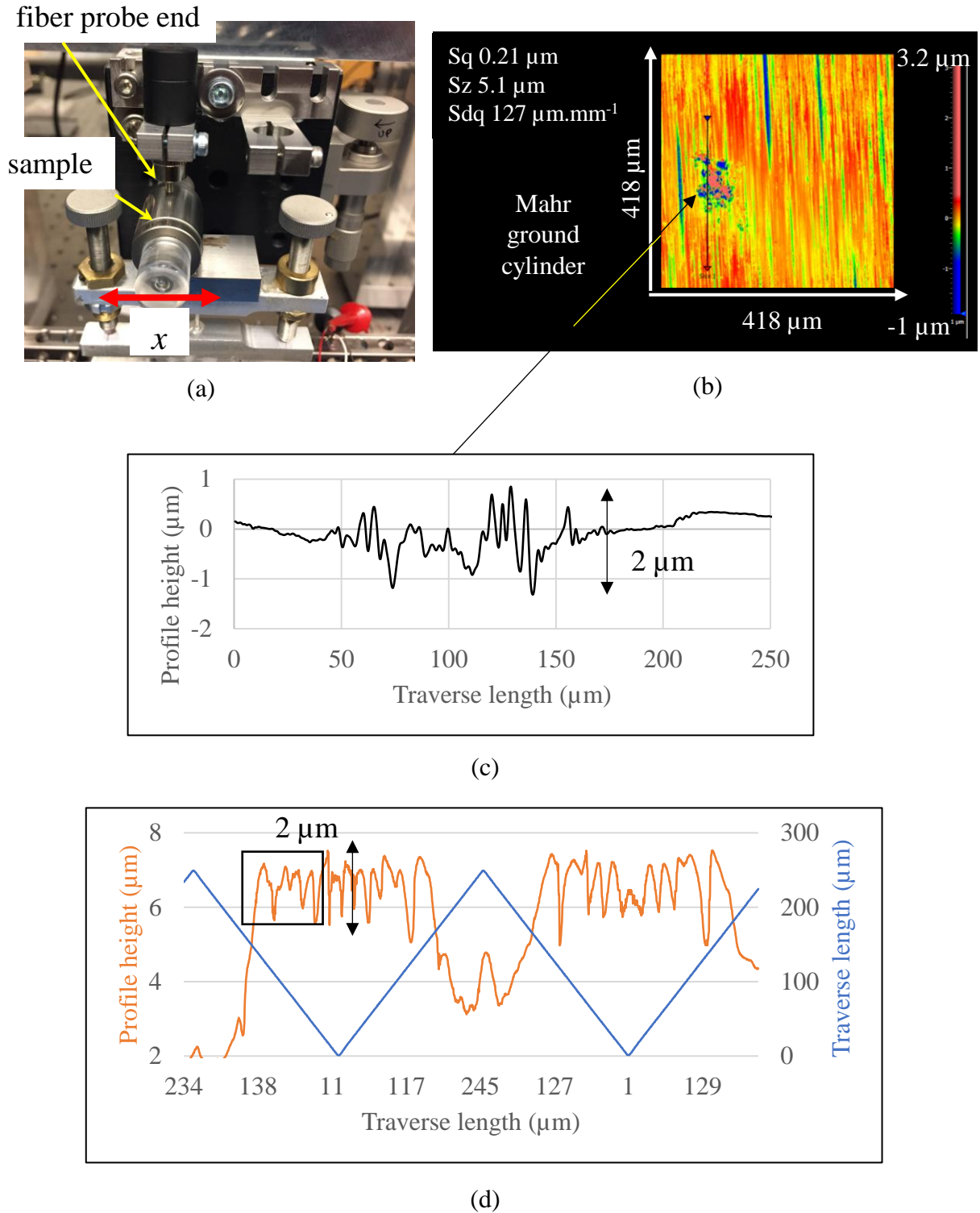


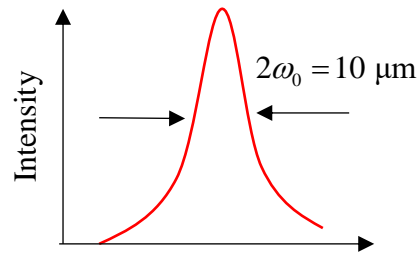
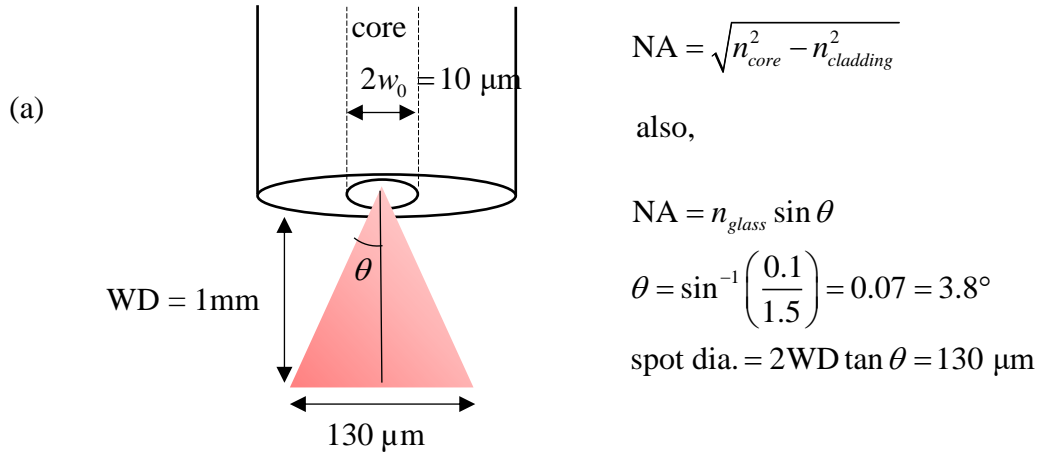
Figure 14: Measurement of a ground cylinder; (a) Cylinder with a ground surface measured using a Coherence Scanning Interferometer (CSI) with a 20X objective lens covering about $0.4 \times 0.4\ mm^2$ area (b) CSI measurement (c) A profile across a pit on the CSI surface measurement (d) Measurement profile of the surface using the fiber-Fabry-Perot profiler.

2.6.4 Spot size enhancement using Gradient Refractive Index lens

As mentioned in section 2.6.3.2, the spot size of the diverging light from the fiber must be reduced to measure surfaces with wavelengths $< 50 \mu\text{m}$. The spot size of the diverging light from the bare fiber tip is estimated by two different ways as shown in Figure 15(a).

- (i) Since the refractive indices of the core and cladding of the bare fiber used in the experiments is not known, a typical value of $\text{NA} = 0.1$ for a single mode fiber is assumed. For this value, the spot diameter on the sample surface at about 1 mm away from the fiber tip would be $130 \mu\text{m}$, see Figure 15(a).
- (ii) One could arrive to a similar conclusion using the beam divergence equation considering a gaussian light beam emitted by the fiber, see Figure 15(b).

To achieve a smaller focus spot of couple of micrometers in diameter, a GRIN lens could be used. The solid model and a fabricated clamp to hold a GRIN lens is shown in Figure 15(b).



also,

$$\theta = \frac{\lambda_0}{\pi w_0} = \frac{1050 \text{ nm}}{\pi \cdot 5 \mu\text{m}} = 0.07$$

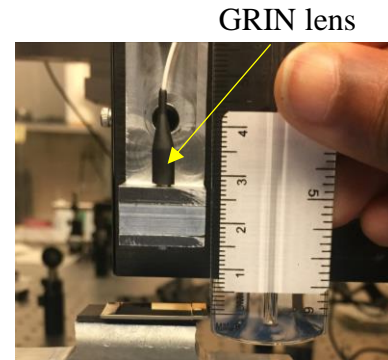
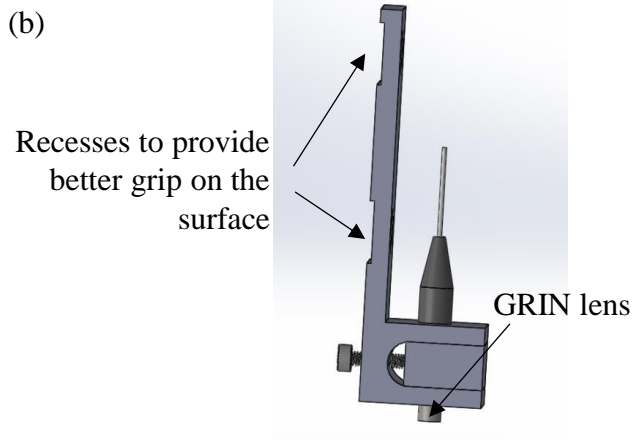


Figure 15: Beam divergence at the fiber output and the GRIN lens; (a) Schematic showing the diverging beam from the fiber and the calculations estimating the spot size on the surface about 1 mm away from the fiber (b) Solid model of the fabricated clamp to hold the GRIN lens during profiling.

2.7 Design studies for producing stress induced modulation of laser sources

2.7.1 Stress induced modulation of laser frequency using a microchip laser

As presented at the end of section 2.6.1, the modulation frequency of the source wavelength using a mechanically oscillated external cavity grating is limited to about 400 Hz due to the mechanical resonance of the system. This frequency limit, in turn, limits the profiling speed to a velocity of less than $v = 0.1 \mu\text{m}\cdot\text{s}^{-1}$ during a displacement, Δz measurement of a copper mirror towards the optical axis of the probe. The frequency of the sinusoidal intensity fringes produced is given by,

$$f_{fringe} = \frac{v_z}{\Delta z} = \frac{v_z}{m \left(\frac{\lambda_0}{2} \right)}$$

Since the source wavelength is $\lambda_0 = 1050 \text{ nm}$, for a single fringe, $m = 1$, it will take about 5 seconds to produce a single fringe i.e., $f_{fringe} = 0.2 \text{ Hz}$ signal. It can be seen that for a 400 Hz modulation frequency, only a $0.1 \mu\text{m}\cdot\text{s}^{-1}$ motion could be discerned using the Lock-in amplifier. Using this as a rule of thumb, to measure the displacements with velocities of millimeters per second, necessary modulation frequency would need to be megahertz or higher. Also, since Lock-in amplifiers are limited to a few MHz of bandwidth, use of high speed processors or, possibly, Field Programmable Gate Arrays (FPGA) would be necessary. It is noted that the Lock-in amplifiers used in our experiments were limited to 20 kHz bandwidth for dual harmonics. To achieve higher modulation frequency, monolithic structures are preferred. One example is Mitsui (1997), who modulated a mirror attached to the surface of a piezo at 600 kHz. Another phenomenon that could increase the modulation frequency (potentially in MHz) is the application of stress on a crystal. Doing this would change the refractive index and other properties of the crystal, referred to as

Stress-optic coefficients [Twyman (1922), Waxler and Weir (1965)]. Literature using this phenomenon to modulate the frequency or phase of the light are briefly discussed below.

2.7.2 Background and literature on mechanical stress control of optical materials for laser source modulation

This second literature review of this chapter discusses research studies that explore the effects of induced stress on crystals as a means of modulating the frequency or phase of the light emanating from it. While there are various potential media, the discussion are focused on glass, Nd:YAG, vanadate and KTP crystals.

a) Silica (Glass)

Photo-elastic constants of fused silica (non-crystalline glass) and Quartz (crystalline glass) were studied by Primak (1959), and Strain-optic coefficients of a single mode fiber was determined by Bertholds (1989). Recently, for frequency modulation in interferometry, Masoud and Smith (2018) have demonstrated the use of Acousto-Optic Modulators (AOM) made of flint glass to achieve a frequency modulation of 10 kHz. A 10 kHz signal is encoded on a 60 MHz carrier frequency like an FM radio to excite the AOM. This technique is termed as ‘Polydyne interferometry’ by the authors. One drawback is that the acousto-optic modulators are typically bulky and expensive. Using FPGA processors modulation frequencies of more than 300 kHz are reported [Masoud, 2019].

b) Neodymium-doped Yttrium Aluminum Garnet (Nd:YAG)

Other media on which stress induced frequency modulation was widely studied is Nd:YAG crystal that produces a 1064 nm infrared light. Owyong (1987) and Zayhowski (1989) have demonstrated frequency tuning on Nd:YAG ‘microchip’ lasers by inducing stress using piezoelectric actuators. The former researcher achieved 0.3 nm (75 GHz, see equation (5)) of

modulation at a 100 Hz modulation frequency, whereas the prototype demonstrated by Zayhowski achieved 0.05 nm of modulation at a 20 MHz modulation frequency. Operating at the acoustic resonance of the crystal (1.1 MHz) enabled the Zayhowski to achieve a 44 times gain in the depth of modulation. Other techniques of frequency modulation implemented using Nd:YAG include:

1. modulation of the current provided to the laser diode. This technique typically has a drawback of thermal emissivity [Nd:Yag - Schulz (1991), Zayhowski (1992)], and
2. modulation of the temperature of the laser diode, which is slow (few Hz) and typically needs a feedback control [Zhou (1985), Gui (2019)].

c) Neodymium-doped Yttrium orthovanadate (Nd:YVO₄) and Potassium Titanyl Phosphate (KTP) crystals

Since Nd:Yag crystals produce infrared light, which is not in the visible spectrum of homosapiens, for interferometric purposes, it is frequently beneficial to implement stress induced modulation on a microchip crystal pair of Nd:YVO₄ (referred to as Vanadate henceforth) and KTP crystals that produces a 532 nm green output, see Figure 16. For this crystal pair to lase, the Vanadate crystal is “pumped” by an 808 nm near-infrared laser source to produce a 1064 nm infrared output. This infrared light enters a frequency doubling (also referred to Second Harmonic Generator) KTP crystal [Bierlein (1989), Kecong (2001), Stus (2003)] and produces a 532 nm green light. These two crystals are optically glued to form a laser cavity with mirrors coated on the 808 nm input side of Vanadate and the 532 nm output side of KTP.

Friel (2000) demonstrated the frequency tunability of this crystal pair by changing the Fabry-Perot cavity length using a piezoelectric actuator and were able to achieve a 14 pm (17 GHz) modulation until the occurrence of a frequency mode hop. It is noted that achieving a higher

modulation frequency was not a goal of their work and the modulation frequency is not mentioned. Mann (1999) studied the variation in the optical output power of the frequency doubling KTP crystal as a function of the input stress applied on the crystal. Hu (2016) modulated the frequency of Vanadate crystal by changing the temperature with a sensitivity of $8 \text{ pm}/^{\circ}\text{C}$. Again, modulation frequencies are not discussed in these reports.

Our efforts to achieve frequency modulation uses the Vanadate-KTP crystal pair and apply stress on the surface orthogonal to the lasing axis using a piezo as schematically shown in Figure 16(e). Application of stress results in the increase of the cavity length due to Poisson's ratio effect, therefore changing the laser wavelength emitted by the crystal pair. The prototypes built for the application of stress, and the experimental details are discussed in section 2.7.3.

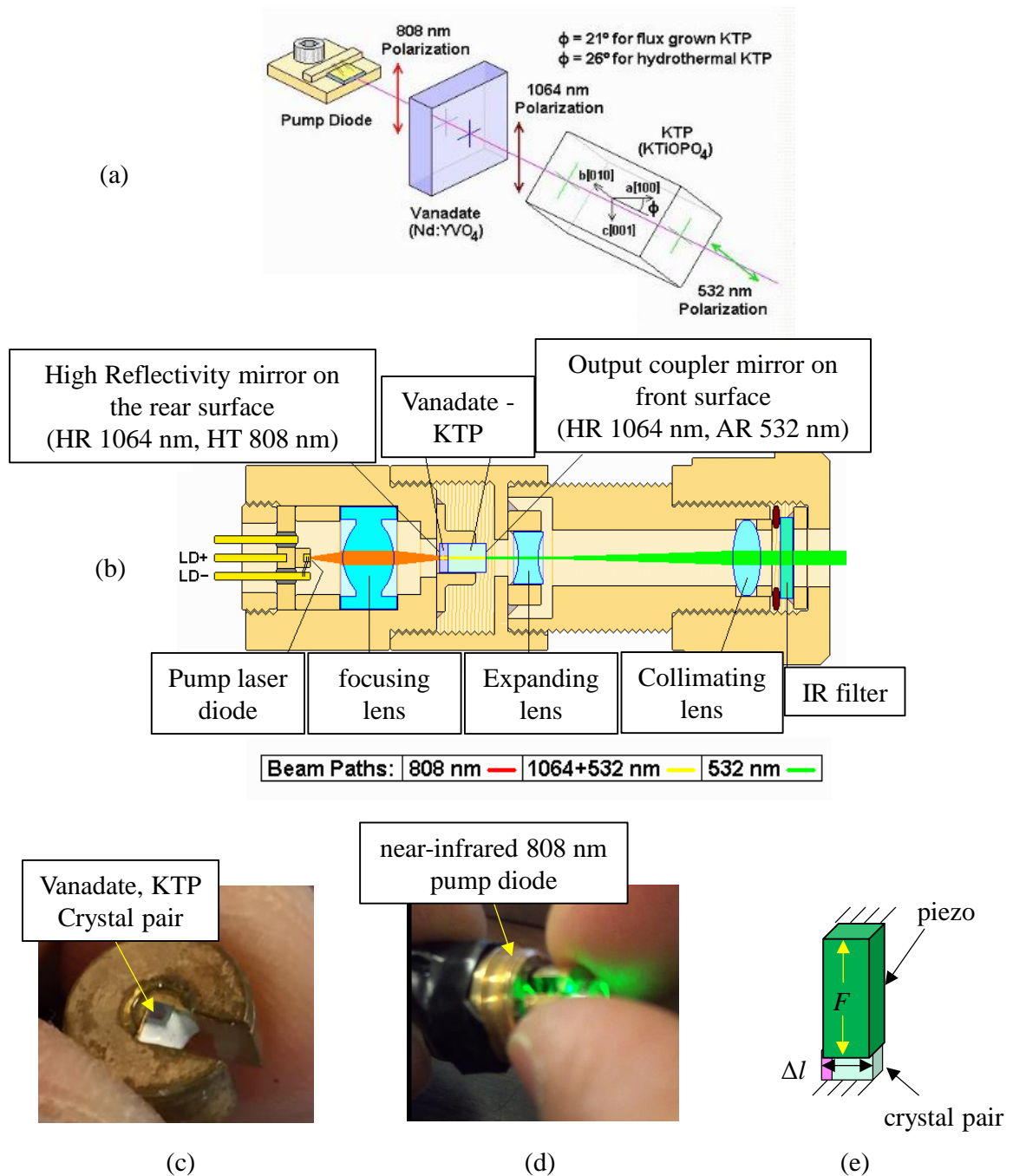


Figure 16: Microchip laser components; (a) Schematic showing the components of the microchip laser producing green light (b) Schematic showing the internal organs of a green laser pointer (courtesy of Sam's lasers repairfaq.org) (c) A crystal pair dissected from a laser pointer (d) placing the crystal pair to the focused light beam from 808 nm pump diode producing a green light (e) schematic of a piezo compressing the crystal pair.

2.7.3 Experiments to modulate the laser frequency by compressing the Vanadate-KTP crystal pair

This section discusses the experiments performed to modulate the frequency of the laser emanating from the vanadate-KTP crystal pair by compressing it using a piezo electric actuator [Arumugam et al., 2017]. In the experiments performed, the crystal pair was held in a commercial clamping mechanism and, to address the issues observed during the experiments a flexure-based gripper mechanism is fabricated and tested.

a) Compression of the crystal pair using a clamp arrangement

The first prototype built to modulate the frequency of the green microchip laser by applying stress is shown in Figure 17(a) and (b). The size of the optically glued crystal pair used in the first prototype is Vanadate: $0.5 \times 1 \times 1 \text{ mm}^3$ KTP: $2 \times 1 \times 1 \text{ mm}^3$, and were taken from a green laser pointer, see Figure 16(b) and (c). This crystal pair is epoxied in between a gage block and a piezoelectric actuator for inducing stress on the crystal as shown in Figure 17(a) and (b). To validate frequency modulation, this prototype was experimented using a Michelson interferometer with an 808 nm diode taken from the laser pointer acting as a pump source, but this experiment did not show any frequency modulation.

The second prototype shown in Figure 17(c) and (d) used a 3 mm^3 crystal pair which was a little larger and easier to handle compared to the previous crystal pair. This crystal pair is held in place using a clamp arrangement, but the surfaces were epoxied. The crystal is pumped with a different 808 nm infrared diode (Lilly electronics, see Appendix A.4 for specifications) producing a maximum optical power of 500 mW, and its current and temperature are controlled using the equipment shown in Figure 18. The displacement of a

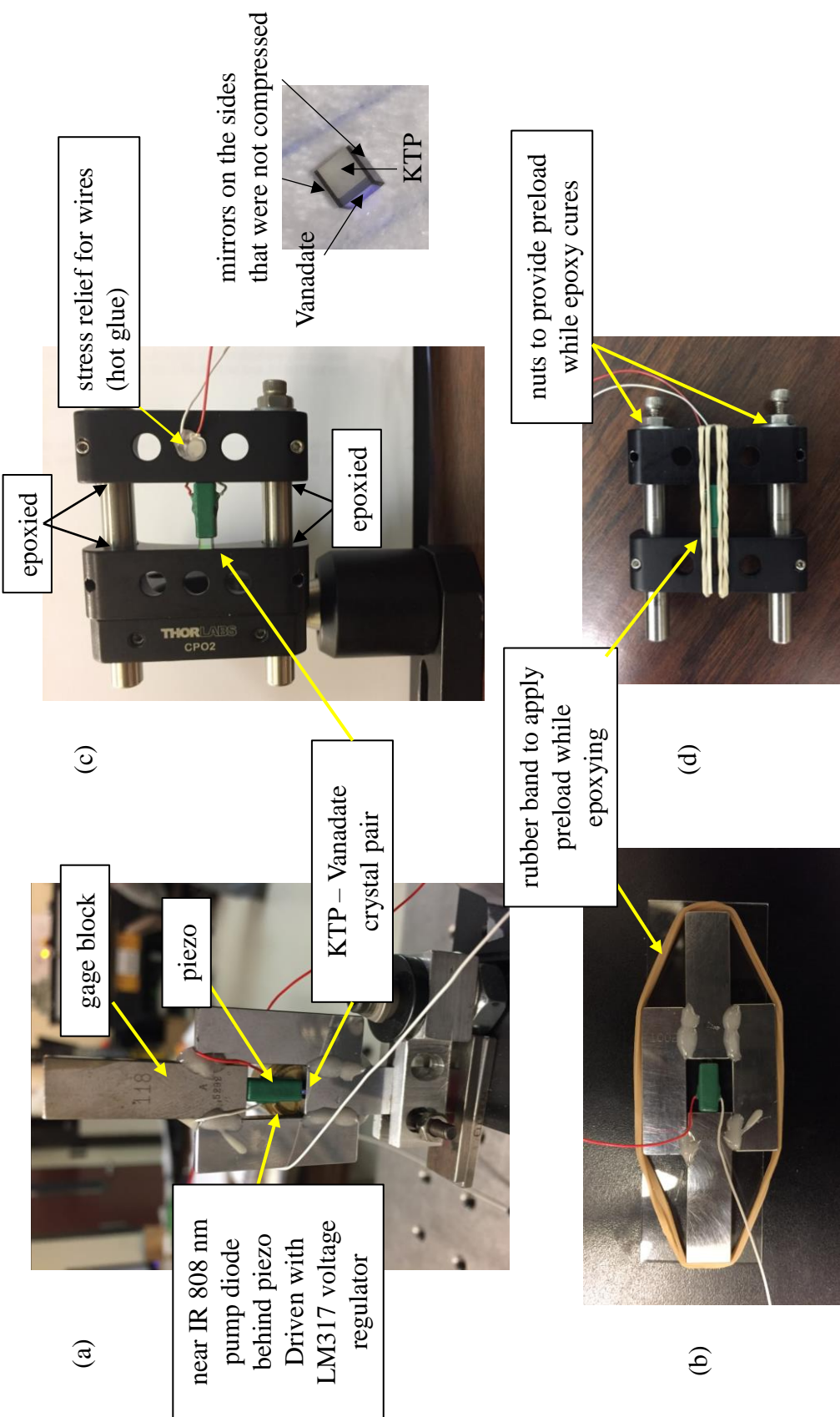
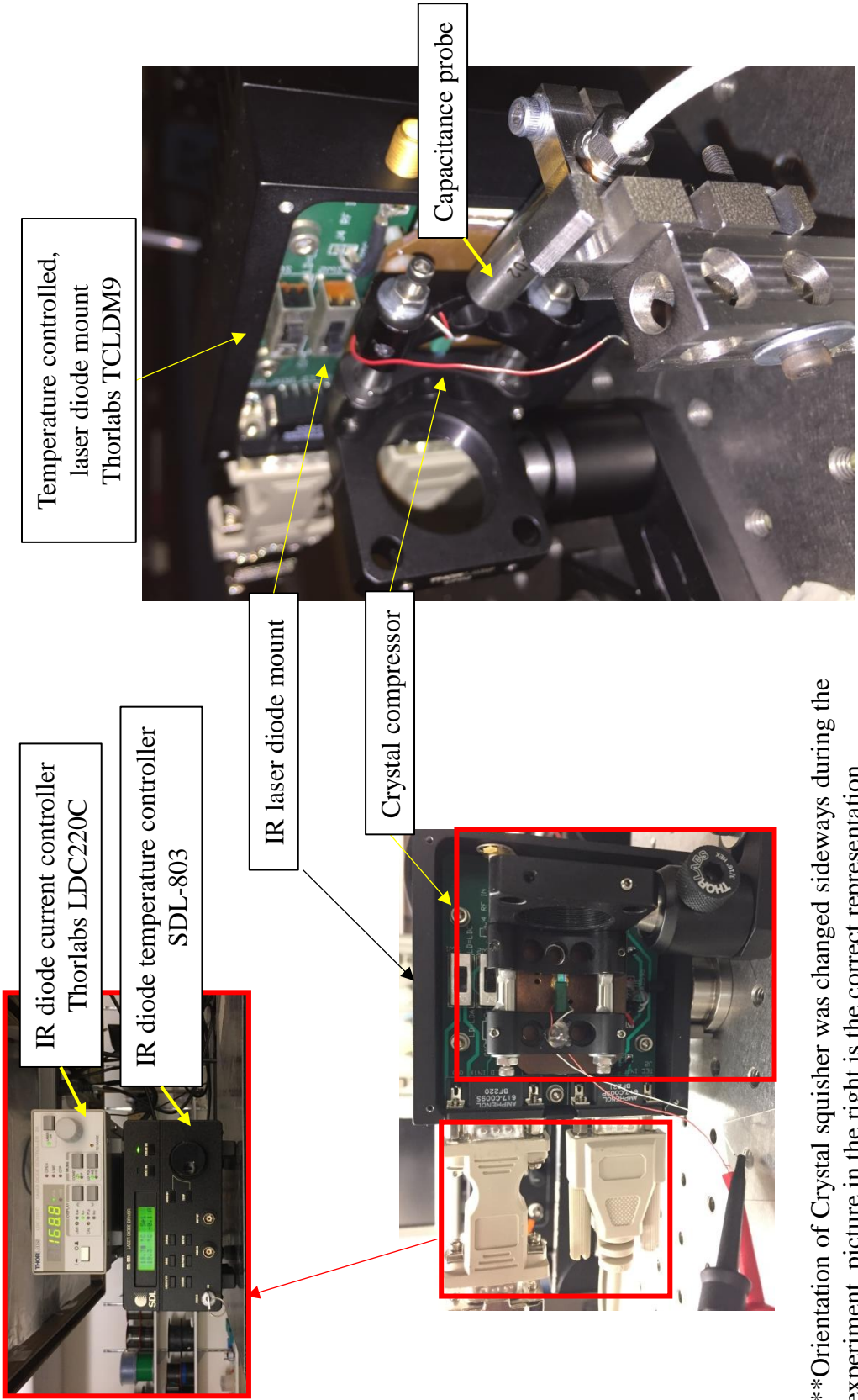


Figure 17: Earlier prototypes of the crystal compressor (a), (b) first prototype built using gage block and a piezo epoxied together (c), (d) crystal pair epoxied to a piezo and clamped together.



**Orientation of Crystal squisher was changed sideways during the experiment, picture in the right is the correct representation

Figure 18: Picture of the 808 nm laser diode mount which controls the current and temperature of the diode using the controller units shown on the left top.

face of the clamp during the actuation of the piezo electric actuator to apply stress is monitored using a capacitance probe. Figure 19(a) shows the Michelson interferometer facility used to validate the frequency modulation during the compression of the crystal. To improve the chance of observing the frequency modulation, two arms of the interferometer (path length) were arranged to be different in length by 5 inches (0.127 m). Doing this increases the number of observable fringes during frequency modulation.

To calculate the number of fringes as a function of laser frequency change, considering the intensity at the photodetector due to the interference of light waves from a two-arm of the Michelson interferometer that is given by

$$I = I_1 + I_2 + 2\sqrt{I_1 I_2} \sin(2k(x_2 - x_1))$$

where, I_1 and I_2 are the intensity of the light from two mirrors (or cube corners) of the interferometer, x_1 and x_2 are the length of the two arms, and $k = \frac{2\pi}{\lambda_0}$ is the number of waves travelled per meter, also referred to as ‘wave number’. The phase of the sinusoidal signal due to the interference of light from two arms is given by

$$\phi = \frac{4\pi}{\lambda_0}(x_2 - x_1)$$

In displacement interferometry, if there is an additional path length difference (Δx) caused due to the motion of a mirror, sinusoidal intensity variations are produced, referred to as “fringes”, and the phase is given by

$$\phi + \Delta\phi = \frac{4\pi}{\lambda_0}(x_2 - x_1 + \Delta x), \quad (7)$$

and the number of fringes (m) (constructive interferences) observed by the photodetector is given by

$$m = \frac{\Delta\phi}{2\pi} = \frac{2\Delta x}{\lambda_0}$$

But, when there is no motion of the mirror (i.e. $\Delta x = 0$), but the frequency of the source is modulated, from equation (7), the change in phase as a function of change in source wavelength is represented as,

$$\frac{d\phi}{d\lambda} = \frac{8\pi}{\lambda_0^2}(x_2 - x_1)$$

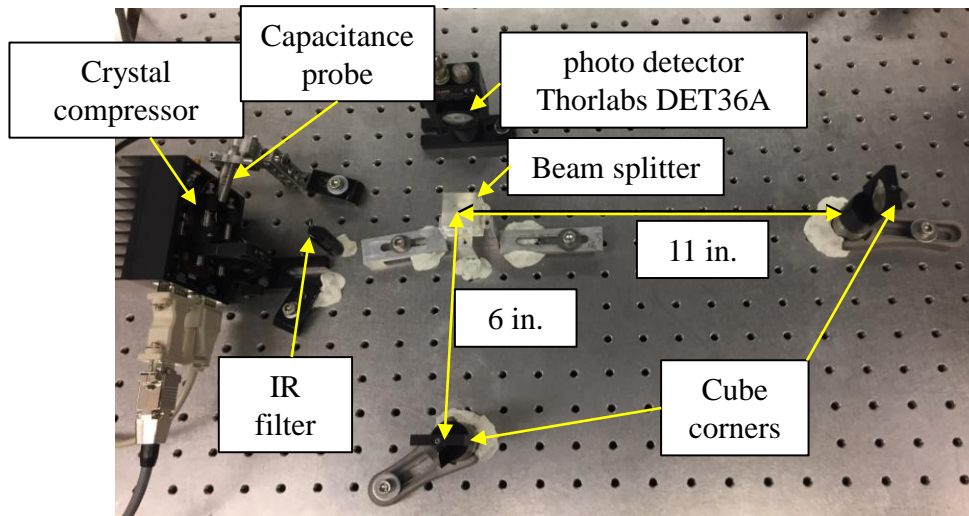
now the number of fringes (m) observed by the photodetector is given by

$$m = \frac{d\phi}{2\pi} = \frac{4(x_2 - x_1)}{\lambda_0^2} d\lambda,$$

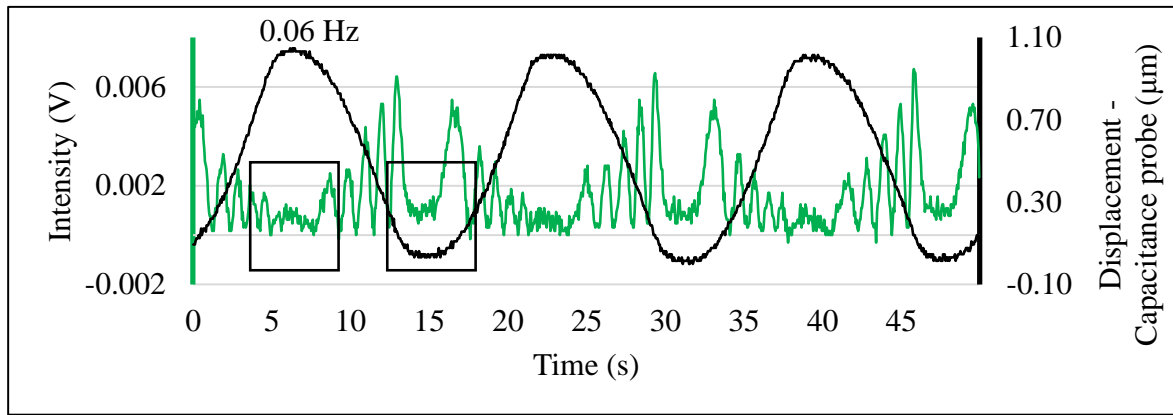
showing the sensitivity of number of observed fringes during modulation to the path length difference ($x_2 - x_1$). Writing in terms of Δ for readability, the amount of modulated wavelength is given by,

$$\Delta\lambda = \frac{m\lambda_0^2}{4(x_2 - x_1)} \quad (8)$$

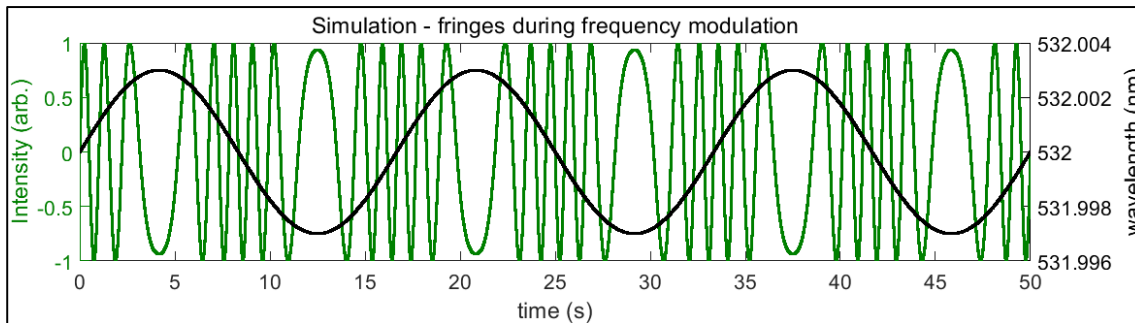
Figure 19(a) shows the Michelson interferometer used in the experiment to validate the modulation of the source wavelength. In Figure 19(b), five fringes are observed during the sinusoidal modulation of the source wavelength (shown in green), and the displacement of the



(a)



(b)



(c)

Figure 19: Result of frequency modulation using the clamp assembly; (a) Michelson interferometer setup to validate the result of frequency modulation (b) Intensity fringes produced during the compression of the crystal pair and the displacement of the clamp measured by the capacitance probe (c) Simulation showing the ideal fringes expected during the compression of the crystal.

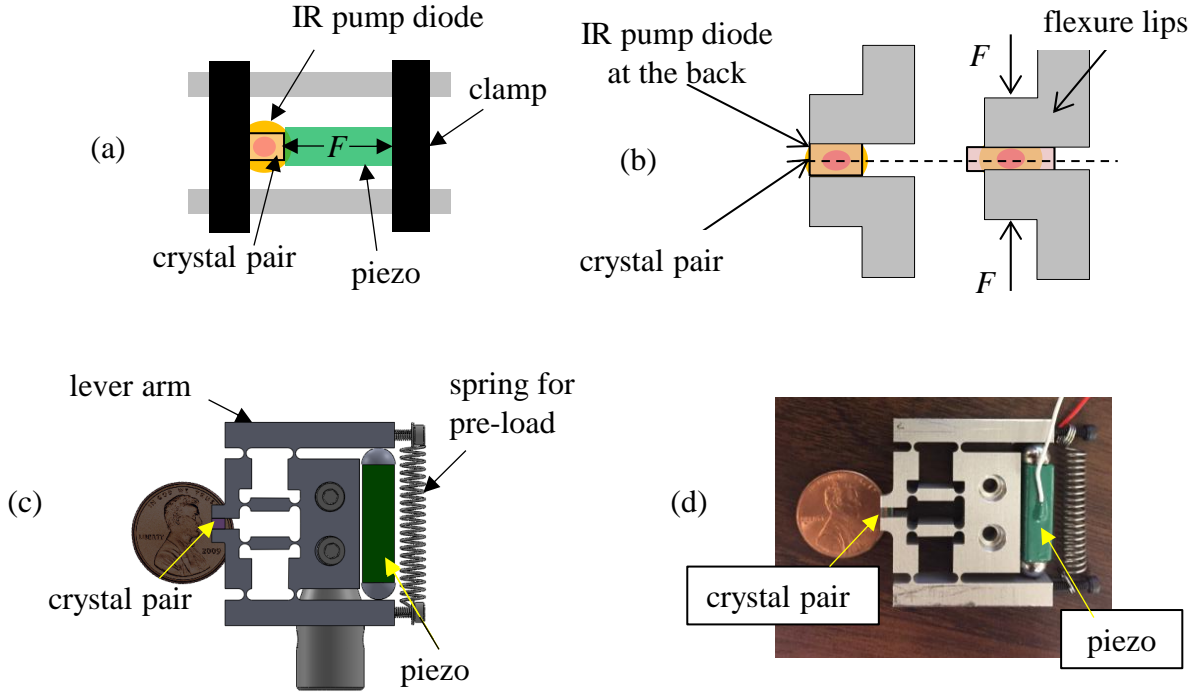


Figure 20: Schematic of the flexure - based crystal compressor; (a) first prototype using a clamp (b) second prototype using a flexure gripper (c) solid model of the mechanisms (d) fabricated mechanism.

clamp holding the crystal measured by the capacitance probe was $1\text{ }\mu\text{m}$. Using equation (8), for five fringes produced, the amount of modulation of the fundamental wavelength of $\lambda_0 = 532\text{ nm}$ is calculated to be $\Delta\lambda = 3\text{ pm}$. It can also be seen that there is an attenuation in the intensity of fringes at both peak and valley of the compression during the experiments which is not desirable. Another prototype encasing the piezo and the crystal pair in a small Aluminum frame is given in Appendix A.5. The fringes produced during the compression of the crystal using this prototype also showed attenuation in fringes but was not repeatable.

Since there is no constraint in the above discussed prototypes to stop the crystal from rotating (yaw) when it is compressed from the top, a flexure mechanism shown in Figure 20(d) was fabricated to compress the crystal symmetrically from both top and bottom. Equations to estimate the stiffness and the natural frequency of this flexure is discussed in Appendix A.6.

b) Compression of the crystal pair using a notch hinge flexure mechanism

Figure 20 (a) and (b) schematically shows the difference in the way the crystal was compressed in the previous clamped configuration, and in the new, flexure-based, configuration shown in Figure 20(c and d). Figure 22(a) shows the Michelson interferometer setup used to validate the frequency modulation with a path length difference of 3 inches. Figure 22(b) shows the crystal placed between the flexure lips and pumped by an infra-red diode taken from a laser pointer (see Figure 15(b)). A capacitance probe is used to measure the displacement of the lever arm of the flexure during the compression of the crystal. Figure 22(c) shows the resulted fringes during the compression, where it can be seen that the attenuation in fringe intensity still occurs, but only at the peak of the compression this time, unlike the earlier case where the attenuation occurred at both peak and valley, shown using a black box in Figure 19(b). Figure 23 shows that the amount of stress exerted on the crystal is estimated to be 0.75 MPa from the strain measured using a strain gage placed on top of the notch hinge in the middle of lever arm C, see Figure 21. It is noted that the signal shown in Figure 23(c) is high pass filtered to remove drift.

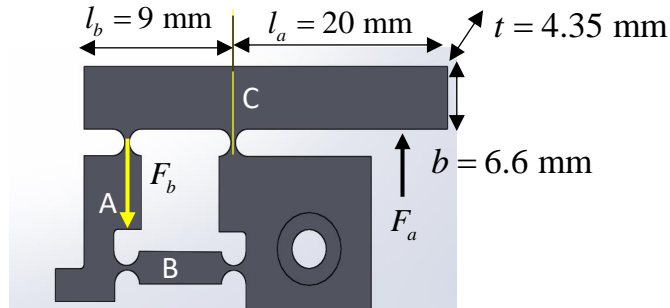


Figure 21: Dimensions of the notch hinge flexure used to calculate the stress exerted on the crystal pair. The strain gage is located on the top surface of the link C, in line with the notch joint.

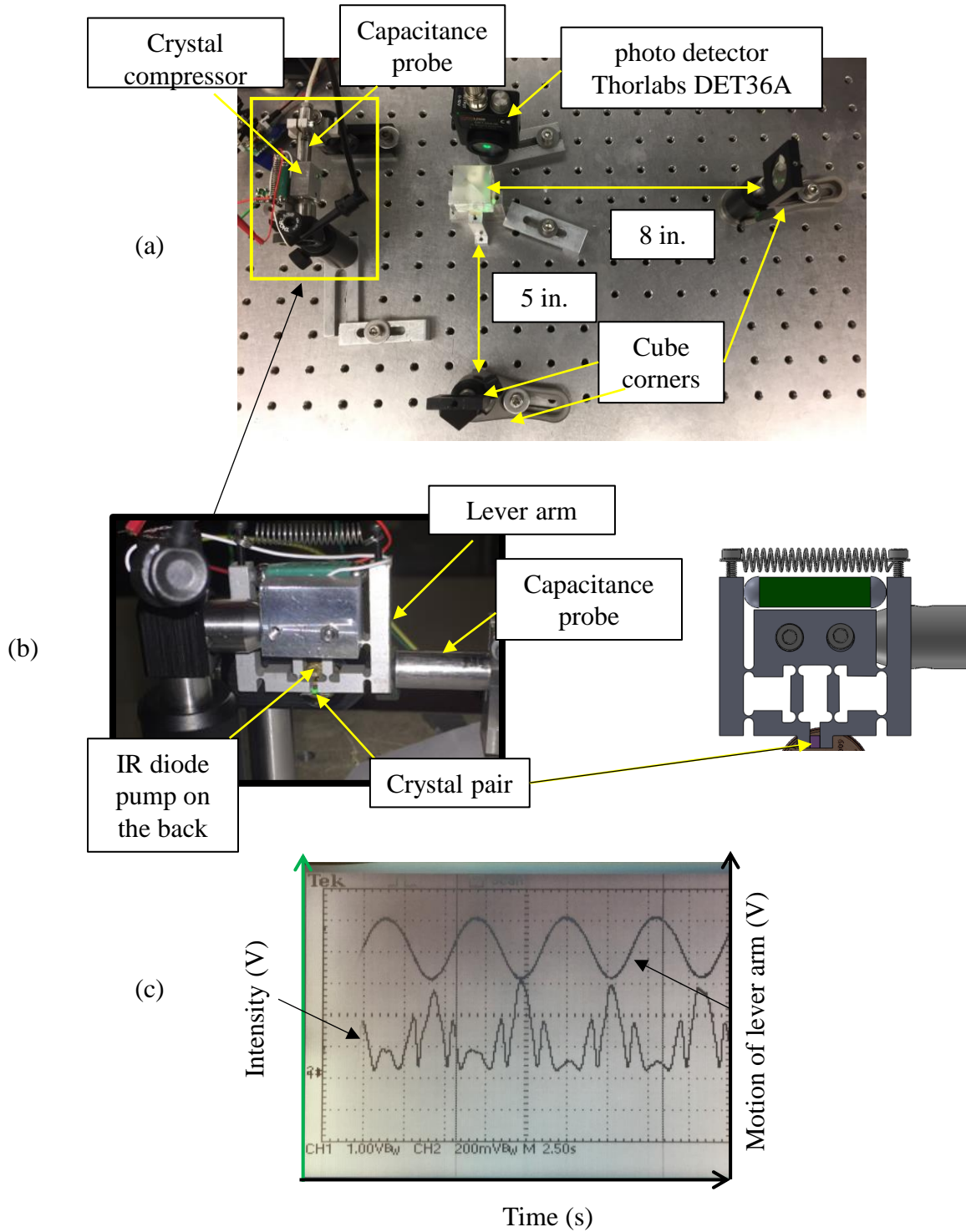


Figure 22: Result of frequency modulation using the flexure gripper; (a) Michelson interferometer facility with a path length difference of 3 inches to validate the modulation of the laser frequency (b) Picture showing the 808 nm pump diode and the capacitance probe measuring the deflection of the lever arm (c) Resulted fringes during compression of the crystal.

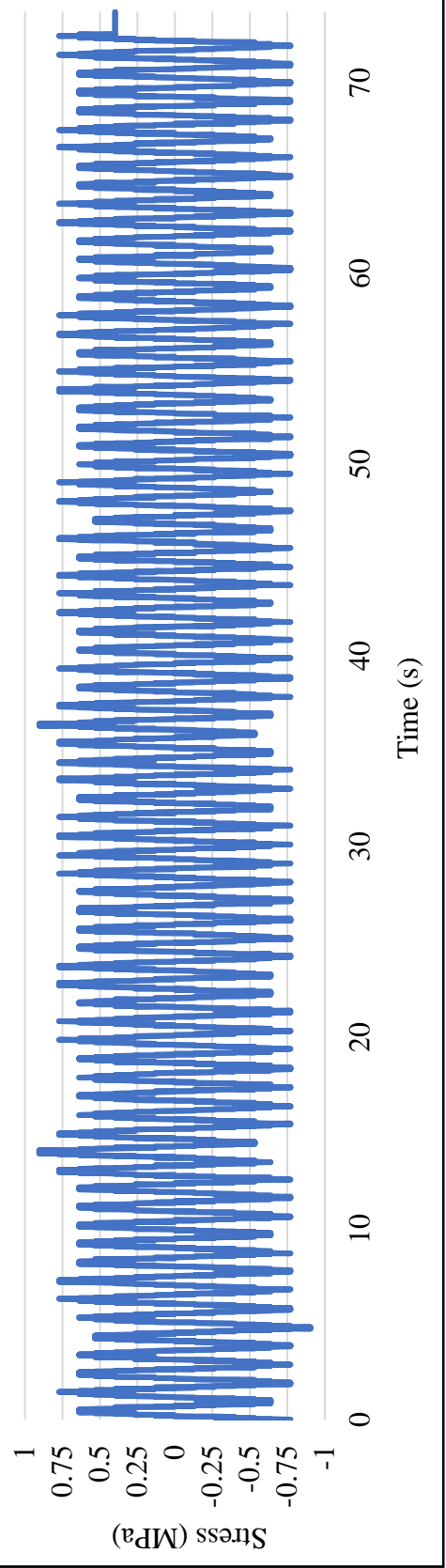
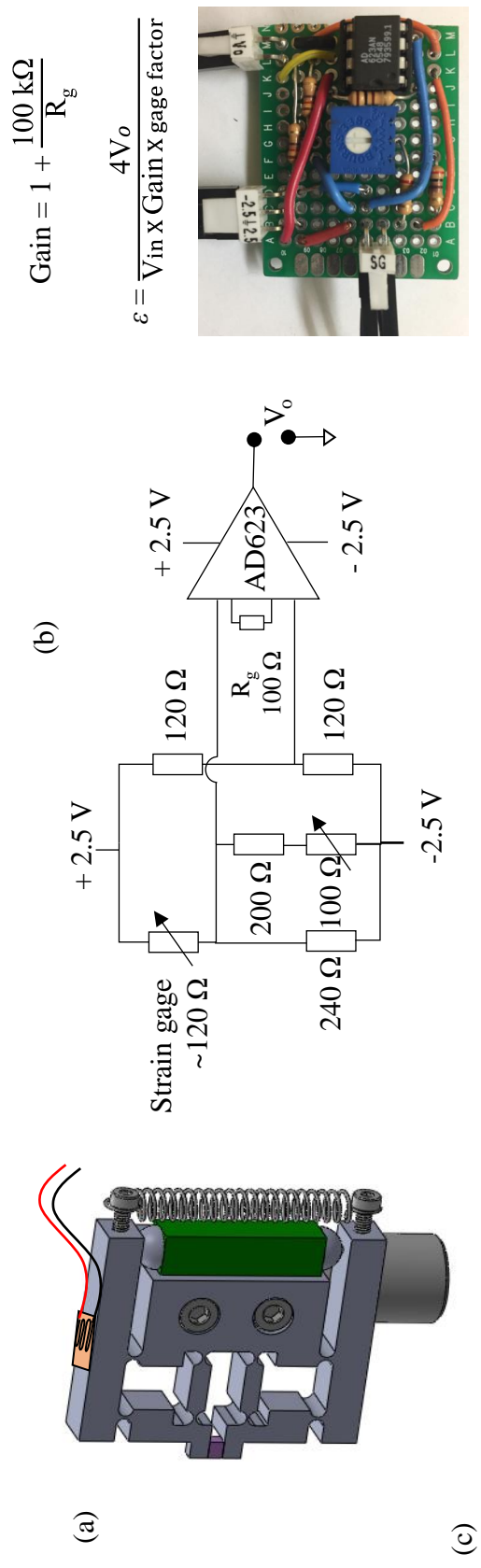


Figure 23: Circuit diagram for strain gage sensing and the calculated stress (a) Solid model showing the strain gage attached on top of the notch hinge of lever arm (b) circuit diagram and the fabricated Wheatstone bridge to measure strain gage signal (c) Sinusoidal stress calculated from the measured stress.

To estimate the stress applied on the crystal, from the measured strain signal (ε), stress at the notch hinge in the middle of lever arm, C is calculated using the Elastic modulus (Aluminum, $E = 70 \text{ GPa}$) as, $\sigma = E\varepsilon$, and plotted in Figure 23(c).

This stress is related to bending moment (M) given by, $\sigma = \frac{My}{I} = \frac{M(t/2)}{bt^3/12}$

Force applied at the end of lever arm due to the expansion of piezo, $F_a = \frac{M}{l_a}$.

From the lever arm ratio, force exerted on the crystal is, $F_b = \frac{F_a l_a}{l_b}$.

For the crystal of area, A , the stress applied on the crystal is calculated as, $\sigma_{crystal} = \frac{F_b}{A} = 0.42 \text{ MPa}$

From the result given in Mann (1999), this amount of estimated stress applied on the crystal is not in the sensitive region of output power change of the second harmonic signal (Green), which is about 1.4 MPa.

To address in the future experiments of compressing the crystal:

1. The crystal pair might still be rotating during compression, and epoxying the crystal-piezo interface might help to reduce (or avoid) the attenuation of fringe intensity.
2. Since the crystal pair in the experiments were optically glued together during the compression studies, it might be an idea to separate them and only compress the KTP crystal which is about 4 times longer than the Vanadate crystal. Although, doing this will increase the cavity length and might produce multiple longitudinal modes (wavelengths) in the laser output.

2.7.4 Multiple longitudinal modes (wavelengths) in a microchip laser

To determine the wavelengths in a microchip green laser, the spectrum of a commercially available laser (Thorlabs CPS532) was measured using a Spectrometer with a 5 pm resolution resulting in the plot shown in Figure 24(a). An infrared filter is used to block 808 nm and 1064 nm light used to pump a KTP crystal and is placed in front of exit beam from the laser so that only the green portion of the spectrum goes into the detector. The measured spectrum shown in Figure 24(b) contains three distinct wavelengths with $\Delta\lambda = 0.1$ nm which is not desirable for the interferometric application of our purposes. On close inspection, there might be two overlapping peaks within each of these three peaks. There was also a fourth wavelength, but its intensity is not appreciable. To ensure that if these three wavelengths are related to different polarizations, a polarizer is put in front of the laser as shown in Figure 24(c), and the measured spectrum is shown in Figure 24(d), which still contains three distinct wavelengths for any given position of the polarizer, but one of the two overlapping peaks is less distinct at the resolution limit of this spectrometer. More spectral measurements of this laser, and other commercial lasers are given in Appendix A.7.

To observe the displacement fringes produced in an interferometer using this microchip laser as a source, a polarization-based interferometer was fabricated, as shown in Figure 25 [Arumugam et al., 2018]. This interferometer produces a quadrature signal using the 90° (ideally) phase shifted polarization signals recorded by the two photodetectors shown in Figure 25. Therefore, frequency modulation of the source is not necessary for obtaining the quadrature in this technique. Figure 26(a) shows the fringes measured for 5 mm displacement of one mirror.

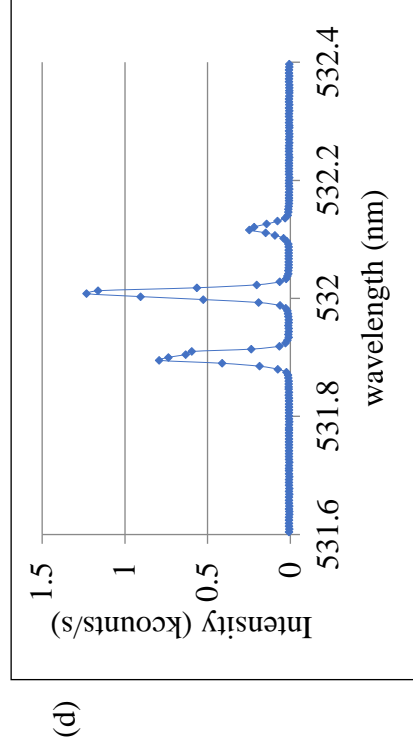
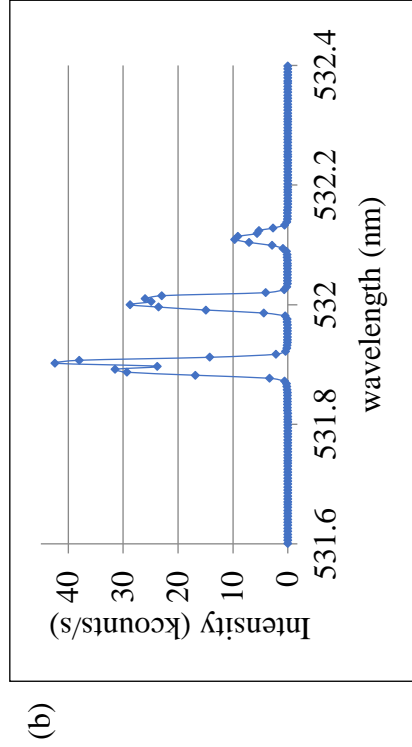
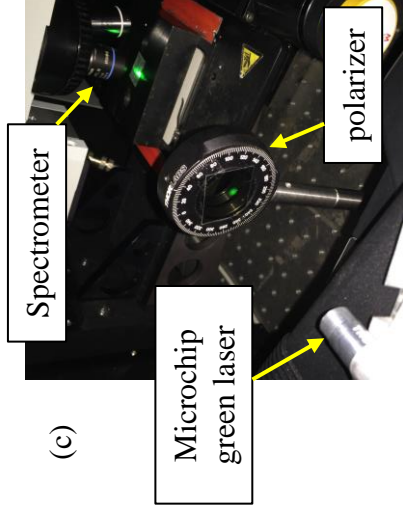
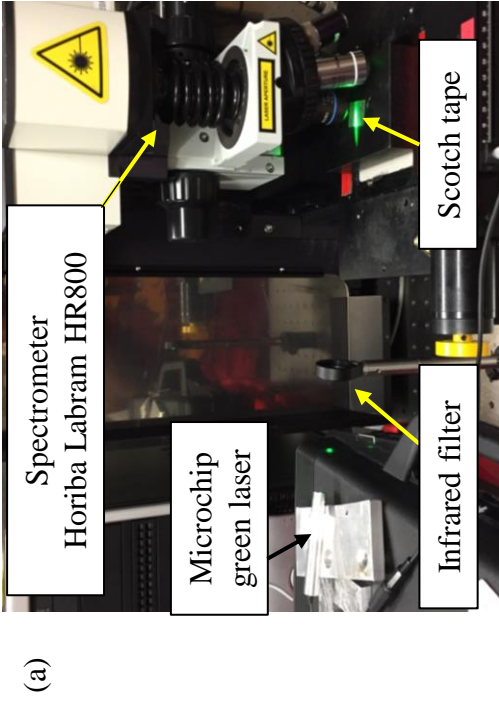
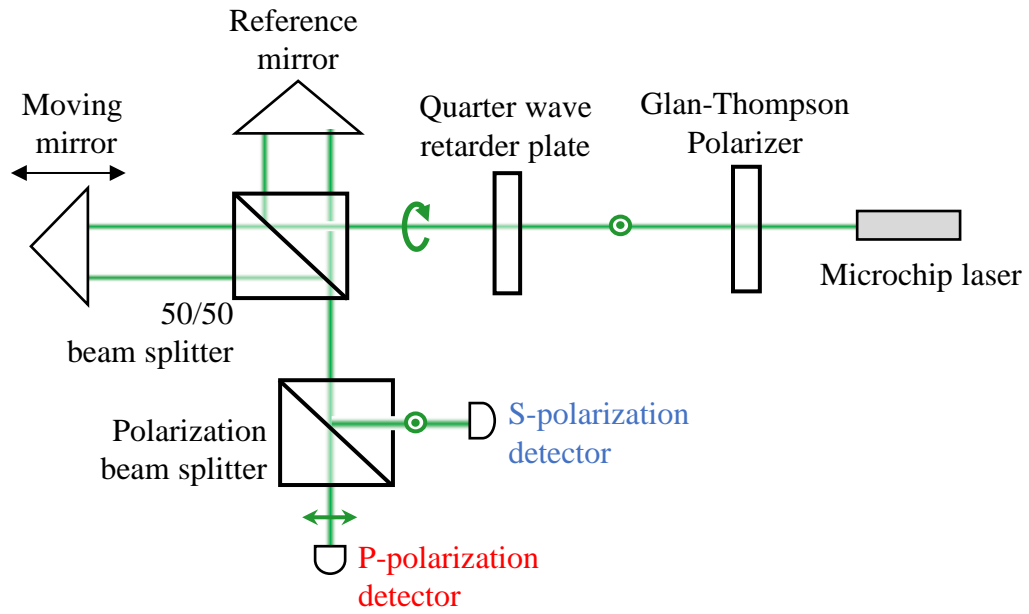
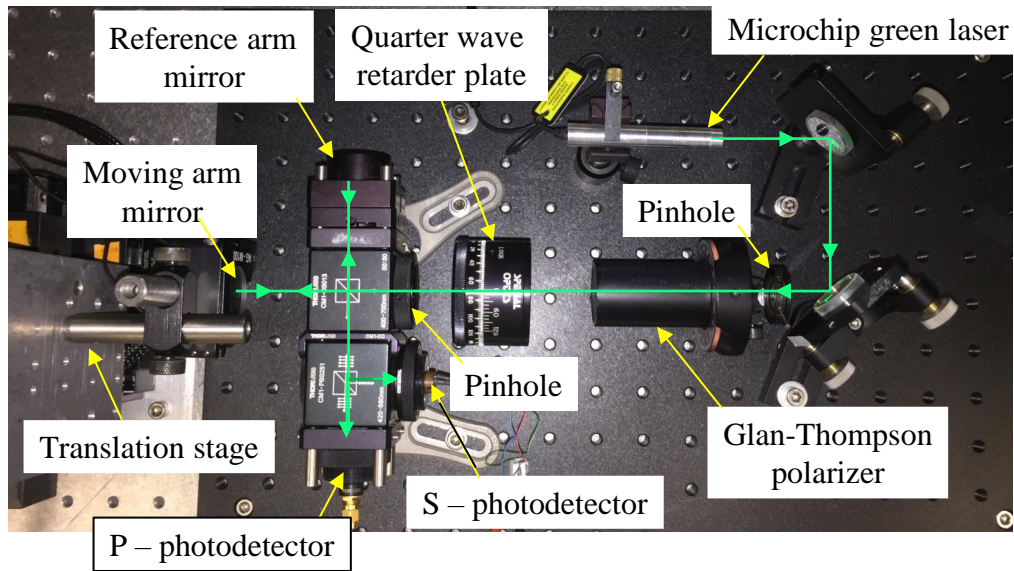


Figure 24: Wavelength spectrum of the microchip laser (a) spectrum of the Microchip laser measured using a Spectrometer with an infrared filter in front of it (b) measured spectrum showing three distinct wavelengths (c) spectrum of the laser measured with a polarizer in front of it, and (d) measured spectrum .



(a)



(b)

Figure 25: Polarization based Homodyne interferometer; (a) Schematic, and (b) Experimental setup.

From this figure it can be seen that the contrast of the signal from both the photodetectors varies ('beats') as a function of displacement with these beats being caused by the three distinct wavelengths present in the laser source. It is noted that the signal shown in Figure 26(a) was subsampled to avoid recording millions of datapoints, and there are about 1000 datapoints in this plot. A portion of the signal from one of the photodetector for a displacement of $x = 1.5$ mm is theoretically fit using the following equation as shown in Figure 26(b).

$$\begin{aligned}
 I &= A_1 (\sin k_1 x) + A_2 (\sin k_2 x) + A_3 (\sin k_3 x) \\
 &= A_1 \left(\sin \frac{4\pi x}{\lambda_1} \right) + A_2 \left(\sin \frac{4\pi x}{\lambda_2} \right) + A_3 \left(\sin \frac{4\pi x}{\lambda_3} \right)
 \end{aligned}$$

where, λ and A represents the three wavelengths and their amplitudes present in the laser spectrum shown in Figure 24, with $\lambda_1=532$ nm being the fundamental wavelength of the laser, $\lambda_2=\lambda_1 + \Delta\lambda$; $\lambda_3=\lambda_1 + 2\Delta\lambda$ with the difference in the wavelength being $\Delta\lambda = 0.1$ nm. It is noted that this theoretical fit (shown in black) contains a million datapoints. The presence of these multiple wavelengths could have also played a role in the attenuation in the intensity of frequency modulated fringes observed in the experiments discussed in Section 2.7.3.

2.7.5 Modulation of the phase of the light source by compressing an optical flat

Modulating the phase of the laser source would produce a similar effect as modulating the frequency, since the former is equivalent to the derivative of the latter, as represented using the following equation.

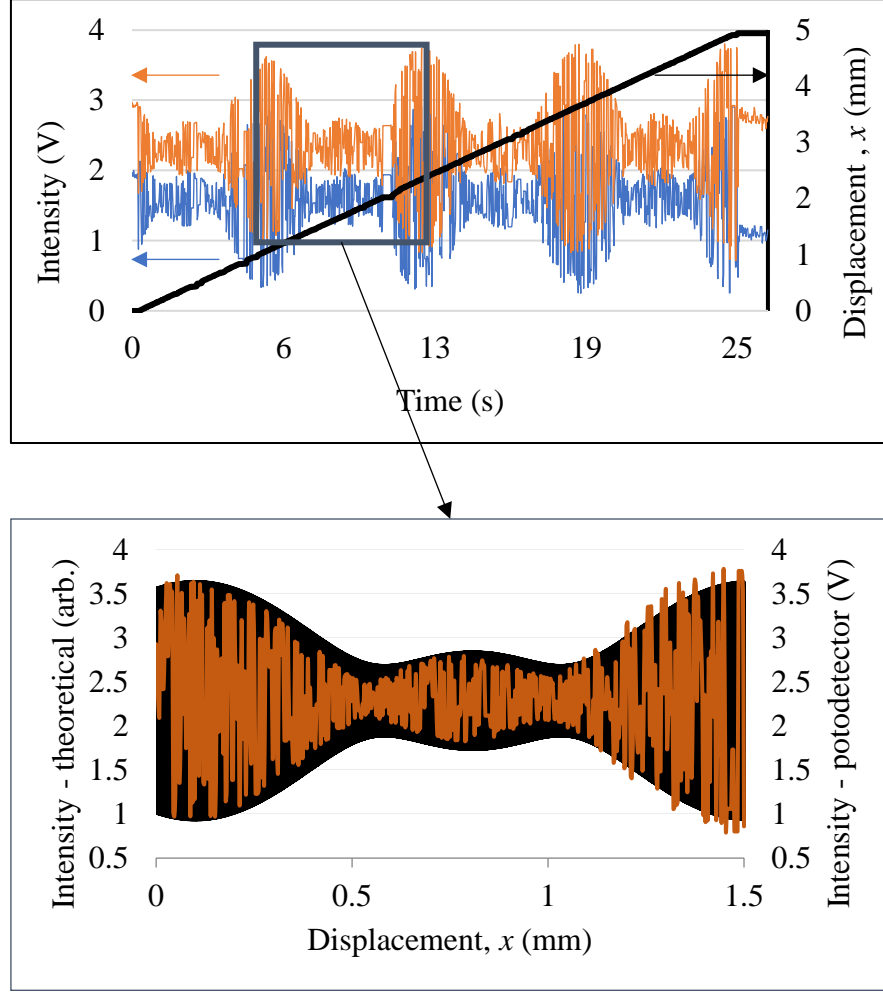


Figure 26: Fringes produced in a Polarization based Homodyne interferometer; (a) during the 1.5 mm travel of mirror showing beats due to the presence of multiple wavelength in the laser source
 (b) Portion of the fringes fit to a theoretical equation representing the multiple wavelengths present in the source.

$$I_{\text{FM}} = I_0 \sin((\omega_0 + \Delta\omega \sin \omega_m t)t)$$

$$I_{\text{PM}} = I_0 \sin(\omega_0 t + \Delta\phi \sin \omega_m t)$$

where,

I_0 and ω_0 are the intensity and the fundamental frequency of the light-source,

I_{FM} and I_{PM} are the intensity of the frequency modulated and the phase modulated source,

$\Delta\omega$ and $\Delta\phi$ are the amplitude (or ‘depth’) of modulated frequency and the phase, and

ω_m is the modulation frequency.

To modulate the phase of the source, laser cavity modulation is not necessary. Figure 30(a) shows a schematic diagram of a transparent medium (say, glass) through which the visible light is transmitted. The wavelength of light inside the medium reduces due to the increase of refractive index of the medium, and then exits the medium. When this medium is compressed as shown in Figure 30(b), the refractive index increases changes, therefore the wavelength inside the medium is larger than the medium in an uncompressed state. And, when the light exits from the medium into air, the phase at the air-glass interface is different from the medium in an uncompressed state, hence, phase modulation.

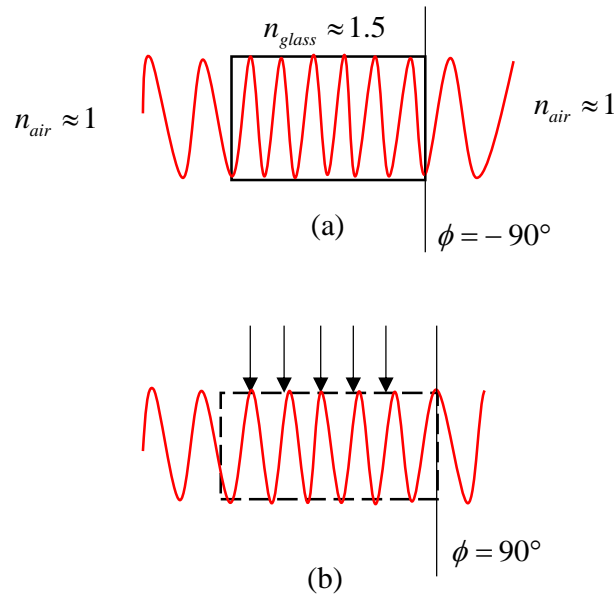


Figure 27: Schematic showing phase modulation; (a) wavelength of the visible light entering from air into an optical medium reduces (b) compressing an optical medium reduces the refractive index of the material and causes a phase shift in the light exiting the medium.

Phase of the light exiting the uncompressed medium of length, l and refractive index, n is

$$\phi_b = \frac{nl}{\lambda} 2\pi$$

Phase of the light exiting the compressed medium due to change in length and the refractive index is given by

$$\phi_a = \frac{(n + \Delta n)(l + \Delta l)}{\lambda + \Delta \lambda} 2\pi .$$

Therefore, the change in phase,

$$\begin{aligned} \Delta \phi &= \phi_a - \phi_b \\ &= \left(\frac{nl + \Delta nl + n\Delta l + \Delta n\Delta l}{\lambda + \Delta \lambda} - \frac{nl}{\lambda} \right) 2\pi \\ &= \left(\frac{(\Delta nl + n\Delta l) - nl \frac{\Delta \lambda}{\lambda}}{\lambda + \Delta \lambda} \right) 2\pi \end{aligned}$$

and for small changes in wavelength,

$$\Delta \phi = \left(\frac{(\Delta nl + n\Delta l)}{\lambda} \right) 2\pi .$$

The change in refractive index is related to the applied stress on the medium (σ) as,

$$\Delta n = \frac{\partial n}{\partial \sigma} \sigma = \beta \sigma$$

Where, β is the stress-optic coefficient with units $[\text{m}^2 \cdot \text{N}^{-1}]$.

The change in length is related to the Poisson's ratio (ν) and the strain of the medium (ε) having an elastic modulus (E) and is given by,

$$\frac{\Delta l}{l} = \nu \varepsilon$$

$$\Delta l = \nu \frac{\sigma}{E} l$$

Therefore, the change in phase can be related to the material properties as,

$$\Delta \phi = \left(\beta + \frac{\nu}{E} \right) \frac{2\pi \sigma l}{\lambda} \quad (9)$$

It is noted that there are two terms inside the parenthesis in the above equation corresponding to the sum of stress optical coefficient and mechanical deformation, respectively.

A Borosilicate optical flat (BK7, $\lambda/4$) of 3 inch diameter and 1/4 inch thickness was cut into small cubes of approximately 5 mm on each side, and used as the transmission medium in our experiments. A diamond grinding wheel was used to cut the slices using the procedure illustrated in Figure 28 (a through f). One of these rectangular blocks was then attached to a piezoelectric actuator that was sinusoidally ‘excited’. When excited at a resonant frequency, a maximum gain in compression could be achieved (referred to as Q factor), see Figure 30(a). Photographs taken during the slicing of the piezoelectric plates are shown in Figure 29.

The equation that relates the velocity of sound (c_{sound}) travelling in a medium to the Elastic modulus ($E_{BK7} = 82 \text{ GPa}$) and the density of the medium, ($\rho_{BK7} = 2500 \text{ kg} \cdot \text{m}^{-3}$) is

$$c_{sound} = \sqrt{\frac{E}{\rho}}$$

For a medium of length ($L = 5 \text{ mm}$), and refractive index ($n_{BK7} = 1.5$), the resonant frequency is given by the below equation, and is calculated to be 1 MHz.

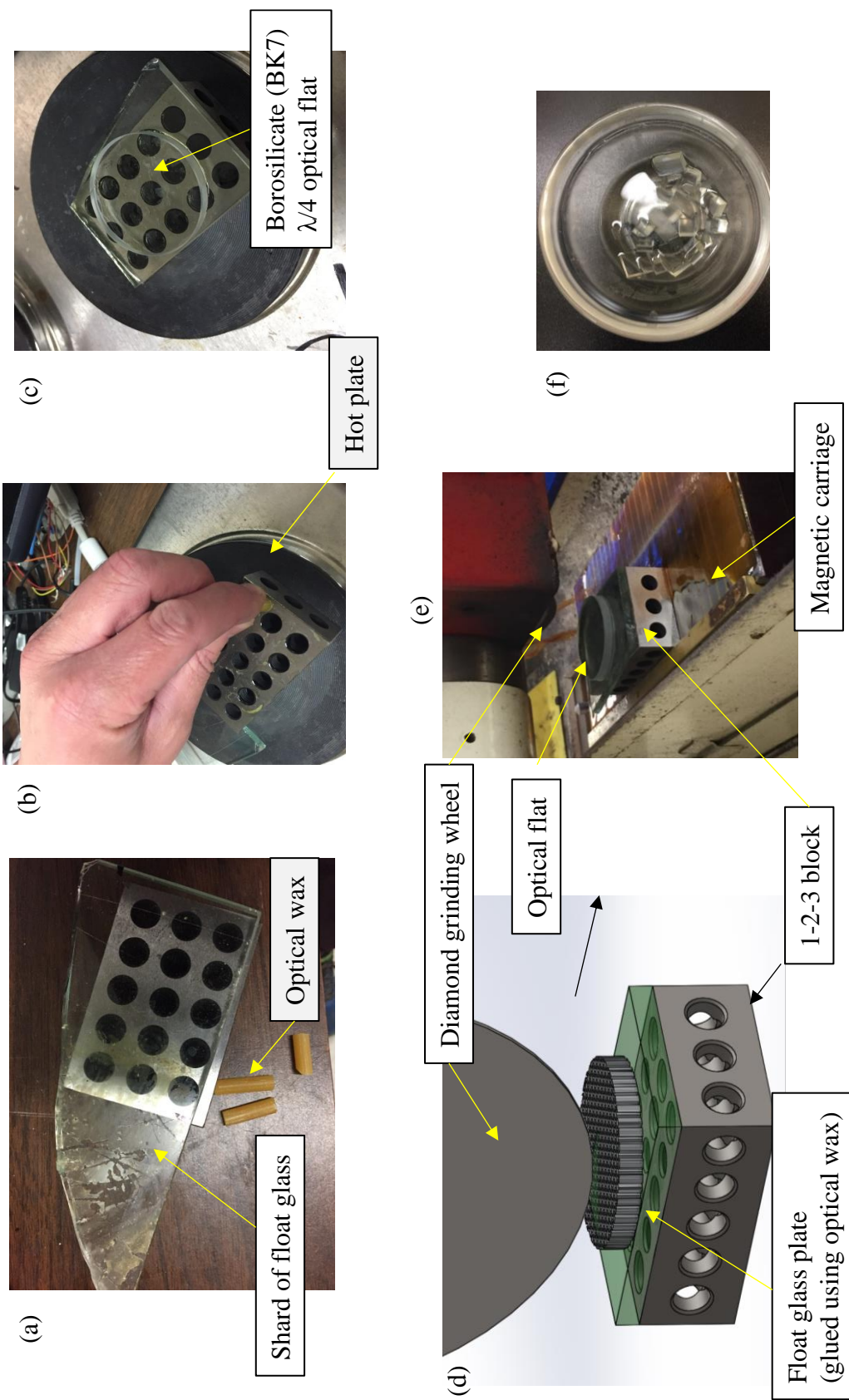


Figure 28: Cutting an optical flat using a grinding wheel; (a),(b) A shard of float glass is glued on to a 1-2-3 block using optical wax (c) Optical flat is glued on top of the shard of glass (d), (e) Solid model and the fabrication process (f) pieces of optical flats

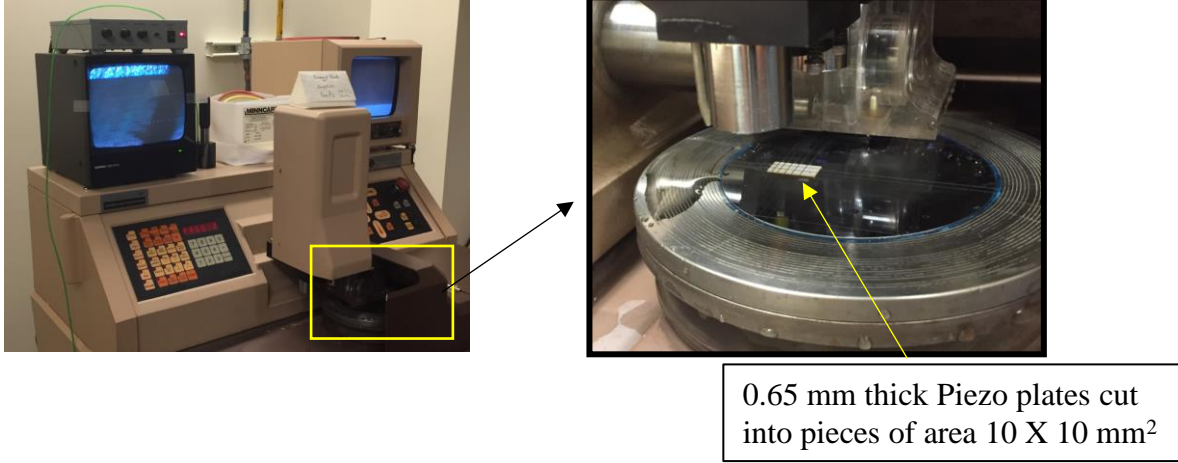


Figure 29: Fabrication of piezo plates by dicing using a diamond wheel (MicroAutomation 1100)

$$f_{resonance} = \frac{n}{L} \sqrt{\frac{E}{\rho}}.$$

Figure 30(e) shows a piezoelectric plate epoxied to the optical flat and provided a sinusoidal voltage input, and a sense resistor is connected between the actuator electrode and ground to monitor charge transfer for which changes in amplitude correspond to changes in displacement. The input and the output signals are shown in Figure 30(c). by increasing the frequency of the applied voltage to the actuator at 180 kHz, an increase in the amplitude of the sense voltage and a 90° phase shift is observed in the output signal indicating a resonant frequency of the system that includes both the flat and the piezo epoxied together, see Figure 30(d).

2.7.5.1 Prototype designs to compress the optical flat and experimental evaluation

To validate phase modulation, this setup is introduced into a Michelson interferometer facility as shown in Figure 30(f) when the piezo is input 20 V_{PV} sinusoidal signal. As of the time of writing, the interference monitored by the photodetector did not shown any fringes representing phase modulation. Phase changes of even 5 degrees would produce visible fringe intensity variation in the interferometer output measured by the photodetector, and nothing was observed.

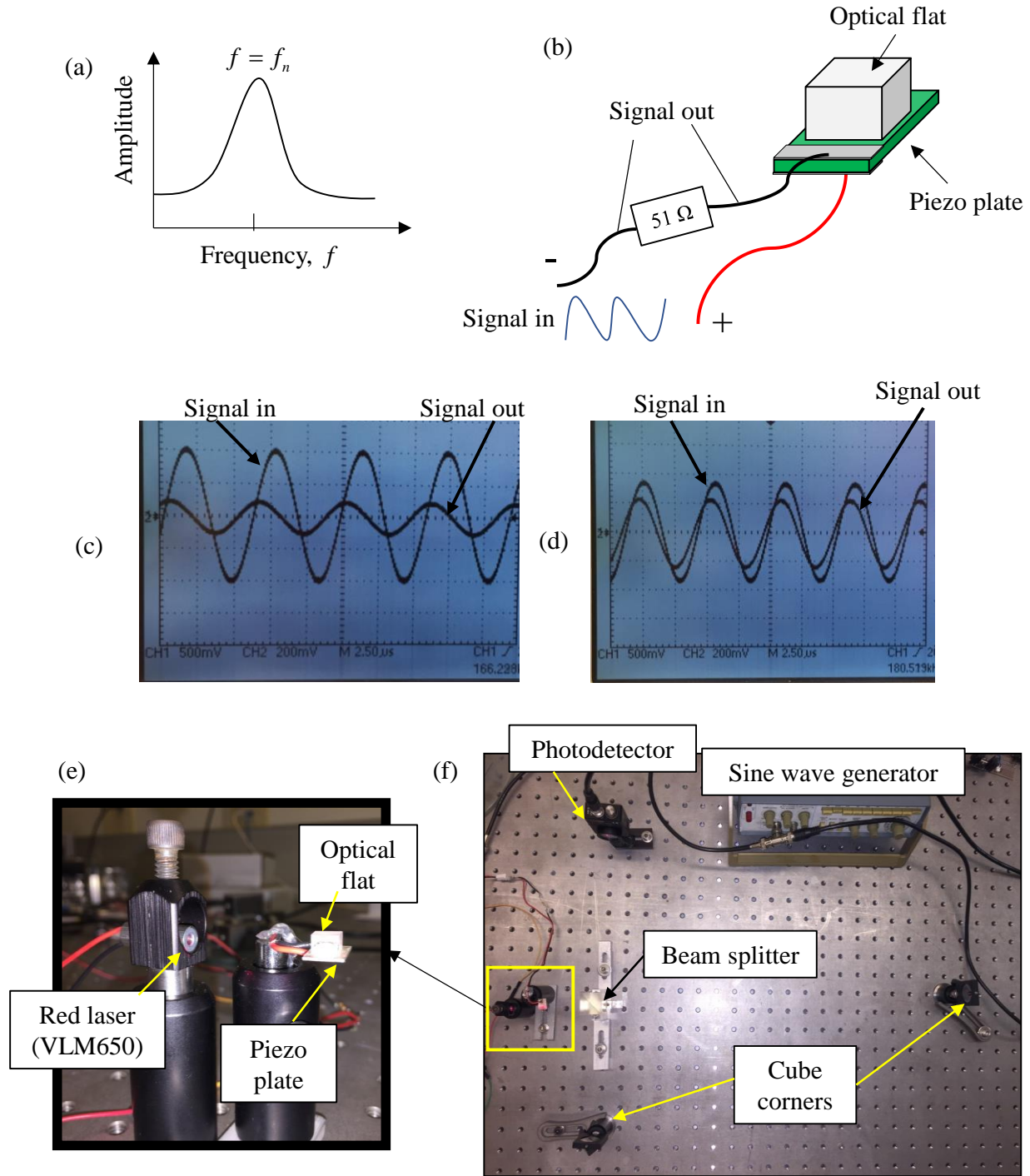


Figure 30: Experimental setup and results of applying stress on an optical flat; (a) Schematic showing the gain of the amplitude at resonant frequency (b) Schematic showing the optical flat attached to the piezo plate (c) Input signal and the sense signal of the piezo not at resonant frequency of the system (d) at resonant frequency showing a 90° phase shift and a gain of 2 (e) picture of the red laser transmitted through the optical flat epoxied to piezo (f) Michelson interferometer to validate phase modulation.

Using equation (9), ignoring the stress optic coefficient (β), to attain a 5° phase change ($\Delta\phi = 0.1$ rad) in a light source of wavelength, $\lambda = 650$ nm, transmitting through a glass optical flat with a refractive index, $n = 1.5$, Poisson's ratio, $\nu = 0.3$, and Elastic modulus, $E = 70$ GPa, it is required to apply a stress of 0.33 MPa. For an expansion as small as $\Delta l = 1$ μm of the flat of length $l = 5$ mm, (strain, $\varepsilon = \Delta l / l$), the expected stress on the flat is $\sigma = E\varepsilon = 14$ MPa.

Following discussions presents the succession of different prototypes to improve the stiffness of the system, none of these produced observable phase variation.

A second prototype with the piezo attached on both top and bottom of the optical flat and a voltage of 60 V_{PV} is provided as shown in Figure 31(a) and (b) using a high voltage amplifier. To provide this voltage at 180 kHz, the amplifier should have a slew rate, $V \cdot 2\pi f_n = 67$ $\text{V} \cdot \mu\text{s}^{-1}$. Therefore, a PA83 (Apex) amplifier with an 80 $\text{V} \cdot \mu\text{s}^{-1}$ slew rate was chosen, see Figure 31(c). This second prototype was also tested within an arm of a Michelson interferometer shown in Figure 31(d).

Since the piezos generally could handle about 5 $\text{kV} \cdot \text{mm}^{-1}$ of its thickness, and the piezo plates we are using is 0.65 mm, they could handle 3.25 $\text{kV} \cdot \text{mm}^{-1}$. Therefore, PA83 amplifier was replaced with a 'ultra-high' voltage amplifier, LEA81-1032 that could provide 0 to 900 V amplified output with a ± 5 V input. But again, the interference monitored by the photodetector did not show any fringes that would indicate phase modulation.

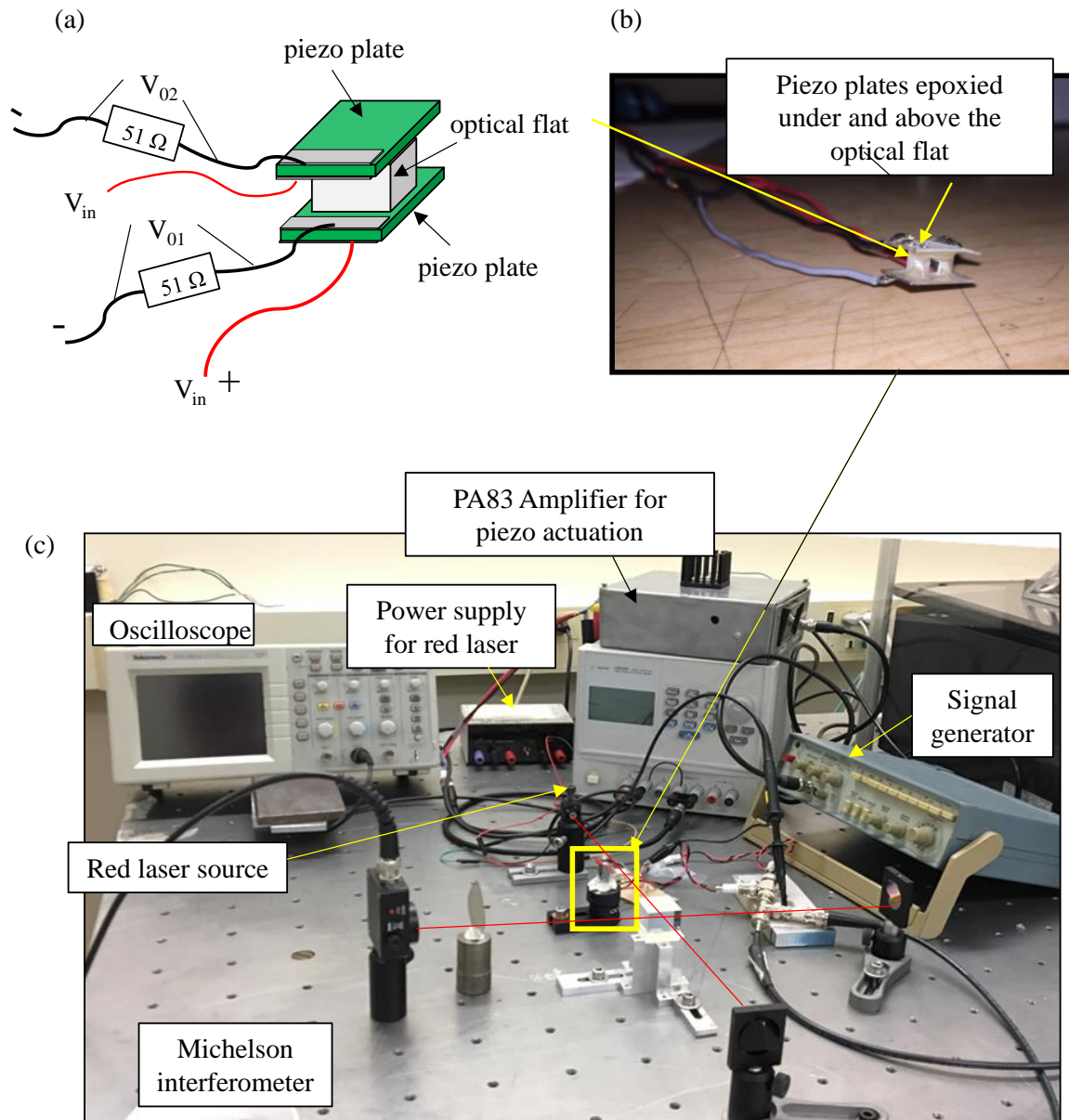
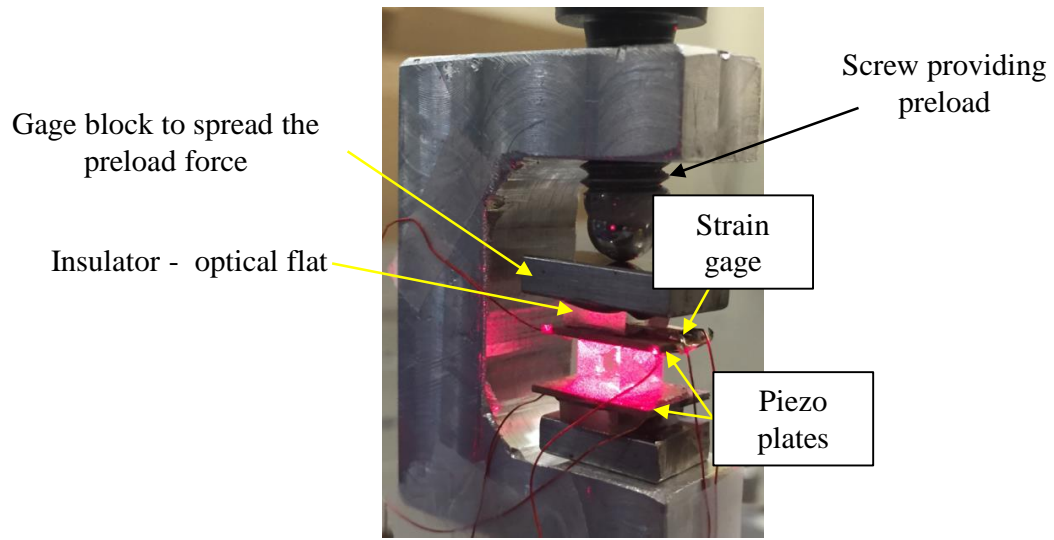
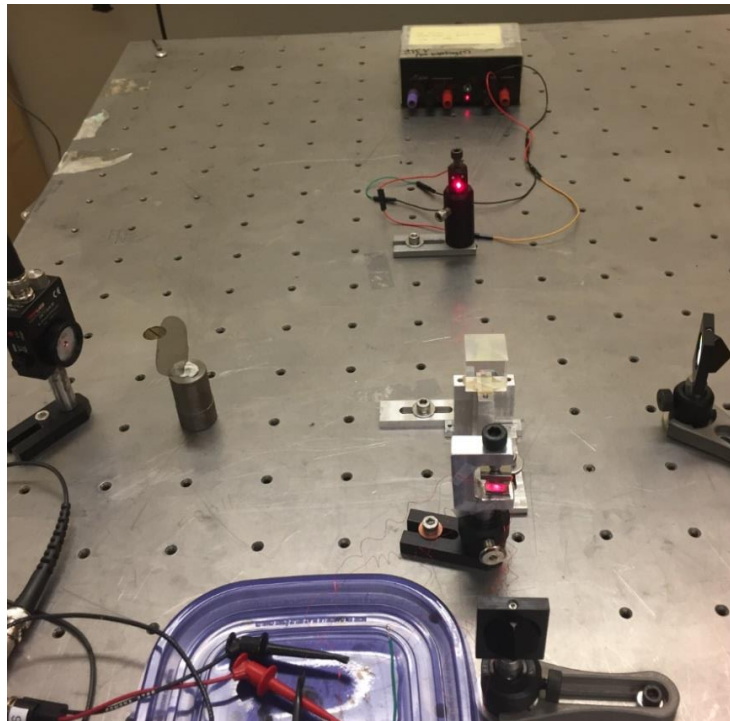


Figure 31: Experimental setup applying stress on top and bottom of an optical flat; (a) Schematic, (b) picture showing the piezos attached to the top and bottom of the optical flat (c) Michelson interferometer used to validate any occurrence of phase modulation.



(a)



(b)

Figure 32: Experimental setup using a stiff clamping assembly; (a) picture showing the screw preloading the piezos attached to the top and bottom of the optical flat (c) Michelson interferometer used to validate any occurrence of phase.

To stiffen up the system, the piezos were epoxied to the top and bottom of the optical flat were and preloaded using a screw through the frame, as shown in Figure 32. This prototype was again tested in a Michelson interferometer, and the interference monitored by the photodetector did not shown any fringes representing phase modulation.

A fourth prototype similar to the clamp setup discussed in section 2.7.3 (a) is tested at one of the arm of the Michelson interferometer shown in Figure 33, but again, the interference signal monitored by the photodetector did not shown any fringes representing phase modulation.

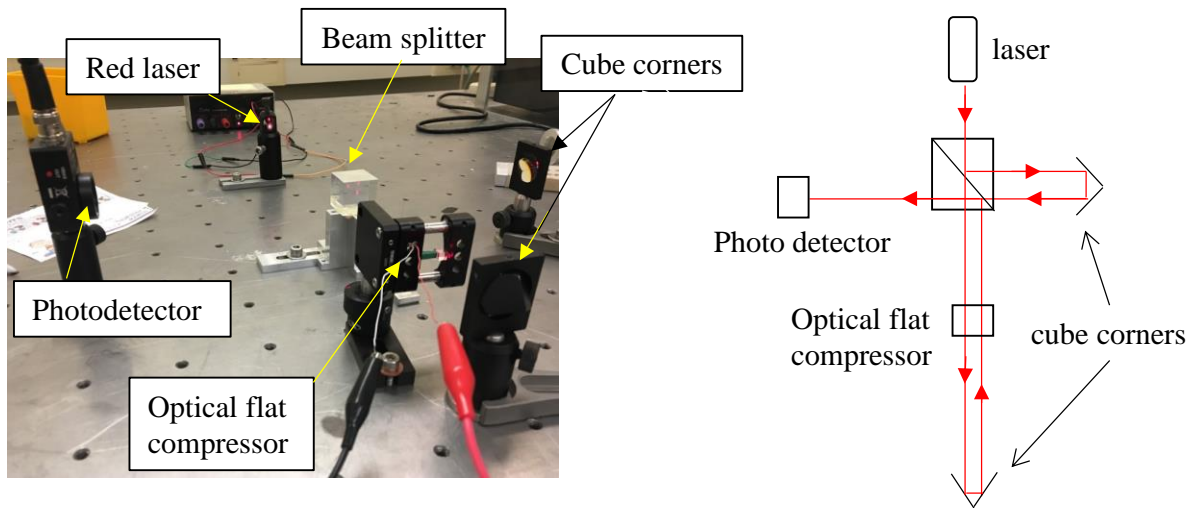


Figure 33: Experimental setup using a piezo stack to compress an optical flat (a) photograph (b) Schematic of the Michelson interferometer used to validate phase modulation of the optical flat compressed by a piezo stack.

Since the optical flat made of BK7 did not result in a detectable phase modulation, as a future work, a different medium such as a Quartz crystal good be coated with electrically conductive layer (copper) with a hole in the middle of the layer to transmit the light.

2.8 Future work

2.8.1 Laser diode coupled to the fiber using a self-aligning bearing

To use a self-fabricated phase or frequency modulated source resulting from the future work, the source must be coupled to a fiber to use it as a profiler. To angularly align the laser to the fiber, Figure 34(a) shows a coupling arrangement in which the laser source is inserted into the inner race of a self-aligning bearing and rotated in pitch and yaw degrees of freedom. Once the angular alignment is achieved, the laser is locked in place using three screws.

2.8.2 Rubidium clock source

To avoid using a lock-in amplifier which are typically limited to few kHz for signal processing to get quadrature harmonics, it can be replaced with an FPGA board. To provide a clock source to it, a Rubidium clock (FE-5680A) providing 10 MHz output with a drift of 2×10^{-11} ticks/day is chosen. The clock and the wiring diagram are shown in Figure 35.

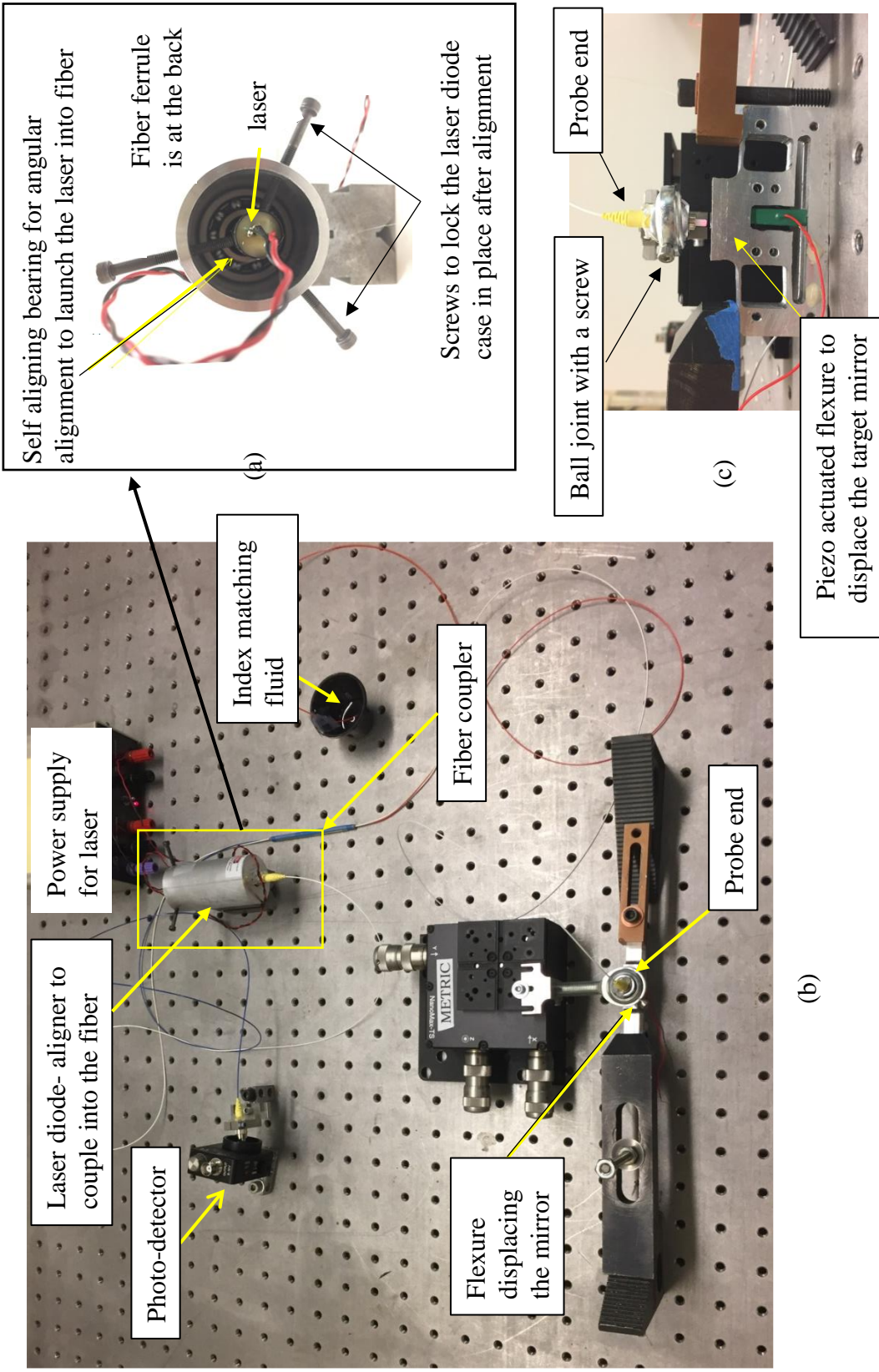


Figure 34: Laser diode coupled to the single mode fiber using a self-aligning bearing (a) A coupler arrangement to align and lock the laser to a fiber ferrule inserted at the back (b) An interferometer facility using the 2X2 fiber coupler (c) Ferrule at the probe end inserted in a ball joint for angular alignment with respect to the target mirror.

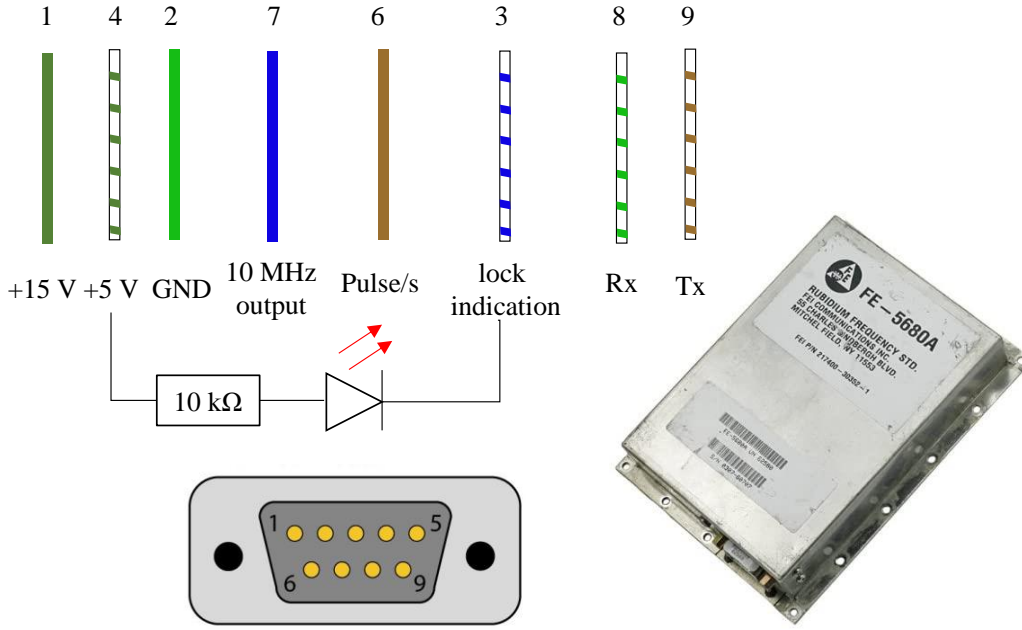


Figure 35: Wiring diagram of Rubidium clock with DB-9 connector.

2.9 Conclusions

An experimental facility using the principle of fiber-based Fabry Perot interferometry has been built and used to measure surface deviations of two sinusoidal reference samples (1 μm PV, 100 μm wavelength, and 1.5 μm PV and 50 μm wavelength) and a ground surface sample. From these measurements, the modulation frequency (400 Hz) of the laser wavelength was found to be a limitation in the speed with which surfaces can be scanned. This is because the modulation required a mechanical oscillation of a laser external cavity diffraction grating. Potentially higher modulation frequencies up to hundreds of kHz are possible by mechanically applying sinusoidal stress to optical crystal components of the laser source. To demonstrate the feasibility of this technique, preliminary studies involving stress applied on a KTP-Vanadate crystal pair inside a green microchip laser source was performed and is discussed in section 2.7.3. Frequency modulation was observed in these studies, and because of the extreme alignment requirements to maintain coupling between the pump laser and the optically glued crystals, the intensity of the

laser was found to decrease at the maximum values of the periodically applied stress. As another approach to dynamically strain an optical element, a piezo-electric plate was attached to a fused silica flat and resonant frequencies up to 180 kHz are demonstrated in section 2.7.5. However, when this assembly was tested in a Michelson interferometer facility, no measurable phase modulation was observed. As a future work an electrode coated Quartz crystal could be used as a medium.

3. OBJECTIVE LENS OSCILLATED MONOCHROMATIC CONFOCAL MICROSCOPE

3.1 Background of the development of confocal microscopy

Since its invention by Minsky in 1955 [Minsky, 1987], confocal microscopy probes are being utilized in the field of biology to locate cell structures often using fluorescence and other dye markers. One of its earlier applications in a manufacturing environment is found in semiconductor industries because of their capability to discern step height changes. Nowadays, confocal probes typically use lasers or LED as its light source, but in its earliest implementation, Minsky used Carbon and Zirconium arc lamps. A variant of this technique, Chromatic confocal microscopy, exploits the chromatic aberration of a simple objective lens using a light source of wider bandwidth, referred to as ‘white light’. Its typical implementation uses a spectrometer to detect the amplitude variation in the spectrum and calculates the surface height variation.

3.2 Motivations for the study

The motivation behind this study is to develop a simple and well understood confocal probe for which the metrological performance can be evaluated. The purpose of this development is to perform measurements of reference surfaces and compare it to the measurements performed by different optical probes including chromatic confocal, and Coherence scanning interferometry. In a chromatic confocal probe, different wavelengths of the broadband light source focuses to different working distances in its optical axis due to the chromatic aberration. To illustrate why a comparison between different optical probes may provide information of their performance limitations, profile measurements of a Silicon nitride roller bearing element measured using a

chromatic confocal probe contained spurious spikes of 2 μm height. These spikes were repeatable for the measurements performed at a given working distance, but would disappear and others appear at unpredictable locations when the measurements are performed at different working distances varied in steps of 50 μm .

Another goal of our work is to use affordable optical elements such as Red diode laser diode, beam splitter, and commercial objective lenses and build a monochromatic confocal probe for surface profiling. A novel feature of this probe is that it will also include a piezo actuated flexure mechanism to oscillate the objective lens stack along its optical axis normal to the surface being profiled. This displacement serves as a means of measuring surface height deviations directly.

Examples of flexure-based oscillation of objective lenses can found in

1. Surface measuring instruments such as Wyko's RST plus which operates both as a Phase shifting Interferometer, and a Coherence Scanning interferometer.
2. P-721 PIFOC high-precision objective scanner sold by Physik instruments for microscopy applications.

These implementations use a parallelogram flexure mechanism that moves the whole objective lens casing (weighing 120 g in the latter example) therefore being a substantial vibration excitation source, and also limiting the bandwidth of oscillation due to the relatively large mass. Our implementation uses an objective lens casing within which flexure leafs are fabricated as a monolith to act as a translation guide. Since only a portion of the casing that carries the lens is oscillated, it could potentially reduce the vibration of the instrument structure and also increase the bandwidth of oscillation.

3.3 Working principle

The embodiment of confocal microscopy used in our work is schematically shown in Figure 36(a), which uses a collimated light source split by a beam splitter cube, into two. One of the two beams reflects and gets diffused by the lapped and later black painted surface of the beam splitter, and the other transmits through the beam splitter. The transmitted beam travels through the objective lens assembly, which is sinusoidally oscillated using a piezo actuator, guided by a flexure mechanism (not shown in the schematic). Due to the period of sinusoidal oscillation, the vertical distance between the focal point and the surface varies continuously. At the instance when the surface coincides with the focal point, the light beam gets reflected back into the objective lens and emerges collimated. And, at other instances of oscillation, the light diverges and scatters along the optical path. Half of the ‘back collimated’ light transmits through the beam splitter to reach the laser, and since the wavelength stability is not a big concern for confocal microscopy, no efforts were taken to block the returning light (for example using objects such as Faraday isolators). Another half of the back collimated light gets reflected from the splitter into another lens assembly where it gets focused through a pinhole to reach a photodetector. For a single period of sinusoidal oscillation, the surface comes in contact with the focused beam two times, once on its way up and other on its way down. Therefore, two intensity peaks are observed per oscillation as shown in Figure 36(b), where the surface being scanned in x axis in steps. The value of the peak intensity observed during the oscillation for a given x step is related to the voltage of the piezo [Uduppa, 2000]. This voltage is converted to the proportional displacement of the piezo, thereby calculating the relative surface height variation for each step in x axis. It is noted that the intensity peak is related to the piezo voltage only for one of the travel directions (either forward or reverse) to avoid the effect of hysteresis in the expansion and contraction of the piezo.

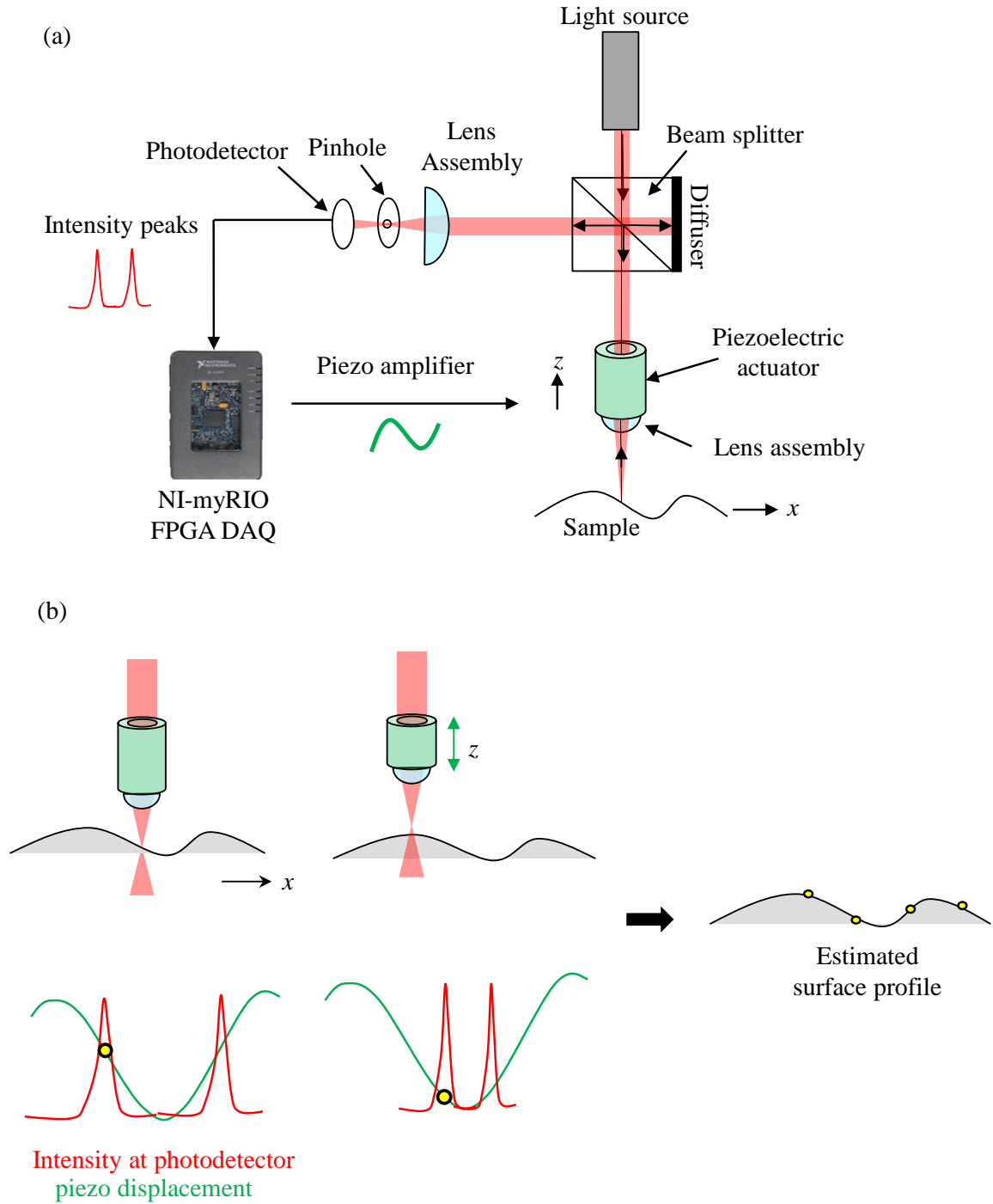


Figure 36: Schematic and a measurement concept of surface profiling using a confocal microscope; (a) Schematic of the monochromatic uniaxial scanning confocal probe showing the intensity peaks observed during the oscillation of the objective lens assembly (b) Schematic showing the scanning of a surface in x axis in steps and the relationship in the observed intensity peak to the displacement of the piezo and the estimated surface profile.

3.4 Literature review

After the description of the confocal microcopy technique in Minsky's patent in 1961, a vast amount of research involving confocal microscopy has been conducted. The papers that are discussed in this literature review are selected for their emphasis on; techniques to improve axial response of the system Full Width Half Maximum (hereafter referred to as FWHM) of the intensity peak, techniques to scan the objective lens and the sample surface, and broader review articles on confocal microscopy. Other topics such as chromatic confocal microscopy, and techniques using fluorescence for scanning biological specimens are not discussed here.

3.4.1 Review articles

Confocal scanning optical microscopy [Kino and Corle, 1989]

Basics of Confocal microscopy and the use of Nipkow disks (a disk typically with a spiral hole pattern) as a scanning mechanism to create an area scan of the sample are discussed. Litchmann's 1994 review article in Scientific American also explains, schematically, the operation of Nipkow disk.

3.4.2 Improvements in axial response sensitivity

Improvement in resolution by near confocal microscopy [Cox et al., 1982]

Improvement in the axial response when the pinhole is offset in its plane is reported. The increased sensitivity is due to the effect of the observed airy pattern (or point spread function) when the sample surface is moved towards or away from the focal point in its optical axis.

Optical profilometer: a new method for high sensitivity and wide dynamic range [Fainman et al., 1982]

The back collimated light from the surface is converged by a lens at the detector end. Before it converges, the light beam is split into two beams using a beam splitter. On one side, a pinhole is kept before the converging point, and on the other side, another pinhole is kept after the converging point. The light beams that pass through the pinholes are recorded by two photodetectors and their outputs are provided as inputs to a differential amplifier. The output of the amplifier is used to measure the surface height variation. A theoretical explanation is given for a reason to use a lens with a longer focal length at the detector side than the objective lens at the sample side and prompted the simplified analysis shown in section 3.5.

Real-time laser differential confocal microscopy without sample reflectivity effects, [Qiu et al., 2014]

This is another article that discusses the same technique of using two photodetectors with theoretical simulations of response curves and measurement results of different sample surfaces.

Non-interferometric differential confocal microscopy with 2-nm depth resolution, [Lee and Wang, 1997]

Since the slope of the intensity peak detected by the photodetector is the least at the apex of the intensity peak, its trailing edge is used as a means of measuring surface height variation.

3.4.3 Scanning techniques

Vertical optical sectioning using a magnetically driven confocal micro scanner aimed for in vivo clinical imaging [Mansoor et al., 2011]

Axial scanning of the objective lens guided by a folded planar leaf spring is demonstrated with a resonant frequency of 378 Hz, and lateral scanning of the sample is achieved by oscillating a fiber to which the light source is coupled at 2 Hz. Solenoids were used as actuators.

MEMS-in-the-lens architecture for a miniature high-NA laser scanning microscope [Liu et al., 2019]

A 3-dimensional MEMS scanner is developed and demonstrated for lateral surface scanning in a transmission type confocal microscope. The scanner is based on a two-axis gimbal actuated by quadrant electrodes placed underneath it.

3.4.4 Other studies

Highly accurate non-contact characterization of engineering surfaces using confocal microscopy [Jordan et al., 1998]

Measurement results of scanning confocal microscopy and micro lens array confocal microscopy are compared with the results using a tactile sensor (Nanostep, 0.1 μm tip radius). Reference samples such as Vickers hardness dent, PTB roughness standard, and a 23 μm high 600 μm wavelength spherical grating are measured and compared.

Confocal axial peak extraction algorithm [Liu et al, 2016]

Intensity peak fitting algorithms such as parabolic, Gauss, and Sinc^2 curves are compared, and Sinc^2 curve fitting yields a more reliable estimate of the peak position.

Fiber optic confocal microscope: FOCON [Dabbs and Glass, 1992]

A 1 x 2 single mode fiber optic cable replaces the beam splitter and the detector pinhole used in the conventional system. Measurement results are comparable to a conventional system.

3.5 Theoretical model for the sensitivity of the confocal FWHM to the focal length of the detector lens

Figure 37(a) shows the configuration of the confocal probe used in our studies. The sample surface is at the focal length (f_1) of the objective lens at the object end (Lens 1), and a pinhole is kept at the focal length (f_2) of the objective lens at the detector end (Lens 2). This configuration is unwrapped and shown in Figure 37(b) with the distance between the lenses being L . Figure 37(c) shows that when the sample is moved a distance, d_1 away from the focal point of the Lens 1, its image is formed at a distance, d_1' away from the back focal length, f_1 of Lens 1 given by the thin lens equation,

$$\begin{aligned}\frac{1}{f_1} &= \frac{1}{f_1 + d_1} + \frac{1}{f_1 + d_1'} \\ \frac{1}{f_1} - \frac{1}{f_1 + d_1} &= \frac{1}{f_1 + d_1'} \\ \frac{d_1}{f_1^2 + f_1 d_1} &= \frac{1}{f_1 + d_1'} \\ d_1' &= \frac{f_1^2 + f_1 d_1}{d_1} - f_1 \\ d_1' &= \frac{f_1^2}{d_1}\end{aligned}$$

The image plane of Lens 1 becomes the object plane of Lens 2, which is at a distance d_2 from its focal point. The final image forms at distance d_2' from the back focal length of Lens 2 given by,

$$d_2' = \frac{f_2^2}{d_2} = \frac{f_2^2}{L - (f_1 + d_1' + f_2)}$$

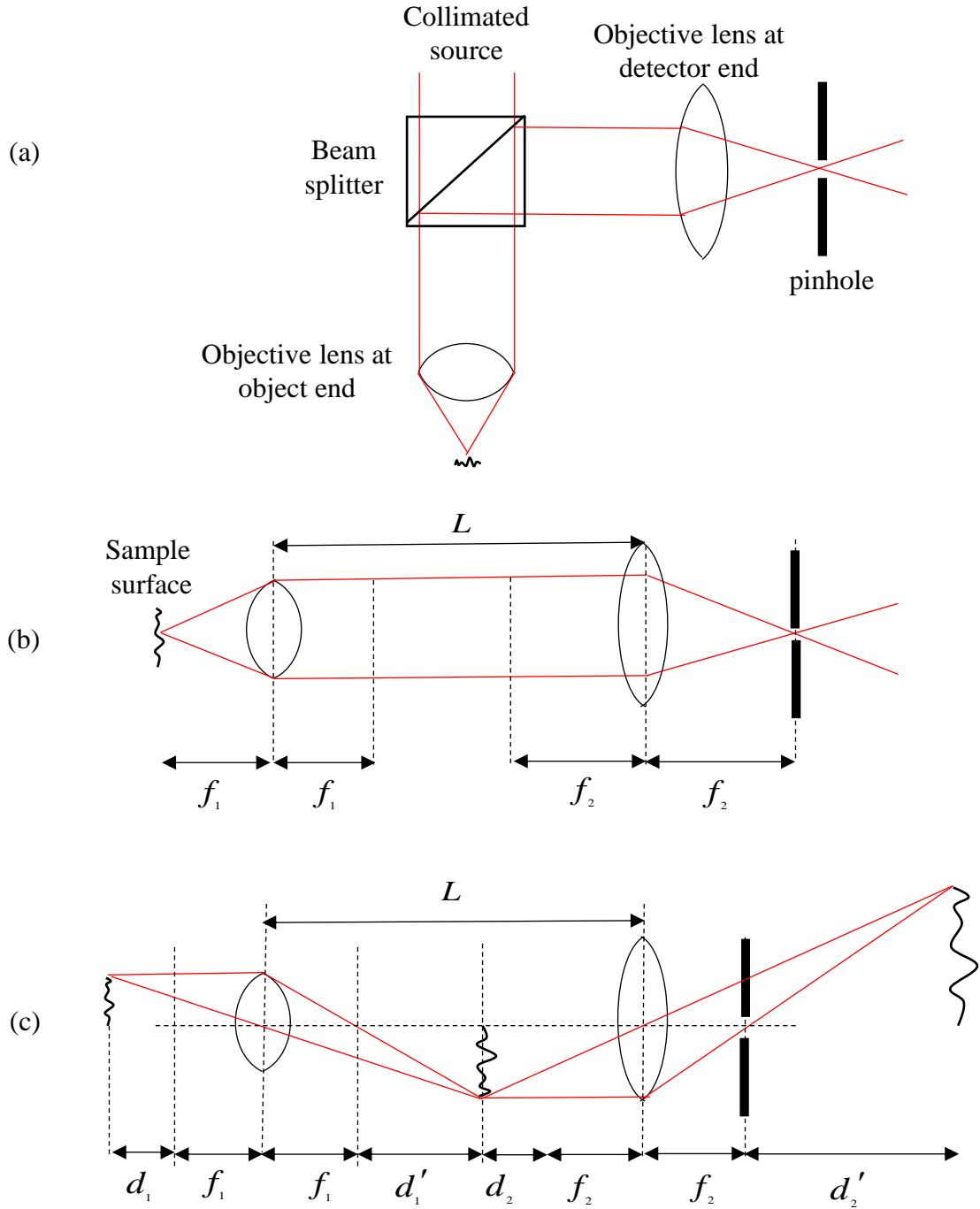


Figure 37: Ray diagram showing the sensitivity of the axial response to the focal length of the lens used at the detector end; (a) Configuration of the lenses used in our system (b) configuration unwrapped in a plane (c) ray diagram showing the object and image planes of the two lenses when the sample surface is away from the focal point of the objective lens at the object end.

$$d_2' = \frac{f_2^2}{L - \left(f_1 + \frac{f_1^2}{d_1} + f_2 \right)} = \frac{f_2^2 d_1}{(L - f_1 - f_2) d_1 - f_1^2}$$

From this equation, the sensitivity of the axial response of the probe is,

$$\begin{aligned} \frac{\partial d_2'}{\partial d_1} &= \frac{f_2^2 \left((L - f_1 - f_2) d_1 - f_1^2 \right) - (f_2^2 d_1 (L - f_1 - f_2))}{\left((L - f_1 - f_2) d_1 - f_1^2 \right)^2} \\ &= \frac{-f_1^2 f_2^2}{\left((L - f_1 - f_2) d_1 - f_1^2 \right)^2} \end{aligned}$$

When the sample surface is at focus, $d_1 = 0$, the sensitivity becomes

$$\frac{\partial d_2'}{\partial d_1} = -\frac{f_2^2}{f_1^2}$$

Therefore, a higher sensitivity is achieved when the focal length of Lens 2 (objective lens at the detector end), f_2 is longer than the focal length of Lens 1 (objective lens at the object end). Therefore, in the recent prototype, when the 60X objective lens at the detector end is replaced with a 20X objective lens, an improved axial response of 10 μm FWHM is achieved. It is also clear that this can, at least with this simple theory, be improved almost arbitrarily by increasing further the focal length of the detection lens.

3.6 Experiments

This section discusses the details of the prototypes that were built to understand the issues in fabricating a confocal probe, and to realize an optimal light source that improves the lateral resolution in the surface measurements.

3.6.1 First prototype using a diode laser source, 40X objective lens, and two pinholes

Figure 38(a) shows the very first prototype which uses a 10 X objective lens at the object end, and a lens of $f = 26$ mm focal length at the detector end of the probe. A red laser diode (Quarton, VLM650, 2.5 mW, 5 V supply) of 650 nm is used as the light source. Dowel pins were fixtured to be parallel using gage blocks and epoxied to microscope glass slides as guides and are used to align the components to the optical axis, and to manually translate a glass microscope slide sample of 0.2 mm thickness at the object end. The motion of the glass sample causes two intensity peaks that corresponds to the reflections from the front and back surfaces of the glass sample, see Figure 38(b). This provided a proof of concept to build the next prototype to improve the axial response. i.e. the FWHM of the observed intensity peaks.

Side views of the Solid model of the next prototype are shown in Figure 39(a and b). This prototype uses a 40X objective lens (AmScope, A40X-V300) to improve the sharpness (FWHM) of the observed peaks, and to reduce the sensitivity of the signal to the tilt of the sample. Two stages of pinhole is used at the detector side, where Pinhole 1 is placed at the focal point of the biconvex lens (Comar 05 VP 04, 5.4 mm focal length, 7.8 mm Dia.) which focuses the back collimated light from the sample surface. The light through the Pinhole 1 diverges and transmits though the Pinhole 2 to reach the photodetector (Osram, BPX61). Use of the second pinhole is to further enhances the sharpness of the observed intensity peaks.

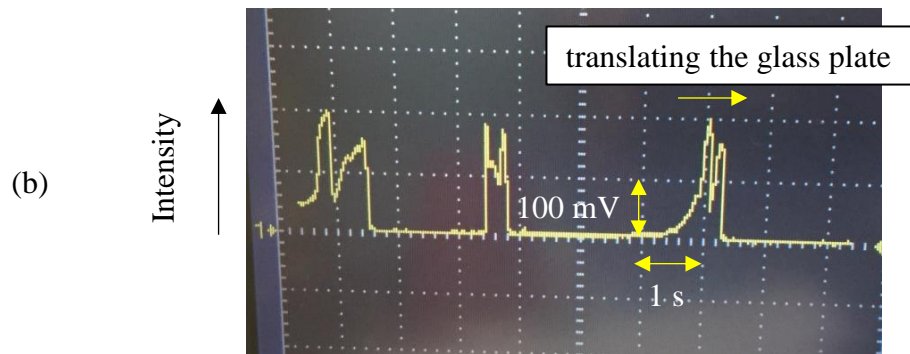
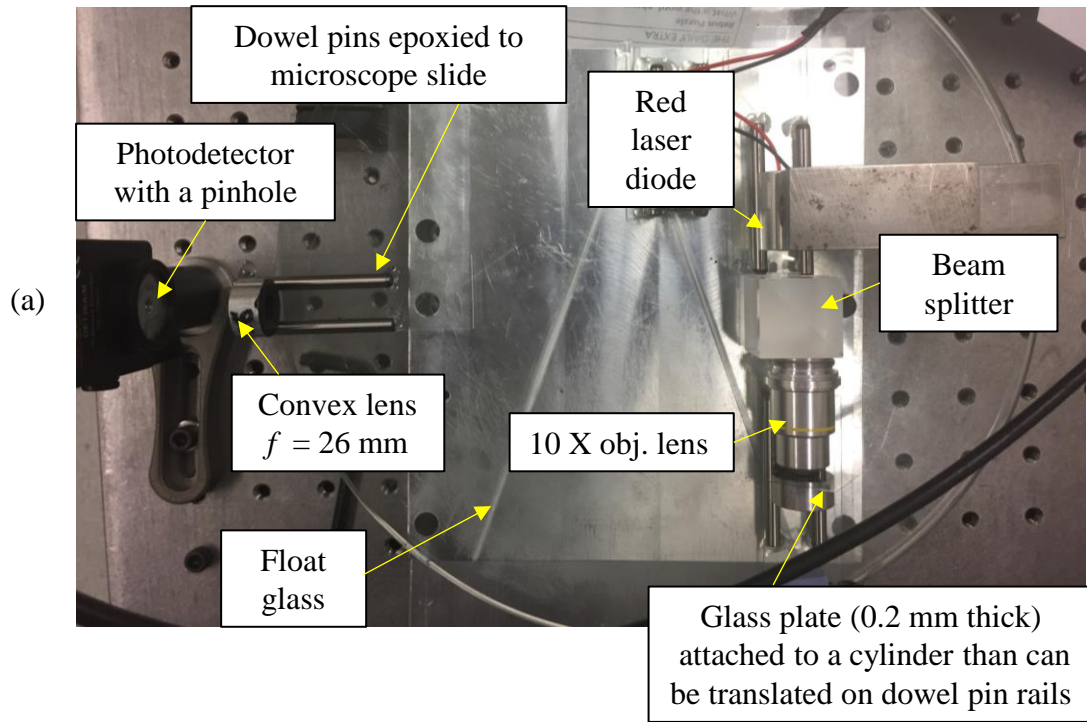


Figure 38: First prototype of the confocal probe assembly; (a) which uses dowel pin rails for translation of the components of the assembly (b) Intensity observed at the photodetector during the motion of the glass sample of 0.2 mm thickness.

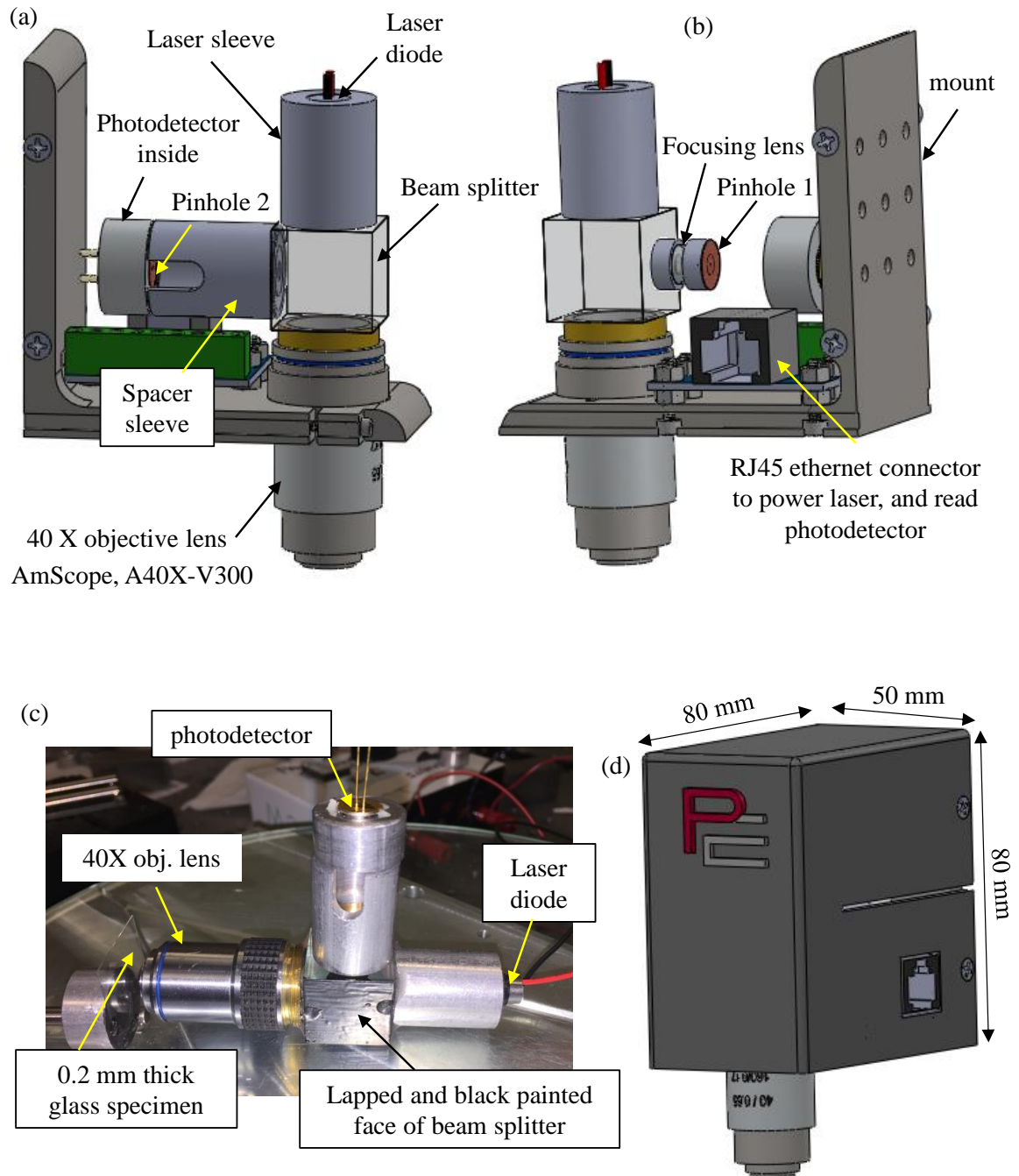


Figure 39: First fabricated prototype of the confocal microscope; (a, b) side views of the solid model showing the two stages of pinhole used at the detector end of the probe (c) Fabricated prototype (d) Solid model of the probe inside the case with an ethernet connector. Solid model courtesy: Dr. Stuart Smith.

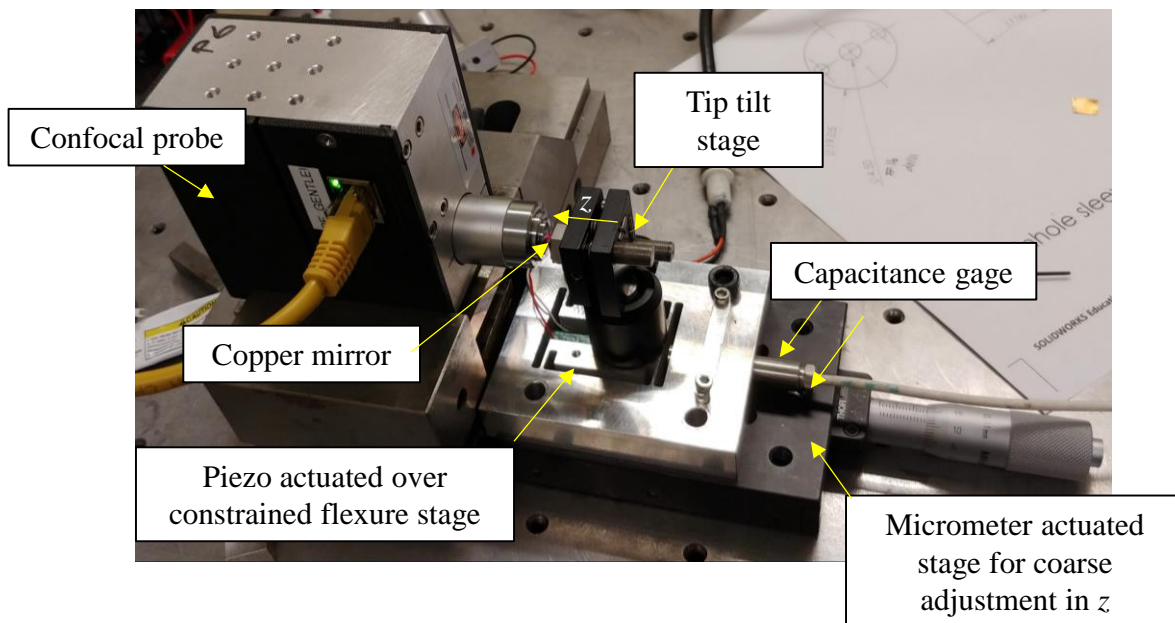
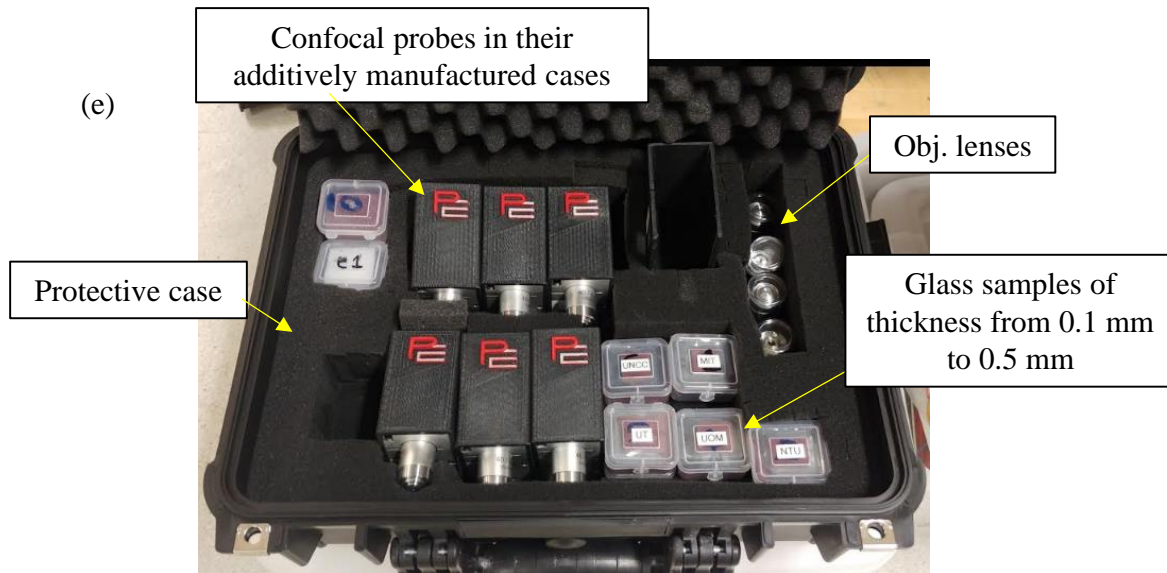


Figure 40: Experimental setup to measure the axial response of the probe; (a) Six of the eight probes used in the student challenge conducted at the ASPE conference (b) Probe being tested to know the FWHM of the intensity peaks when a Copper sample is translated using a piezo actuated flexure stage whose displacement is monitored by a capacitance gage.

Figure 39(c) shows the fabricated prototype. Details of the fabrication process is pictorially explained in Appendix B.1. Figure 39(d) shows the solid model of the probe casing with an RJ45 ethernet connector that supplies the power to the laser, photodetector and its amplifier from a myRIO microcontroller. The intensity measurement from the photodetector signal after amplification is sent to the myRIO through the same connector. Figure 40(a) shows the six of the eight probes that were built for an international Student challenge organized by the American Society of Precision Engineering (ASPE) in their annual conference in 2018. The probes were utilized by the students to measure the thickness of glass samples varying from 0.1 mm to 0.5 mm.

Figure 40(a) shows one of the probes (P6) being tested for the FWHM of the intensity peaks observed when a copper mirror at a working distance of about 0.5 mm is towards the objective lens using a flexure stage actuated by a piezo. The intensity peaks observed during a sinusoidal translation of the copper mirror are shown in Figure 41. It is interesting to observe two peaks for a travel in one direction, and the combined FWHM of the two peaks is 100 μm . It was also found that the distance between these peaks increases when the tilt of the copper sample is increased, indicating that the two observed peaks could be due to the squareness in the travel of the stage. It is also noted that the dual peaks were not observed in the other probes that were built.

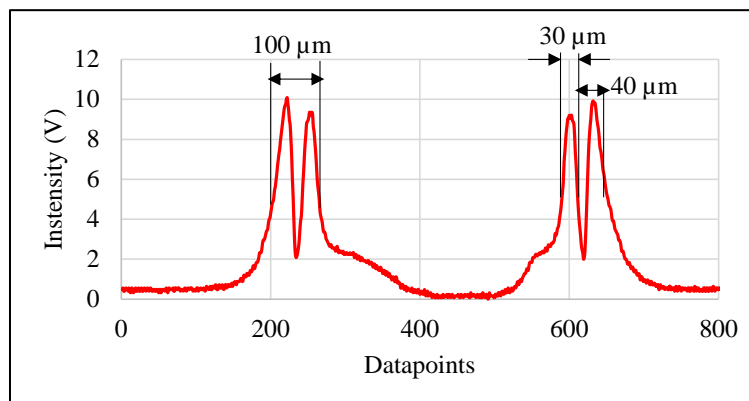


Figure 41: Intensity peaks observed by the probe for a single period of sinusoidal translation of the copper mirror towards the probe using a flexure stage.

3.6.2 Second prototype using a red mLED source and 60X objective lenses

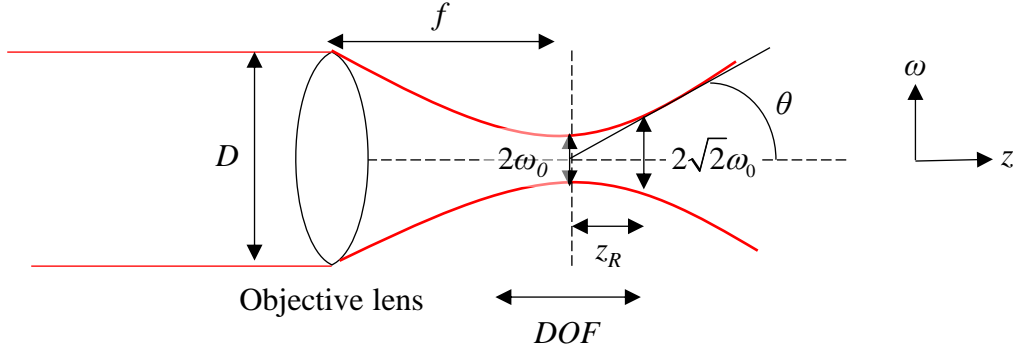


Figure 42: Schematic of a collimated beam converged by a lens indicating the spot size and the depth of focus.

To enhance the axial response (i.e., to reduce the FWHM of the intensity peak), and increase surface slopes that can be detected, it is ideal to illuminate the full aperture of the objective lens with the collimated light beam as shown in Figure 43(a), producing a shorter depth of focus, DOF . Figure 42 shows a collimated light beam of wavelength, λ converged by a lens to a spot with a waist diameter (also referred to as spot size) of $2\omega_0$. Rayleigh length of this converged beam is given by

$$z_R = \frac{\pi\omega_0^2}{\lambda},$$

Rayleigh length is defined as the length along the optical axis (z) from the focused spot at which the area of the cross section of the focused beam doubles. At this distance, the spot size, $2\omega_0$ becomes $2\sqrt{2}\omega_0$. The depth of focus is represented as $DOF = 2z_R$.

The radius of the beam, ω related to the Rayleigh length as a function of distance, z as,

$$\begin{aligned}\omega &= \omega_0 \sqrt{1 + \left(\frac{z}{z_R}\right)^2} \\ &= \frac{\omega_0}{z_R} \sqrt{z_R^2 + z^2}\end{aligned}$$

For a distance, $z \gg z_R$, the small angle approximation of the half divergence angle of the beam is,

$$\theta \approx \tan \theta = \frac{\partial \omega}{\partial z} = \frac{\omega_0}{z_R}.$$

The angle, θ is also given by,

$$\theta = \frac{D/2}{f}$$

where, D and f are the aperture and the focal length of the converging lens, respectively. Using this relation, the spot size is derived as,

$$\begin{aligned}\frac{\omega_0}{z_R} &= \frac{D/2}{f} \\ \omega_0 &= \frac{\pi \omega_0^2}{\lambda} \frac{D/2}{f} \\ 2\omega_0 &= \frac{4\lambda}{\pi} \frac{f}{D}\end{aligned}$$

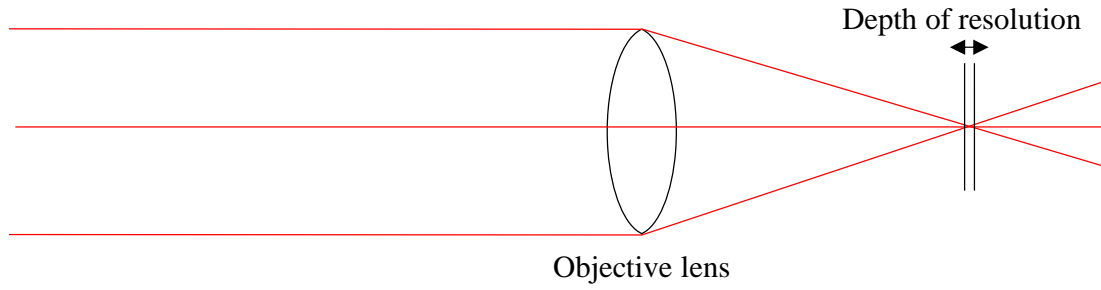
A 60X objective lens with a typical focal length of $f = 3$ mm and an aperture of $D = 5$ mm, converging a red light beam $\lambda = 650$ nm, would be produce a spot size of $0.5 \mu\text{m}$, theoretically. The depth of focus for the same arrangement is $0.6 \mu\text{m}$, given by

$$DOF = \frac{2\pi \omega_0^2}{\lambda} = \frac{8\lambda}{\pi} \left(\frac{f}{D}\right)^2$$

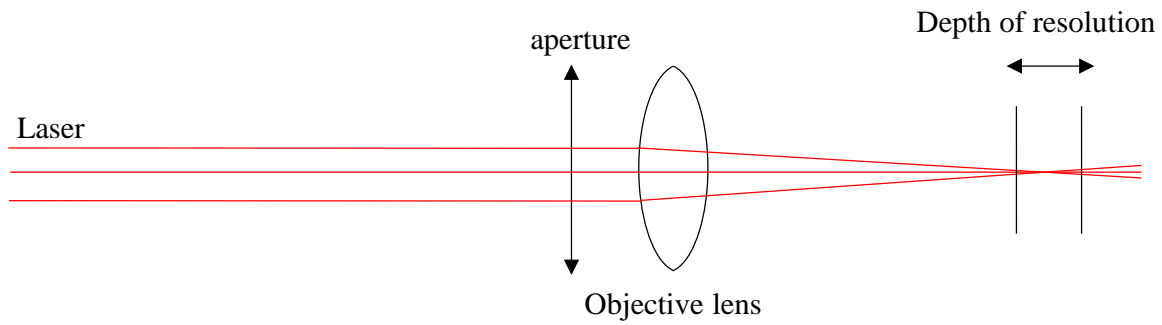
In the earlier prototype, the diameter of the laser beam was only 2 mm illuminating only a portion of the 5 mm aperture of the objective lens. Due to this, the converging light beam will have a larger depth of focus, see Figure 43(b). To overcome this, a micro-Light Emitting Diode (mLED) source is used. Since mLEDs produce a diverging light from a relatively small source (less than 0.5 mm^2 area), it can be considered a point source, see Figure 43(c). The diverging mLED light source is first collimated using a lens and then focused using an objective lens at the object end of the probe.

Also, from the test result shown in Appendix B.2, the spot size produced when a red laser source used with a 40X objective lens in the previous prototype is $290 \text{ }\mu\text{m}$. Since, the spot size determines the lateral resolution of the probe to use it as a surface profiler, the first prototype is not suitable to use in surface roughness or waviness measurement applications. From the spot size experiments performed, it was determined that a spot size of $19 \text{ }\mu\text{m}$ is achievable when a 60X objective lens is used. Appendix B.2 shows the experimental results, and the procedure to calculate the spot size when red laser and red and blue mLED light sources are used with 40X and 60X objective lenses.

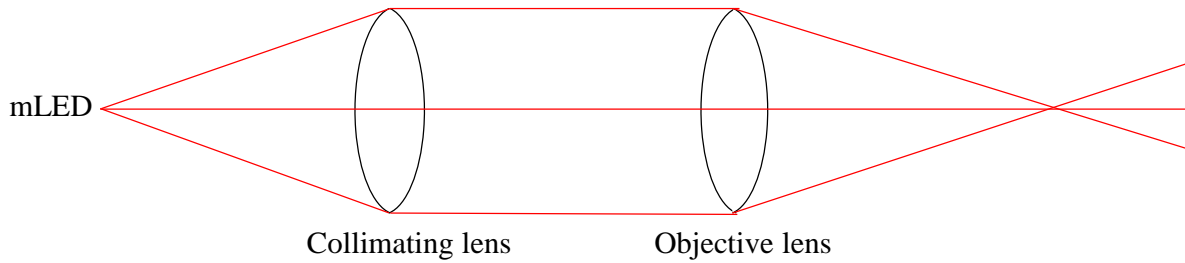
The second prototype shown in Figure 44(a) uses a red mLED (LTST-C191KRKT) collimated by a lens element of 9 mm Dia., and 18 mm back focal length. 60X objective lenses are used at both the object and the detector ends of the probe. Objective lenses of higher magnification than the 60X lens typically operate in an oil immersion medium to provide a larger numerical aperture. Use of oil immersion is not feasible in a large scale manufacturing environments limiting all designs to a 60X objective lens. To enhance the axial response of the probe, a $25 \text{ }\mu\text{m}$ pinhole is used, replacing the self-drilled $300 \text{ }\mu\text{m}$ pinholes used in the previous prototype. Also, for



(a)



(b)



(c)

Figure 43: Ray diagrams of a light source focused by a lens element; (a) collimated light illuminating the full aperture of a lens is getting focused to a shorter depth of resolution (b) collimated light illuminating only a portion of the aperture of a lens is getting focused to a longer depth of resolution (c) full aperture illumination is achieved using a point source.

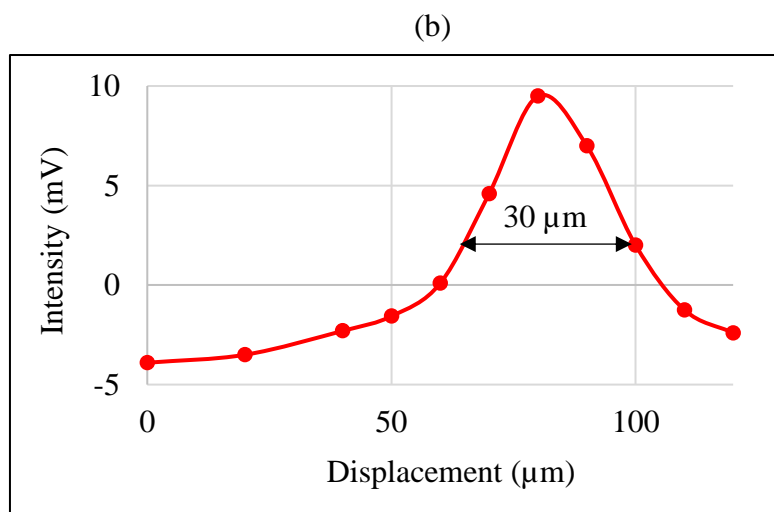
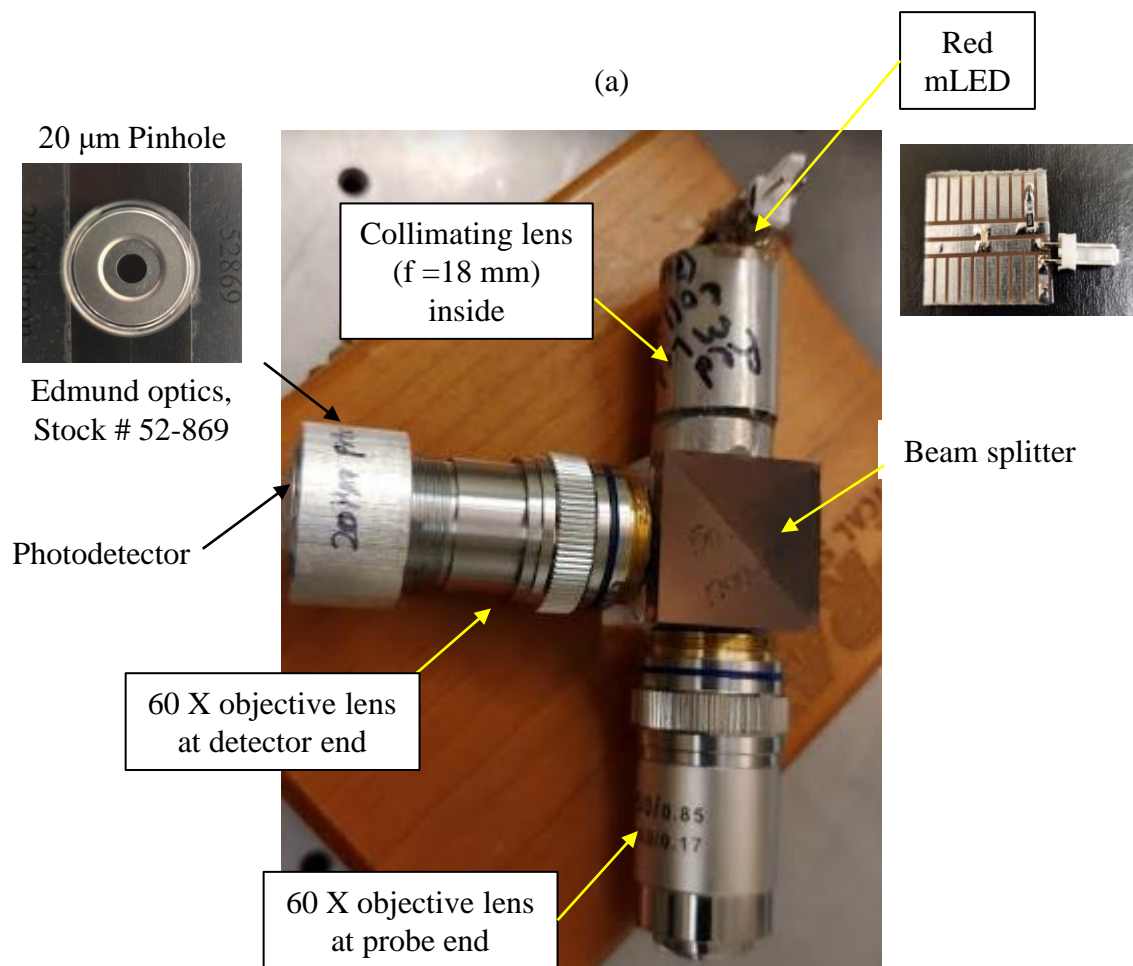


Figure 44: Second prototype using a red mLED source and its axial response; (a) Fabricated Prototype using a red mLED source, 60X objective lenses, and a 20 μm pinhole (b) FWHM of the intensity peak observed during a translation of a copper mirror towards the objective lens at the probe end.

simplicity, a single pinhole is used in this setup. Fabrication of this prototype is detailed in Appendix B.3. Figure 44 (b) shows the intensity peak observed when a copper mirror is translated towards the object lens at the probe end, demonstrating an FWHM of 30 μm . One main drawback of this prototype is that the intensity of the observed peak is only 10 mV, resulting in a low signal to noise ratio during data acquisition.

3.6.3 Third prototype using a red diode laser, and 60X objective lenses

To increase the signal to noise ratio, a 30 mW red laser diode (5 V supply) is used (as opposed to 5 mW red laser and 10 mcd mLED sources of previous prototypes), see Figure 45(a and b). The light beam diverging from the laser diode is focused using a lens that is screwed on the laser diode casing that can be used to change the focal point. The light beam after converging, again diverges to illuminate the aperture of the collimating lens with a 32.7 mm focal length, see Figure 45(b). The light from the collimating lens transmits through the beam splitter cube to the 60X objective lens at the object end. To maintain the collimated light co-axial to the objective lens, a tip-tilt aligner using spherical washers is used as shown in Figure 46(a). The tip-tilt alignment is achieved by actuating the M2.5 screws. Building procedure of an earlier prototype without the tip-tilt aligner, and of the current prototype with the tip tilt aligner are detailed in Appendix B.5.

To improve the axial response of the probe, a pinhole of 5 μm is used with the objective lens at the detector end. To align the pinhole with the optical axis of the objective lens at the detector end, an alignment mechanism shown in Figure 46(b) is used. This mechanism uses three fine screws (8 mm long, M2 \times 0.2 Thorlabs, F2ES8) to adjust the pinhole in its xy plane, see Figure 46(b and c) and another fine screw (15 mm long, M2 \times 0.2 Thorlabs, F2ES15) from the top pushes against a flat region on the spring loaded objective lens casing to provide the adjustment in z axis,

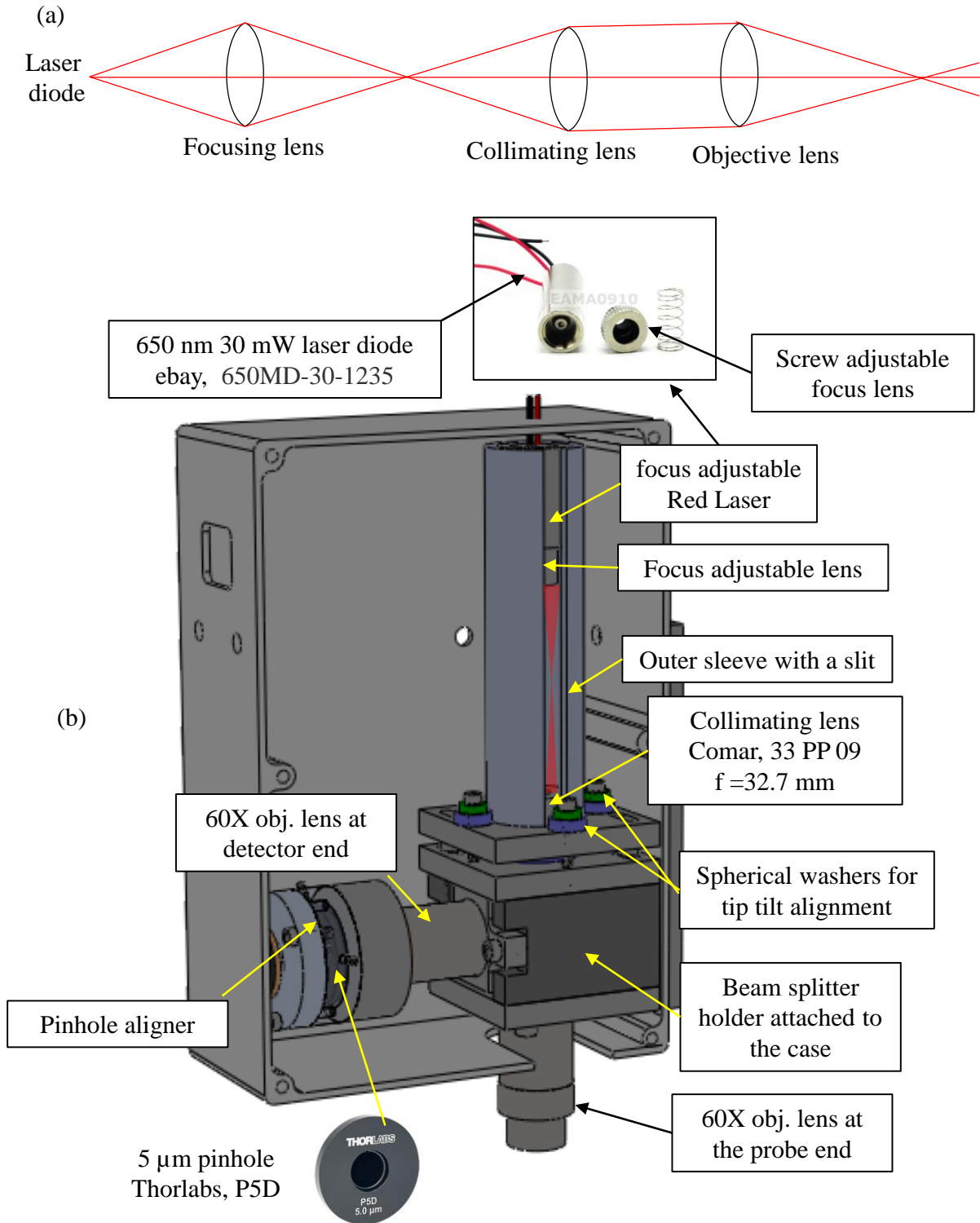


Figure 45: Third prototype using a 30 mW red laser; (a) Ray diagram of the laser source which uses an adjustable focusing lens and a collimating lens to collimate the beam to the objective lens (b) Solid model of the fabricated prototype that uses a focus adjustable red laser, collimating lens, a tip-tilt alignment mechanism, and a pinhole alignment mechanism.

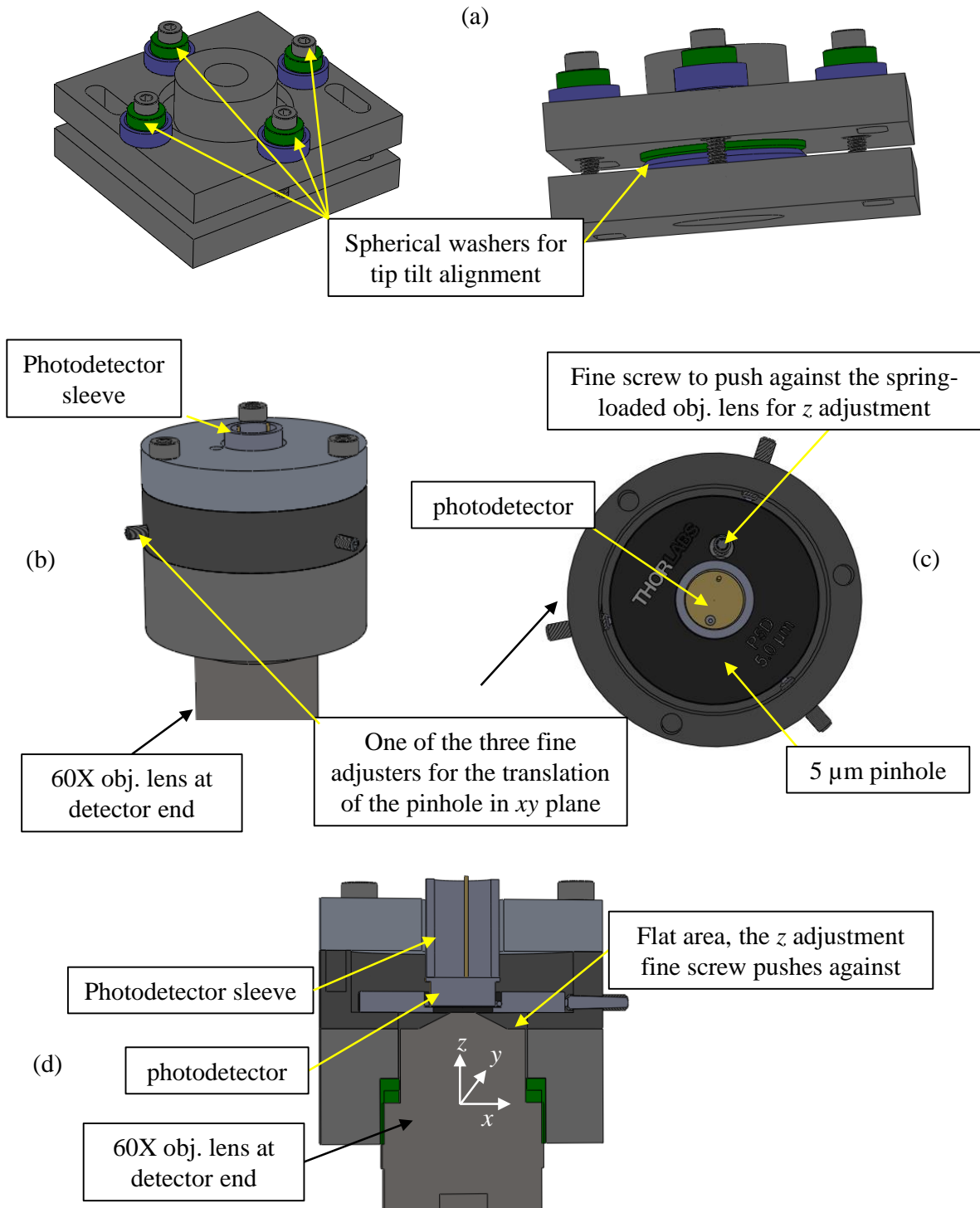


Figure 46: Tip-tilt aligner for the laser source, and the pinhole alignment mechanism; (a) Solid model of the tip-tilt aligner that uses spherical washer on top and the pivot pint between the moving platform and the base (b) Solid model of the pinhole alignment mechanism -isometric view (c) top view showing the three fine screws translating the pinhole in xy plane, and another fine screw pushing against a flat region on the spring loaded objective lens providing adjustment in z axis (d) cross sectional view.

see Figure 46(d). An earlier prototype of a different pinhole alignment mechanism is shown in Appendix B.4.

A probe fabricated using the above discussed components (Figure 45, Figure 46) is shown in Figure 47. To assess the axial response of the fabricated probe, a copper mirror is translated towards the objective lens using an over constrained flexure stage for fine travel, and a micrometer stage for coarse adjustments. To determine the working distance of the objective lens, the copper mirror attached to a tip tilt aligner is translated towards the probe using the micrometer stage until it makes contact and pushes against the spring loaded objective lens. The intensity measured by the photodetector and the displacement of the back surface of the tip-tilt aligner measured using a capacitance probe (Lion precision, C9.5-5.6 with a range of 2 mm) are plotted in Figure 48. The distance between the rising edge of the intensity peak and when the displacement signal of the capacitance gage becomes flat determines the working distance of the probe that was measured to be 0.1 mm. The displacement remains flat until the copper mirror overcomes the spring force and travels further with a slower slope afterwards.

To determine the axial response of the probe, the copper mirror was translated towards/away from the probe and the measured FWHM is 30 μm , see Figure 49. This value is almost same as the previous prototype indicating that aligning the collimated laser beam coaxial to the objective lens and using a smaller pinhole did not make a significant difference.

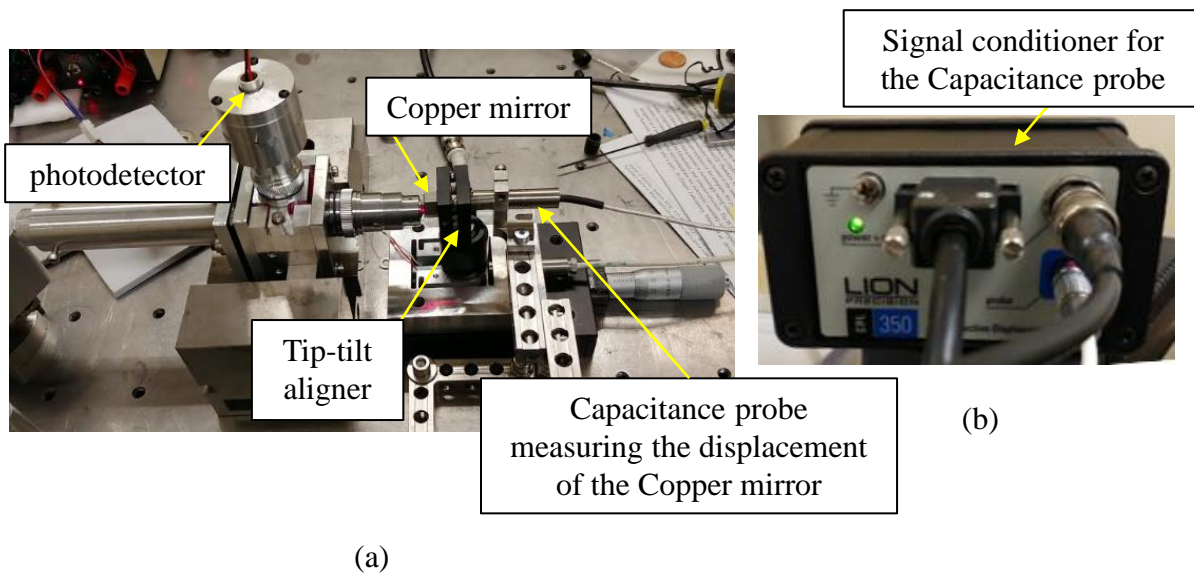


Figure 47: Experiment to measure the working distance and axial response of the probe; (a) photograph of the apparatus, (b) signal conditioning unit for the capacitance probe.

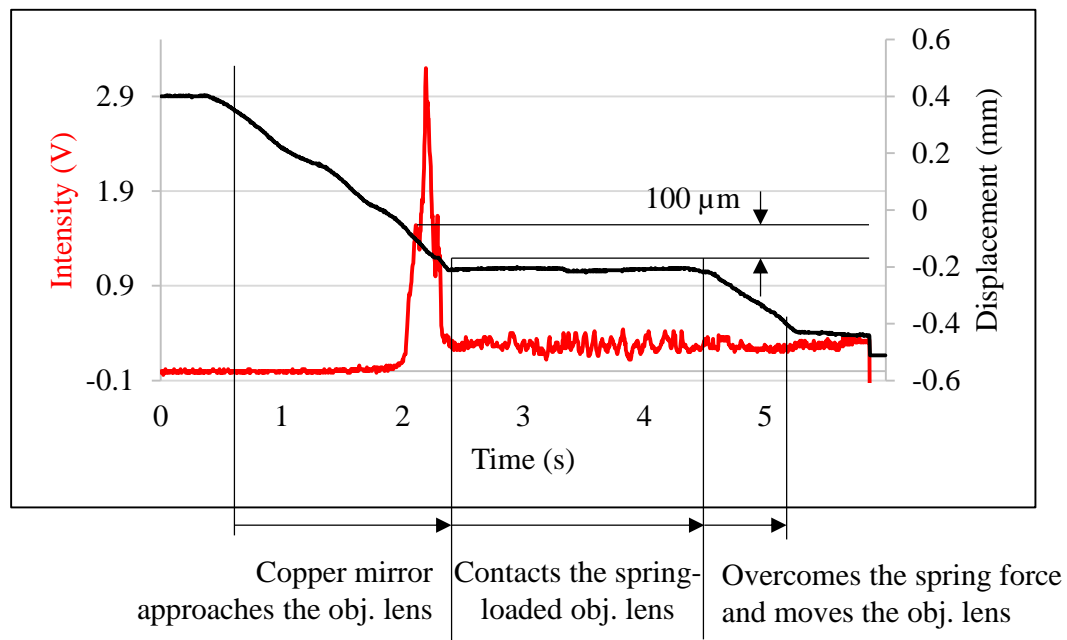


Figure 48: Intensity recorded when the copper mirror is moved until it contacts the spring-loaded object lens.

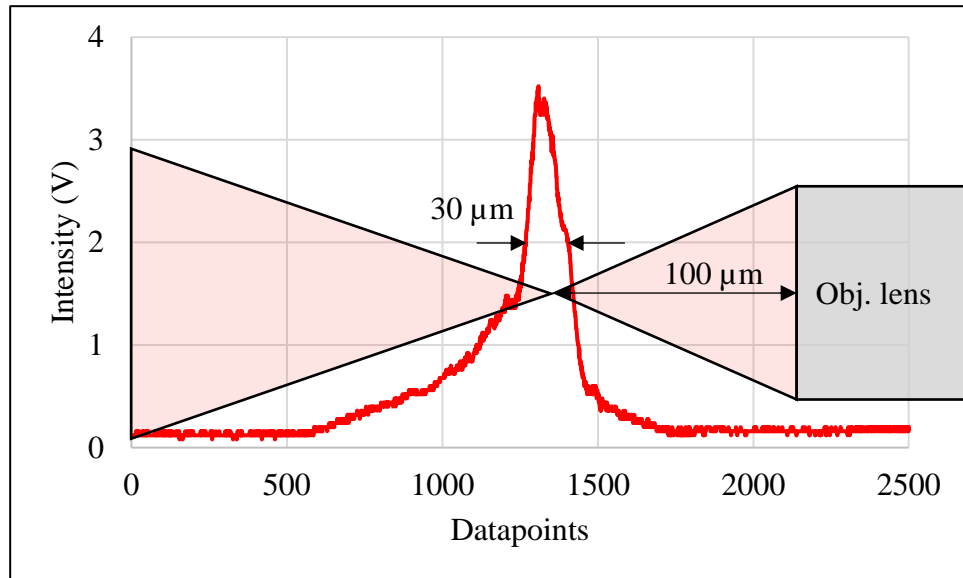


Figure 49: Intensity recorded by the photodetector when a copper mirror is moved towards or away from the objective lens to determine the FWHM of the probe representing its axial response.

3.6.4 Fourth prototype using a red diode laser with a pin hole, and 60X and 20X objective lenses

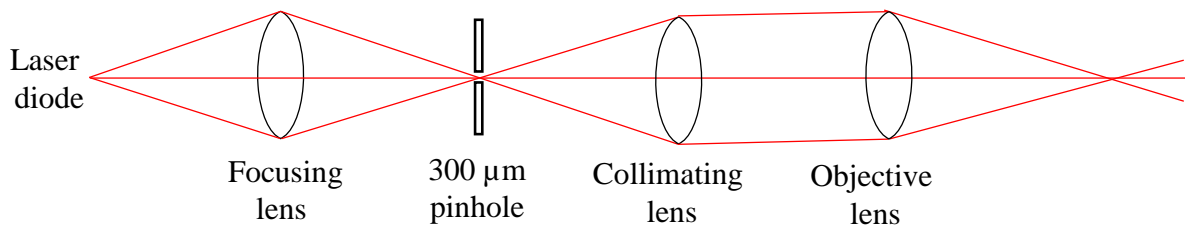


Figure 50: Ray diagram of the assembly using an adjustable focusing lens, a pinhole, and a collimating lens to collimate the beam to reach the objective lens

In the new prototype shown in Figure 51(a) and Figure 52(c), to improve the axial response, a 300 μm pinhole drilled on a Beryllium copper sheet of 0.1 mm thickness is used as a ‘spatial filter’ and is inserted at the focused spot of light coming from the focusing lens see Figure 50. The focal length of the collimating lens is chosen with a shorter focal length of 15 mm (5 mm Dia.

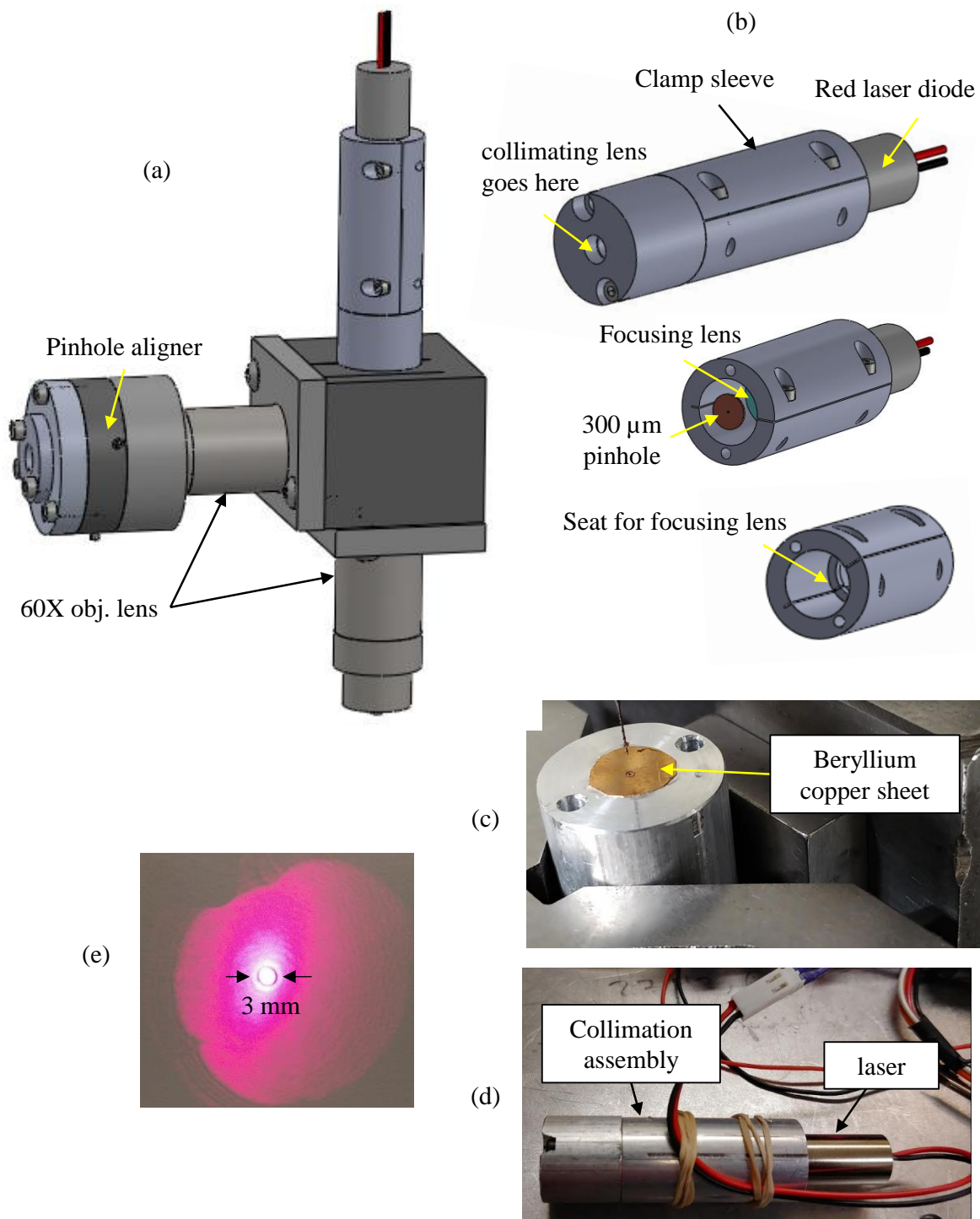


Figure 51: Fourth prototype using a 30 mW red laser with a pinhole; (a) Solid model of the new prototype (b) solid model of the collimating assembly showing the clamping sleeve for the laser, 300 μm pinhole, and the focusing and collimating lenses (c) drilling the 300 μm pinhole on a Beryllium copper sheet epoxied to the back of the cylinder that contains the collimating lens (d) fabricated collimating assembly (e) collimated beam of about 3 mm diameter

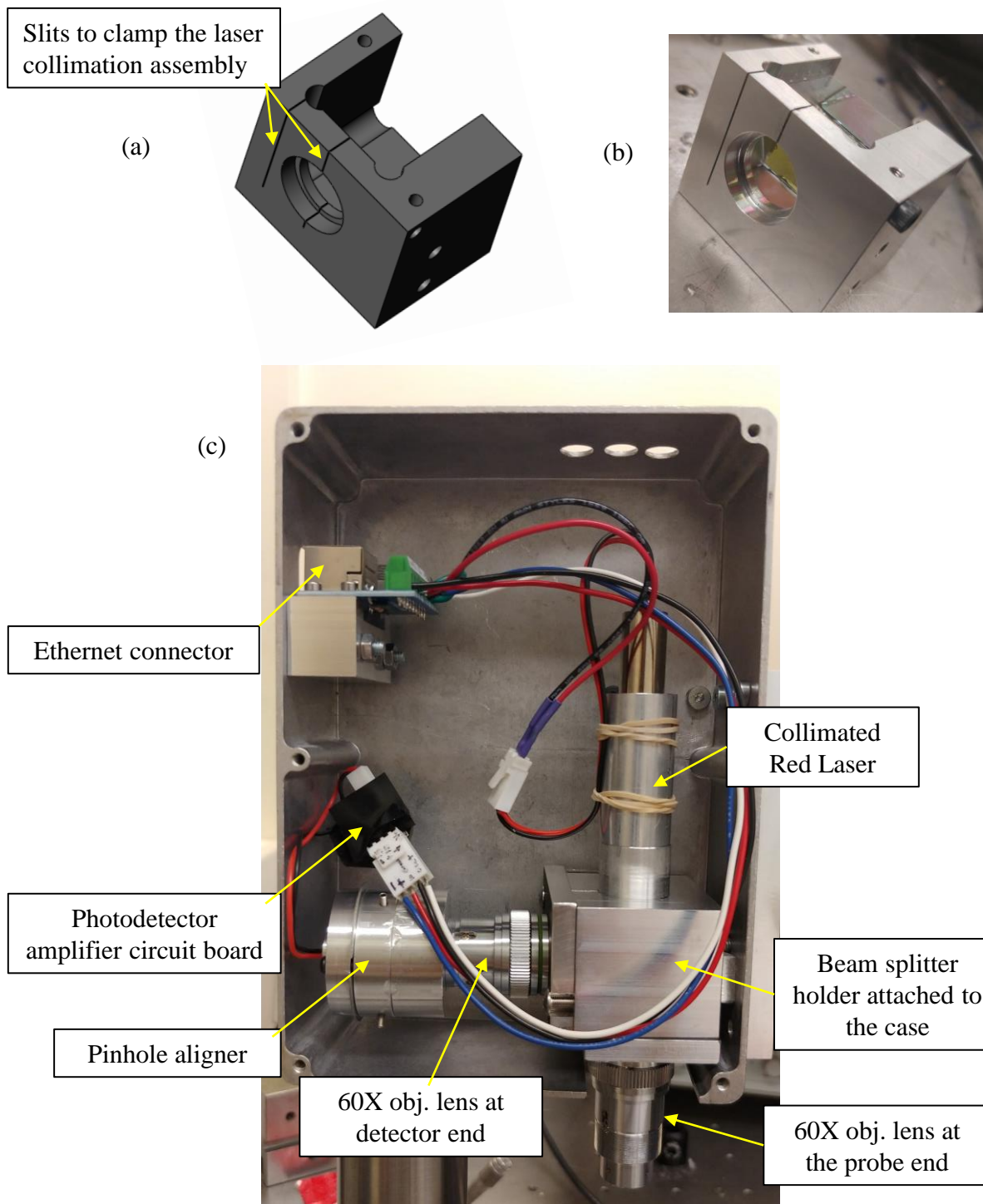


Figure 52: Fabricated fourth prototype; (a) solid model (b) fabricated beam splitter holder with a slit made using a wire EDM to clamp the collimating assembly of the (c) fabricated prototype.

Edmund optics, stock# 63-532) so that the length of the collimating assembly is shorter than the previous prototype. This prototype also uses a beam splitter holder to which a slit is made using a wire EDM so that the collimating assembly could be clamped instead of being epoxied in the previous prototypes, see Figure 52.

To determine the axial response, the copper mirror is translated towards the objective lens at the object side to produce the signal shown in Figure 53 with a FWHM of $50\text{ }\mu\text{m}$, which is larger than the previous prototype. In a later design the 60X objective lens at the detector side is replaced with a 20X objective lens to obtain an FWHM of $10\text{ }\mu\text{m}$. The theoretical reason for this was explained in section 3.5.

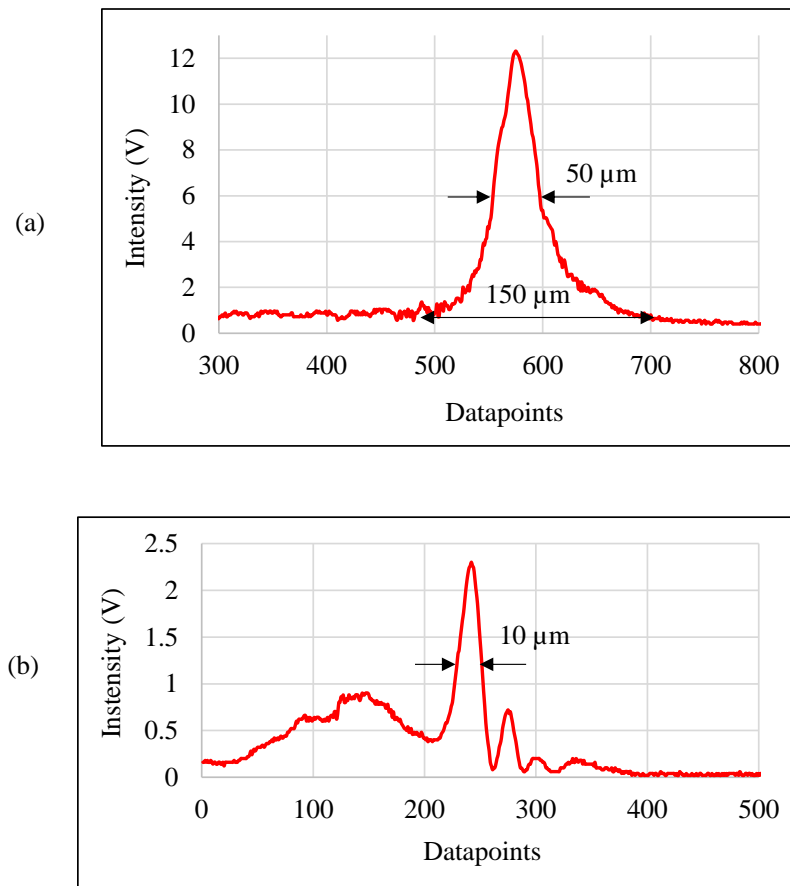


Figure 53: Axial response when a copper mirror is translated towards the 60X objective lens at the object side; (a) $50\text{ }\mu\text{m}$ FWHM when 60X objective lens is used at the detector side (b) $10\text{ }\mu\text{m}$ FWHM when 20X objective lens is used at the detector side.

3.6.5 Oscillation of the objective lens using a piezo actuated flexure mechanism

Figure 54 shows a piezo actuated disc coupling flexure casing housing a lens stack used in the 60X objective lens. This would replace the objective lens used at the object end eliminating the use of the over constrained flexure to oscillate in z axis. The calculations and the machining instruction for the fabrication of the flexure is given in Appendix B.7. To evaluate the oscillation bandwidth, frequency response of the flexure is measured using the experimental setup shown in Figure 55(a). The results given in Figure 56 shows the sinusoidal input voltage to the piezo and the displacement recorded by the capacitance probe measuring the motion of the flexure based objective head, and their Lissajous' curves for frequencies of 2, 20, 50, 100, 120, 150, 160, 200 Hz. During these experiments, resonant frequencies are observed at 120 Hz and 160 Hz, which can be seen from the Lissajous' curves shown in Figure 56(j and n). The displacement recorded by the capacitance probe stays sinusoidal up to 100 Hz, making 80 Hz a reasonable oscillating frequency (bandwidth).

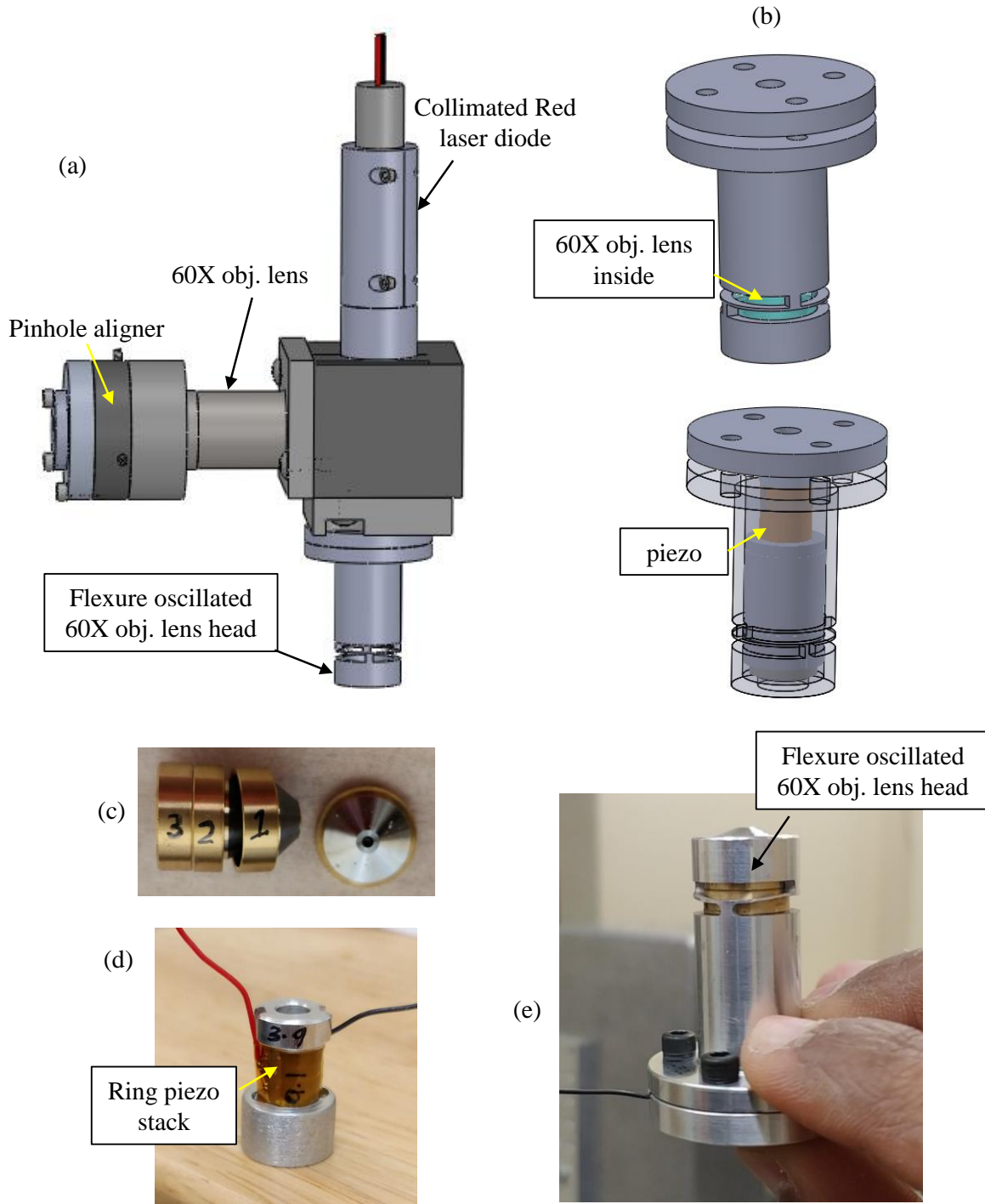


Figure 54: Fabrication of the flexure based oscillator for the objective lens; (a, b) solid model showing a disc coupling flexure containing the lens stack of a 60X objective lens at the object end of the confocal probe (c) lens stack taken from a 60X objective lens (d) ring piezo stack epoxied to the hollow spacer cylinders (e) lens stack and the piezo epoxied together maintaining the concentricity and then assembled into the flexure housing. One can notice that the flexure showing deflection due to the preload.

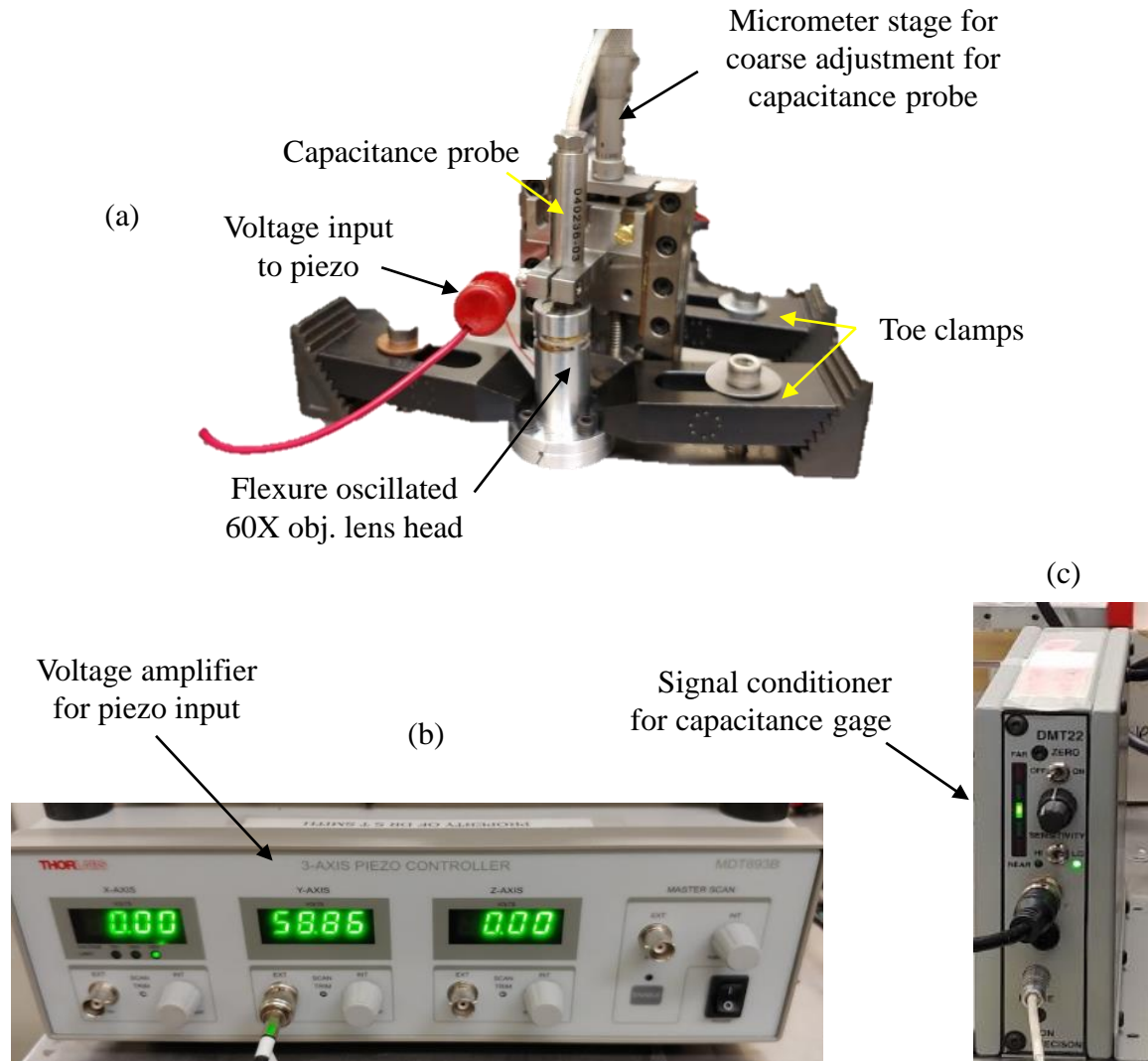
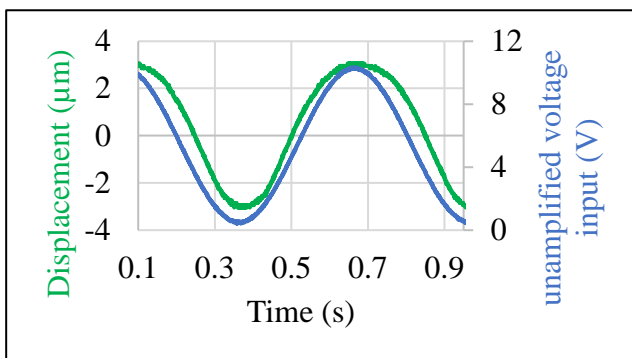
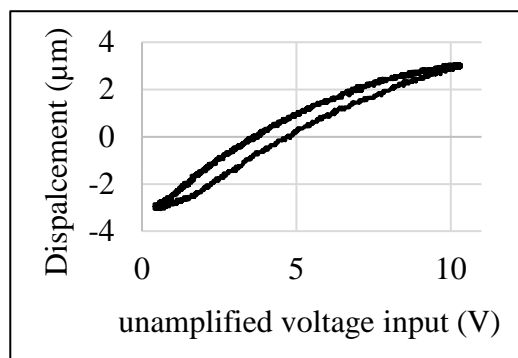


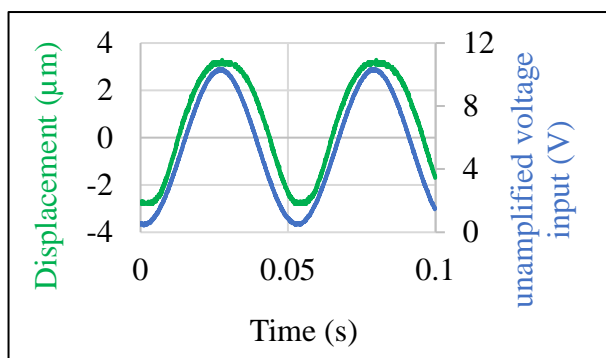
Figure 55: Experimental setup to observe the frequency response function of the flexure-based oscillator; (a) oscillation of the disc coupling flexure recorded by a capacitance probe (b) piezo amplifier (Thorlabs, MDT6938) used to actuate the piezo inside the flexure housing (c) signal conditioner for the capacitance probe (Lion precision, DMT22).



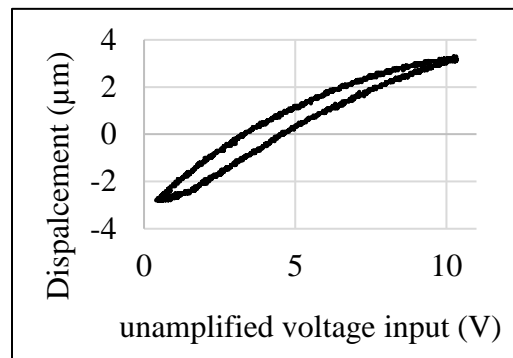
(a)



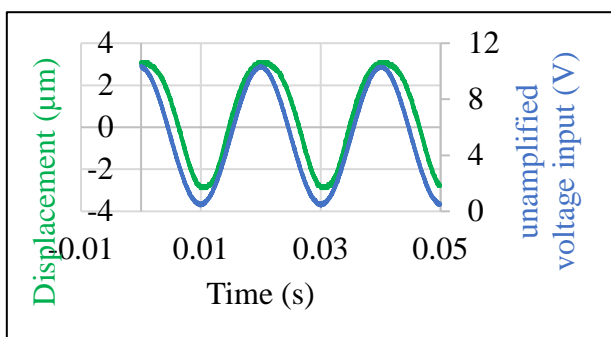
(b)



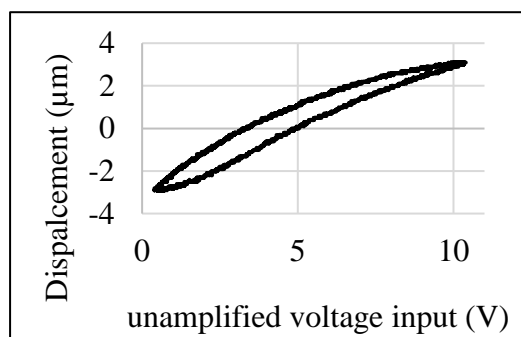
(c)



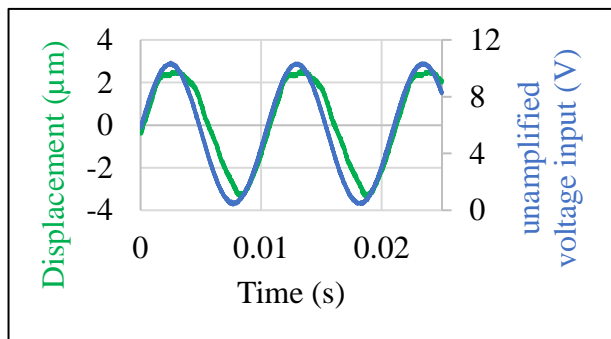
(d)



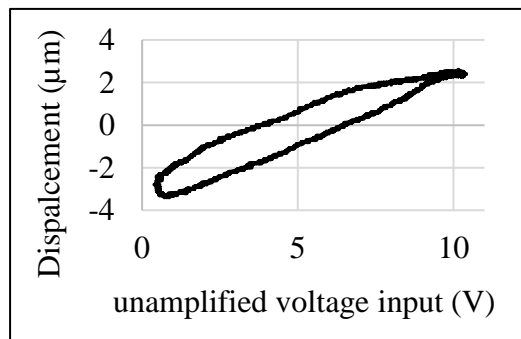
(e)



(f)



(g)



(h)

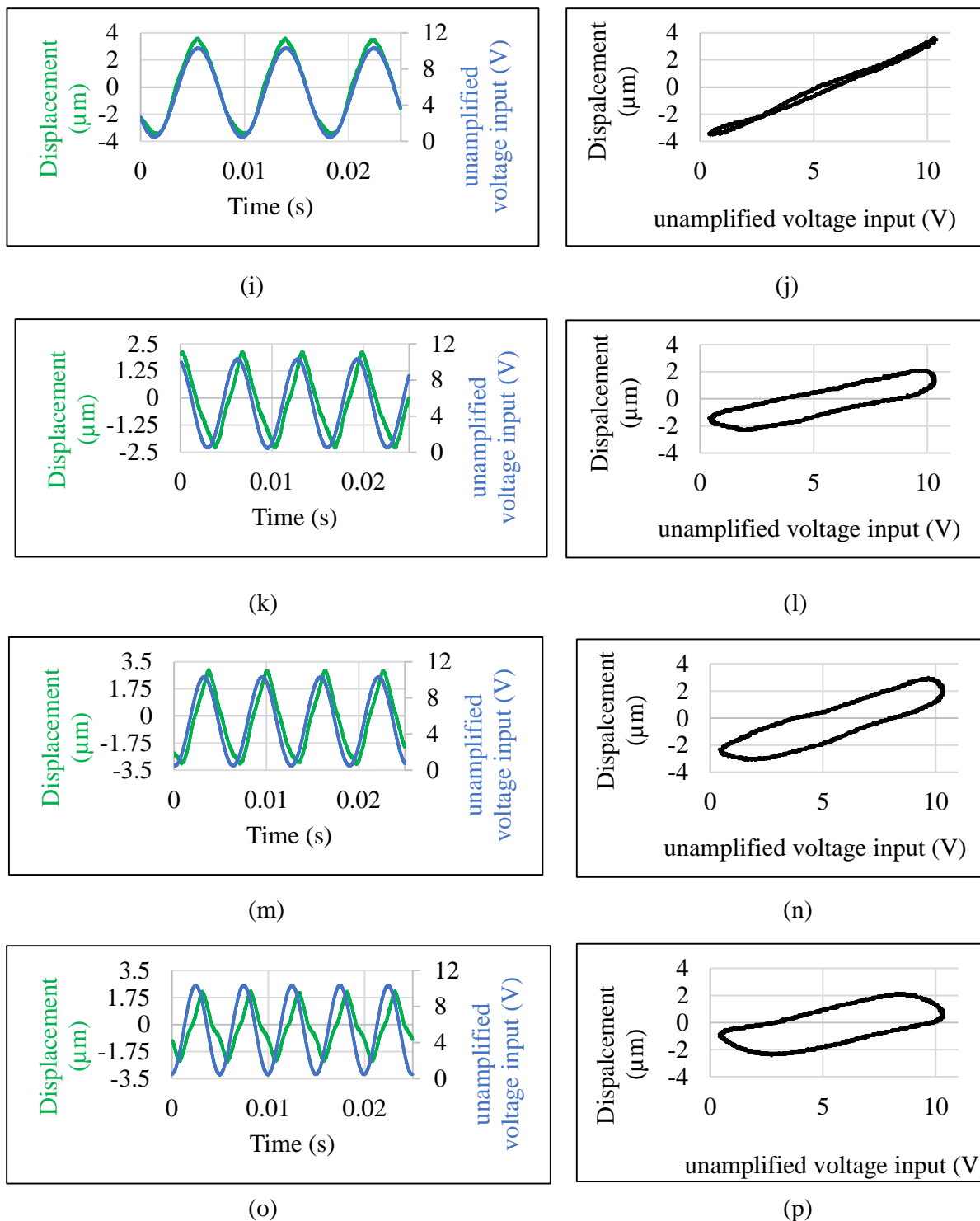


Figure 56: Left: Input sinusoidal signal to the piezo actuator and the recorded displacement from the capacitance probe plotted as a function of time for frequencies of 2, 20, 50, 100, 120, 150, 160, 200 Hz, Right: Lissajous curves.

The flexure oscillated objective lens head is integrated with the other components of the assembly shown in Figure 54(a), and is encased in an Aluminum casing and is tested for its axial response using a copper mirror translated towards the probe as shown in Figure 57(a), and the FWHM of the recorded intensity peak is $10\text{ }\mu\text{m}$, see Figure 57(b).

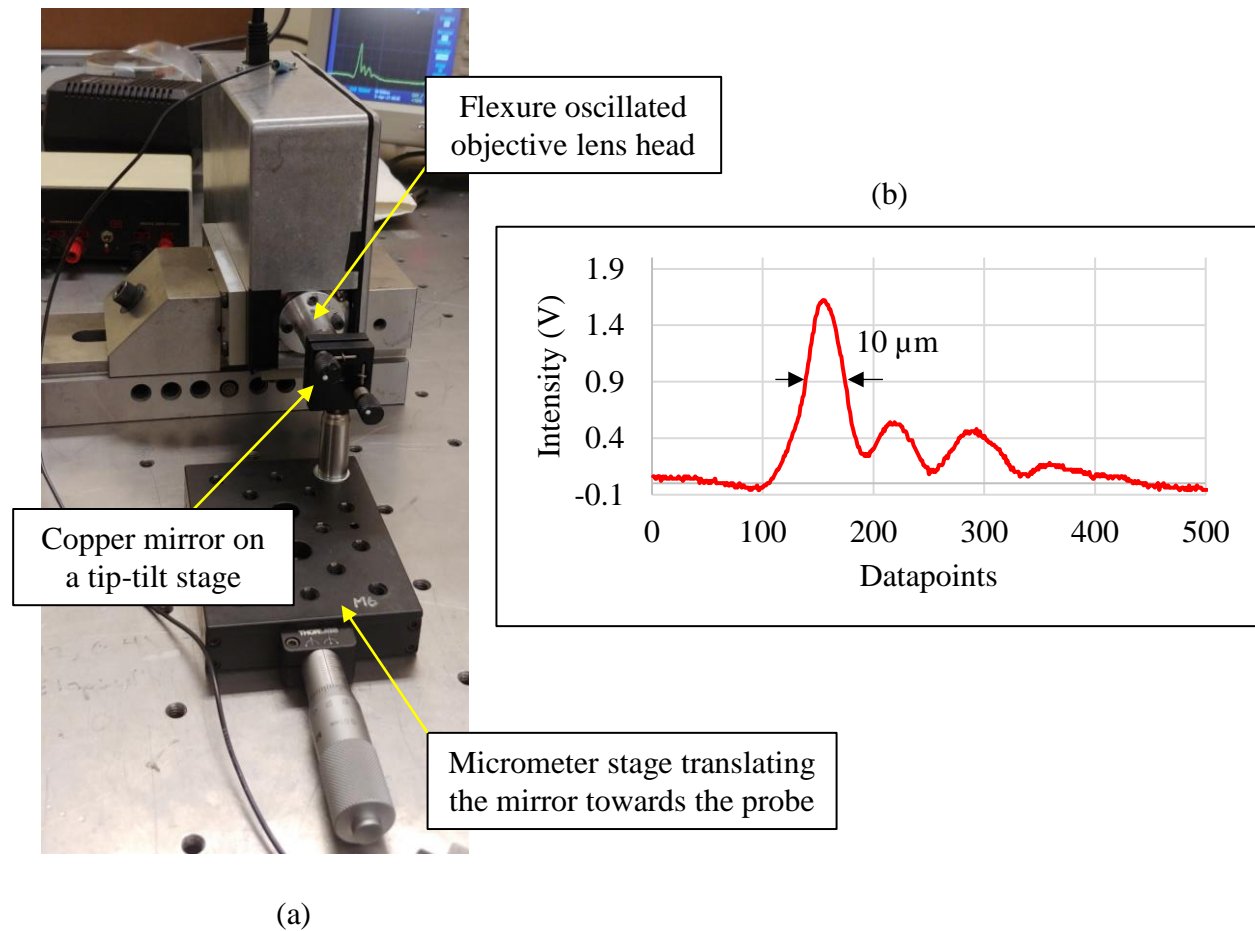


Figure 57: Testing the prototype using the flexure oscillated object lens head for axial response; (a) experimental setup (b) measured axial response with a $10\text{ }\mu\text{m}$ FWHM.

3.6.6 Sinusoidal reference surface

To validate the use of the recent prototype as a surface profiler, a sinusoidal surface with a height of 2 μm PV and five different frequencies from 0.5 mm to 0.15 mm is fabricated to serve as a reference sample, see Figure 58(b). The sample was manufactured using a diamond turning machine with a tool radius of 0.5 mm (courtesy: Mr. Brian Dutterer).

The height of the sinusoidal surface as a function of distance x is given by,

$$z = A \sin\left(\frac{2\pi x}{\lambda}\right),$$

Where, A is the amplitude, λ is the wavelength of the sinusoids. From this equation, the radius of curvature, R can be derived as

$$\frac{1}{R} = \frac{d^2 z}{dx^2} = \frac{4A\pi^2}{\lambda^2} A \sin\left(\frac{2\pi x}{\lambda}\right).$$

The maximum radius of curvature is given by,

$$R_{\max} = \frac{\lambda^2}{4A\pi^2}.$$

$R_{\max} = 0.5$ mm corresponds to the radius of the diamond tool used to fabricate the surface. For a desired amplitude of $A = 1$ μm , the minimum achievable wavelength is 140 μm .

The fabricated sample is measured using a stylus profilometer shown in Figure 59 for comparison, with a stylus force of 0.5 mN and a scanning velocity of 0.5 mm.s⁻¹. From the result shown in Figure 60, the measured amplitude and wavelengths are comparable to the prescription shown in Figure 58(b). Zoomed in picture of the result is given in Appendix B.6.

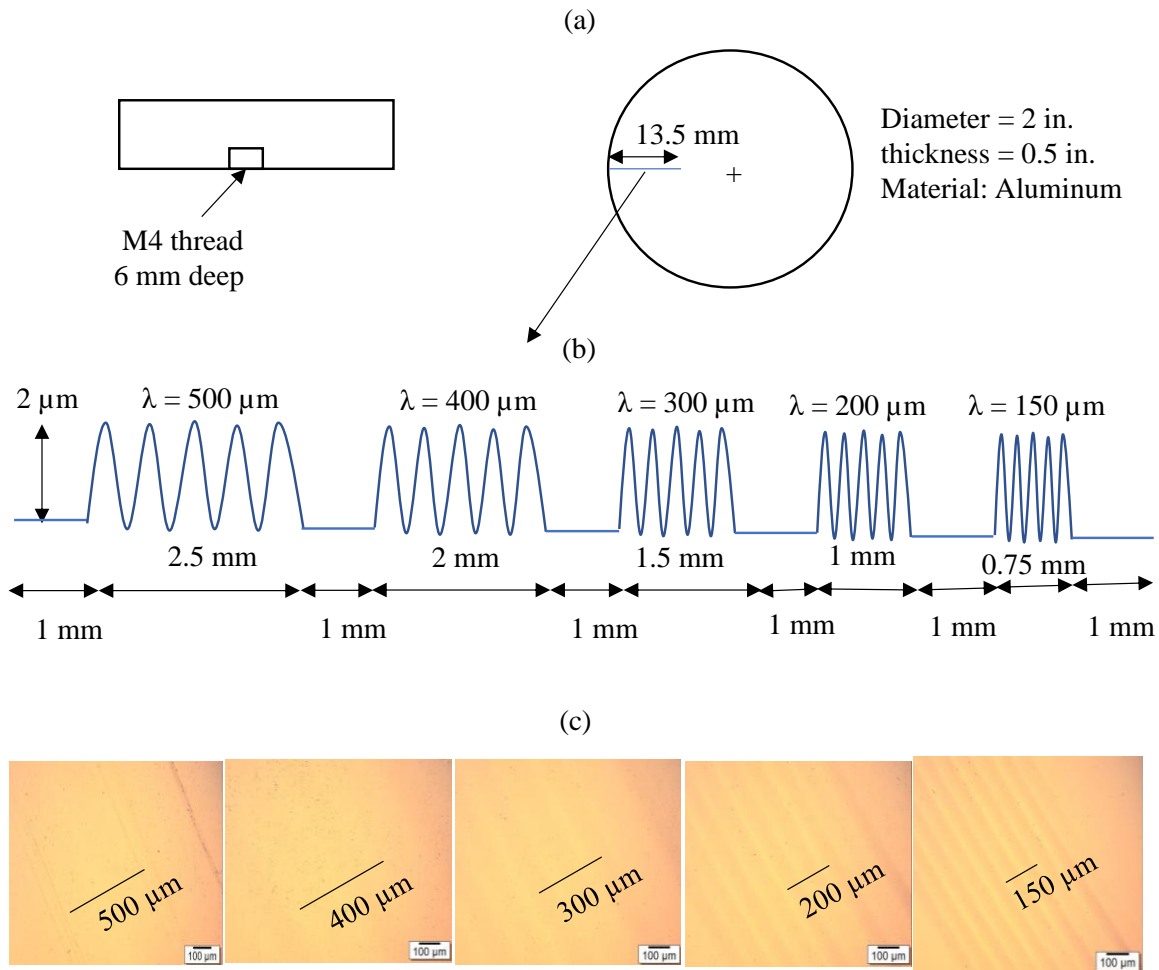


Figure 58: Sinusoidal reference sample; (a) Overall dimension of the reference sample (b) amplitude and the wavelengths of the sinusoids in the sample (c) microscope images of the sinusoids of each wavelength.

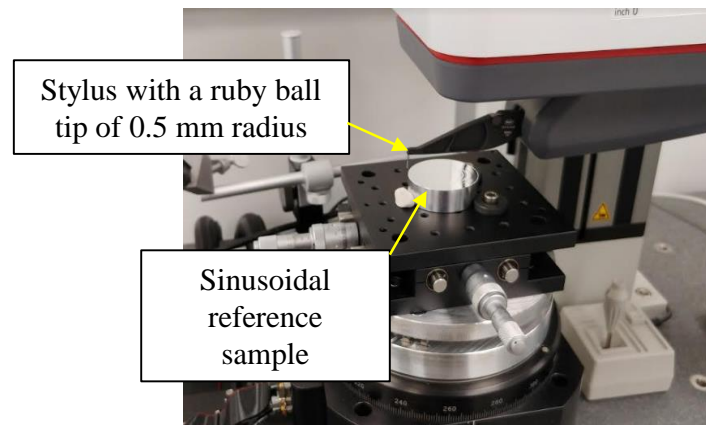


Figure 59: Stylus profiler (Mahr LD260) measuring the sinusoidal reference sample.

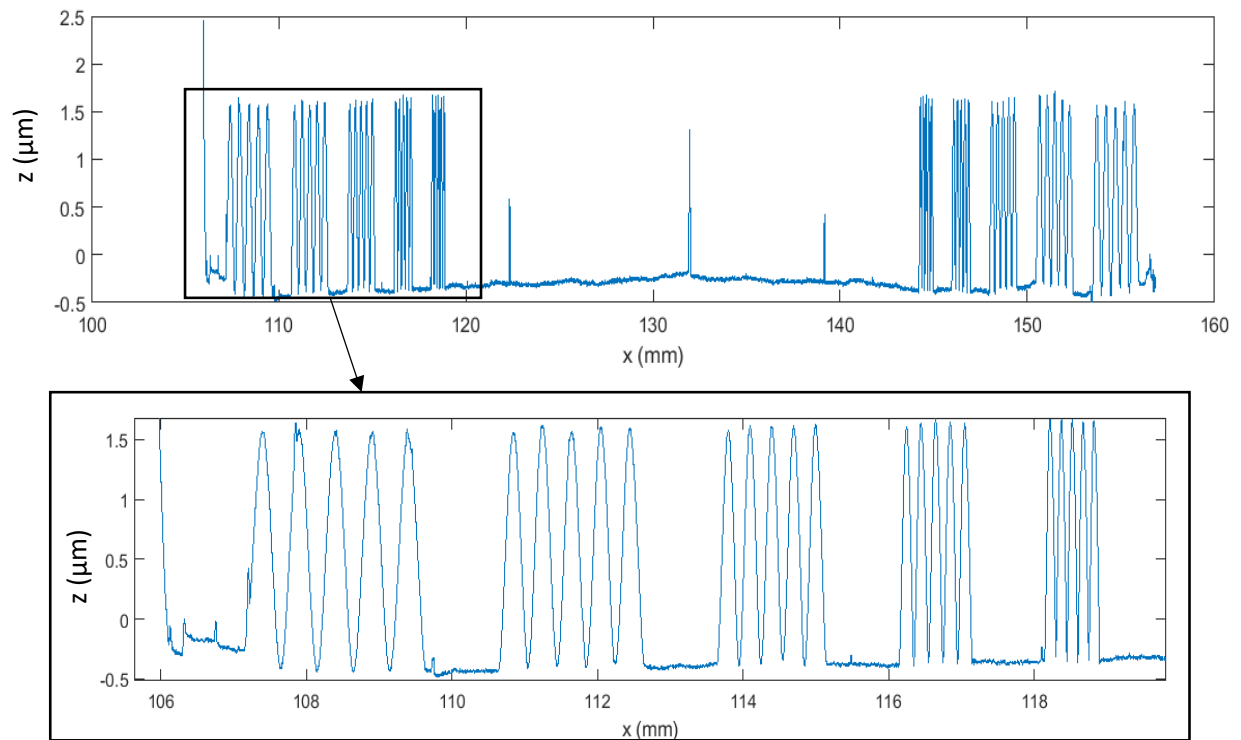


Figure 60: A profile measured on the sinusoidal reference sample using a stylus profiler with the inset showing left half of the profile.

3.7 Conclusions and future work

Prototypes were developed to understand the issues in building a monochromatic confocal profiler using commercially available inexpensive objective lenses and laser diodes. From these prototypes, design modifications to reduce the FWHM involved; using smaller pinholes, the necessity for micrometer level adjustments and fastening requirements, and the benefit of increasing the focal length of the lens element at the detector end. The final prototype at the time of writing this dissertation uses a 20X objective lens at the detector end, and a 60X objective lens at the object end. The 60X objective lens is chosen for its spatial resolution in surface texture measurements and higher numerical aperture increasing the surface slopes that can be measured. Experimental characterization of the spot size created by the objective lens was also performed. From these experiments, using a razor blade and a photodetector, the spot size is found to be 19 μm at a working distance of 100 μm . Objective lenses of a larger magnification than the 60X lenses typically require an oil immersion medium that is not desirable in most engineering measurements.

A flexure assembly housing the lens stack taken from a 60X objective head was fabricated and the frequency response measured. As a future work, this flexure-based objective lens integrated to the confocal probe assembly would be used to measure sample surfaces such as the sinusoidal reference surface presented in section 3.6.6. To automate the scanning of surfaces, a flexure based stage with a linear encoder feedback, and the LabVIEW program to operate the stage are described in Appendix B.8 and B.9. To align the surface sample normal to the confocal probe, a flexure-based tilt aligner also described in Appendix B.8 would be used. Also, design, fabrication, and performance studies of fiber-based confocal microscope may provide benefits for surface profiling in confined space.

4. CHARACTERIZATION OF A STYLUS PROFILER FOR AREAL FORM MEASUREMENTS

4.1 Background

The goal of our work is to evaluate a stylus profiler (MahrLD260) for measuring areal form of objects with major dimensions of up to 200 mm by making individual profiles on the part, and is described in subsequent sections. Following is a brief review of the basic operational principles and the development of stylus profilometry. Profilometry is a localized measurement of height variation on a specimen surface as a function of distance along the surface relative to the fixed frame of the instrument. Stylus tips made of a ruby ball, sapphire cone, or diamond pyramid attached at the tip of a pivoting arm still serves as a quick, contact-based measurements in industrial settings. This is especially true for thin film measurements, where the smallest measurable thickness for coherence scanning interferometers is limited by the coherence length of the light source, and the Atomic Force Microscopy technique is time consuming.

Profilometry is the predecessor of all the surface profiling techniques available today, and fittingly referred to as “Surface meters” in the past (Clay, 1944). Whitehouse (1994) attributes the invention of profilometer to Schmalz (1929) in his famous “handbook of surface metrology” (chapter 4), and the name ‘Profilometer’ came from the registered name of the instrument improved and marketed by Abbot (1933, 1936). Others who made significant contributions to the technique include Perthen, Reason, and Tomlinson. One disadvantage of using a contact-based stylus profiler over non-contact optical techniques is the potential damage caused to the optically smooth surface during the measurement, although this could be avoided if an appropriate stylus

force (say, 1 mN for a stylus radius of 0.5 mm) is used depending on the material. Advantages of stylus profiling over optical techniques include its immunity to optical reflectivity of the material, environmental robustness (some instruments will operate in manufacturing environments where large temperature swings and vibrations are present), the ability to profile in the presence of contaminant (liquid) films, and comparative affordability.

An example of why contact or non-contact profilometers are still a versatile measurement technique compared to Phase shifting interferometers (PSI) such as Fizeau is discussed. To measure form of a surface using a PSI used on shop floors and, more typically in temperature and particle controlled environments ('clean rooms'). To measure freeform surfaces using this technique requires the generation of holograms to insert between the reference surface (transmission sphere or flat) and the measurement object. In a mass manufacturing facility, a master freeform optic could be produced, and its functionality can be validated in the intended assembly. A master optic could be used as a reference surface in the subsequent interferometry measurements to qualify the performance of the manufactured parts. Because the interferometry measurements would require a master for every new design this is not appropriate for facilities that manufactures different freeform optics with frequent design changes. Therefore, point probing techniques such as confocal microscopy, CMM, and profilometers are the obvious options because they do not need another conformal reference surface.

4.2 Motivations for the study

As mentioned in the introduction, the goal of our work is to evaluate the errors inherent to a stylus profiler (MahrLD260) for measuring areal form of objects with major dimensions of up to 200 mm by making individual profiles on the part. A major driving factor is to use this stylus profiler, and a Universal Measuring Machine (Moore UMM100) that uses a chromatic confocal

probe (Precitech) for intermittent measurement of freeform mirrors manufactured at the Center for Freeform Optics, UNC Charlotte for the ‘Next generation’ optical telescope.

The resulting ‘form’ measurements using the stylus profiler are influenced by the errors in the motion of the carriages that move the stylus and the part. Even if these errors are repeatable and corrected within some uncertainty, since covering a surface area of the part by individually profiling takes longer time, and thermal variations from internal and external sources during this period is not straightforward to correct.

In our studies, ‘primitive’ objects such as flats, prisms, and spheres are used as reference objects (artefacts) to characterize the carriage errors using novel measurement techniques for error extraction. Also considered is the deviation of the stylus from its intended linear travel in the x axis due to the normal forces from the surface slope of the test object. This effect is referred to as ‘side-loading’ henceforth. A Geometric model of the machine is developed, and a Monte-Carlo simulation is performed to estimate the uncertainty of the measurements performed by the profiler. This model is important because it includes the influence of the nominal shape of the part in the evaluated uncertainty.

4.3 Literature review

The surfaces of reference objects used for these experiments are first measured using a Fizeau interferometer for comparison. To appreciate the broader context of this work, this section presents a review of literature discussing; geometry and dynamics of styluses used in profilometers, Fizeau interferometric form measurement techniques, kinematics of supporting optical flats during measurements, and freeform surface metrology by profiling.

4.3.1 Stylus geometry and dynamics

Algorithms to deconvolve stylus geometry from surface profile measurements [DeVries and Li, 1985]

Since the shape of the stylus tip convolves with the surface being measured, algorithms to deconvolve this effect are presented, making the deconvolved profile a better representation of the ‘true surface’. Sinusoidal and statistical (also referred to as stochastic or random) profiles are simulated, and considered as true profiles. The measurement profile is represented by relating the coordinates of the points of interaction of the stylus and the simulated profile and the, assumed ideal, radius of the stylus tip. Using the local slope and curvature of the measured profile, an estimate for the deconvolved profile is reconstructed.

A revised philosophy of surface measuring systems [D J Whitehouse, 1988]

This paper presents a theoretical analysis of the dynamics of the stylus during profiling with the stylus being modelled as a mass-spring-damper system, and its interaction with, assumed rigid, sinusoidal and random surfaces. The measured signal is related to the amplitude, and wavelengths or randomness of the true theoretical profile by a transfer functions consisting of mass, stiffness, and the damping ratio of the profiler system. Other non-geometric parameters such

as coefficient of friction, and damping are also discussed. The optimal damping ratio of 0.6 improves surface-stylus fidelity.

Improvement of the fidelity of surface measurement by active damping control [Liu et al., 1993]

A profilometer is modified to follow a simulated force signal (a simulated surface) by feedback control when it scans in x axis. The displacement feedback is provided by a Linear Variable Differential Inductor (LVDI) and a force can be applied to the stylus using a voice coil. The feedback control system used is a PD controller. The response of the system to the simulated force input is studied with different derivative gain terms (damping ratios). Variations in the calculated surface parameters (such as R_a , R_q , D_q) of simulated signal as a function of damping ratio, and scanning velocity is reported. Damping ratio of 0.6 yields a closer approximation of the simulated surface in the measurement results although deviations are small for damping ratios varying from 0.4 – 0.8. Variation of the calculated surface parameters during the measurements of mild steel and copper sample surfaces are also presented as a function of damping ratio, and scanning velocity.

4.3.2 Comparison studies of stylus and optical profilers

Measurement of freeforms and complex geometries by use of tactile profilometry and multi-wavelength interferometry [Wendel, 2019]

In this study, a stylus profiler (Talysurf) with a 2 μm radius diamond tip is used to make stripe profiles, and a Multi-wavelength interferometric probe (Luphoscan) is used to make spiral profiles on three test surfaces and the results are compared. The difference in the measured form of

- a) a 150 mm long, 50 mm wide, 3 mm sag diamond turned heads-up display is 10 nm PV.

b) a 40 mm diameter and a 2 mm sag bi-conic surface is 200 nm PV, which is attributed to the 2 mm spacing in the adjacent stripes made using the stylus profiler. Notwithstanding that, the difference in the RMS is 4 nm.

c) a 65 mm diameter, 100 mm and 300 mm radius of curvature ground concave toric surface is 50 nm PV. Aliasing was observed in the results of stylus profiler due to the spacing of the profiles.

Comparison of tactile and chromatic confocal measurements of aspherical lenses for form metrology [Nadim et al., 2014]

A profilometer using a stylus probe with a diamond tip radius of 2 μm , and a chromatic confocal probe is constructed following the Abbe's principle. The metrology frame is made of Invar to reduce the thermal expansion to $1 \frac{\mu\text{m}}{\text{m}^\circ\text{C}}$, and the test object is mounted on a Zerodur platform. The thermal expansion of the Zerodur platform and Invar frame combined is less than 3 nm for the temperature variations in the laboratory. The motion of the Zerodur platform is monitored using displacement interferometers and used to correct for the Abbe errors in the encoder feedback x , y , z carriages translating the probe. An aspherical surface of area 3.5 mm² measured using the chromatic confocal probe reports a residual form of 1 μm PV, whereas the stylus profiler measures it to be 200 nm PV. The residuals are reported after removing the fit to the asphere performed following a quasi-Newtonian method called L-BFGS (Limited memory Broyden- Fletcher- Goldfarb- Shanno) algorithm.

4.3.3 Form measurement techniques in Fizeau interferometry

4.3.3.1 Three-flat test

Absolute calibration of optical flat [Fritz, 1984]

Form measurement using a Fizeau interferometer not only contains the form of the test object, but also of the reference surface (typically a flat, or a sphere). To obtain the form of test object along its vertical axis, three different flats could be measured in three tests. During these test, the three flats are interchanged as reference surfaces and test objects. These three tests are referred to as “three-flat test”. In the work of Fritz, to obtain the form of the entire surface (not only the vertical profile), in one of the three-flat tests, one flat was rotated in azimuth, and a 4th measurement is made. 36-term Zernike polynomials were fit to all four measurements, and Zernike coefficients were obtained. By relating the coefficients from the four measurements, coefficients of individual flats were determined to represent the form of each flat with a repeatability of $\lambda/500$ (1.2 nm) and measurement uncertainty of less than $\lambda/100$ (6 nm).

4.3.3.2 Skip flat test

Self-Calibration : Reversal, Redundancy, Error Separation, and 'Absolute Testing' [Evans et. al, 1996]

This paper is a survey of various reversal and error separation techniques used in machine tool and optical metrology. This paper briefly describes a technique called ‘skip flat’ test (see Figure 244(a) in appendix C.2.7), which could be used to measure rectangular test objects of lengths larger than the transmission flat of the interferometer. During the measurement, the test object is place in between the reference flat and a return flat in an oblique angle (azimuthally) therefore illuminating the entire surface area thereby facilitating the form measurement of the whole area.

4.3.3.3 Random ball test

A Practical Implementation of the Random Ball Test [Parks, 2006]

Different spherical caps of a ball are measured using a Fizeau type interferometer, and subsequently averaged. Since the spherical cap areas of a polished ball are uncorrelated to each other, the average represents the form error of the transmission sphere. The idea of Random ball test was introduced by Parks et al. in 1999, a short but a clear paper was written by Parks in 2006.

4.3.4 Kinematic support of flats

Determination of Planeness and Bending of Optical Flats [Emerson, 1952]

An equation to calculate the sag of a flat supported on three points 120° azimuthally from each other is given. This equation is a function of applied load, radius at which the three mounting points are located, radius and thickness of the flat, Poisson's ratio, and elastic modulus. The equation is also validated experimentally within 5 nm difference, and it was observed that the flat supported at 0.7 times its radius produces the minimal sag.

Optimum Kinematic Support of Rectangular Flat Plates [Loewen, 1967]

Loewen extended the work of Emerson for square and rectangular plates and provided the optimal location of the three points resulting in minimum deflection, for a given length to width ratio of the plates. Optimal mounting locations for a square and two rectangular glass plates are first determined experimentally. Using the data, a dimensionless ratio is provided to use in a theoretical equation for a given length to width ratio of the plate.

4.3.5 Freeform surfaces

Manufacturing and measurement of freeform optics [Fang et al., 2013].

This paper presents a broad review of fabrication and measurement approaches for the production of freeform surfaces. Consequently, this covers a large number of topics including;

- a) applications in imaging, concentration, and illumination.
- b) design methodologies
- c) Diamond machining techniques such as slow slide servo, and fast tool servo, ‘ultra-precision’ milling, fly cutting, grinding, polishing, and molding
- d) contact and non-contact measurement systems such as CMMs, profilometers, auto focus probe, fringe projection, and other on machine measurement implementations
- e) stitching of data, probe correction, alignment of data using datums machined during the generation of freeform

The section on measurement that is relevant to our study lists the current techniques that are utilized, and some performance measures are briefly mentioned.

Strategy for a flexible and noncontact measuring process for freeforms [Beutler, 2016]

Strategies to measure freeform surfaces using a cylindrical coordinate measuring machine MarForm MFU200 is discussed. The system includes both a stylus probe and a white light interferometric optical probe. Use of reference spheres to kinematically locate the test surface and define the coordinate system by profiling these spheres using the above mentioned probing techniques is discussed. After defining the coordinate system, profiles comprising concentric circles or spokes could be performed to measure the form of a test surface. Other reference features such as reference pin on a fixture holding an ophthalmic lens, and direct measurement of edges of test objects using the stylus probe is also suggested. The results of the measurement of a cylindrical

lens with a 30 mm radius and the outer dimension of $6 \times 9 \text{ mm}^2$ subtracted from its nominal form leaving a residue of 1 to 2 μm PV, with the higher number being an influence of lateral shifts and rotation of the nominal fit.

4.3.6 Error modeling and task specific uncertainty

Thesis- Freeform Optical Surface Form Metrology with Serial Data Acquisition [Noste, 2020]

A universal measuring machine (Moore Nanotech) has been installed and adapted in the CPM (Center for Precision Metrology, UNC Charlotte) laboratory to measure freeform and conventional surfaces using a chromatic confocal probe. This probe is attached to a linear carriage to move in its optical axis. This linear carriage rides on another linear carriage that moves in an orthogonal direction to profile the test surface. The part is mounted using a vacuum chuck on the spindle rotating around the optical axis of the probe. Motion errors of the carriages are measured and compensated in the measured results using the geometrical model of the machine. Also, a task specific uncertainty is evaluated via Monte Carlo simulation, with a 65 nm standard deviation.

4.4 Experimental facility

The profilometer used in our work is a Marsurf LD260, and is shown in Figure 61. This profiler uses a stylus with a ruby ball tip (LP R 14-10-2/60°) of 0.5 mm radius that pivots on a carriage that can travel horizontally in the x direction with a maximum range of 260 mm. To accommodate the measurement of a part, this X carriage can be moved vertically in the z direction, and also can be rotated about the y axis using a coarse carriage represented by the parameter, H . Once an optimal location is found for the measurement of a part, coarse H carriage is fixed (or locked) at its position until the measurements are completed. The profiler also has a Y carriage that travels 200 mm. On top of the Y carriage, a rotary carriage, C is attached, that can rotate 360° around z axis. Both Y and C carriages are guided by air bearings, and their manufacturer performance specifications are given in Appendix C.1. On top of the rotary stage, a ‘3 ball-3 dowel pin groove’ kinematic plate is attached, see Figure 61(c). A two axis (xy) micrometer stage (not shown) is sometimes attached on top of the kinematic plate when centering of the part with respect to the axis of rotation of rotary carriage, C , becomes necessary. If centering of the part is not necessary, it is directly placed on the 3-ball kinematic plate and poster tack is used to hold it down.

4.5 Areal profiling approaches

This multiple carriage arrangement enables two approaches for areal profiling of a part as shown in Figure 62. The two approaches are:

- (i) Stripes (linear grid) - make a profile by moving the stylus using X carriage, step over in y axis using the Y carriage and make subsequent profiles to cover the area of measurement.
- (ii) Spokes (polar grid) - make a profile by moving the X carriage, rotate the part using the C carriage, and make subsequent profiles to cover the desired area of measurement.

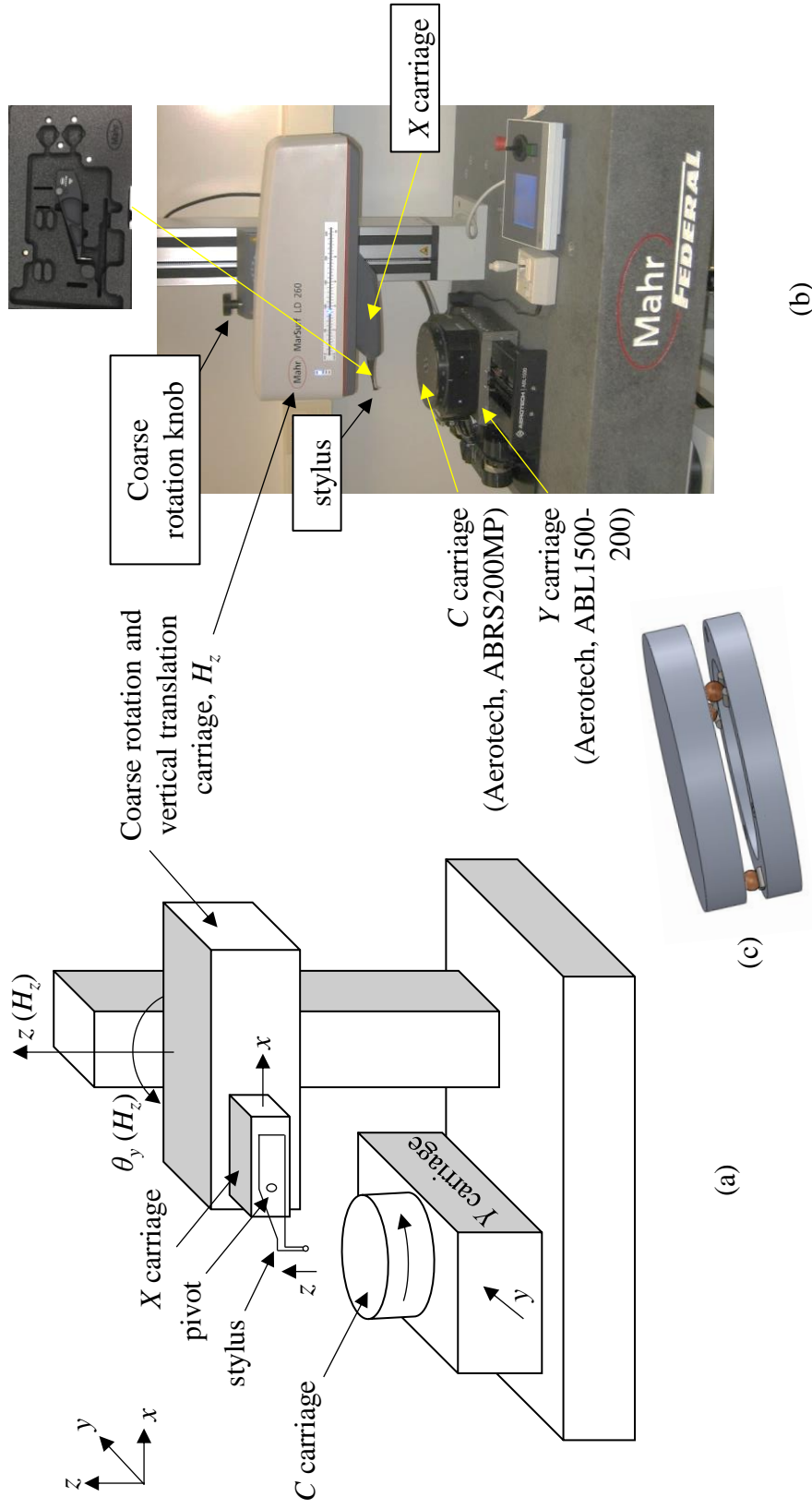


Figure 61: Profilometer system; (a) Schematic of the profilometer system characterized in our work (b) photograph of the system (c) Solid model of the 3-ball kinematic plate attached on top of the rotary stage.

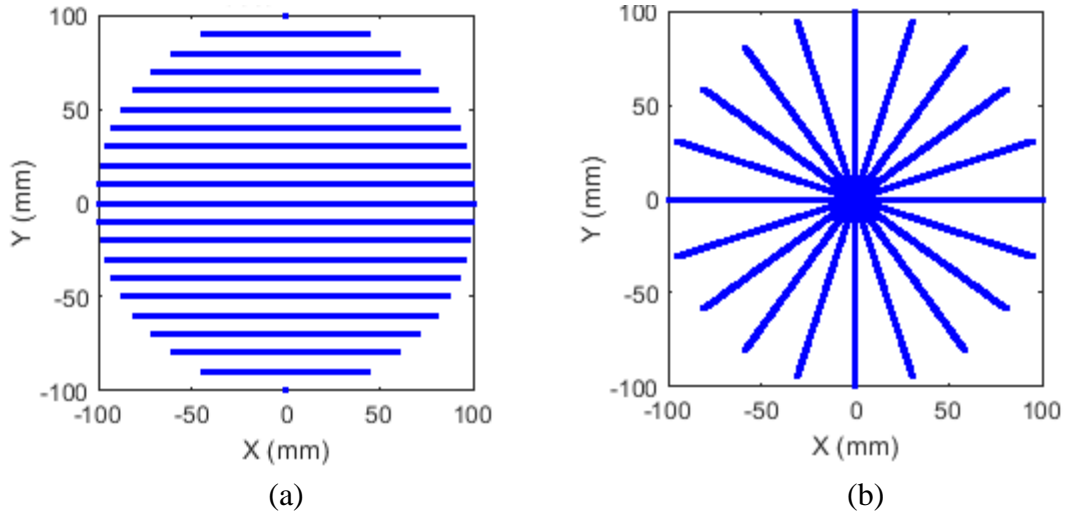


Figure 62: Areal profiling approaches simulated on a 200 mm diameter flat disk specimen; (a) stripes or incremental linear profiles (b) spokes made using incremental angular profiles.

4.5.1 Merits and limitations of the stripes approach

One of the advantages of profiling using stripes due to the potential to correct for thermal drifts by using the additional profiles made after rotating the part azimuthally by 90° . To understand how this compensation is implemented, Figure 63(a) shows a simulation where twenty profiles are made on a flat with a linear thermal drift of $0.25 \text{ nm}\cdot\text{mm}^{-1}$. To assess the out of flatness of a flat, it is a practice to fit a plane to the measured data and subtract it from the data to remove tilt of the measured surface due to the stage supporting the flat, and non-parallel faces of the top and bottom surfaces of the flat. Figure 63(b) and (c) shows a plane fit to the simulated data with added thermal drift and this plane fit is subtracted to yield a residue of 80 nm PV. Figure 63(d) shows the profiles made on the flat after it is rotated by 90° using the *C* carriage, and four more stripes are made in a short time span, referred to as ‘Tie lines’. The twenty profiles and the four tie lines are overlapped to determine their intersection points, shown in black in Figure 63(f). The twenty profiles are offset in the *z* axis and rotated in *y* axis with respect to these intersection points as shown in Figure 63(g). Residue from a plane fit to this adjusted data is only 0.8 pm PV, see

Figure 63(i). It is noted that the tie lines are influenced by the motion errors of Y carriage, which is not considered in this simulation. Another feature of the stripes method of measurement is that the data spacing in Cartesian coordinates (Δx , Δy) is the same.

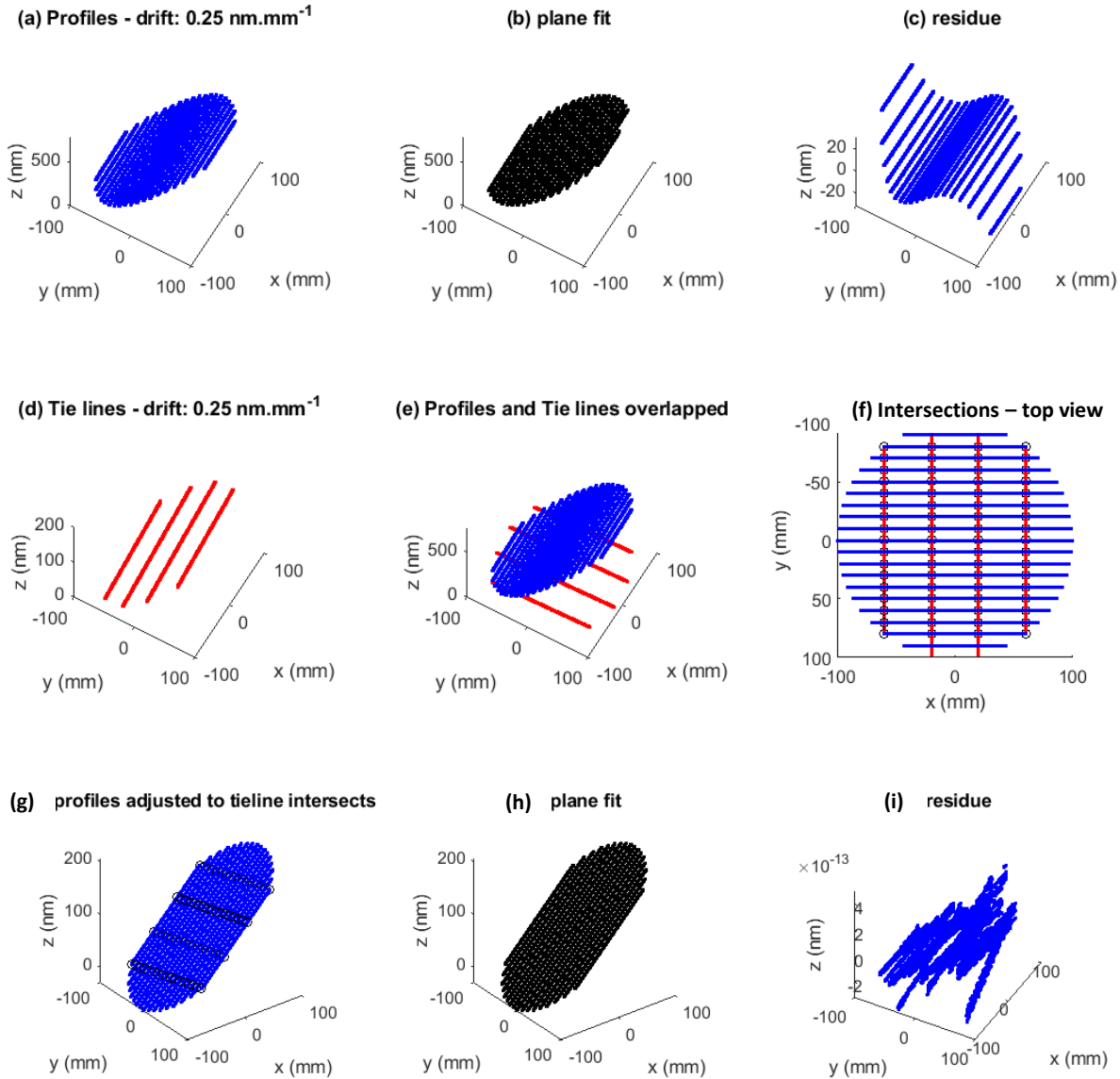


Figure 63: Simulation showing the use of tie lines to compensate for the linear thermal drift.

One disadvantage of profiling using the stripes approach is the varying interaction of the ball stylus with the test object in its non-meridian region. For example, when measuring surfaces

such as spheres in stripes manner, the region of the ball stylus interacting with the part is not along its meridian except for the profile made across the top of the sphere. Due to this, conventional morphology filtering techniques that deconvolves the part stylus morphology is not applicable, because they typically assume that the interaction is along the meridian of the stylus. Another effect of stylus interaction in non-meridian region is that the probe-surface interaction forces will cause the stylus to bend and will result in the substantial changes in the force vector transmitted through the magnetically held kinematic seat of the stylus.

4.5.2 Merits and limitations of the spokes approach

An advantage of Spokes method of measurement is the interacting region of the stylus is always moving across its meridian, at least for test objects such as spheres and aspheres. For freeform surface of varying surface slopes this may not be true. Another advantage over the Stripes method is that the range of travel of *Y* carriage used to make stripes is 200 mm, which limits the measurable aperture of the test object, whereas spokes method of measurement can use the full 260 mm travel span of the *X* carriage. An issue with the spokes approach is that the density of datapoints decreases from the center to the edge.

4.5.3 Zernike polynomial fit to stripes and spokes

Representing the form of surfaces with circular aperture using Zernike polynomials is an established practice in metrology. Therefore, it is important to know if there are any differences between the polynomial fit to the surfaces measured using stripes and spokes. To evaluate this, two datasets are generated from a simulated concave surface with a 200 mm aperture and a radius of curvature of 300 mm, see Figure 64(a and d). A Zernike polynomial fit to these datasets consisting of piston, defocus, primary, secondary, and tertiary spherical terms are plotted in Figure 64(b to e). The difference between the fit and the measured data are shown in Figure 64(c to f)

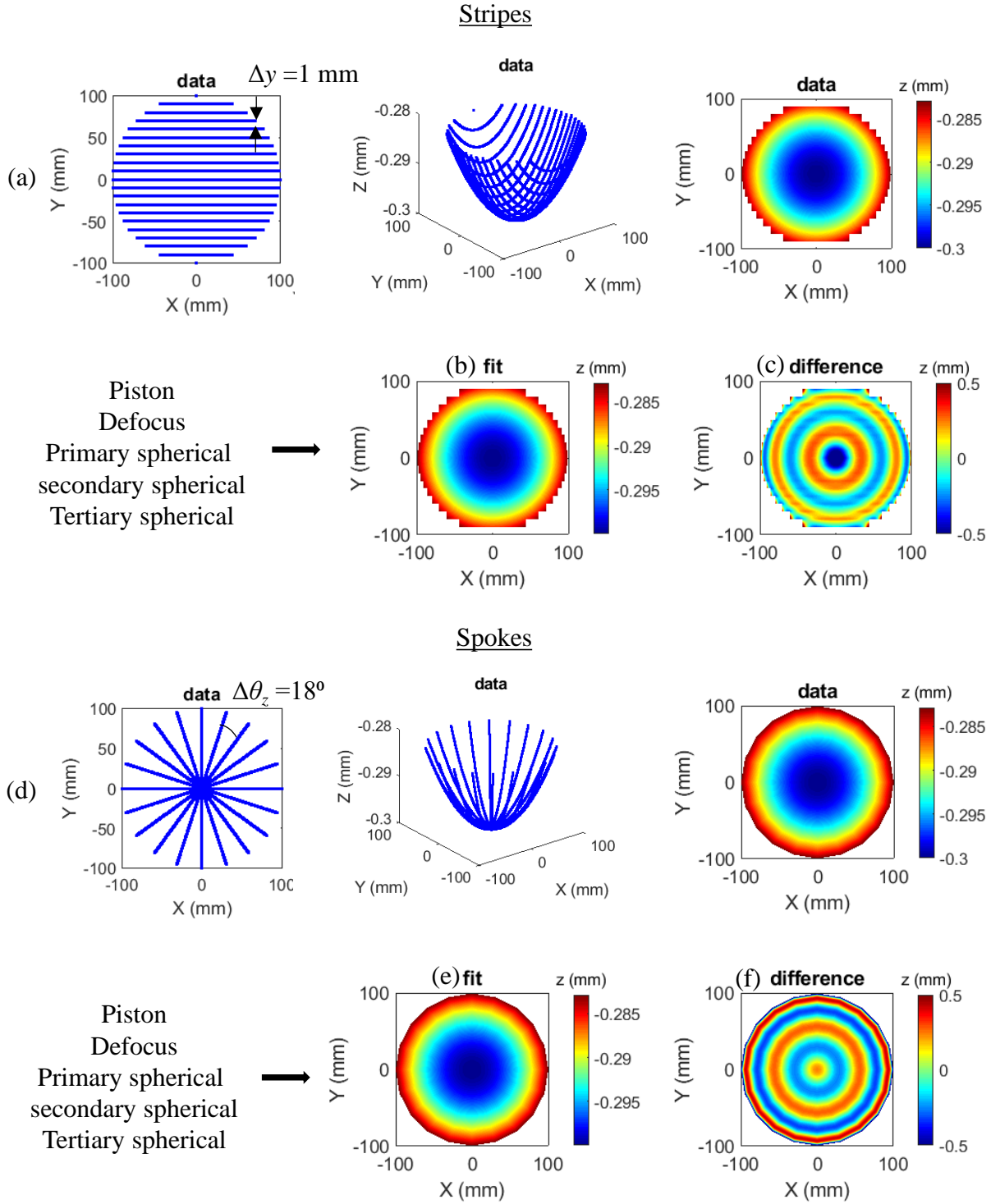


Figure 64: Comparison between Zernike fitting for the simulated measurements using stripes and spokes approaches of profiling; (a) simulated data of a concave surface measured in stripes manner (b) Zernike fit to this data (c) difference between the simulated data and the fit for stripes measurement (d to f) similar plots for a concave surface measured in spoke manner.

which is 1 nm PV. This simulation indicates that differences in the representation of a measured surfaces using Zernike polynomial fit for a surface measured by stripes and spokes manner is negligible.

4.5.4 Time taken for stripes and spokes

It is straightforward to compute the time taken to measure in spokes manner for a given velocity of stylus travel, distance each profile, and the number of profiles. If the stylus travels at $1 \text{ mm}\cdot\text{s}^{-1}$, for the simulation shown in Figure 64(d) the time taken for making nine spokes profiles of 200 mm long covering a total length of 1800 mm is 30 minutes. For the 19 profiles measured in stripes manner shown in Figure 64(a), the distance travelled by the stylus is given by

$d = 2r + 4 \sum_{n=1}^{10} \sqrt{r^2 - (n \cdot \Delta y)^2}$, where n is the number of profiles to cover top or bottom half, r is

half the aperture size, Δy is the spacing in y axis, see schematic shown in Figure 65. For a stylus travelling with a velocity of $1 \text{ mm}\cdot\text{s}^{-1}$, time taken for the ‘stripes’ measurement shown in Figure 64(a) is 52 minutes and the total distance travelled is $d = 3100 \text{ mm}$.

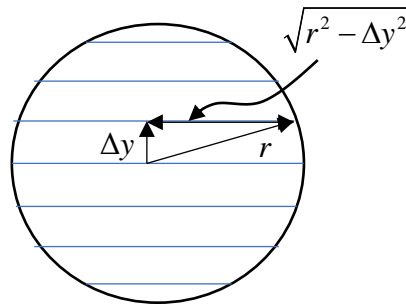


Figure 65: Schematic showing the half length of a profile according to the chord lengths in a circular area.

4.6 Geometrical model

To be able to determine the measurement error due to the errors in the motion of carriages used in the profilometer system, a rigid body geometrical model of the profilometer system that includes the desired degrees of freedom of carriages and the undesired motions ('errors') is developed in this section. Figure 66 shows the origin of the coordinate systems of Y and C carriages, O_Y and O_C respectively overlapping at the reference (or Frame) coordinate, O_F . The origin of the coordinate system of the X carriage at a distance l_a in x axis, and l_s in z axis which corresponds to the distance of the stylus ball center from its pivot point.

To bring the center of the stylus ball to this location, the X carriage is commanded to 131.383 mm, the Y carriage is commanded to -101 mm after homing their line scales (linear encoder). Experimentally determined resolution of the X carriage line scale is ± 25 nm (see Figure 141(a)), and the manufacturer specified Y carriage positioning accuracy is ± 0.5 μm . The z height of the stylus is adjusted using the H carriage to read zero. To determine this 'fiducial' location, the calibration sphere of radius 22.4834 (Mahr, calibration no., FMR 150126) is centered using an electronic indicator colinear with respect to the axis of rotation of the rotary carriage, C . Then, x and y values of the apex of the sphere were obtained by 'crowning' the sphere.

When the carriages are commanded to translate or rotate during measurements, the result will be the motion to a point given by the reading from the encoders and the motion errors in six degrees of freedom. This is schematically shown in Figure 67(a). The distance between the origin of the coordinate system of each carriage and the origin of the coordinate system of the carriage it is attached to is given by the vector diagram shown in Figure 67(b).

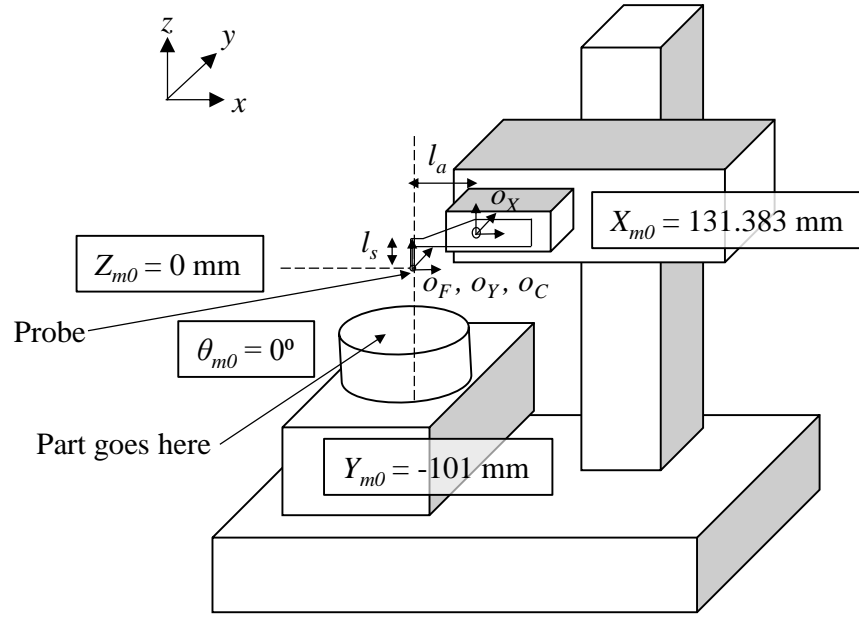


Figure 66: Schematic showing the components of the profilometer system, and the locations of the X, Y, and C carriages and the stylus that brings the center of the probe ball to reference coordinate, O_F .

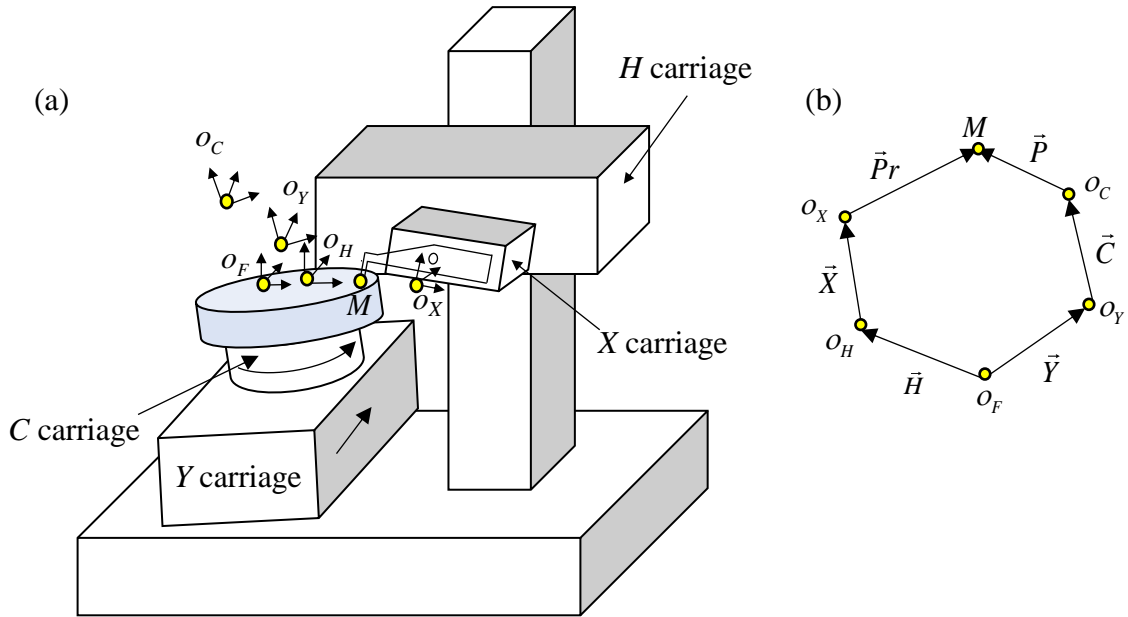


Figure 67: Translation and rotation of carriages during the measurement; (a) Schematic showing the exaggerated motion of carriage coordinates due to the intended travel and the errors in motion during the measurements. (b) vector diagram showing the distance between the origin of the closest coordinate systems due to the motion of the carriages.

The distance of the measurement point, M from the origin of the reference coordinate system, O_F traced through the coordinate origins O_H , O_X and O_Y , O_C are equal, given by,

$$\begin{bmatrix} \vec{P}_r \end{bmatrix}_F + \begin{bmatrix} \vec{X} \end{bmatrix}_F + \begin{bmatrix} \vec{H} \end{bmatrix}_F = \begin{bmatrix} \vec{P} \end{bmatrix}_F + \begin{bmatrix} \vec{C} \end{bmatrix}_F + \begin{bmatrix} \vec{Y} \end{bmatrix}_F$$

where the component of the left side of the equation is given by

$$\begin{aligned} \begin{bmatrix} \vec{H} \end{bmatrix}_F &= \begin{bmatrix} \vec{H} \end{bmatrix}_F \\ \begin{bmatrix} \vec{X} \end{bmatrix}_F &= R_{HF} \begin{bmatrix} \vec{X} \end{bmatrix}_H \\ \begin{bmatrix} \vec{P}_r \end{bmatrix}_F &= R_{HF} R_{XH} \begin{bmatrix} \vec{P}_r \end{bmatrix}_X \\ \begin{bmatrix} \vec{Y} \end{bmatrix}_F &= \begin{bmatrix} \vec{Y} \end{bmatrix}_F \\ \begin{bmatrix} \vec{C} \end{bmatrix}_F &= R_{YF} \begin{bmatrix} \vec{C} \end{bmatrix}_Y \\ \begin{bmatrix} \vec{P} \end{bmatrix}_F &= R_{YF} R_{CY} R_{C,nom} \begin{bmatrix} \vec{P} \end{bmatrix}_C \end{aligned}$$

Using this, the part coordinate is represented with respect to the C carriage it sits on

$$\begin{aligned} R_{HF} R_{XH} \begin{bmatrix} \vec{P}_r \end{bmatrix}_X + R_{HF} \begin{bmatrix} \vec{X} \end{bmatrix}_H + \begin{bmatrix} \vec{H} \end{bmatrix}_F &= R_{YF} R_{CY} R_{C,nom} \begin{bmatrix} \vec{P} \end{bmatrix}_C + R_{YF} \begin{bmatrix} \vec{C} \end{bmatrix}_Y + \begin{bmatrix} \vec{Y} \end{bmatrix}_F \\ \begin{bmatrix} \vec{P} \end{bmatrix}_C &= \left(R_{YF} R_{CY} R_{C,nom} \right)^{-1} \left[R_{HF} R_{XH} \begin{bmatrix} \vec{P}_r \end{bmatrix}_X + R_{HF} \begin{bmatrix} \vec{X} \end{bmatrix}_H + \begin{bmatrix} \vec{H} \end{bmatrix}_F - R_{YF} \begin{bmatrix} \vec{C} \end{bmatrix}_Y - \begin{bmatrix} \vec{Y} \end{bmatrix}_F \right] \end{aligned} \quad (10)$$

where, vectors containing the translation errors of the carriages given by

$$\begin{aligned} \begin{bmatrix} \vec{P}_r \end{bmatrix}_X &= \begin{bmatrix} -l_a \\ 0 \\ -l_s \end{bmatrix}; \quad \begin{bmatrix} \vec{X} \end{bmatrix}_H = \begin{bmatrix} (X_m - X_{mo}) + \delta_x(X) \\ \delta_y(X) + (X_m - X_{mo})\alpha_{z,X} \\ \delta_z(X) - (X_m - X_{mo})\alpha_{y,X} \end{bmatrix}; \quad \begin{bmatrix} \vec{H} \end{bmatrix}_F = \begin{bmatrix} \delta_x(H) + H_m\alpha_{y,H} \\ \delta_y(H) - H_m\alpha_{x,H} \\ H_m + \delta_z(H) \end{bmatrix}; \\ \begin{bmatrix} \vec{C} \end{bmatrix}_Y &= \begin{bmatrix} \delta_x(C) \\ \delta_y(C) \\ \delta_z(C) \end{bmatrix}; \quad \begin{bmatrix} \vec{Y} \end{bmatrix}_F = \begin{bmatrix} \delta_x(Y) - (Y_m - Y_{mo})\alpha_{z,Y} \\ (Y_m - Y_{mo}) + \delta_y(Y) \\ \delta_z(Y) + (Y_m - Y_{mo})\alpha_{x,Y} \end{bmatrix} \end{aligned}$$

and the rotation matrices, R_{HF} , R_{XH} , R_{YF} , R_{CY} , $R_{C,nom}$ contains the angular errors of the H , X , Y and C carriages, and the nominal rotation of the C carriage respectively given by,

$$R_{HF} = \begin{bmatrix} 1 & -\varepsilon_z(H) & \varepsilon_y(H) \\ \varepsilon_z(H) & 1 & -\varepsilon_x(H) \\ -\varepsilon_y(H) & \varepsilon_x(H) & 1 \end{bmatrix}$$

$$R_{XH} = \begin{bmatrix} 1 & -\varepsilon_z(X) & \varepsilon_y(X) \\ \varepsilon_z(X) & 1 & -\varepsilon_x(X) \\ -\varepsilon_y(X) & \varepsilon_x(X) & 1 \end{bmatrix}$$

$$R_{YF} = \begin{bmatrix} 1 & -\varepsilon_z(Y) & \varepsilon_y(Y) \\ \varepsilon_z(Y) & 1 & -\varepsilon_x(Y) \\ -\varepsilon_y(Y) & \varepsilon_x(Y) & 1 \end{bmatrix}$$

$$R_{CY} = \begin{bmatrix} 1 & -\varepsilon_z(C) & \varepsilon_y(C) \\ \varepsilon_z(C) & 1 & -\varepsilon_x(C) \\ -\varepsilon_y(C) & \varepsilon_x(C) & 1 \end{bmatrix} ; R_{C,nom} = \begin{bmatrix} \cos(\theta_m - \theta_0) & \sin(\theta_m - \theta_0) & 0 \\ -\sin(\theta_m - \theta_0) & \cos(\theta_m - \theta_0) & 0 \\ 0 & 0 & 1 \end{bmatrix}$$

Figure 68 defines the symbols used to represent the motion errors of the carriages contained in the vectors and matrices listed above. with arrows pointing towards the positive directions following the right hand rule, when the index finger, middle finger, and thumb points respectively along the positive directions of x , y and z axes of the profilometer system shown in Figure 66. Since the H carriage is used once for a given set of stripes or spokes, it would change the squareness of X carriage due to the angular errors and offset the probe point due to its translation errors. If the freeform surfaces uses fiducial marks [Beautler, 2016], the squareness error could be removed. Therefore, the H carriage errors are assumed to be zero, making the vector $[H]_F = 0$, and rotational matrix R_{HF} an identity matrix.

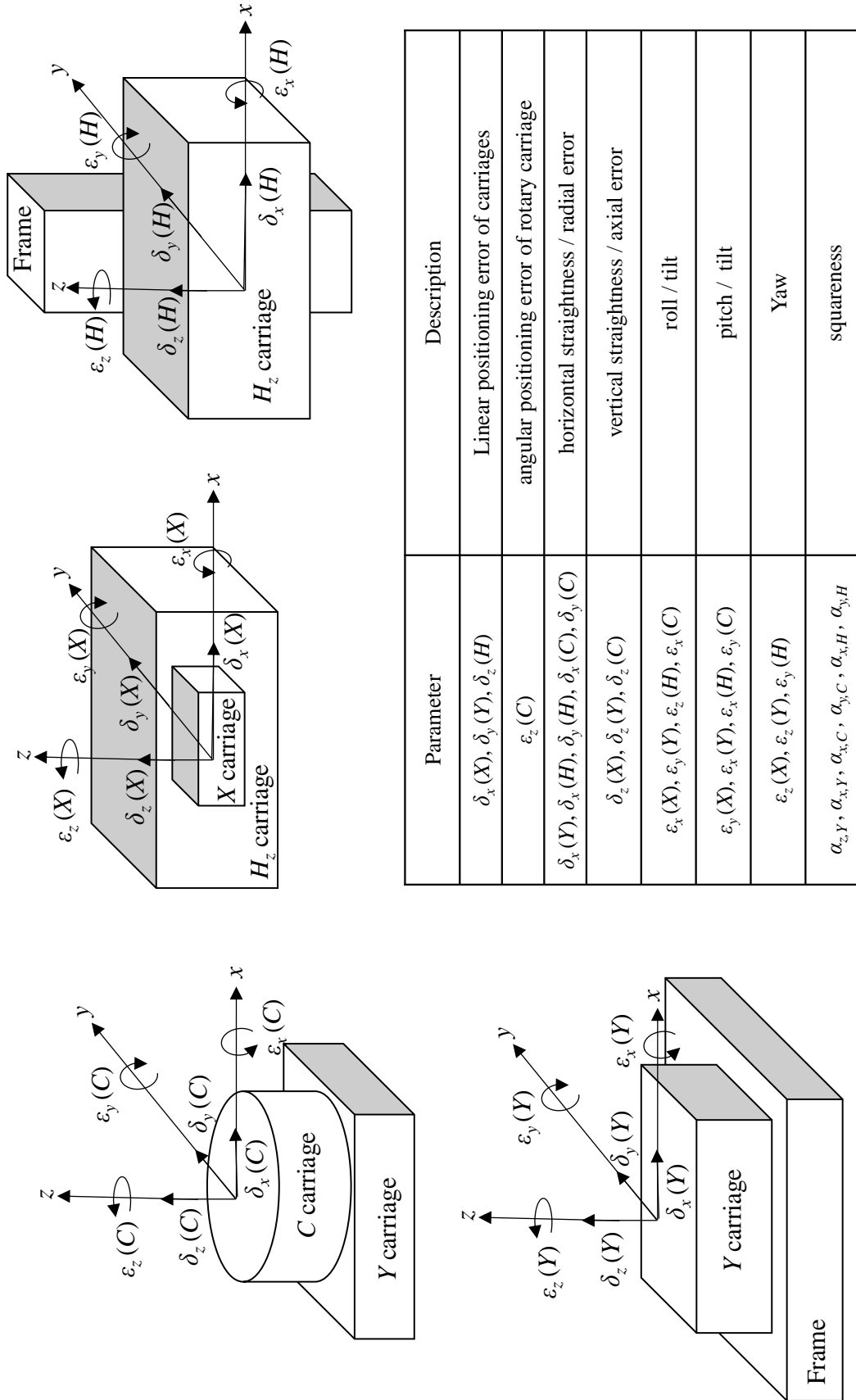


Figure 68: Symbols representing the errors in the motion of the carriages used in the profilometer system.

4.6.1 Simplified geometrical models for stripes and spokes methods of measurements

For stripes method of measurement, the C carriage is not utilized therefore making its translation vector, $[C]_Y = 0$ and Rotation matrices; R_{CY} and $R_{C,nom}$ as identity matrices, simplifying equation (10) to

$$[\vec{P}]_C = R_{YF}^{-1} \left[R_{XH} [\vec{P}_r]_X + [\vec{X}]_H - [\vec{Y}]_F \right] \quad (11)$$

For spokes method of measurements, the Y carriage is not utilized therefore making its translation vector, $[Y]_F = 0$ and Rotation matrix, R_{FY} as an identity matrix, simplifying equation (10) to

$$[\vec{P}]_C = (R_{CY} R_{C,nom})^{-1} \left[R_{XH} [\vec{P}_r]_X + [\vec{X}]_H - [\vec{C}]_Y \right] \quad (12)$$

4.6.2 Vector containing the X carriage errors and probe displacement terms

The equation (11) could be directly used for measuring machines such as a CMM in a FXYZ configuration [Hocken and Pereira, 2012] where the X , Y , and Z carriages are commanded to touch the surface of a test object using a probe. The point of contact (measurement point) is given by the locations of the X , Y , and Z carriages in the cartesian coordinate system at the triggering point of the probe. Profilometers do not contain an active Z carriage during the measurement. Here, a stylus probe attached to the X carriage is placed on a test object and ‘dragged’ using the X carriage, causing the stylus probe to pivot as a function of the z height variation of the surface. The z height values could be calculated by monitoring the rotation of the stylus around its pivot point and deconvolving the traverse and rotation to estimate the contact point of the probe on the surface.

As a first simplified model to evaluate stylus deconvolution, a two dimensional schematic of the X carriage and the stylus measuring a flat is shown in Figure 69(a). A spring attached to the

far end of the stylus is modeled as a means of measuring stylus displacement. When the stylus moves upwards in z , the spring extends, denoting the positive travel of the stylus. And, when the X carriage rotates or vertically translates upwards due to the pitch $\varepsilon_y(X)$ or vertical straightness $\delta_z(X)$ errors respectively, the spring compresses, making the measured z values negative, see Figure 69(b to d). Figure 69(e) shows the negative rotation of the stylus due to the positive rotation (clockwise) of the X carriage, because of the pitch error $\varepsilon_y(X)$. Figure 69(f) shows the motion of stylus ball center in x and z axis for a given arm length, l_a and stylus length, l_s given by their small angle approximation as,

$$\begin{aligned}\Delta x &= l_a (1 - \cos \varepsilon_y) + l_s \sin \varepsilon_y \approx l_s \varepsilon_y \\ \Delta z &= l_a \sin \varepsilon_y + l_s \cos \varepsilon_y - l_s \approx l_a \varepsilon_y\end{aligned}$$

Figure 69(g and h) shows the motion of the stylus during the roll and yaw of the carriage ($\varepsilon_x(X), \varepsilon_z(X)$) respectively, and the equations representing the motion of the stylus ball center in the third dimension (y), and their small angle approximations are given below.

$$\begin{aligned}\Delta x &= 0 \\ \Delta y &= l_s \sin \varepsilon_x \approx l_s \varepsilon_x \\ \Delta z &= l_s - l_s \cos \varepsilon_x \approx 0 \\ \Delta x &= l_a - l_a \cos \varepsilon_x \approx 0 \\ \Delta y &= l_a \sin \varepsilon_z \approx l_a \varepsilon_z \\ \Delta z &= 0\end{aligned}$$

Therefore, when a flat is measured using the profiler as shown in Figure 70(a), the motion of the center of the stylus ball with respect to the reference coordinate origin, O_F is given by,

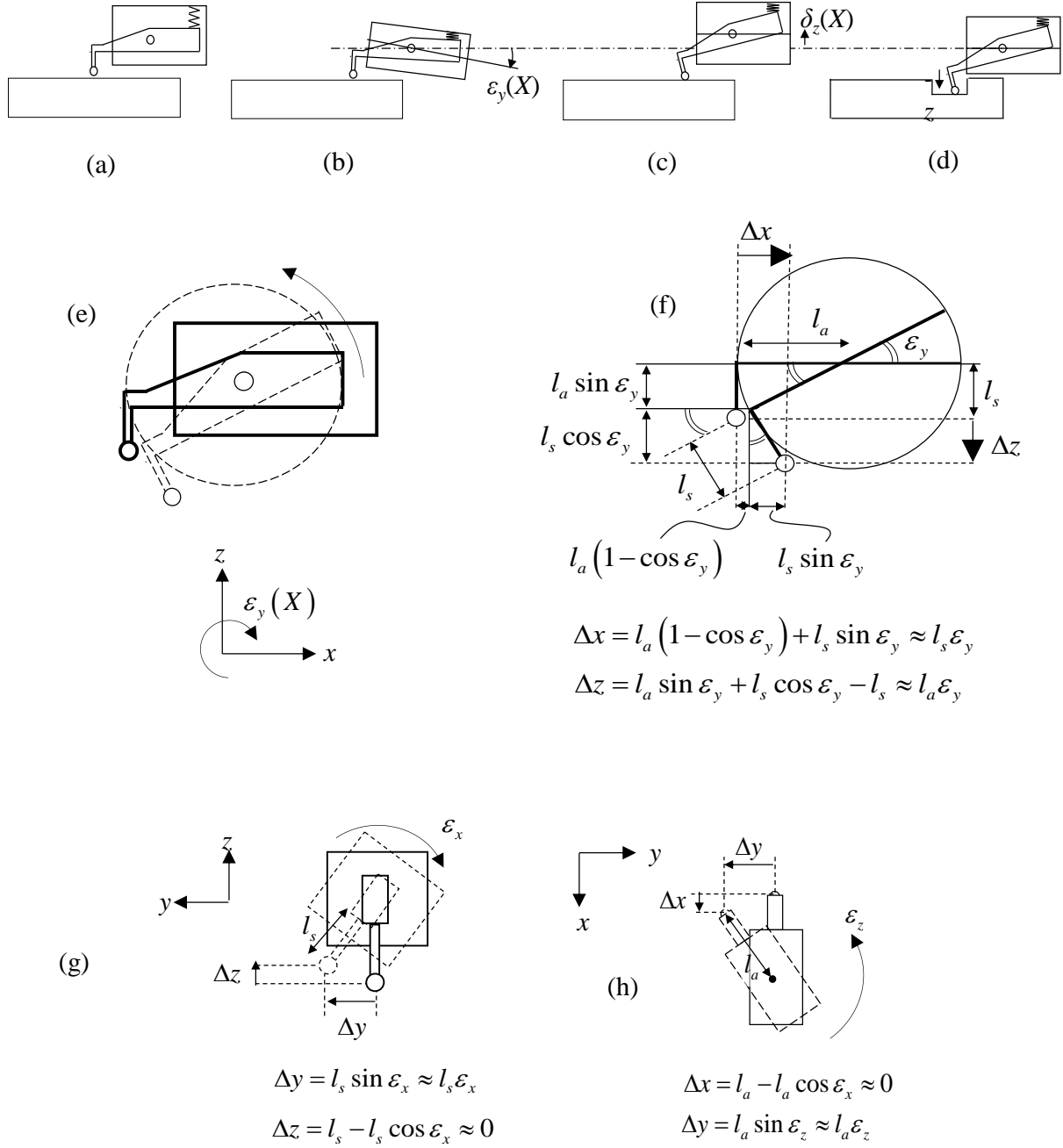


Figure 69: Schematics showing the motion of stylus with respect to the errors in the motion of X carriage (a to d) sign of output z values due to the x carriage travel error (e) counterclockwise rotation of stylus (f) motion of probe due to the rotation (g) motion of the stylus due to the roll and (h) yaw of X carriage.

$$R_{XH} \begin{bmatrix} \vec{P}_r \end{bmatrix}_X + \begin{bmatrix} \vec{X} \end{bmatrix}_H = \begin{bmatrix} (X_m - X_{m0}) + \delta_x(X) - l_a + l_s \varepsilon_y(X) \\ \delta_y(X) - l_a \varepsilon_z(X) + l_s \varepsilon_x(X) \\ -(\delta_z(X) + l_a \varepsilon_y(X)) - l_s \end{bmatrix}$$

The reported x values by the profiler contains the measured x position, offset due to stylus arm length, and the arcuate correction influenced by the pitch error of the X carriage, $x = X_m - l_a + l_s \varepsilon_y(X)$, and the reported z values by the profiler contains the influence of vertical straightness of X carriage and the arcuate correction influenced due the pitch error of the X carriage, $z = -(\delta_z(X) + l_a \varepsilon_y(X))$. It is noted that this vector forms the component of the X carriage and probe in equations (11) and (12).

A simulation of a measurement of a ‘perfect’ flat is shown in Figure 71(c), for an assumed vertical straightness, $\delta_z(X)$ of $0.5 \mu\text{m PV}$ approximated by a parabola. The pitch error $\varepsilon_y(X)$ is sampled from a uniform distribution of $\pm 1 \mu\text{rad}$.

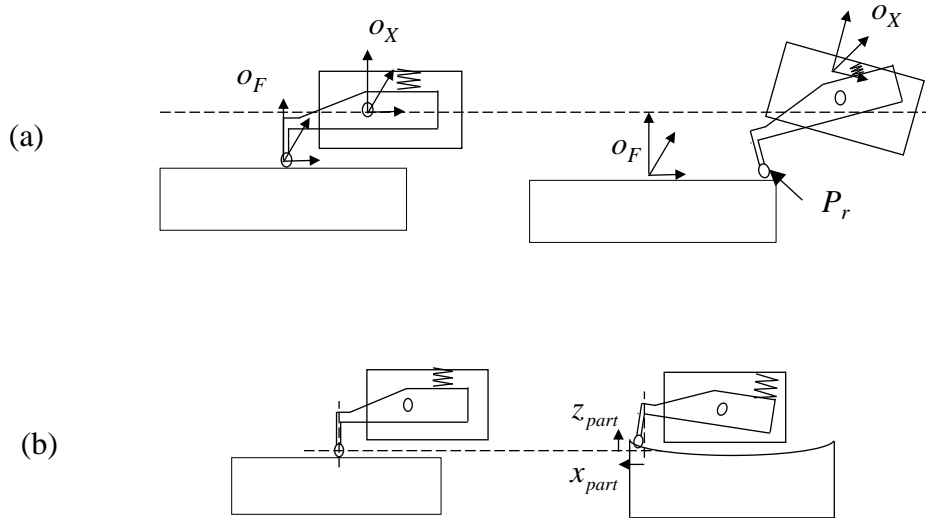


Figure 70: Schematic of (a) perfect flat measured by the stylus (b) concave surface measured by the stylus.

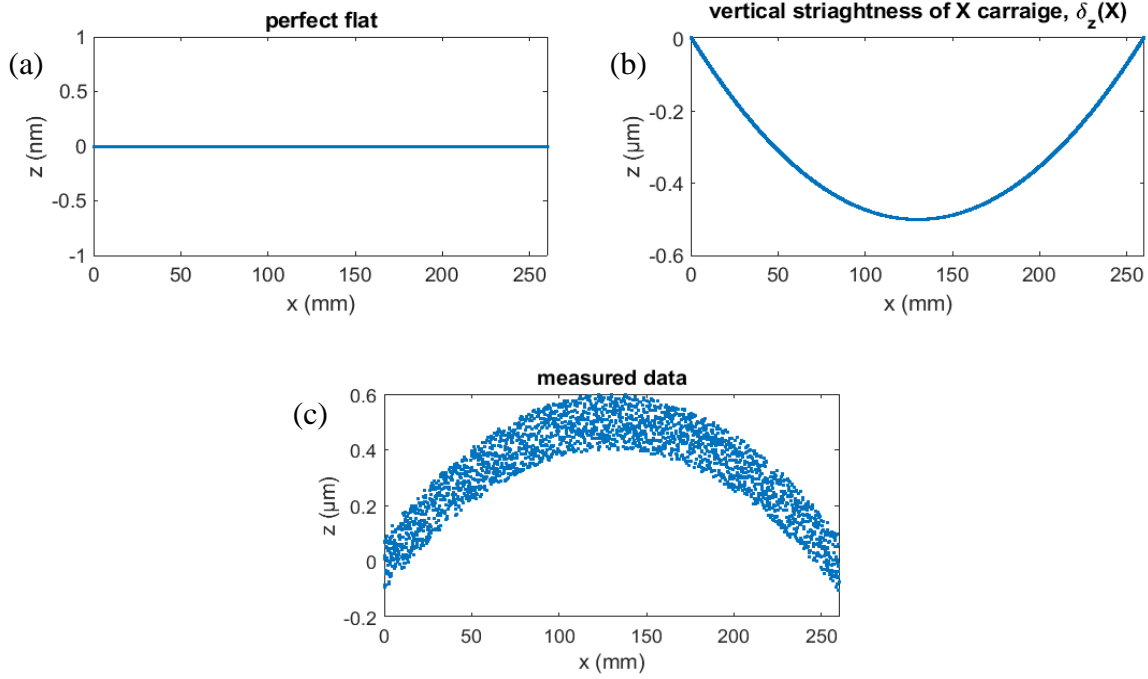


Figure 71: Simulation of the effect of vertical error of the X carriage on the resulted measurement; (a) Simulated data of a perfect flat, (b) vertical straightness of 0.5 μm PV (c) resulted profile measurement.

If the object measured by the profiler is a concave surface as schematically shown in Figure 70(b), the motion of the center of the stylus ball in cartesian coordinate is given by,

$$R_{XH} \begin{bmatrix} \vec{P}_r \end{bmatrix}_X + \begin{bmatrix} \vec{X} \end{bmatrix}_H = \begin{bmatrix} (X_m - X_0) + \delta_x(X) - l_a + l_s \varepsilon_y(X) + x_{part} \\ \delta_y(X) - l_a \varepsilon_z(X) + l_s \varepsilon_x(X) \\ -(\delta_z(X) + l_a \varepsilon_y(X)) - l_s + l_a \sin \varepsilon_y + l_s (1 - \cos \varepsilon_y) + z_{part} \end{bmatrix} \quad (13)$$

where, $x_{part} = l_a (1 - \cos \theta_y) + l_s \sin \theta_y$, $z_{part} = l_a \sin \theta_y + l_a (\cos \theta_y - 1)$, and θ_y is the rotation of the stylus due to the slope of the part being measured. It is noted that the horizontal straightness roll, and yaw errors of X carriage ($\delta_y(X)$, $\varepsilon_x(X)$, $\varepsilon_z(X)$) causing the probe tip offset in x and z axes due to the surface slope are ignored in equation (13).

4.7 Flat surface measurements for profiler performance evaluation

To study the performance of the profilometer in measuring flat surfaces, two optical flats are used as reference objects,

- (i) a 6 in. dia. (~150 mm) , 1 in. thick, Fused Silica flat with a manufacturer specified flatness of $\lambda/10$ (Edmund optics, Stock #01-612-000), and
- (ii) a 4 in. dia. (~100 mm), 3/4 in. thick, Zerodur flat with a manufacturer specified flatness of $\lambda/10$ (Edmund optics, stock #31-392-000)

4.7.1 Interferometric measurements of reference optical flats

The optical flats used in this study were measured using a phase shifting interferometer in Fizeau configuration (Zygo – Verifire) with the results from these measurement plotted in Figure 72. Complete details necessary to reproduce the measurements are given in Appendix C.2.1 and C.2.4. To know the orientation of the flats during the interferometric measurements, circular fiducials of 2 mm diameter made of plastic with adhesive back surface are stuck on the surface of the flats and can be seen in Figure 72(b and d). Figure 72(a to c) shows the measurement of the Fused Silica flat indicating a 40 nm PV deviation. Since the aperture of this flat (6 in.) is greater than the aperture of the transmission flat (4 in.) used in the Fizeau interferometer, the Fused Silica flat was translated vertically to two overlapping locations and two interferograms were captured. The two fiducials in the overlapping region are used to collocate the two interferograms and stitch them using the least sum of squares method. For more detailed description of the stitching procedure, see Appendix C.2.1 (e). It is noted that this stitched interferogram also includes the

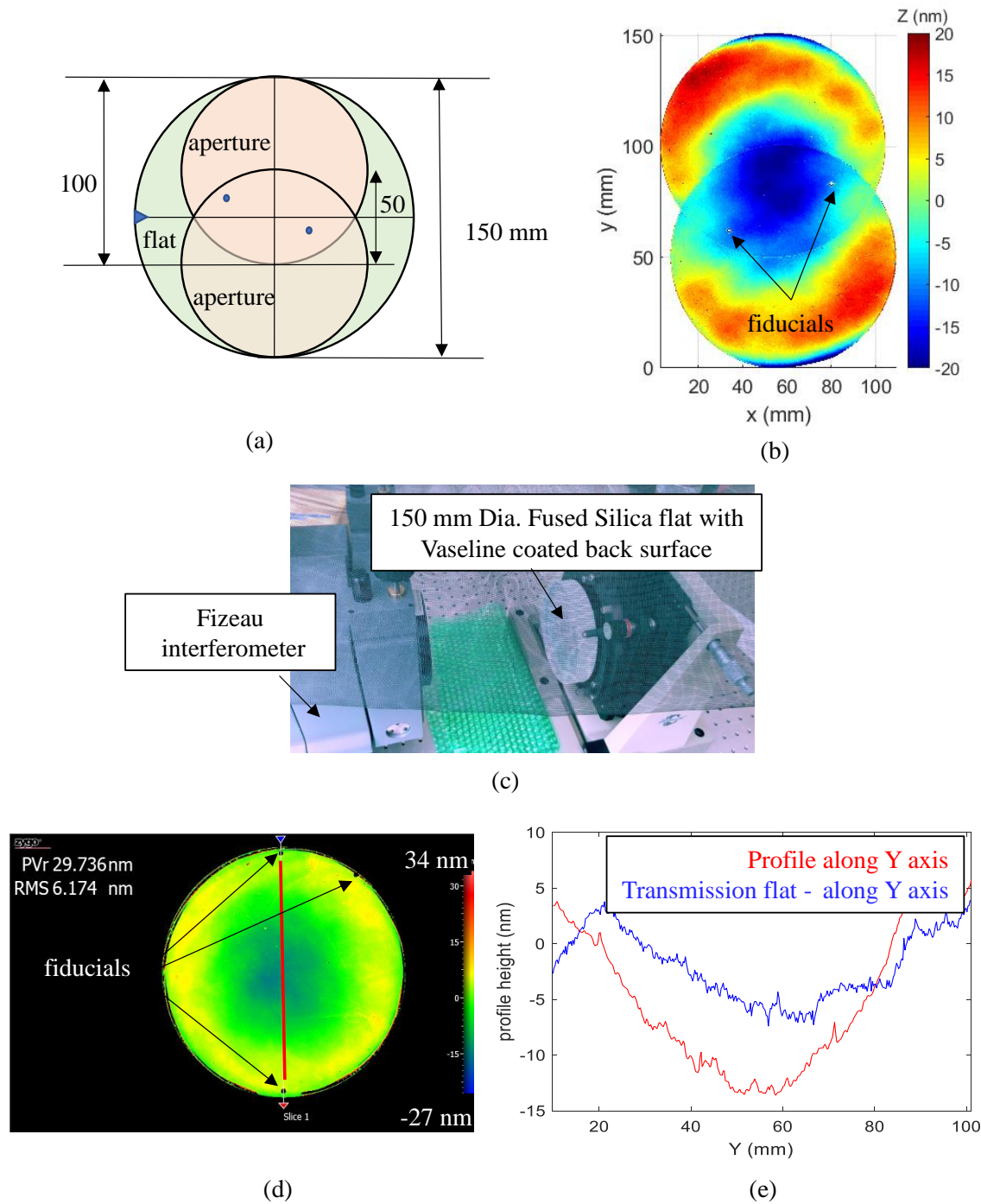


Figure 72: Interferometric measurements of the reference optical flats; (a) Schematic showing the Fused Silica flat of diameter larger than the aperture of transmission flat, measured by locating in two positions with an overlapping area (b) Stitched interferograms of the two measurements (c) Fused Silica flat being measured using a Fizeau interferometer (d) Interferogram of the Zerodur flat measured using a Fizeau interferometer (e) A profile along the vertical diameter of the interferogram with 20 nm PV compared to the profile of the transmission flat used in the measurement obtained via. three flat test.

effect of the out of flatness of the transmission flat, which is estimated to be about 10 nm PV from a 3-flat test (see Appendix C.2.4, Figure 227). Figure 72(d) shows the interferogram of the Zerodur flat with a 30 nm PV estimate.

A profile along the vertical diameter of the transmission flat obtained via. “3-flat test” is shown alongside the profile from the interferogram, see Figure 72(b). In another measurement of the Zerodur flat using a different Fizeau interferometer in vertical configuration, it is estimated to have a less than 10 nm PV (see Appendix C.2.4, Figure 236).

By measuring these flats using the profiler, the following characteristics of the profilometer are studied:

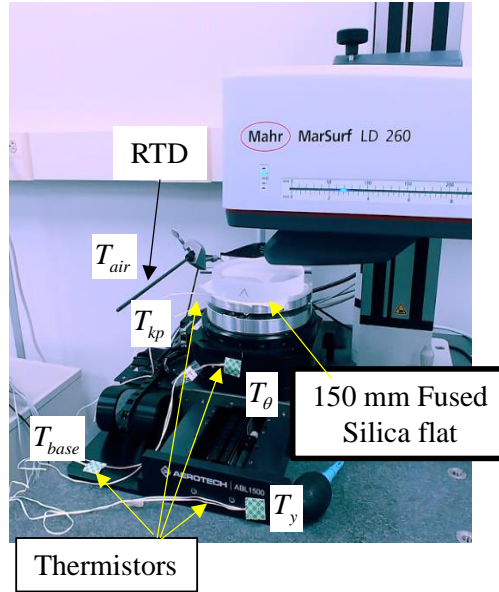
- (a) static electrical noise, static and dynamic thermal drift in the system
- (b) repeatability in measurements
- (c) motion of the stylus due to the pressure variation in the air supply to the Y and C air bearing carriages
- (d) force feedback control of the stylus
- (e) a combined vertical straightness $\delta_z(X)$ and pitch error $\varepsilon_y(X)$ of the X carriage
- (f) surface measurements by stripes and spokes methods, which not only provide the overall performance of the profiler for areal measurements, but also provided estimates of combined vertical straightness $\delta_z(Y)$ and pitch $\varepsilon_z(Y)$, and roll error $\varepsilon_x(Y)$ of the Y carriage, tilt $(\varepsilon_x(C), \varepsilon_y(C))$ and axial errors $\delta_z(C)$ of the C carriage. Using a Tie line for thermal compensation is also demonstrated.

Assessment of each of these measures are presented in the following subsections of this section. It is noted that the expected gravitational sag of the Zerodur flat is calculated to be 2 nm as discussed in section 4.7.5.2 (a). And the diameter (150 mm) to thickness ratio (20 mm) of the Fused Silica flat is 7.5:1, therefore minimizing the gravitational sag.

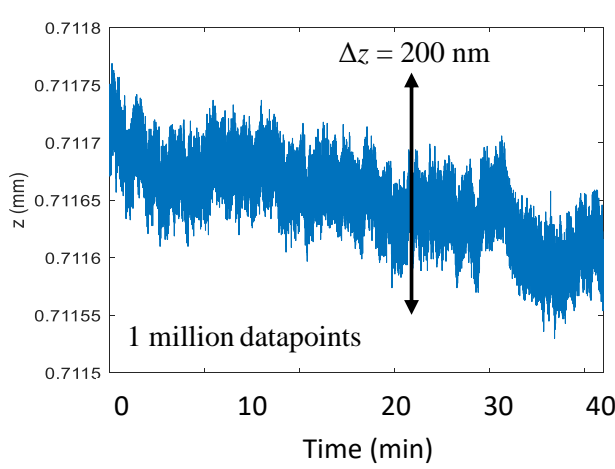
4.7.2 Static electrical noise and thermal drift

To study the variation in the z height values reported by the profiler due to the electrical noise and the static thermal drift in the system, the stylus is rested on the Fused Silica flat for 40 minutes and the z values reported by the profiler is monitored. To record the temperature of the atmosphere during this measurement, a RTD (Resistance Temperature Detectors) is placed in air. To record the temperature changes on the different components of the system, using a 3MTM double sided tape four thermistors were attached to the surfaces of: the kinematic plate under the flat, the rotary carriage, the Y carriage, and the base (or frame). Details of calibration of the temperature sensors are given in Appendix C.3. Motion of the stylus due to the drift in the system is recorded for about 40 minutes and had a PV deviation of 200 nm, see Figure 73(b). This signal includes the effect of temperature drift, force feedback control of the stylus, and the electrical noise in the system. To reject the long term temperature drift, this signal is high pass filtered that results in a 100 nm variation predominantly caused by electrical noise in the sensor and the signal processing equipment, see Figure 73(c).

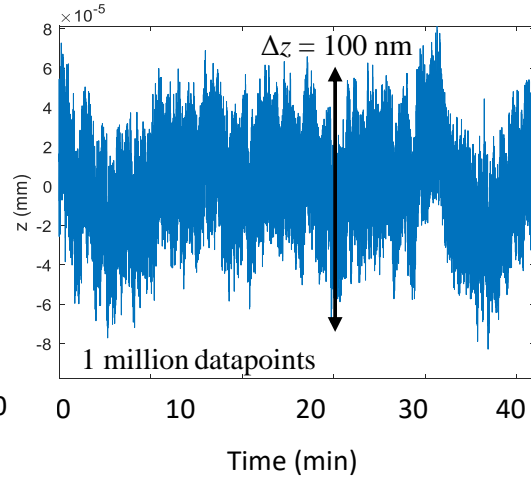
Plots showing the relationship between the drift and the temperature at the different location of the profilometer system are shown in Figure 74. The signal of the stylus motion (drift) is low pass filtered to 60 seconds before being plotted. From Figure 74(a), the variation in air temperature monitored by the RTD is less than 0.1 °C, which is the within the allowable temperature variation in the laboratory. There is also a significant correlation between drift of the



(a)



(b)



(c)

Figure 73: Experiment measuring the drift in the system and the temperature variation of the components in the system; (a) Profilometer system with RTD and thermistors to monitor temperature variations of air and other components in the system (b) Drift in the system showed by the motion of stylus (c) Drift removed to show electrical and other high frequency noise in the system.

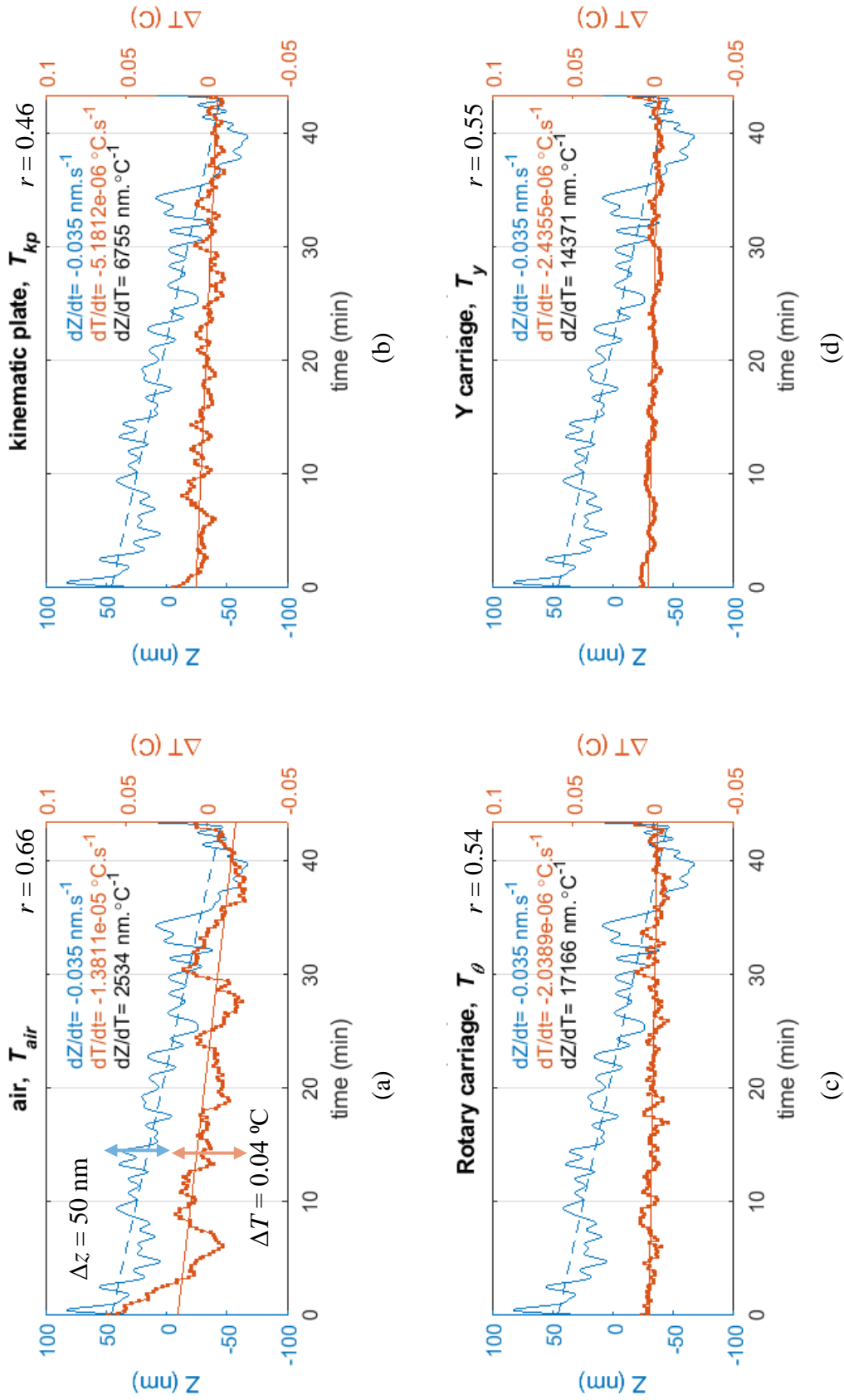


Figure 74: Drift , and the temperature of (a) air, and surfaces of (b) kinematic plate, (c) rotary carriage, and (d) Y carriage plotted as a function of time.

stylus reading and the air temperature monitored by the RTD, correlation coefficient, $r = 0.66$. The temperature monitored by the thermistors at other surfaces of the profilometer system varied less than $0.02\text{ }^{\circ}\text{C}$.

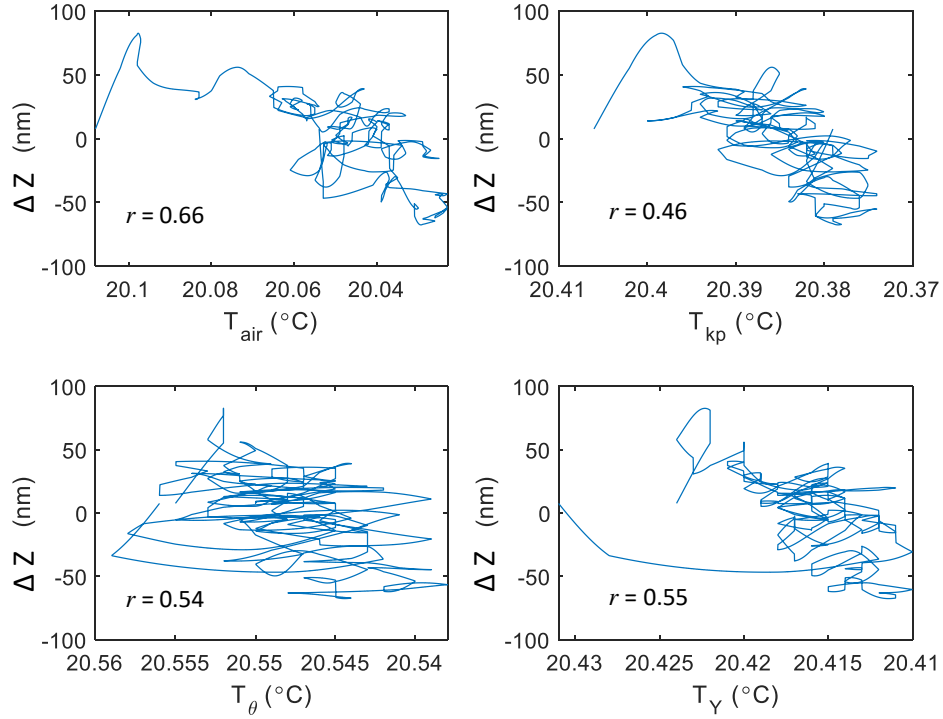
The drift is also plotted with respect to the temperature and is shown in Figure 75(a). A theoretical estimate, that does not include drift in the signal conditioning electronics or the dynamic variations with components having different thermal capacity, of thermal expansion (ΔL) considering the thermal expansion coefficients of the material (α) and the length of the components (L) with respect to the change in temperature (ΔT) is given by,

$$\Delta L = \left((\alpha_{\text{castiron}} L_{\text{base}} + \alpha_{\text{steel}} L_{\text{screw}}) - (\alpha_{\text{carbonfiber}} L_{\text{stylus}} + \alpha_{\text{fusedsilica}} L_{\text{part}} + \alpha_{\text{aluminum}} (L_C + L_Y)) \right) \Delta T$$

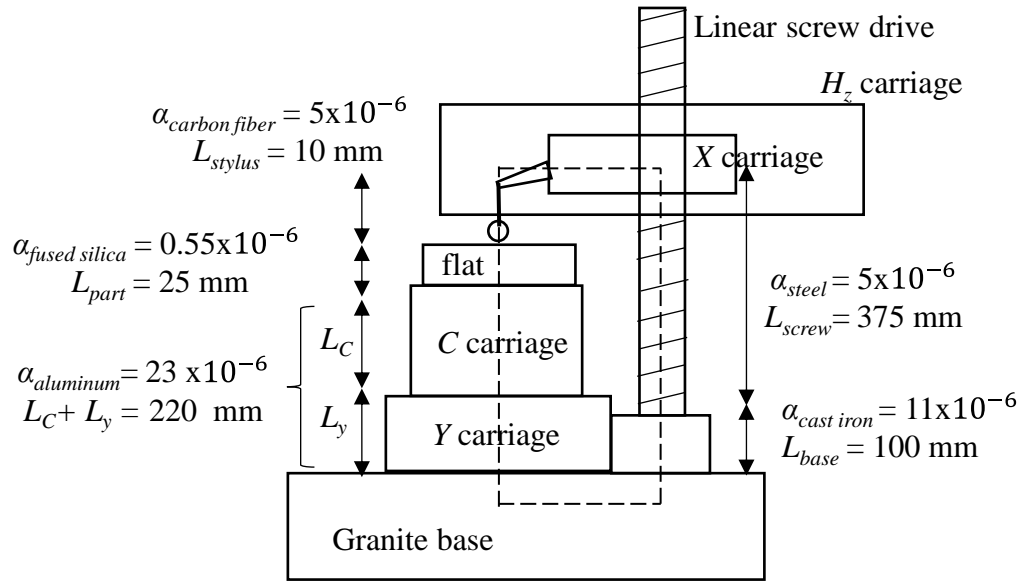
and is about $35\text{ nm}/0.1\text{ }^{\circ}\text{C}$. See Figure 75(b) for dimensions and thermal expansion coefficients of the different material of the components in the profilometer system. From the experimental result shown in Figure 74(a), thermal drift is about $100\text{ nm}/0.1\text{ }^{\circ}\text{C}$.

4.7.3 Effects of pressure variation in the air supply to the carriages

To know the displacement of the stylus due to the pressure variation in the air supplied to the Y and C carriages, a pressure sensor that streams data via USB (Universal Serial Bus) to the computer is connected at the air source before being filtered, see Figure 76(b and c). The stylus is rested on top of the micrometer stage as shown in Figure 76(a), and its motion is recorded and plotted along with the pressure variation in Figure 76(c). These data are low pass filtered to 60 seconds and plotted as a function of time, and against one another in Figure 76(c and d) respectively. The correlation coefficient of the low pass filtered data is, $r = 0.03$, indicating there are no significant effects caused by the air bearing pressure variation to the motion of the stylus.

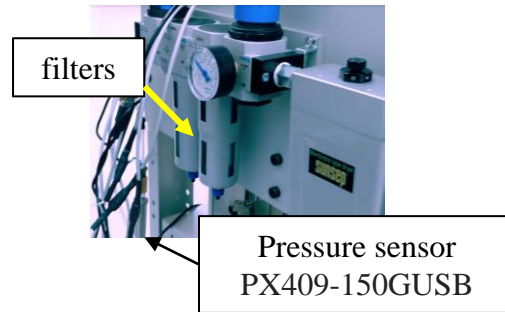
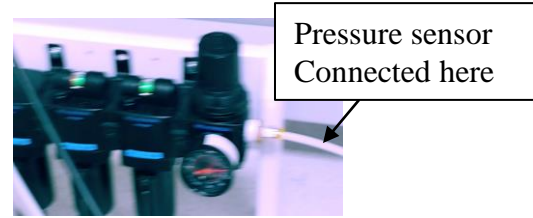
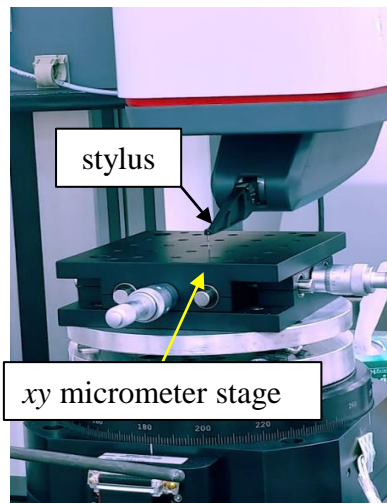


(a)



(b)

Figure 75: Thermal expansion coefficients of the material, and the height of the components in the profilometer system (a) Drift in measurement plotted as a function of temperature of air, and surfaces of kinematic plate, rotary stage, and Y stage (b) Schematic of the system showing the lengths and thermal expansion coefficients of the material of different components.



(a)

(b)

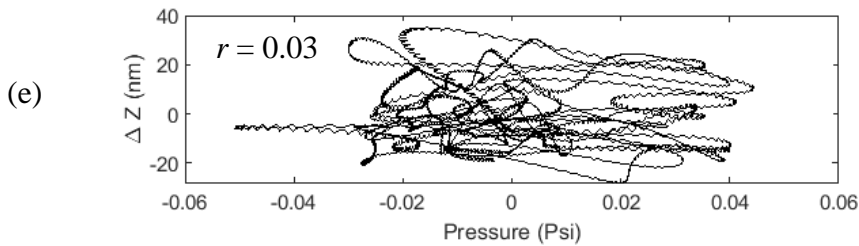
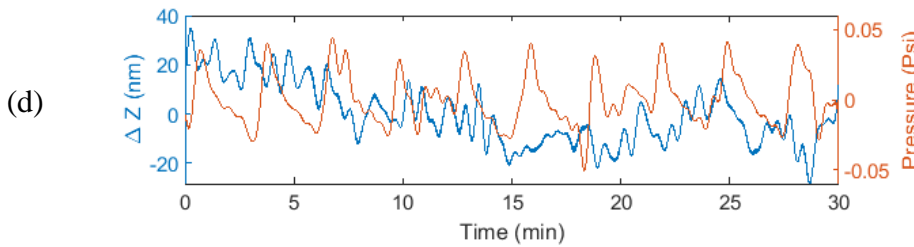
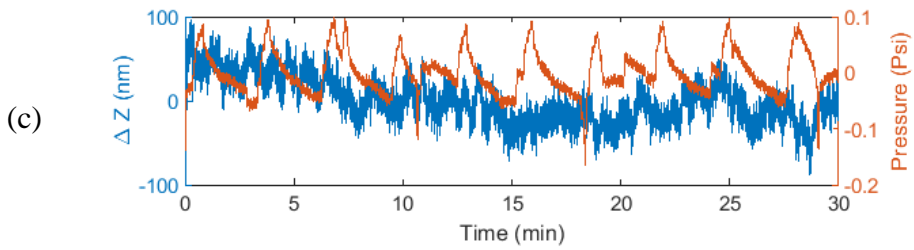


Figure 76: Measurement to observe the air pressure variation in the air bearing stages and its effect on the motion of the stylus; (a) Stylus resting on top of the micrometer stage (b) Location of the pressure sensor (c) Data showing stylus motion in blue, and air pressure variation in orange (d) data low pass filtered to 60 seconds (e) stylus displacement and pressure variation plotted against one another.

4.7.4 Vertical error in the profiles measured in the middle 130 mm travel in x axis

To observe the correction for the vertical straightness and pitch of the X carriage, the stylus was ran ‘in air’ (when it is not in contact with a sample surface) at a constant velocity of $1 \text{ mm} \cdot \text{s}^{-1}$. During this traverse, the stylus is not expected to displace. Acceleration when the carriage gets up to speed and decelerated to stop, will create moments if the center of mass of the stylus is not coincident with the pivot point, but no noticeable effect is observed in the data. The measured profile is expected to majorly consist of electrical noise only. A profile made by traversing the profiler in air for a mid-travel range of 130 mm ($x = 70 \text{ mm}$ to 200 mm) is shown in blue in Figure 77(a). The 1000 nm PV variation in this profile indicates a manufacturer’s correction curve input to the software. This correction curve should have been obtained by profiling a calibrated optical flat, schematically presented in Figure 78(a). The resulting profile could be subtracted from the calibration flat’s out of flatness to reveal the errors in the motion of X carriage, mainly vertical straightness, $\delta_z(X)$, and pitch, $\varepsilon_y(X)$ combined.

To validate this correction, a profile of same length was made on the Fused Silica optical flat and a line is subtracted to remove the tilt of the part resulting in a 250 nm PV, plotted in orange in Figure 77(a). It was not expected to see a 250 nm PV error if the calibration was performed correctly or if the errors of the X carriage had not changed since calibration. It is noted that the out of flatness of this flat measured interferometrically is only 40 nm PV, see Figure 72(d). To remove the high frequency content of the measurement, it is low pass filtered to 1 mm, showing oscillations of about 50 nm amplitude with 5 mm periods, see Figure 77(b). This 5 mm period could be an effect of the lead screw errors coupling into the X carriage. A parabola is removed from the low pass filtered signals to show the similarity in the phase of the 5 mm periods in the ‘air profile’ and the profile made on the flat, see Figure 77(c).

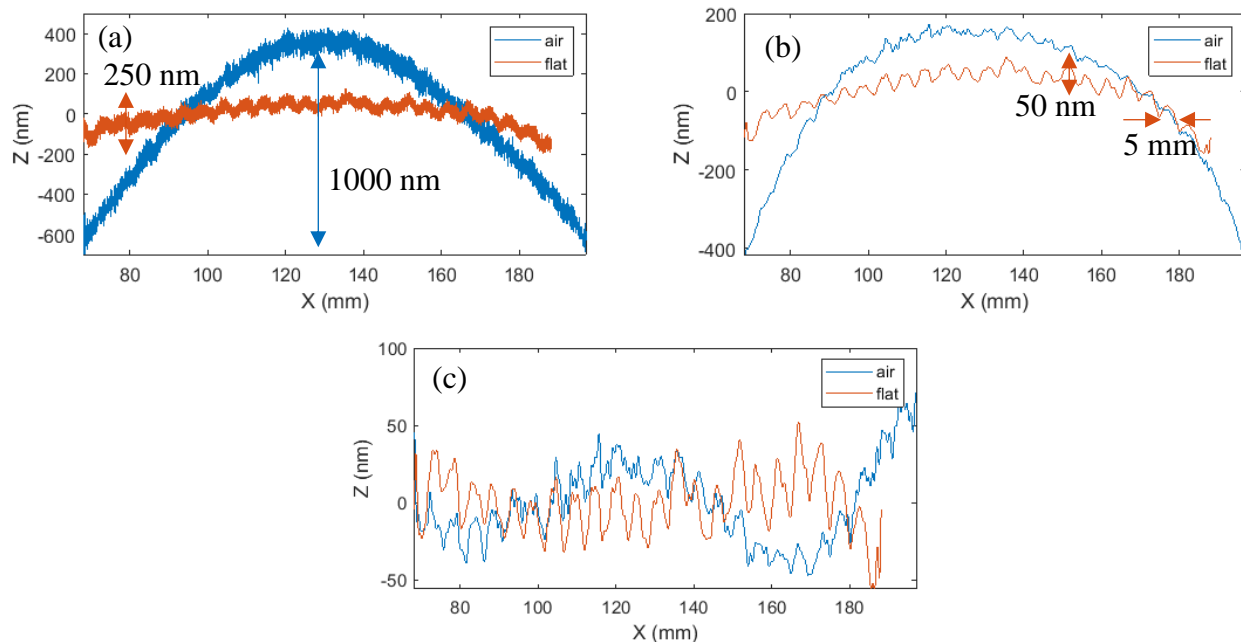


Figure 77: Plots showing the results of profiling in air and on an optical flat; (a) profile in air is shown in blue, and on the Fused Silica optical flat is shown in orange, (b) Signals low pass filtered at 1 mm, (c) Parabola removed from the low pass filtered signals showing 5 mm periodic oscillations and the similarity in their phase.

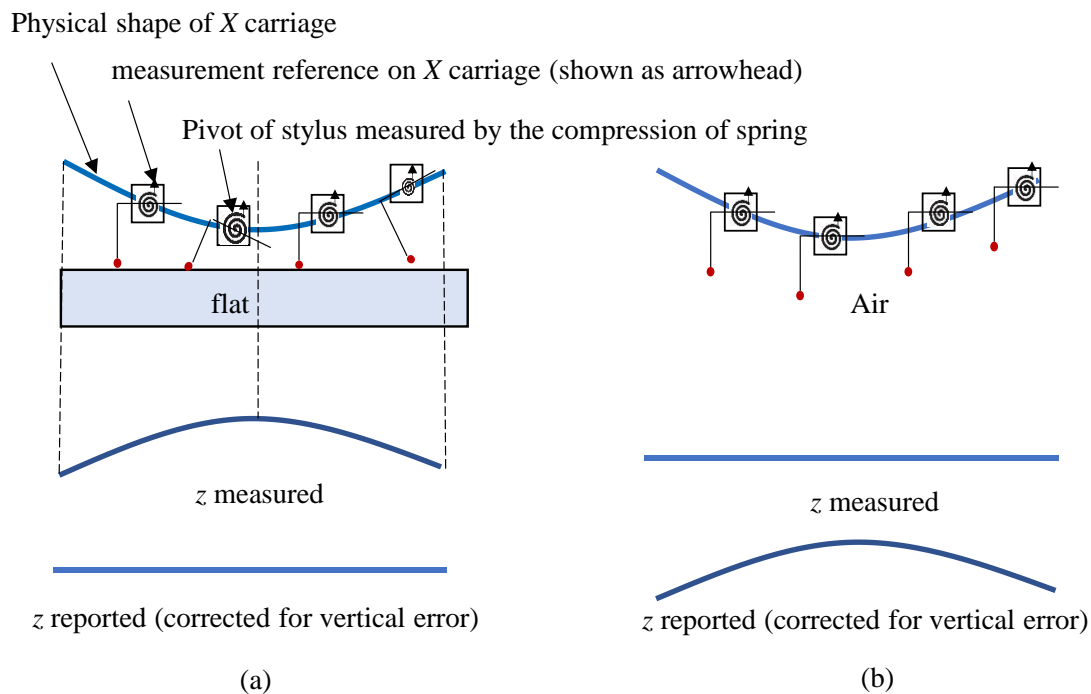


Figure 78: Schematic (a) of a measurement of an ideal optical flat showing the X carriage error (b) Reported measurement in air containing the correction curve

From here on, this 250 nm PV error due to the vertical straightness and pitch error of the X carriage is referred together as ‘vertical error’ of X carriage which is caused either due to the vertical straightness and pitch of Y carriage or a residue in the correction performed by the manufacturer. It is noted that the above discussed measurements are only performed over a range of 130 mm travel over the central region of the x direction carriage. The following section discusses the experiments to determine the vertical error for the full 260 mm x axis travel of the profiler.

4.7.5 Vertical error in the profiles measured in the full x axis travel

4.7.5.1 Nitralloy Straight edge

To estimate the vertical error for the full 260 mm x axis travel, a Nitralloy straight edge [Moore, 1970, p.83] with a 5 μm . (125 nm) out of flatness shown in Figure 79(a) is measured. The measured is shown in Figure 79(b), and a 100 point moving average of this signal with a 600 nm PV is shown in Figure 79(c) representing the vertical error for the full x travel.

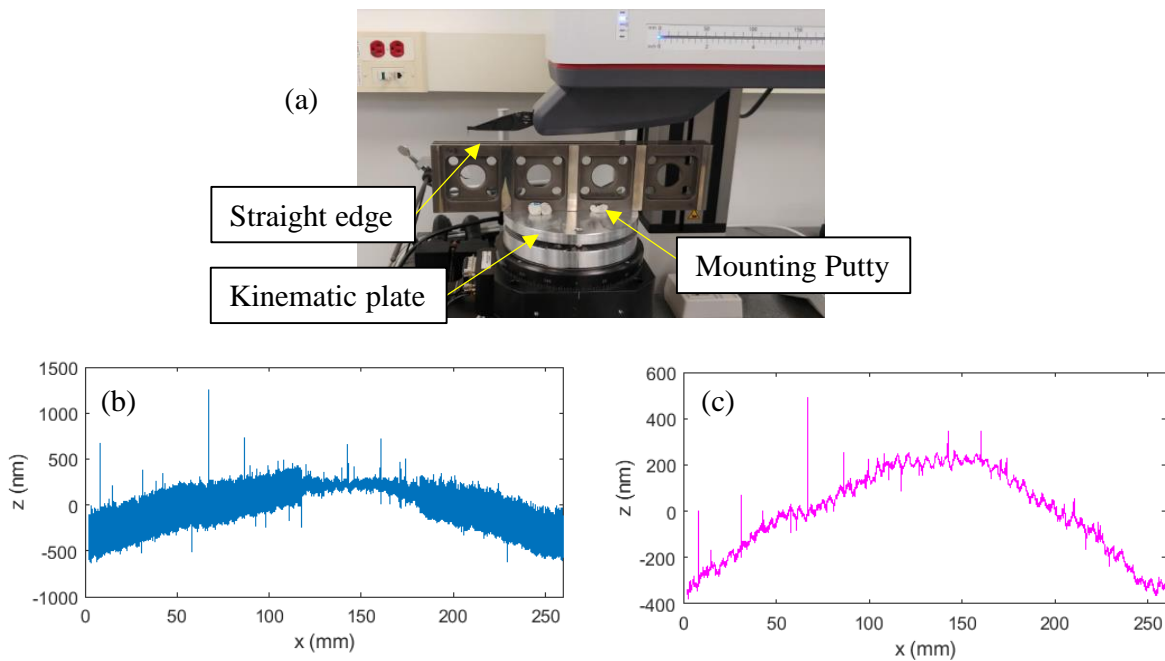


Figure 79: Measurement of a straight edge made of Nitralloy (a) Photograph of the straight edge being measured using the profiler (b) line subtracted data with 1 μm data spacing in x (c) a 100 point moving averaged data to reduce high frequency component of the measurement.

4.7.5.2 Zerodur flat piecewise measurement

Since the out of flatness of the straightedge is about 20% of the measured vertical error, a Zerodur flat of 100 mm diameter, less than 30 nm out of flatness shown in Figure 72(d) is measured in a piece-wise manner to estimate the vertical error of the X carriage. For these experiments, the flat is measured in 4 locations along the x axis of the profilometer with about 30% overlap thereby covering the full 260 mm horizontal travel of the profiler. Figure 80(a) shows schematically the profiles on the flat with overlapping locations in x , i.e., the first overlapping segment is 27 mm. Each of the four profiles will have different z offsets and tilts at their location which is removed using least sum of squares analysis at the overlapping locations, resulting in a stitched profile representing the vertical error of the X carriage for its full span.

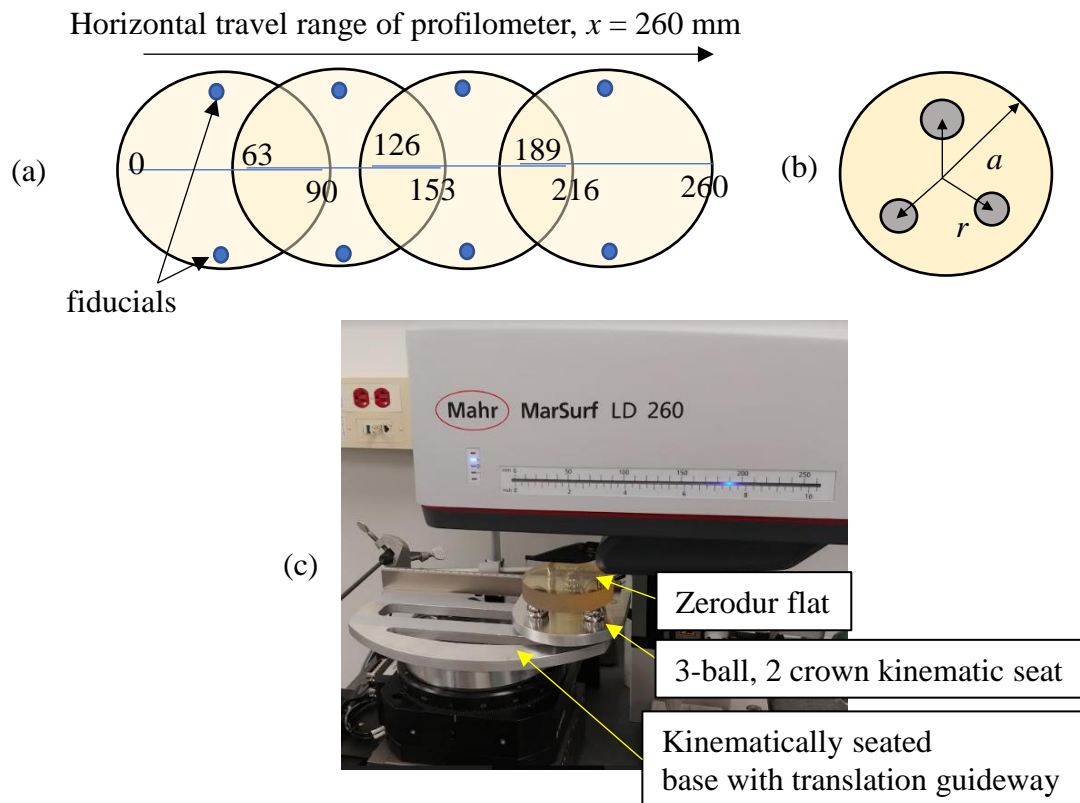


Figure 80: Piece-wise measurement of a Zerodur flat; (a) Schematic showing the piecewise measurement of the flat with overlapping locations in x axis (b) Flat supported on a kinematic seat at the final location of measurement.

The following sections discuss the kinematic assembly used to support and translate the flat during the measurements, measurement procedure and the results, and stitching procedure. Also discussed is a comparison of the estimated vertical error using the stitched profiles with the calibration result of the X carriage performed by the manufacturer at their manufacturing location and our laboratory when it was installed.

a) Assembly to support and translate the flat

Figure 81(a and b) shows a top and front views of the solid model and a photograph of the assembly on which the 100 mm Dia. Zerodur flat is mounted. This assembly has a base plate (shown in orange) with three stainless steel hemispheres on its bottom (shown in the front view of Figure 81(a)) that gets attached to three kinematic dowel pin grooves on top of the attachment on the rotary carriage of the profilometer system, see Figure 61(c). An Ultrahigh Molecular weight polyethylene tape is attached on top of the base plate acting as a bearing surface for the kinematic seat for the optical flat, see Figure 81(c). This kinematic seat comprises three stainless steel hemispheres in its bottom (Baltec 500-TB) that slides on the polyethylene tape, constraining (z, θ_x, θ_y) and two more stainless steel hemispheres on the edge that slides on the translation guideway made of Nickel coated Carbon steel rectangular bar with a thickness tolerance of $\pm 50 \mu\text{m}$ supported against two dowel pins. This constrains (y, θ_y) , thereby allowing only the freedom to translate in x .

On top of the kinematic seat, three stainless steel hemispheres of 1 in. dia. (Baltec 100-TBR-T) are attached, on which the Zerodur optical flat will be seated, constraining (z, θ_x, θ_y) . The size of the hemispheres are chosen to reduce the pressure that the bottom surface of the flat endures. A Hertzian analysis of the flat-hemisphere interface is given in Appendix C.4. These three hemispheres are arranged in 120° from each other, and at a radial distance of 0.7 times the

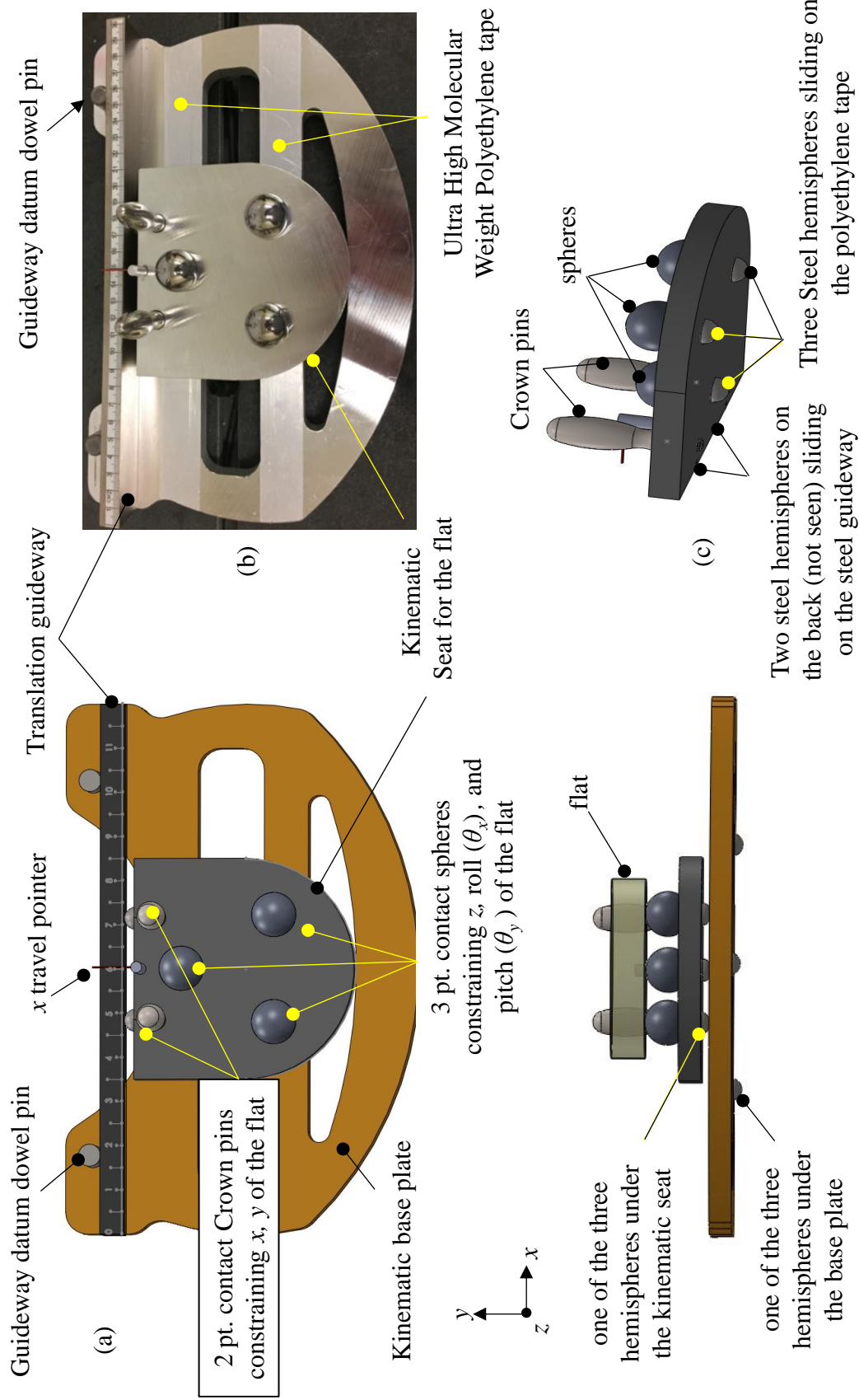


Figure 81 Experimental assembly used in the piecewise measurement of the Zerodur flat; (a) Solid model of the top and front views (b) Photograph of the kinematic assembly used to support and translate the optical flat during the piece wise measurement (c) kinematic seat on which the flat is supported.

radius of the flat, see Figure 80(b). This arrangement is chosen to reduce the, z_{sag} , of the flat computed from

$$z_{sag} = \frac{\rho g}{4E} \left[\left(\frac{1}{t^2} \right) \frac{3}{4} (1 - \nu^2) \left(\frac{5 + \nu}{1 + \nu} (a^2 - r^2) \right) + (3 + \nu) \right] (a^2 - r^2) \text{ [Emerson, 1952]}$$

where,

density of Zerodur, $\rho = 2530 \text{ kg.m}^{-3}$

acceleration due to gravity, $g = 9.81 \text{ m.s}^{-2}$

Elastic modulus of Zerodur, $E = 90.3 \text{ N.m}^{-2}$

thickness of the flat, $t = 19 \text{ mm}$

Poisson's ratio of Zerodur, $\nu = 0.24$

radius of the flat, $a = 50.8 \text{ mm}$

distance of the steel balls from the center, $r = 0.7a$

For the parameters of this assembly a self-weight sag of 1.3 nm is predicted. The edge of the flat is pushed gently against the two 'Crown pins' shown in Figure 81(a and b) constraining (x , y) leaving only the freedom of azimuth rotation of the flat (θ_z). The kinematic seat of the flat is moved and positioned at each x location of the piece wise measurement with the help of a pointer and a measurement scale fastened with adhesive backing on the top edge of the guideway, see Figure 81(a and b).

b) Piecewise measurement of the flat

The profiler was automated to make ten repeated profiles on the flat at each x location without the presence of the operator to avoid thermal and other disturbances. When the flat with its kinematic seat moved to its desired x location, it was allowed to ‘soak out’ for an hour, then the operator walks in and start the warmup run of the profiler and exits the room, and the period of warmup run is one hour. The reason to perform this warmup routine is to reduce the thermal drift caused during the travel of the profiler, and this is discussed in detail in section 4.7.6. Once the warmup run completes, the stylus makes contact on the surface of the flat and performs ten repeated, 90 mm long, profiles with a data spacing of 1 μm which takes about 15 minutes, and this process is repeated for the remaining three x locations of measurements. The raw data obtained from these measurements are plotted in Figure 82(a). It is noted that the H carriage height was the same, but the pivot angle of the stylus changes to make contact on the surface at each location. A line is subtracted from the raw data revealing the outliers datapoints, typically in the range of a few micrometers and, being vertical, are most likely dust or adhered dirt, see Figure 82(b).

Outliers that are greater than 3σ standard deviation are removed from the raw data shown in Figure 82(a), and again a line is fitted and subtracted to obtain the profiles shown in Figure 82(c). It is noted that with or without removing the outliers the slope of the raw data computed from the line fit differs less than a microradian. Averages of the 10 repeated measurements at each x location is shown in Figure 82(d), and their standard deviation representing the repeatability of the measurements which was consistently less than 50 nm, see Figure 83(a). A 100 point moving average is applied to the data a plotted in Figure 82(d) to remove high frequency content. These filtered curves represent the local vertical error over a 90 mm range. To obtain the vertical error for the full x span, the profiles are stitched together, as follows.

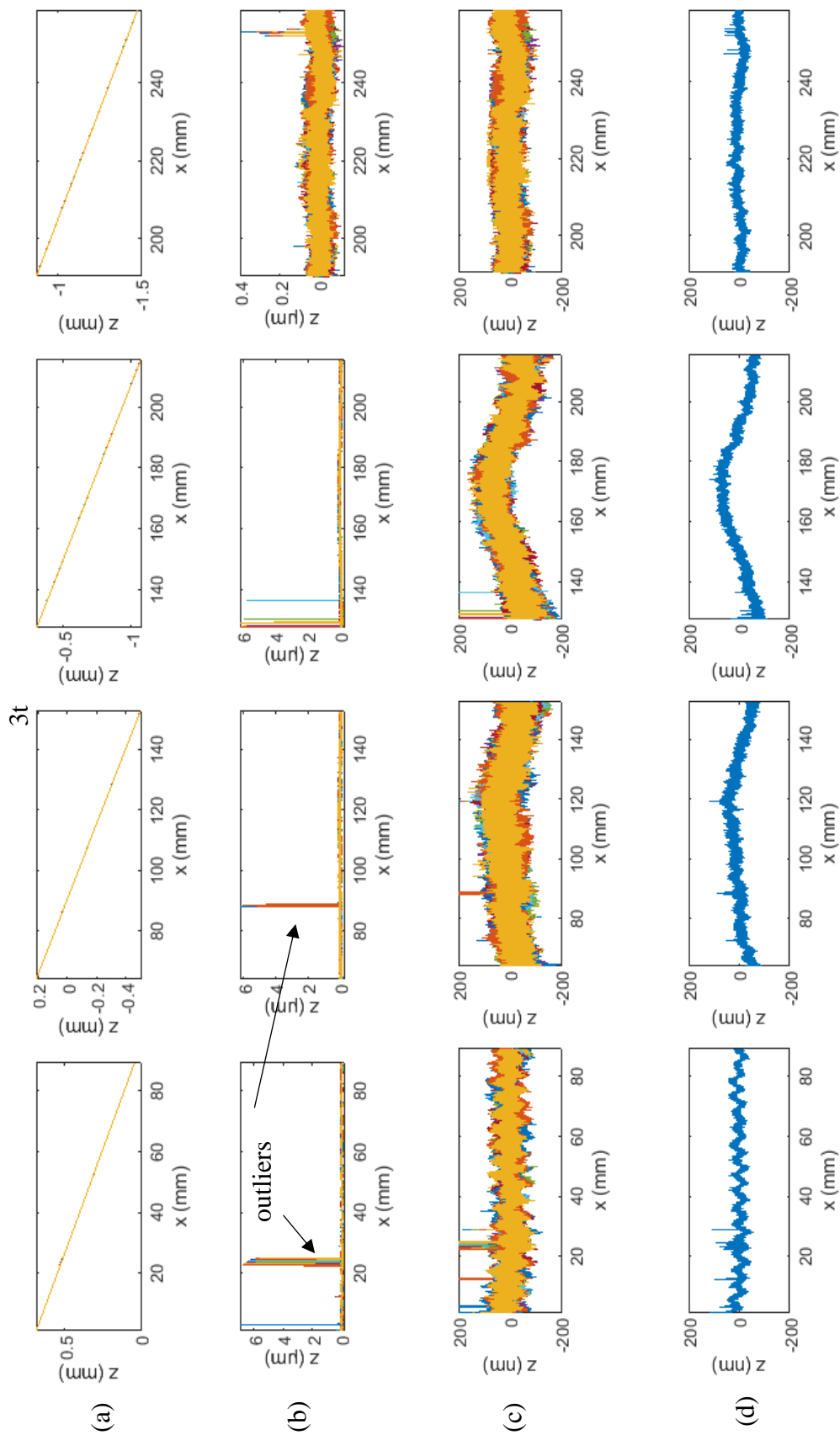


Figure 82: Results of the profiles measured in piecewise manner (a) Raw data showing the tilt and offset of the measurement at each x location (b) line subtracted from the raw data showing outliers (c) outlier greater than 3σ deviation are removed (d) average of ten profiles.

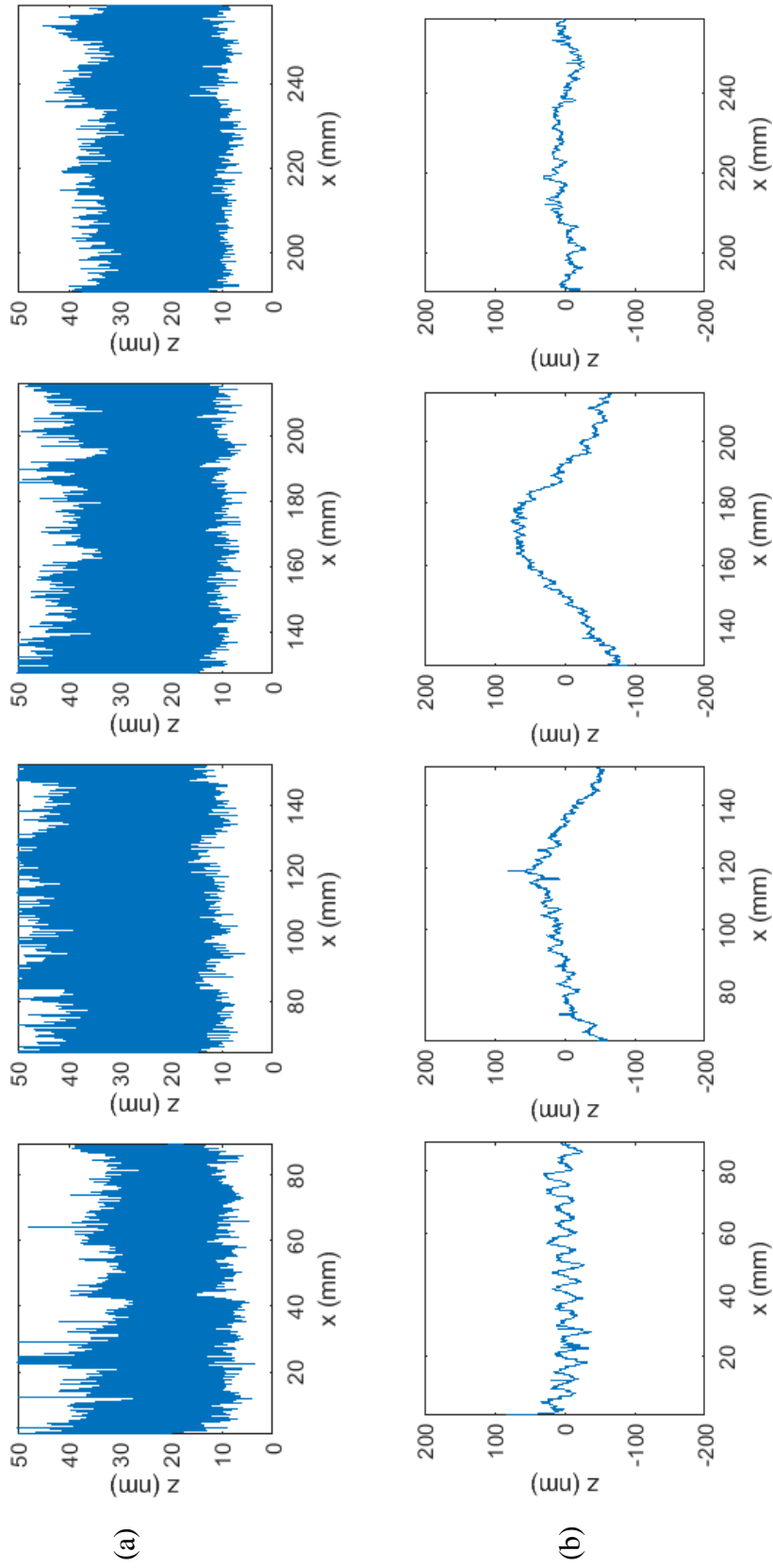


Figure 83: Standard deviation of the profiles measured in piecewise manner; (a) Standard deviation of the ten repeated profiles at a given x location less than 50 nm (b) A 100 point moving average of the ten profiles representing the vertical error locally at a given 90 mm x range

c) Stitching piecewise measurement profiles

Figure 84(a) shows the average of ten repeated profiles at each x location with their tilts and z offsets. The data at the overlapping region of each pair of profiles is used to tilt and offset one of the profile with respect to the other by using least sum of squares method, and shown in Figure 84(b), the difference between the profiles in the overlapping region after tilting and offsetting is shown in Figure 84(c), and it is 50 nm PV. The data of the profile pairs at the overlapping region is averaged, to obtain a single profile as shown in Figure 84(d). A line is fit to this profile and subtracted to estimate the vertical error of the profiler for the full horizontal travel of 260 mm as shown in Figure 84(e). A 100 point moving average is applied to this data to remove the high frequency content and the resultant data is plotted in Figure 84(f).

It is interesting to see the 5 mm periodic oscillation present in the left half of the curve, but not so much on the right half. In comparison with the Straightedge measurement which contains the oscillations throughout the curve, see Figure 85. Ignoring outliers, the maximum difference between the Zerodur flat piecewise measurement and the Straightedge measurement is about 150 nm PV, and it is noted that the out of flatness of the Straight edge is 125 nm.

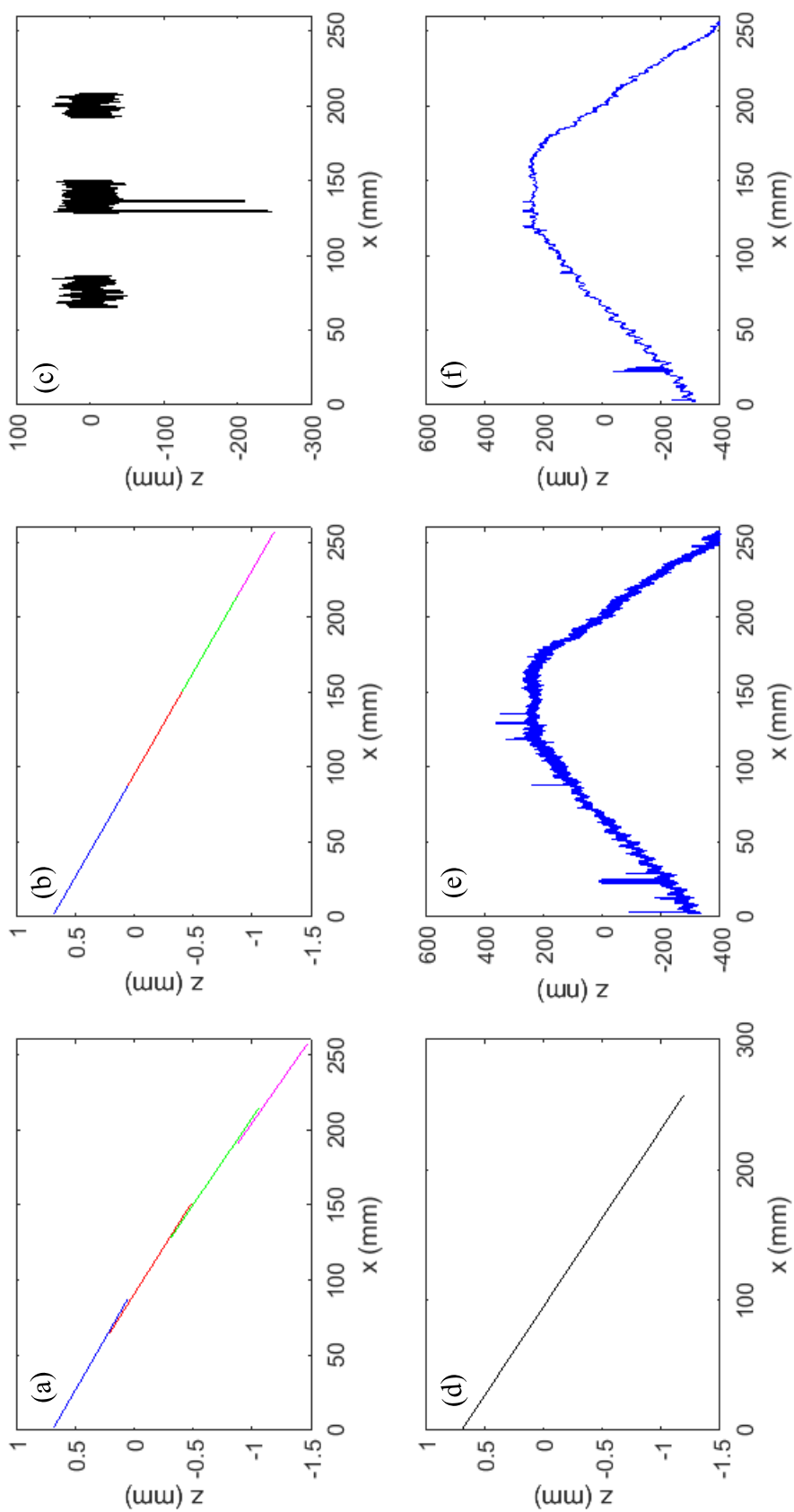


Figure 84: Procedure to stitch the overlapping profiles measured in piecewise manner; (a) mean of ten repeated profiles at each x location (b) profiles tilted and offsetted with respect to the closest profile using least sum of squares (c) difference in the overlapping region after tilting and offsetting the profiles (d) A single profile obtained by averaging the data in the overlapping region (e) data obtained by subtracting a line (f) a 100 point moving average reduces the high frequency content of the signal with 5 mm periodic oscillation on the left half of the curve.

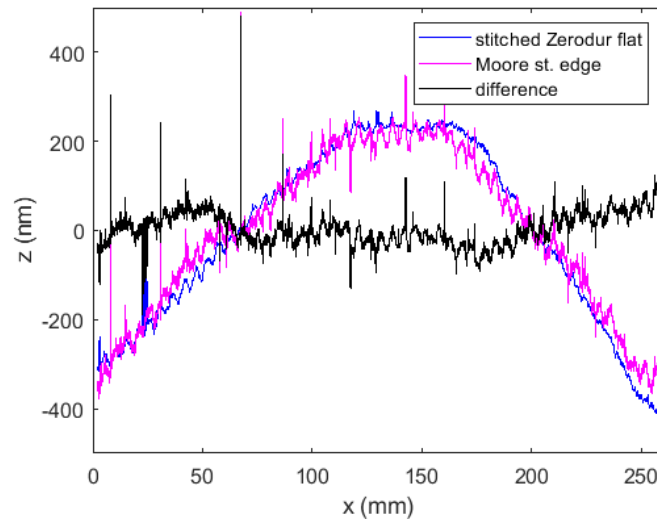


Figure 85: Comparison of the vertical error estimated using the stitched piecewise measurements of Zerodur flat to the Straightedge measurement

d) Vertical error comparison with the calibration data from the manufacturer

The profiler was first calibrated using a flat reference object at the manufacturing site in Germany, and later in the laboratory at UNC Charlotte. These calibration curves and the difference between them are shown in Figure 86(a & b). The comparison of the calibration difference and the Zerodur flat and Straight edge measurements are shown in Figure 86(c to h) indicating the vertical error of the X carriage is probably due to the difference in the calibration performed by the manufacturer and the correction curve input to the software of the profilometer system.

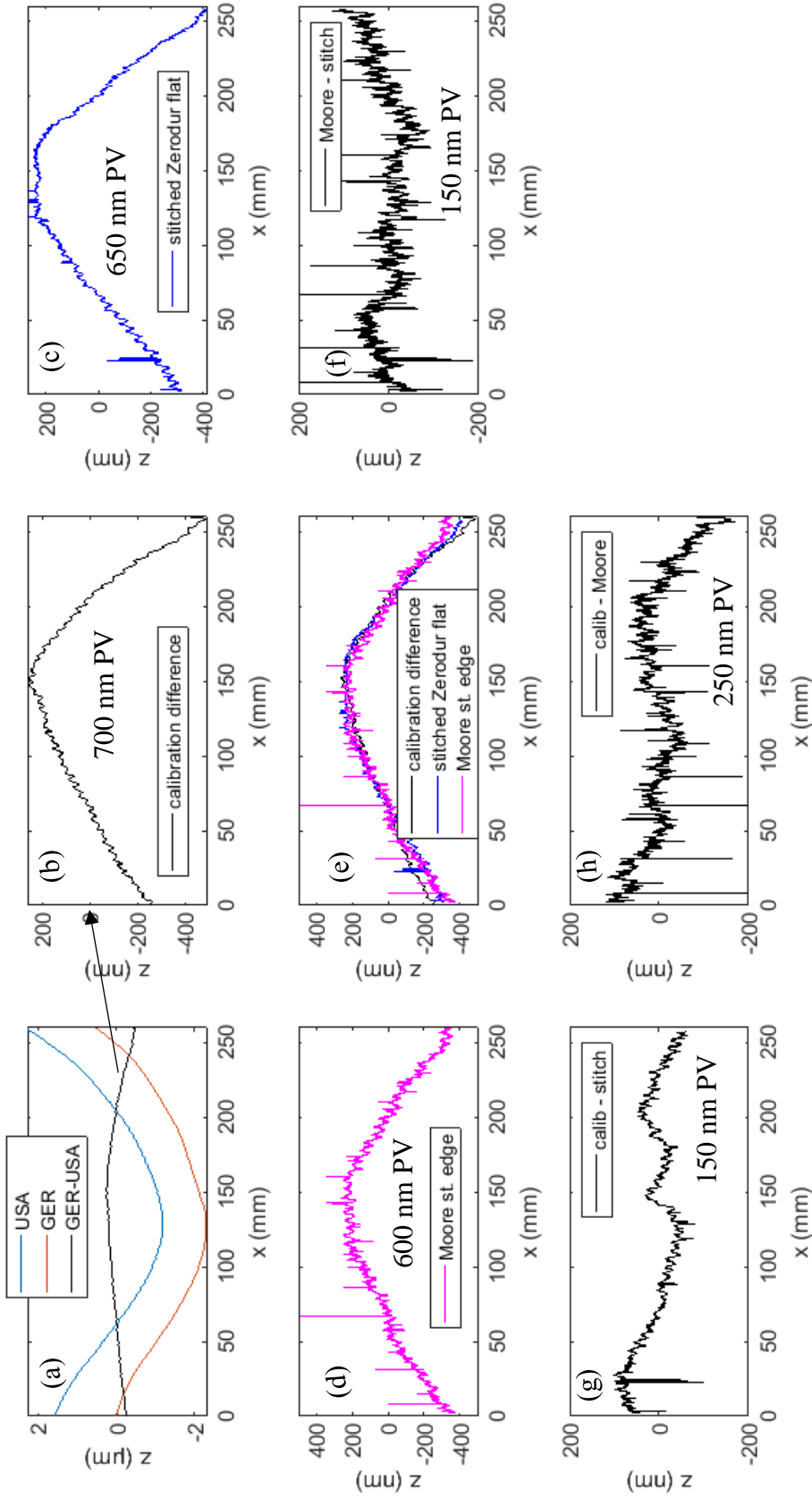
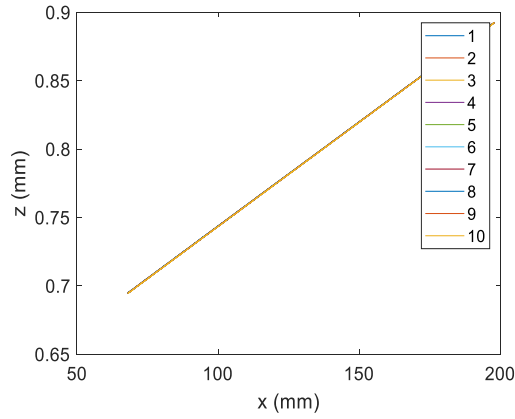


Figure 86: Comparison of the measured vertical error to the calibration curve of the profilometer (a) Calibration performed by the manufacturer in two locations and their difference (b) difference (c) vertical error estimate from the stitched piecewise measurement of the Zerodur flat (d) Straightedge (e) plotted together to see the similarity (f) difference between the straightedge and Flat measurements (g) difference between the calibration difference and the Flat measurement (h) difference between the calibration difference and the straightedge measurement.

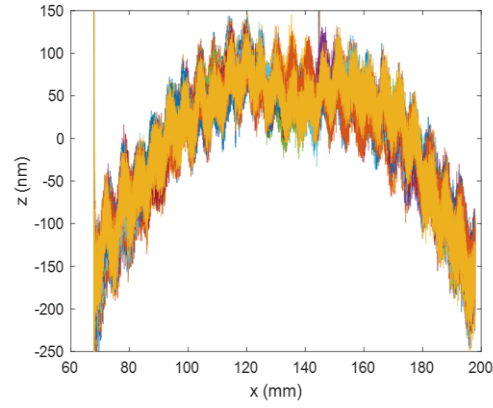
4.7.6 Dynamic thermal drift

To study the thermal drift of the system during the x axis motion of stylus, ten repeated profiles were made on the Fused Silica optical flat shown in Figure 72 (a to c). To reduce the external thermal sources during the measurements, once the flat is setup, it is allowed to ‘soak out’ for 30 minutes, then the operator walks into the room, clicks the button to make ten repeated profiles, and leaves the room. The profiles are of 130 mm long with a travel velocity of the stylus being $1 \text{ mm}\cdot\text{s}^{-1}$, and the time-delay between each profile is about 15 seconds.

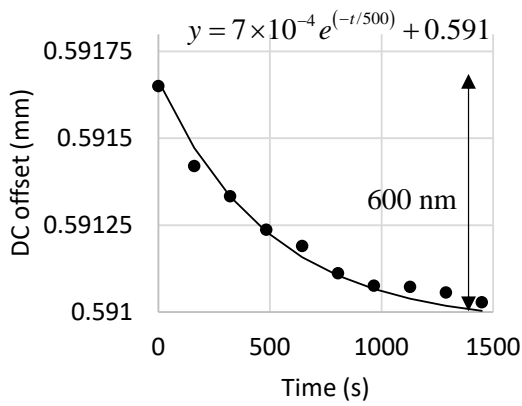
Figure 87(a) shows the raw data of the ten profiles and, after the slope and DC offset are removed, in Figure 87(b). It is noted that this parabolic curve is due to the vertical error of the X carriage discussed in the previous chapter. Values of the DC offset (y-intercept) and the slope in each profile are shown in Figure 87(a) (c) and (d) respectively. The variation in DC offset represents the drift in between the time taken for each profile, and it is 600 nm with a time constant of 500 seconds. The variation in slope represents the drift during the time each profile is made, and it is about $2 \text{ }\mu\text{rad}$ with a time constant of 250 seconds. To know the repeatability in the drift repeated profiles are made on three different days (Feb 4th to 6th, 2020) with number of profiles being 60, 55, and 100 respectively. DC offsets and the slope of the profiles are plotted in Figure 88(a) and (b) respectively with their time constants and steady state variations listed. From these measurements it is estimated that the machine takes at least an hour to reach its steady state temperature with 100 to 200 nm variations being typical over this time period. To validate this, the profiler was ran in air for two hours, and then 20 repeated profiles were made on the flat, with the subsequent measurement results shown in Figure 89(a).



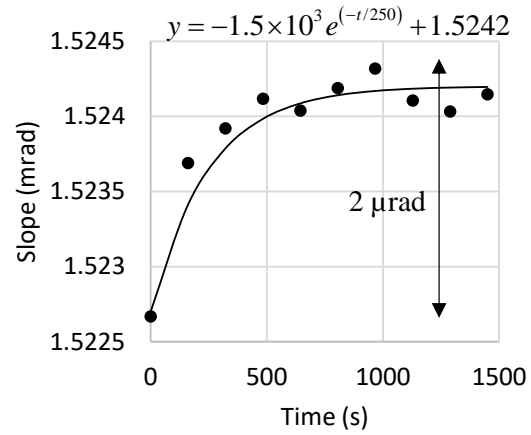
(a)



(b)



(c)



(d)

Figure 87: Experimental results of a Fused Silica flat measurement to determine the dynamic thermal drift of the profiler; (a) Ten repeated profiles made on the Fused Silica flat (b) line removed profile (c) DC offset and slope removed from each raw profile.

An average of 20 profiles were subtracted from each profile to estimate the repeatability in the measurements to be 100 nm PV. This data is low pass filtered to 2.5 mm according to ISO 10110-8 for form measurements and is 40 nm PV as shown in Figure 89(c). DC offset representing the dynamic drift is shown in Figure 89(d) and is 200 nm which is at least a three-time improvement comparing the drift shown in Figure 88(a). DC offset between each profile of 130 mm (2 minutes) is about 50 nm as shown in Figure 89(e), and the variation of slope is about 1 μ rad as shown in Figure 89(f).

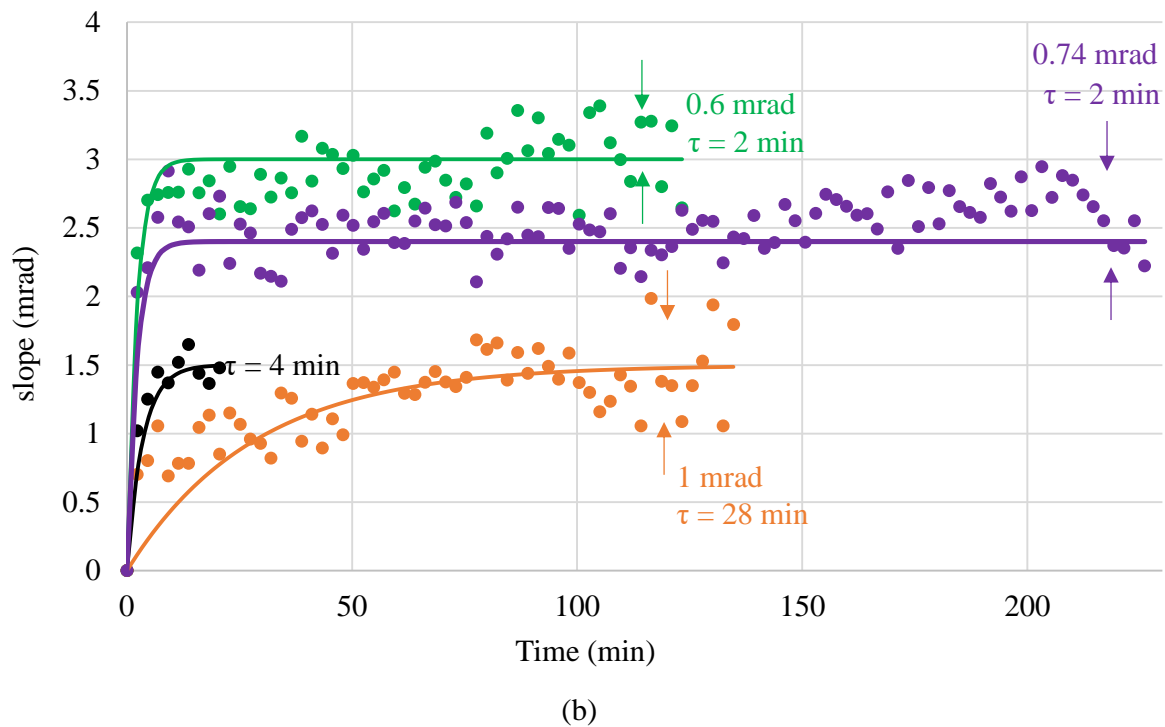
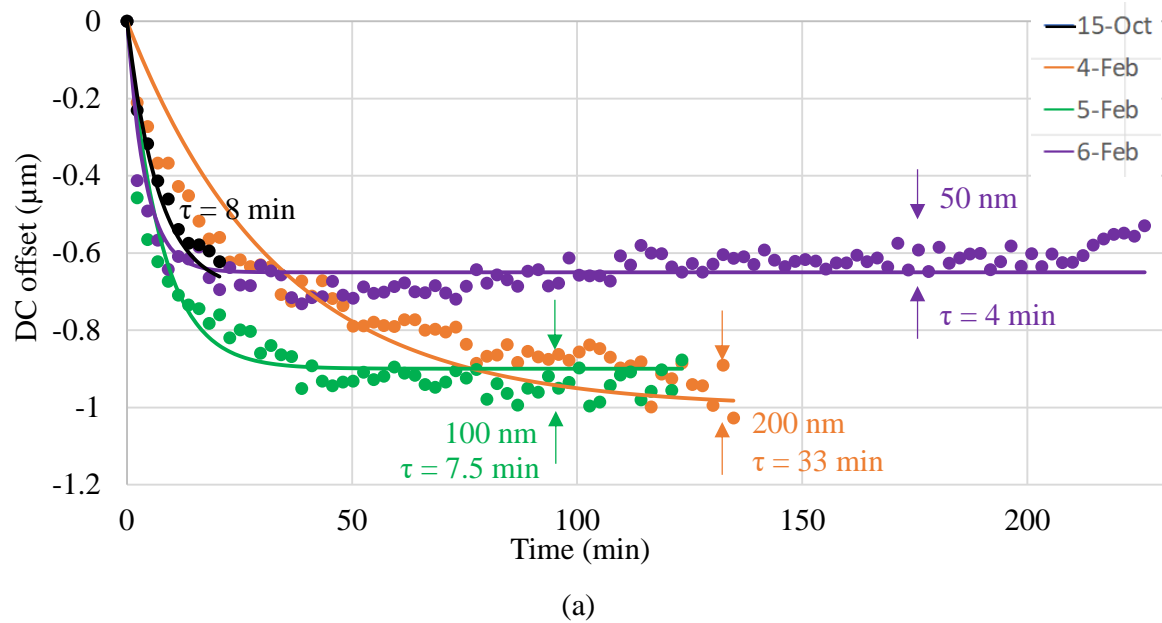


Figure 88: Drift of the repeatedly measured profiles (a) DC offsets and (b) slopes in the profiles measured on three different days.

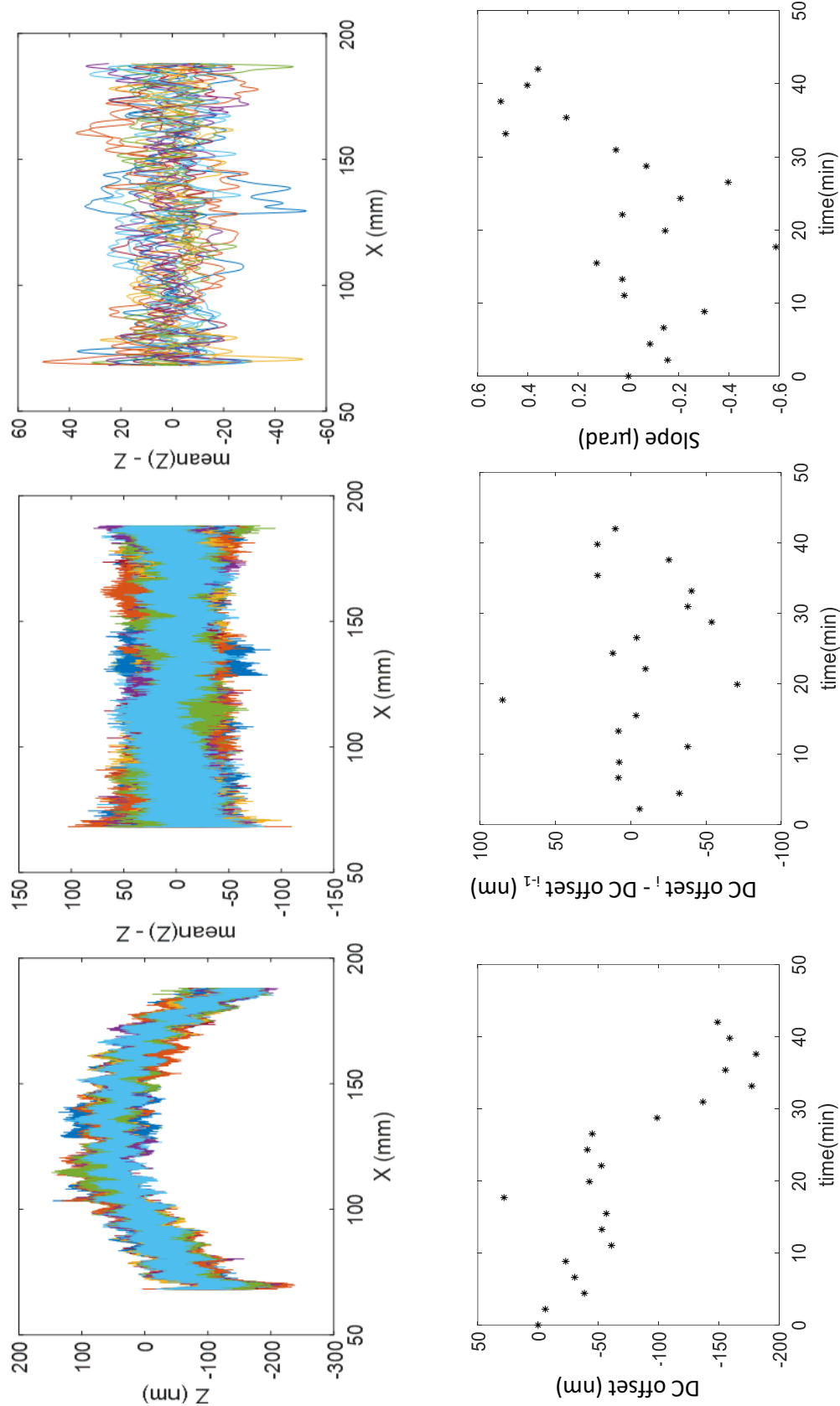


Figure 89: Results of twenty repeated profiles of the Fused silica optical flat; (a) after removing the z offset (z intercept) and the slopes of the profiles (b) Standard deviation of the repeated profiles, (c) Standard deviation low pass filtered to 2.5 mm, (d) z intercepts of each profiles, (e) difference in the z intercepts of subsequent profiles, (f) slopes of the repeated measured profiles

4.7.7 Validation of force feedback control

To validate that the above discussed DC offset of repeated profiles are caused due to thermal drift, and not due to the error in the force feedback control of the stylus to keep it in contact with the surface being profiled, the following experiment is performed. After running the profiler in air for an hour to get ‘warmed up’, it is rested for thirty minutes on top of the surface of the kinematic plate shown in Figure 79(a) with a preload force of 1 mN, while the z values were recorded. The stylus is lifted and left static in air for two minutes, then the stylus is placed back on the kinematic plate and the z values are recorded for two more minutes. This two minute ‘lift and rest’ process is repeated ten times and plotted in Figure 90(a), with a variation in z values being less than 100 nm PV, see Figure 90 (b). The mean of the z values at each instance of measurement is less than 40 nm PV as shown in Figure 90(c) ensuring that the DC offset observed in repeated profiling is not due to the errors in force feedback control of the stylus.

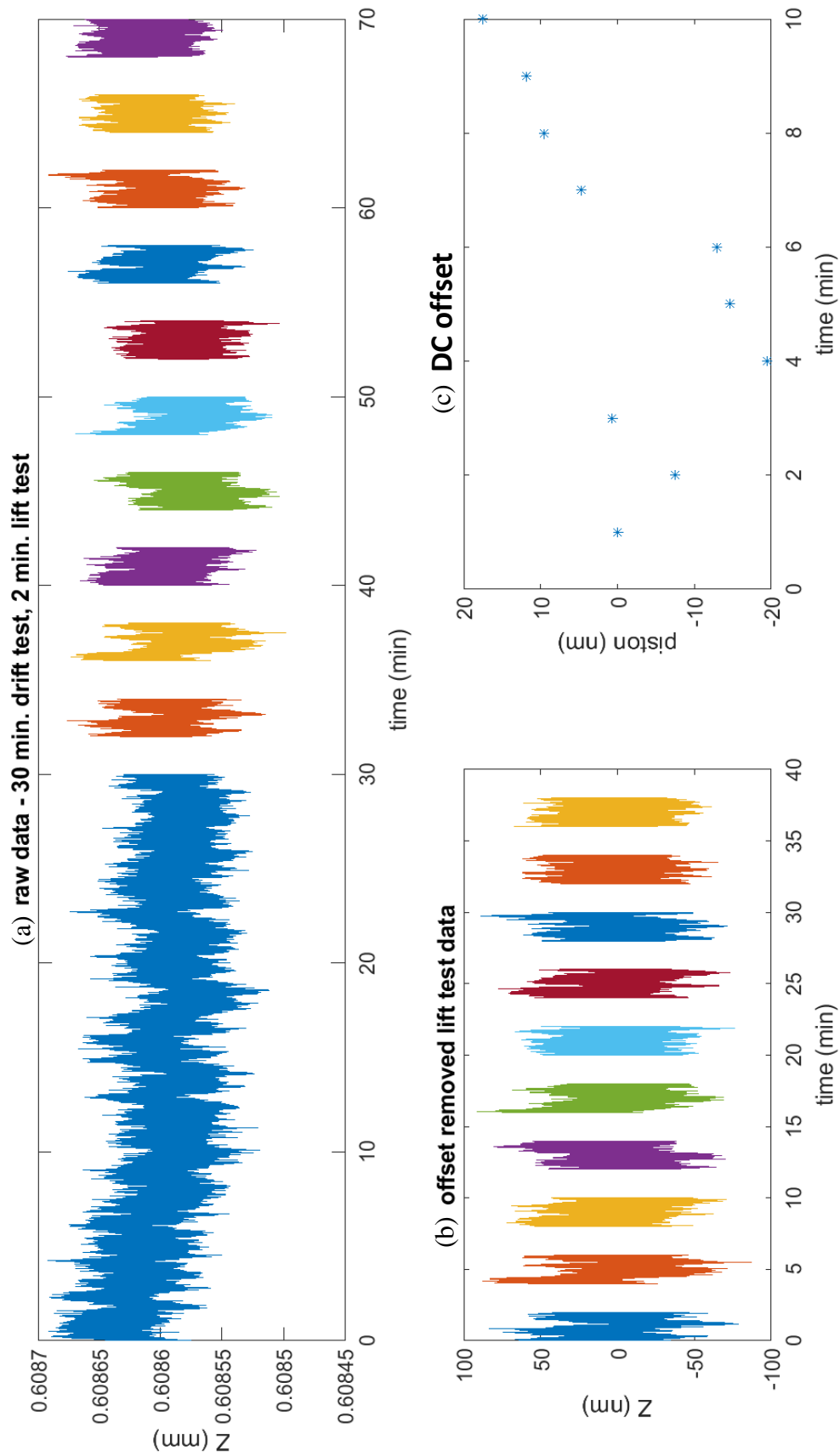


Figure 90: Repeatability assessment for z height relocation and stability; (a) Measured z values when stylus is intermittently kept static on the surface of the kinematic plate (b) DC offset removed data showing the noise in the measured z values (c) DC offset in each instance of static test

4.7.8 Areal surface measurements of a flat over an 85 mm aperture

To study the performance of the profilometer while measuring the areal form of an object, stripes and spokes are made on the Zerodur flat shown in Figure 91(a). It is noted that from the interferometric measurement of this flat shown in section 4.7.1, Figure 72(d), we know that its out of flatness is less than 30 nm. Therefore, any deviations greater than this observed in the profilometer measurements would indicate the errors in the motion of X , Y , and C carriages, and the thermal drift during measurements. Following are the two experiments performed after warming up the machine by running the profiler in air for an hour, see Figure 91(b and c).

- (i) stripes were made on the flat with a y axis spacing of 1 mm, and then the flat is rotate by 90° to make five tie lines that could be used to correct for thermal drift. After this, spokes were made by rotating the flat using the rotary carriage (C) for each profile. Sections 4.7.8.1, 4.7.8.4 and 4.7.8.5 discuss the results of these experiments.
- (ii) to study the repeatability of the measurements, and the Y carriage vertical straightness error, stripes were made on the flat repeatedly covering its area three times. Sections 4.7.8.2 and 4.7.8.3 discuss the results of these experiments.

4.7.8.1 Stripes on the Zerodur flat and use of a tie line to correct for the Y carriage errors and thermal drift in the system

Measurement of stripes, schematically illustrated in Figure 91(b), are plotted in Figure 91(d), and this measurement took about 2 hours to completer. Whereafter a plane is fit to this data, and subtracted to remove part tilt and vertical squareness error $(\alpha_x(Y))$ of the Y carriage, and plotted in Figure 91(e) and shows a 200 nm PV variation. Slope and z offset in each profile are

subtracted to remove roll ($\varepsilon_y(Y)$), vertical straightness ($\delta_z(Y)$), and pitch ($\varepsilon_x(Y)$) of the Y carriage and plotted in Figure 91(f).

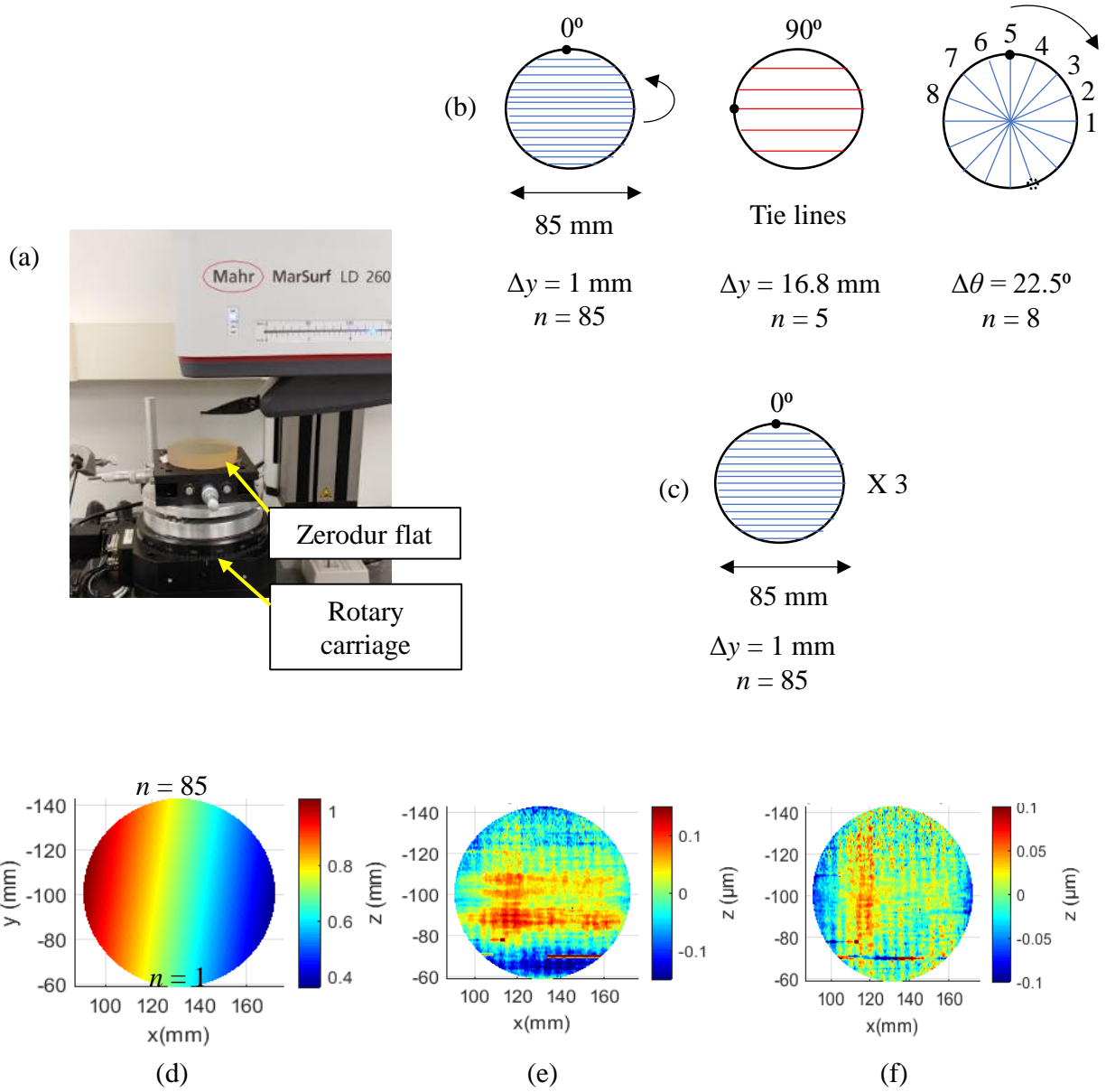


Figure 91: Results of the areal surface measurement of the Zerodur optical flat; (a) Zerodur flat being measured using the profilometer system (b) Schematic of stripes profiles, and five tie lines to correct for thermal drift, and spokes profiles (c) Three repeated stripes measurements (d) Stripes measurement of the Zerodur flat, (e) after subtracting a plane from this measurement (f) after subtracting the slope and z offsets of each profile.

To use all five tie lines (shown in red in Figure 91(b)) to correct for thermal drift as discussed in section 4.5.1, they must be first corrected for vertical offsets and tilts experienced due to the motion of Y carriage. These errors must be measured separately using machine tool metrology methods [Evans, 1996, Salsbury, 2003] in the future. For the analysis presented here, only the middle tie-line is used in this section in an attempt to correct for the drift. Figure 92(a) shows the stripes and the middle tie line plotted in the measurement coordinates. A line is fit to the tie line and is translated to a (0,0,0) origin by subtracting the mean of x and y values, and then rotated counterclockwise by 90° , translated back to measurement coordinates as given in the equation below, and plotted in Figure 92(b).

$$\begin{bmatrix} x' \\ y' \\ z' \end{bmatrix} = \begin{bmatrix} 1 & 0 & \bar{x} \\ 0 & 1 & \bar{y} \\ 0 & 0 & 1 \end{bmatrix} \begin{bmatrix} \cos \theta & -\sin \theta & 0 \\ \sin \theta & \cos \theta & 0 \\ 0 & 0 & 1 \end{bmatrix} \begin{bmatrix} 1 & 0 & -\bar{x} \\ 0 & 1 & -\bar{y} \\ 0 & 0 & 1 \end{bmatrix}$$

Out of the 85 stripes, the tie line fit goes through only 81 of them, two extreme profiles at each edge of the y axis are not intersected and are therefore discarded. The minimum distance between the tie line and each of the stripes in the y axis is considered to be the point of intersection, and this distance is within $0.5 \mu\text{m}$. The z values of the intersecting points of the tie lines and the stripes are plotted in red and blue respectively in Figure 92(c). The difference between the z values of these datapoints are calculated and plotted in Figure 92(d). It is noted that this difference accounts for vertical squareness $(\alpha_x(Y))$, vertical straightness $(\delta_z(Y))$, and pitch error $(\varepsilon_x(Y))$ in the motion of the Y carriage, and also the thermal drift during the process of measuring stripes. The stripes are translated vertically to correct for this height difference as shown in Figure 92(e), to which a plane is fit and subtracted to plot in Figure 92(f) with 200 nm PV.

Dec 17, 2020

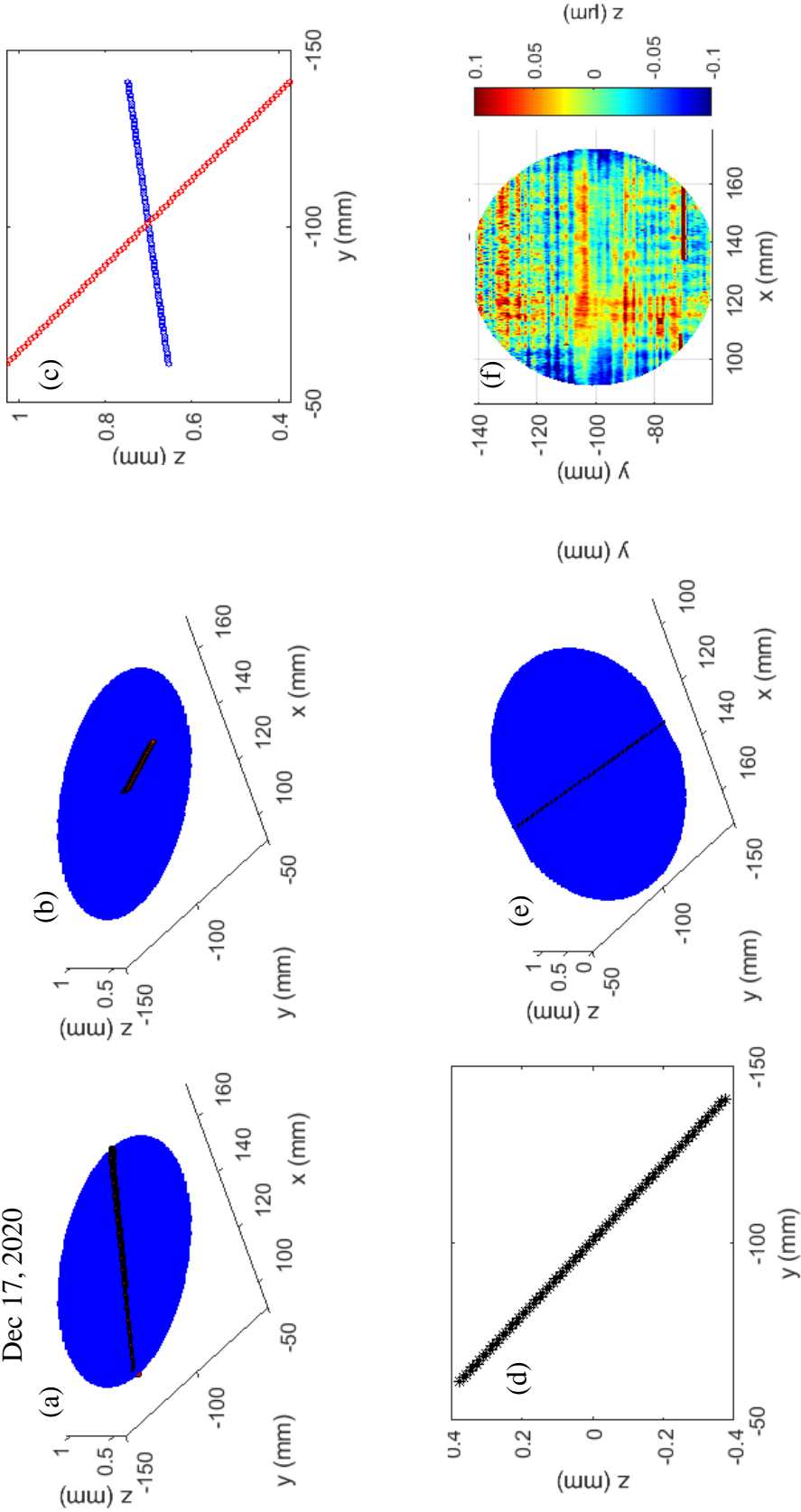


Figure 92: Using a tie line to correct for the Y carriage vertical straightness and thermal drift in the measurements by stripes approach; (a) Stripes and the middle tie line plotted in measurement coordinates (b) tie line rotated by 90° (c) y intersects of stripes and the tie line (d) difference between them (e) stripes translated vertically to correct for this difference (f) after correction, a plane is fit and subtracted

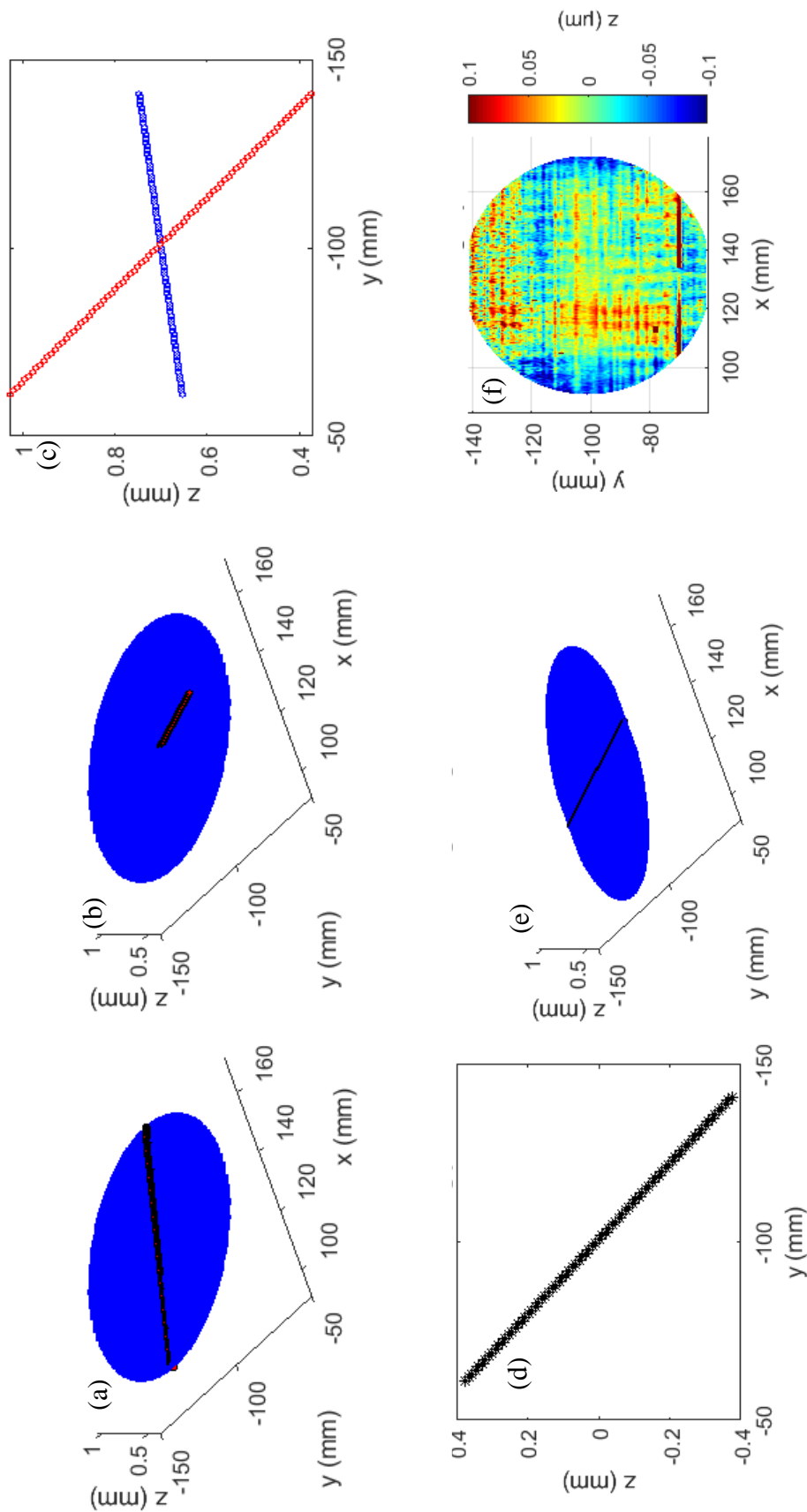


Figure 93: Using a tie line to correct for the Y carriage roll, vertical straightness and vertical squareness errors, and the thermal drift in the measurements by stripes approach; (a) stripes and the middle tie line plotted in measurement coordinates (b) slopes of each profile along x axis is removed, and tie line rotated by 90° (c) y intersects of stripes and the tie line (d) difference between them (e) stripes translated vertically to correct for this difference (f) after correction, a plane is fit and subtracted

To also correct for the roll error of the Y carriage ($\varepsilon_y(Y)$), and the linear thermal drift during each profile of the stripes, slopes of the individual profiles along x axis shown in Figure 93(a) are removed and the resultant data plotted in Figure 93(b). The same procedure discussed earlier to vertically translate the stripes with respect to the tie line intersects is followed and the plane subtracted profilograms is shown in Figure 93(f) with 200 nm PV, which majorly includes X carriage vertical straightness and pitch error, and nonlinear thermal drift within a single profile of the stripes.

4.7.8.2 Estimation of vertical error of Y carriage from the repeated stripes measurements of the flat

Figure 94(a to c) shows the three repeated areal measurements, after subtracting a plane to remove the part tilt and the vertical squareness of X and Y carriage ($\alpha_y(X), \alpha_x(Y)$), they are plotted in Figure 94(d to f) with 200 nm PV. Average of these three repeated measurements, standard deviation (60 nm PV), and range of variation are shown in Figure 94(g to i).

To estimate the vertical straightness of the Y carriage ($\delta_z(Y)$), plane subtracted data of the three repeated measurements shown in Figure 94(d to e) are used. An x intercept line within a resolution of 5 μm about x axis is used to find the z height values of the intercepting line, see Figure 95(b and c). It is noted that the x data spacing in these measured profiles is 10 μm . Average of these z values, and a second order polynomial fit to this data are shown in Figure 95(d) representing vertical error of Y carriage of 100 nm PV for a mid y travel range of 85 mm. The polynomial fit shown in Figure 95(d) is extended in x axis and plotted in Figure 95 (e), which is then subtracted from the third repeat of the measurements and plotted in Figure 95 (f).

Jan 7, 2021

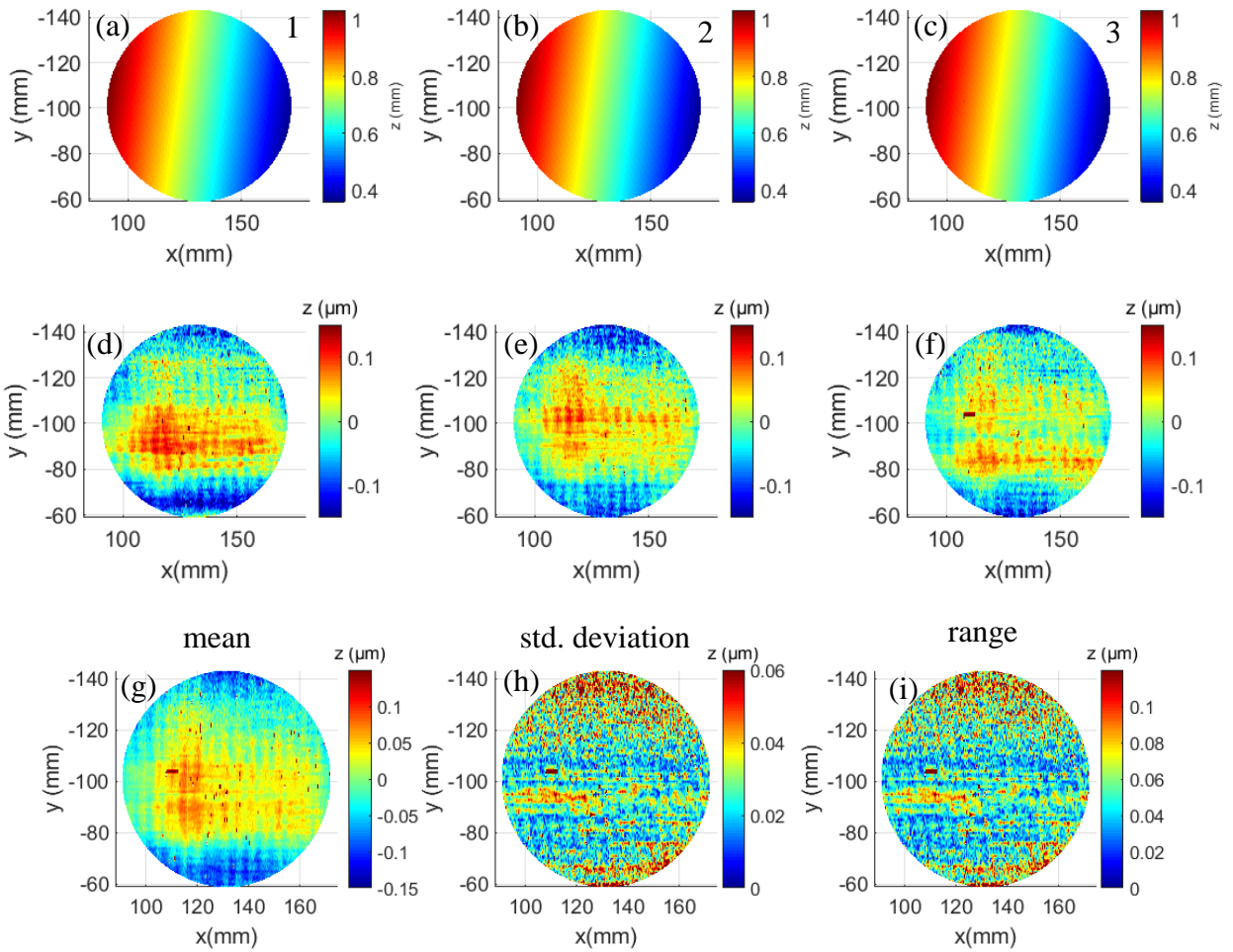


Figure 94: Repeated areal measurements of the Zerodur flat using stripes approach; (a to c) Three repeated area surface form measurements (d to f) after subtracting a plane, (g to i) mean, standard deviation, and range of variation in the measurements.

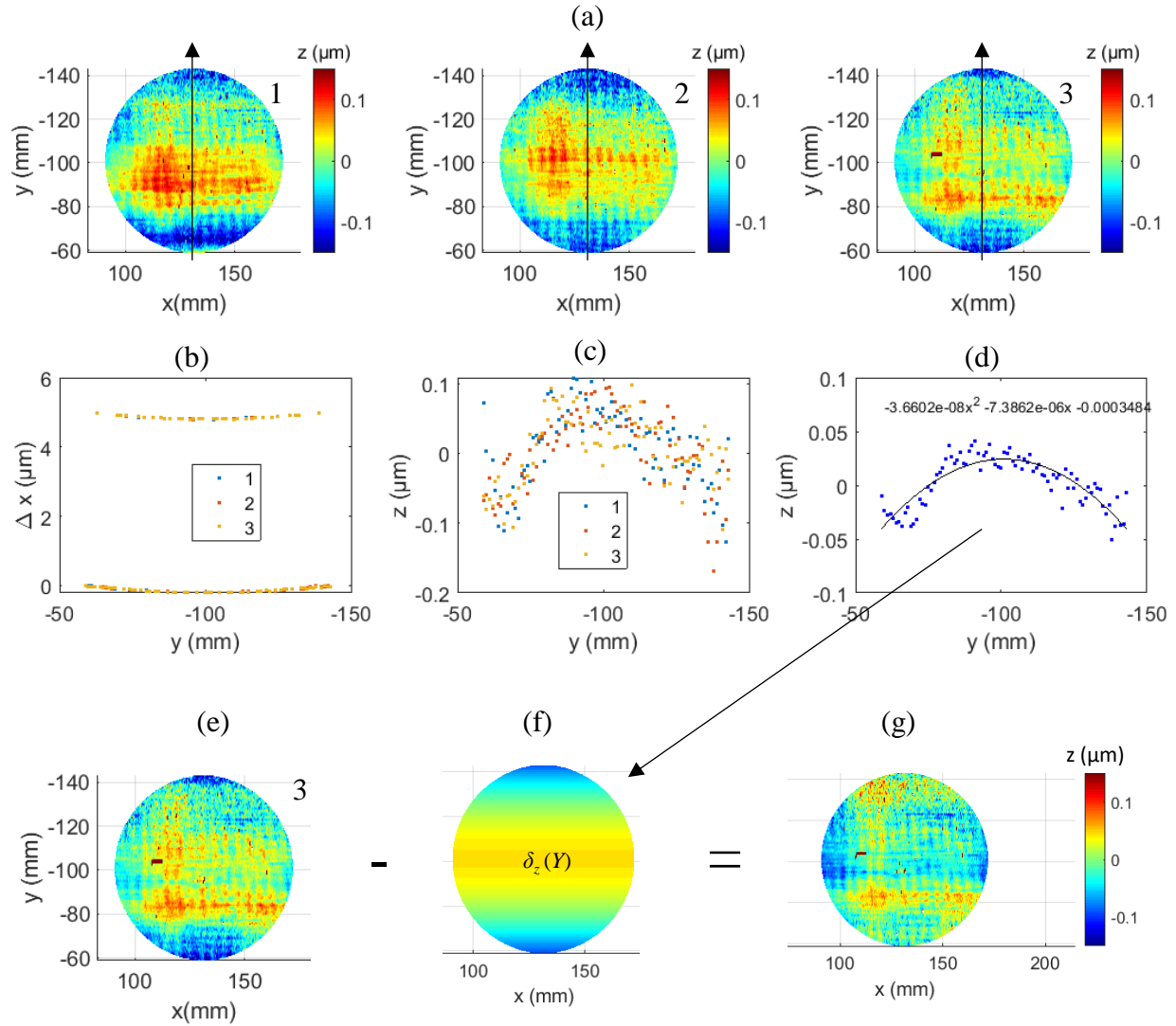


Figure 95: Estimation of vertical straightness of Y carriage using the repeated areal stripes measurements of the Zerodur flat and its correction; (a) x intercept line along the three repeatedly measured surface (b) values of x intercepts (c) z values at the interception (d) mean of the z values and a second order polynomial fit representing vertical straightness of Y carriage (e) plane subtracted measurement from third repeat (f) vertical straightness of Y carriage extended in x axis (g) measurement after removing vertical straightness of Y carriage.

4.7.8.3 Removing vertical error of X carriage from the areal measurement data of the flat

A 100-point moving average of the combined vertical error of X carriage ($\delta_z(X)$, $\varepsilon_y(X)$) estimated by a piece wise measurement of the Zerodur flat discussed in 4.7.5.2 is shown in Figure 96(a). For the x axis travel range of 85 mm (89 mm to 174 mm) used in the areal form measurements discussed in this section, the vertical error of the X carriage is plotted in Figure 96(b). A line is subtracted from this data and plotted in Figure 96(c).

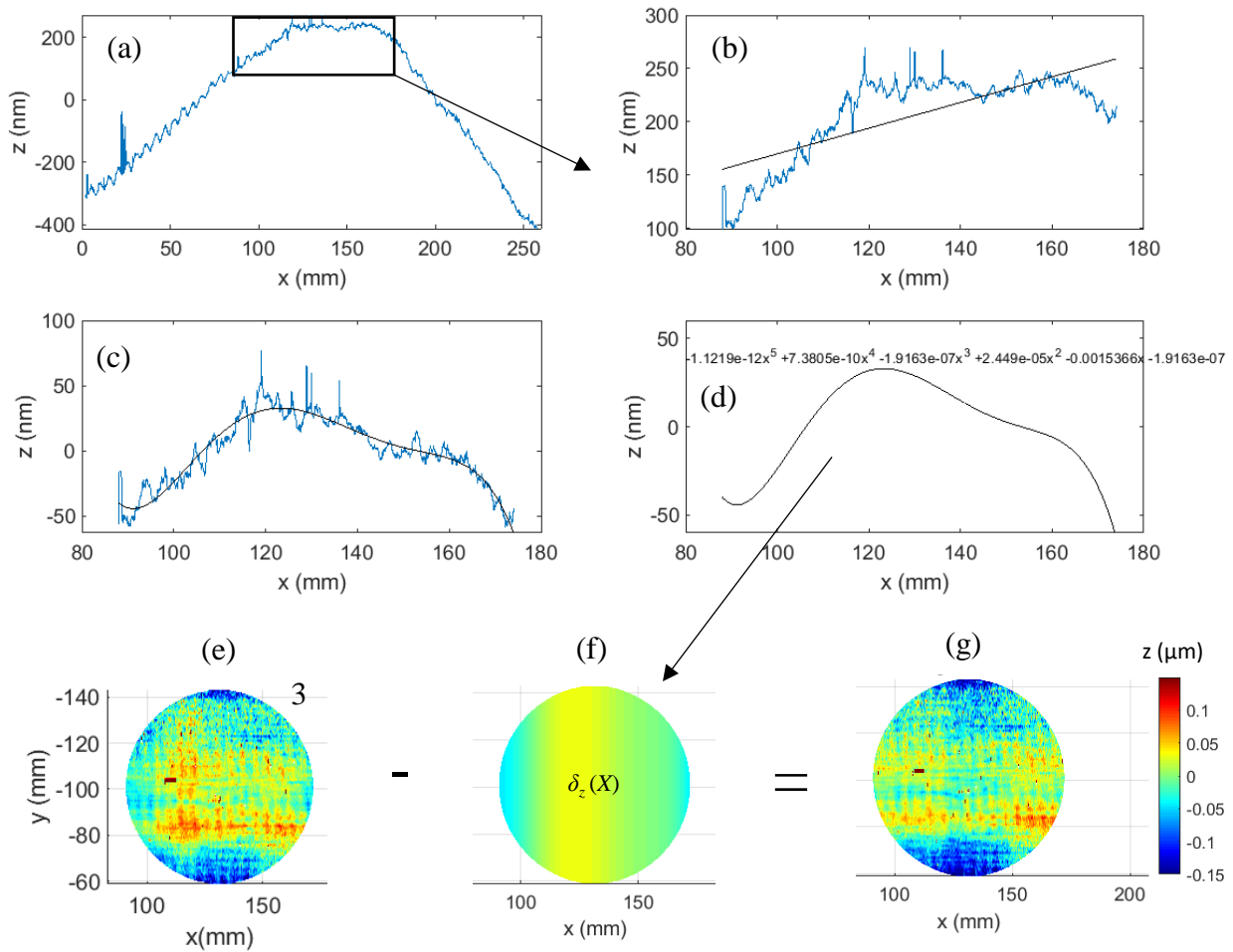


Figure 96: Correcting for vertical error of the X carriage in the areal measurements of the Zerodur flat; (a) A 100 point moving average of the vertical error of X carriage (b) plotted in the range of areal form measurements discussed in this section (c) after subtracting a line (d) 5th order polynomial fit (f) extended in x axis (g) after subtracting from the 3rd repeat of the areal measurement shown in (e).

A 5th order polynomial is fit to represent the vertical error of X carriage is shown in Figure 96(d), which is extended in y axis and plotted in Figure 96(f). The third repeat of the areal surface measurement is subtracted from X carriage vertical error and shown in Figure 96(g). Both the vertical errors of the X and Y carriages are subtracted from the areal form measurement (200 nm PV) and this is shown in Figure 97(a) and results in reducing the form deviation to 100 nm PV. The estimated vertical error of X carriage could also be rotated azimuthally and used to correct for the measurements performed in spokes manner shown in Figure 98(g) and Figure 97(a). Azimuthally rotated vertical error and the corrected areal form with 100 nm PV deviation are shown in Figure 97(c and d) respectively.

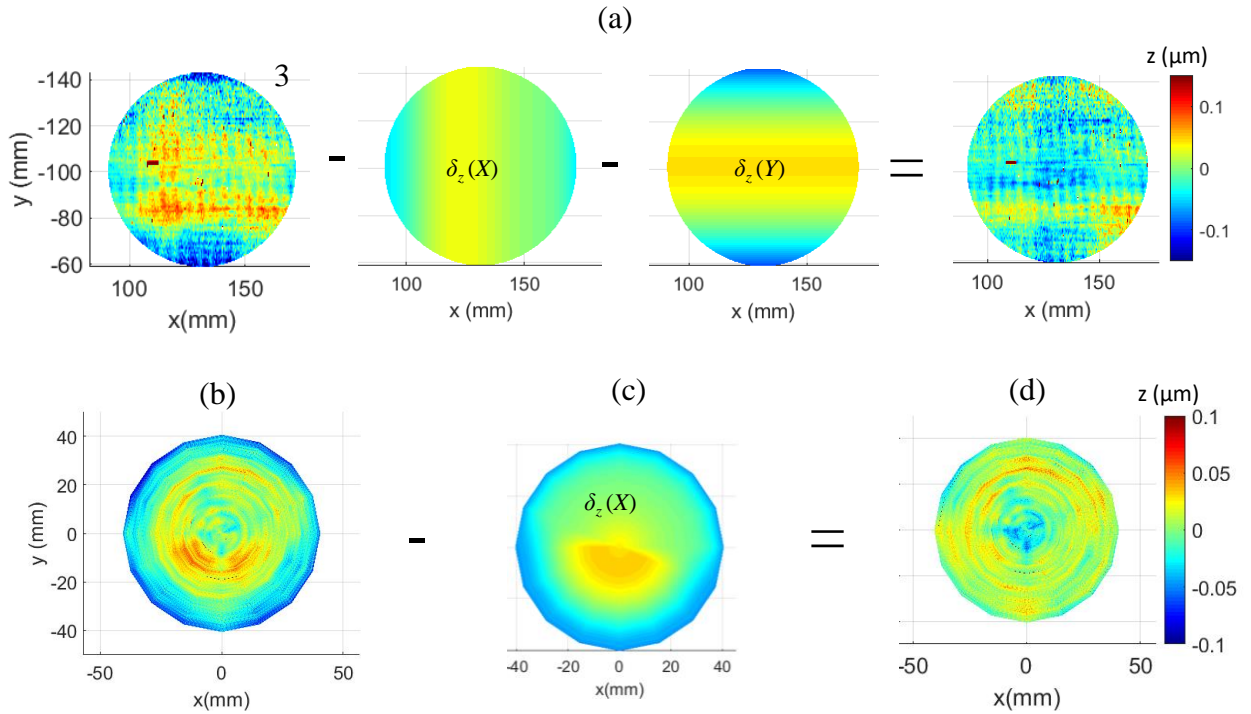


Figure 97: Correcting for vertical error of the X carriage and vertical straightness of the Y carriage in the areal measurement of Zerodur flat; (a) Vertical error of X and Y carriages subtracted from the areal form measured by stripes method (b) Flat measured using spokes method (c) Vertical error of X carriage rotated azimuthally (d) vertical error subtracted.

4.7.8.4 Spokes measurements on the Zerodur flat

Eight spokes profile measurement schematically shown in Figure 91(b) is performed and the raw data is plotted in Figure 98(a) in measurement coordinates. From this data, the x values were subtracted from their mean (\bar{x}) and plotted in Figure 98(b). Slopes (m) and DC offsets (z_0) of these profiles are plotted in Figure 98(c and d), which were subtracted from their profiles and the resultant data is plotted in Figure 98(e). These profiles mainly include the out of form of the flat and the X carriage errors. Using the rotational transformation

$$\begin{bmatrix} x' \\ y' \\ z' \end{bmatrix} = \begin{bmatrix} \cos \theta & -\sin \theta & 0 \\ \sin \theta & \cos \theta & 0 \\ 0 & 0 & 1 \end{bmatrix} \begin{bmatrix} x - \bar{x} \\ 0 \\ z - (m(x - \bar{x}) + z_0) \end{bmatrix},$$

these profiles are rotated counterclockwise to obtain the y values to generate the spokes as plotted in Figure 98(f and g).

Slope and offset removed profiles are shown in Figure 98(e), and a 5th order polynomial fit is plotted in Figure 99. The mean difference between the fit and experimental data is 100 nm PV as plotted in Figure 100(b) that represents the X carriage vertical error and the out of flatness of the flat which is less than 30 nm PV. Standard deviation, and range of these polynomial fits are also shown in Figure 100(c and d).

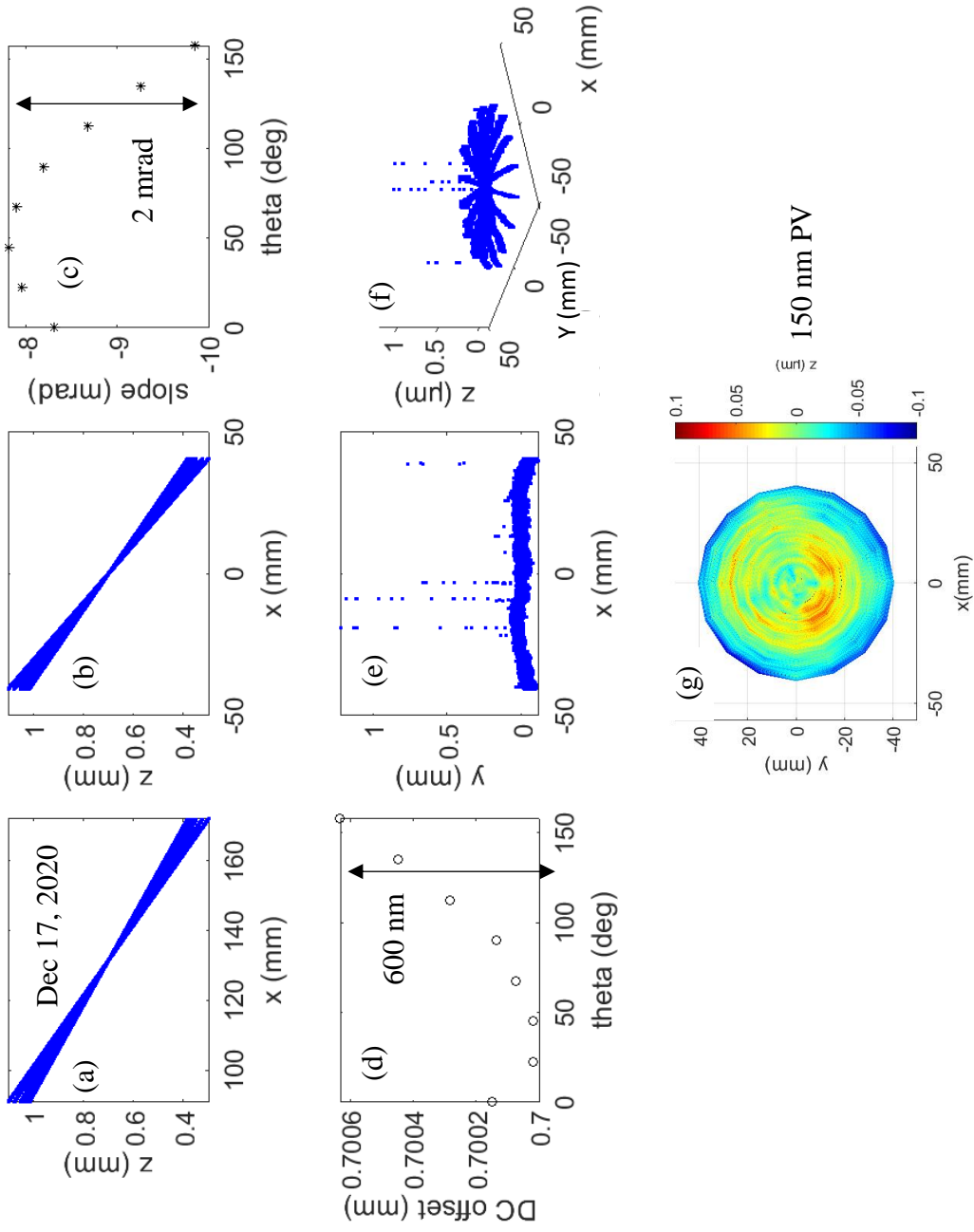


Figure 98: Zerodur flat measured using the spokes approach (a) eight spokes profiles plotted in measurement coordinates (b) profiles with their x values subtracted from their mean (c) slope of each profile (d) z offset of each profile (e) slope and offset subtracted from the profiles (f) profiles rotated azimuthally to represent the form of the surface (g) heat map.

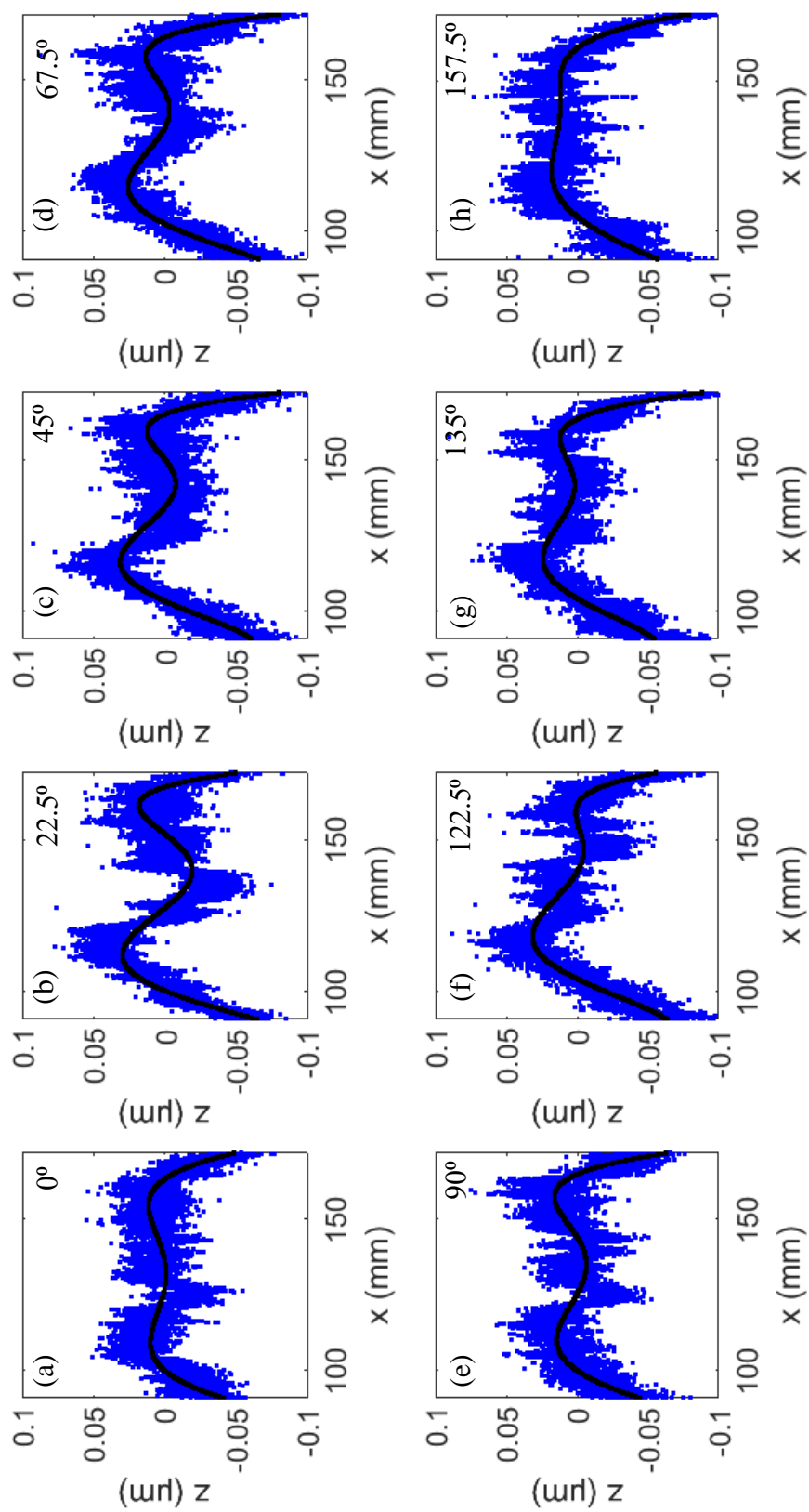


Figure 99: Slope and offset removed from each profile and their 5th order polynomial fit.

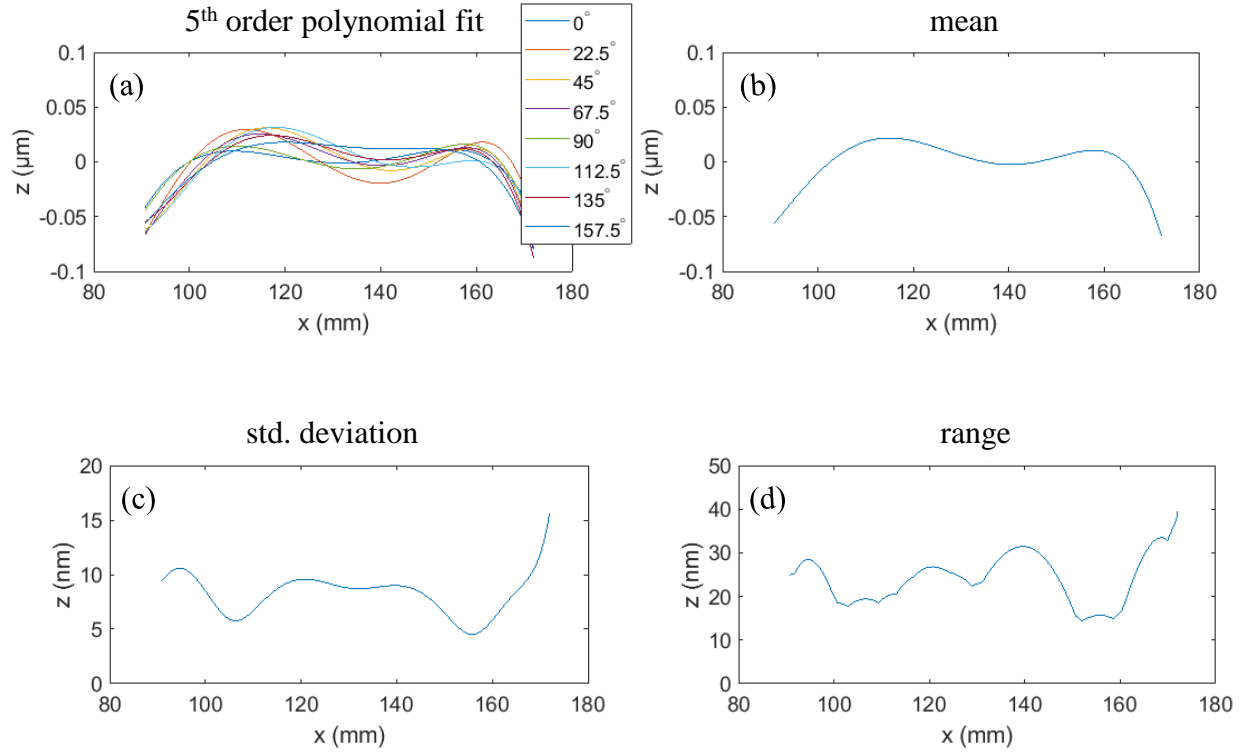


Figure 100: Results of the 5th order polynomial fit to the eight spokes profiles made on the flat (a) 5th order polynomial fit (b) mean of the eight fits to the profiles (c) standard deviation of the fit (d) range of variation (max-min).

4.7.8.5 Estimation of Rotary carriage axial and tilt errors from spokes measurement

Figure 101(a) shows the raw measurement data of the Zerodur flat measured using eight spokes profiles on two different days. Lines are fit to this data using the least sum of squares method and its calculated slope values are shown in Figure 101(b) respectively. A sinusoidal trend seen in the slope values is typically due to the wedge angle of the part and is 2 mrad PV, which is larger than the manufacturer specified parallelism of the flat of 0.15 mrad. This sinusoidal trend is removed to represent the tilt error of the rotary carriage of 2 μrad PV as shown in Figure 101(d) which is comparable to 3.4 μrad synchronous tilt error specified by the manufacturer (see Appendix C.1.2). DC values of the profiles shown in Figure 101(c) is calculated by finding the mean of the z values of measured profiles. The sinusoidal trend seen in the DC offset values of the

is possibly due to the effect of the tilt error causing the flat to translate horizontally due to the lever arm created by the height at which it is located above the rotary carriage. Removing this sinusoidal trend leaves a residue of 40 nm PV as shown in Figure 101(e), which is comparable to the synchronous axial error of 100 nm specified by the manufacturer.

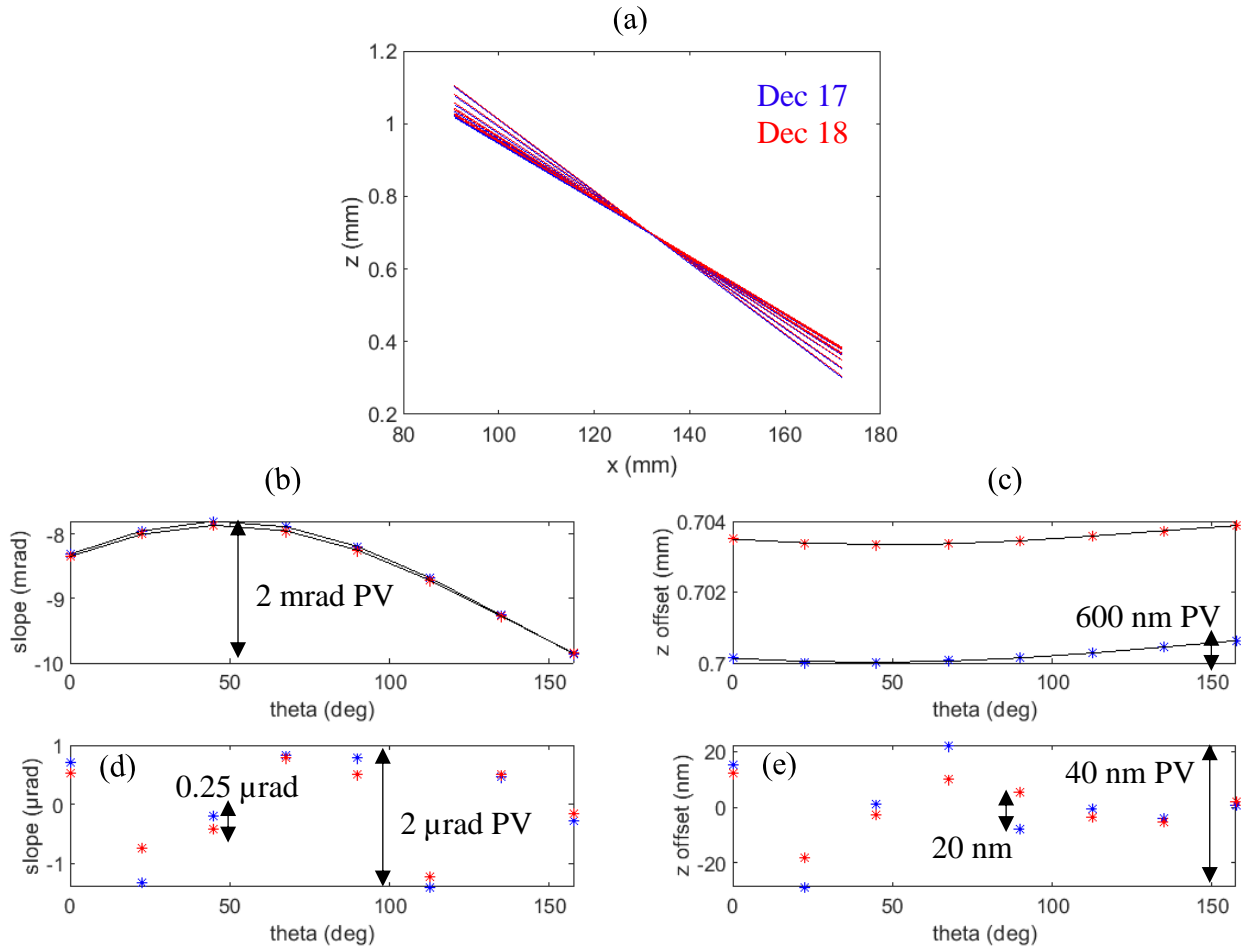


Figure 101: Estimation of tilt and axial errors of the C rotary carriage; (a) raw data of the spokes made on the Zerodur flat (b) slopes calculated by fitting a line (c) DC offset calculated by finding the mean of measured z heights (d) after removing the sinusoidal trend in slope values representing tilt errors of the rotary carriage (e) after removing the sinusoidal trend in DC offset values representing axial error of the rotary carriage

4.8 Prism measurements

In the measurements of flat surfaces, the range of z travel utilized is only about 2 mm due to the tilt of the part and Y and C carriage stack ups' underneath it. To study the performance of the profiler for the full 13 mm z travel of the stylus, a right-angled prism with 90° pyramid angle is used as a reference object (Edmund optics Stock #47-790). The ground face on which alphabet 'F' is engraved is designated the front face of the prism, see Figure 103(b). Interferograms of the on and off ramp surfaces of this prism measured using the Fizeau interferometer (Figure 103(c)), shows the out of flatness is less than 20 nm PV, which is three times better than the vendor's specification of $\lambda/10$ (< 60 nm). Details of this experiment are given in Appendix C.2.8.

Inclination angles of the prism surfaces are measured using a multi-surface tester (Zygo Verifire) and the values from these measurements are included in Figure 102. Because the direction of tilt during this measurement was not recorded, the angle measured in surface 1 could be either 45.00088° or 44.99912° .

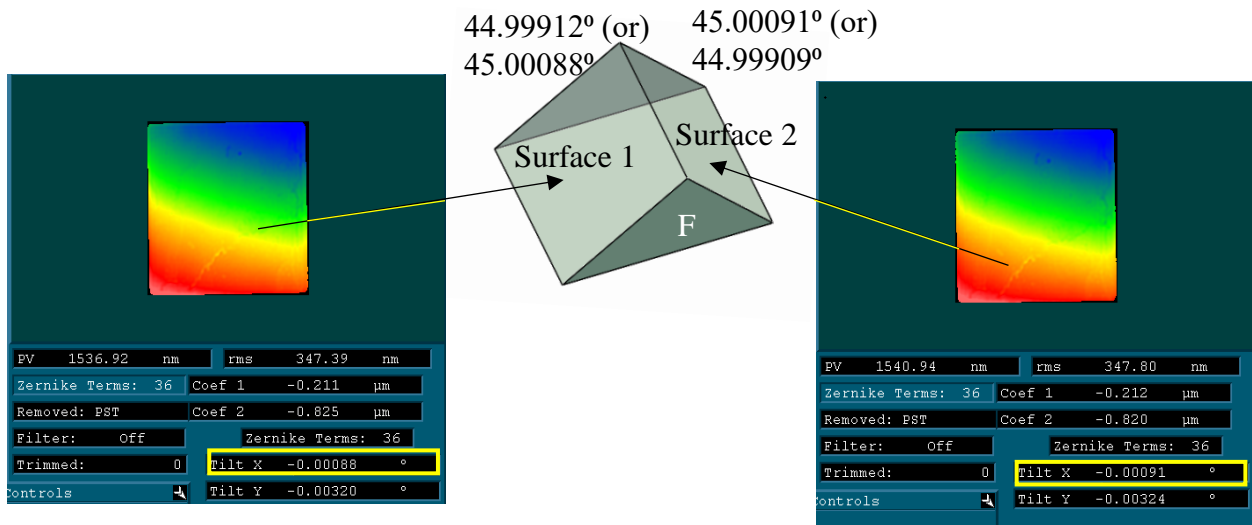


Figure 102: Results of the angle of inclination of the prism measured using a Multi-surface tester.

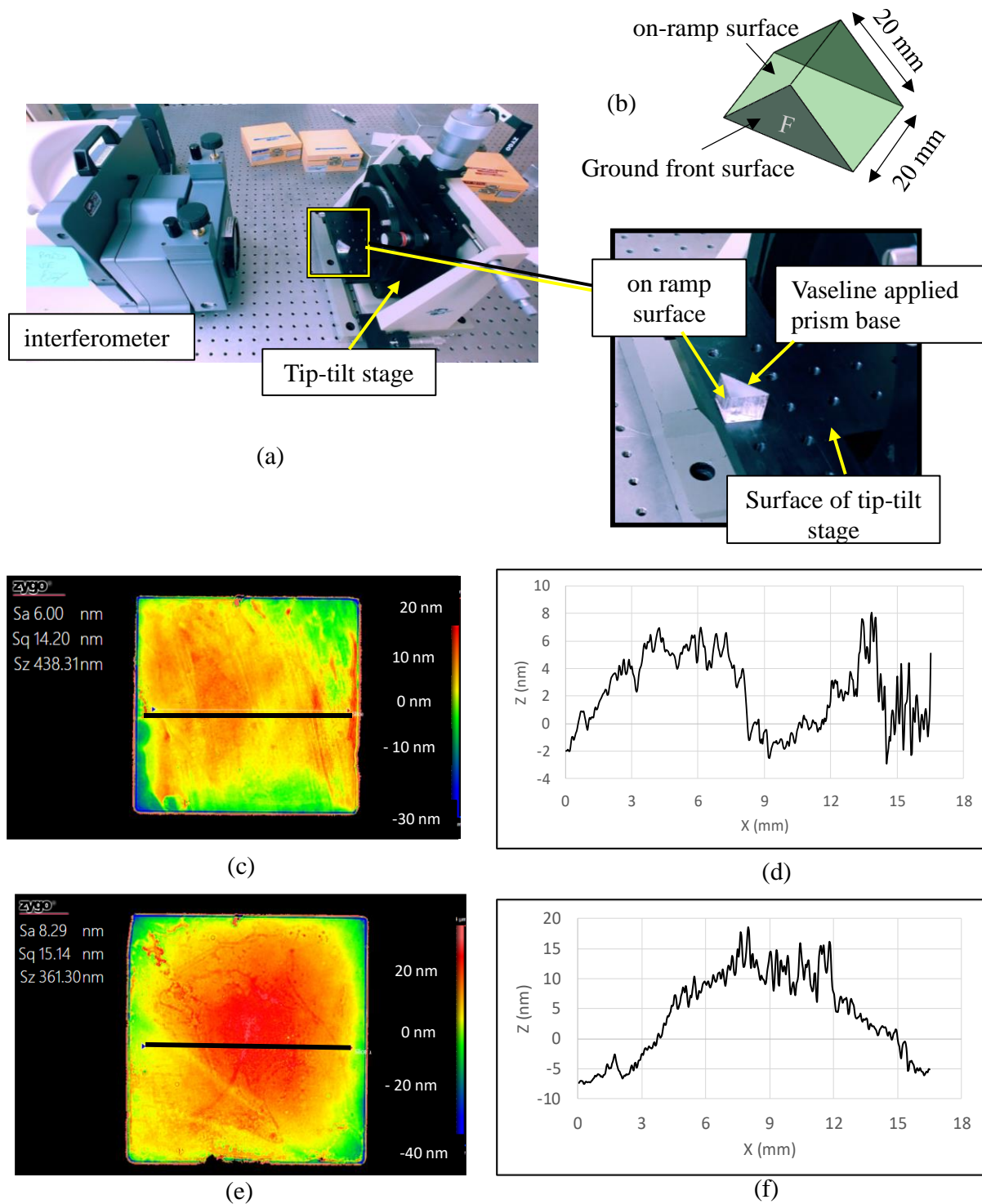


Figure 103: Interferometric measurements of the prism surfaces; (a) Prism measured using a Fizeau interferometer (b) indication to know the orientation of the prism during the measurements (c) interferograms of on ramp surface, and (d) a profile across its horizontal axis (e), (f) same for the off ramp surface.

4.8.1 Experimental assembly and alignment

This prism is measured using the profiler when it is mounted on a kinematic assembly shown in Figure 104(a and b). Delrin polymer material is chosen for the platform so that the glass surface of prism is protected from getting scratched. The prism is pushed into the dove tail groove of the platform, and three plastic set screws (120° from one another) through the bottom of the platform pushes the bottom surface of the prism, up against the surfaces of the groove, making the inclined surfaces of prism contact the surfaces of the groove. The dovetail groove constrains the translation of the prism in x axis, and the plastic screws constrain the z axis translation, roll and pitch (θ_x, θ_y) of the prism. The prism is also pushed against a dowel pin to constrain its translation in y axis (along the dovetail).

To align the profiler's x axis orthogonal to the ramp surfaces of the prism, it was initially planned to use the two hemispheres placed adjacent to the prism. The platform could be translated in the y axis using the Y carriage and rotated in θ_z using the rotary carriage until a profile can be made such that it passes through the meridians of both the hemispheres. But due to the operator feasibility, the polymer platform is centered with respect to the axis of the rotary carriage using an electronic tactile indicator (Appendix C.1.3) around the circular edge of platform while translating it using a micrometer stage. A downside of centering this way is, only the polymer platform is centered, not the prism. As a result, profiles taken across the prism when the rotary stage is oriented at 0° and 180° are offset in x axis by 4 mm, see Figure 104(c).

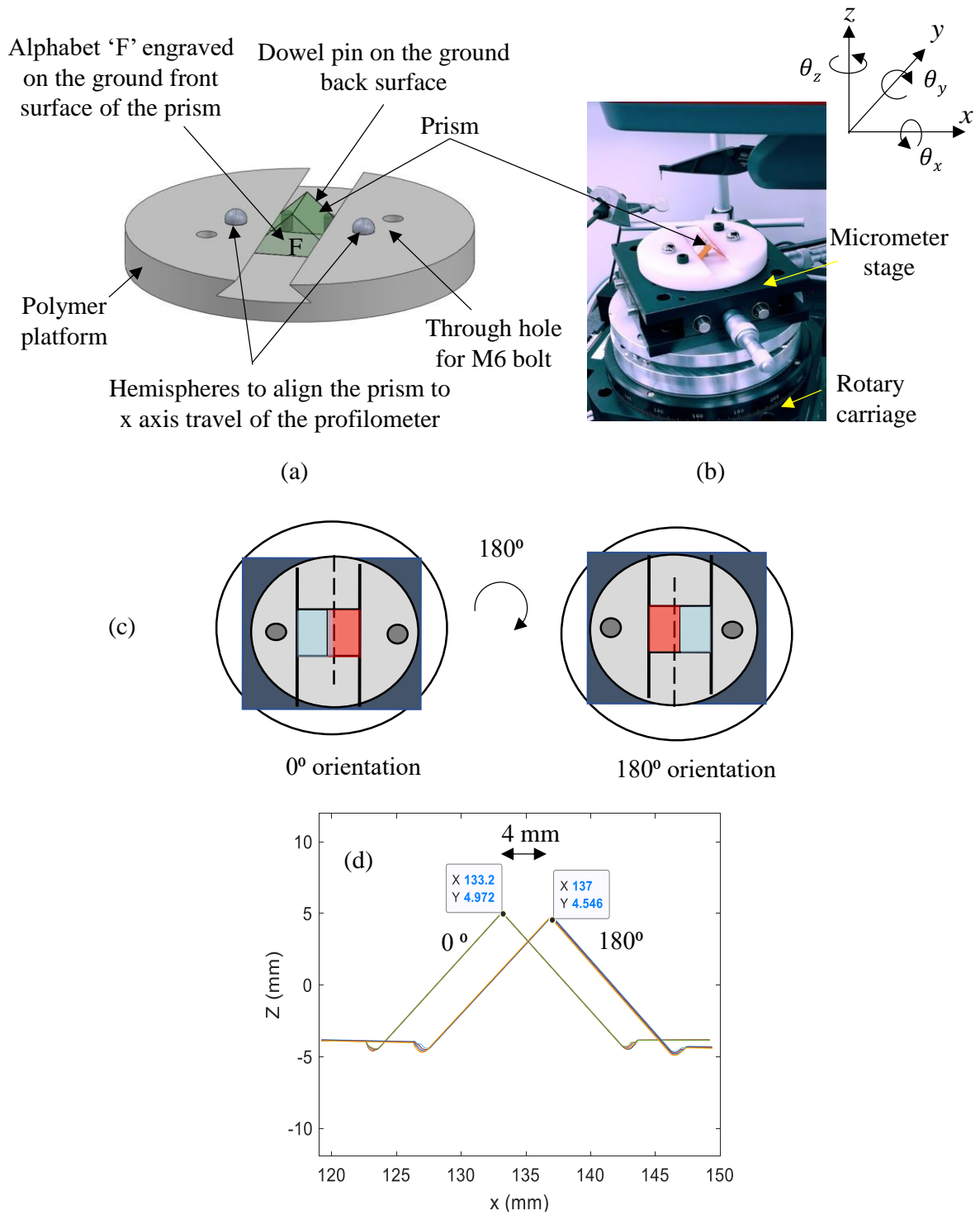


Figure 104: Mounting and orienting the prism in the profilometer, (a) Solid model of the kinematic assembly for measuring the prism (b) Photograph of the experimental setup (c) Schematic showing the off-centered prism during its two azimuth orientations (d) profiles on the prism showing a 4 mm offset in x axis.

4.8.2 Arcuate correction of reported X carriage values due to the pivoting stylus

The x and z values reported by the profiler for the measurement of a prism are plotted as a function of the number of datapoints collected in Figure 105(b). From this figure it is apparent that the number of datapoints of the z values reported on-ramp of the prism is less than that of the off-ramp. This is due to the pivoting action of the stylus as it travels on the surface of the prism as illustrated schematically in Figure 105(a). For the same distance, a travelled by the stylus carriage, X , the z height of the off-ramp surface of the prism changes rapidly compared to the on-ramp surface. This results in a smaller number of datapoints in the off-ramp of the prism as shown in Figure 105(b). Also shown in Figure 105(b) is the reported x values of the carriage travel which is not linear as expected. This is due to the correction applied to the reported x values due to the pivoting stylus of arm length, l_a and stylus length l_s for a given carriage travel (x_{travel}), as shown schematically in Figure 105(c). Therefore, when the reported x and z values are plotted against one another, a symmetric profile of the prism is realized as shown in Figure 105(d). When the stylus travels on the off-ramp of the prism, large oscillations are apparent in Figure 106, where the data in orange is the difference between the adjacent x datapoints reported.

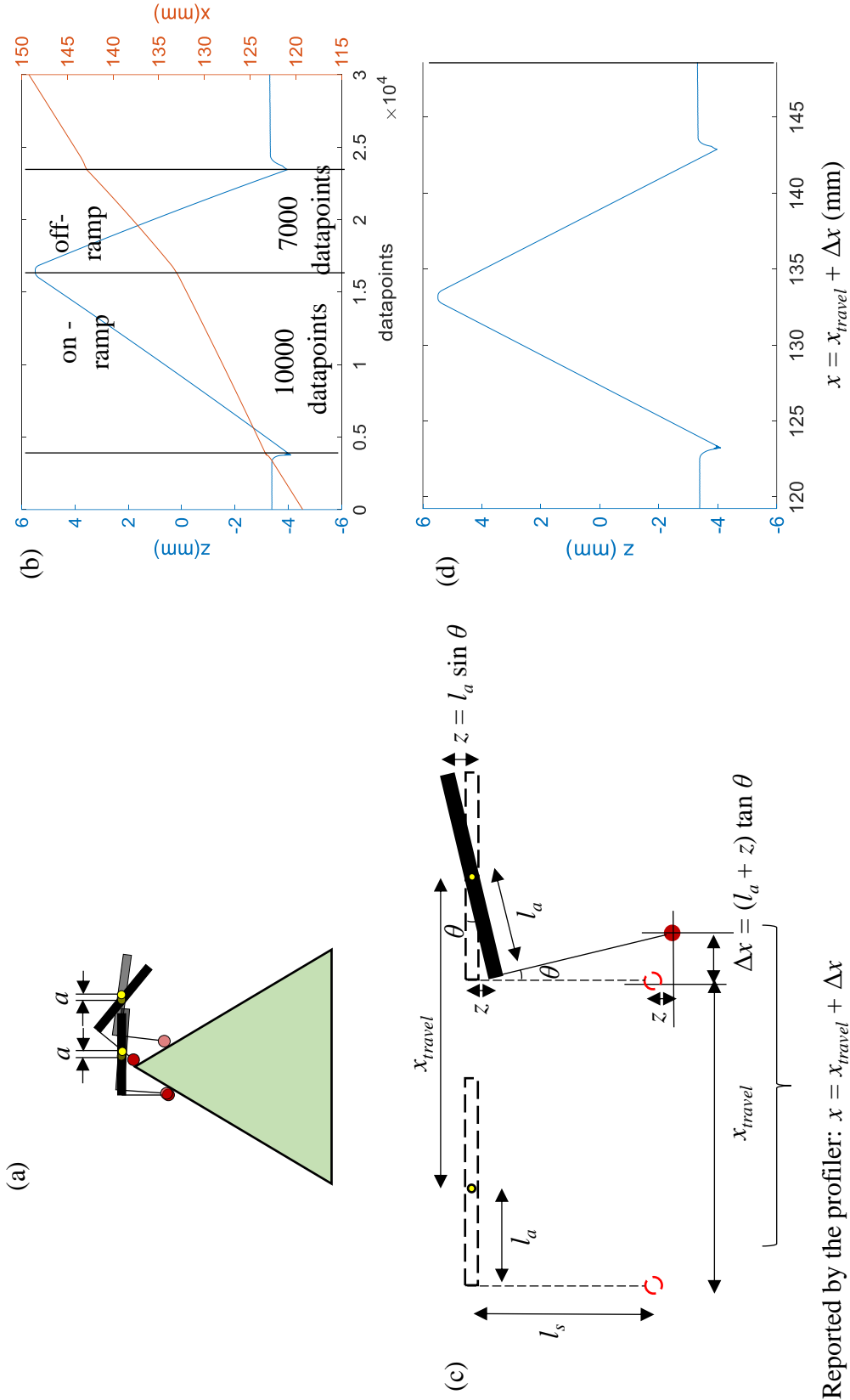


Figure 105: Measurement results of profiling the prism (a) Schematic showing the x carriage of stylus being longer on-ramp (b) Reported x and z values for a profile made on the prism (c) Possible equation showing the correction applied to the reported x values (d) reported x and z values plotted against one another.

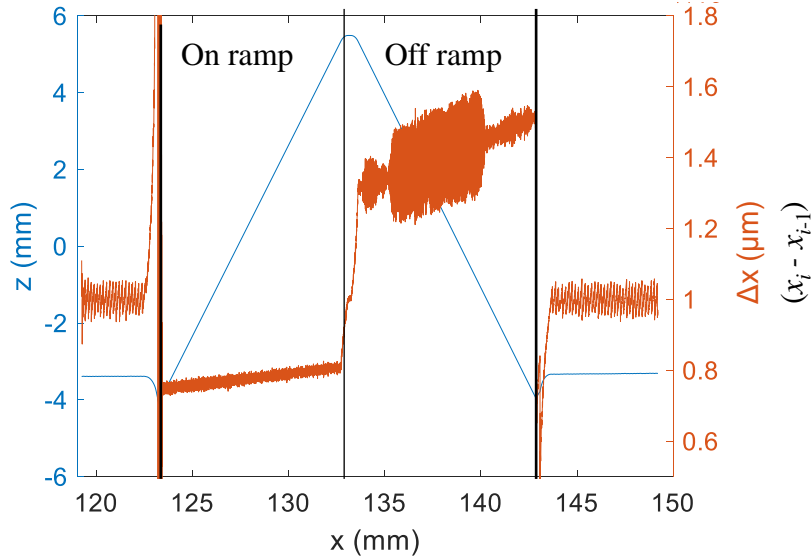


Figure 106: Plot showing the difference in the data spacing of x values reported (in orange) when the stylus travel on ramp and off ramp of the prism.

4.8.3 Filtering for stylus morphology

The stylus tip used in the profiler is a ruby sphere of 0.5 mm radius, therefore, when the stylus travels on features of curvature smaller than 0.5 mm, it is expected to produce a ‘rounded’ feature in the measured signal. This influence of the stylus geometry on the measured profile is called stylus convolution and can be noticed at the apex of the prism shown in Figure 107(c). The profilometer also provides a dataset that is filtered for this ‘morphology’ approximating the apex that appears to have a plateaued flat at the top, see Figure 107(f). It is also noticed that the variation in the adjacent x values in the morphology filtered data is constant, see Figure 107(d).

4.8.4 Vertical error measured on the inclined surfaces of the prism

After the polymer platform of the prism is centered with respect to the C carriage (0° azimuth orientation), the stylus was repeatedly ran over the surface of the prism ten times and the Y carriage was stepped over in 5 locations along y axis with a spacing of 3 mm for each y location.

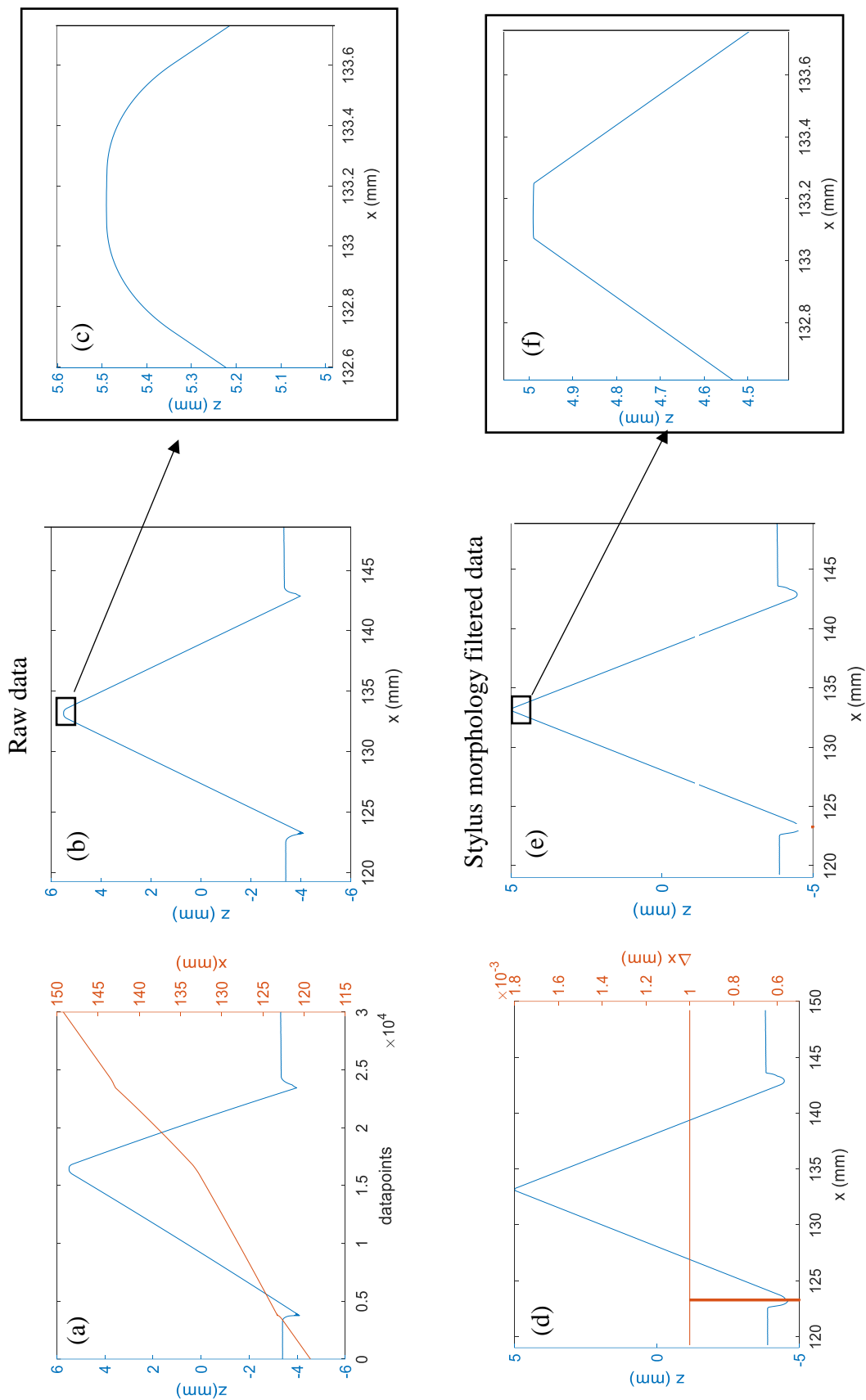


Figure 107: Raw and morphology filtered results of the measurement of the prism; (a) reported x and z values (Raw data) plotted as a function of number of datapoints (b) plotted against one another (c) rounded feature of the apex of the prism (d) Morphology filtered x and z values plotted as a function of number of datapoints (e) plotted against one another (f) deconvolved sharp features at the apex of the prism.

Following these measurements, the prism was rotated 180° azimuthally using the *C* carriage and the measurement was repeated. In the schematic shown in the top row of Figure 108, blue and red areas represent the on-ramp and off ramp surfaces measured earlier interferometrically (Figure 103). On-ramp and off-ramp measurements at the 0° azimuth orientation of the prism are shown in the middle row of Figure 108(a and c), and similar measurements at the 180° azimuth orientation of the prism are shown in Figure 108(b and d).

From the vertical error of *X* carriage established using the measurements of the Zerodur flat shown in Figure 85, the expected variation in the prism measurement for the *x* axis range of 120 mm to 150 mm is less than 100 nm, plus the out of flatness of the surfaces of the prism which is less than 20 nm. Lines are fit to the datapoints highlighted in black (middle row of Figure 108), and subtracted and plotted bottom row of Figure 108. It is noted that, the 3σ outliers of the data are removed and the signal is low pass filtered to 0.8 mm (retains waviness and form) before being plotted in the bottom row. The vertical height variation in these profilograms is less than 150 nm indicating that the vertical error for the full stylus travel in *z* almost about the same as the observed error during the flat measurements when the stylus travelled only about 2 mm in *z* axis. Also, the arcuate motion correction performed by the manufacturer's software does not seem to cause any appreciable amount of error in the measurements of inclined surfaces. Each of these profilograms shown in the bottom row is a culmination of majorly,

- (a) the out of flatness of the prism only along its *x* axis,
- (b) the vertical errors associated with the *X* carriage, and
- (c) the thermal drift of the profilometer system

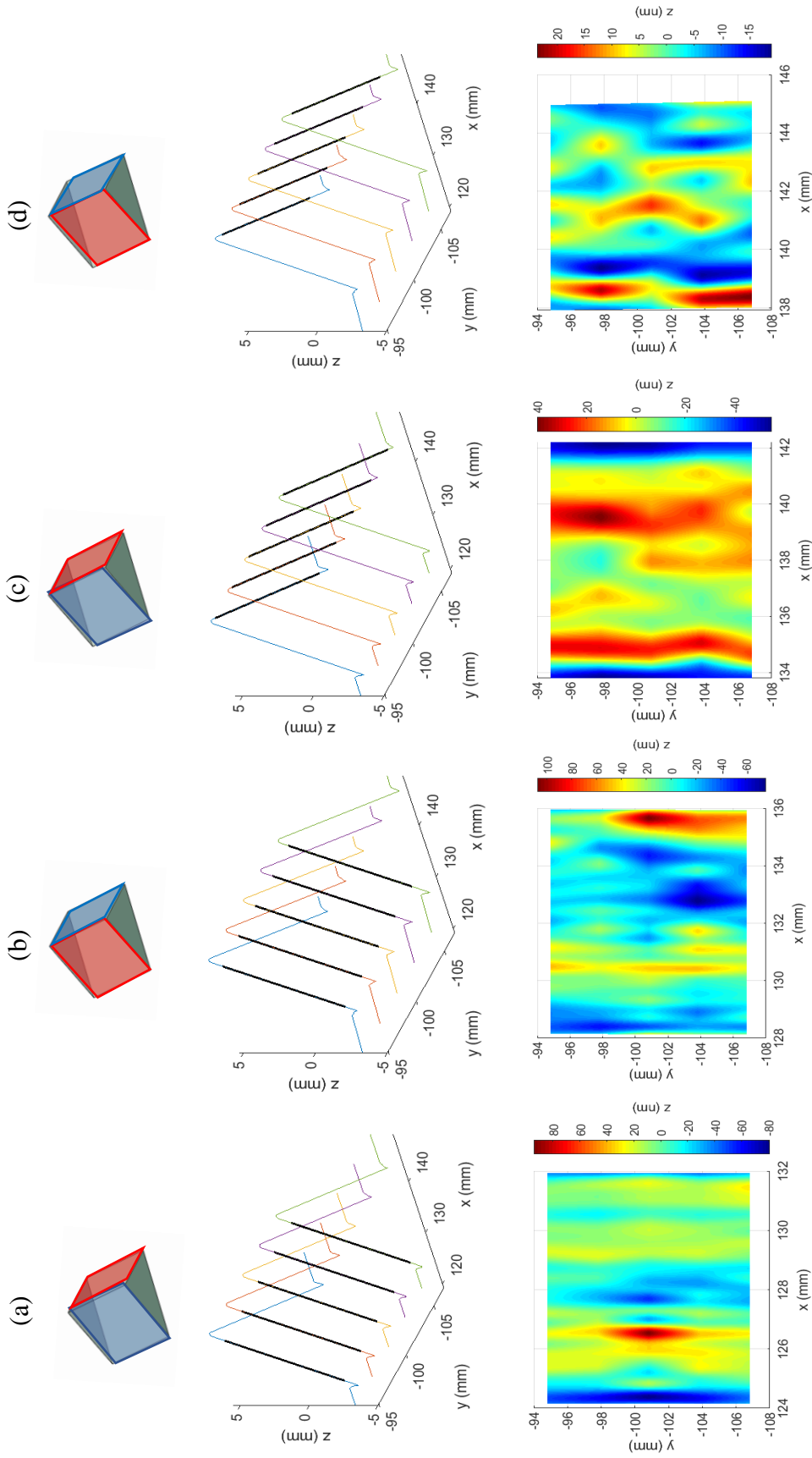


Figure 108: Profiles measured on a prism by stepping in x axis. Top row: Orientation of the prism during measurements; middle row: average of ten profiles made at five y locations using the profiler; bottom row: line subtracted from each profile and plotted as profilograms (a) 0° azimuth orientation of prism when stylus travelling on ramp (b) 180° azimuth orientation, stylus travelling on-ramp (c) 0° azimuth orientation, stylus travelling off-ramp (d) 180° azimuth orientation, stylus travelling off-ramp.

It is noted that prism is housed on a platform made of polymer, and the operator was present during the measurements. From the results discussed in section 4.7.6, and from this, the warmup time of one hour and the removal of operator from the vicinity of the measurement were recommended. Given that these cautions were not known nor followed during the prism measurements performed in these early experiments, the results are likely to include thermal instabilities at the observed magnitudes.

4.8.5 Varying slope profile on the prism and its comparison with a profile on an optical flat

When the stylus travels on a test surface of continuously varying slope, the region of interaction of the stylus ball will not be along its meridian, and the stylus-surface interaction forces will be exerted in the directions in which the stylus is constrained. To study its performance while travelling on a surface with linearly varying slope, the prism is rotated azimuthally by 51° as shown in Figure 109(b) and profiled ten times repeatedly. Then the prism is rotated by another 180° using the rotary carriage, and profiled another ten times. Average of these two sets of measurements are shown in Figure 110(a and b).

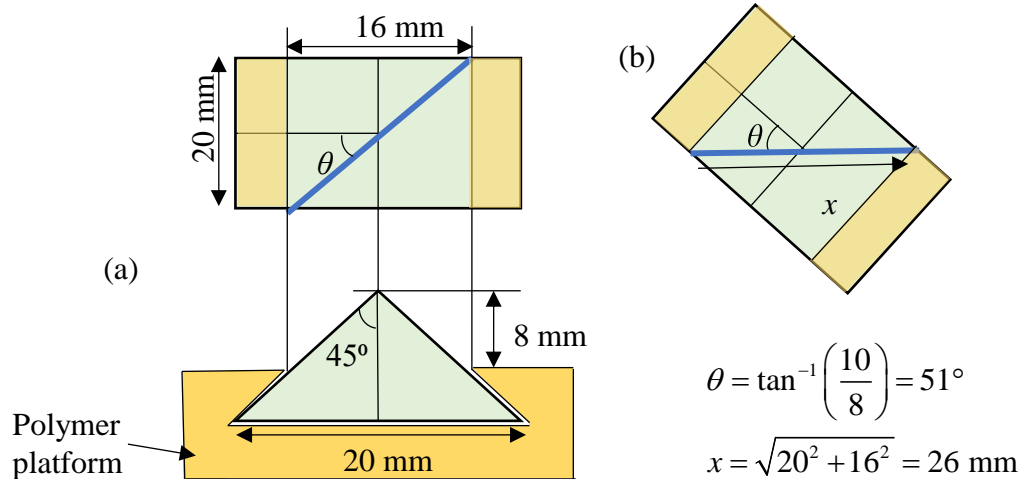


Figure 109: Schematic of (a) top and front view of the prism mounted on the polymer platform and its dimensions and (b) prism rotated to 51° azimuthally to profile along a linearly varying surface slope.

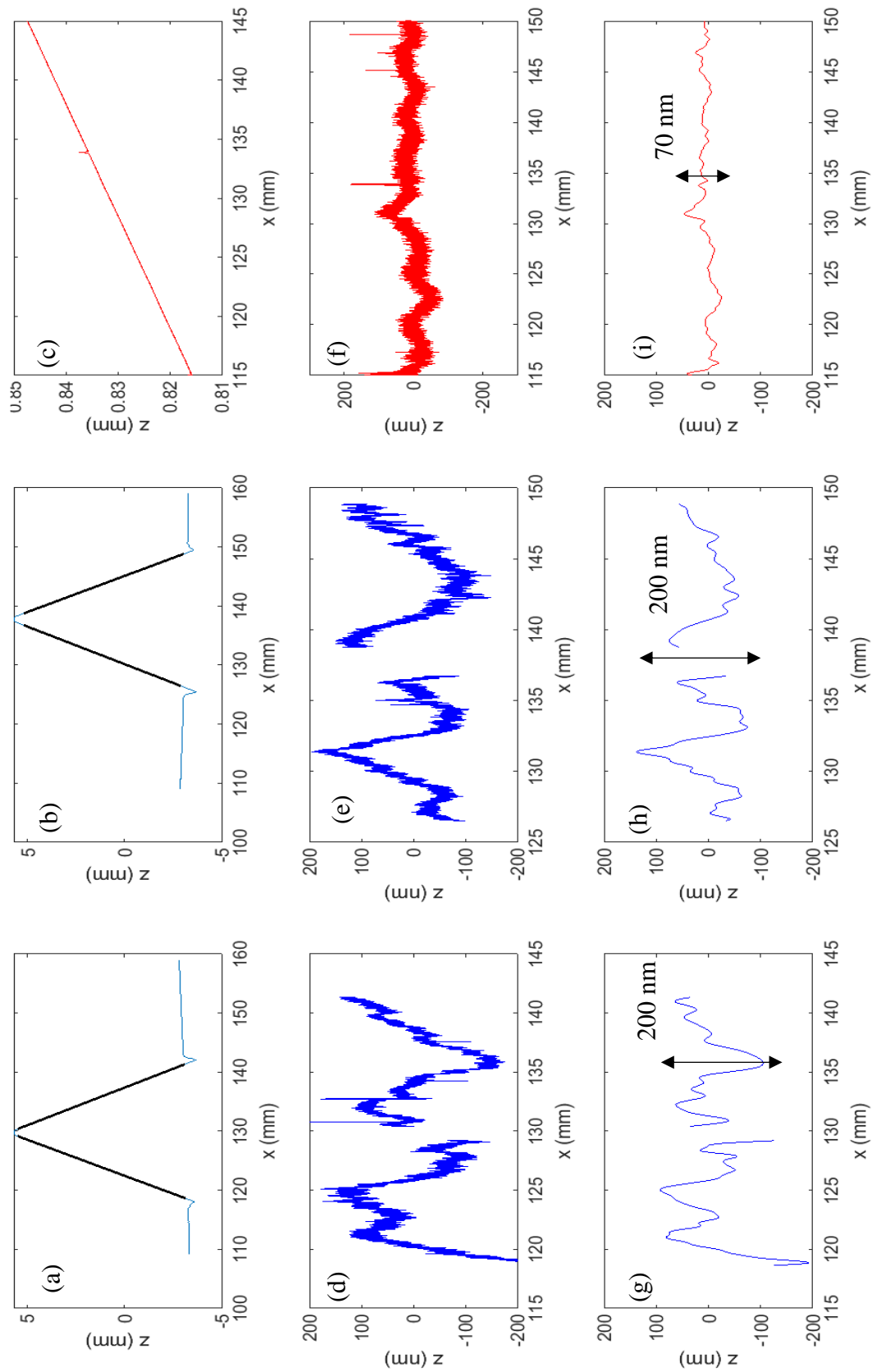


Figure 110: Comparison between the profiles measured on a prism and the profile measured on a Zerodur flat; (a) average of ten diagonal profiles on the prism oriented at 51° azimuthally (b) prism rotated by another 180° azimuthally (d) , (e) line subtracted signals (g), (h) signals low pass filtered at $\lambda_c = 0.8$ mm retaining waviness and form (c) profile on the 4 in. Dia. Zerodur flat (f) line

A line is subtracted from the inclined region of the averaged data and plotted in Figure 110(d and e), which is then low pass filtered to 0.8 mm to remove roughness of the surface and allowing waviness and form (ISO 10110-8) and plotted in Figure 110(e and f), with the vertical error in the measurements being 200 nm PV. As a comparison, vertical error in the measurement of the Zerodur flat for the same x travel is shown in Figure 110(i) with a 70 nm PV.

4.8.6 Estimation of inclined surface angles of the prism

To estimate the angles of ramps of the prism, the tilt of the prism in θ_y must first be removed. To do this, an average of morphology filtered data from ten repeated profiles at one y location is used, shown in blue in Figure 111(a) (unfiltered data could also have been used for this purpose). Tilt is found by calculating the slope between the first and last z datapoints of the data, which is removed and plotted in red. Datapoints highlighted in black in Figure 111 (b), which avoids the apex and troughs of the ramp, is used to compute the angles of the ramp surfaces to be 45.25° and 44.76° , consequently making the pyramid angle 90.01° . The following two sections discuss the computed angles using all the subsequent profiles made on the prism.

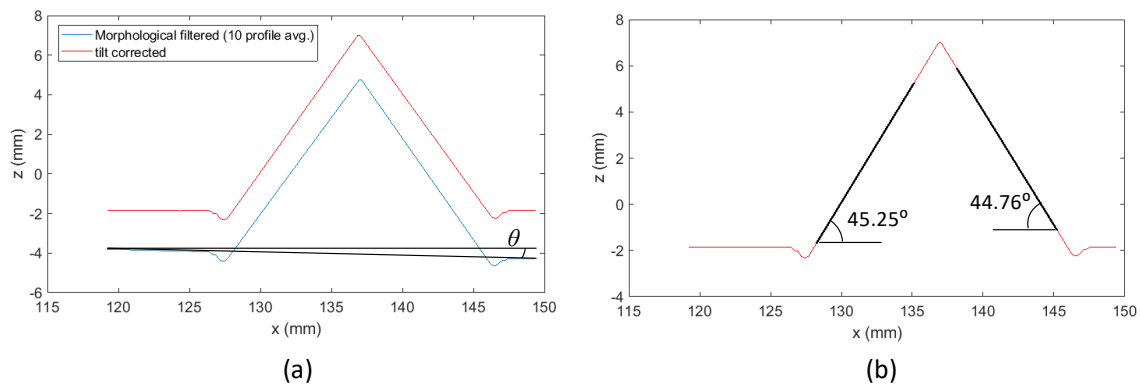


Figure 111: Procedure to estimate the ramp angles of the surfaces of the prism (a) Morphology filtered data at 180° azimuth orientation of the prism (in blue), its tilt is removed and plotted in red (b) Angle of the ramp surfaces computed by fitting a line to the region shown in black.

4.8.7 Estimation of angles using profiles at each Y location

To estimate the angles of the inclined surfaces of the prism, the experimental data shown in Figure 112(a and b) are used, which are the mean of ten repeated profiles on the prism at each y location of measurement when the rotary stage is oriented azimuthally (at 0° and 180° respectively). The inclination angles of these profiles are calculated and plotted in Figure 112(c and d). Triangles in Figure 112 represents the computed angles of Surface 1, using the profiles when the rotary stage is oriented at 0° , and stylus travels up the on-ramp. Squares in Figure 112 (c) represents the computed angles of the same surface, when the rotary stage is oriented at 180° , and, this time, the stylus travels downward along the off-ramp. Correlation coefficients of the computed angles and the y location of the profiler are also given. Similar data processing for the other prism surface is shown in Figure 112(d). It is interesting that by rejecting the single outlier identified in Figure 112(d), the value of correlation coefficient increases to 0.98999. The ‘error bars’ shown in the plots are the standard deviation magnified by 20 times.

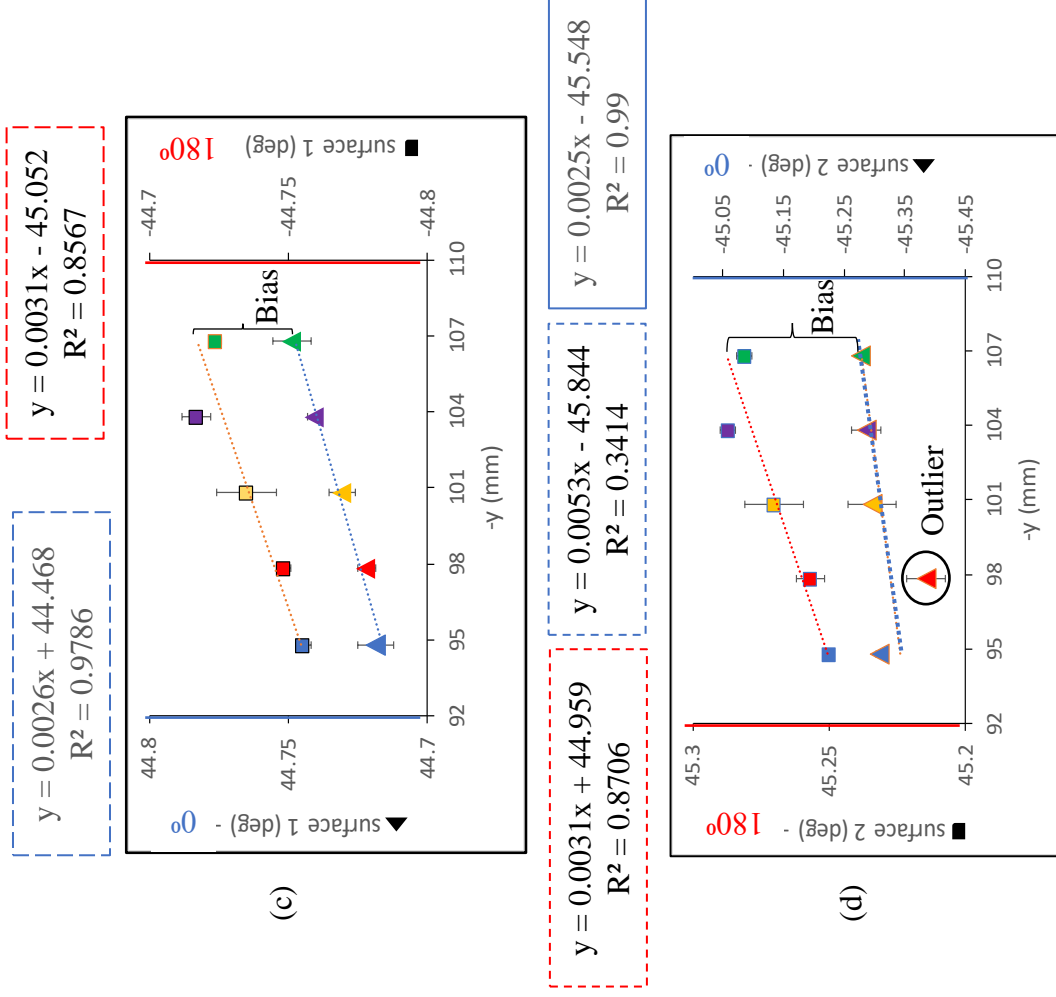
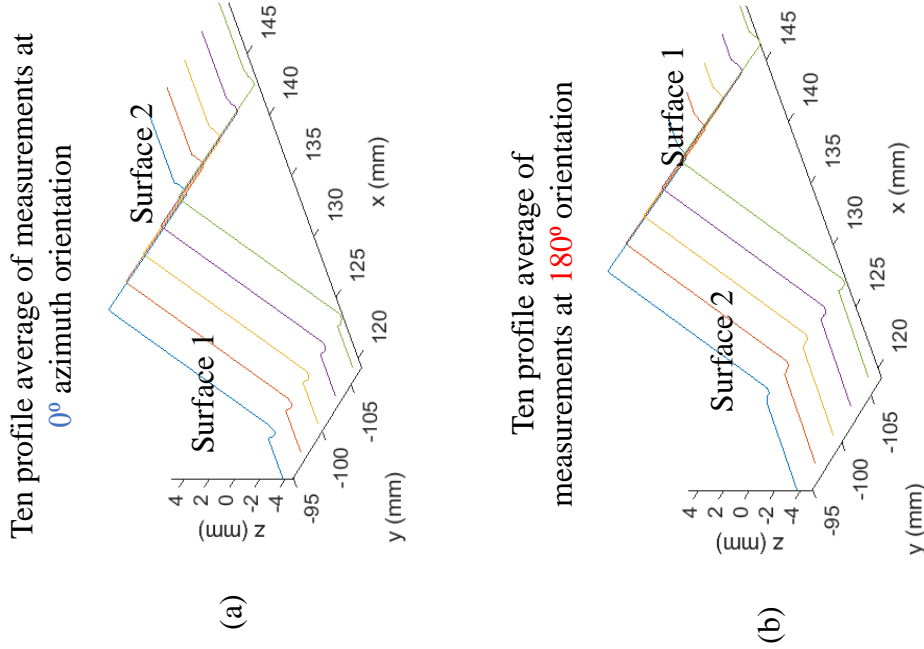


Figure 112: Estimation of the inclination angles of the prism surfaces; (a) Measurements of the prism when the rotary stage is oriented at 0° (b) 180° (c) computed angles of surface 1 of the prism, triangles: stylus travel on-ramp, rotary stage oriented is 0° , squares: triangles: stylus travel off-ramp, rotary stage oriented is 180° (d) computed angles of surface 2 of the prism, triangles: stylus travel on-ramp, rotary stage oriented is 180° , squares: stylus travel off-ramp, rotary stage oriented is 0° .

The bias in the computed angles is probably because the prism is not oriented azimuthally ‘perfectly’ orthogonal to the x axis of the profiler causing the stylus to travel on different slope in left and right surfaces of the prism. One possible reason for the linear relationship between the computed angle and y position is, yaw and pitch of the Y carriage causing the stylus to travel in a larger slope of the surface as illustrated in Figure 113. Figure 114(a and b) shows the mean values of the inclined angles computed and plotted in Figure 112(c and d). For example, the value 44.73° in Figure 114 (a) is the mean of all the triangles shown in Figure 112(c). Figure 114(c and d) shows the angles of the inclined surfaces computed by fitting a plane to the measurements.

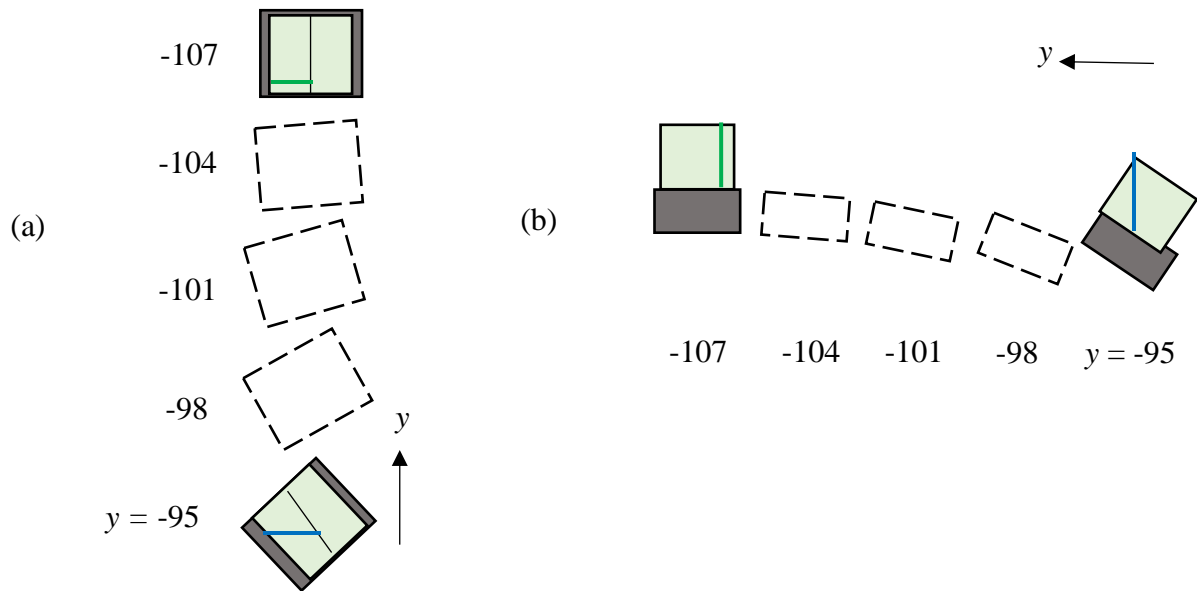


Figure 113: Schematic showing the (a) Yaw of the Y carriage (top view of prism) and (b) Pitch of the Y carriage (side view of prism) during the step over to make profiles on the prism.

4.8.8 Summary of estimated inclination angle

A summary of the inclination angles estimated from the above discussed methods are presented in Table 2. It is noted that the manufacturer’s tolerance for inclination angle and pyramid angle are 1.1 mdeg and 1.7 mdeg respectively. From the measurement using a Multi-surface testing interferometer, the estimated inclination angles are a magnitude better than the manufacturer’s

specification. From profilometric measurements, they are a magnitude worse than the manufacturer's specification.

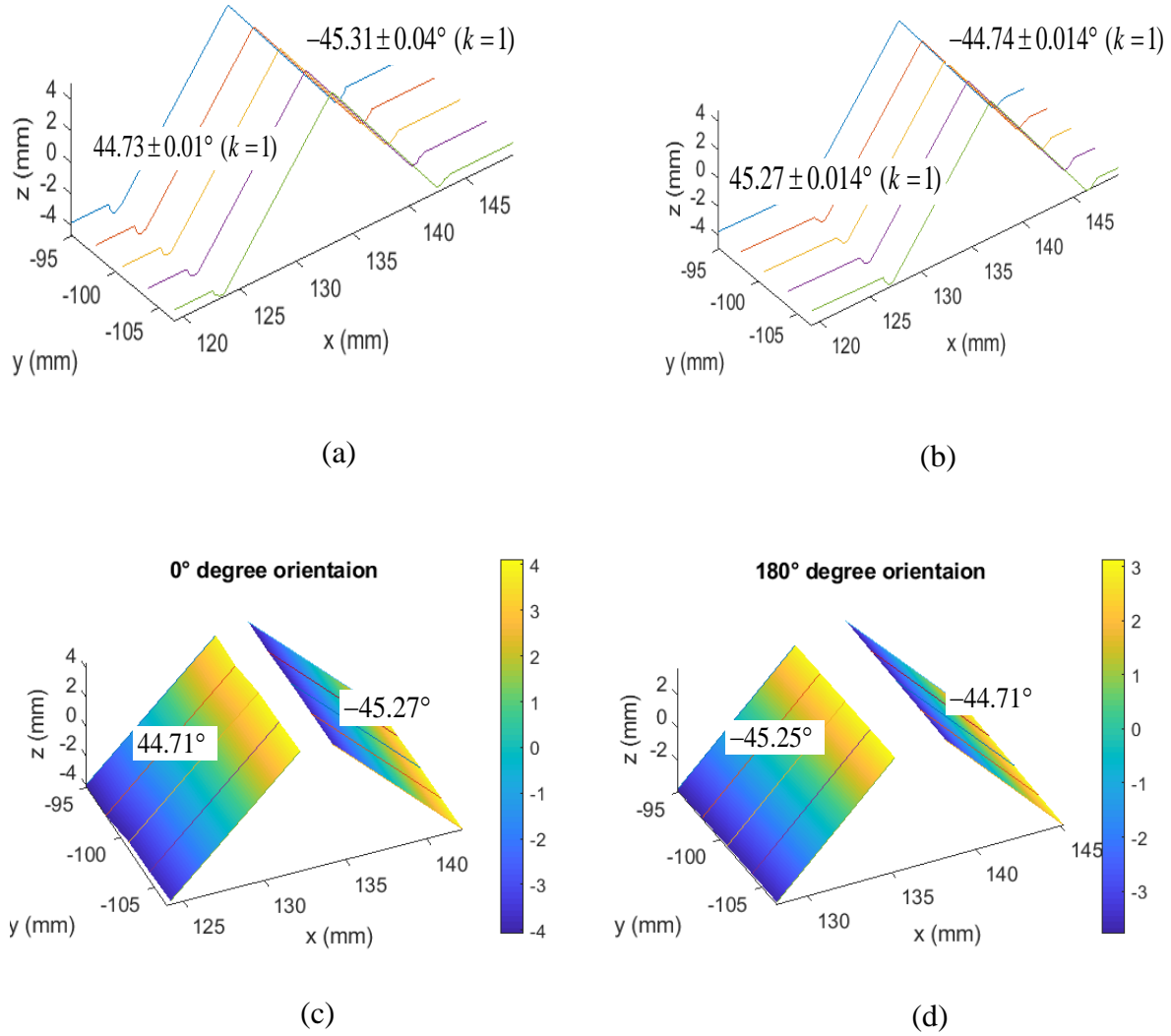


Figure 114: Ramp angles estimated by fitting a plane to the profiles made on a prism; (a) average value of the inclined angle of the surfaces computed using the measurements performed when the rotary stage is oriented at 0° (b) rotary stage is oriented at 180° (c) inclined angle of the surfaces computed by fitting a plane to the measurements performed when the rotary stage is oriented at 0° (d) rotary stage is oriented at 180° .

Table 2: Summary of the computed angle of inclination surfaces and the pyramid angle

Method	Rotary carriage orientation	Inclination angle Surface 1	Inclination angle Surface 2	Pyramid angle
Mean of angle computed from each profile	0°	44.73 ±0.01	45.31 ±0.04	90.04 ±0.05
	180°	44.74 ±0.014	45.27 ±0.014	90 ±0.028
Plane fit to the profiles	0°	44.71	45.27	89.98
	180°	44.71	45.25	89.96
Multi-surface testing interferometer	NA	44.99912 (or) 45.00088	45.00091 (or) 44.99909	90.00003 (or) 89.99997
Manufacturer specification	NA	45±0.011	45±0.011	90±0.0017

In this section, measurements of an object with a constant surface slope (a prism) was studied, and the computed pyramid angles indicate that the algorithms to correct for the arcuate motion of the stylus are within $\pm 0.05^\circ$ for the measurements performed in this study. In the following section, measurements of an object with a continuously varying surface slope (a sphere) is studied.

4.9 Spherical cap measurements

This section discusses the measurements performed on a 50 mm Silicon nitride sphere and two concave mirrors of 75 mm Diameter, and 2.4 mm sag. The former is used to assess the effect of the normal forces exerted on the stylus causing it to deviate from its intended path of travel, referred to as ‘side-loading’. The dimensions of the concave mirrors are equivalent to the tertiary freeform mirror of the ‘next generation’ telescope to be measured using the profiler in the future. Therefore, the measurement results of the concave mirrors would indicate the expected uncertainty in the measurements of the tertiary mirror.

4.9.1 Silicon nitride sphere

To study the performance of the profiler on test surfaces with continuously varying slope, a Silicon nitride sphere (Ortech inc., Lot # SPB757G5KFE, Grade 28, worst case out of roundness of $0.75\text{ }\mu\text{m}$) of 50.8 mm (2 in.) diameter is used in the experiments.

When a small ball (stylus) moves on the surface of a large sphere, the contact point follows the path of the normal vectors from the surface of the sphere. As shown schematically in Figure 115(a), the stylus is constrained to pivot ideally about the y axis as the carriage travels in a linear path directed along the x axis. During its travel on a sphere, normal force vectors in the constrained directions of the stylus would try to unseat the stylus from its magnetically held kinematic seat. This ‘sideloading’ effect will cause deviations from the ideal path of travel of stylus causing an error between the reported values and the actual location of the stylus on the sphere, schematically shown in Figure 115 (b). This effect becomes more influential as the profiles are made further away from the meridian of the sphere, which is the case when the sphere is measured in a stripes manner.

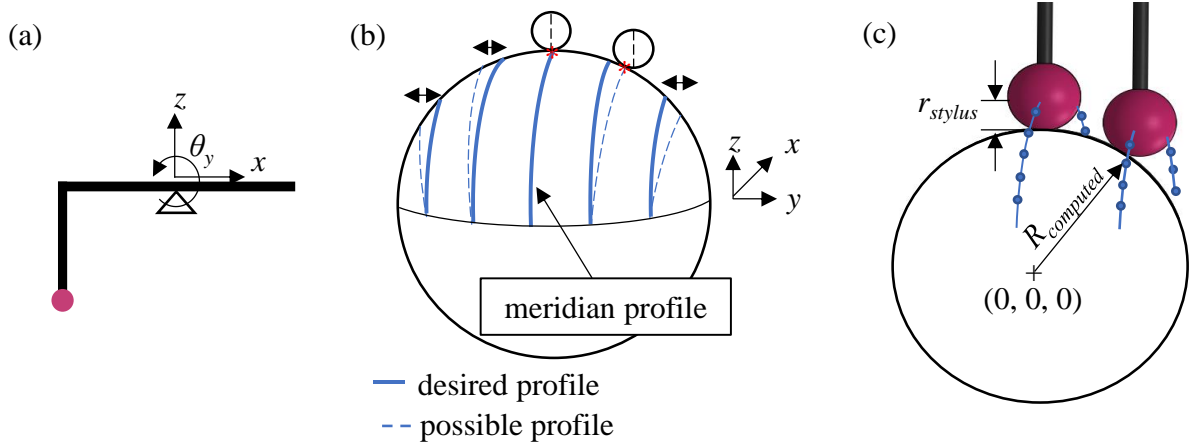


Figure 115: Schematic diagrams showing (a) the degrees of freedom of the stylus, (b) desired profile and possible profiles due to side loading, (c) the measured datapoints on the sphere

Therefore, one cannot use the morphology filtered data for data analysis because the meridian of the stylus interacts with the sphere only when it is profiled along its meridian. For profiles adjacent to the meridian of the sphere, this is not the case, shown as red asterisks in Figure 115(b), making the software implementation of morphology filter by the manufacturer suitable only for the profile along the meridian.

4.9.1.1 Experimental setup

Before the measurements, the profiler was continuously ran in air for an hour to get ‘warmed up’. A solid model of the Silicon nitride sphere and the 3-ball kinematic seat it is supported on, are shown in Figure 116(a and b). The 3-balls are arranged in a way that the Silicon nitride sphere sits deep enough so that it does not get unseated even if unexpected lateral forces of couple of newtons are exerted on it. To align the vertical axis of the sphere with respect to the axis of the rotary carriage, a Chrome steel sphere of 2 in. diameter (Grade 25) is used, see Figure 116(c). This is done to avoid impact of unseating and reseating the brittle Silicon nitride sphere from the kinematic seat when an inductive probe (Millimar EHE-2048) is used at the equator of the sphere and align it using the xy micrometer stage. The

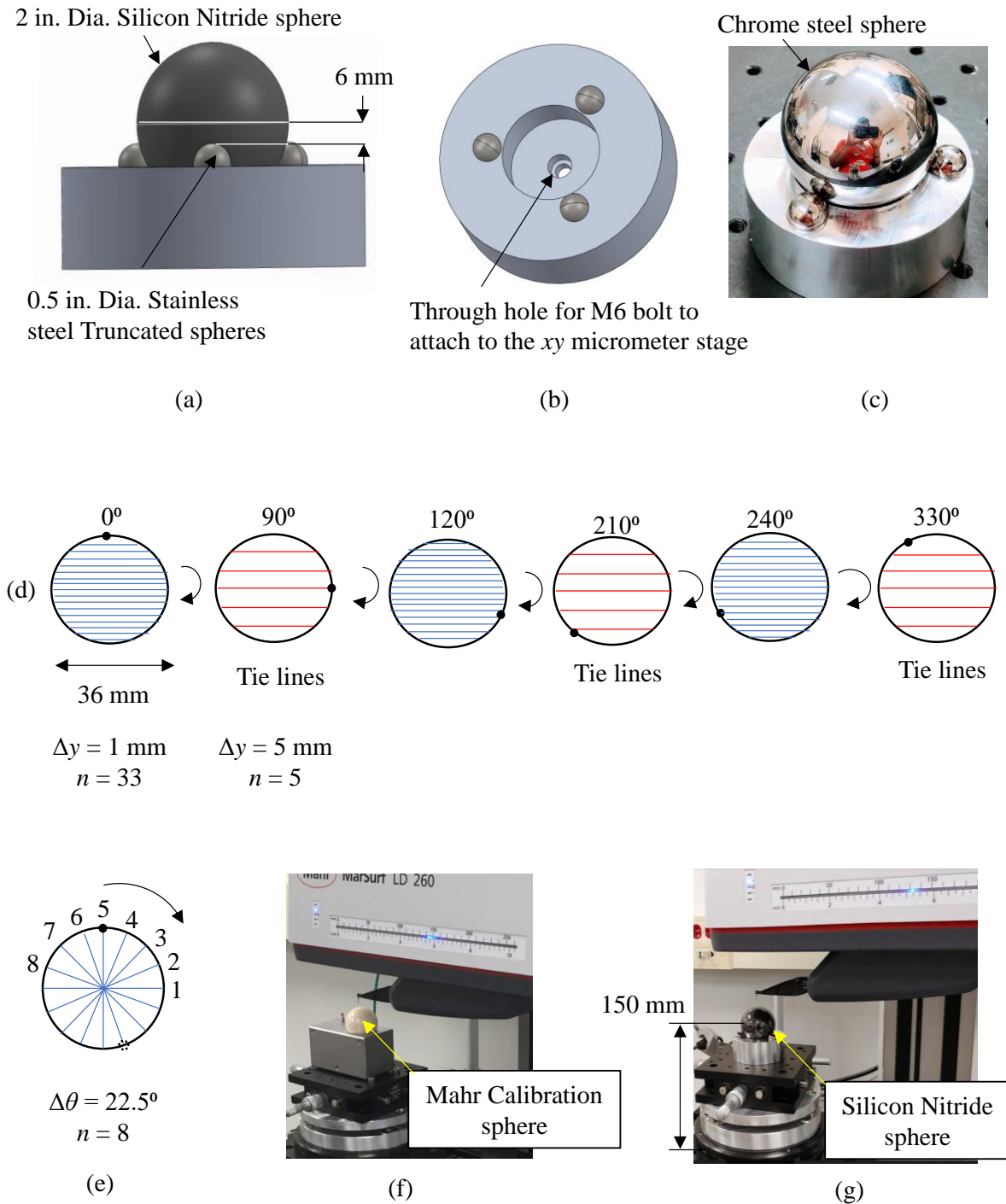


Figure 116: Experimental setup and the measurement procedure to measure a Silicon nitride sphere; (a), (b) Solid model of the Silicon nitride sphere supported in a 3-ball kinematic nest (c) Chrome steel ball used to align its vertical axis with respect to the rotary carriage axis (d) Schematic showing the experiment procedure of stripes method to remove rotationally varying errors in the measurement (e) Spokes measurement method (f) Probe calibration using the calibration sphere (g) Silicon nitride sphere being measured.

specification of the inductive probe, and a Hertzian analysis of the sphere supported on the 3-ball kinematic seat is given in Appendix C.5.

4.9.1.2 Measurement procedure

To remove the rotationally variant form error of the sphere (astigmatism, coma, trefoil, etc.), it was measured in 3 azimuth orientations differing by 120° , and 33 stripes were made to cover its spherical cap, see Figure 116(d). The average of the radial residues computed from these measurements would mainly comprise of the side loading effect on the stylus, and X , Y carriage related errors. In between the measurements at each azimuth orientation, the sphere is rotated by 90° and 5 tie lines were also made. Once the stripes measurements are complete, eight spokes were made by rotating the sphere using the rotary carriage with a 22.5° azimuth spacing between each spoke as shown in Figure 116(e). Before measurements, the stylus tip is calibrated using a Alumina calibration sphere of radius 22.4834 mm and out of roundness of $0.068 \mu\text{m}$ (Mahr, calibration no., FMR 150126) as shown in Figure 116(f) and the result of one such measurement is shown in Figure 123(f). The Silicon nitride sphere is then placed on the 3-ball nest attached to the micrometer xy stage, which sits about 150 mm above the rotary carriage, see Figure 116(g).

4.9.1.3 Results- Stripes

The measurement data of the spherical cap when the rotary carriage is at sphere 0° is shown in Figure 117(a). Circles are fit individually to the measured profiles using the least sum of squares method [Shunmugam, 1986] shown in equation (14), to estimate their radius ($R_{profile}$) and x , z origin values ($x_{0,c}$, $z_{0,c}$), and are plotted in Figure 117(c and d). It is noted that the backslash operator is used in the Matlab program for finding the inverse of matrix B . i.e., $C = B^{-1}A$ in equation (14) is programmed as $C = B/A$.

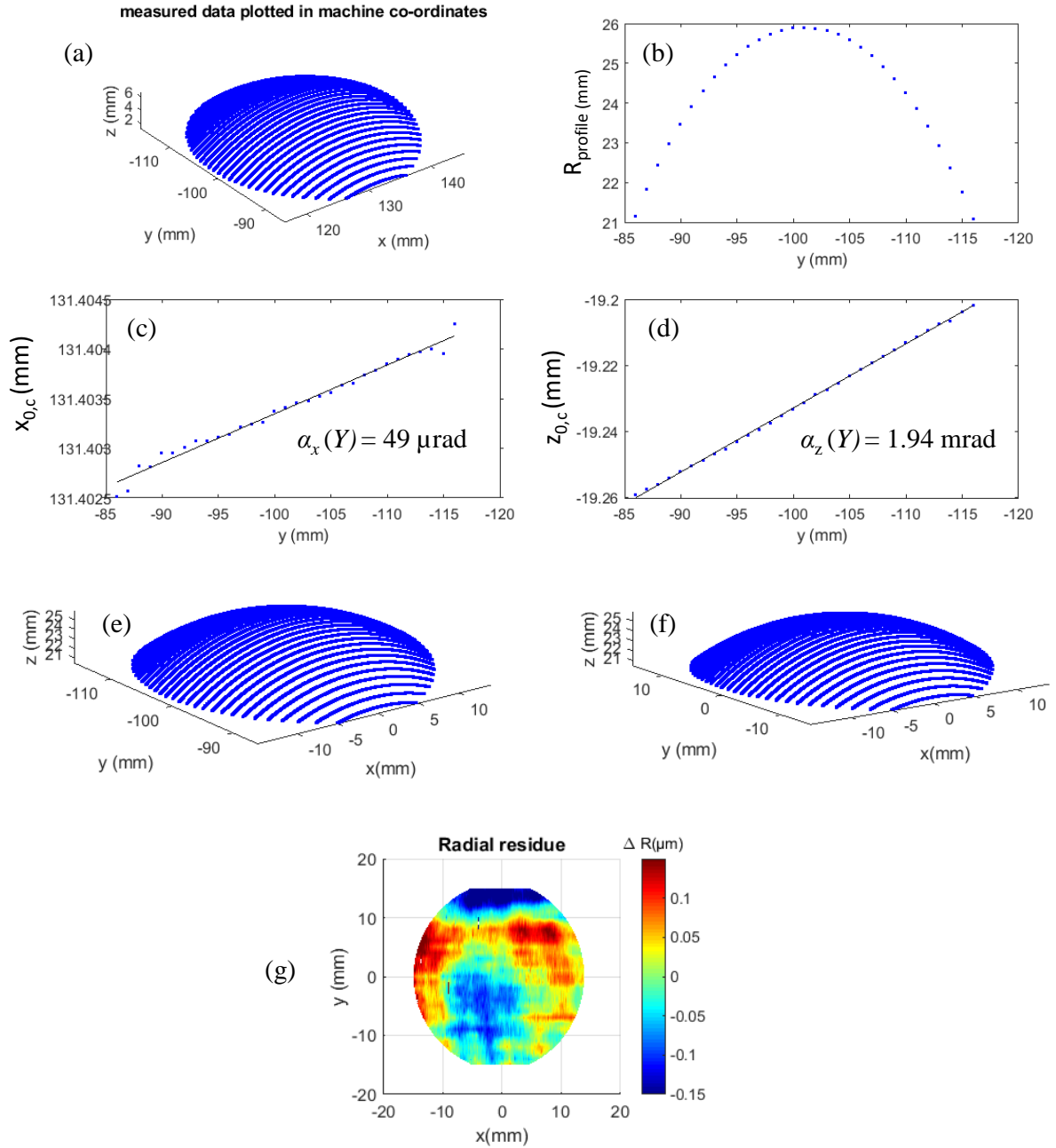


Figure 117: Estimation of Y carriage squareness and the calculated radial residue in the measurement of a Silicon nitride sphere; (a) measured data with the first and last profiles discarded, (b) radius of the circles fit to individual profiles, (c) x , and (d) z origin of the profiles representing the squareness of Y carriage (e) data corrected for the squareness (f) data moved to (0,0,0) origin (g) computed radial residue with a 300 nm PV.

$$\begin{aligned}
& (x - x_{0c})^2 + (z - z_{0c})^2 = R_{profile}^2 \\
& x^2 + z^2 = 2xx_{0,c} + 2zz_{0,c} - x_{0,c}^2 - z_{0,c}^2 + R_{profile}^2 \\
& \begin{bmatrix} x_i^2 + z_i^2 \\ x_{i+1}^2 + z_{i+1}^2 \\ \cdot \\ \cdot \\ x_n^2 + z_n^2 \end{bmatrix} = \begin{bmatrix} 2x_i & 2z_i & 1 \\ 2x_{i+1} & 2z_{i+1} & 1 \\ \cdot & \cdot & \cdot \\ \cdot & \cdot & \cdot \\ 2x_n & 2z_n & 1 \end{bmatrix} \begin{bmatrix} x_{0,c} \\ z_{0,c} \\ -x_{0,c}^2 - z_{0,c}^2 + R_{profile}^2 \end{bmatrix} \quad (14)
\end{aligned}$$

$$A = BC$$

$$C = B^{-1}A$$

Lines are fit to the origin values (x_0, z_0) as a function of y location to estimate the horizontal and vertical squareness of Y carriage as $\alpha_z(Y) = 49 \mu\text{rad}$ and $\alpha_x(Y) = 1.94 \mu\text{rad}$ respectively, see Figure 117(c and d). The subscripts z and x denotes the out of squareness axes of rotation. It is noted that, since these origin values of the first and last profile of the measurement had a larger deviations from the line fit, they were ignored in the computation of the squareness's. Estimated squareness from the measurements at 120° and 240° locations of the rotary carriage are shown in Figure 118(a and b). Standard deviation of the estimated x and z origin, and the radii of each circular profile are given in Figure 118(d to f).

To correct for the squareness errors, for the given y location of the profiles shown in Figure 117(a), x and z values of their datapoints are subtracted from the respective x_0 and z_0 values from the fit shown in Figure 117(c and d) respectively. The squareness corrected profiles are plotted in Figure 117(e). Using the least sum of squares method given by equation (15), a sphere is fit to this cloud points of data to estimate its origin (x_0, y_0, z_0) and the radius of the sphere, R_{sphere} .

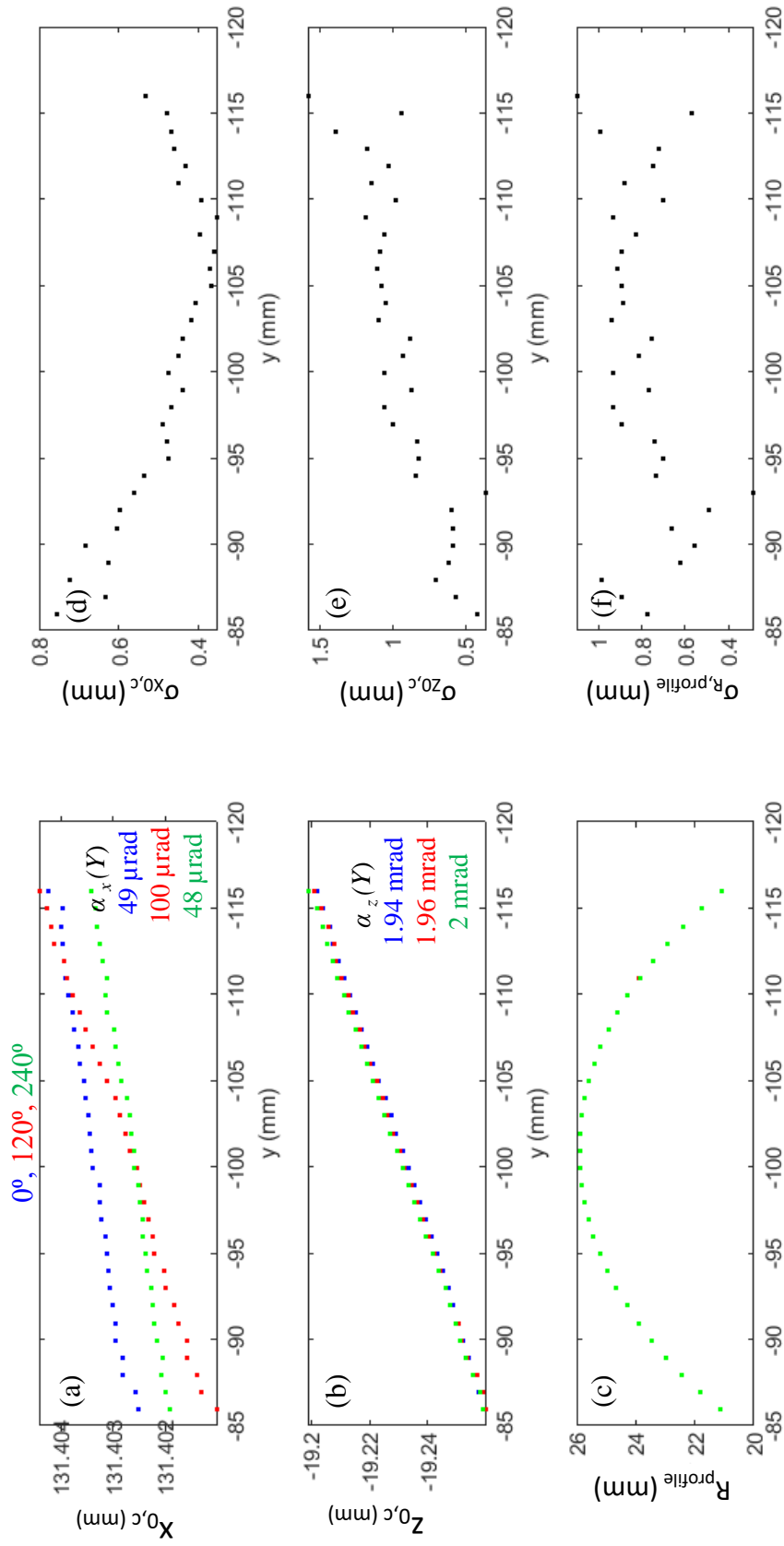


Figure 118: Estimation of Y carriage squareness using the measurement of a Silicon nitride sphere in three azimuth orientations; (a) x origin of each circular profile from the stripes measurement at three azimuth orientation estimated by fitting circles to it using least sum of squares method (b) z origin (c) radius of each circular profiles (d) radius of x origin, (e) z origin (f) radius of circular profiles.

$$\begin{aligned}
& (x - x_0)^2 + (y - y_0)^2 + (z - z_0)^2 = R_{sphere}^2 \\
& x^2 + y^2 + z^2 = 2xx_0 + 2yy_0 + 2zz_0 - x_0^2 - y_0^2 - z_0^2 + R_{sphere}^2 \\
& \begin{bmatrix} x_i^2 + y_i^2 + z_i^2 \\ x_{i+1}^2 + y_{i+1}^2 + z_{i+1}^2 \\ \vdots \\ x_n^2 + y_n^2 + z_n^2 \end{bmatrix} = \begin{bmatrix} 2x_i & 2y_i & 2z_i & 1 \\ 2x_{i+1} & 2y_{i+1} & 2z_{i+1} & 1 \\ \vdots & \vdots & \vdots & \vdots \\ 2x_n & 2y_n & 2z_n & 1 \end{bmatrix} \begin{bmatrix} x_0 \\ y_0 \\ z_0 \\ -x_0^2 - y_0^2 - z_0^2 + R_{sphere}^2 \end{bmatrix} \quad (15)
\end{aligned}$$

$$A = BC$$

$$C = B^{-1}A$$

The x , y and z values of the datapoints shown in Figure 117(e) are subtracted from the estimated origin of the sphere, therefore moving its center to (0,0,0) and is plotted in Figure 117(f). The distance from center to each datapoint is calculated as $R_{computed} = \sqrt{X^2 + Y^2 + Z^2}$ and the difference between this and the estimated radius of the sphere is plotted in Figure 117(g) with 300 nm PV. Ideally, the distance, $R_{computed}$ should be equal to the sum of radius of the sphere and radius of stylus tip (see Figure 115(c)), but due to the errors such as the X carriage motion, side loading, and the out of roundness of sphere, this distance will vary for each datapoint. This variation is referred to as ‘Radial residue’.

The radial residues estimated at all the three azimuth orientations are shown in Figure 119(a to c), and their average that removes the rotationally varying form error of the Silicon nitride sphere is plotted in Figure 119(d), with 200 nm PV including the effect of side loading and other uncertainties in the measurement. It is interesting to see the curved streaks that is probably be due to the 5 mm periodic oscillations present in the vertical error of the X carriage, see Figure 77(c). Standard deviation (less than 150 nm PV) and the range (max - min) of the radial residue measurements are plotted in Figure 119(e and f) respectively.

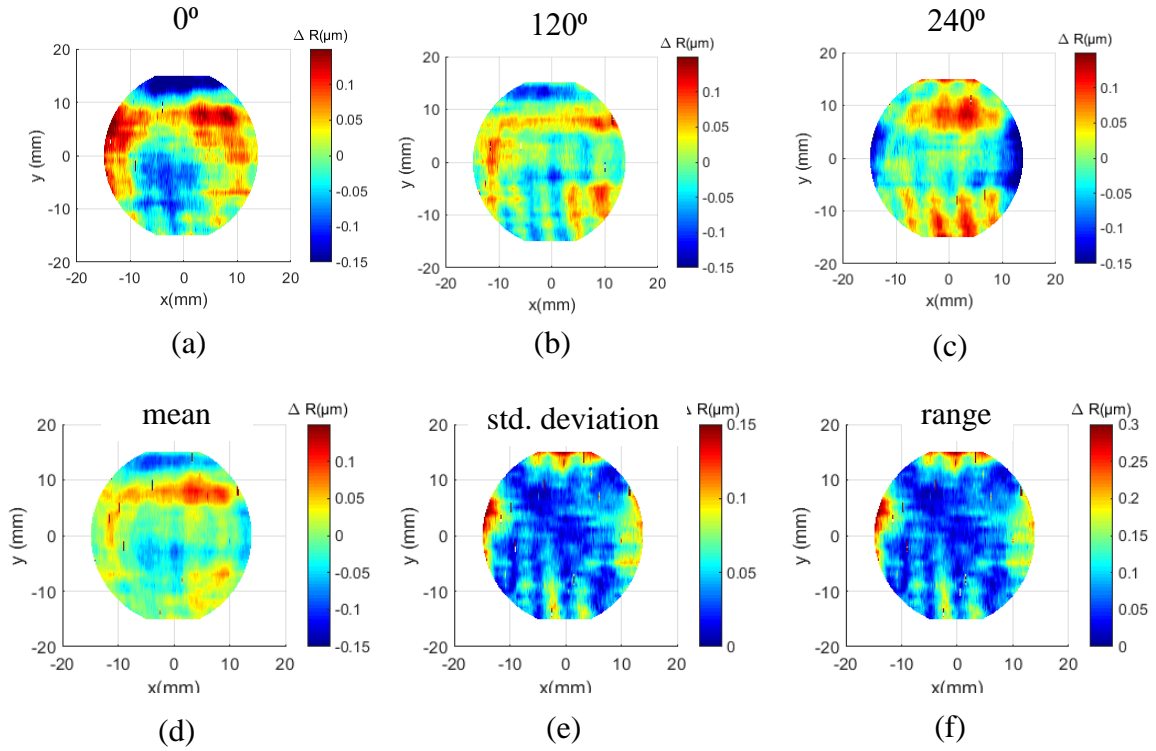


Figure 119: Radial residues calculated from the measurements of the Silicon nitride sphere in three azimuth orientations; (a),(b), (c) Radial residue at 0° , 120° , and 240° azimuth orientations (d) average of radial residue at the three orientations removing the rotationally varying form error (e) standard deviation, and (f) range of radial residue.

(a) Uncertainty in the estimation of the squareness of Y carriage

To estimate the horizontal and vertical squareness of the Y carriage, the origin of each circular profile estimated using the least squares fit to each measurement profile are used. Measurements were done over four days, and each measurement comprises datasets at three azimuth orientations (0° , 120° , 240°), making a total of 12 datasets. Figure 121(b and c) shows the x and z origin values, and Figure 121(d and e) shows a lines fit to this data. The values of the slope of these fit lines are plotted in Figure 121(f and g) provide estimates for the horizontal and vertical squareness's of Y carriage to be $70 \pm 30 \mu\text{rad}$ and $-1.97 \pm 0.03 \text{ mrad}$ respectively, and the variation at each azimuth orientation is about $20 \mu\text{m}$. For example, Figure 120 shows a schematics that helps to determine the sign of the estimated horizontal squareness value using the 'right hand rule'. A line is subtracted from the data and plotted in Figure 121(h and i), which majorly consists of Y carriage vertical straightness, pitch, thermal and other errors associated with the measurements.

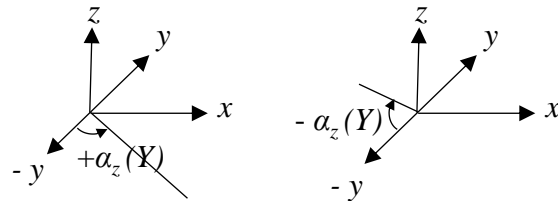


Figure 120: Example illustration of sign convention for the estimated horizontal squareness values.

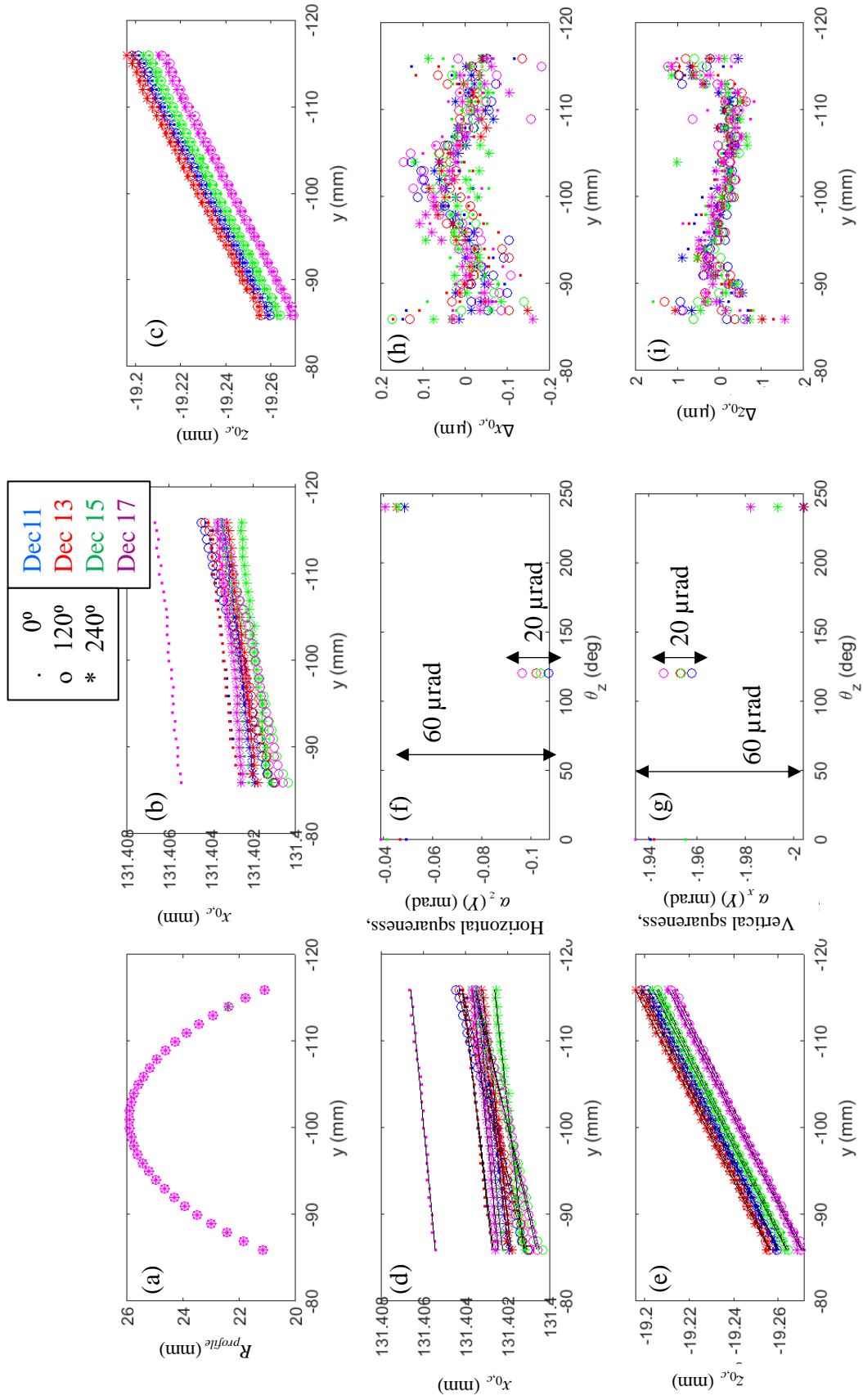


Figure 121: Estimation of Y carriage squareness using the measurement of the Silicon nitride sphere in three azimuth orientations on four different days; (a) Radius, (b) x origin, (c) z origin of each circular profile from the stripes measurement at three azimuth orientation estimated by fitting circles to it using least sum of squares method (d), (e) line fit to the x and z origin (f), (g) slope of the line fit representing the horizontal and vertical squareness of the Y (h), (i) after subtracting the line from the estimated x and z origin.

(b) Radial residue of individual profiles

To study the effect of side loading on the basis of individual profiles, radial distance of each datapoint (see Figure 117(a)) for a given profile is computed as

$$R_{computed} = \sqrt{(x - x_{0,c})^2 + (z - z_{0,c})^2}, \text{ where } x_{0,c} \text{ and } z_{0,c} \text{ are the origin of the profile, and } R_{profile}$$

is the radius of the profile estimated by fitting circles to it, as discussed in the beginning of the section 4.9.1.3. Radial residue of each profile is calculated as $\Delta R = R_{computed} - R_{profile}$. Figure 122(a to c) shows the radial residues at each azimuth orientation of measurement, and Figure 122(d) shows their average which removes the rotationally variant form error of the sphere with 100 nm PV.

(c) Importance of probe calibration after reinstalling the stylus

Whenever the stylus is attached to the X carriage of the profiler, it is necessary to recalibrate it using the calibration sphere shown in Figure 116(f) so that the correction performed by the software to account for arcuate motion of the stylus is valid. Failure to do so results in spurious measurements, for example, the radial residue of a spherical cap measurement is shown in Figure 123(b). Also, an S shaped radial residue is observed in each profile, for example, radial residue of the meridian profile shown in Figure 123(c) displays the S shaped curve indicating that the probe calibration is outdated. After recalibrating the probe, the computed radial residue does not contain the S shape as shown in Figure 123(d), and is less than 50 nm PV.

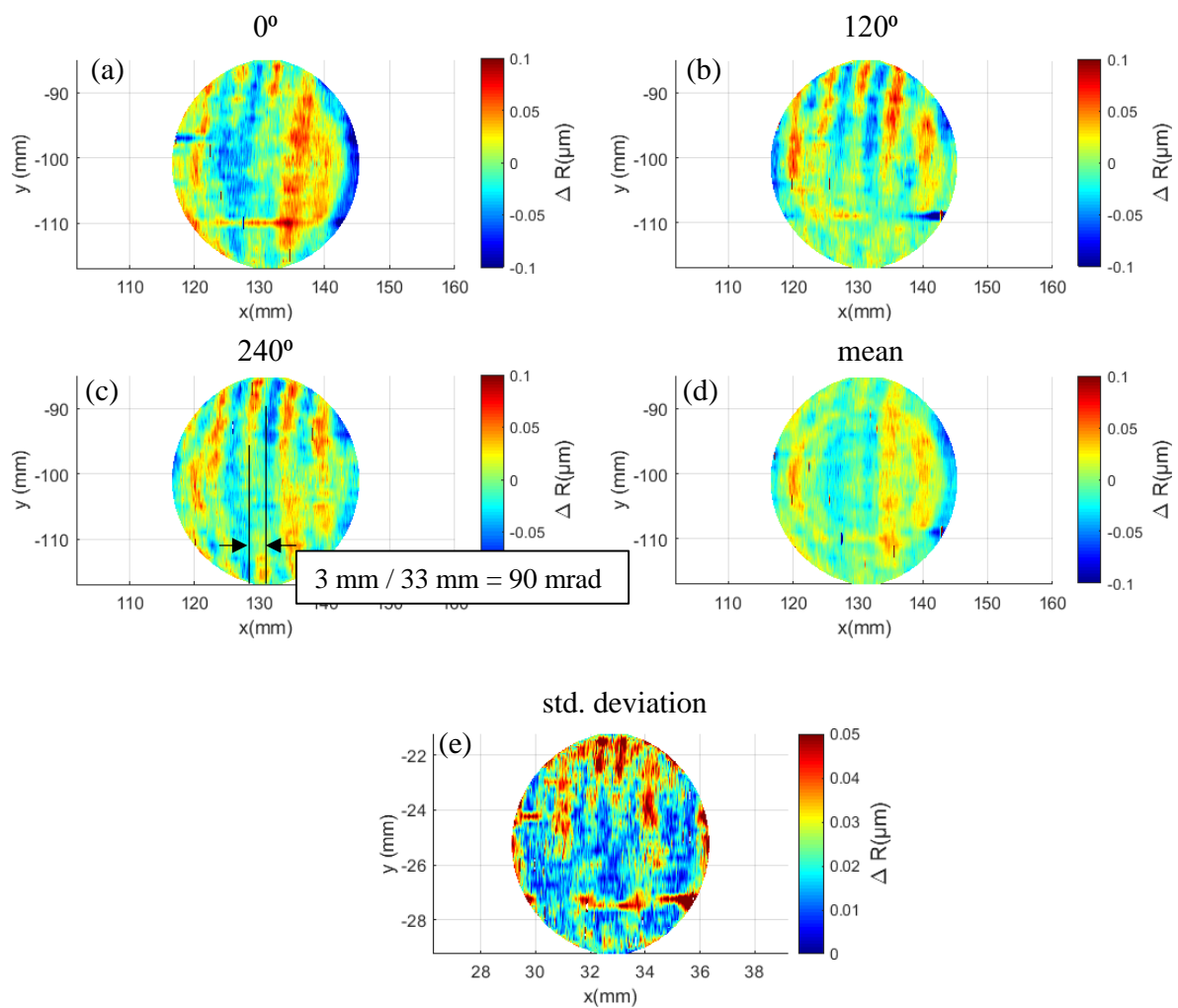


Figure 122: Radial residue of individual profiles of the measured spherical cap of the Silicon nitride sphere measured at (a) 0° (b) 120° (c) 240° (d) average, and (e) standard deviation.

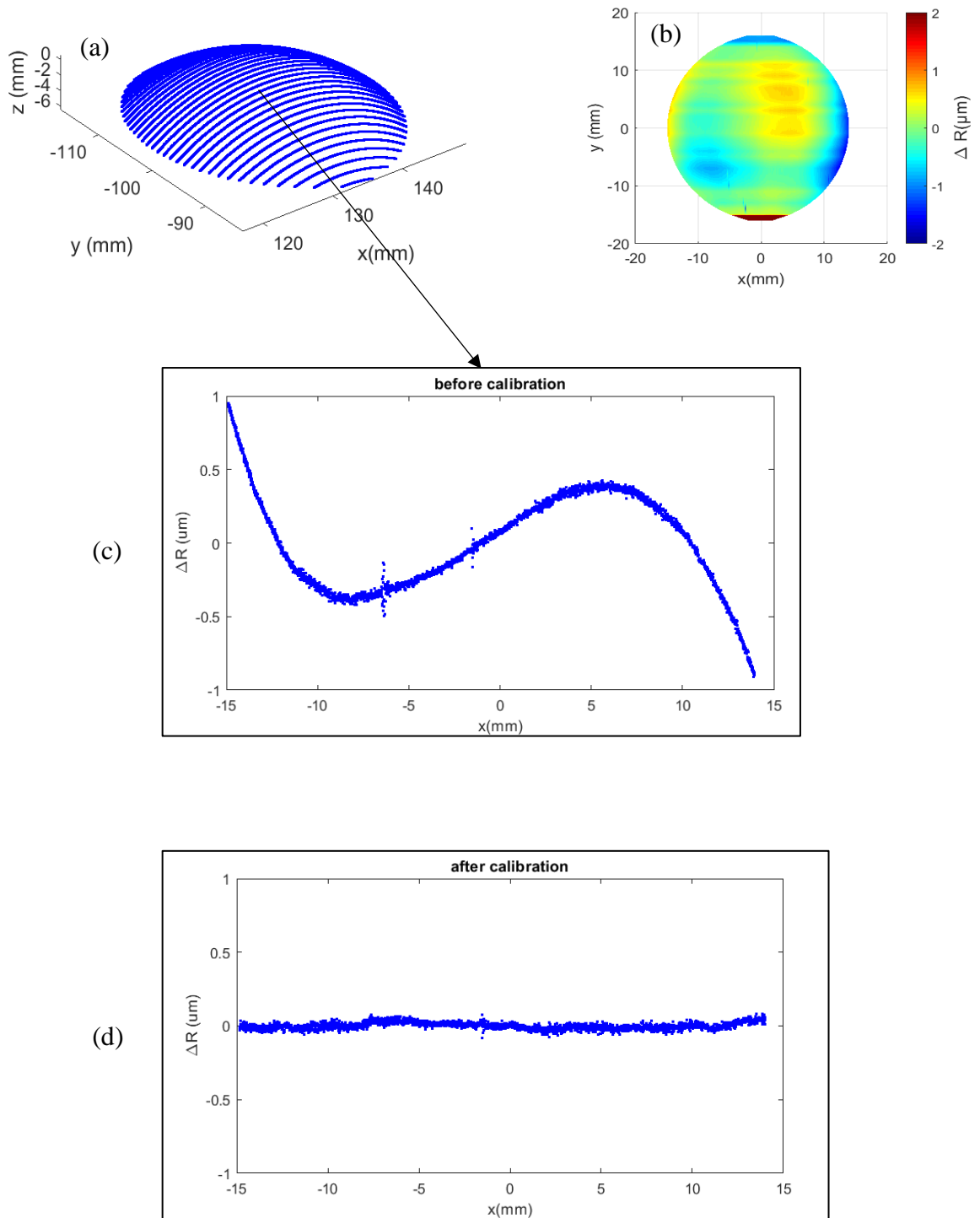


Figure 123: Radial residue of a meridian profile on the Silicon nitride sphere indicating the need for recalibrating the stylus; (a) Measurement of a spherical cap of the Silicon nitride sphere without recalibrating the probe (b) radial residue from the measurement (c) radial residue of the prime meridian profile (d) radial residue of the prime meridian profile after probe recalibration.

(d) Use of tie lines to compensate for thermal drift

As discussed in section 4.9.1.2 and shown in Figure 116(d), after making stripes on the Silicon nitride sphere, it was rotated azimuthally by 90° and five tie line profiles made. In principle, these can be used to compensate for the thermal drift during the measurements. Since tie lines also experience translation and angular errors due to the motion of Y carriage, the tie lines must be corrected for these errors before using all the five tie lines to correct for thermal drift as discussed in section 4.5.1. Therefore, only the middle tie line is used in this section to correct for the drift during stripe measurements. Figure 124(a) shows the circles fit to the stripes made on the spherical cap of the Silicon nitride sphere in blue, and the circle fit to the middle tie line in red, plotted in the measurement coordinates of the machine. Since the tie lines are profiled after rotating the sphere by 90° clockwise, to place the tie line in the part coordinates, it is rotated back counterclockwise by 90° and plotted in Figure 124 (b). To visualize this, a yellow dot is placed at the beginning of the tie line. Out of the 33 stripes the tie line goes across only 28 of them (intersecting points are indicated by red dots), as seen in Figure 124 (b and c), and these intersecting points are found within $0.5\ \mu\text{m}$ resolution in y axis and plotted in Figure 124(d). The difference between the z values of these datapoints are calculated and plotted in Figure 124(e). The stripes intersecting the tie line are corrected for this height difference and plotted in Figure 124(f and g), and it is noted that this difference does not only account for the thermal drift, but also for the vertical squareness, vertical straightness, and pitch error in the motion of the Y carriage while making those stripes. The radial residue of the datapoints shown in Figure 124(g) are computed and plotted in Figure 124(h and i) with a $4\ \mu\text{m}$ PV, compared to the $200\ \text{nm}$ PV residue that did not use the tie line for thermal drift compensation, see Figure 117(g). This larger residue could be due to the fact

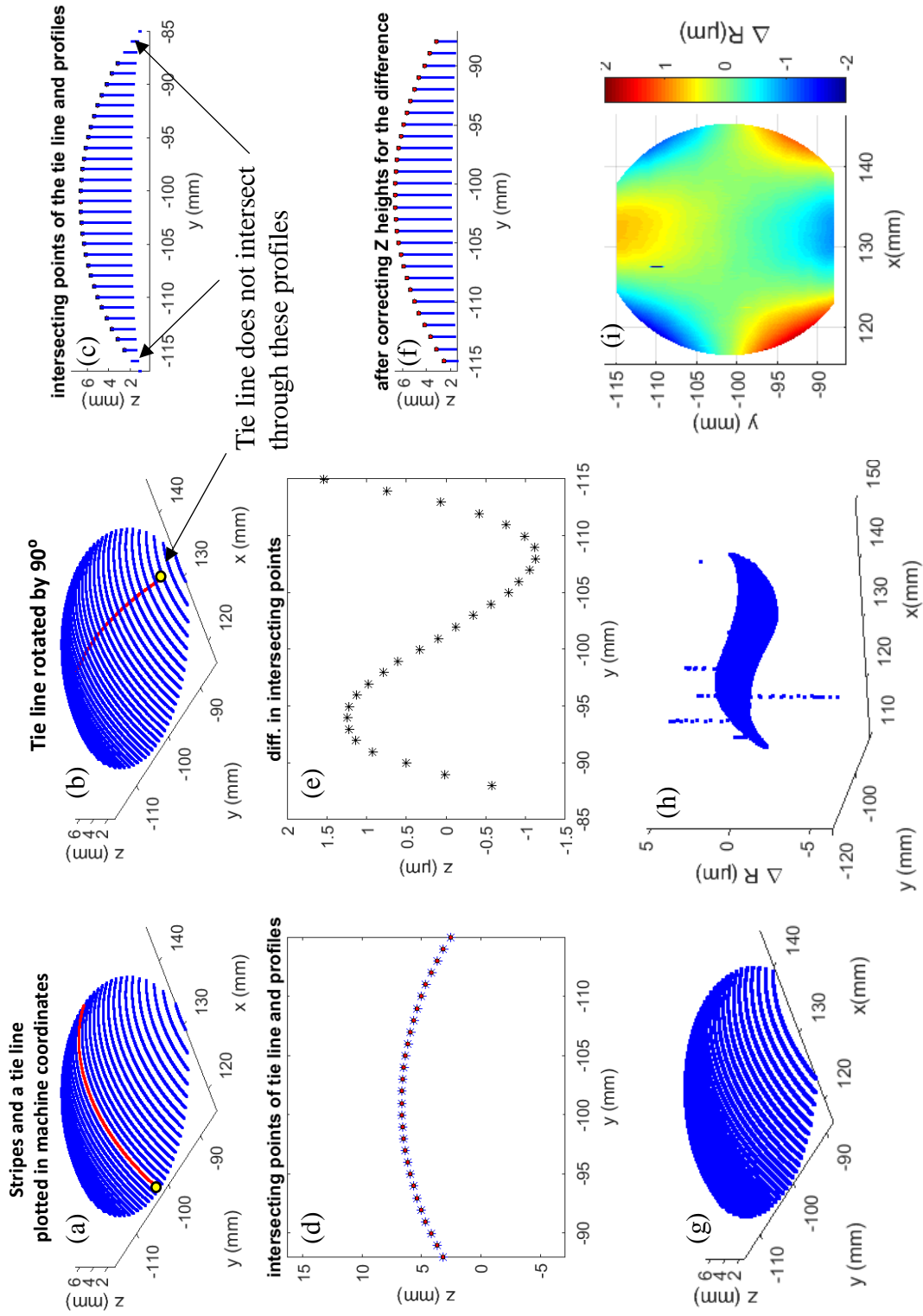


Figure 124: Using a tie line to correct for the Y carriage vertical squareness, and vertical straightness errors, and thermal drift; (a) stripes made on the Silicon nitride sphere and the middle tie line plotted in measurement coordinates (b) tie line rotated by 90° (c) Side view showing the stripes intersecting with the tie line (d) intersecting datapoints (e) difference in z

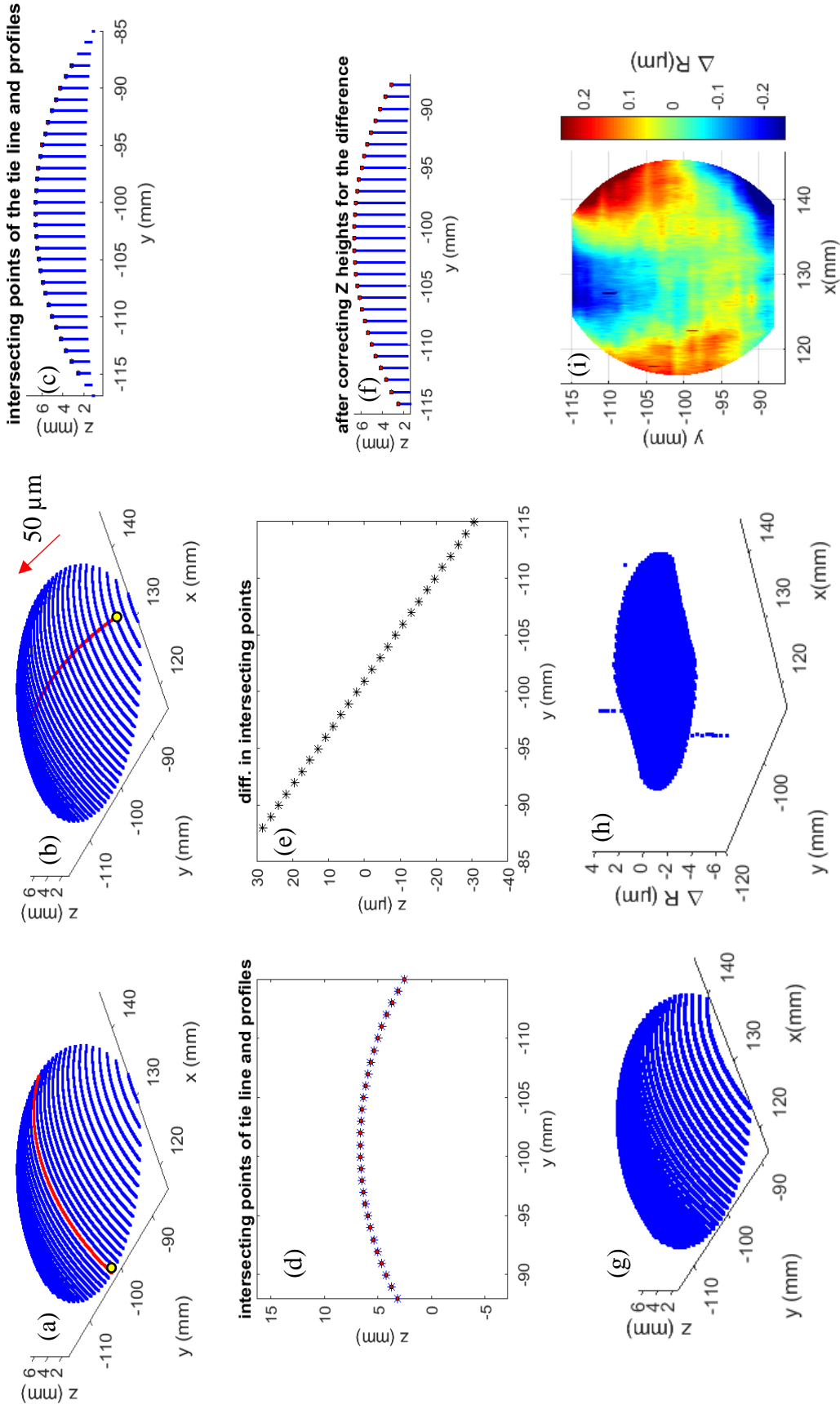


Figure 125: Using a tie line to correct for the Y carriage vertical squareness and vertical straightness errors, and thermal drift by iteratively translating the tie line along y axis; (a) stripes made on the Silicon nitride sphere and the middle tie line plotted in measurement coordinates, (b) tie line rotated by 90° and translated in y axis by $50 \mu\text{m}$, (c) Side view showing the stripes intersecting with the tie line. (d) intersecting datapoints, (e) difference in z height between the intersecting datapoints, (f) Side view: Stripes

that the rotary carriage might tilt and offset the Silicon Nitride sphere radially and axially causing the tie line not to be ‘perfectly’ orthogonal to the stripes. To evaluate the effect of rotary stage motions, the tie line shown in Figure 125(b) is iteratively translated in y axis by $50\text{ }\mu\text{m}$, and following the above mentioned procedure, a radial residue down to 500 nm PV is obtained, see Figure 125(i).

From the manufacturer’s specification of the rotary carriage, its radial error is $\delta_x(C) = 0.5\text{ }\mu\text{m}$, and tilt error is $\varepsilon_y(C) = 10\text{ }\mu\text{rad}$. For this tilt, Silicon nitride sphere sitting $d = 0.15\text{ m}$ above the rotary stage would have only offsetted by $\Delta x = 1.5\text{ }\mu\text{m}$, see Figure 126. Therefore, it is not clear why the tie line must be translated by $50\text{ }\mu\text{m}$ to obtain a minimum value for the radial residue. It is also possible that the tie line was not profiled through the sphere meridian.

4.9.1.4 Results – Spokes

As shown in Figure 116(e), the Silicon nitride sphere was rotated clockwise using the rotary carriage, and eight Spoke profiles were made, and these are plotted in Figure 127(a) using two-dimensional cartesian coordinates (x, z) . Since these profiles are made near the meridian of the sphere, the expected effect of side loading is minimal. Since for each spoke

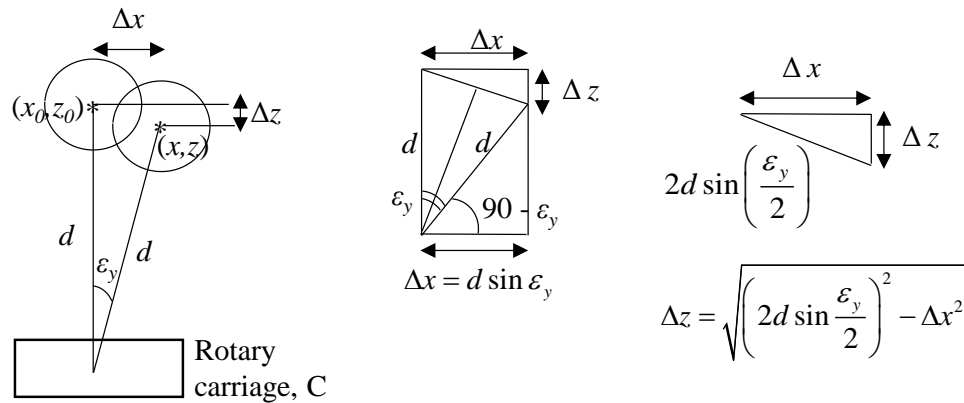


Figure 126: Schematic showing the expected offset of the sphere due to the tilt of the rotary carriage

only the azimuth angular orientation of the Silicon nitride sphere is reported by the C carriage, data must be rotated around the z axis in steps of 22.5° so that corresponding y values could be computed to represent the data in three dimensional cartesian coordinates (x, y, z) as plotted in Figure 127(e), with the procedure for this computation being as follows. Circles are fit to each profile shown in Figure 127(a) using the least sum of squares method shown in equation (14) and the estimated origin of each profile, x_0 and z_0 are shown in Figure 127(b and c). Using x_0 and z_0 values to rotate the profiles around the z axis resulted in spurious radial residues estimated to be about $2 \mu\text{m PV}$, see Figure 127(f). Therefore, the maximum z values of each profile (z_{max}) is used as a way of rotating the profiles, which were obtained after filtering each profile using a ten point moving average method, and the ‘max’ function in Matlab, see Figure 127(d). Using the x_0 and z_{max} values, a counterclockwise rotation matrix given in the equation below, and is used to obtain the y values to generate the spokes plotted in Figure 128(a).

$$\begin{bmatrix} x' \\ y' \\ z' \end{bmatrix} = \begin{bmatrix} \cos \theta & -\sin \theta & 0 \\ \sin \theta & \cos \theta & 0 \\ 0 & 0 & 1 \end{bmatrix} \begin{bmatrix} x - x_0 \\ 0 \\ z - z_0 \end{bmatrix}$$

A sphere is fit to this data using a least squares method as shown in equation (15) and the radial residues are plotted in Figure 128(b). For this method there is a 300 nm PV radial residue which is comparable to the result obtained from stripes method of measurement, which is prone to side loading, see Figure 117(g).

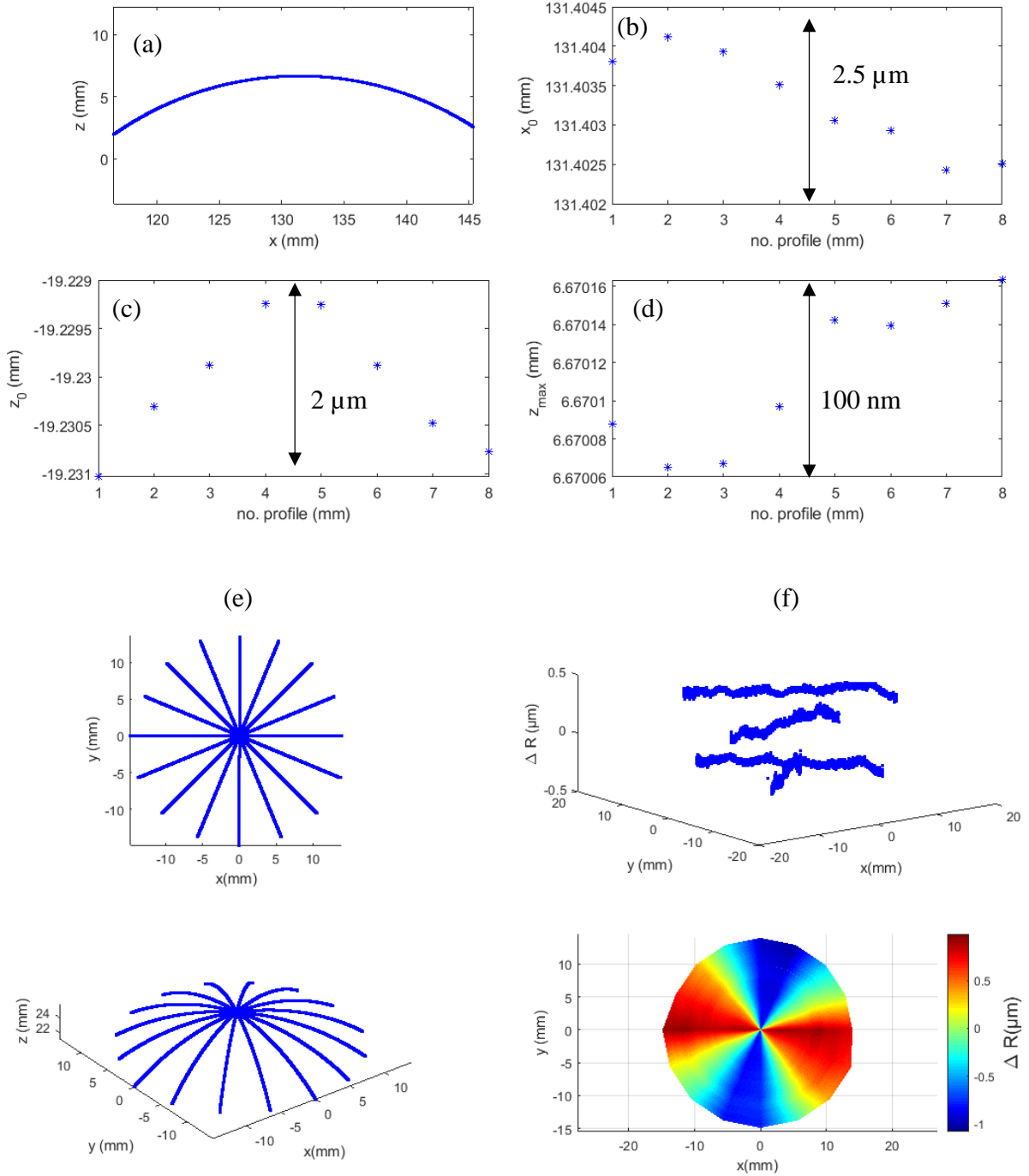


Figure 127: Results of the Silicon nitride sphere measured using the spokes approach; (a) Measurement data of 8 spokes profiles, (b,c) origin of the profiles estimated using the least sum of squares, (d) maximum z value of each profile (e) Spokes obtained using the rotation matrix (f) radial residue obtained from fitting a sphere to the spokes and subtracting the estimated radius.

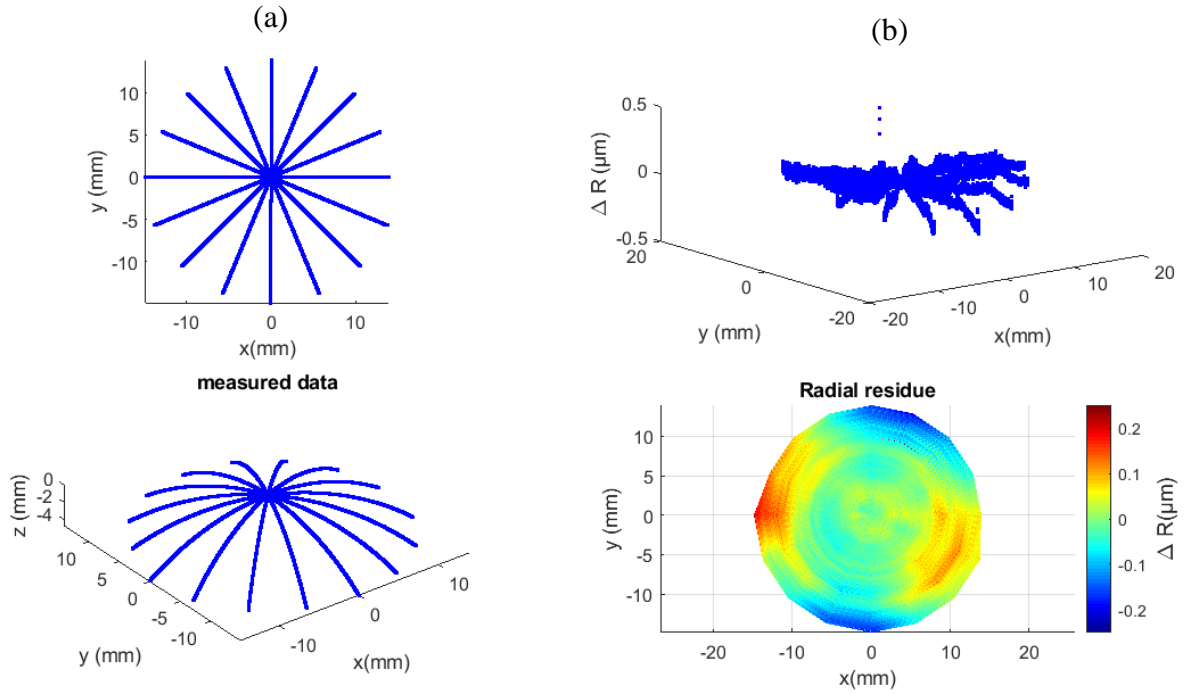


Figure 128: Radial residue estimated in the spokes approach of profiling; (a) Spokes obtained using the rotation matrix (b) radial residue obtained from fitting a sphere to the spokes and subtracting the estimated radius.

To evaluate the repeatability in the measurements, spokes measurements were made on the sphere over a period of three days is used to compute the radial residue, the data from these measurements is plotted in Figure 129(e to h). Estimated origin (x_0 , z_0) and maximum z values (z_{max}) on each day of measurement is plotted in Figure 129(b to d). Average of the computed radial residues with a 300 nm PV, standard deviation and the range of variation are shown in Figure 130(a to c) respectively.

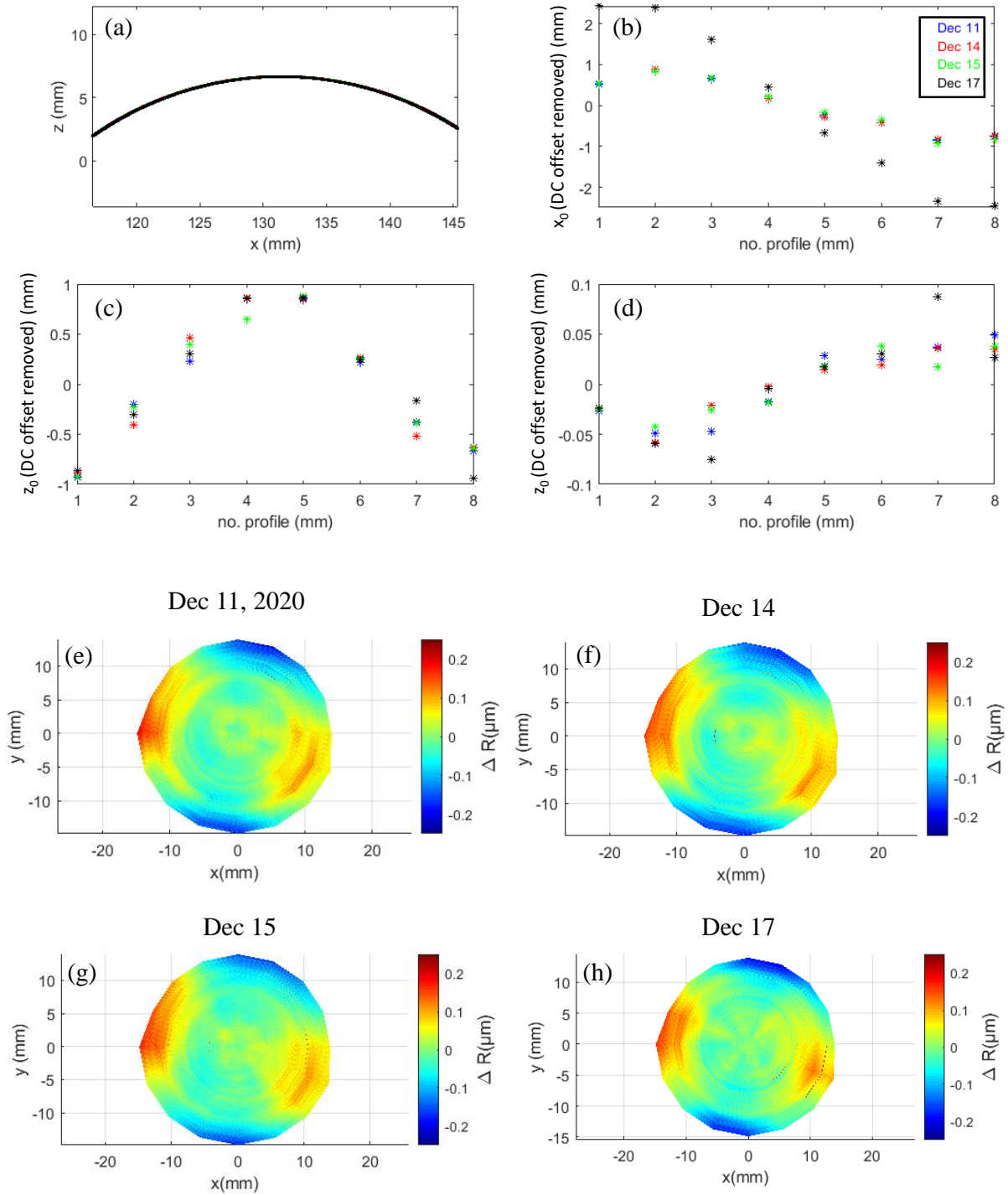


Figure 129: Radial residue calculated from the spokes measurements made on the Silicon nitride sphere on four different days (a) Measurement data of 8 spokes profiles made on each day, (b,c) origin of the profiles estimated using the least sum of squares, (d) maximum z value of each profile, (e to h) Radial residues computed from each day of measurement.

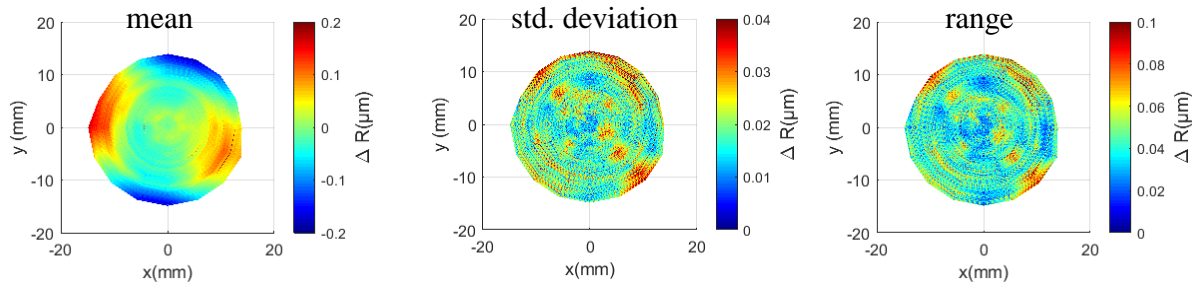


Figure 130: Results of the spokes measurement over four days; (a) Mean of radial residues computed from four days of measurement, (b) standard deviation, and (c) range of variation.

4.9.2 Borosilicate concave mirrors

Two concave spherical mirrors (Edmund optics, stock # 32-826) of surface slope much smaller than the previously measured sphere are measured using the profiler in this section. These Borofloat® mirrors are $D = 3$ in. Dia. (~ 75 mm) with an effective focal length, $EFL = 152.4$ mm, and the radius of curvature $R = 2EFL = 305$ mm. Sag of these mirrors is given by

$$\text{sag} = R - \sqrt{R^2 - \left(\frac{D}{2}\right)^2} = 2.4 \text{ mm.}$$

These mirrors are comparable in dimensions to a freeform mirror intended to be measured and qualified using our profilometer system ($D = 92$ mm, sag = 3.55 mm, $R = 300$ mm). The freeform mirror forms a tertiary mirror in an optical telescope system being built at the Center for Freeform optics, USA. These mirrors are measured using an interferometer to compare it with the measurements performed on the profilometer. The interferograms captured using a Fizeau interferometer and a transmission sphere is shown in Figure 131 (b and c). Details of the qualification of transmission sphere using a ‘Random ball test’, and the measurements of the concave mirrors are given in Appendix C.2.9.

4.9.2.1 Simulation- Stripes and spokes

To know the minimum number of stripes or spokes required in the profilometer measurements that enables to obtain the Zernike polynomial coefficients values comparable with the values obtained from the interferometry measurement, a simulation is performed. A 36 term Zernike polynomial is fit to the interferometric measurement of concave mirror 1 shown in Figure 131 (b), see Figure 132 (a). From the resulted Zernike coefficients, values that

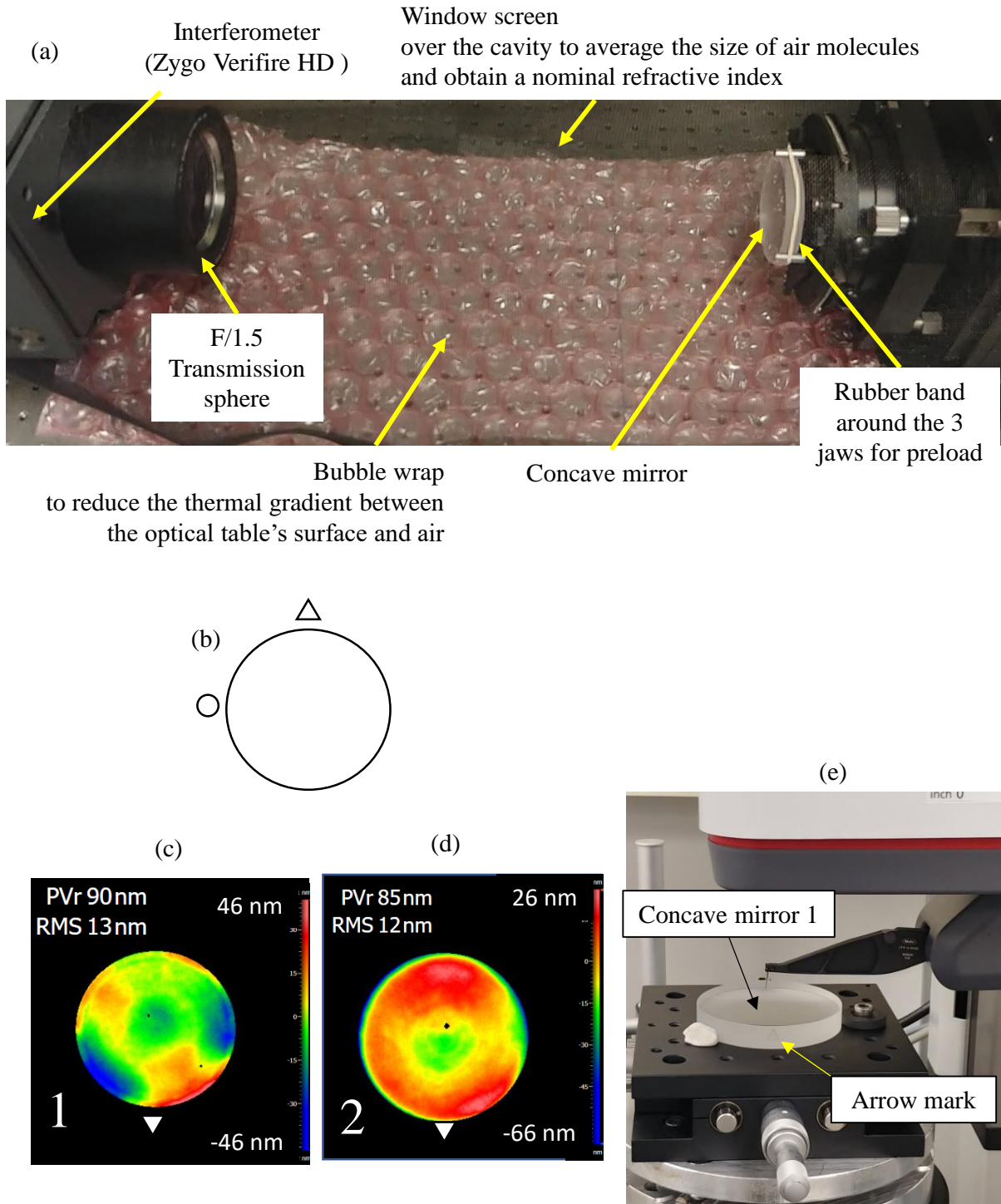


Figure 131: Interferometric measurement of the concave reference surfaces; (a) Fizeau interferometry experimental facility measuring the concave mirror 1 (b) orientation of the concave mirrors during the measurement marked by an arrow mark on the top edge (c) interferogram of concave mirror 1 (d) interferogram of concave mirror 2 (e) concave mirror being measured using the profilometer.

Table 3: Zernike coefficients of values greater than 4 nm for concave mirror 1

Zernike term	formula	PV normalized Zernike coefficient values (nm)
Horizontal tilt	$\rho^2 \cos 2\theta$	-12
Vertical tilt	$\rho^2 \sin 2\theta$	-19
Horizontal coma	$(-2\rho+3\rho^3) \cos \theta$	5
Vertical coma	$(-2\rho+3\rho^3) \sin \theta$	4
Oblique trefoil	$\rho^3 \cos 3\theta$	-18
Vertical trefoil	$\rho^3 \sin 3\theta$	8
Secondary vertical coma	$(3\rho-12\rho^3+10\rho^5) \sin \theta$	-6
Secondary spherical	$-1+12\rho^2-30\rho^4+20\rho^6$	9

are greater than 4 nm are chosen (see Table 3) and a surface is simulated and plotted in Figure 132 (b). Using this simulated surface, z values corresponding to the given x and y values of stripes and spokes are determined, see Figure 132(c and d). A thirty six term Zernike polynomial was fit to this data to obtain the coefficients and compared with the values shown in Table 3 and the differences were indistinguishable for more than three stripes and three spokes. However, during the profilometer measurements, 73 stripes and 8 spokes were made to obtain a ‘dense’ dataset and results from these experiments are discussed in sections 4.9.2.2 and 4.9.2.3 respectively.

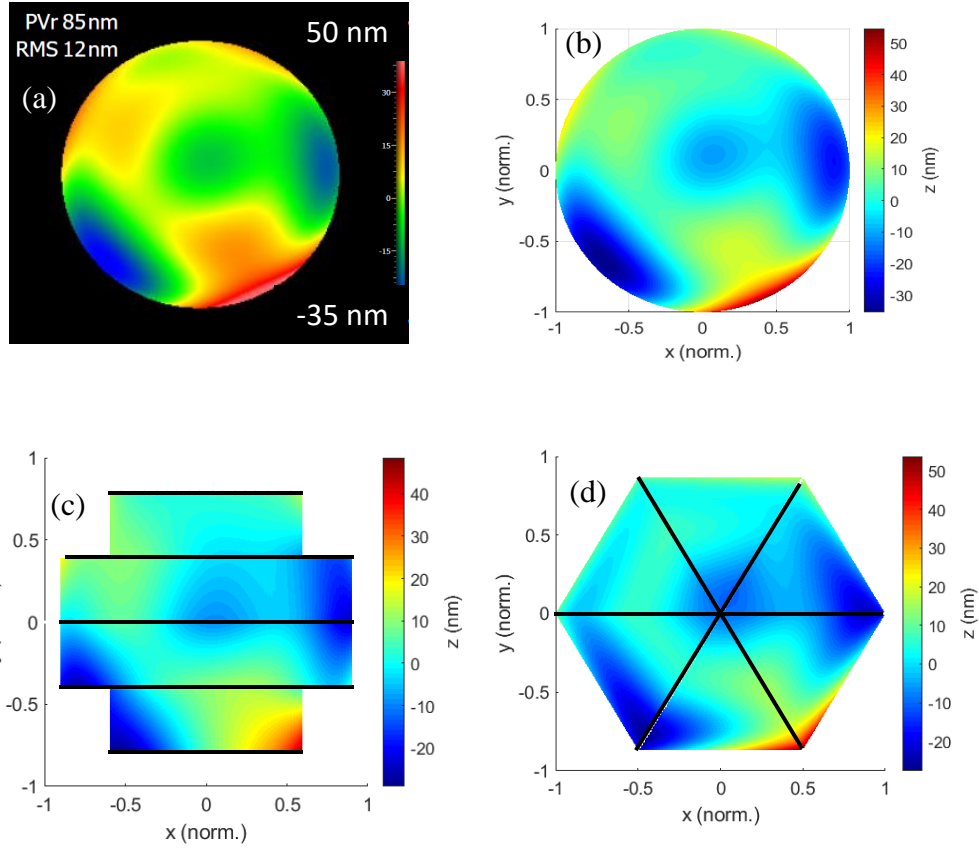


Figure 132: Zernike polynomial fit to the interferometric measurements of the concave reference surfaces; (a) A 36 term Zernike fit to the interferogram measurement of concave mirror 1 (b) Simulated surface using the Zernike terms greater than 4 nm (c) minimum number of stripes and (d) spokes enables to retrieve the values of the Zernike terms.

4.9.2.2 Stripes measurements

Figure 131(e) shows the profilometer making 73 lines to cover the aperture of the concave surface, and this process was repeated 3 times. The raw measurement data of concave mirrors 1 and 2 are given in Figure 133(a and c) respectively. A sphere is fit to these data using the least sum of squares method given by equation (15) to estimate the origin (x_0, y_0, z_0) and the radius (R_{sphere}) . From which the z height for a given x and y values are calculated (z_{fit}) using the following equation, and subtracted from the reported z values and plotted in Figure 133(b and d) for concave mirrors 1 and 2 respectively.

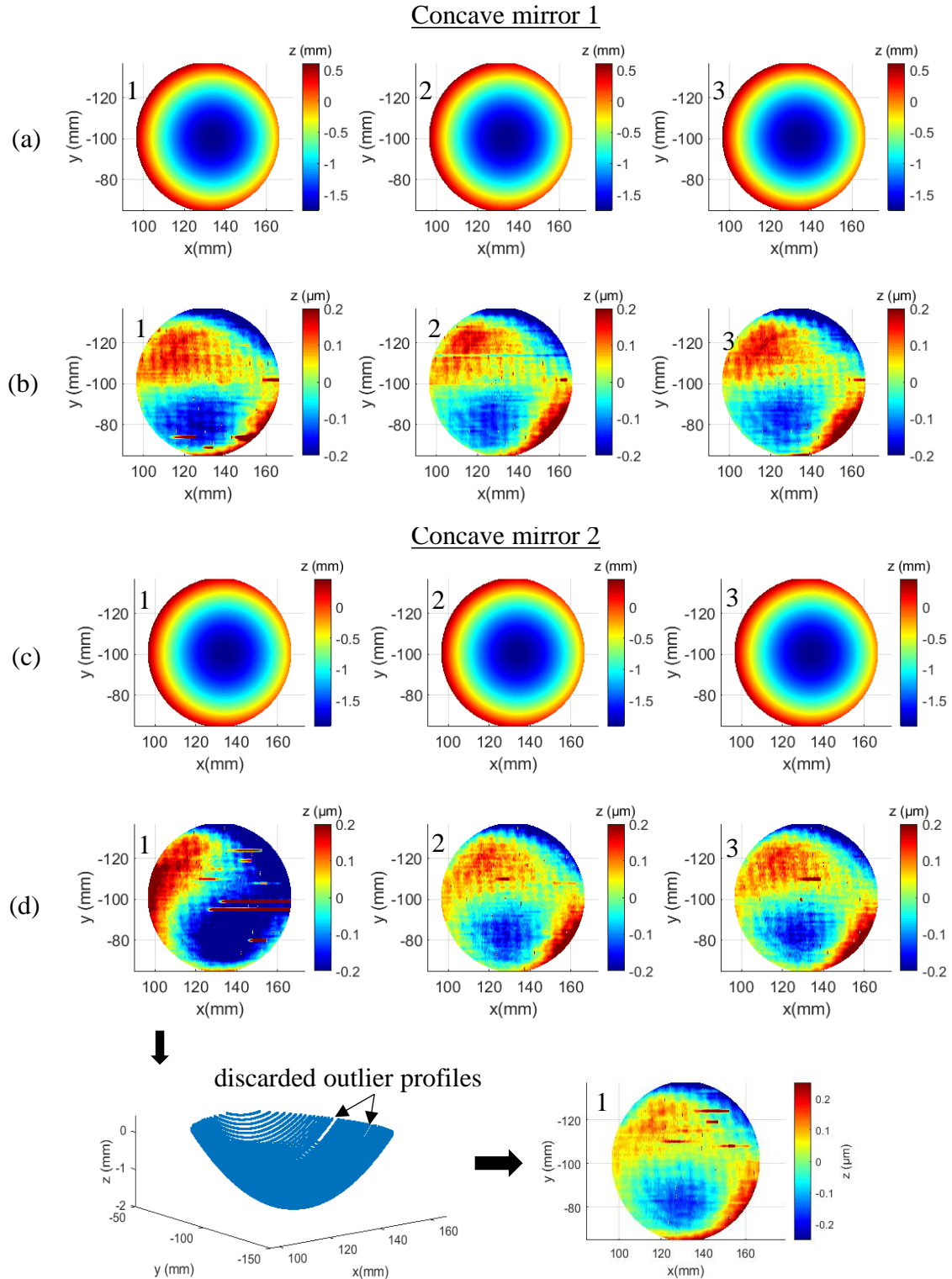


Figure 133: Profilometer measurement of concave mirrors 1 and 2 (a) Surface plot from profilometer measurement of concave mirror 1 (b) Sphere removed from the data using Least sum of squares method (c) Measurement of concave mirror 2 (d) Sphere removed data, outlier profiles were discarded for the first measurement.

$$z_{fit} = \sqrt{R_{sphere}^2 - (x - x_0)^2 - (y - y_0)^2} + z_0$$

$$\Delta z = z - z_{fit}$$

It is noted that due to the presence of the outliers in the recorded profile during the first measurement of concave mirror 1, the sphere removed data shown in Figure 133 (d (1)) looks different than the next two repeats. Therefore, the profiles containing the outliers were discarded and then a sphere is removed from this data and plotted in the bottom right. Data shown in Figure 133(b and d) contains the effect of horizontal and vertical squareness of the Y carriage $(\alpha_z(Y), \alpha_x(Y))$. The origin of each profile made on the concave mirror (x_0, z_0) is found using a least sum of squares circle fit method (discussed in the beginning of section 4.9.1.3) given by equation (14), and plotted Figure 134 (a and b). Lines are fit to these origins, and their slopes represent the squareness of Y carriage and are listed below in Figure 134 (a and b). These values are comparable to the estimated squareness from the measurements of a Silicon nitride sphere, see Figure 121(f and g). The lines are subtracted from the data shown in Figure 134 (a and b) and the residues are plotted in Figure 134 (c and d) where the deviations of the first set of measurement made on both the concave mirrors shows a downward trend even after subtracting the line indicating potential outliers. This downward trend of the line removed origins x_0 and z_0 being $2 \mu\text{m}$ and $100 \mu\text{m}$ respectively.

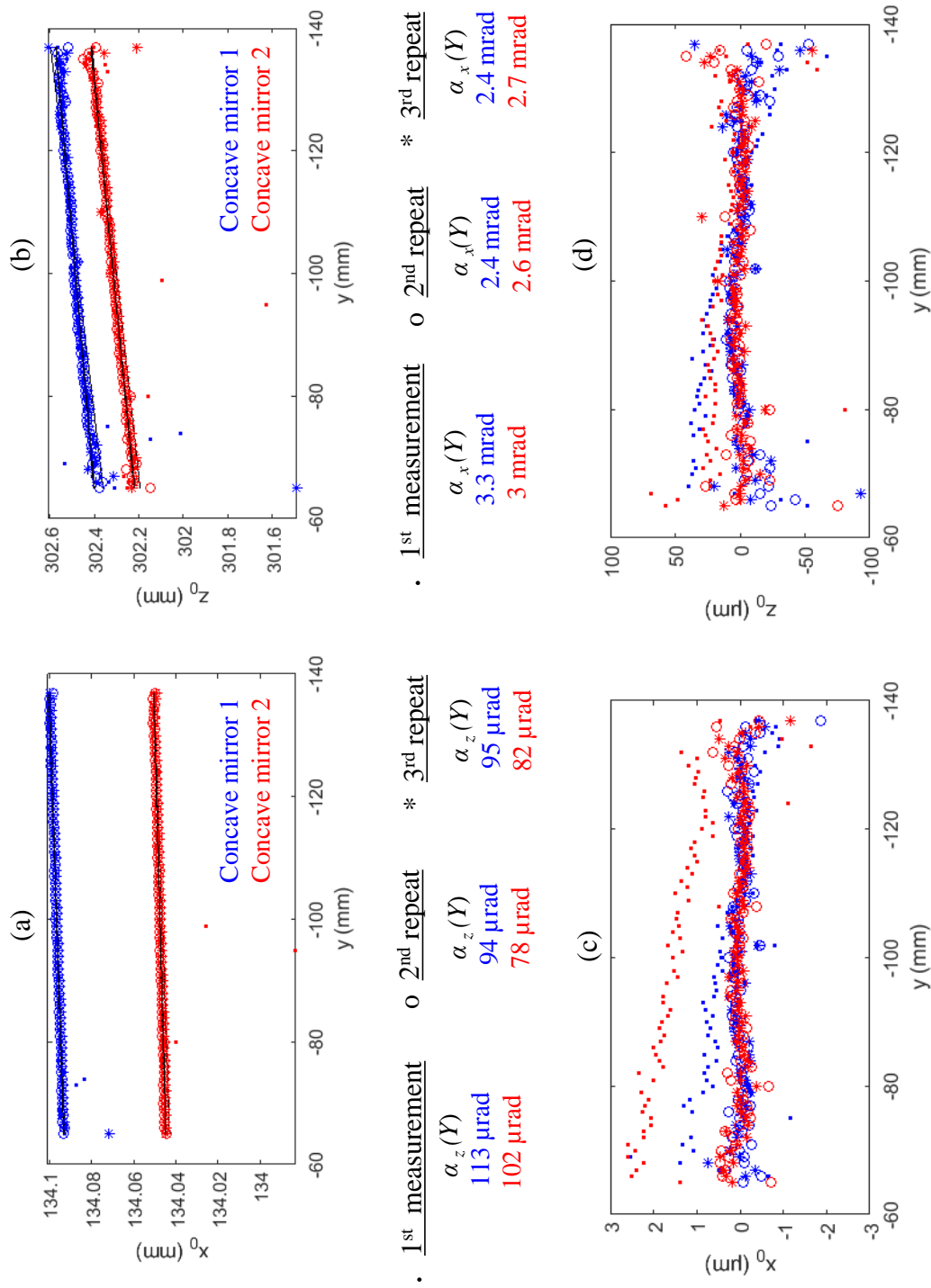


Figure 134: Estimation of squareness of the Y carriage from the profilometer measurements of the concave surfaces; (a) x origin of profiles made on concave mirror 1 and 2 estimated from a least sum of squares fit and a line fit to the estimated origins (b) z origin estimates and line fits (c) after subtracting the line from the x origins (d) after subtracting the line from the z origins

Evaluation of corrections for X and Y carriage errors

This section discusses the effort to remove the errors of the motion in the X and Y carriages from the measurements of the concave mirrors. After subtracting these errors, a residue of 200 nm PV shown in Figure 135(d) and Figure 136(d) from the measurements of concave mirrors 1 and 2 respectively primarily indicates the uncertainty in the estimated errors from the carriages and the thermal drift in the system.

(a) Horizontal and vertical squareness of Y carriage $(\alpha_z(Y), \alpha_x(Y))$

The estimated origin (x_0, z_0) of each profiles of the 3rd repeat shown in Figure 133(a) were subtracted from their measured x and z values, thereby correcting for the squareness error of the Y carriage. Then equation (15) is used to fit a sphere to this data, from which the z height for a given x and y values are estimated (z_{fit}) , which is later subtracted from the reported z values and plotted in Figure 135(b) with a 250 nm PV.

(b) Vertical errors of Y and X carriage $(\delta_z(Y), \delta_z(X))$

Vertical error of Y carriage estimated from the measurements of Zerodur flat shown in Figure 95(f) is subtracted from Figure 135(b) and plotted in Figure 135(c). Vertical error of X carriage estimated from the piece wise measurements of Zerodur flat shown in Figure 96(f) is subtracted from Figure 135(c) and plotted in Figure 135(d) with 200 nm PV, which is larger than the 90 nm PV estimated from the interferometric measurement shown in Figure 131 (b)

Above mentioned procedure is also followed for the 3rd repeat of the measurement of concave mirror 2 and plotted in Figure 136, with a similar 200 nm PV result. The procedure is also given as a flowchart in Figure 137.

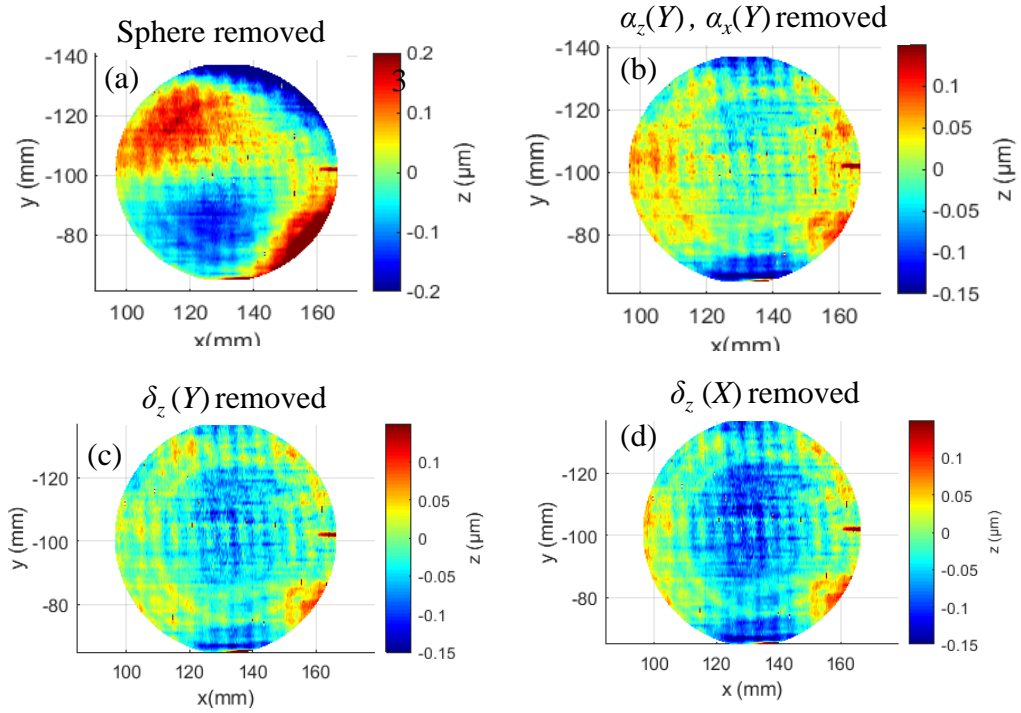


Figure 135: Profilometer measurement of Concave mirror 1 using the stripe approach; (a) after removing a sphere (b) after removing squareness of Y carriage (c) after removing vertical straightness of Y carriage (d) after removing squareness of X carriage.

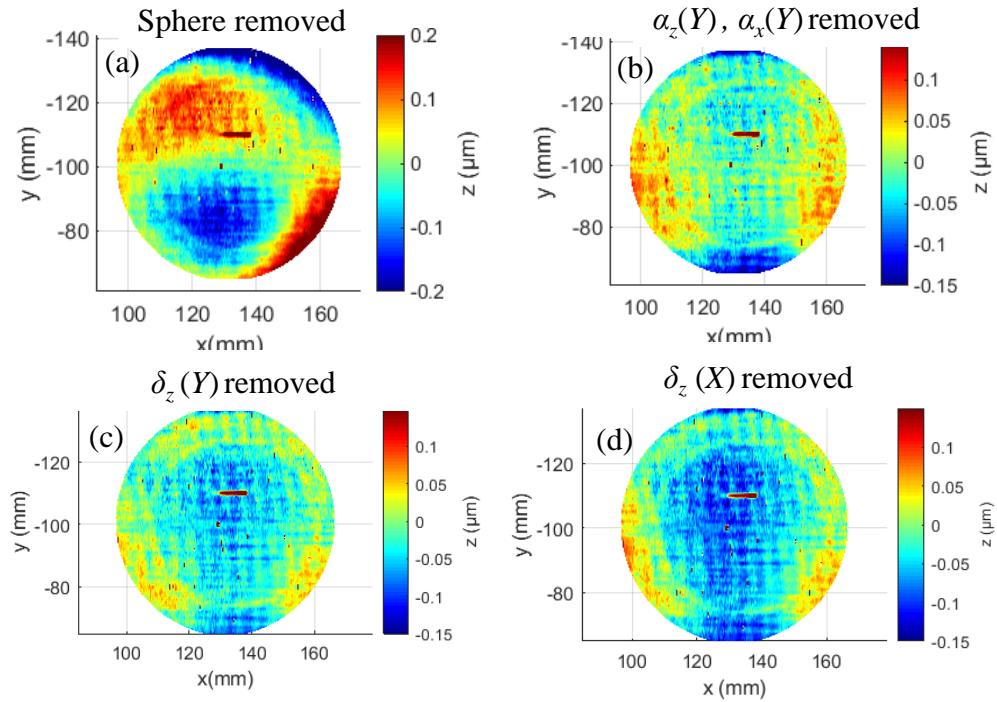


Figure 136: Profilometer measurement of Concave mirror 2 using the stripes approach.

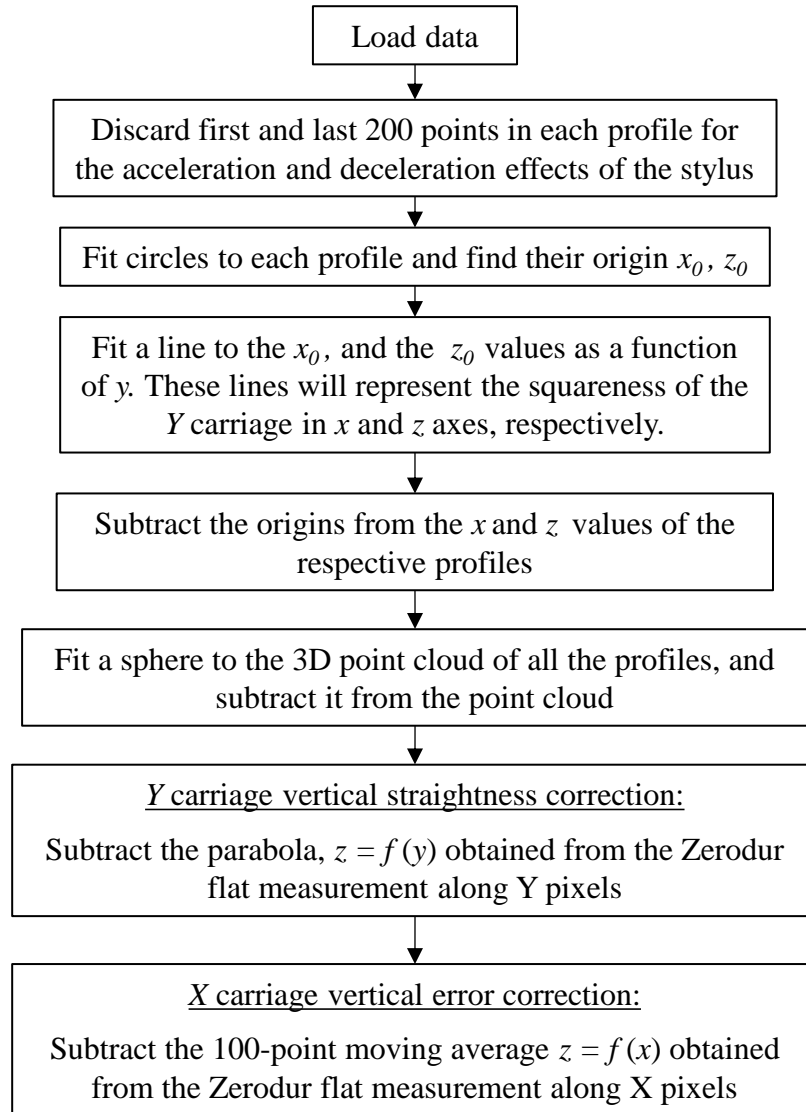


Figure 137: Flowchart showing the procedure to use the raw measurement data of a concave mirror and correct for the carriage errors.

4.9.2.3 Spokes measurements

Two dimensional measurement data (x,z) of the Concave mirror 1 measurement using spokes manner is rotated azimuthally by following the procedure discussed in section 4.9.1.4 and the measured data from these experiments are plotted in Figure 138(a). A sphere is removed using the least sum of squares method and plotted in Figure 138(b). Vertical error of X carriage shown in Figure 138(c) is subtracted from this and plotted in Figure 138(d) with 150 nm PV. This same procedure and analysis is used for the 3rd repeat of the measurement of concave mirror 2 and the results plotted in Figure 139.

4.9.2.4 Profilograms corrected for carriage errors in comparison with interferograms

Figure 140(b and c) shows the profilograms of concave mirror 1 measured by stripes and spokes method and corrected for errors of X and Y carriages in comparison with the interferometer measurement shown in Figure 140(a). Similar results for concave mirror 2 is shown in Figure 140(d to e). From these results it can be seen that stripes method of measurement after correcting for carriage errors look similar for two different optics, see Figure 140(b and e). This indicates that the uncertainty in the machine errors majorly contribute to the resulted profilograms with a 200 nm PV. Whereas there is a noticeable difference in spokes method of measurement of the concave mirrors Figure 140(c and f).

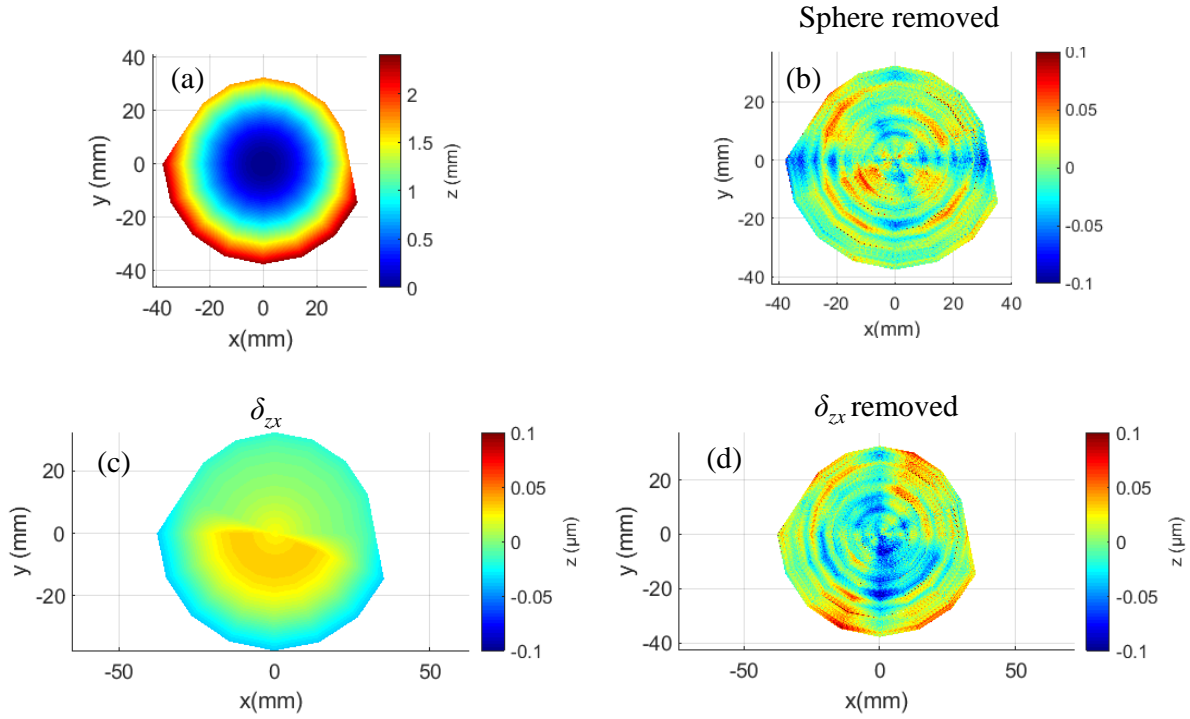


Figure 138: Profilometer measurement of the Concave mirror 1 using the spokes approach; (a) Spokes measurement of concave mirror 1 (b) after subtracting a sphere (c) vertical error of X carriage for the measurement aperture (d) after removing the vertical error.

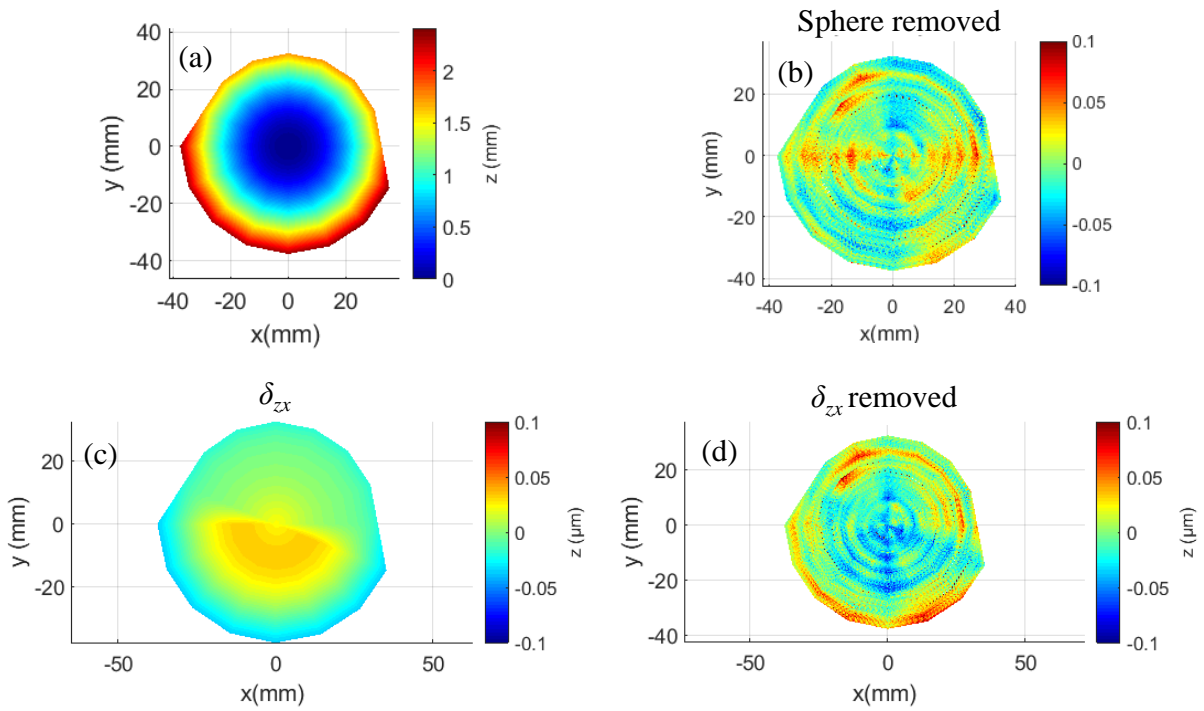


Figure 139: Profilometer measurement of the Concave mirror 2 using the spokes approach

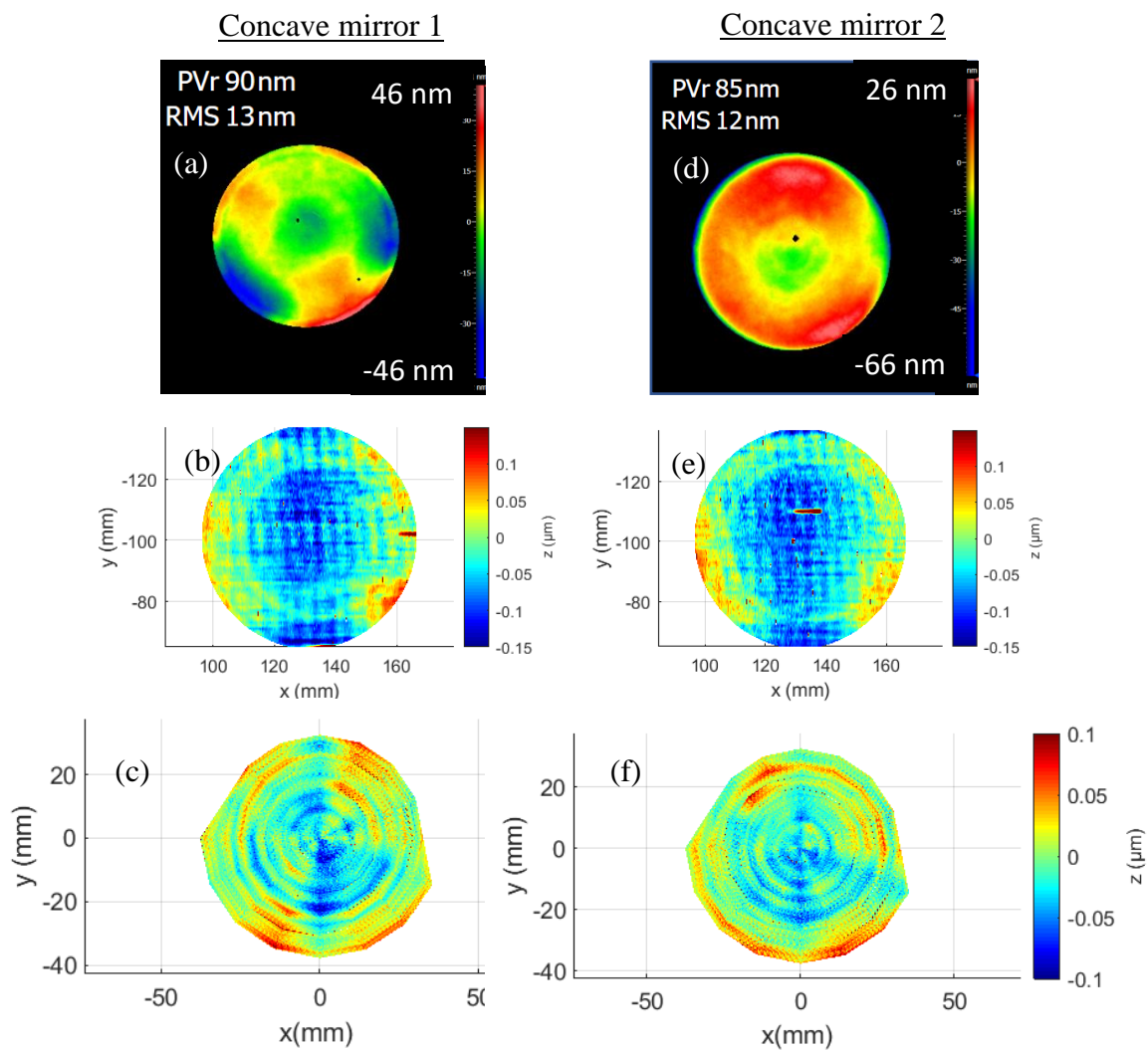


Figure 140: Comparison of the profilograms of the concave mirror measurements with the interferograms from PSI; (a) interferogram of concave mirror 1 (b) profilograms by stripes method after correcting for carriage errors (c)) profilograms by spokes method after correcting for carriage errors (d to f) same for concave mirror 2

4.10 Uncertainty evaluation using Monte Carlo simulation

In this section simulations are performed with the inputs being the uncertainty in the measured carriage errors discussed in the earlier sections, and the manufacturer specifications for the errors that were not quantified. Simulations were performed for both stripes and spokes methods of measurement.

4.10.1 Monte Carlo – stripes

A Monte Carlo simulation is performed to evaluate the uncertainty in areal form measurement of a perfect optical flat shown in Figure 143(a). The measurement is performed by making stripes on the surface to cover its 100 mm aperture. Even though the profilometer system is capable of performing areal measurements of 200 mm aperture, the uncertainty evaluation is limited to 100 mm. This is because the areal measurements performed to measure the *Y* carriage errors used a Zerodur flat of 100 mm diameter, therefore our knowledge of carriage errors is limited to this range, see Figure 141(d to g).

Figure 141(a) shows the positioning accuracy of the *X* carriage estimated by plotting the difference in the reported *X* values from one of the flat measurements and is ± 25 nm. The ideal sample spacing of the reported *X* values is 5 μm . It is true that the in between each profile, the thermal drift would influence the repeatability in the *X* position for subsequent profiles. Since before any areal form measurements, the machine is warmed up by running the stylus in air to reach thermal equilibrium, the thermal drift effect is not considered. The vertical error of the *X* carriage is estimated by measuring the flat in a piece wise manner, and is shown in Figure 141(b), and for the uncertainty evaluation range of mid 100 mm, it is shown in Figure 141(c). The residue from the 5th order polynomial fit is ± 12.5 nm, and is chosen as the uncertainty in the estimation of vertical error of the *X* carriage. It is noted that this vertical error is a

combination of vertical straightness and the pitch error of the X carriage and they cannot be separated from a flat measurement.

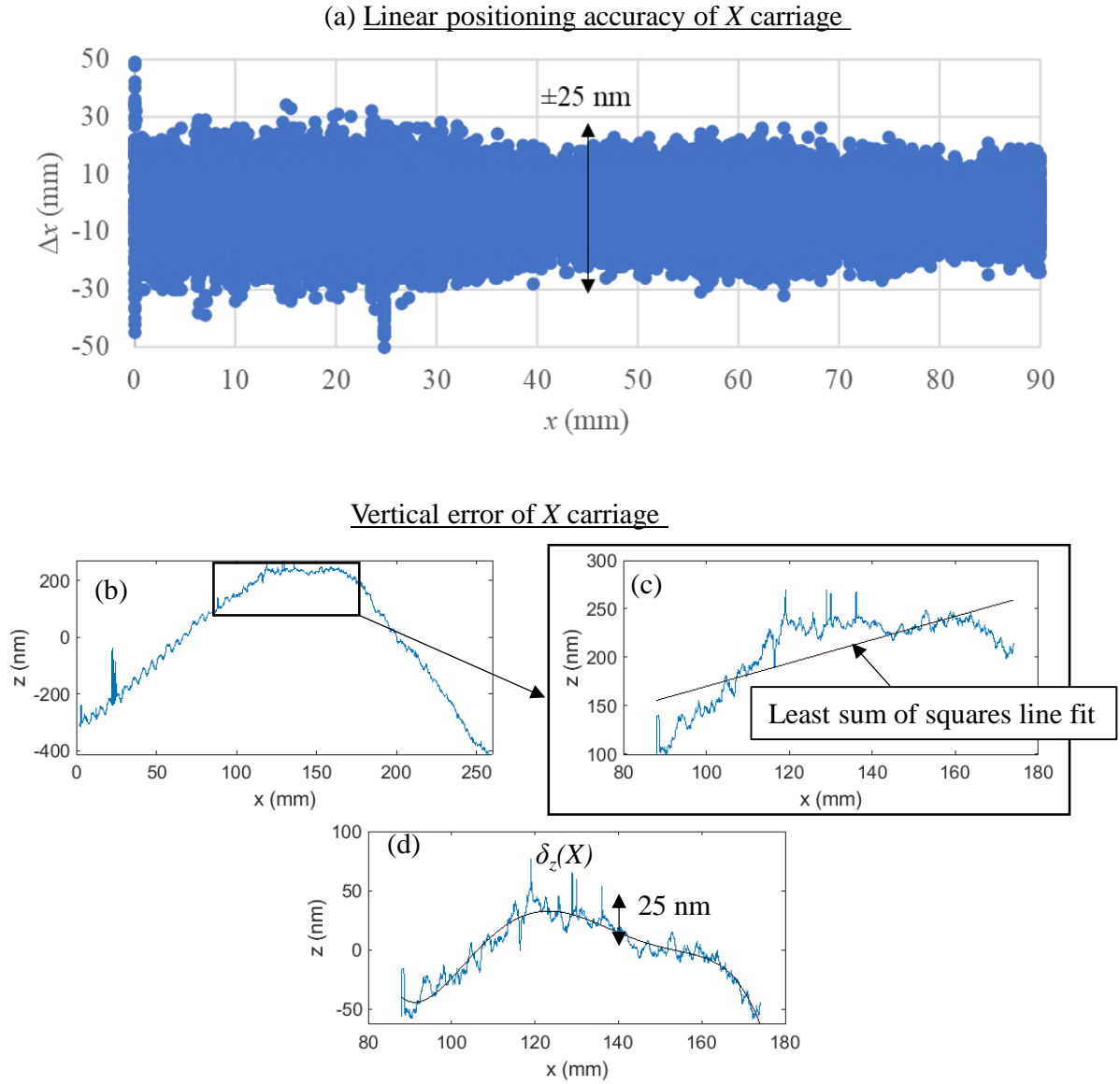


Figure 141: X carriage errors; (a) linear positioning accuracy of X carriage estimated by plotting the differences in the reported x value from a measurement made on an optical flat (b to d) Vertical straightness error of X carriage estimated using a piece wise profile measurement of the flat stitched together

Figure 142(a) shows the areal measurement of the flat using the profiler ('profilogram'). z height of a profile along its y axis shown in Figure 142(b) represents the vertical straightness of Y carriage. It is noted that this z height variation would also be influenced by the pitch error of Y carriage, but very minimal (in picometers). Figure 142(d) shows the roll error of Y carriage estimated by finding the slope of each profile that generates the raw profilogram shown in Figure 142(c).

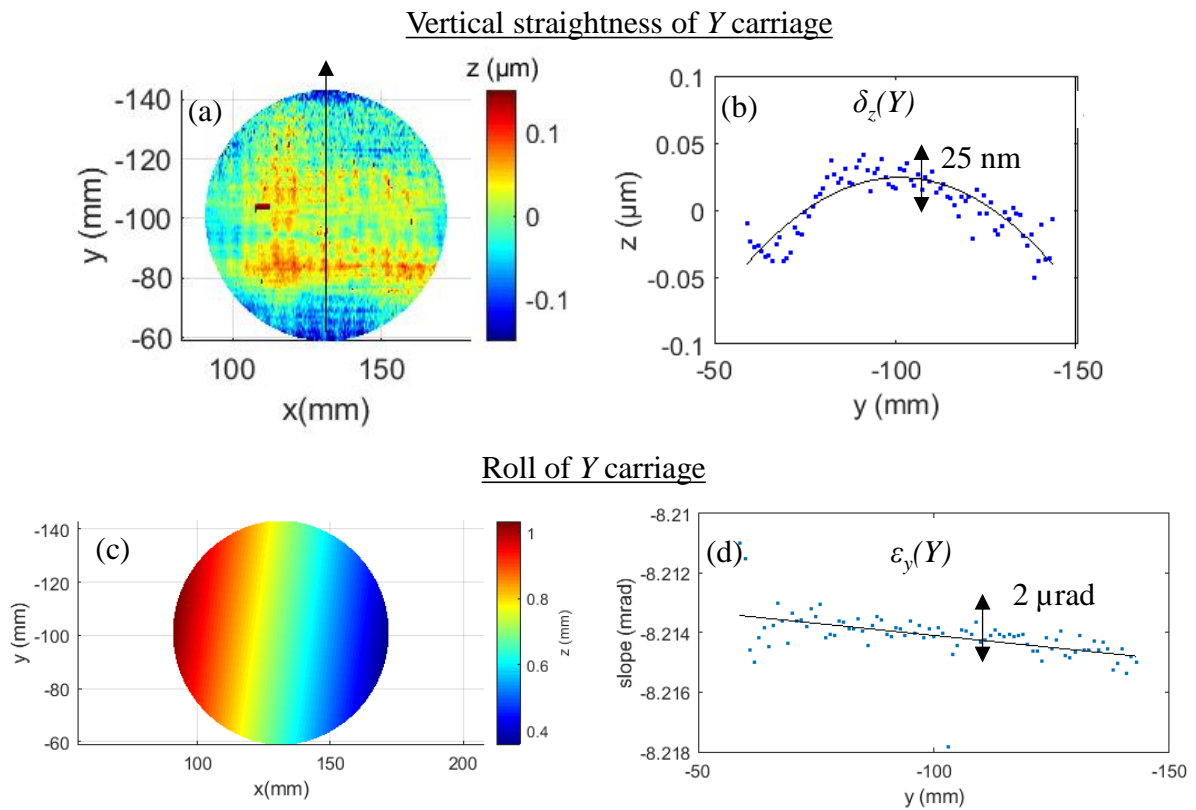


Figure 142: Y carriage errors; (a and b) vertical straightness error of Y carriage (c and d) Roll error of Y carriage and the raw profilograms used to estimate it.

It is assumed that the Monte Carlo simulated areal measurement discussed henceforth is corrected for the measured vertical straightness errors of X and Y carriages shown earlier. Uncertainties in their measurement, and uniformly distributed manufacturer specification of other errors are used as inputs to the simulation, see Table 4.

Table 4: Uncertainty of X and Y carriage errors input to the Monte Carlo simulation.

Parameter	Description	Uncertainty
$\delta_x(X)$	Positioning accuracy of X carriage	± 25 nm scale error
$\delta_y(X)$	Horizontal straightness of X carriage	Unknown
$\delta_z(X)$	Vertical straightness of X carriage	± 12.5 nm from a piecewise Zerodur optical flat measurement
$\varepsilon_x(X)$	Roll of X carriage	Unknown
$\varepsilon_y(X)$	Pitch of X carriage	Assumed to be zero, because it is not easy to separate this from $\delta_z(X)$ from the measured profile
$\varepsilon_z(X)$	Yaw of X carriage	Unknown
$\delta_x(Y)$	Horizontal straightness of Y carriage	± 0.5 μm manufacturer specification
$\delta_y(Y)$	Linear positioning error of Y carriage	± 0.5 μm manufacturer specification
$\delta_z(Y)$	Vertical straightness of Y carriage	± 12.5 nm from an areal form measurement of Zerodur optical flat
$\varepsilon_x(Y)$	Pitch of Y carriage	Not measured
$\varepsilon_y(Y)$	Roll of Y carriage	± 1 μrad from an areal form measurement of Zerodur optical flat
$\varepsilon_z(Y)$	Yaw of Y carriage	± 10 μrad manufacturer specification
$\alpha_x(Y)$	Horizontal squareness of Y carriage	± 30 μrad from a measurement of Silicon nitride sphere
$\alpha_z(Y)$	Vertical squareness of Y carriage	± 30 μrad from a measurement of Silicon nitride sphere

The result of the simulation for a single iteration of the simulation is shown in Figure 143(b) with a 200 nm PV, and the PV estimates of 100 iterations is given in Figure 143(c). Standard deviation of the result of these 100 iterations represents the uncertainty in the measurements [JCGM 101:2008] using the profiler in stripes manner and is 60 nm, see Figure 143 (d). It is noted that the squareness errors of *Y* carriage are not applicable for flat measurements, because a plane will be removed from the raw measurement data thereby removing the effect of squareness errors. However, it becomes necessary to consider their uncertainties during the measurement of non-flat objects. A simulated data of a concave surface with a radius of curvature of 300 mm is shown in Figure 143(e). Estimated uncertainty from 100 iterations of Monte Carlo simulation is 80 nm, see Figure 143(h).

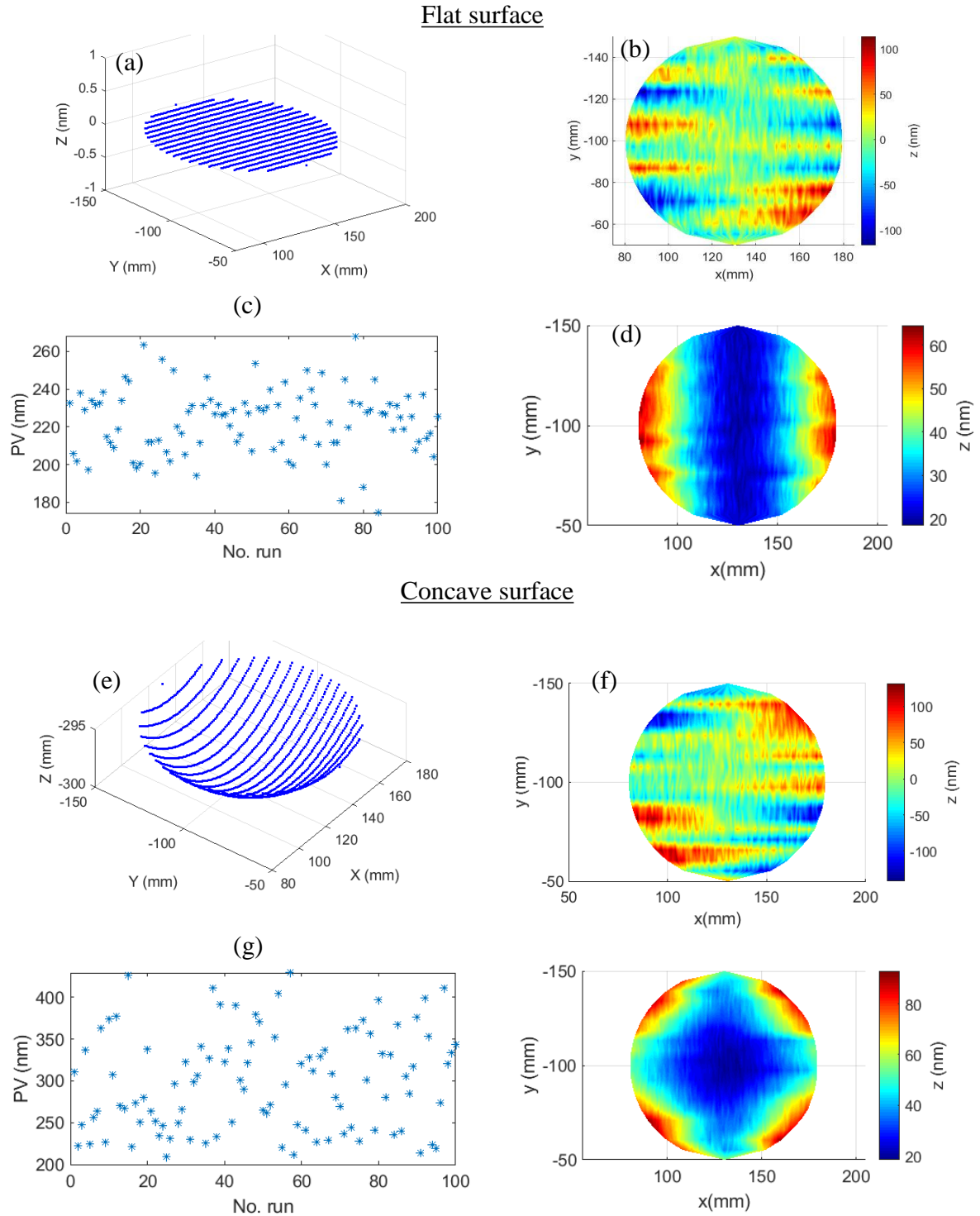


Figure 143: Monte Carlo simulation of a flat surface, and a concave surface measured using the stripes approach; (a,e) Simulated data (b,f) Output of a single iteration of Monte Carlo simulation to estimate the uncertainty of an areal measurement of a flat and a concave surface after removing a sphere (c,g) PV results of 100 iterations (d, h) standard deviation of 100 iterations representing the measurement uncertainty.

4.10.2 Monte Carlo – spokes

A Monte Carlo simulation is performed to estimate the uncertainty in areal form measurement of a perfect optical flat. The measurement is achieved by making spokes on the surface to cover its 100 mm aperture. To estimate the tilt and radial error of rotary carriage, *C*, Figure 101(a) shows raw measurement profiles of the Zerodur flat measured in a spokes manner on two different days. Lines are fit to this data using the least sum of squares method, and slopes are calculated and plotted in Figure 101(b). A sinusoidal trend seen in the slope values at each azimuth orientation of the flat is typically due to the wedge angle of the part and is 2 mrad PV, which is larger than the manufacturer specified parallelism of the flat of 0.15 mrad. This sinusoidal trend is removed to represent the tilt error of the rotary carriage, and is 2 μ rad PV as shown in Figure 101(d), which is comparable to the 3.4 μ rad synchronous tilt error specified by the manufacturer, see Appendix C.1.2. *z* offset values of the profiles shown in Figure 101(c) is calculated by finding the mean of the *z* values of measured profiles. The sinusoidal trend seen in the offset values is possibly due to the effect of the tilt error causing the flat to translate horizontally due to the lever arm created by the height at which it is located above the rotary carriage. Removing this sinusoidal trend leaves a residual of 40 nm PV as shown in Figure 101(e), which is lesser than the synchronous axial error of 100 nm specified by the manufacturer.

It is assumed that the Monte Carlo simulated areal measurement discussed henceforth is corrected for the measured rotary carriage tilt and axial errors. Uncertainties in these error measurements, and uniformly distributed manufacturer error specifications for radial error are used as inputs to the Monte Carlo simulation, see Table 5.

Table 5: Uncertainty of rotary carriage errors input to the Monte Carlo simulation.

Parameter	Description	uncertainty
$\delta_x(C), \delta_y(C)$	Radial errors of C carriage	$\pm 0.25 \mu\text{m}$ manufacturer specification
$\delta_z(Y)$	Axial error of C carriage	$\pm 20 \text{ nm}$ from an areal form measurement of Zerodur optical flat
$\varepsilon_x(C), \varepsilon_y(C)$	Tilt errors of C carriage	$\pm 0.25 \mu\text{rad}$ from an areal form measurement of Zerodur optical flat
$\varepsilon_z(C)$	Positioning error of C carriage	$\pm 10 \mu\text{rad}$ manufacturer specification
$\alpha_x(C)$	Horizontal squareness of C carriage	unknown
$\alpha_z(C)$	Vertical squareness of C carriage	unknown

The result of the simulation of a flat for a single iteration is shown in Figure 144(b) with an 80 nm PV, and PV variation during 100 iterations is given in Figure 144(b). Standard deviation of the results of these 100 iterations represents the uncertainty of the flat measurement using the profiler in a spokes manner and is 25 nm, see Figure 144(c). Simulated data of a concave surface with a radius of curvature of 300 mm is shown in Figure 144(e), and the estimated uncertainty from 100 iterations of Monte Carlo simulation is 30 nm. The evaluated uncertainties in the measurement by spokes manner is two time less than the uncertainties evaluated in the measurements using stripes manner. Although it is observed that the evaluated uncertainty in both methods of measurement is sensitive to the linear positioning accuracy of X carriage ($\delta_x(X)$).

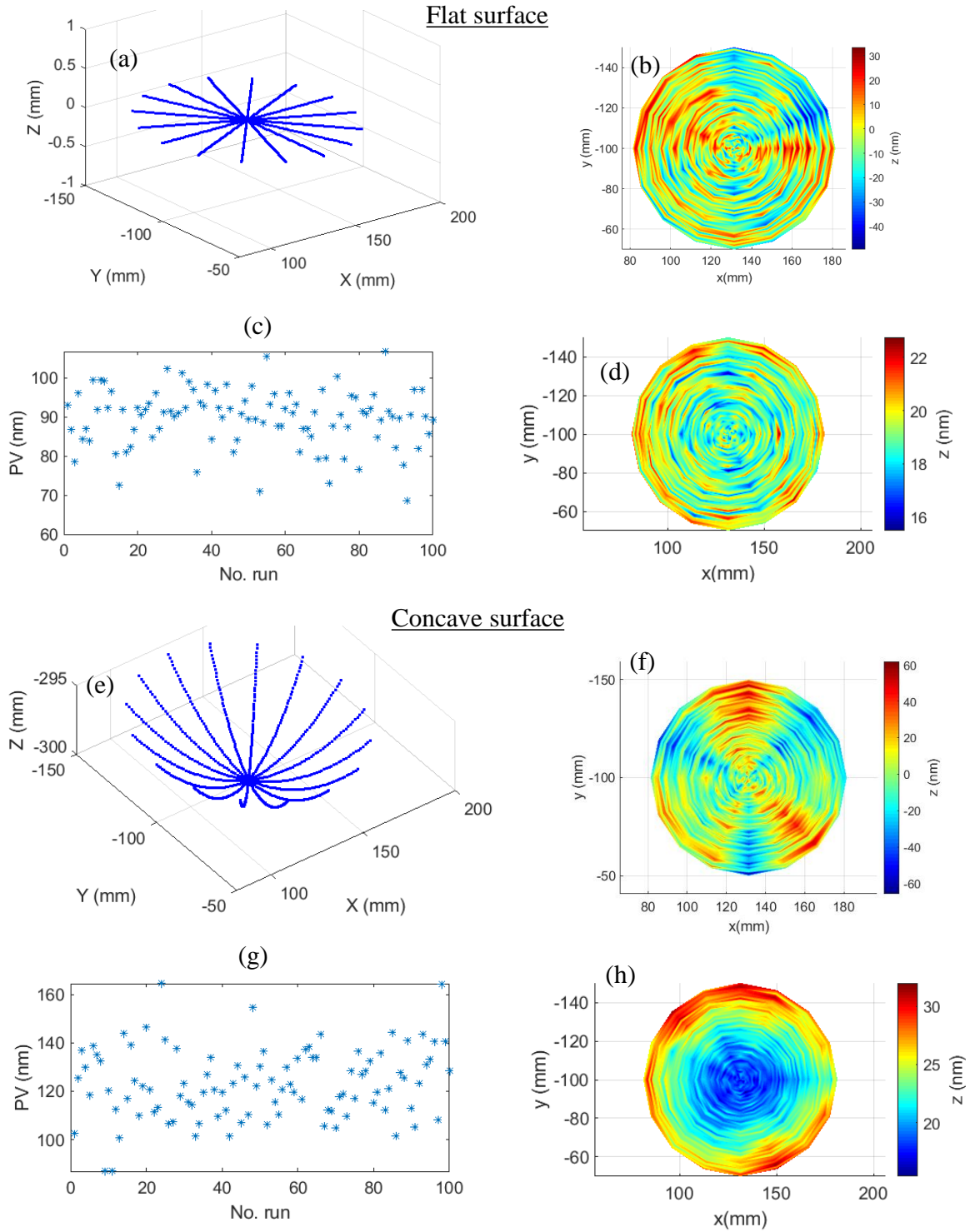


Figure 144: Monte Carlo simulation of a flat surface, and a concave surface measured using the spokes approach; (a,e) Simulated data (b,f) Output of a single iteration of Monte Carlo simulation to evaluate the uncertainty of an areal measurement of a flat and a concave surface after removing a sphere (c,g) PV results of 100 iterations (d,h) standard deviation of 100 iterations representing the measurement uncertainty.

4.11 Future work

While combined vertical straightness and pitch error of X carriage is established, horizontal errors that include horizontal straightness, yaw, and roll of the X carriage are yet to be established.

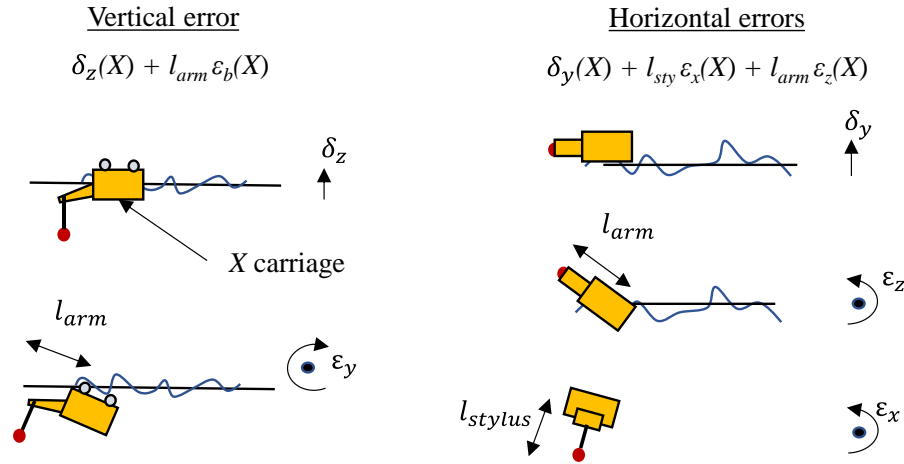


Figure 145: Schematics of the motion errors of the X carriage

Even though indirect estimates of Y carriage errors were made based on the measurements of reference surfaces, they are limited to only about 100 mm aperture, therefore a set of machine tool metrology measurements must be performed to estimate the errors for the full travel range of the Y carriage. Figure 146 to Figure 149 show the effect of carriage errors in the measured stripes and spokes of a concave surface as an example, and the suggested methods of machine tool metrology [Evans, 1996, Salsbury, 2003] to estimate these errors. Other factors to study are

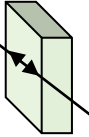
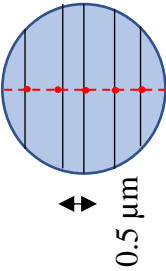
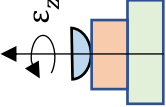
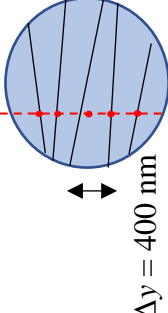
- (i) probe wear of the ruby stylus as a function of the length of profiles and the material of the parts being measured.

- (ii) To study the performance of the profiler on surfaces with large tilts, sinusoidal samples such as the ones made by Rubert Co. Ltd. could be measured in a tilted manner, and the results could be compared with the known amplitude and wavelength of the sample.

- (iii) When a non-flat objects such as a sphere measured in a stripes manner, the meridian of the stylus interacts with the surface of the sphere only when the sphere is profiled along its meridian. Since the current software implementation of the morphology filter by the manufacturer does not take this into consideration, algorithms must be developed considering the x , y , z coordinates at which the stylus and the test surface interacts.

Y carriage errors	schematic	Consequence in measuring a concave surface of 75 mm Dia., slope of $dz/dx = 0.1$	Metrology method
Horizontal straightness δ_x (Y)			Measure a rectangular mirror when displaced using Y carriage, using an interferometer placed orthogonal to the mirror surface, subtract the yaw of Y carriage
Roll ϵ_y (Y)			Use electronic level, create space to attach it by moving the H_z carriage higher
Vertical straightness δ_z (Y)			Rectangular flat measured by moving the Y carriage, subtract the pitch of Y carriage
Pitch ϵ_x (Y)			Electronic level

Figure 146: Machine tool metrology methods to estimate the Y carriage motion errors (straightness, roll, and pitch)

Y stage errors	schematic	Consequence in measuring a concave surface of 75 mm Dia., slope of $dz/dx = 0.1$	Metrology method
Positioning error δ_y (Y)	$\delta_y = 0.5 \mu\text{m}$ 	 $0.5 \mu\text{m}$	Interferometer, retro reflector
Yaw ϵ_z (Y)	$\epsilon_z = 10 \mu\text{rad}$ 	 $\Delta y = 400 \text{ nm}$	Angular interferometer sub arcsec ($< 0.3 \text{ mdeg}$)

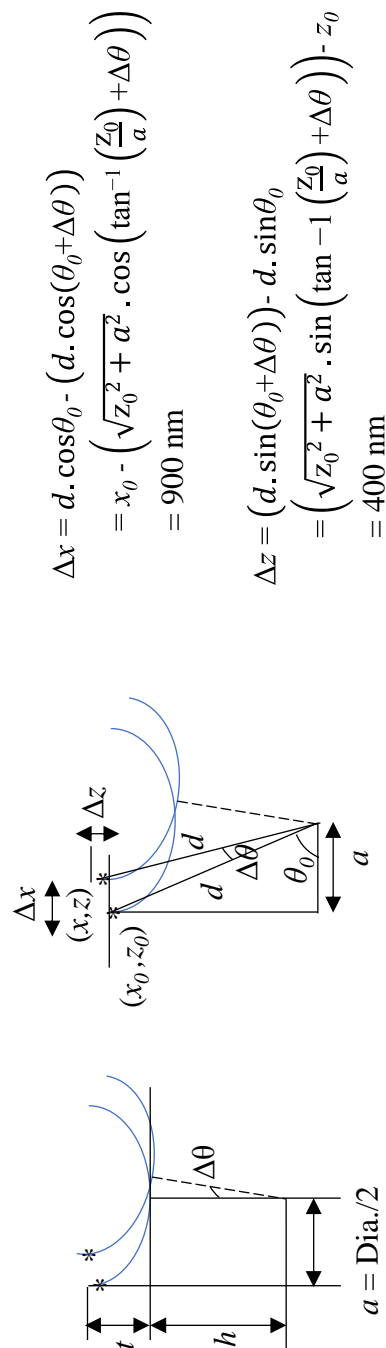


Figure 147: Machine tool metrology methods to estimate the Y carriage motion errors (positioning error, and yaw)

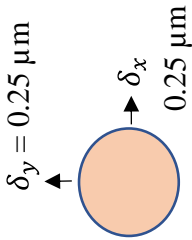
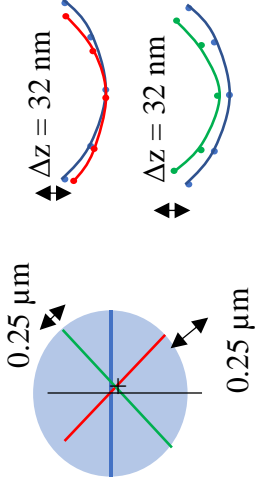
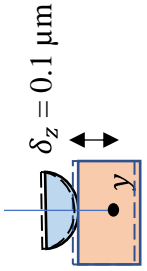
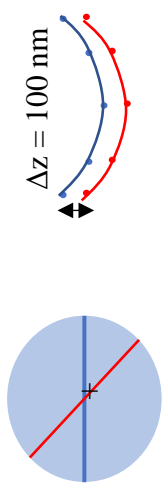
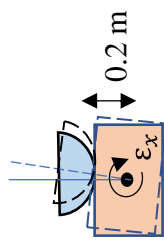
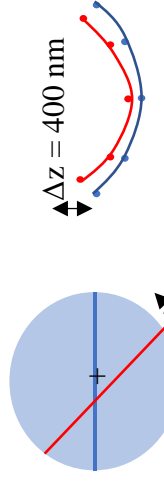
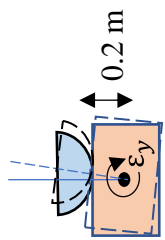
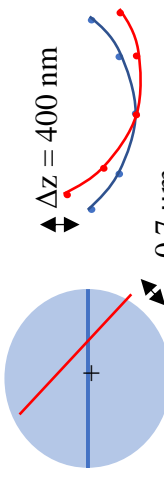
Rotary carriage errors	schematic	Consequence on a concave mirror (TMA equivalent) measurement	Metrology method
Radial errors $\delta_x(C)$, $\delta_y(C)$			Donaldson ball reversal using a capacitance probe
Axial error $\delta_z(C)$			Estler's reversal method using the stylus profiler measure an optical flat
Pitch $\epsilon_x(C)$			
Roll $\epsilon_y(C)$			

Figure 148: Machine tool metrology methods to estimate the C carriage motion errors

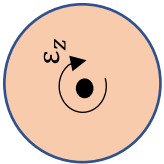
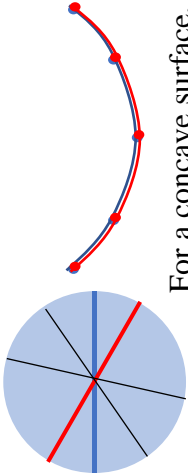
Rotary carriage errors	schematic	Consequence on a concave mirror (TMA equivalent) measurement	Metrology method
Positioning error $\varepsilon_z(C)$	 <p> $\varepsilon_z = 40 \text{ arc sec (200 urad, 10 mdeg)}$ From Aerotech calibration data </p>	 <p> For a concave surface, positioning error does not matter, but for freeform surfaces, it would matter </p>	A.G Davis secondary stage rotary calibrator, Needs air supply to operate (0.2 arc sec/ 60 μdeg) (weight - 8 kg) 1° manual indexing

Figure 149: Machine tool metrology method to estimate the *C* carriage positioning error

4.12 Conclusion- considerations to use the machine and process the measurement data

From the results discussed in this chapter of the thesis, the following are the considerations and practices that should be followed to use the machine efficiently for areal form measurement

- (i) Uncertainty in the areal form measurements of 100 mm aperture is ± 100 nm. i.e. this stylus profilometer is a $\lambda/3$ instrument.
- (ii) Warmup the machine for at least an hour by running the stylus in x axis in air.
- (iii) X carriage vertical error of 600 nm PV must be removed for measurements of 260 mm long profiles.
- (iv) To avoid their thermal influence, the operator must not be proximal to the machine during measurements and preferably an hour before.
- (v) Morphology filtered data cannot be used for areal measurements of non-flat objects measured using stripes approach, because of the non-meridian region of the stylus interacting with the surface
- (vi) Squareness of the Y carriage must be corrected for measurements of non-flat surfaces

Data, and Matlab programs to analyze the data can be found in a flash drive attached at the back cover. The folders are named according to the section numbers. One can also contact the author via email.

5. REFERENCES

5.1 Surface metrology

- Arumugam, K. et al. (2019). "Methods of optically profiling surfaces." *Proceedings of the ASPE 34th annual conference*, 71, 225-229.
- Hagemeier, S. et al. (2019). "Sensor characterization by comparative measurements using a multi-sensor measuring system." *J. Sens. Sens. Syst.*, 8, 111–121.
- Hocken, R. et al. (2005). "Optical Metrology of Surfaces." *CIRP Annals*, 54(2), 169–183.
- ISO 4287:1997, Geometrical Product Specifications (GPS) — Surface texture: Profile method — Terms, definitions and surface texture parameters.
- Peklenik, J. (1967). "New developments in surface characterization and measurements by means of random process analysis.", *Proc. Instn. Mech Engrs.*, 182(11), 108-126.
- Wang, Y. et al. (2017). "Review of surface profile measurement techniques based on optical interferometry." *Optics and Lasers in Engineering*, Elsevier Ltd, 93(January), 164–170.
- Williamson, J. (2016). "Dispersed reference interferometry for on-machine metrology." PhD thesis, univ. Ruddersfield.

5.2 Fiber-based Fabry-Perot interferometric profiler

- Arablu, M., and Smith, S. T. (2018). "Polydyne displacement interferometer using frequency-modulated light." *Review of Scientific Instruments*, 89(5).
- Arumugam, K. et al. (2018). "Limitations caused by rough surfaces when used as the mirror in displacement measurement interferometry using a microchip laser source" *Proceedings of the ASPE 33rd annual conference*.
- Bosbach, C. et al. (2002). "Fiber optic interferometer for absolute distance measurements with high measuring frequency." *Seventh International Symposium on Laser Metrology Applied to Science, Industry, and Everyday Life*, 4900(July 2002), 408–415.
- Bruland, K. J. et al. (1999). "Thermal tuning of a fiber-optic interferometer for maximum sensitivity." *Review of Scientific Instruments*, 70(9), 3542–3544.
- Drake, A. D., and Leiner, D. C. (1984). "Fiber-optic interferometer for remote subangstrom vibration measurement." *Review of Scientific Instruments*, 55(2), 162–165.
- Dufour, M. L. et al. (2006). "Surface inspection of hard to reach industrial parts using low-coherence interferometry." *Photonics North 2006*, 6343(September 2006), 63431Z.
- Hernandez, C. et al. (2014). "Fabry-Perot interferometer with enhanced visibility with tapered fiber tips." *Latin America Optics and Photonics Conference, LAOP 2014*, 20–22.
- Hirschmann, T. Ch., and Bödefeld, C. (2018). "Profilometry on micron sized objects", *Application note senI, Attocube systems AG*.

ISO 25178-3. (2012). "Geometrical product specifications (GPS) – Surface texture: Areal – Part3: specification operators, International Organization for Standardization, Geneva"

Liu, Z. et al. (2015). "High-resolution fiber profilometer for hard-to-access areas." *Applied Optics*, 54(24), 7205.

Nan-Nan, Z., and Jun, Z. (2016). "Surface roughness measurement based on fiber optic sensor." *Measurement: Journal of the International Measurement Confederation*, Elsevier Ltd, 86, 239–245.

Nowakowski, B. K. et al. (2016). "Highly compact fiber Fabry-Perot interferometer: A new instrument design." *Review of Scientific Instruments*, 87(11).

Yoshino, T. and Ohno, Y. (1981). "Fiber Fabry-Perot interferometers." *Integrated Optics and Optical Fiber Communication, OSA Technical Digest*, paper WL2.

Riesen, N. et al. (2021). "Lensed GRIN Fiber-Optic Fabry-Perot Interferometers." JTU7D.4.

Rugar, D. et al. (1988). "Force microscope using a fiber-optic displacement sensor." *Review of Scientific Instruments*, 59(11), 2337–2340.

Rugar, D. et al. (1989). "Improved fiber-optic interferometer for atomic force microscopy." *Applied Physics Letters*, 55(25), 2588–2590.

Schulz, M., and Lehmann, P. (2013). "Measurement of distance changes using a fibre-coupled common-path interferometer with mechanical path length modulation." *Measurement Science and Technology*, 24(6).

Wilkinson, P. R., and Pratt, J. R. (2011). "Analytical model for low finesse, external cavity, fiber Fabry-Perot interferometers including multiple reflections and angular misalignment." *Applied Optics*, 50(23), 4671–4680.

Yoshino, T. (2020). "Precise phase theory for accuracy improvement in a fiber probe interferometer for nanometric sensing, taking into account fiber coupling." *Journal of the Optical Society of America B*, 37(7), 2026.

Zhang, Y., Li, Y., Wei, T., Lan, X., Huang, Y., Chen, G., and Xiao, H. (2010). "Fringe visibility enhanced extrinsic Fabry-Perot interferometer using a graded index fiber collimator." *IEEE Photonics Journal*, 2(3), 469–481.

Zheng, J. (2006). "Optical frequency-modulated continuous-wave interferometers." *Appl. Opt.* 45, 2723-2730.

5.2.1 Stress induced frequency and phase modulation of light source

Arablu, M. (2019). "Polydyne displacement interferometer using frequency modulated light.", *PhD thesis, univ. North Carolina at Charlotte*.

Arumugam, K. et al. (2017). "Stress induced frequency modulation of a microchip green laser" *Proceedings of the ASPE 33rd annual conference*, 67 (253-256).

- Bertholds, A., and Dändliker, R. (1988). "Determination of the Individual Strain-Optic Coefficients in Single-mode Optical Fibers." *Journal of Lightwave Technology*, 6(1), 17–20.
- Bierlein, J. D., and Vanherzeele, H. (1989). "Potassium titanyl phosphate: properties and new applications." *Journal of the Optical Society of America B*, 6(4), 622.
- Chenault, D. B. et al. (1994). "Electro-optic coefficient spectrum of cadmium telluride." *Applied Optics*, 33(31), 7382.
- Friel, G. J. et al. (2000). "Compact and efficient Nd:YVO₄ laser that generates a tunable single-frequency green output." *Applied Optics*, 39(24), 4333.
- Gui, K. et al. (2019). "Frequency difference thermally and electrically tunable dual-frequency Nd:YAG/LiTaO₃ microchip laser." *Applied Sciences (Switzerland)*, 9(10).
- Heine, F. F., and Huber, G. (1998). "Tunable single frequency thulium:YAG microchip laser with external feedback." *Applied Optics*, 37(15), 3268–3271.
- Kecong, Z. and Ximin, W. (2001). "Structure sensitive properties of KTP-type crystals." *Chin.Sci.Bull.* 46, 2028–2036.
- Mann, G. et al. (1999). Influence of mechanical stress on the conversion efficiency of KTP and LBO." *Laser Metrology and Inspection*, 3823(June), 289–297.
- Nagai, H. et al. (1992). "Low-Noise Operation of a Diode-Pumped Intracavity-Doubled Nd:YAG Laser Using a Brewster Plate." *IEEE Journal of Quantum Electronics*, 28(4), 1164–1168.
- Ohmi, M. et al. "High-sensitivity two-dimensional thermal- and mechanical-stress-induced birefringence measurements in a Nd : YAG rod." 6368–6372.
- Owyoung, A., and Esherick, P. (1987). "Stress-induced tuning of a diode-laser-excited monolithic Nd : YAG laser." *Opt. Lett.* 12(12), 999–1001.
- Primak, W., and Post, D. (1959). "Photoelastic constants of vitreous silica and its elastic coefficient of refractive index." *Journal of Applied Physics*, 30(5), 779–788.
- Schulz, P. A., and Henion, S. R. (1991). "Frequency-modulated Nd:YAG laser." *Opt. Lett.* 16(8), 578–580.
- Stus, N. V. et al. (2004). "The mechanical properties of KTiOPO₄ single crystals." *Journal of Alloys and Compounds*, 366(1–2), 0–3.
- Twyman, F., and Perry, J. W. (1921). "The determination of poisson's ratio and of the absolute stress-variation of refractive index." *Proceedings of the Physical Society of London*, 34(1), 151–154.
- Waxler, R. M., and Weir, C. E. (1965). "Effect of hydrostatic pressure on the refractive indices of some solids." *Journal of Research of the National Bureau of Standards Section A: Physics and Chemistry*, 69A(4), 325.
- Zayhowski, J. J., and Keszenheimer, J. A. (1992). "Frequency Tuning of Microchip Lasers Using Pump-Power Modulation." *IEEE Journal of Quantum Electronics*, 28(4), 1118–1122.

- Zayhowski, J. J., and Mooradian, A. (1989). "Frequency-modulated Nd:YAG microchip lasers." *Opt. Lett.* 14(12), 618–620.
- Zhang, K., and Wang, X. (2001). "Structure sensitive properties of KTP-type crystals." *Chinese Science Bulletin*, 46(24), 2028–2036.
- Zhou, B. et al. (1985). "Efficient , frequency-stable laser-diode-pumped Nd : YAG laser." 10(2), 62–64.

5.3 Objective lens oscillated monochromatic confocal microscope

- Cox, I. J. et al. (1982). "Improvement in resolution by nearly confocal microscopy." *Applied Optics*, 21(5), 778.
- Dabbs, T., and Glass, M. "Fiber-optic confocal microscope : FOCON." *Applied Optics*, 31(16), 3030-3035.
- Dabbs, T., and Glass, M. (1992). "Single-mode fibers used as confocal microscope pinholes." *Applied Optics*, 31(6), 705.
- Fainman, Y. et al. (1982). "Optical profilometer: a new method for high sensitivity and wide dynamic range." *Applied Optics*, 21(17), 3200.
- Jordan, H et al. (1998). "Highly accurate non-contact characterization of engineering surfaces using confocal microscopy." *Measurement Science and Technology*, 9(7), 1142–1151.
- Lee, C. H., and Wang, J. (1997). "Noninterferometric differential confocal microscopy with 2-nm depth resolution." *Optics Communications*, 135(4–6), 233–237.
- Liu, J. et al. (2016). "Confocal axial peak extraction algorithm." *Confocal Microscopy*.
- Liu, T. et al. (2019). "MEMS-in-the-lens architecture for a miniature high-NA laser scanning microscope." *Light: Science and Applications*, Springer US, 8(1).
- Minsky, M. (1987). "Memoir on Inventing the Confocal Scanning Microscope." *Scanning*, 10, 128–138.
- Mansoor, H. et al. (2011). "Vertical optical sectioning using a magnetically driven confocal microscanner aimed for in vivo clinical imaging." *Optics Express*, 19(25), 25161.
- Qiu, L. et al. (2014). "Real-time laser differential confocal microscopy without sample reflectivity effects." *Optics Express*, 22(18), 21626.
- Udupa, G. et al. (2000). "Characterization of surface topography by confocal microscopy: I. Principles and the measurement system." *Measurement Science and Technology*, 11(3), 305–314.
- Xiao, G. et al. (1988). "Real-time confocal scanning optical microscope." *Applied Physics Letters*, 53(8), 716–718.

5.4 Characterization of a stylus profiler for areal form measurements

- Beutler, A. (2016). "Strategy for a flexible and noncontact measuring process for freeforms." *Optical Engineering*, 55(7), 071206.
- DeVries, W. R., and Li, C. J. (1985). "Algorithms to deconvolve stylus geometry from surface profile measurements." *Journal of Manufacturing Science and Engineering, Transactions of the ASME*, 107(2), 167–174.
- Emerson, W. B. (1952). "Determination of planeness and bending of optical flats." *Journal of Research of the National Bureau of Standards*, 49(4), 241.
- Evans et al. (1996). "Self-calibration: Reversal, redundancy, Error separation, and 'absolute testing'" *CIRP Annals*, 45(2), 617-634.
- Fang, F. Z., Zhang, X. D., Weckenmann, A., Zhang, G. X., and Evans, C. (2013). "Manufacturing and measurement of freeform optics." *CIRP Annals - Manufacturing Technology*, CIRP, 62(2), 823–846.
- Fritz, B. S. (1984). "Absolute Calibration Of An Optical Flat." *Optical Engineering*, 23(4).
- Hampshire, S. (2007), "Silicon nitride ceramics – review of structure, processing and properties", *Journal of achievements in materials and manufacturing engineering*, 24(1), 43-50.
- Hocken, R and Pereira, P. (2012), "Coordinate measuring machines and systems", second edition, *CRC press*.
- JCGM 101:2008, "Evaluation of measurement data — Supplement 1 to the "Guide to the expression of uncertainty in measurement" — Propagation of distributions using a Monte Carlo method"
- Leach, R., and Smith, S. (2018), "Basics of precision engineering", CRC Press
- Leach, R., et al. (2021), "Metrological characteristics for the calibration of surface topography measuring instruments: a review", *Meas. Sci. Technol*, 32(3), 1-16.
- Liu, X., Chetwynd, D. G., Smith, S. T., and Wang, W. (1993). "Improvement of the fidelity of surface measurement by active damping control." *Measurement Science and Technology*, 4(12), 1330–1340.
- Loewen, E. G. (1967). "Optimum Kinematic Support of Rectangular Flat Plates." *CIRP Annals*, XV(1), 345–348.
- Moore, W. (1970). "Foundations of mechanical accuracy." *The Moore special tool company*, p.83.
- Nadim, E. H. et al. (2014). "Comparison of tactile and chromatic confocal measurements of aspherical lenses for form metrology." *International Journal of Precision Engineering and Manufacturing*, 15(5), 821–829.
- Noste, T. (2020) "Freeform Optical Surface Form Metrology with Serial Data Acquisition", PhD thesis, Univ. North Carolina at Charlotte.
- Parks, R. (2006) "A Practical Implementation of the Random Ball Test", *Optical Perspectives Group, LLC*

- Salsbury, J. (2003). "Implementation of the Estler face motion reversal technique". *Precision Engineering*, 27(2), 189-194.
- Schott (2004). "TIE-33: Design strength of optical glass and ZERODUR"
- Schott (2011). "Catalog- Zerodur®, Zero Expansion Glass Ceramic"
- Shunmugam, M.S. (1986). "On assessment of geometric errors", *Int. J. Prod. Res.*, 24(2), 413-425.
- Smith, S. (2000). "Flexures- Elements of elastic mechanisms", *CRC press*
- Vannoni, M. (2014). "Absolute flatness measurement using oblique incidence setup and an iterative algorithm A demonstration on synthetic data." *Optics Express*, 22(3), 3538-3546.
- Wendel, M. (2019). "Measurement of freeforms and complex geometries by use of tactile profilometry and multi-wavelength interferometry." *Proc. of SPIE*, 1117109.
- Whitehouse, D. J. (1988). "A revised philosophy of surface measuring systems." *Proceedings of the Institution of Mechanical Engineers, Part C: Journal of Mechanical Engineering Science*, 202(3), 169.

APPENDIX A

A.1 Frequency modulation of the laser by oscillating the grating

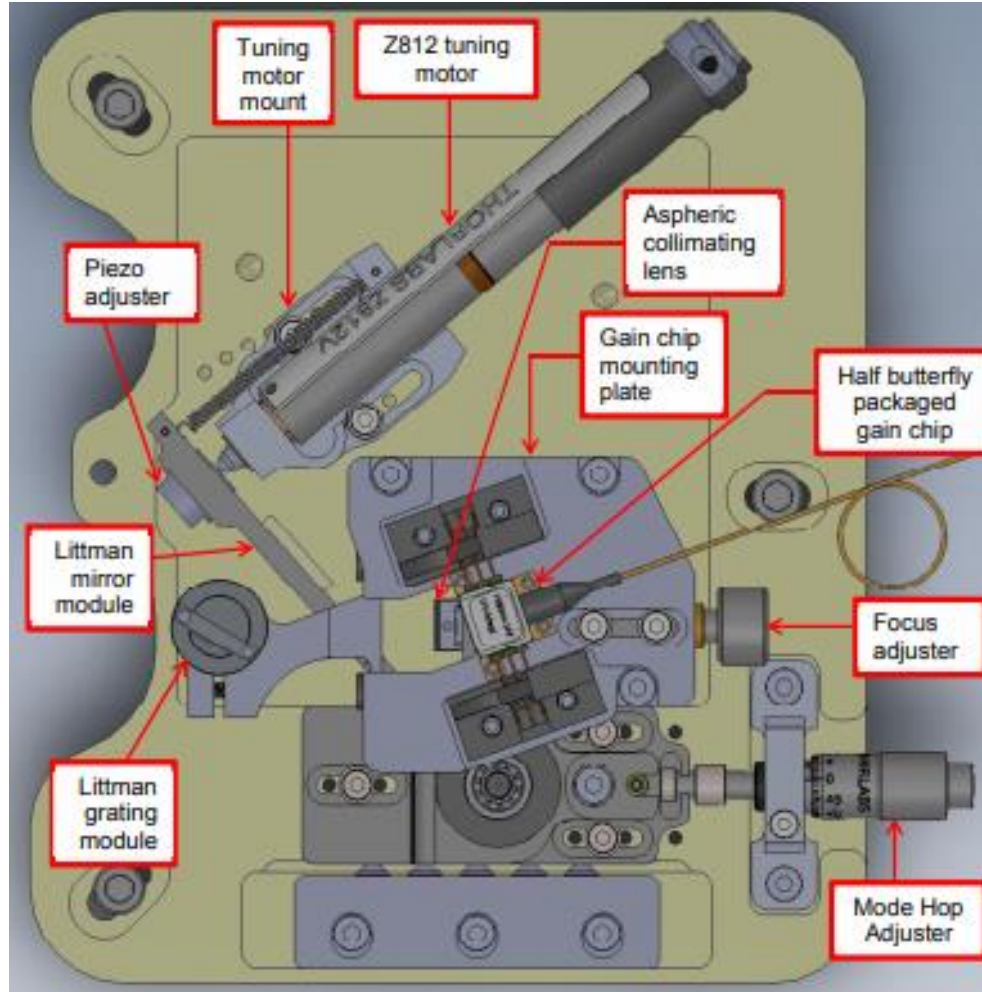
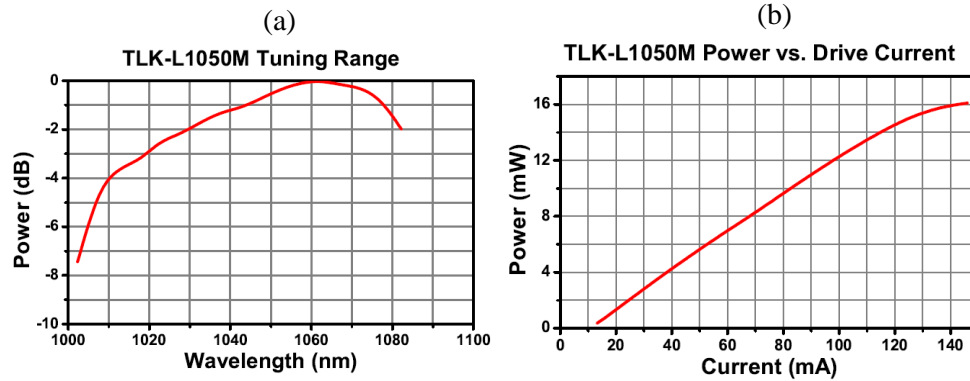


Figure 150: Solid model of the laser frequency modulator

Figure 151(a) shows that the tuning range (frequency modulation range) of the laser module shown in Figure 150 is about 60 nanometers and can be achieved using the stepper motor. Since, in our experiments we use the piezo shown in Figure 151(d), fine tuning of up to 90 pm is achievable.



(c)

	Min	Typ	Max
Center Wavelength	1040 nm	1050 nm	1060 nm
Tuning Range (10 dB)	45 nm	60 nm	-
Peak Power	5 mW	8 mW	-
Wavelength Tuning Resolution	2 pm	-	-
Tuning Speed (using Z812)	-	-	23 nm/s
Linewidth	-	100 kHz	130 kHz
Side Mode Suppression Ratio	45 dB	-	-
Polarization Extinction Ratio	-	N/A	-
Power Stability (30 s)*	1%	-	-
Power Stability (24 hr)*	10%	-	-
Wavelength Stability (30 s)*	-	-	4 pm
Wavelength Stability (24 hr)*	-	-	50 pm
Operating Current	-	120 mA	150 mA
Chip Forward Voltage	-	-	2.5 V
TEC Forward Current	-	-	2.1 A
TEC Forward Voltage	-	-	3.6 V
Fiber Output	1.5 m, HI1060, FC/APC		

*Measurements taken with laser operating in open loop.

(d) Fine-Tuning Piezo Actuator

- ▶ Wavelength Tuning Open-Loop Piezo Actuator
- ▶ Use in Tandem with Main Tuning Actuator
- ▶ 9.1 μm Max Displacement
- ▶ 150 V Max, 100 V Recommended Drive Voltage
- ▶ 0.75 $\mu\text{F} \pm 20\%$ Capacitance @ 1 kHz, 1 V_{RMS}



This piezo module attaches to the grating pivot arm (Littrow) or mirror pivot arm (Littman) via its M12 x 1.25 threaded housing to provide fine wavelength tuning of a Tunable Laser Kit. The standard tuning actuator is a Z812 DC servo motor, which offers 12 mm of travel and a minimum incremental movement of 0.05 μm . The piezo module is used in tandem with the Z812 tuning actuator, allowing the user to access the full tuning range, while also having the ability to finely tune the wavelength. The TLK-PZT1 has a BNC connector for use with Thorlabs open-loop piezo controllers. The table below lists the incremental wavelength tuning of the tunable laser kits when the TLK-PZT1 is integrated into them.

Littman Item #	TLK-L780M	TLK-L1050M	TLK-L1300M	TLK-L1550M	TLK-L1900M
Incremental Tuning	7 pm/ μm	10 pm/ μm	13 pm/ μm	15 pm/ μm	20 pm/ μm
Littrow Item #	TLK-L1220R	TLK-L1300R	TLK-L1550R	TLK-L1950R	
Incremental Tuning	10 pm/ μm	7 pm/ μm	14 pm/ μm	18 pm/ μm	

Figure 151: Frequency modulation characteristics of the laser

A.2 Scanning stage used in fiber Fabry-Perot interferometry

Figure 152 shows the stage mechanism used to translate the sample surface to profile it along x axis using the fiber Fabry-Perot interferometer. This stage uses flexure leafs made of spring steel with Elastic modulus, $E = 215$ GPa arranged in a double compound parallelogram configuration [Smith, 2000]. The dimension of the leafs is length, $l = 38$ mm, width, $b = 12.7$ mm, and thickness, $t = 0.3$ mm, and the stiffness of the mechanism is given by,

$$k = \frac{12EI}{l^3} = \frac{Ebt^3}{l^3} = 1343 \text{ N} \cdot \text{m}^{-1}$$

The stage is actuated using a linear motor made of a 3-phase coil and an array of magnets placed on both sides of the coil. The position of the stage is feedback controlled using a linear encoder. Figure 153 shows the signal conditioning components used to operate the stage which includes, a myRIO microprocessor, amplifiers to provide a three sinusoidal input currents to the coils which are out of phase by 120° . The circuitry of these amplifier is shown in Figure 155(b). Figure 154 shows the box that houses these current amplifiers with two of its sinusoidal input voltages provided by 12-bit DAC's on connector C of the myRIO. The third input is “derived” from these two inputs using a difference amplifier shown in Figure 155(a).

Also shown Figure 153 is an interpolator board used to convert the sinusoidal signal from the encoder during the displacement into a square wave interpolated to 64 times, therefore converting the $20 \mu\text{m}$ sinusoidal period into 314 nm square periods, counted by a counter board. Figure 156 shows the layout of the box that houses the interpolator and the counter boards.

Figure 157(a) and (b) Shows the control structure showing the operation of the stage with the sinusoidal 120° phase shifted voltages produced by myRIO and are used to derive the

third 240° phase shifted wave. These voltage inputs are provided into the current amplifier which provides the current output to the three copper coils. The displacement of the moving stage is sensed by the linear encoder and is used for the feedback control of the stage position. Figure 157(c) and Figure 158 shows the LabVIEW GUI, and the program to operate the stage respectively.

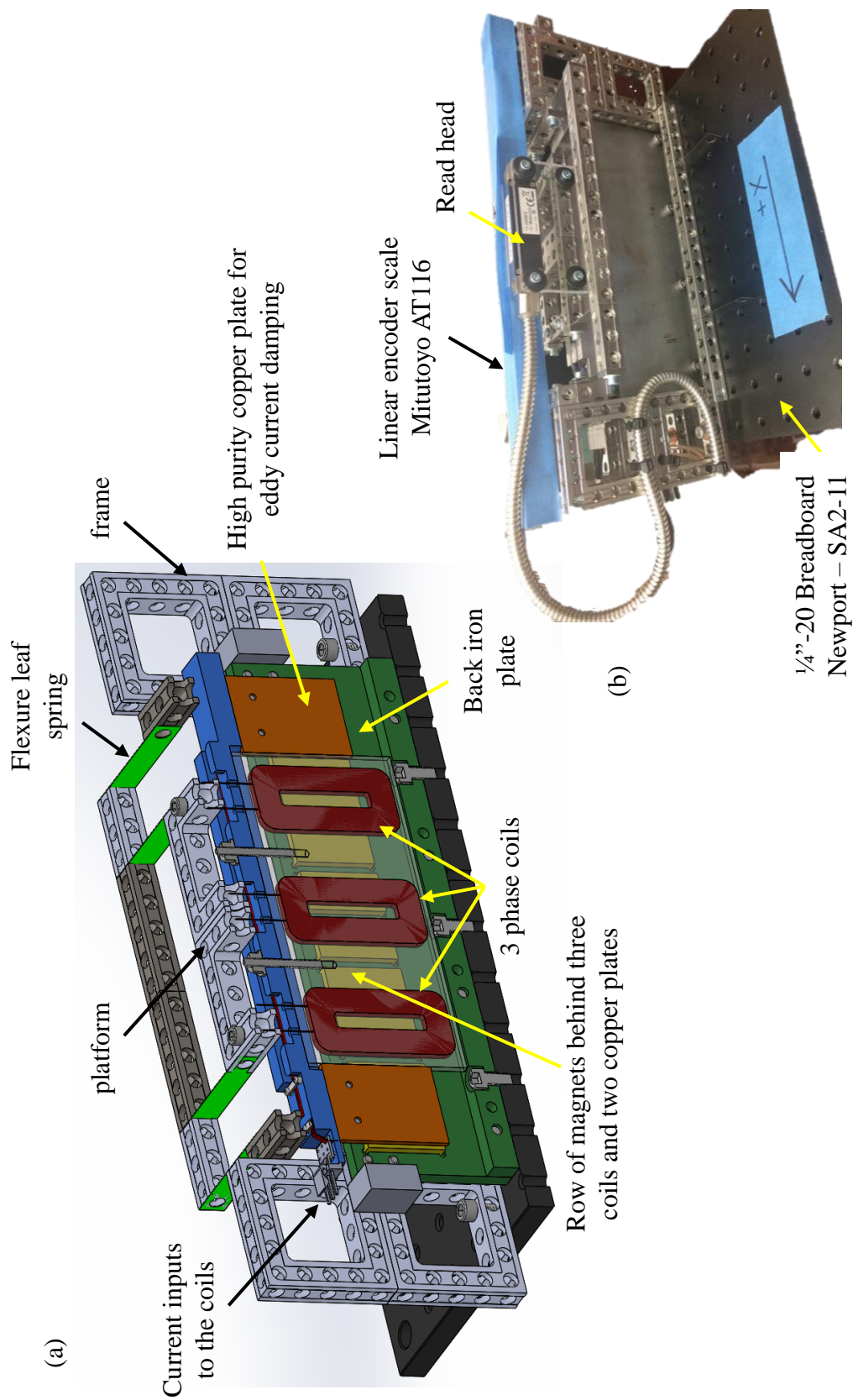


Figure 152: x axis scanning stage used in the Fiber interferometric profiler studies; (a) cross sectional view of the Solid model of the scanning stage showing the coils and arrays of magnets used to actuate the stage (b) Picture of the stage showing the linear encoder read head used to feedback control the position

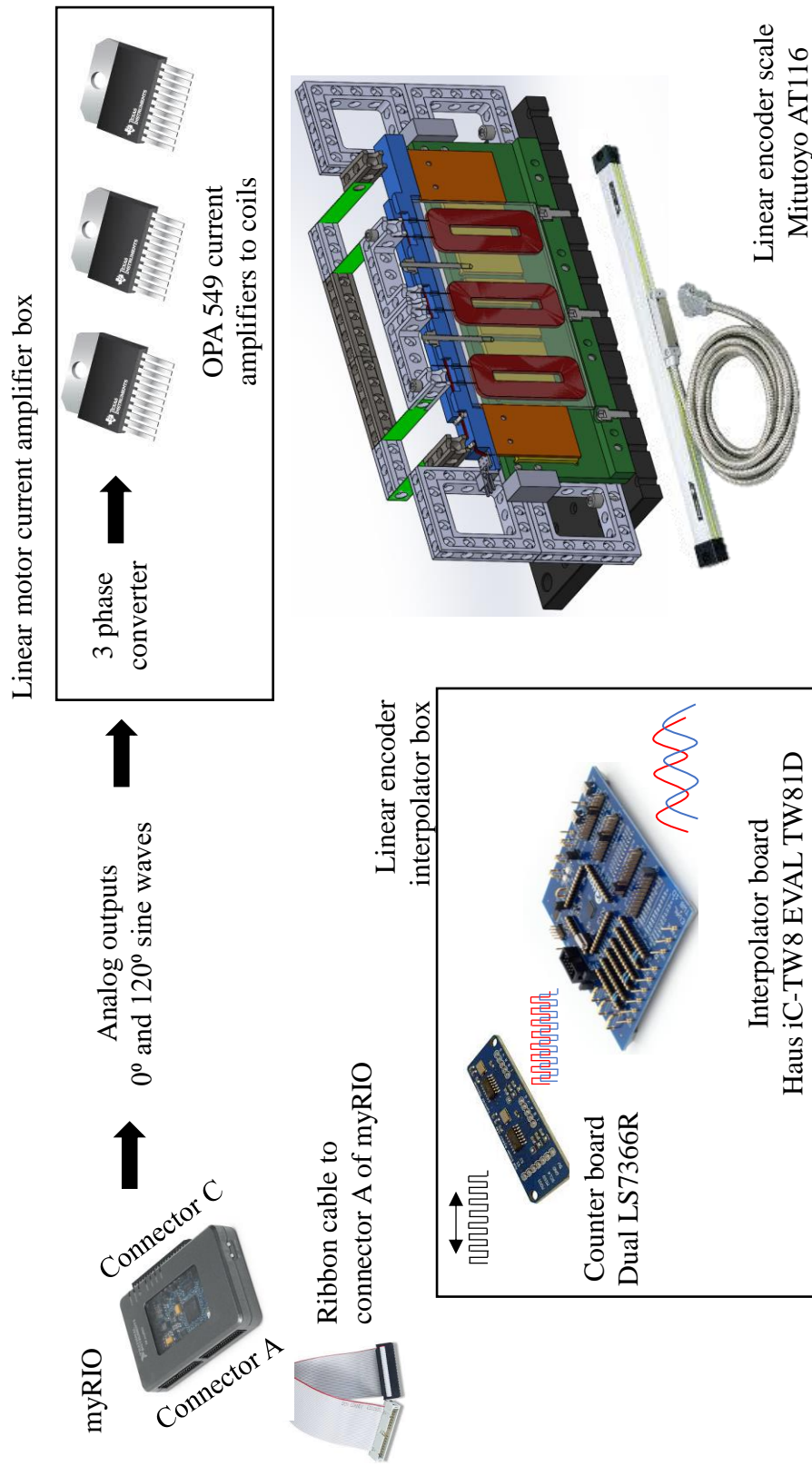


Figure 153: Components used in controlling the scanning stage: myRIO microprocessor, OPA549 current amplifier to provide current to the coils, Interpolator for converting the sinusoidal encoder signal to square waves

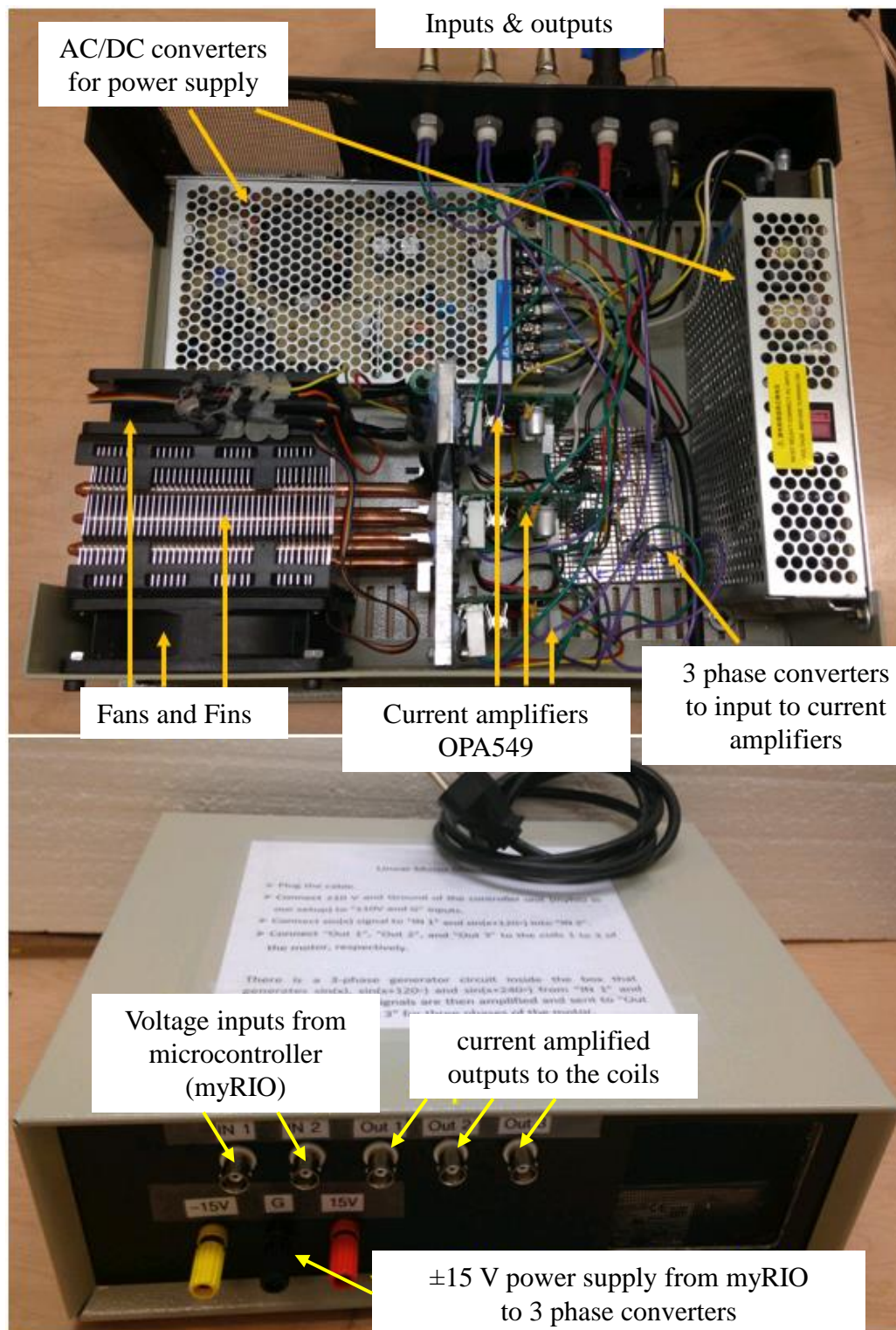


Figure 154: Amplifier box providing three current outputs phase shifted by 120° with its signal inputs from myRIO's 12-bit DAC's on connector C. Courtesy of Dr. Masoud Arablu

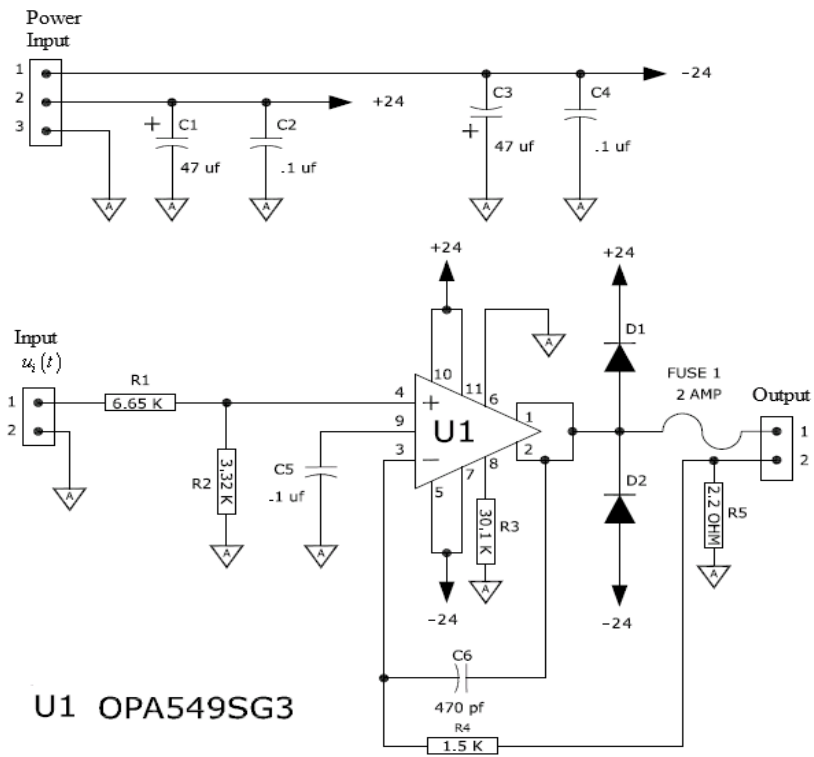
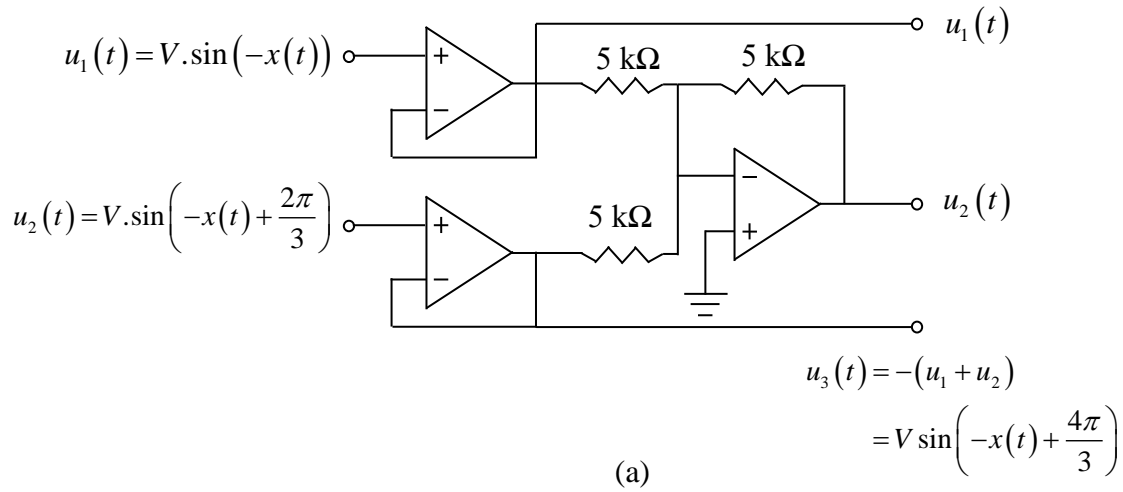


Figure 155: Circuits to actuate the x axis scanning stage; (a) Difference amplifier to derive the 240° phase shifted sinusoidal voltage input to the current amplifier (b) Current amplifier to provide phase shifted sinusoidal current inputs to the coils, Courtesy of Dr. Masoud Arablu and John Brien

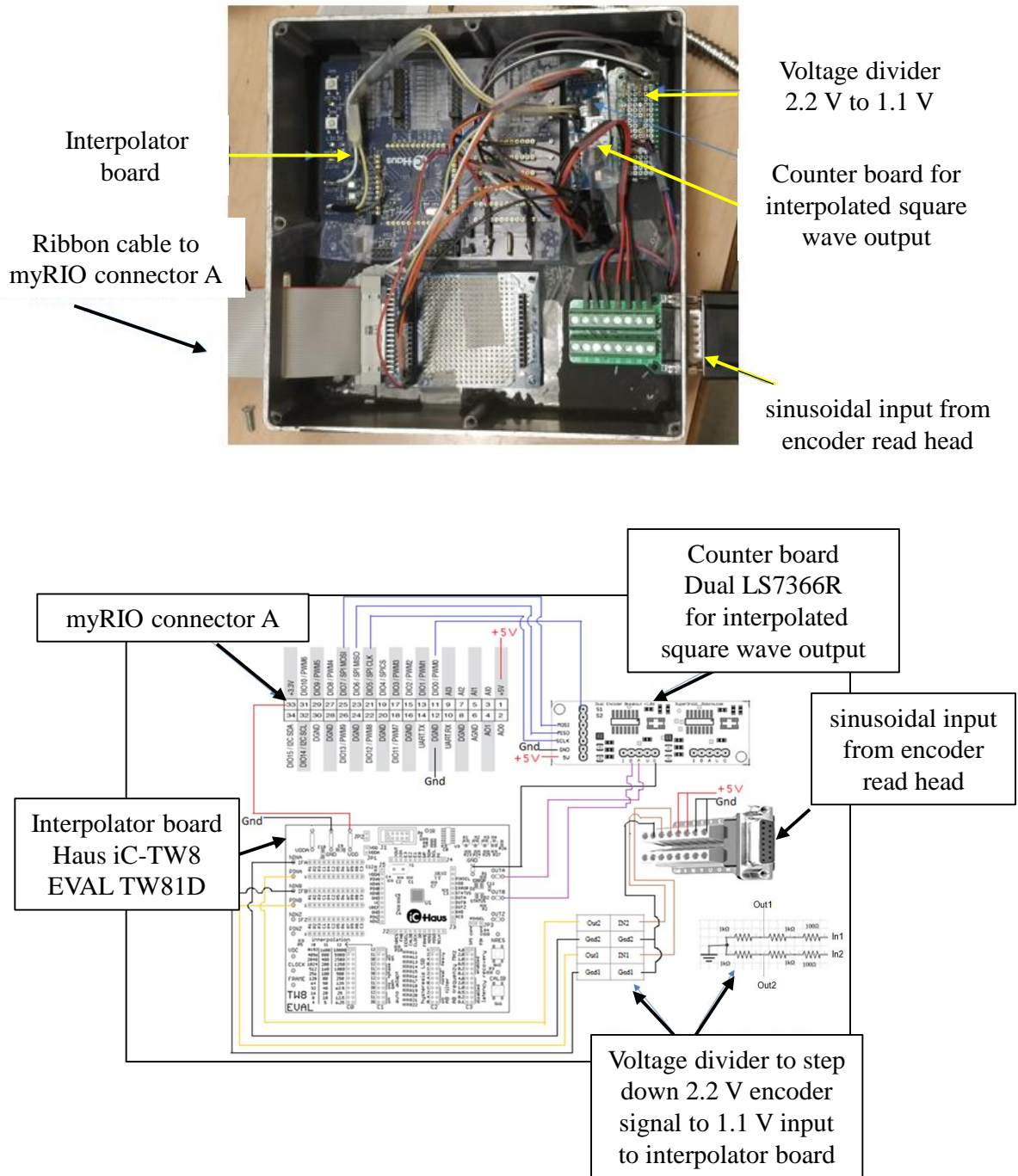
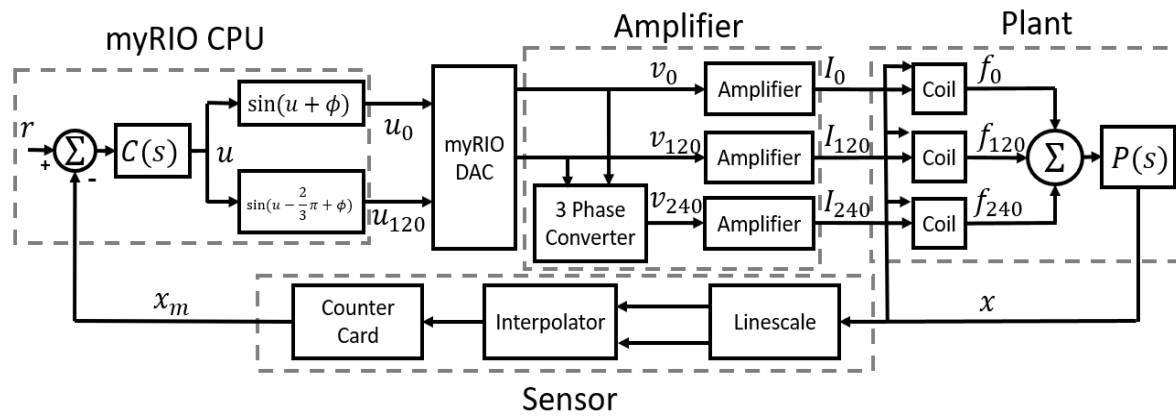
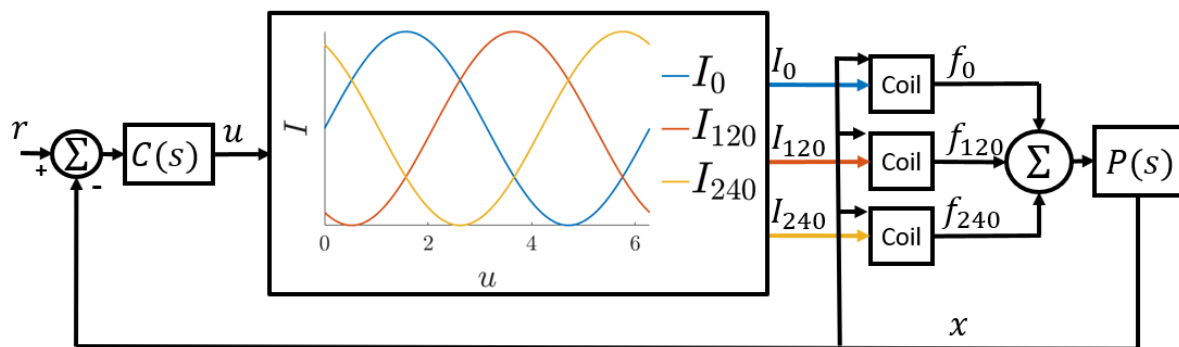


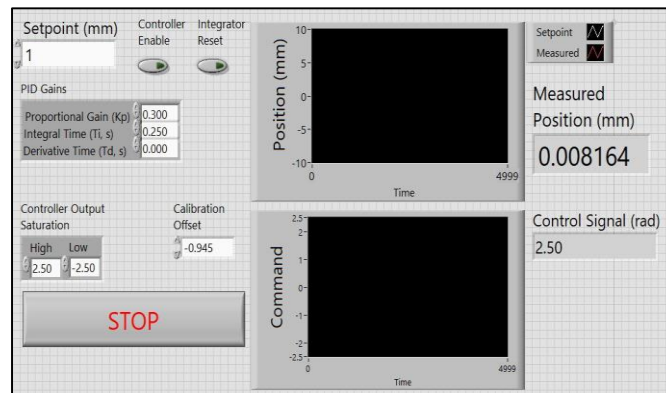
Figure 156: Layout of the interpolator board to convert the 20 μm sinusoidal signal from the linear encoder into a 314 nm periodic square waves, and the counter board to count the number of periods of the square waves generated



(a)



(b)



(c)

Figure 157: Feedback control of the stage; (a) Control structure (b) 120° phase shifted sinusoidal current inputs to the coils (c) LabVIEW GUI to operate the stage, Courtesy of Dr. Mitchell Cobb

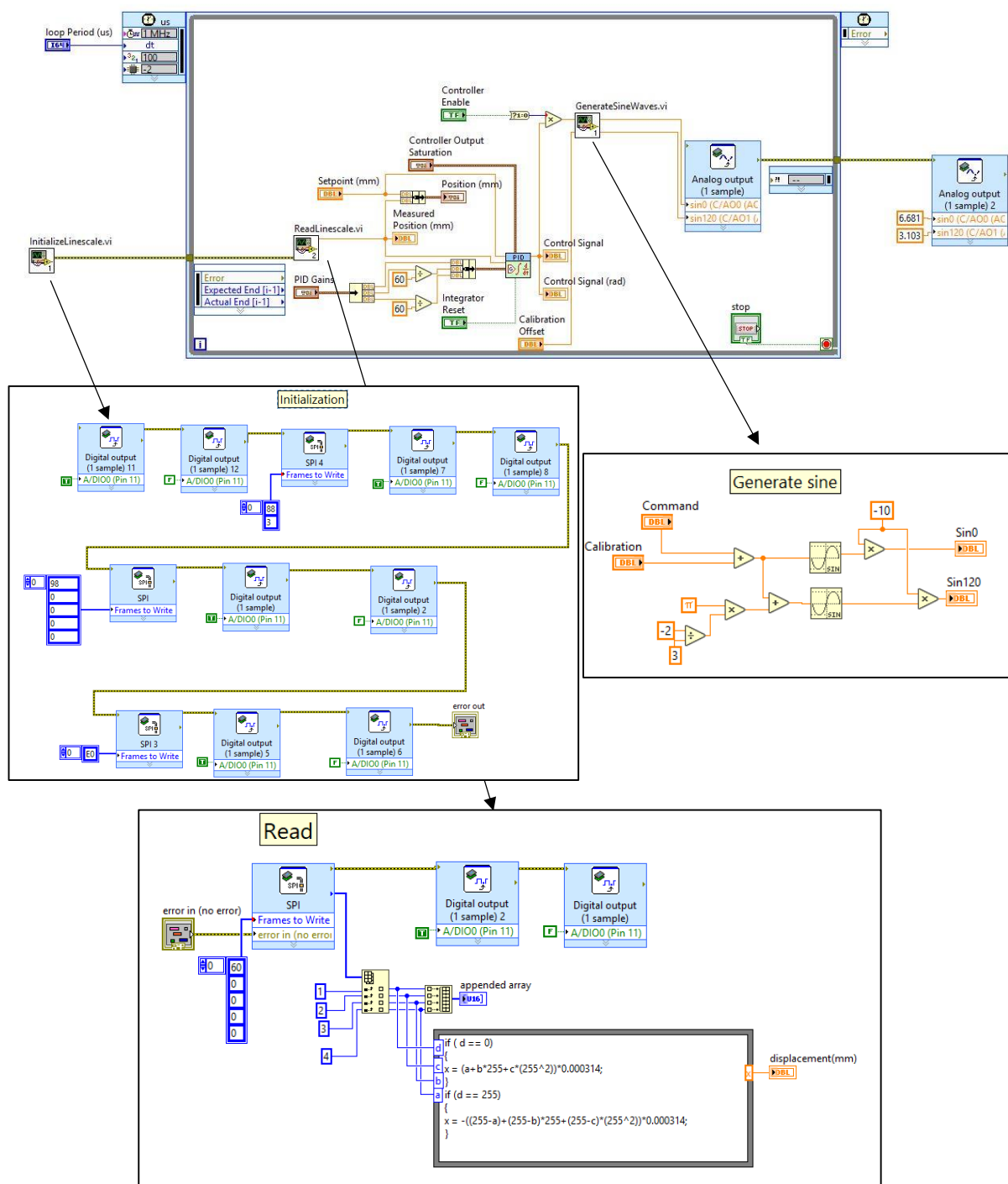


Figure 158: LabVIEW program with a timed loop to execute a PID controller, to initialize and read the counter board outputting the number of interpolated square waves during the motion of the stage

A.3 Rod flexure based tilt aligner used in fiber Fabry-Perot profiler

A rod flexure mechanism designed to remove the tilt of the sample surface is shown in Figure 159. This tilt mechanism sits on top of the over constraint flexure stage to translate the sample surface in z axis.

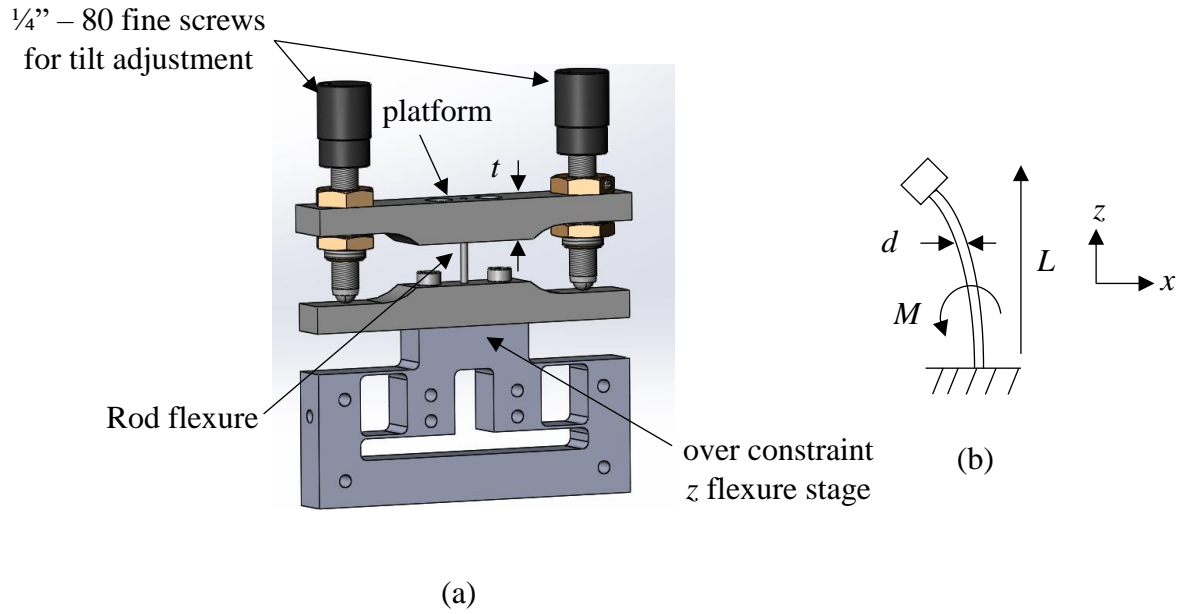


Figure 159: A rod flexure mechanism used to remove the tilt of the sample surface measured using the Fiber Fabry-Perot interferometric profiler

The stiffness (k_{θ}) of the rod flexure undergoing a cantilever deformation is related to the applied moment, (M) and the angular deflection (θ) as,

$$M = EI \frac{d^2 z}{dx^2}$$

$$Mx = EI\theta$$

$$k_{\theta} = \frac{M}{\theta} = \frac{EI}{x}$$

where, E is the elastic modulus of the material, and $I = \frac{\pi d^4}{64}$ is the second moment of area.

The stress on the flexure due to the applied moment is given by

$$\sigma = \frac{Mr}{I} = \frac{E\theta d}{2L}$$

For this to be less than the yield stress, the required length of the rod for a desired angular deflection of 0.01 rad is given by

$$L > \frac{E\theta_{desired}d}{2\sigma_{yield}}$$

For a rod of diameter, $d = 1.6$ mm made of steel (Elastic modulus, $E = 200$ GPa and yield stress, $\sigma_{yield} = 350$ MPa), the length of the rod must be greater than 4.5 mm. Therefore, a length of 10 mm is chosen.

A.3.2 Thickness of the platform

The length of the hole (thickness of the platform) through which the rod is pushed through and epoxied must be long enough to avoid plastic deformation of the platform, see Figure 160(a). Therefore, an Hertzian analysis [Leach and Smith, 2018] was performed for a

cylindrical rod of radius, R_1 inside a cylindrical hole in the platform of radius, R_2 , for which

the half contact width is given by $b = \sqrt{\frac{4f_n R^*}{\pi E^*}}$,

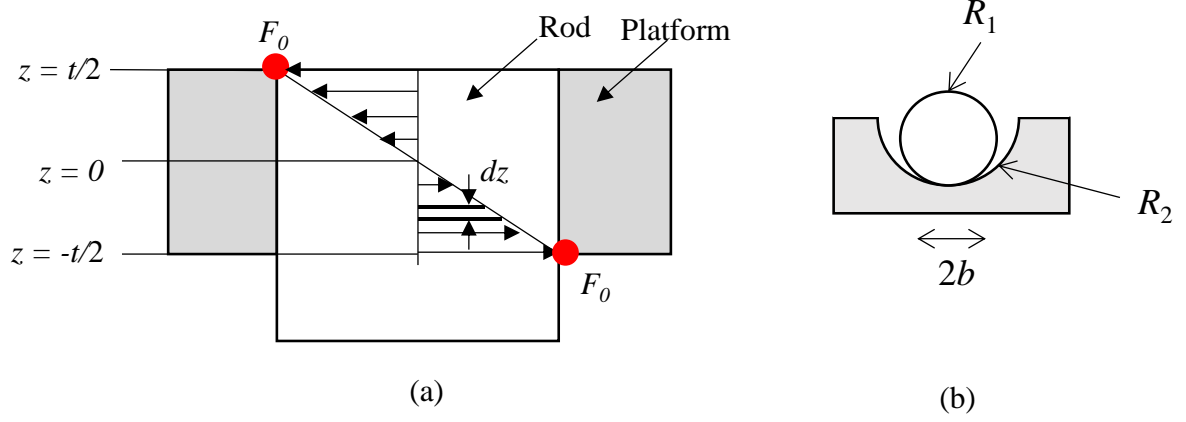


Figure 160: Schematic showing the flexure rod inserted to the platform (a) Front view (b) Top view

where, $\frac{1}{E^*} = \left(\frac{1-\nu_1^2}{E_1} + \frac{1-\nu_2^2}{E_2} \right)$, $\frac{1}{R^*} = \left(\frac{1}{R_1} + \frac{1}{R_2} \right)$

$\nu_1 = \nu_2 = 0.32$ is the Poisson ratio of the materials approximately,

$E_1 = 215$ GPa $E_2 = 70$ GPa are the elastic modulus of the steel rod and the Aluminum platform, making $E^* = 58$ GPa,

$R_1 = R_2 = 0.8$ mm is the radius of the inner and outer cylindrical surfaces respectively, making

$R^* = 0.4$ mm, and

f_n is the force per unit length of the surface.

The contact pressure between the cylindrical surfaces is given by $p_0 = \frac{2f_n}{\pi b}$, and p_0 is about 0.3 times the shear stress (τ) (τ) of the material, which in turn is about half of the equivalent tensile stress (σ). Therefore, $\sigma = \frac{0.3f_n}{\pi b}$ should be less than the yield strength ($\sigma_{yield, Al} = 135 \text{ MPa}$) of the material, and is written as

$$\sigma = \frac{0.15\sqrt{f_n}}{\sqrt{\pi(R^* / E^*)}}$$

When the rod bends, the maximum force (F_0) is exerted at the top and bottom corners of the platform, shown as red circles in Figure 160(a). The force at any instance, dz shown in Figure 160 is given by $f_n(z) = F_0 \frac{2z}{t}$. From which the bending moment is calculated as

$$M = \int_{-t/2}^{t/2} f_n(z) \cdot z \cdot dz = \frac{F_0 t^2}{6},$$

making $f_n(z) = \frac{12Mz}{t^3}$. Therefore, at the corners of the platform $f_n(t/2) = \frac{6M}{t^2}$. From this, the tensile stress is calculated as,

$$\sigma = 0.9 \sqrt{\frac{M}{\pi t^2 (R^* / E^*)}}$$

Solving this equation for the yield strength of the platform, and approximating $0.9 \sim 1$, gives the required thickness of the platform,

$$t = \sqrt{\frac{M}{\pi (R^* / E^*) \sigma_{yield}^2}}$$

and the bending moment, $M = k_{\theta} \theta_{desired}$

where, the stiffness of the rod for a cantilever deflection is $k_{\theta} = \frac{E_{steel} I}{L}$

where, the second moment of area of the rod, $I = \frac{\pi d^4}{64}$, making

$$t = d^2 \sqrt{\frac{E_{steel} \theta_{desired}}{64 L (R^* / E^*) \sigma_{yield}^2}}$$

For $d = 1.6$ mm, $E_{steel} = 215$ GPa, thickness of the platform is calculated as $t = 13.2$ mm.

A.4. Specifications of a 808 nm laser pump diode

■ Absolute Maximum Ratings($T_c=25^\circ\text{C}$)							
Parameter		Symbols	Ratings		Units		
Optical Output		Po	500		mW		
Reverse Voltage		Vr	2		V		
Operating Temperature		Top	-10~+40		$^\circ\text{C}$		
Storage Temperature		Tstg	-40~+85		$^\circ\text{C}$		

■ Electrical and Optical Characteristics($T_c=25^\circ\text{C}$)							
Parameter		Symbols	Conditions	Min.	Typ.	Max.	Units
Threshold Current		Ith	Po=500mW	-	70	100	mA
Operating Current		Iop	Po=500mW	-	540	590	mA
Operating Voltage		Vop	Po=500mW	-	1.9	1.95	Volts
Slope Efficiency		η	375mW-125mW	0.8	1.1	-	mW/mA
			I _{375mW} -I _{125mW}				
Beam Divergence (FWHM)	Parallel	θ_{\parallel}	Po=500mW	-	10	-	deg.
	Perpendicular	θ_{\perp}	Po=500mW	-	31	-	deg.
Lasing Wavelength*		λ	Po=500mW	803	808	811	nm

◎ θ_{\parallel} and θ_{\perp} are defined as the angle within which the intensity is 50% of the peak value.

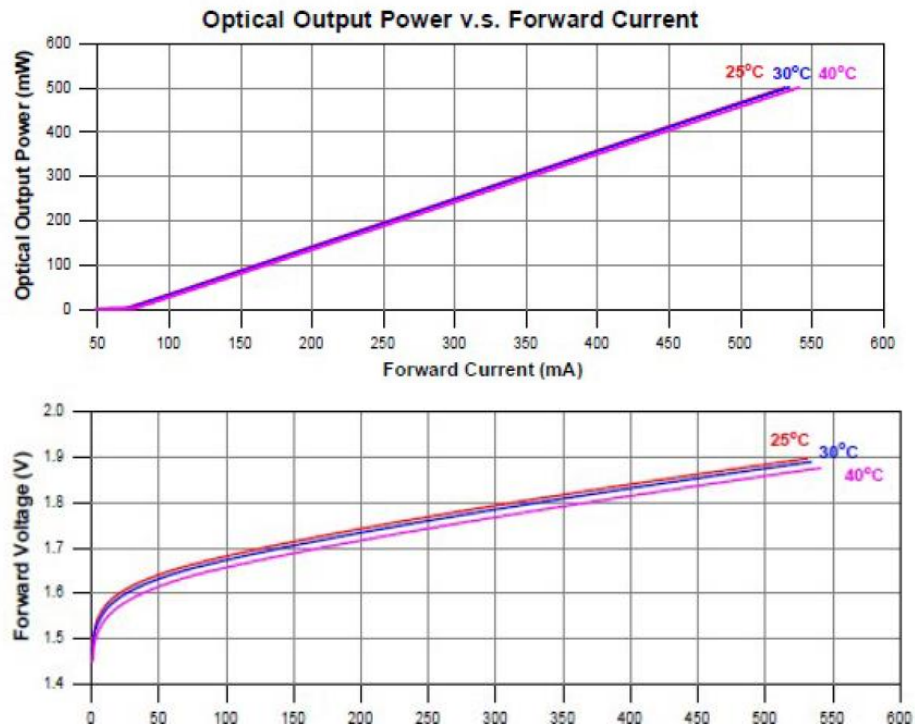


Figure 161: Specifications of the 808 nm infrared laser pump diode used in the experiments to frequency modulate a Vanadate-KTP microchip laser by applying stress

A.5. A prototype compressing a microchip laser crystal pair for frequency modulation

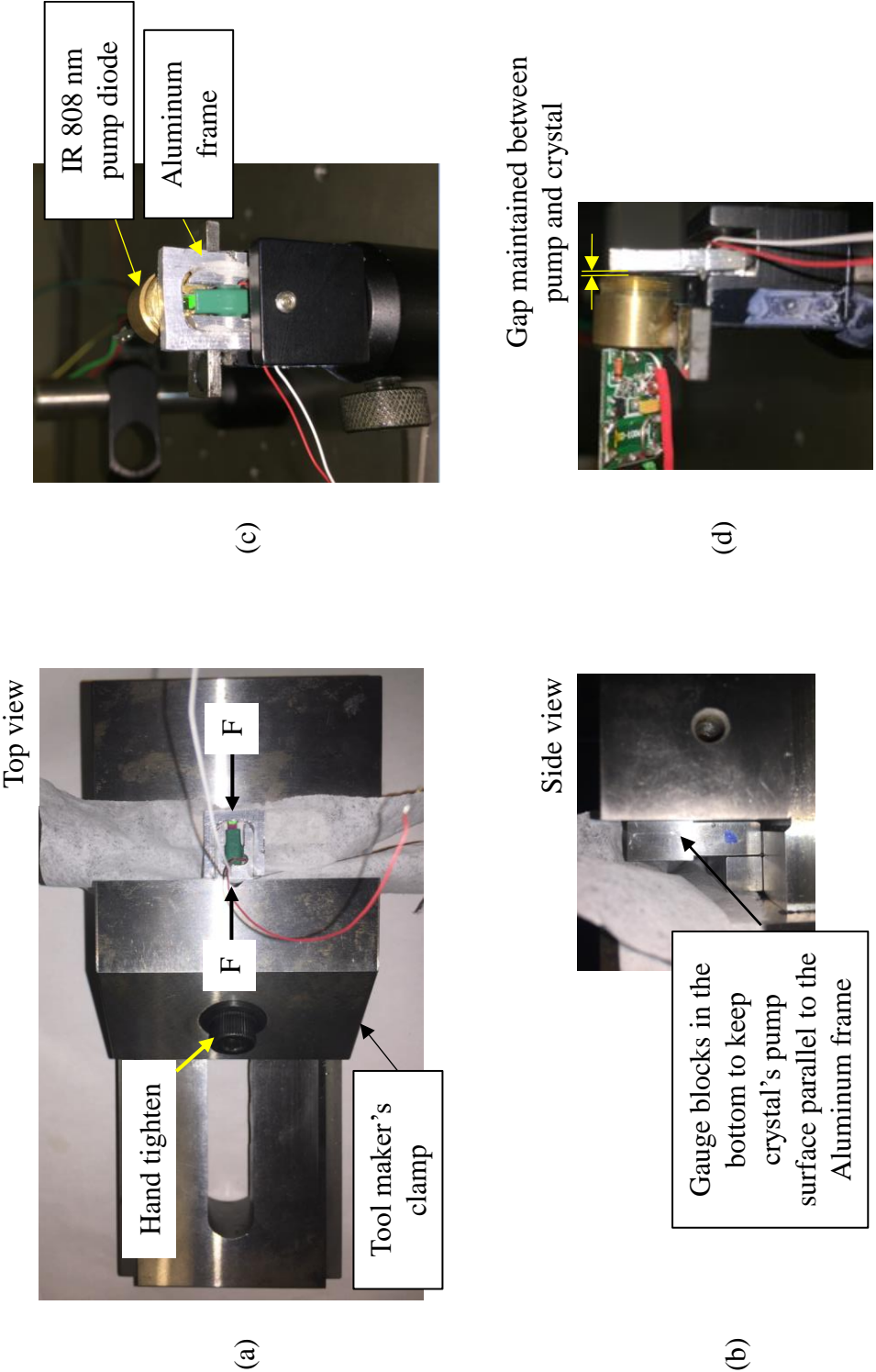


Figure 162: Prototype to compress the Vanadate-KTP crystal pair; (a), (b) preloading the prototype using a toolmaker's vice after epoxying the laser-piezo interface (c), (d) pictures showing the crystal pair pumped by the 808 nm laser from a handheld laser pointer

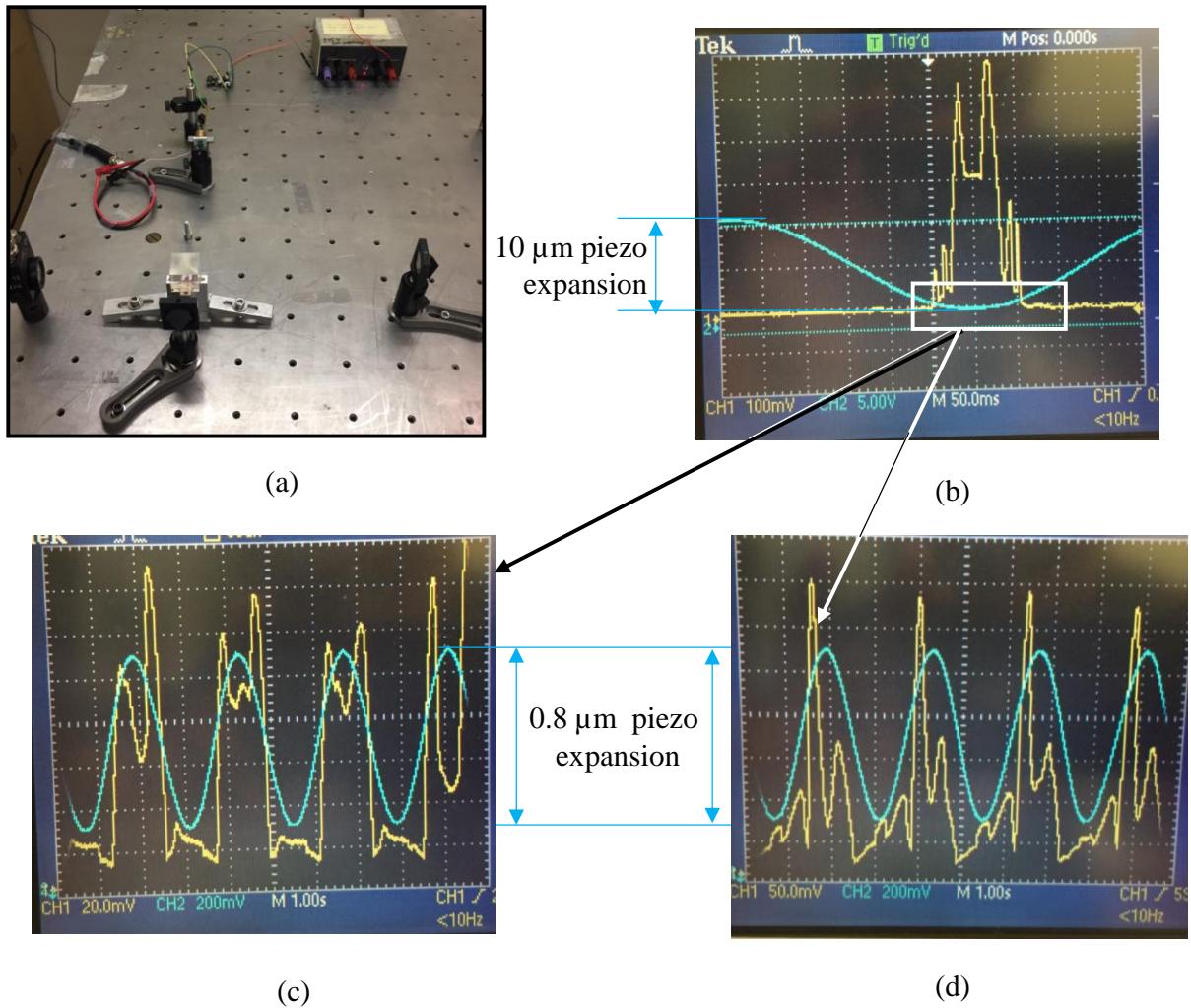


Figure 163: Experiment to observe the frequency modulation of the laser output; (a) Michelson interferometer to validate frequency modulation (b) Signal detected by the photodetector during the compression of the crystal pair with a 10 μm expansion of piezo (c), (d) localized modulation of piezo where the fringes occurred previously with the 10 μm expansion of piezo showing the non-repeatability

A.6. Design of flexure based crystal compressor

Dimensions of the notch hinges in the flexure used to compress the Vanadate-KTYP crystal pair is shown in Figure 164(a). From these values, the stiffness of a notch hinge made of Aluminum ($E = 70 \text{ GPa}$) can be calculated as,

$$k = \frac{2Ebt^{5/2}}{9\pi a_x^{1/2}} = 3.39 \text{ Nm}^{-1}$$

A finite element simulation of the flexure mechanism shows a displacement of $16 \text{ }\mu\text{m}$ for a 1 N simulated force, see Figure 164(b). Therefore, the fine element estimate of the stiffness of the mechanism is, $k_{FEA} = 62.5 \text{ kN} \cdot \text{m}^{-1}$

The natural frequency of the mechanisms can be theoretically determined by calculating the kinetic and potential energy. Figure 164(c) shows the top symmetric half of the mechanism, where the link A and C only translates, and link B translates and rotates. Therefore, the kinetic energy,

$$T = \frac{1}{2}m_A\dot{q}_A^2 + \frac{1}{2}I_C'\dot{\theta}_C^2 + \frac{1}{2}m_B\dot{q}_B^2 + \frac{1}{2}I_B\dot{\theta}_B^2$$

where,

$$I_B = \frac{m_B l_B^2}{12} \text{ and } I_C = \frac{m_C l_c^2}{12} \text{ are the second moment of mass of links B and C}$$

m_A , m_B and m_C are the masses of links A, B and C

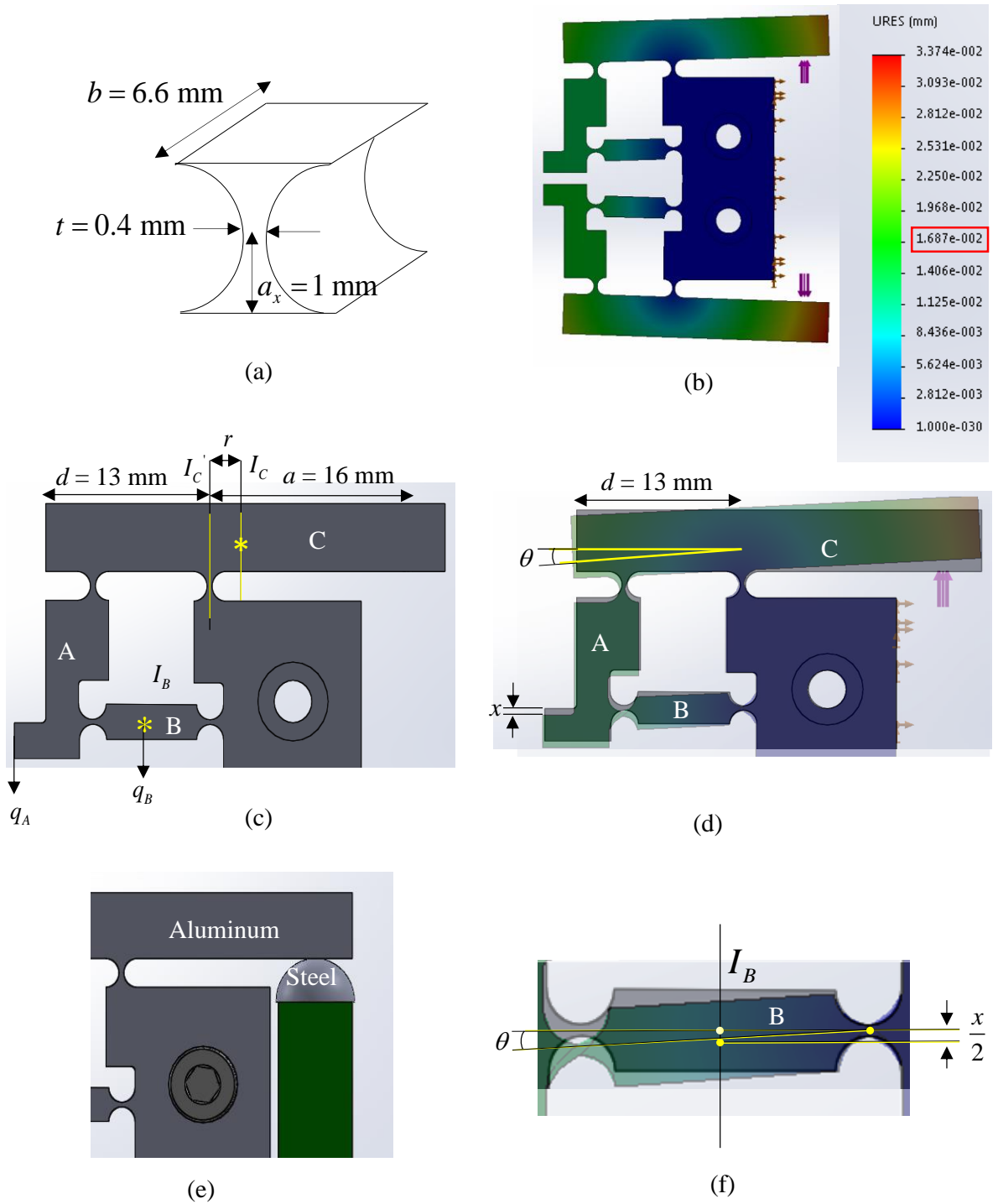


Figure 164: Design of the notch hinge flexure to compress the crystal pair; (a) dimension of the notch hinges used in the mechanism (b) Finite element analysis of the mechanism (c) dimensions of the lever arm and the dependent degrees of freedom (d),(f) Motion of the mechanism showing the angular and linear deflections

From Figure 164 (c),(d) and (e), it can be seen that $\dot{q}_A = \dot{x}$, $\dot{\theta}_C = \dot{\theta}_B = \frac{\dot{x}}{d}$, $\dot{q}_B = \frac{\dot{x}}{2}$, making

$$T = \frac{1}{2}m_A\dot{x}^2 + \frac{1}{2}I_C'\left(\frac{\dot{x}}{d}\right)^2 + \frac{1}{2}m_B\left(\frac{\dot{x}}{2}\right)^2 + \frac{1}{2}I_B\left(\frac{\dot{x}}{d}\right)^2$$

and from the parallel axis theorem, the second moment of mass at the middle of link C (shown with an asterisk in Figure 164(c) is given by, $I_C' = I_C + m_C r^2$, with $r = 2.54$ mm, making

$$T = \frac{1}{2}\left[m_A + \frac{I_C + m_C r^2}{d^2} + \frac{m_B}{4} + \frac{I_B}{d^2}\right]\dot{x}^2 = \frac{1}{2}m_{eq}\dot{x}^2$$

The equivalent mass is calculated to be, $m_{eq} = 0.0026$ kg .

Potential energy of the notch springs and the piezo actuator is given by,

$$V = \frac{1}{2}(k_1 + k_2 + k_3 + k_4)\left(\frac{q}{b}\right)^2 + \frac{1}{2}k_{piezo}\left(\frac{q}{n}\right)^2$$

where,

$k_1 = k_2 = k_3 = k_4 = k$ is the stiffness of a notch hinge,

$k_p = \frac{E_p b_p t_p}{l_p} = 0.12 \text{ GNm}^{-1}$ is the stiffness of the piezo actuator, with

$E_p = 63 \text{ GPa}$, $b_p = 6 \text{ mm}$, $t_p = 6 \text{ mm}$, $l_p = 19 \text{ mm}$, and

$n = d / a$ is the lever ratio.

$$V = \frac{1}{2}k\left(\frac{x}{d}\right)^2 + \frac{1}{2}k_{piezo}\left(\frac{a}{d}x\right)^2$$

Using Lagrangian,

$$\frac{d}{dt}\left(\frac{\partial T}{\partial \dot{x}}\right) + \left(\frac{\partial V}{\partial x}\right) = 0$$

$$m_{eq}\ddot{x} + \left(\frac{k}{d^2} + \left(\frac{a}{d}\right)^2 k_{piezo}\right)x = 0$$

Theoretical stiffness of the mechanism is $k_{th,withpiezo} = \left(\frac{k}{d} + \frac{a}{d}k_{piezo}\right) = 0.17 \text{ GN} \cdot \text{m}^{-1}$.

To compare with the FEA estimation of the stiffness of the mechanism, $k_{FEA} = 62.5 \text{ kN} \cdot \text{m}^{-1}$,

theoretical stiffness without the piezo is calculated to be $k_{theory} = \frac{k}{d} = 77 \text{ kN} \cdot \text{m}^{-1}$

From this, the natural frequency of the mechanism with the piezo actuator is calculated to be

$$f_n = \sqrt{\frac{k_{th,withpiezo}}{m_{eq}}} = 260 \text{ kHz}$$

A.7. Spectrum of some of the commercially available lasers

Thorlabs
CPS532

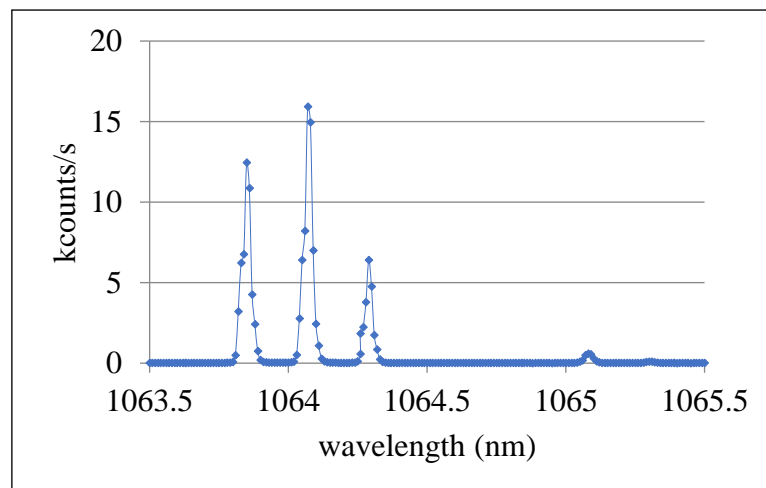
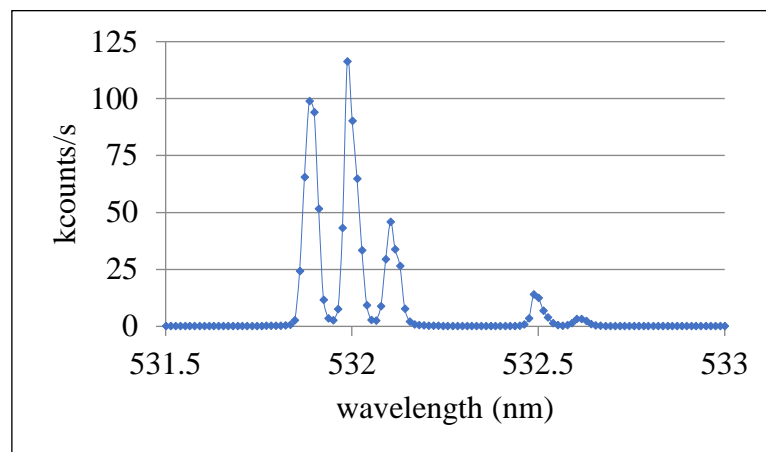


Figure 165: Spectrum of Thorlabs CPS532 green laser

Ebay- INDUSTRIAL/LAB 532nm 5mW 3.7-5V
Green Laser DOT Module Diode w/ Driver & Spring

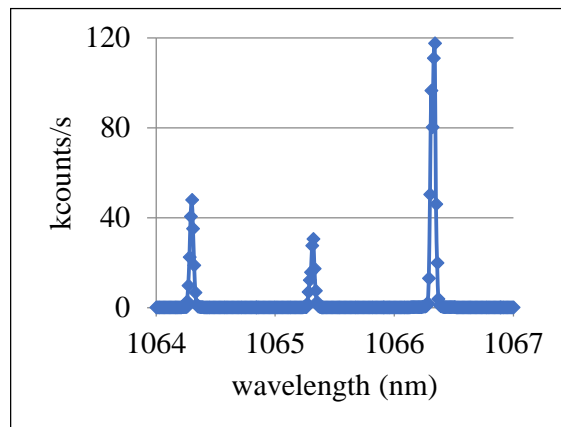
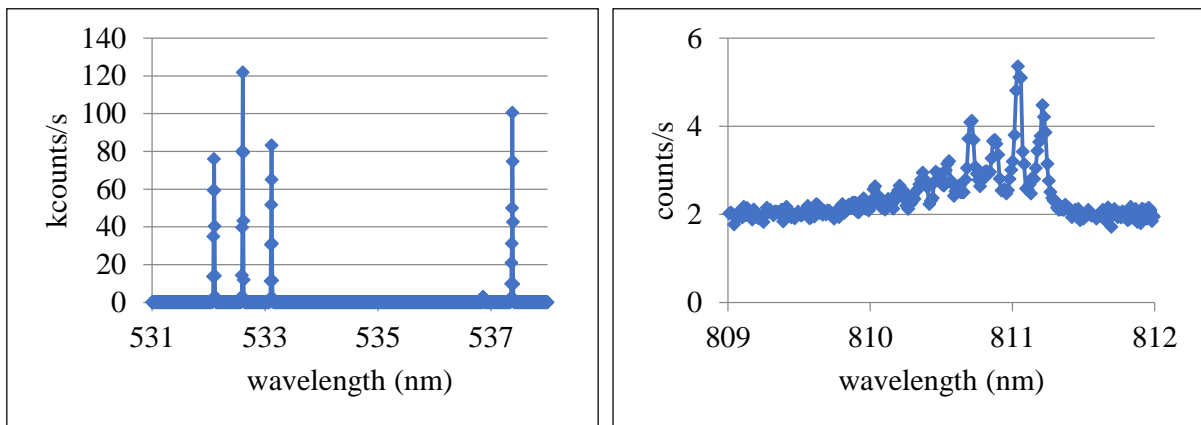


Figure 166: Spectrum of Ebay green laser

Sparkfun
COM-09906

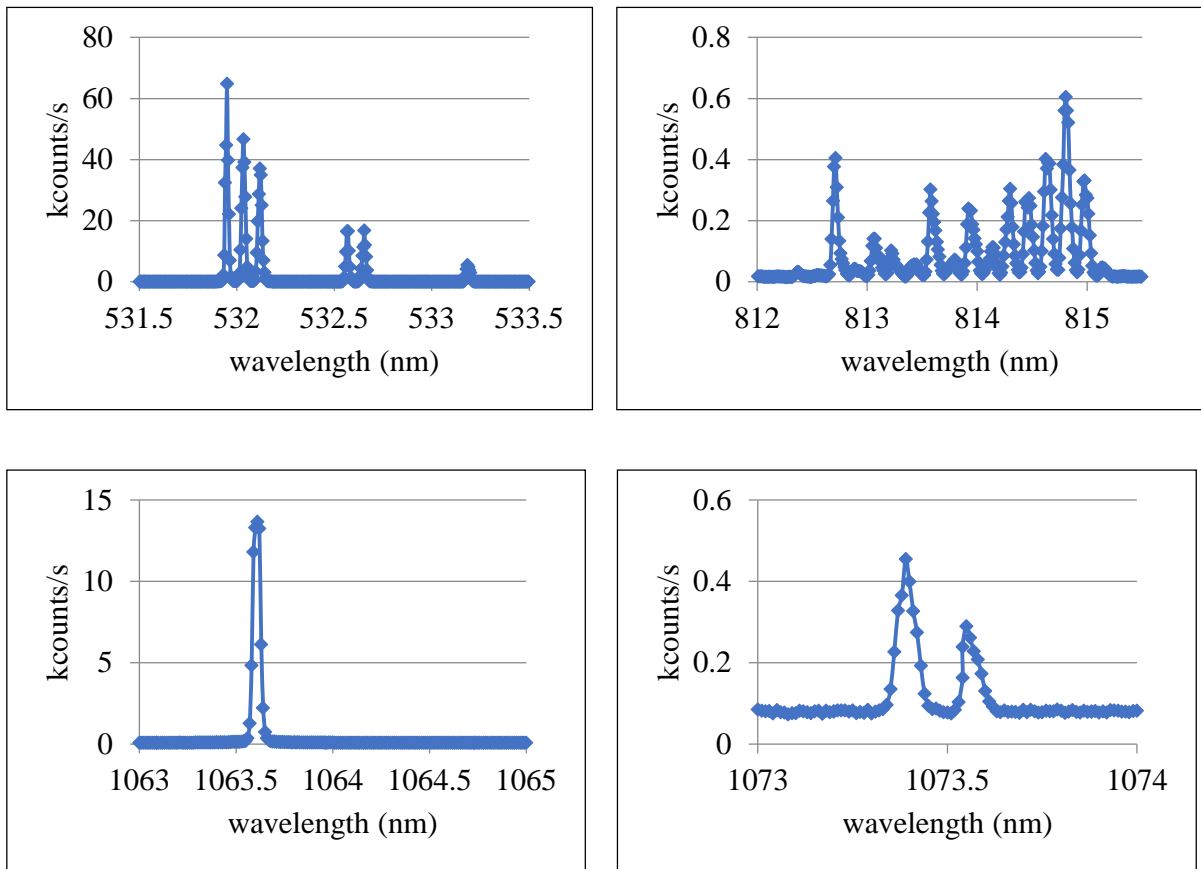


Figure 167 Spectrum of Sparkfun green laser

VLM-650-03-LPA

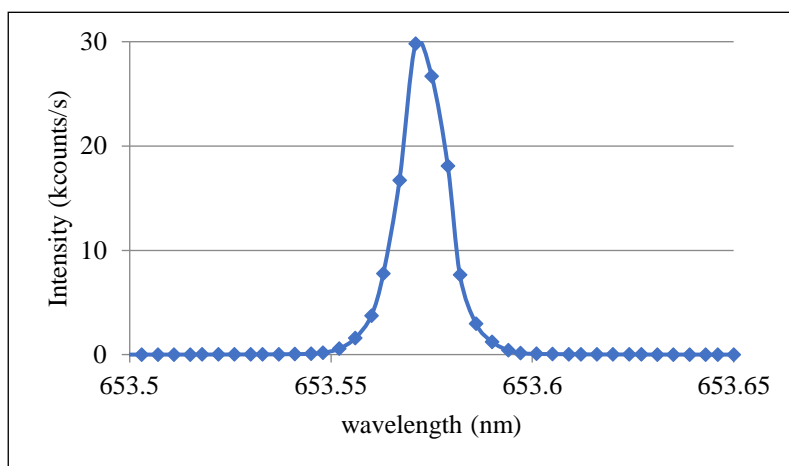
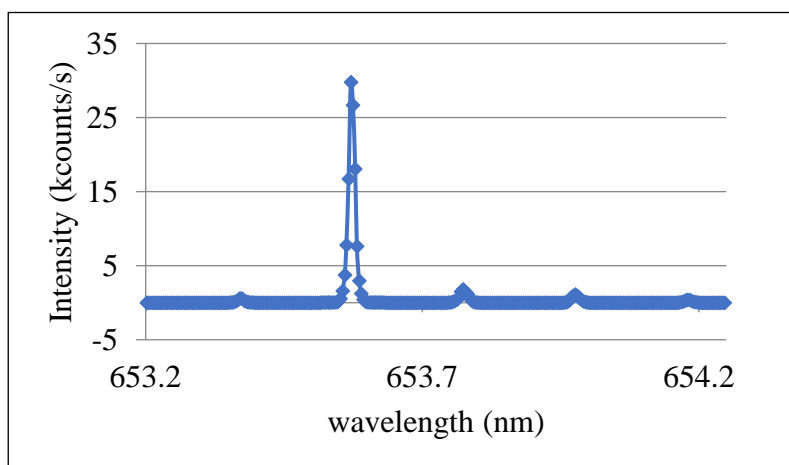


Figure 168: Spectrum of Quarton Inc. red laser

APPENDIX B

B.1 Procedure followed to build the first prototype

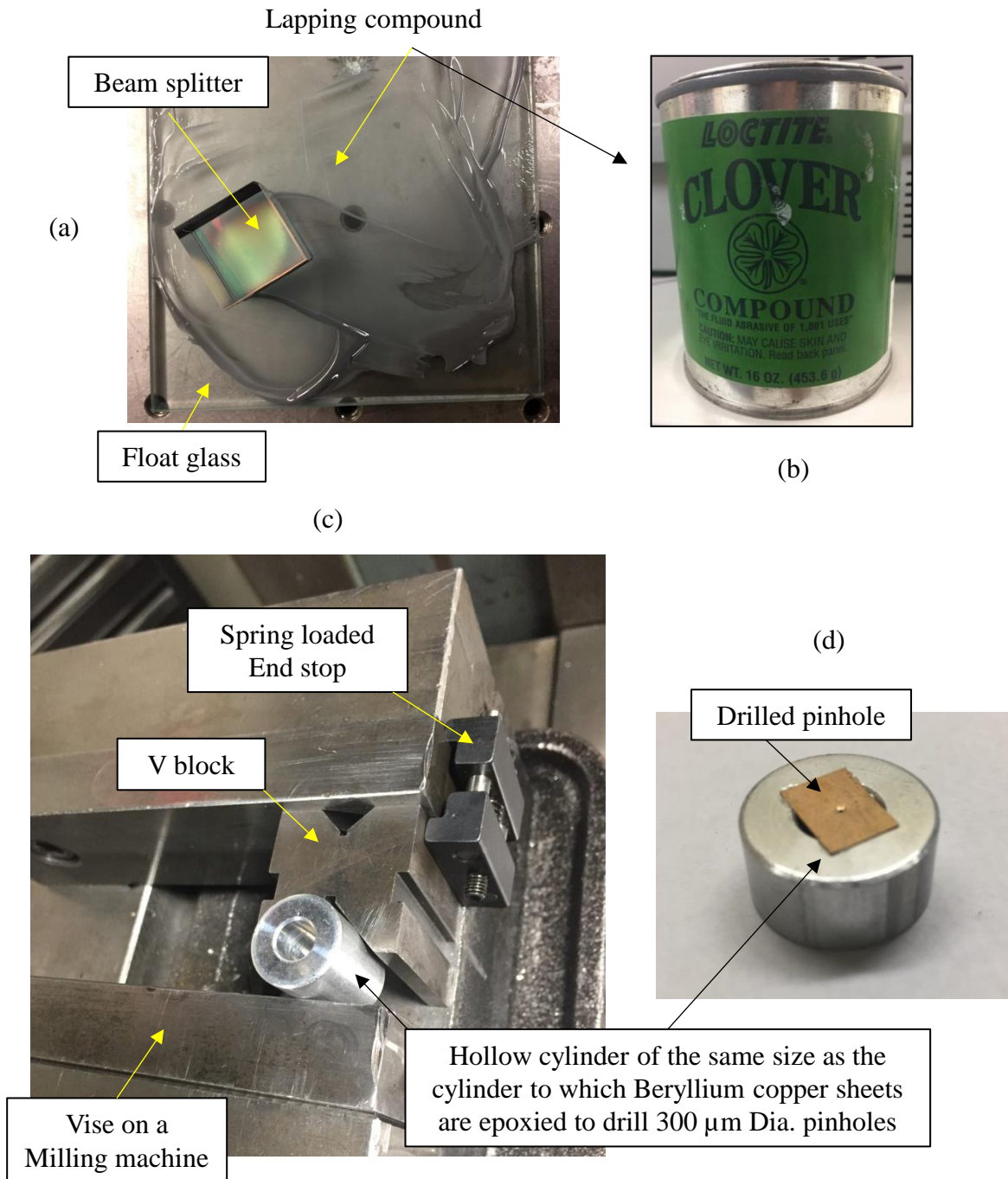


Figure 169: Lapping the beam splitter cube and drilling pinholes in a copper sheet; (a) Beam splitter being lapped on the surface of float glass which is typically very flat (b) Lapping compound used (c) Cylinder supported using a V block and the vise, and end stop to help the repeated manufacturing of pinholes by keeping the center of cylinders the same (d) Beryllium copper sheet of 0.1 mm epoxied on the cylinder and a 300 μm pinhole is drilled

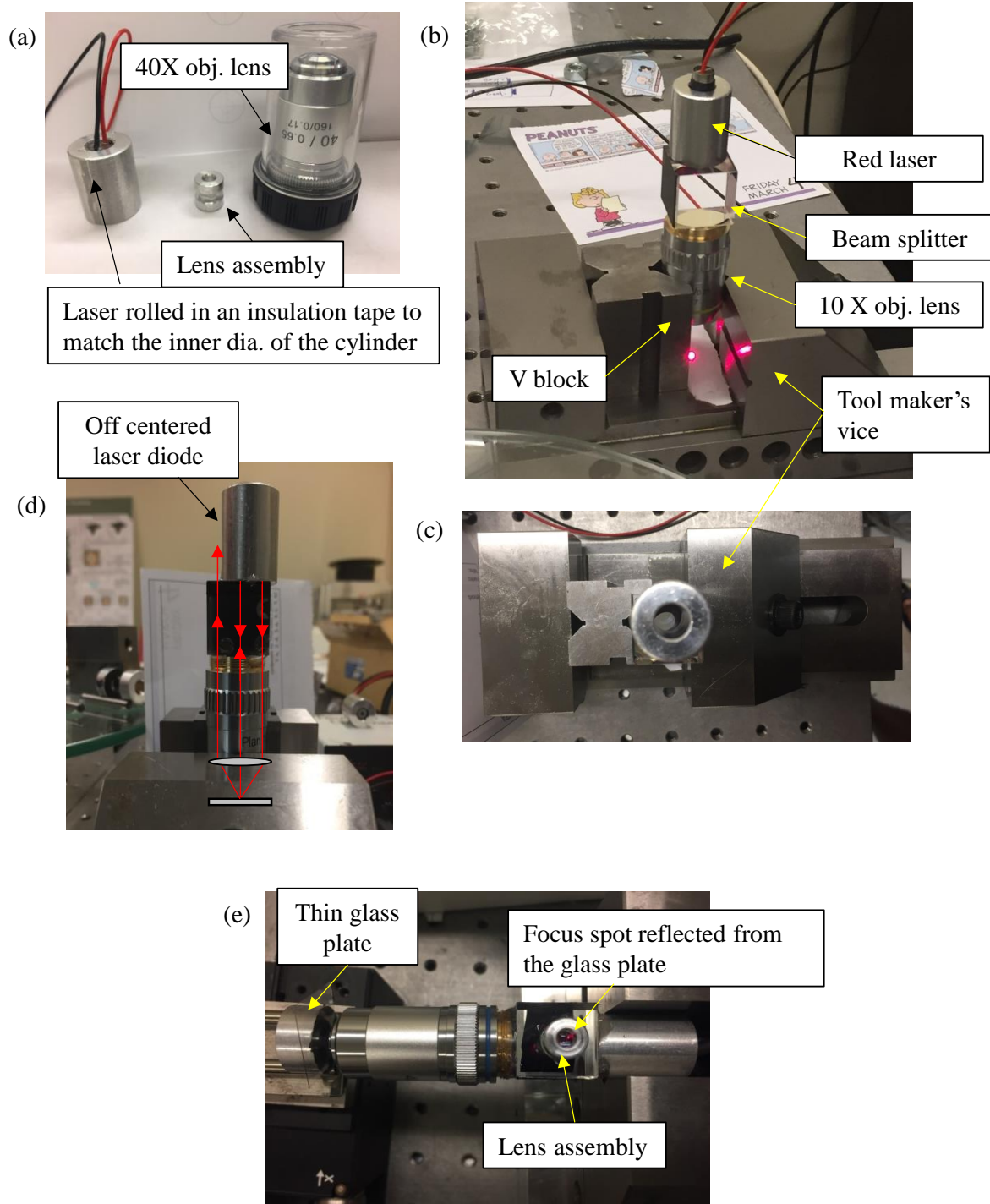


Figure 170: Fabrication of the first prototype; (a) Optical components used in the assembly (b, c) Laser, beam splitter and 40X objective lens aligned coaxially and epoxied (d) in the previous prototype using the 20X objective lens, the laser was offsetted so that the back reflection from the sample surface does not cause instability in the laser. This idea was dropped later because the entrance aperture of 40X objective lens smaller than the 20X objective (e) Lens assembly on the detector side showing the focused light spot due to the back collimated light from the sample glass plate when it is at focus

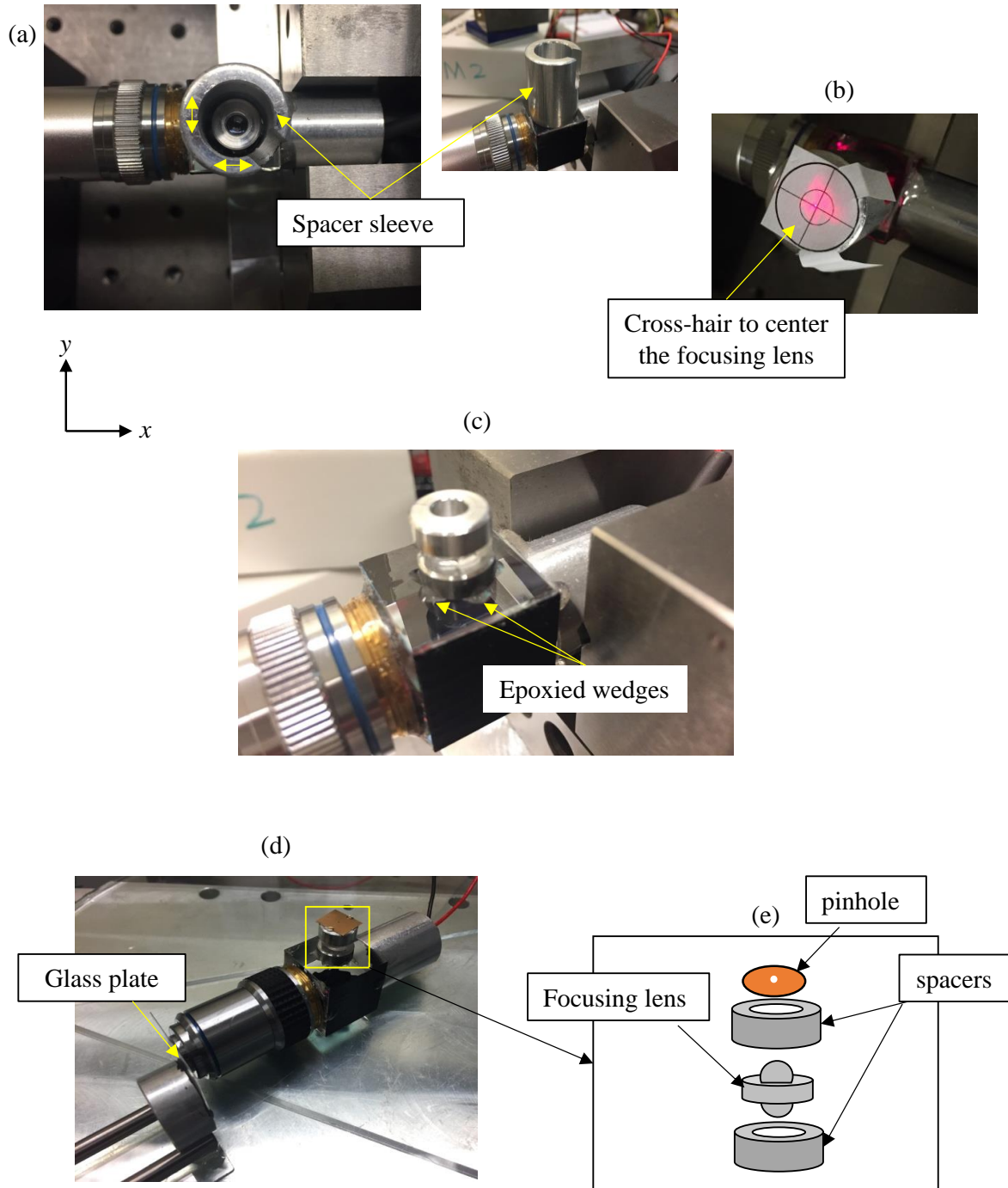


Figure 171: Alignment of the pinhole with respect to the focused spot at the detector end of the confocal probe; (a) A cylindrical sleeve around the thin lens assembly is translated in xy plane so that the lens assembly is coaxial with the cylindrical sleeve (b) verified using a cross hair (c) once centered, the lens assembly is epoxied carefully using a toothpick without disturbing it (d) Pinhole 1 epoxied on top of the lens assembly (e) Schematic of the lens assembly

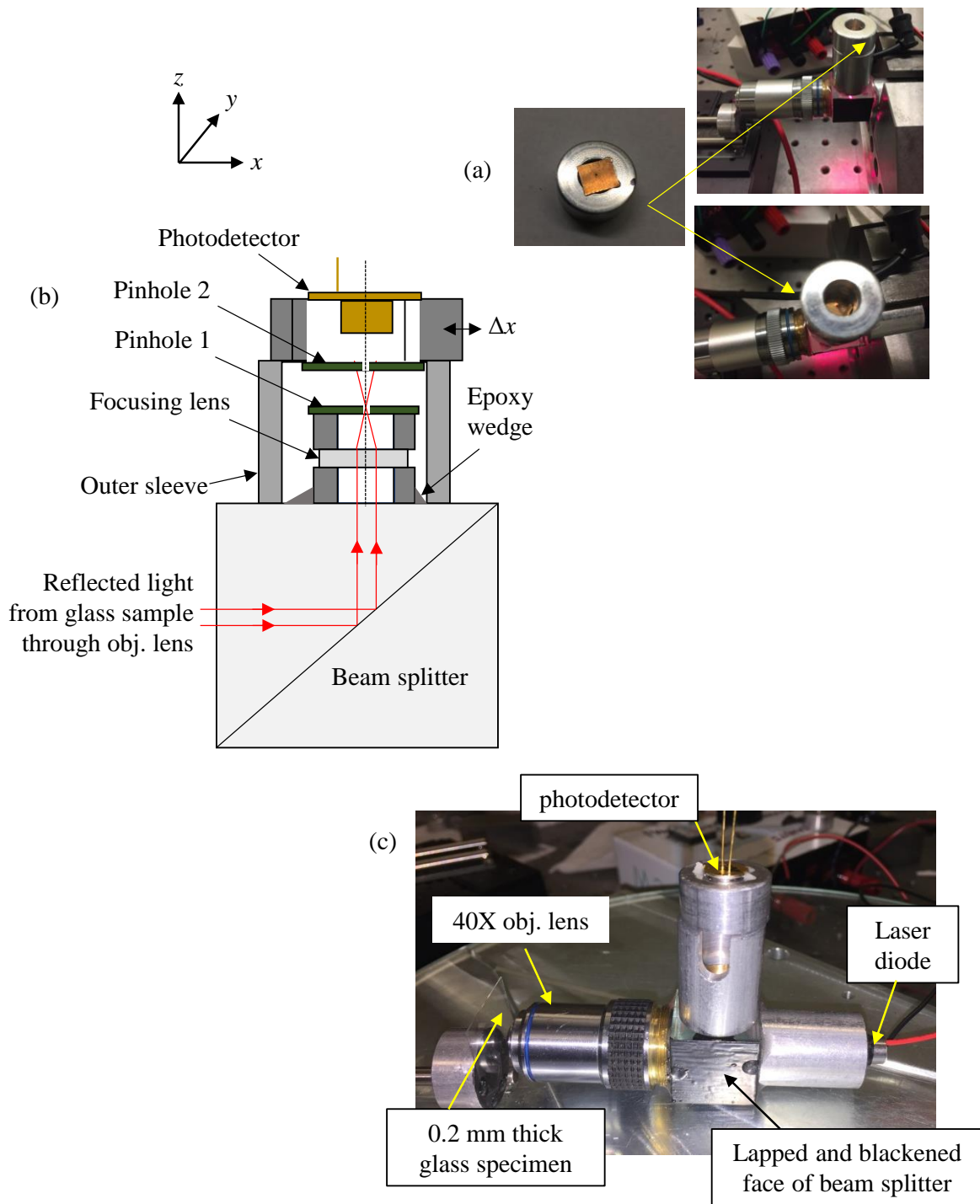
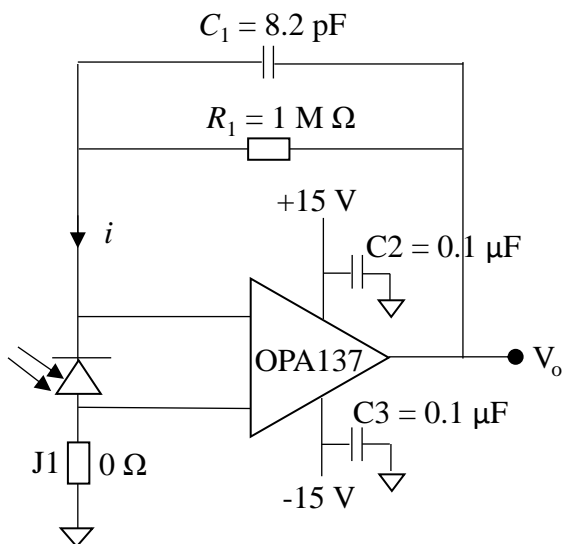


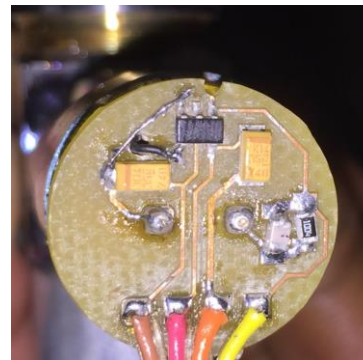
Figure 172: Fabricated prototype; (a) Pinhole 2 (300 μm Dia.) drilled earlier is translated in xy plane until the light transmits through it and then epoxied (b) Schematic of the assembly on the detector side (c) Because the casing of the photodetector is connected to its signal pin, its outer edge is covered with insulation tape and then inserted into the back of the cylinder with the Pinhole 2 and epoxied to complete the prototype

(a) Photovoltaic transimpedance amplifier

$$f_c = \frac{1}{2\pi R_1 C_1} \approx 20 \text{ kHz}$$

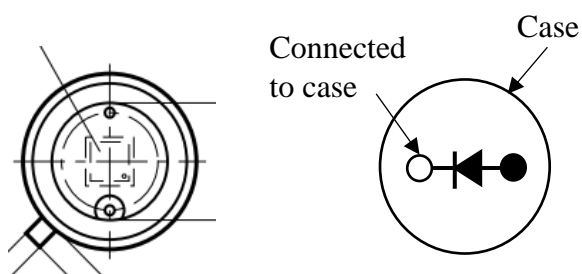


(b) 1st generation PCB

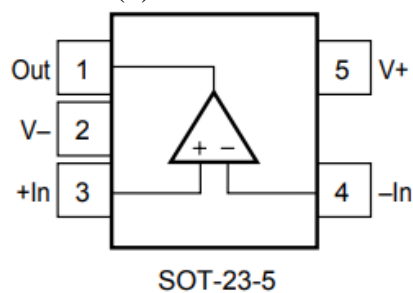


-15 +15 GND Vo

(c) photodetector model: BPX61



(d) OPA137



(e) 2nd generation PCB

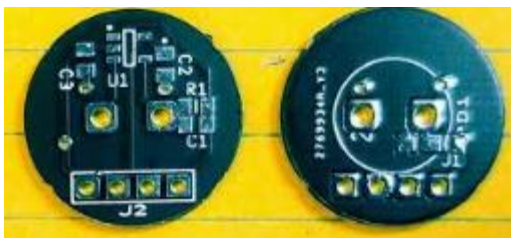


Figure 173: Circuit diagram of the photodetector amplifier; (a) with its cut-off frequency of 20 kHz (b) First generation PCB (c) schematic showing the cathode and anode of the photodetector (d) schematic of the operational amplifier (e) 2nd generation PCB with no modifications in the circuit

Picture courtesy: Osram, Texas instruments

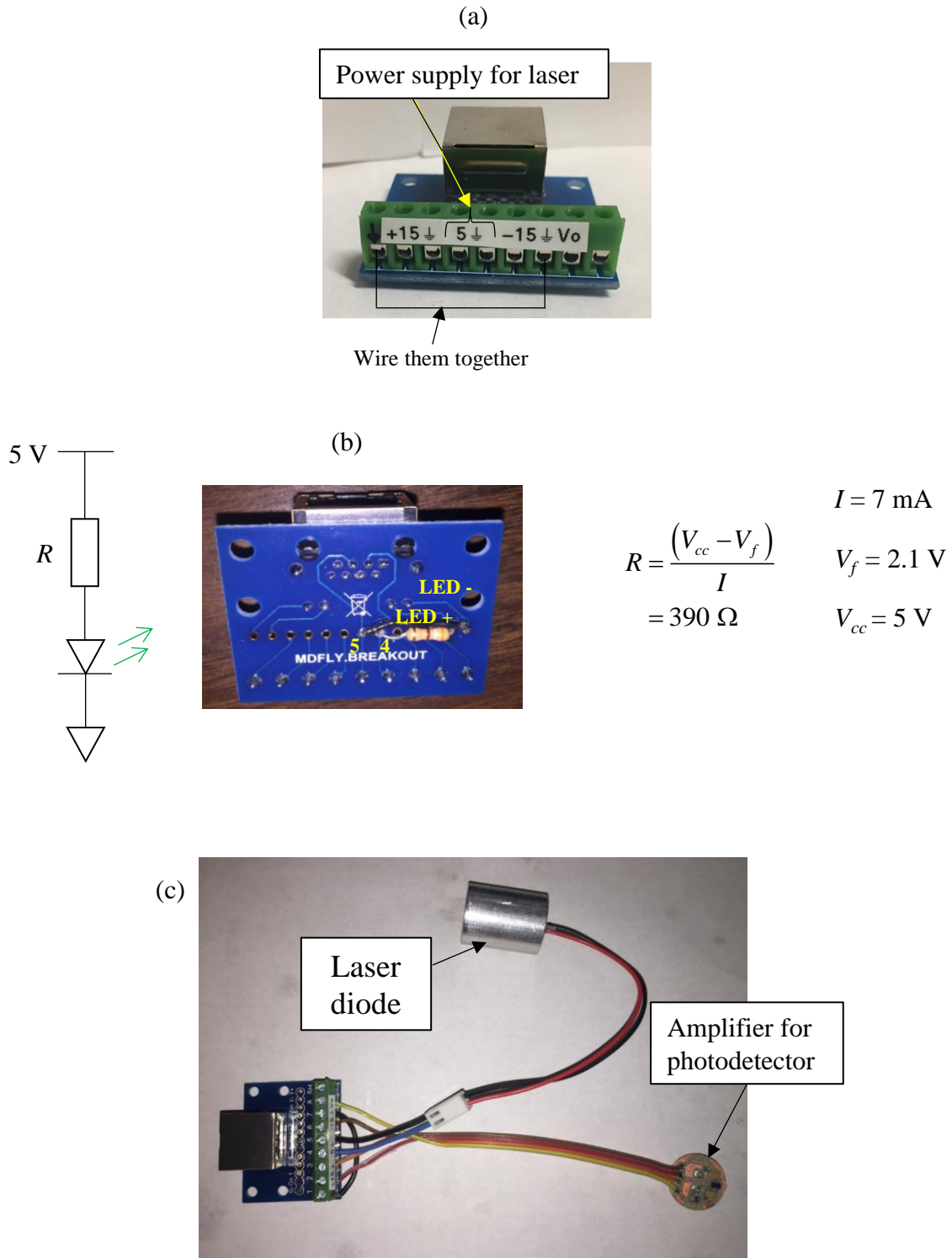


Figure 174: Ethernet connector breakout board used to power the laser, power and read the photodetector circuit using the myRIO; (a) photograph, (b) value of the resistor chosen according to the forward voltage and the current rating for the Green LED on the connector listed in the datasheet of Amphenol RJ45 modular jack, (c) laser diode and the photodetector circuit connected to the breakout board.

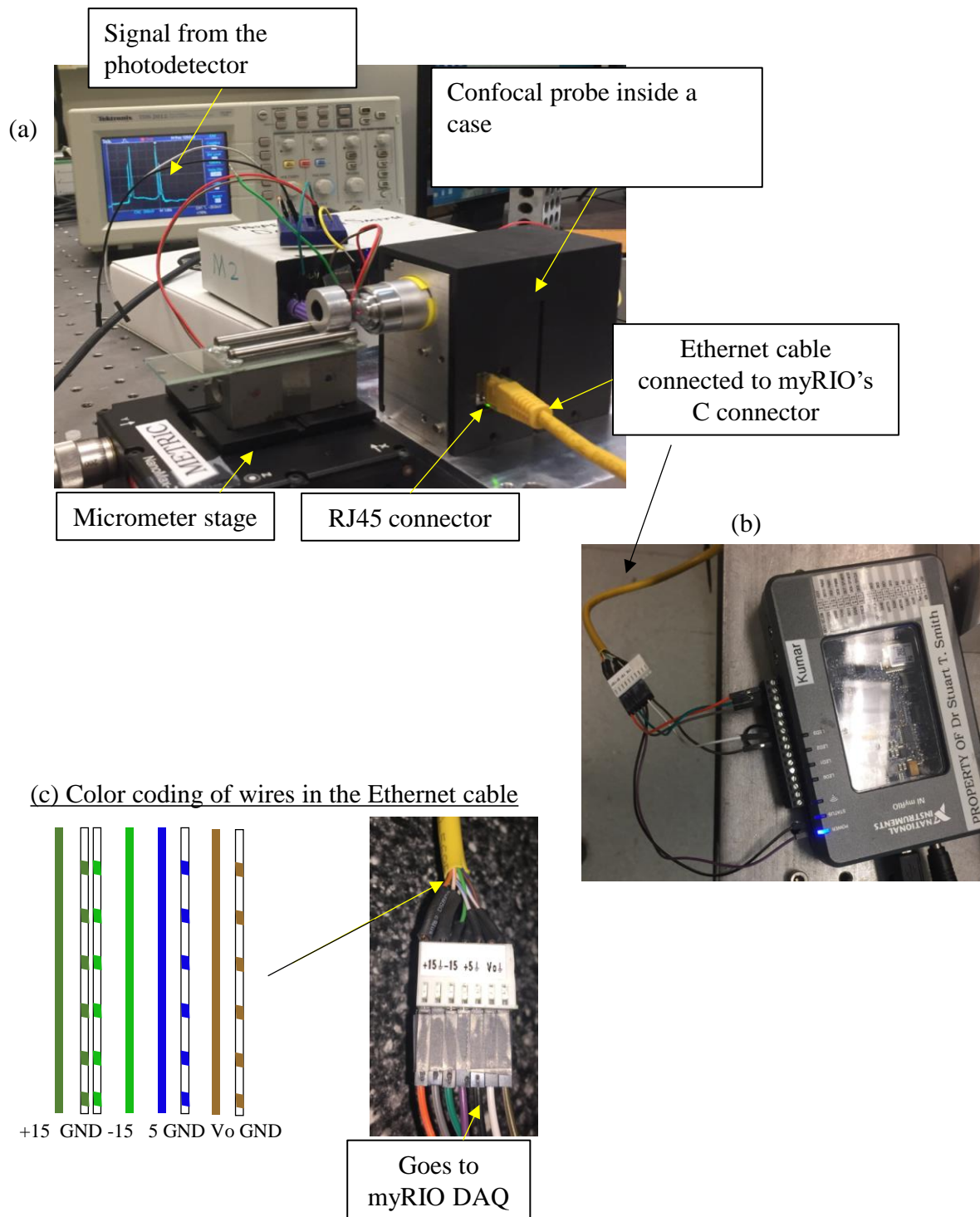


Figure 175: Intensity peaks measured using the first prototype; (a) Confocal probe being tested showing the two intensity peaks on the oscilloscope for the travel of the glass sample using a micrometer stage (b) Ethernet cable connected to the myRIO (c) Color coding of the wires in the Ethernet cable and the signals with respect to them

B.2 Spot size estimation of various light sources focused by 40X and 60X objective lenses

Section courtesy: Alex Caviness, Tara Newman

Figure 176 shows the experimental setup to determine the spot size of the light focused using an objective lens. The intensity profile at the focal point is given by the Gaussian function,

$$I(x) = a \exp\left(-\frac{(x-\mu)^2}{2\sigma^2}\right),$$

where, a is the intensity amplitude, μ is the position of the peak in x , and σ is the standard deviation.

The intensity measured by the photodetector when a razor blade is scanned at the focal plane is given by the integration of the Gaussian function with respect to the position of the razor blade in x axis. This integral is referred to as cumulative distribution function, and is related to the error function as,

$$F(x) = \frac{\left[\operatorname{erf}\left(\frac{(x-\mu)}{\sigma\sqrt{2}}\right) + 1 \right]}{2}.$$

Following equation can be used to fit to the intensity measured by the photodetector when a razor blade is scanned during the experiment.

$$A \cdot \operatorname{erf}\left(\frac{(x-b)}{c}\right) + d$$

From the fit, spot size at the beam waist (FWHM) is given by $2\sigma\sqrt{2\ln 2}$.

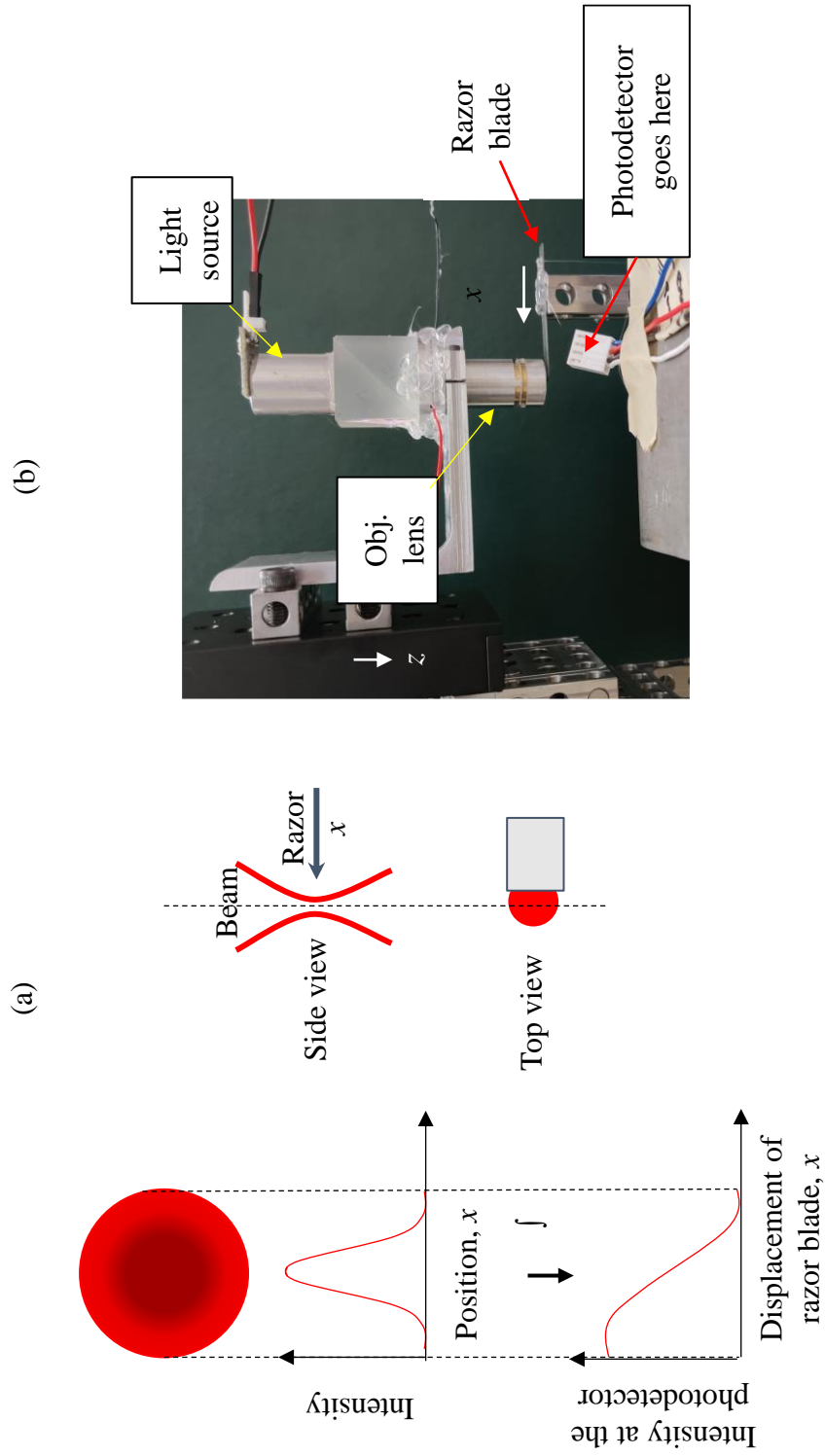


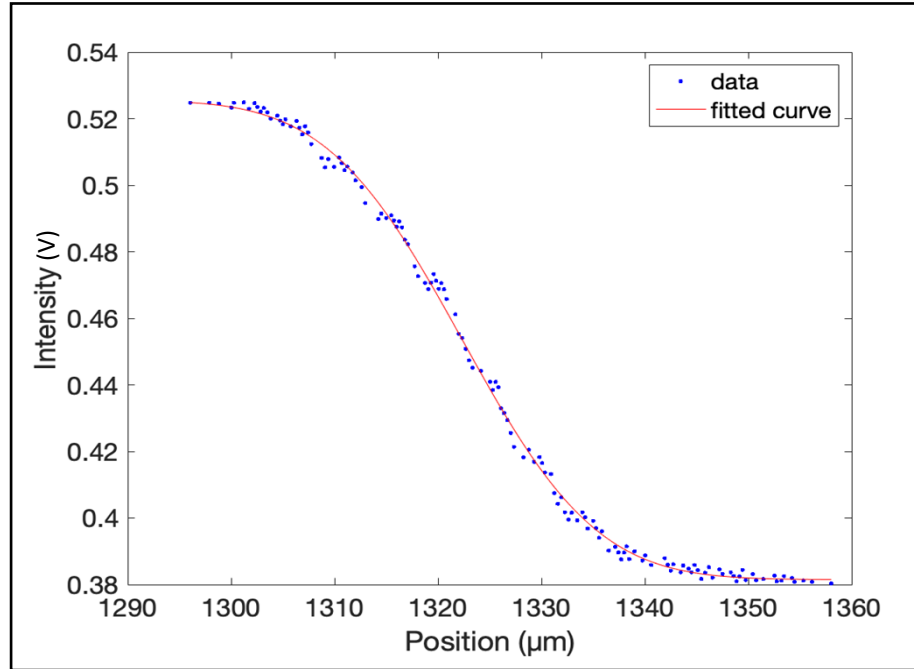
Figure 176: Experimental facility to estimate the spot size of the converging beam from an objective lens; (a) Schematic showing the intensity across the cross section of a focused light beam, and the intensity observed by the photodetector when a razor blade is run across the beam, which is given by the integration of the former (b) Experimental setup showing the probe attached to a micrometer to translate vertically to get waist of the focused beam to the plane of razor blade

Figure 177(a) shows the intensity measured by the photodetector when the razor blade is translated in x axis, when a red mLED source is focused using the 40X objective lens. An erf function is fit to the data to calculate the value of FWHM. The FWHM values calculated at each z height by moving the objective lens by the micrometer is shown in

Figure 177(b), and the lowest value corresponds to the beam waist, representing the spot size of the focused beam. In this case, it is 31 μm .

Figure 178 shows the some of the objective lens - light source combinations experimented to determine their spot sizes, and Figure 179(a and b) shows the intensity measured and normalized during the experiments. Figure 179(c) lists all the objective lens - light source combinations used and the calculated spot size values. From these results, 60X objective lens yields the smallest value of 19 μm .

(a)



(b)

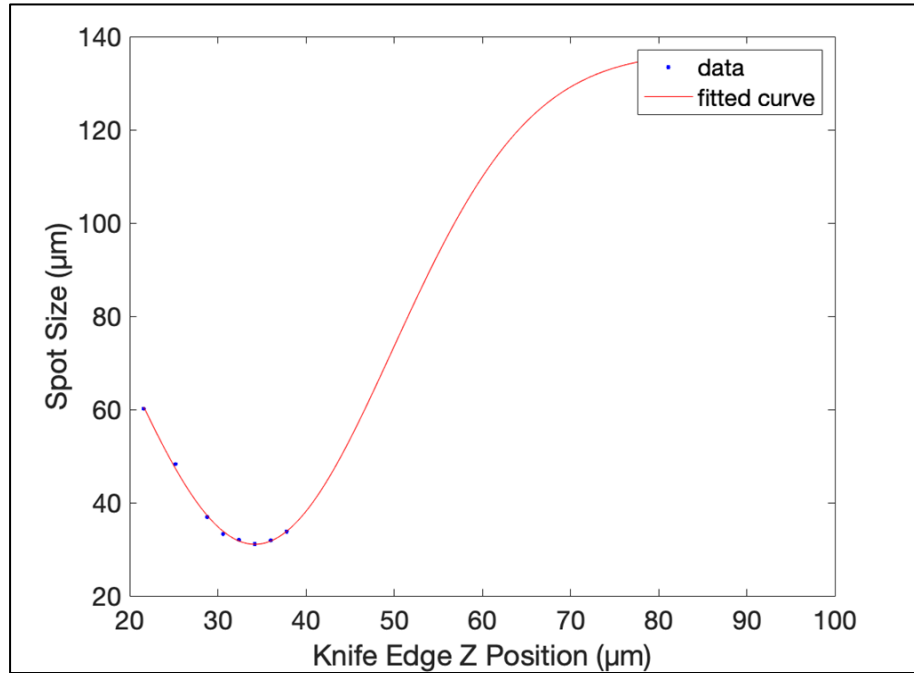


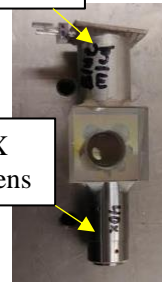
Figure 177: Erf function fit to the measurement results; (a) Intensity measured as a function of the translation of razor blade in x axis (b) Spot size calculated from experiments at each z heights to iteratively arrive at the waist of the beam.

AmScope,
A40X-V300



Blue mLED

40X
obj. lens



AmScope,
A60X-V300



Lens assembly taken
from a 60X obj. lens



Blue mLED

Disc coupling
flexure housing

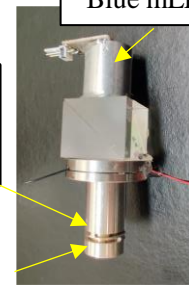
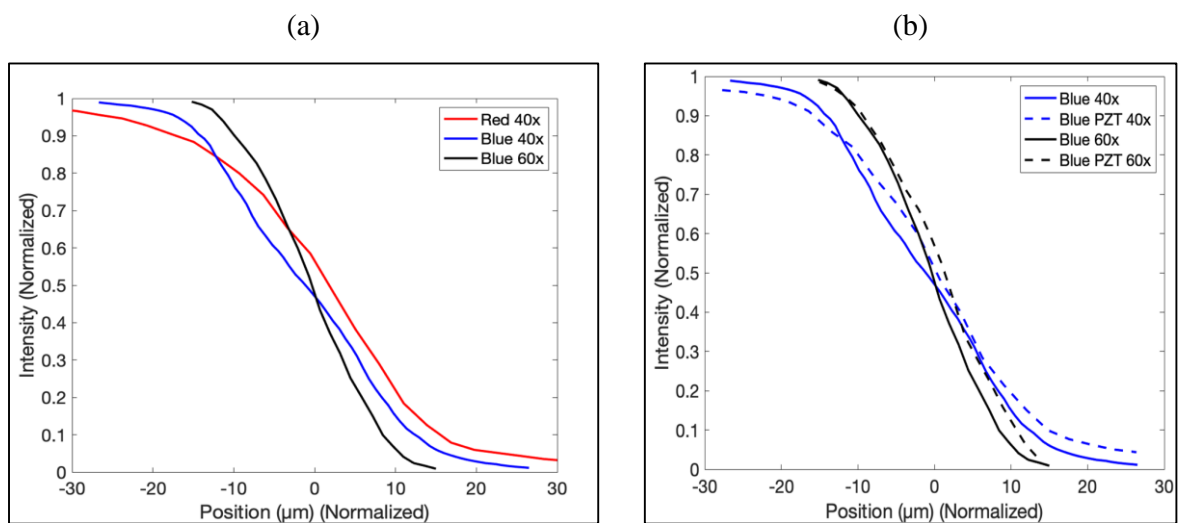


Figure 178: Some of the light source - objective lens combinations used in the experiments



(c)

Light source	Focusing lens	Numerical Aperture	Spot size
Red laser	40x Obj	0.65	290 μm
Red mLED	40x Obj	0.65	31 μm
Blue mLED	40x Obj	0.65	25 μm
Blue mLED	40x Obj, and piezo inside Flexure housing	0.65	24 μm
Blue mLED	60x Obj, and piezo inside Flexure housing	0.85	19 μm

Figure 179: Spot size estimates of various objective lens- light source combinations; (a, b) Intensity measured and normalized (c) table listing the combinations and the calculated spot size.

B.3 Procedure followed to build the second prototype

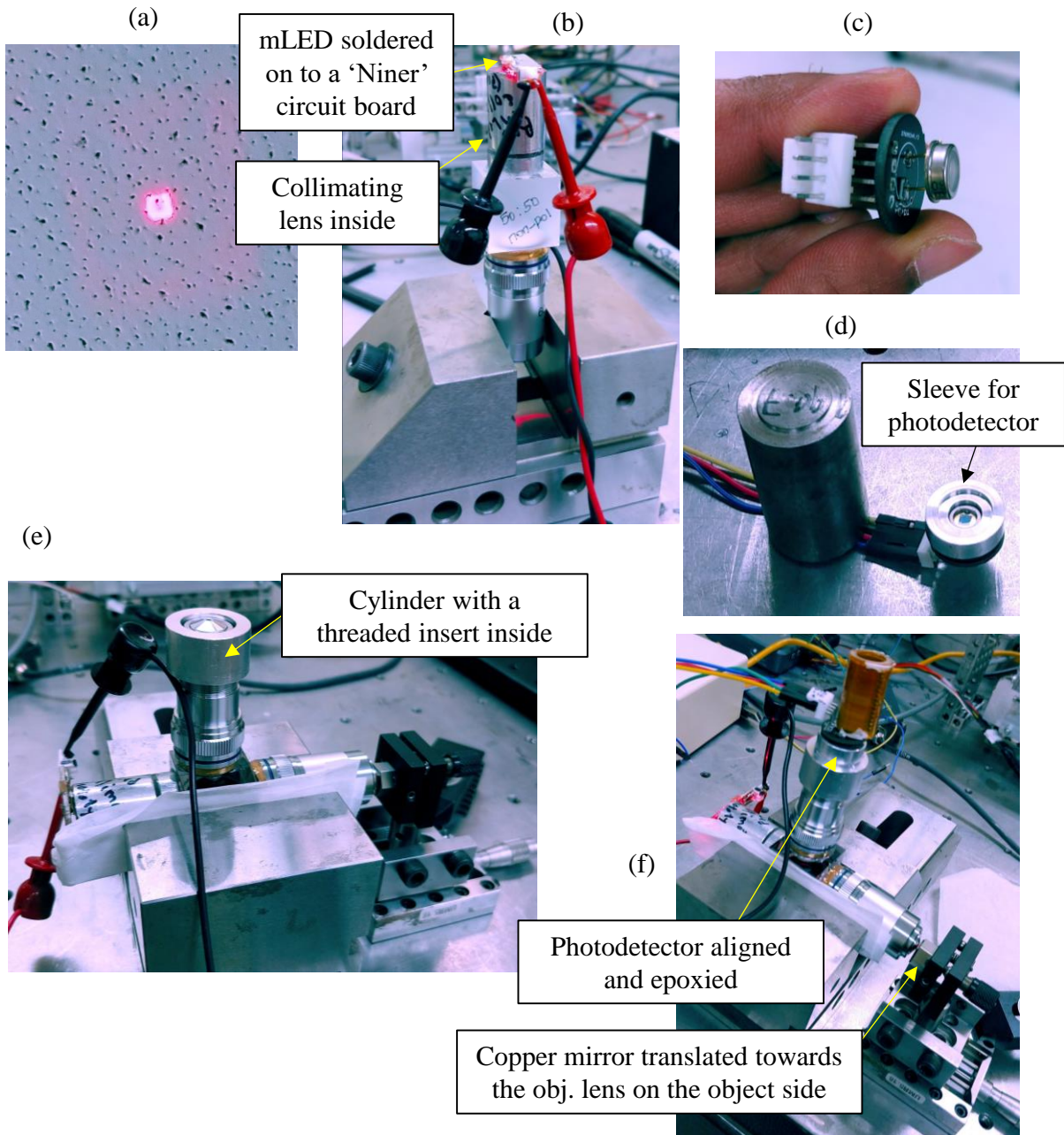


Figure 180: Build of the second prototype that uses a Red mLED; (a) Red mLED after being collimated showing the square shape of the LED source (b) after centering and epoxying it to the beam splitter and the objective lens (c) Photodetector soldered to the second generation PCV (d) Photodetector attached to its sleeve (e) Cylinder to which a threaded insert is epoxied is spun around the objective lens on the detector side. This cylinder provides a datum to translate and epoxy the photodetector sleeve, and the threaded insert is a component of a commercial objective lens (d) Photodetector is attached above the objective lens on the detector side

B.4 An earlier prototype of pinhole alignment mechanism

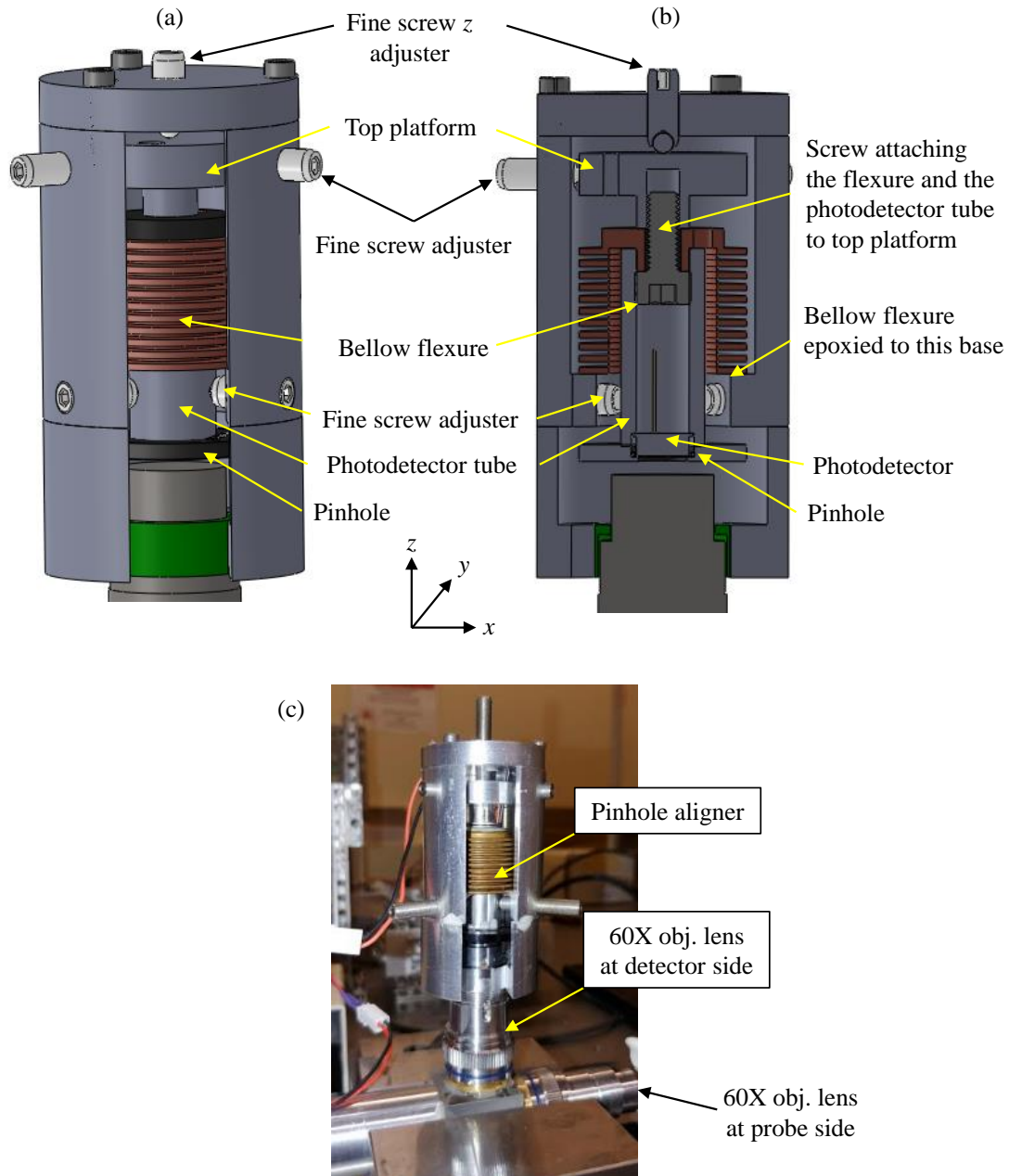


Figure 181: An earlier prototype of the pinhole alignment mechanism using a bellow flexure;

(a, b) Solid models showing the front and cross sectional view of a pinhole alignment mechanism, where the pinhole and the photodiode are attached to a cylinder that hangs from the top platform of a bellow flexure. The bottom of the flexure is epoxied to a fixed base. The platform and the cylinder are pushed using fine screws to provide translate and tip and tilt the pinhole in x , y . The platform is also pushed by a fine screw from the top translate the pinhole in z to get it to the focal point of the 60X objective at the detector side (c) Fabricate prototype with which alignment could not be achieved because we do not know the location of the focused beam to initiate the alignment due to the absence of line of sight.

B.5 Procedure followed to build the third prototype with and without the tip-tilt

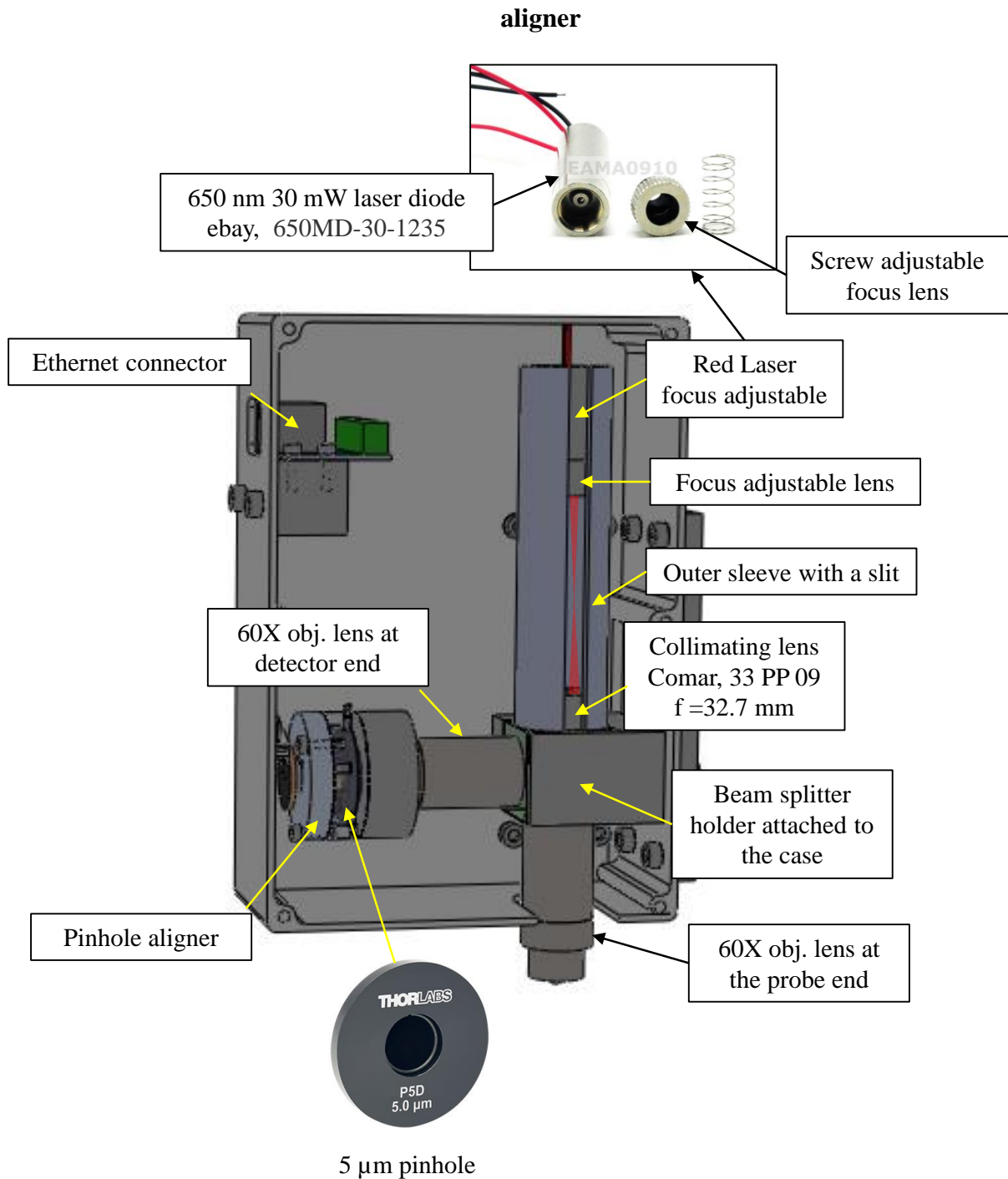


Figure 182: Solid model of the fabricated prototype that uses a focus adjustable red laser, a collimating lens, and a pinhole alignment mechanism

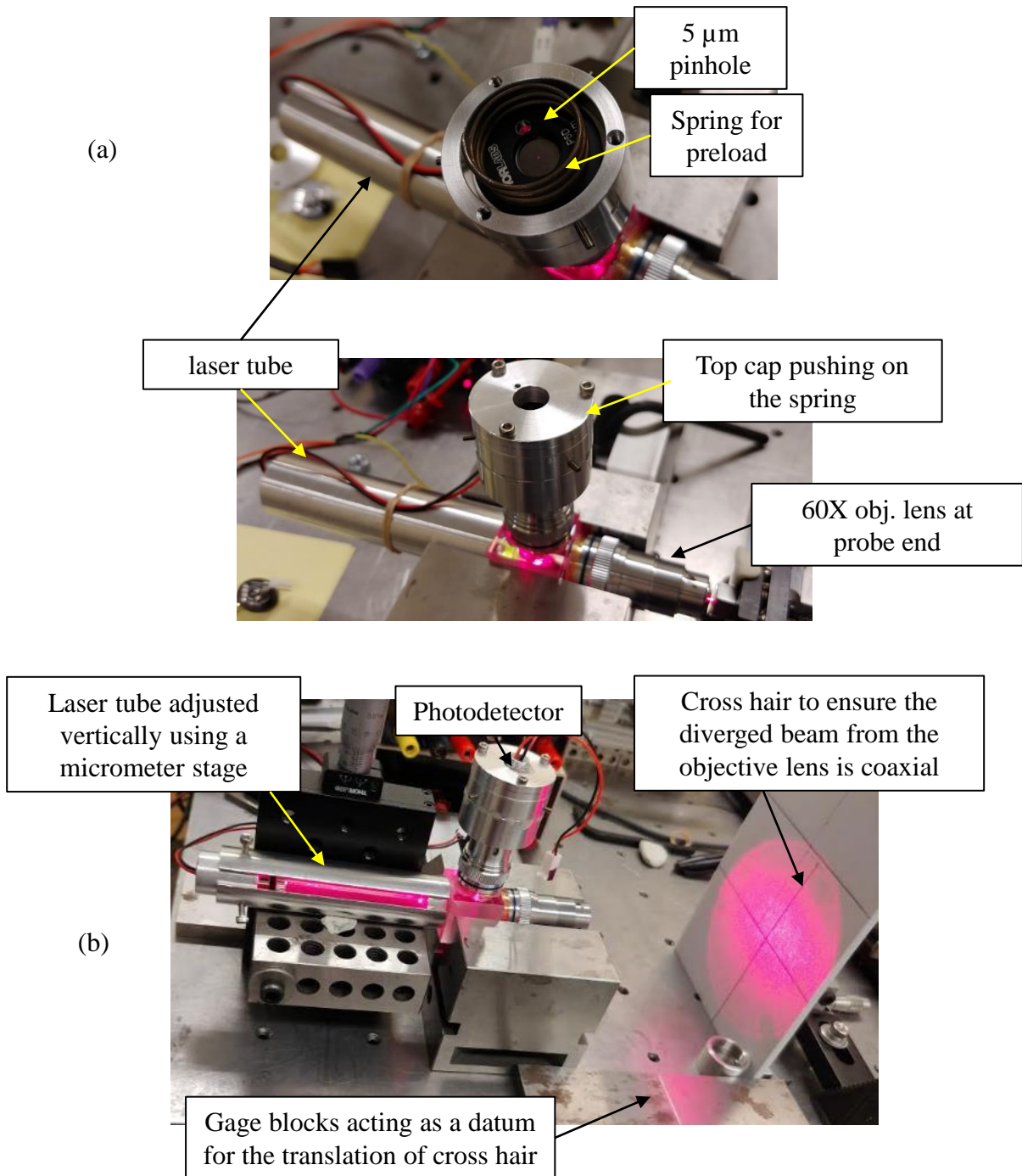


Figure 183: Building procedure of a prototype that do not use a tip-tilt aligner; (a, b) 5 μm pinhole and a preload spring (Century springs, H-37CS, 210 N.m⁻¹) inside the casing of the pinhole alignment mechanism, laser tube containing the collimating lens (c) The laser tube translated vertically using a micrometer stage so that the laser is aligned coaxial to the 60X objective lens at the object side

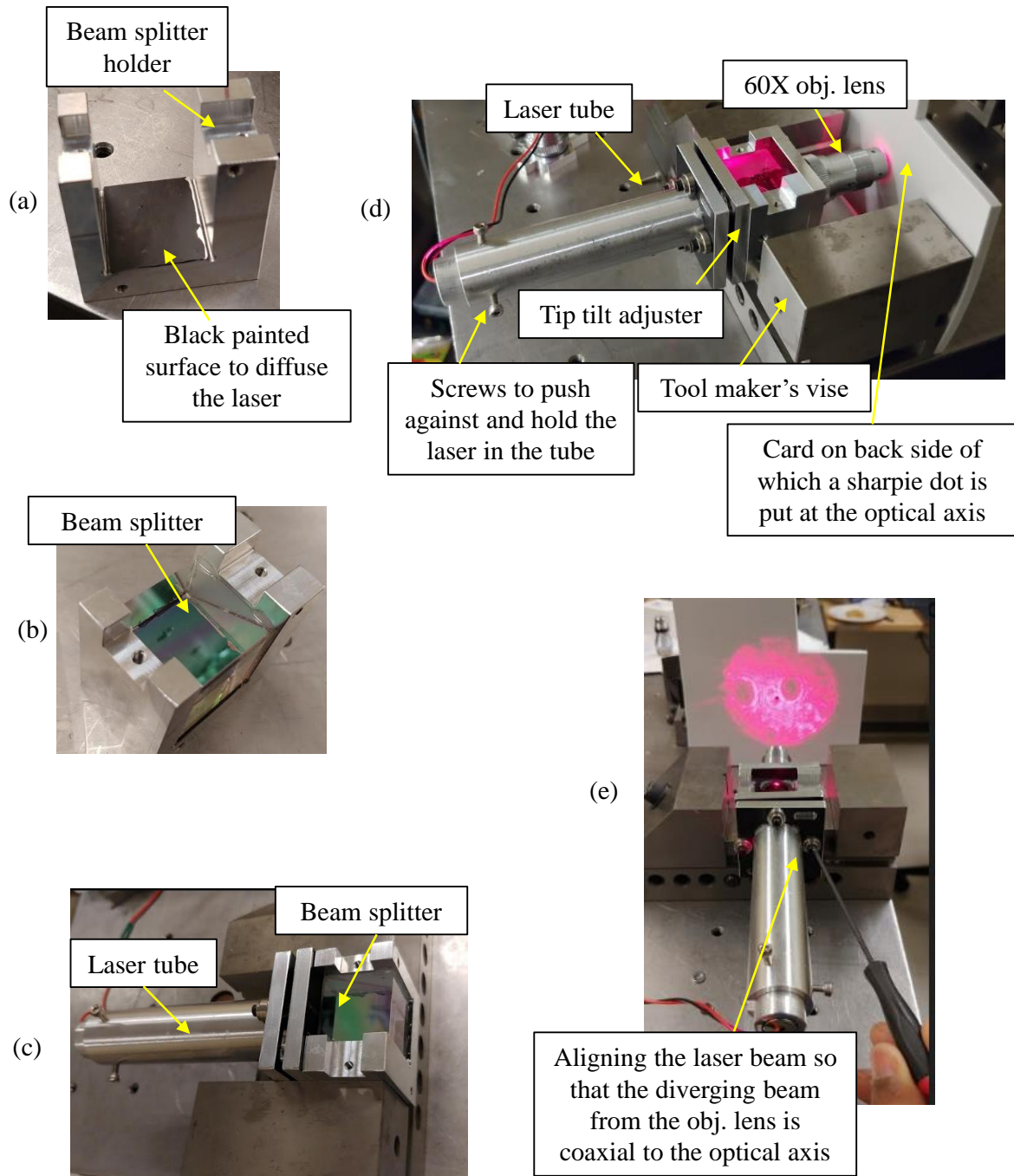
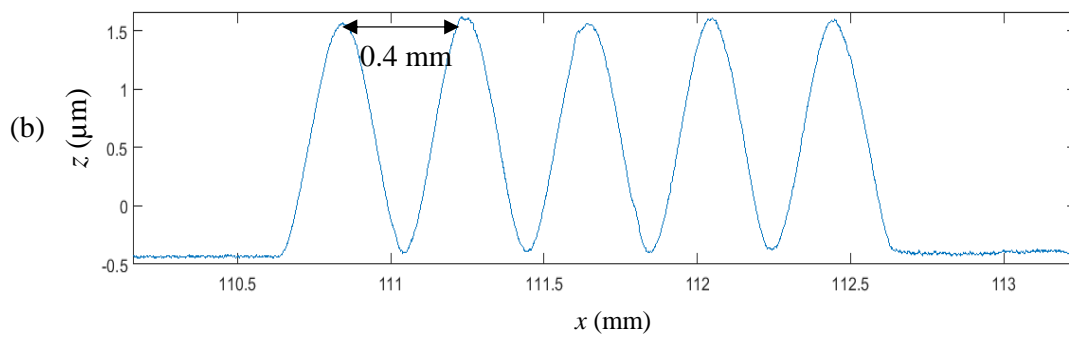
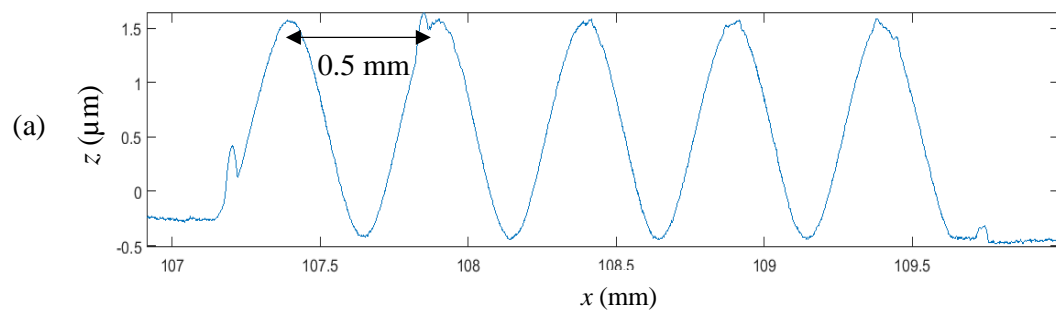
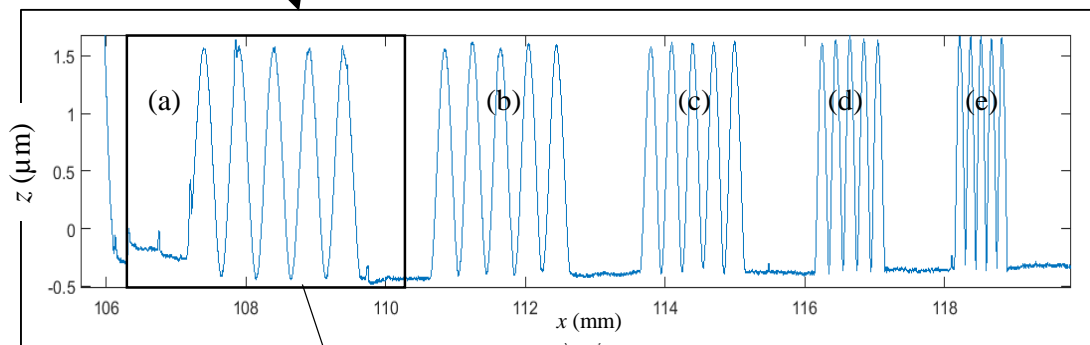
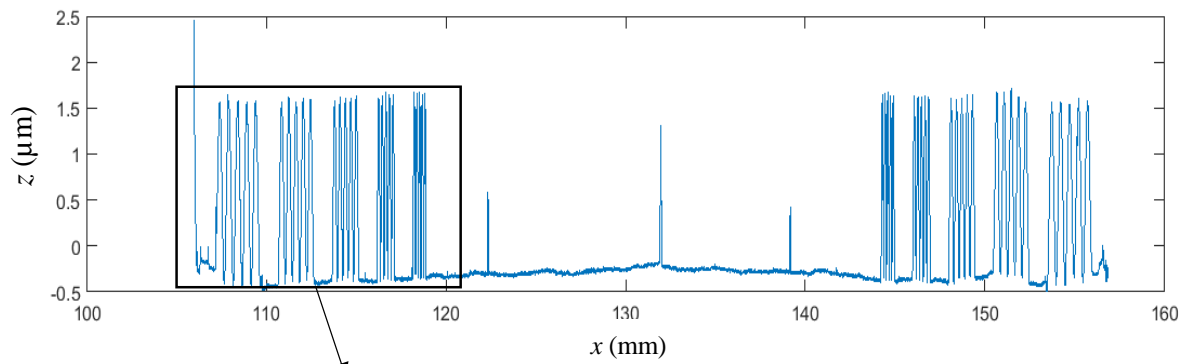


Figure 184: Building procedure of a prototype that uses a tip-tilt aligner; (a) Beam splitter holder painted black, and the beam splitter with a ground surface kept against an epoxied at the edges is (c) Laser collimating assembly and its tip tilt aligner is attached to the beam splitter holder (d) experimental assembly (e) aligning the laser using the tip-tilt aligner so that the diverging beam is coaxial to the objective lens

B.6 Stylus profilometer measurement result of sinusoidal reference sample



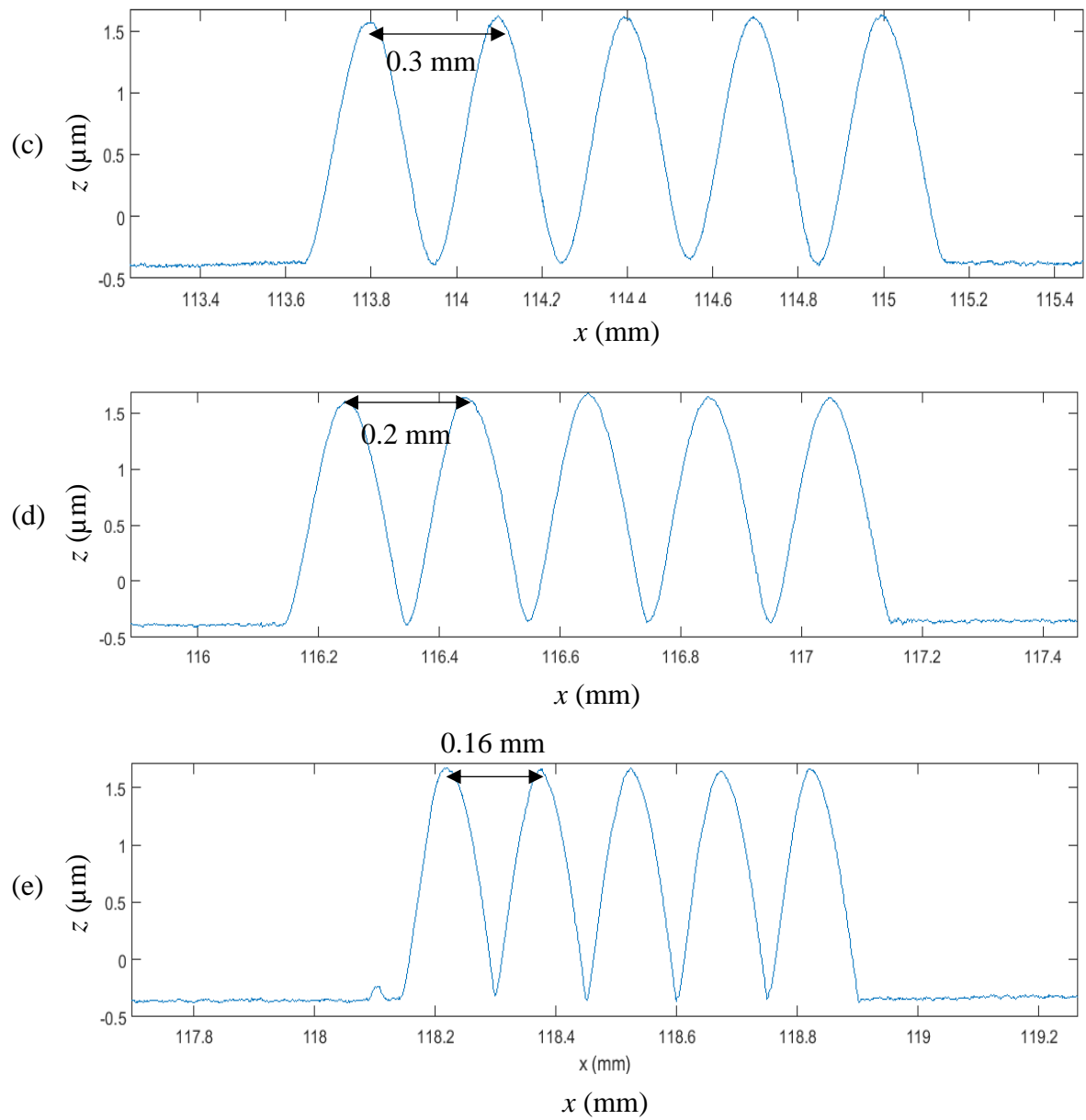


Figure 185: Zoomed in results of the stylus profilometer measurement of the sinusoidal reference sample

B.7 Disc coupling flexure for oscillating the objective lens stack

Section courtesy: Alex Caviness

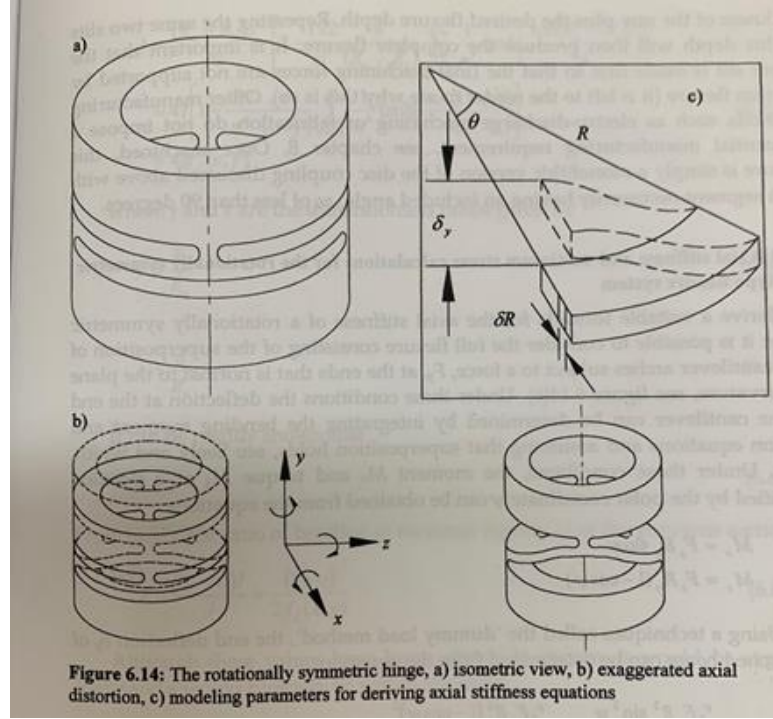


Figure 186: Schematic of a disc coupling flexure [Smith, 2000]

To machine this flexure out of a 1" long, 3/4" OD, 3/8" ID aluminum cylinder (Young's Modulus $E = 70$ GPa), five parameters that need to be controlled are: included angle θ , outer radius R_o , inner radius R_i , flexure thickness t , and deflection length δ_y . The value of the dimensionless ratio R_o/R_i is given by γ , and should be within the range of $0.75 < \gamma < 0.95$, and the ratio t/R_o is given by ϵ , and should be within the range of $0.01 < \epsilon < 0.1$. The axial stiffness of the flexure is given by,

$$k = \frac{2E(1-\gamma)t\epsilon^2}{3(1+3\gamma+3\gamma^2+\gamma^3)} \left[\left(\frac{\theta}{2} - \frac{\sin \theta}{2} \right) + 2\lambda \left(\frac{3\theta}{4} - 2\sin\left(\frac{\theta}{2}\right) + \frac{\sin \theta}{4} \right) \right]^{-1},$$

and the stress experienced by the flexure for a given deflection of δ_y is given by,

$$\sigma = \frac{6Et}{2R_i^2\theta^2} \delta_y .$$

To provide an inner diameter that fits the objective lens stack, inner diameter of the flexure is chosen to be $D_i = 0.51$ in. To provide a γ within acceptable bounds shown above, while also providing a ledge on the bottom of the flexure for attachment, $D_o = 0.65''$ ($\gamma = 0.78$). The deflection length used in the calculation is $\delta_y = 0.1$ mm, used as an approximation of the deflection combination of the preloading and the piezo expansion. However, due to the modifications during the assembly of the lens stack, the deflection of the flexure due to the preload was about 1 mm. The flexure thickness was chosen as $t = 0.4$ mm and the angle as $\theta = 75^\circ$ (1.309 radians) ($k = 36871 \text{ N.m}^{-1}$, $\sigma = 117$ MPa). The notch width is given by the following equation, where R_m is the average of the inner and outer radii.

$$s = R_m \left(\frac{\pi}{2} - \theta \right) = 0.073 \text{ in.},$$

Machining instructions:

1. Use an Aluminum cylinder of 1'' long, $\frac{3}{4}''$ OD as the raw material on the lathe, and bore a 0.510'' diameter hole through the center of the cylinder 0.937'' deep
2. Flip the cylinder around, and turn the outside diameter down to 0.65'', 0.875'' deep
3. Put the cylinder flange in a $\frac{3}{4}''$ collet on the mill, and using a slitting saw at a location around $\frac{2}{3}$ up the cylinder, mill a slit on the right side 0.289'' into the part
4. Bring the saw around to the left side and mill another slit 0.289'' into the part
5. Raise the table 0.016'' plus the thickness of the slitting saw and mill 0.289'' slits into the two other faces.

B.8 Flexure-based tilt aligner and a translation stage for surface scanning

Figure 187 shows the solid model of the flexure-based tilt aligner with a 6° travel range that uses fine screws to align the sample normal to the confocal probe.

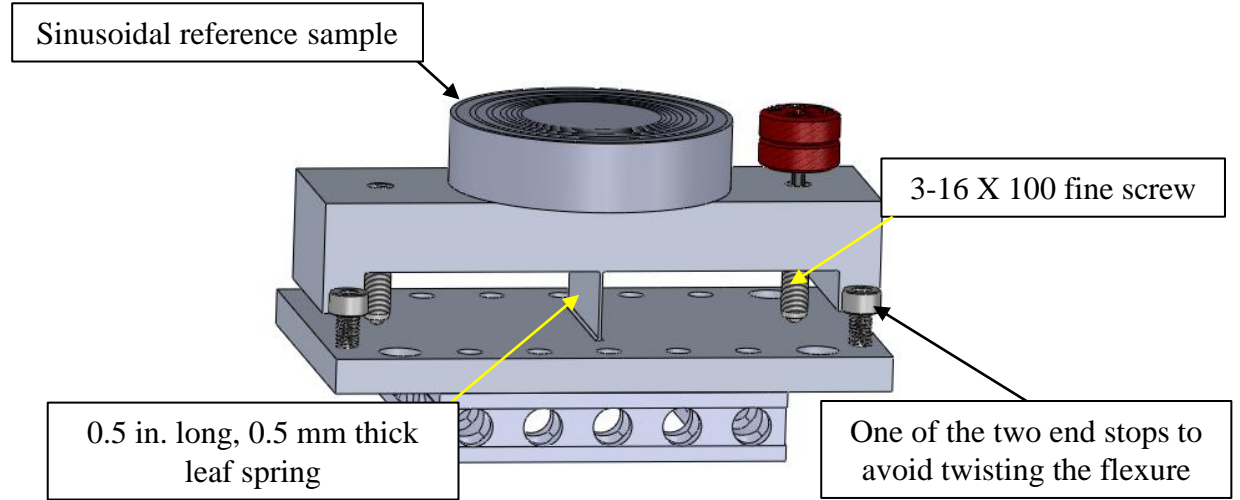


Figure 187: Flexure-based tilt aligner to align the surface sample normal to the confocal probe.

Figure 188 shows a flexure based stage to scan the sample surfaces actuated using a voice coil with a sensitivity of $13 \text{ N}\cdot\text{A}^{-1}$ with its input from an amplifier (OPA549) capable of providing $\pm 1.5 \text{ A}$, making the maximum force about $F = \pm 20 \text{ N}$. The flexure leafs of length, $l = 35 \text{ mm}$, width, $b = 12.7 \text{ mm}$, thickness, $t = 0.6 \text{ mm}$ made of spring steel (Elastic modulus, $E = 215 \text{ GPa}$) are arranged in a double compound parallelogram manner. The stiffness of the mechanism is given by,

$$k = \frac{Ebt^3}{l^3} = 17.5 \text{ kN}\cdot\text{m}^{-1}$$

Therefore, a travel range of $x = F/k = \pm 1 \text{ mm}$ is expected. The displacement of the stage is sensed using a linear encoder and is positioned using an integral controller.

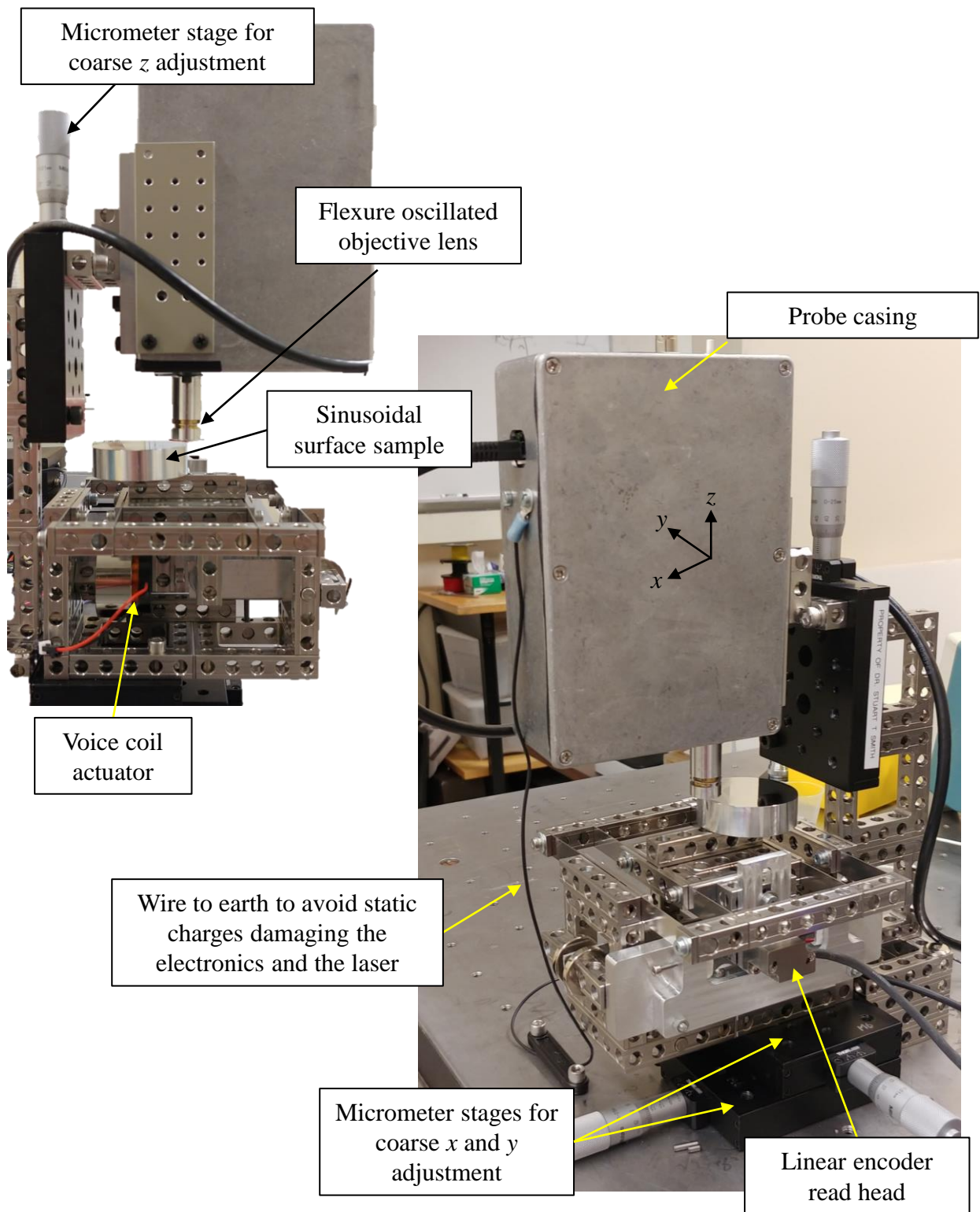


Figure 188: Voice coil actuated flexure based stage with a linear encoder feedback to scan surface samples.

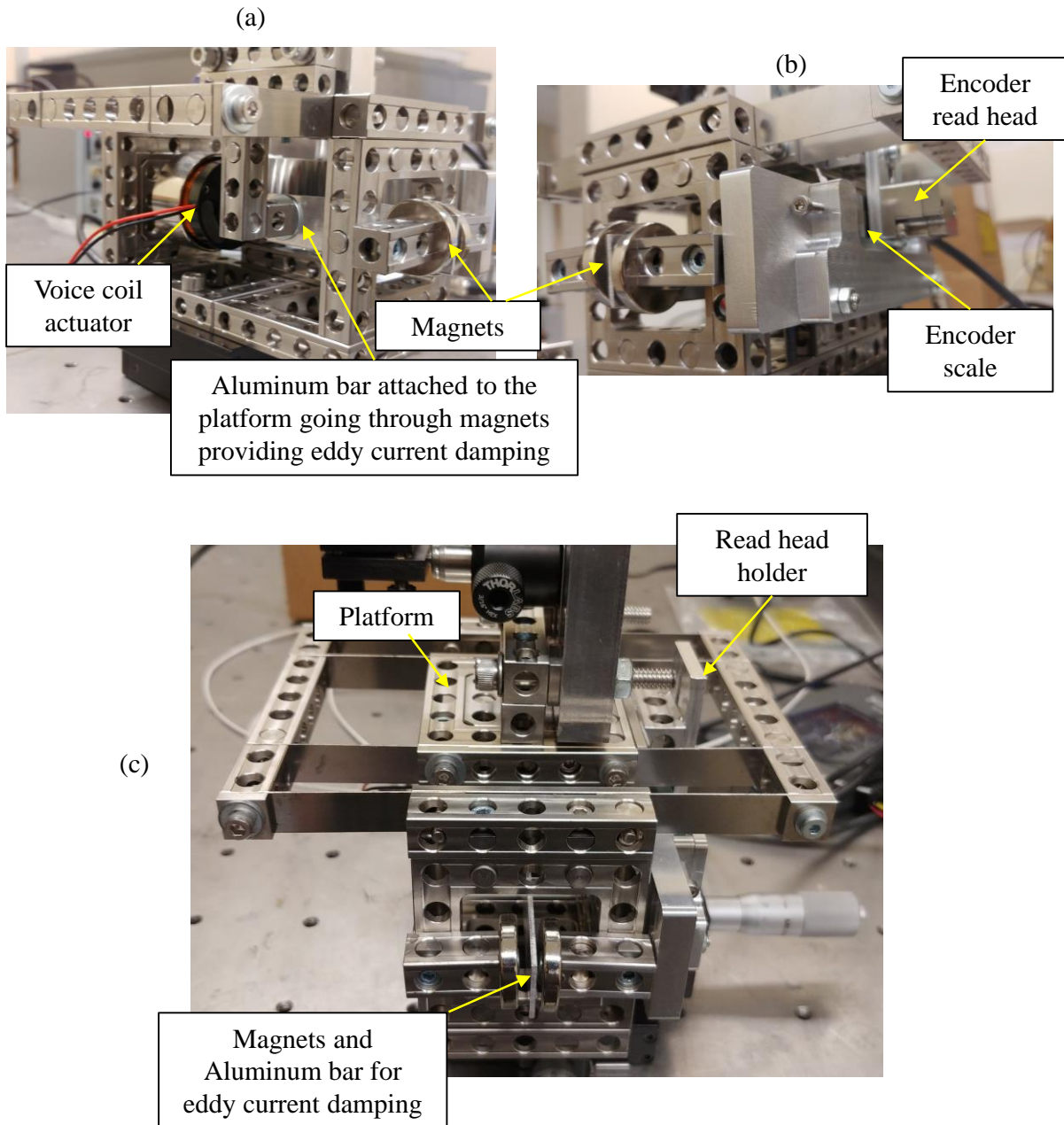
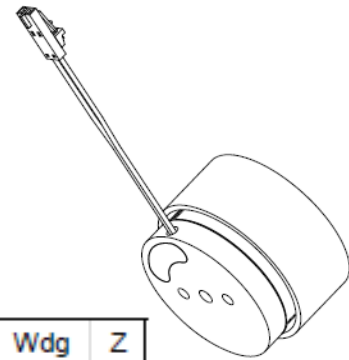


Figure 189: Flexure-based x axis scanning stage used with the confocal microscope;(a) Voice coil actuating the stage, Aluminum bar magnet pair providing eddy current damping (b) Linear encoder scale and its read head attached to the platform (c) Front-top view of the stage



Winding Constants *	Units	Tol	Symbol	Wdg	Z
DC Resistance	Ohms	$\pm 12.5\%$	R	8.58	
Voltage @ F_p	Volts	Nominal	V_p	26.0	
Current @ F_p	Amps	Nominal	I_p	3.03	
Force Sensitivity	LB/Amp	$\pm 10\%$	K_F	2.97	
	N/Amp	$\pm 10\%$		13.2	
Back EMF Constant	V/(ft/sec)	$\pm 10\%$	K_B	4.0	
	V/(m/sec)	$\pm 10\%$		13.2	
Inductance ****	milli-henry	$\pm 30\%$	L	2.8	
Linear Actuator Parameters *	Units	Symbol	Value		
Peak Force **	LB	F_p	9.0		
	N		40.0		
Continuous Stall Force ***	LB	F_{cs}	2.65		
	N		11.8		
Actuator Constant	LB/ $\sqrt{\text{Watt}}$	K_A	1.01		
	N/ $\sqrt{\text{Watt}}$		4.51		
Electrical Time Constant	milli-sec	τ_E	0.33		
Mechanical Time Constant	milli-sec	τ_M	2.3		
Theoretical Acceleration	ft/sec ²	a_T	3003		
	m/sec ²		915.3		
Max Theoretical Frequency @ Full Stroke & Sinusoidal/Triangular Motion	Hz	f_{max}	87.21/96.9		
Power I^2R @ F_p	Watts	P_p	78.8		
Stroke: BI-DIRECTIONAL	\pm in		0.12		
	\pm mm		3.05		
Clearance on Each side of Coil	in		0.05		
	mm		1.22		
Thermal Resistance of Coil in still air	$^{\circ}\text{C/Watt}$	θ_{TH}	12.6		
Maximum Allowable Coil Winding Temp	$^{\circ}\text{C}$	Temp	155		
Weight of Coil Assembly	OZ	WT_C	1.54		
	G		43.7		
Weight of Field Assembly	OZ	WT_T	6.2		
	G		175.8		

* AT MID-STROKE POSITION AND @ 25°C AMBIENT TEMPERATURE
 ** 10 SECONDS @ 25°C AMBIENT & 155°C COIL TEMPERATURE
 *** @25°C AMBIENT & 155°C COIL TEMPERATURE
 **** MEASURED AT 1000 Hz.

Figure 190: Characteristics of the voice coil actuator, BEI, Kimco magnetics division

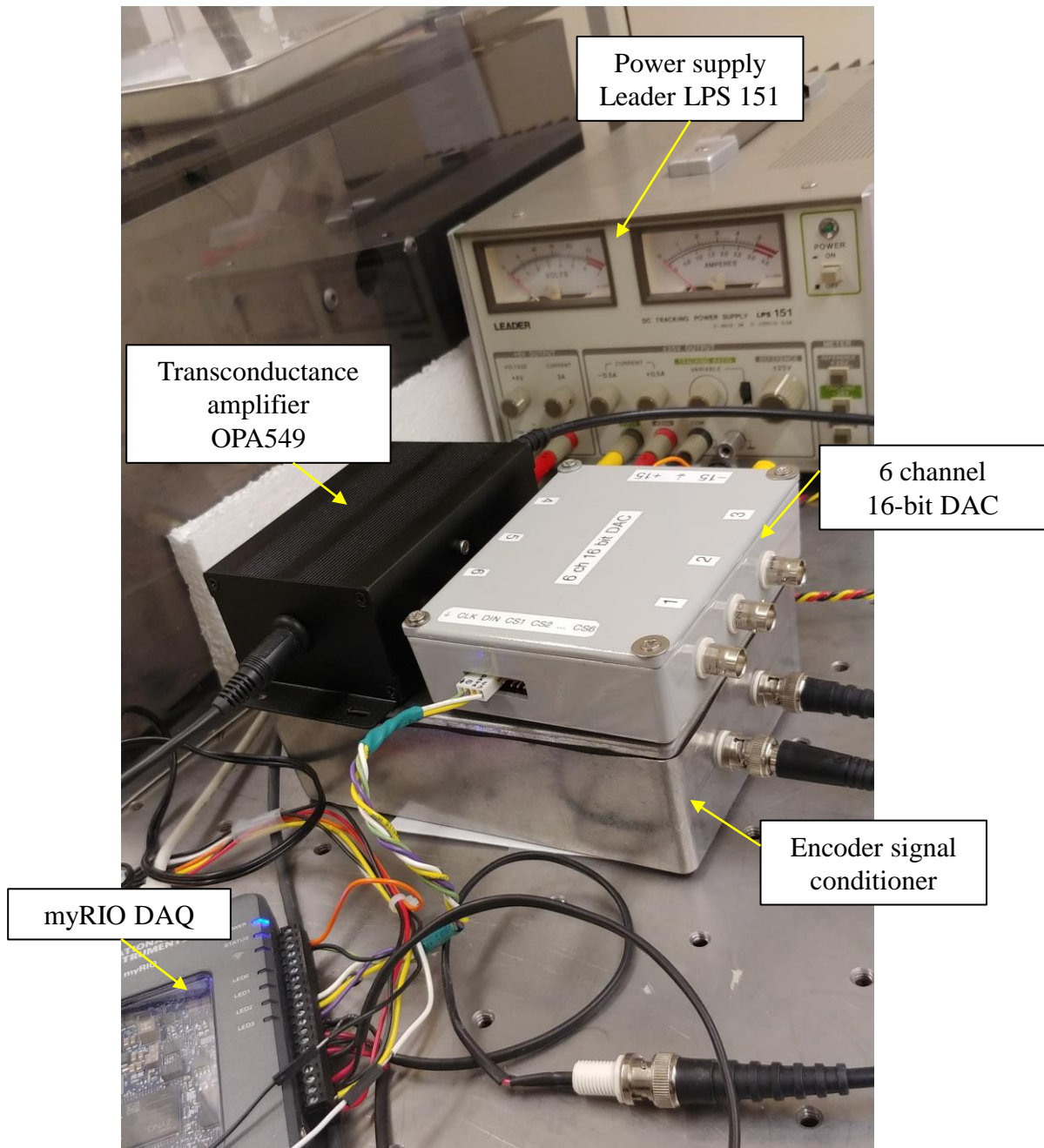
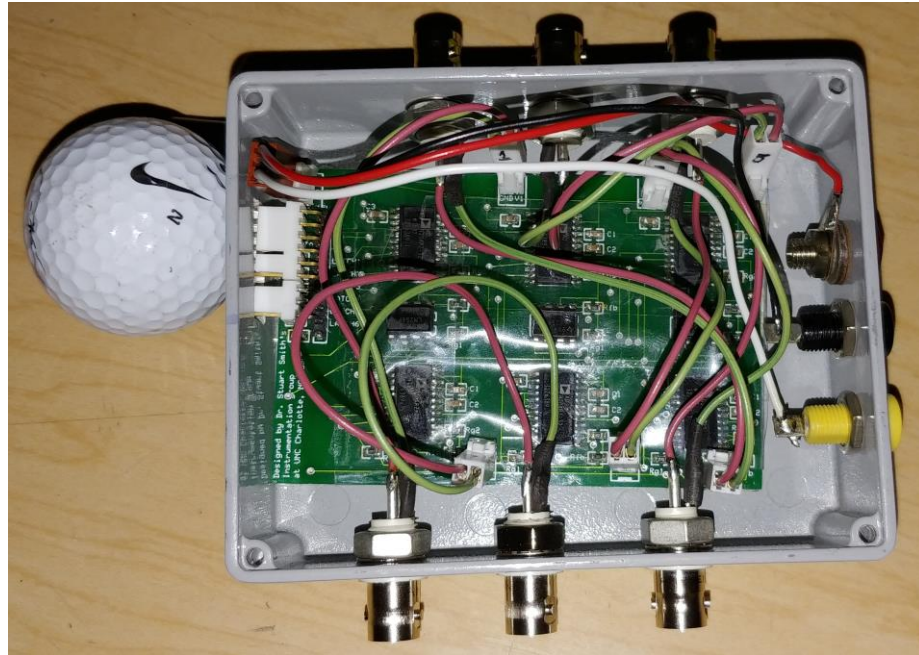
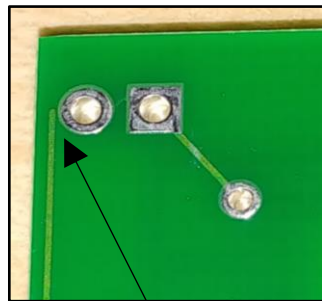


Figure 191: Photograph of the circuit boxes used with the stage. Transconductance amplifier from which the voice coil receives its current input. The current amplifier receives its voltage input from one of the output channels of the 6 channel 16-bit DAC. Digital inputs to the DAC comes from the myRIO. Power supply that provides a low noise amplified encoder signal outputs from its signal conditioner

(a)



(b)



Had to use a razor blade to remove the insulation on the copper path, and then solder the copper path to the circular via on its right

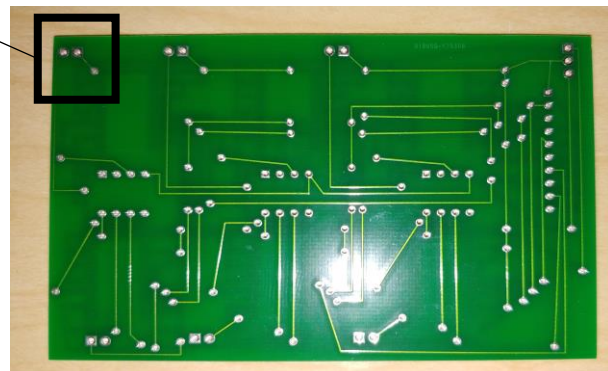


Figure 192: (a) Fabricated PCB for the 6 channel DAC (b) necessary modification to get one of the channel to work

$$C_1 = C_2 = 0.01 \mu\text{F}$$

(a)

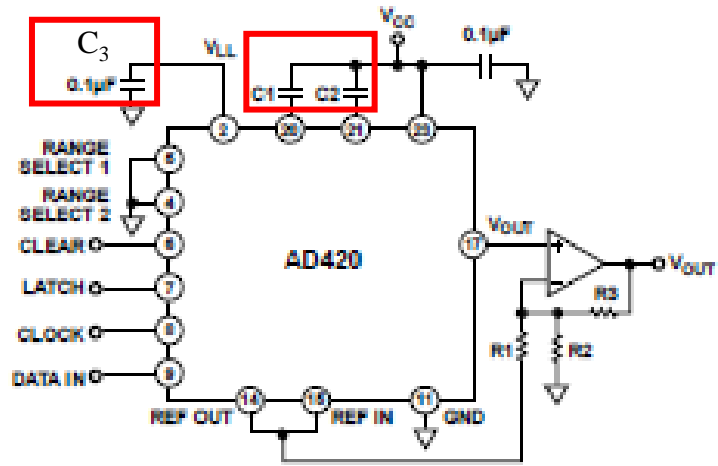


Figure 7.

Ref: AD420 Datasheet

(b)

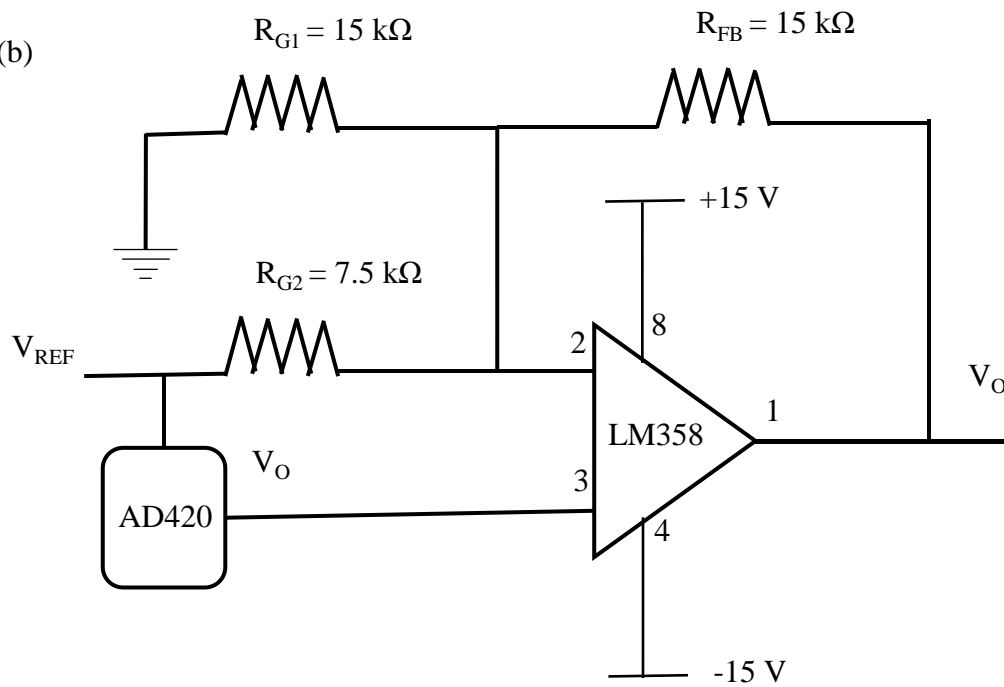
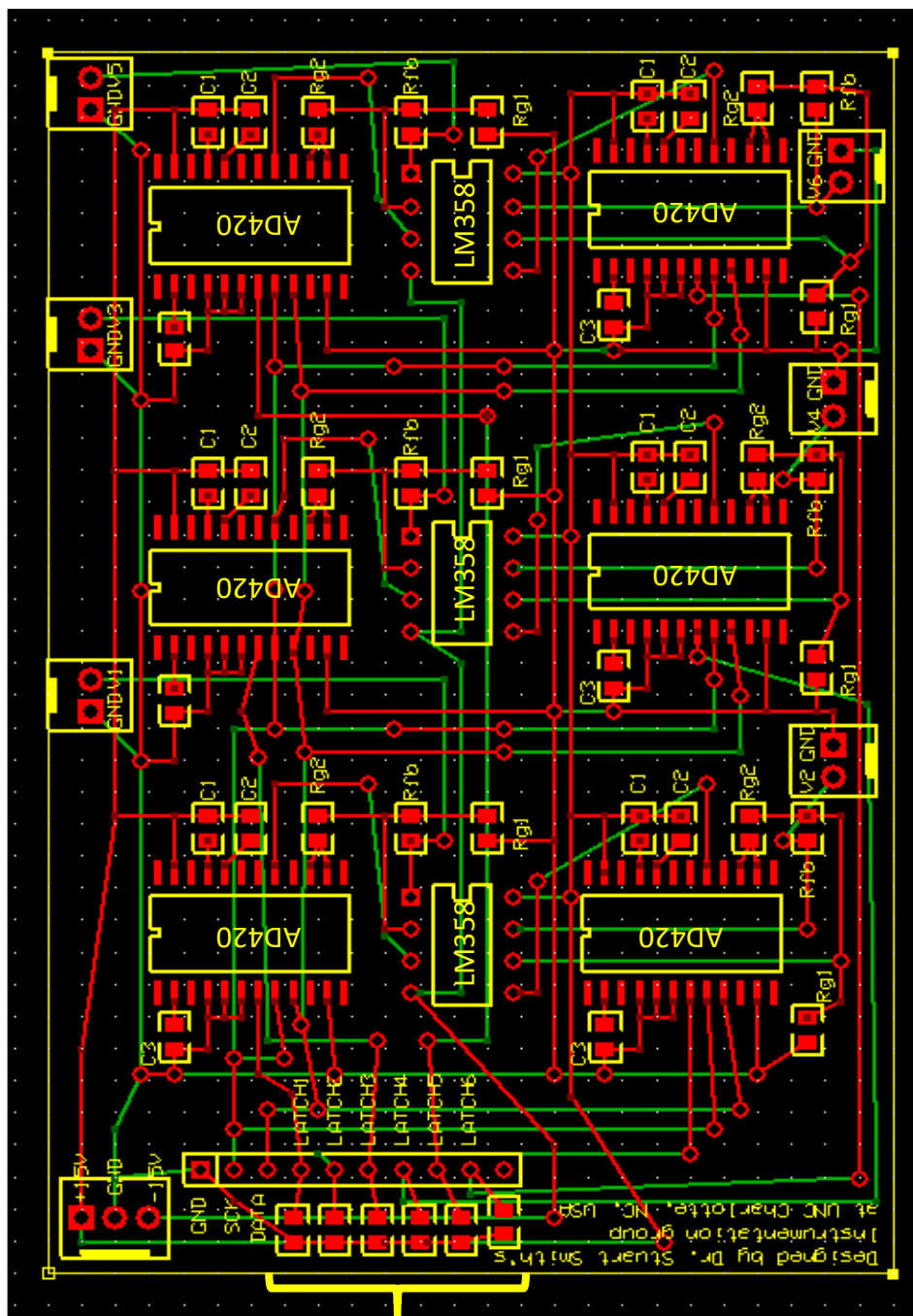


Figure 193: circuit diagram of (a) AD420 DAC (b) the buffer amplifier converting 0 to 5 V input to a +/- 10 V output



20 kΩ current
limiting
resistors for
latch inputs

Figure 194: Layout of the PCB for a 6 channel DAC

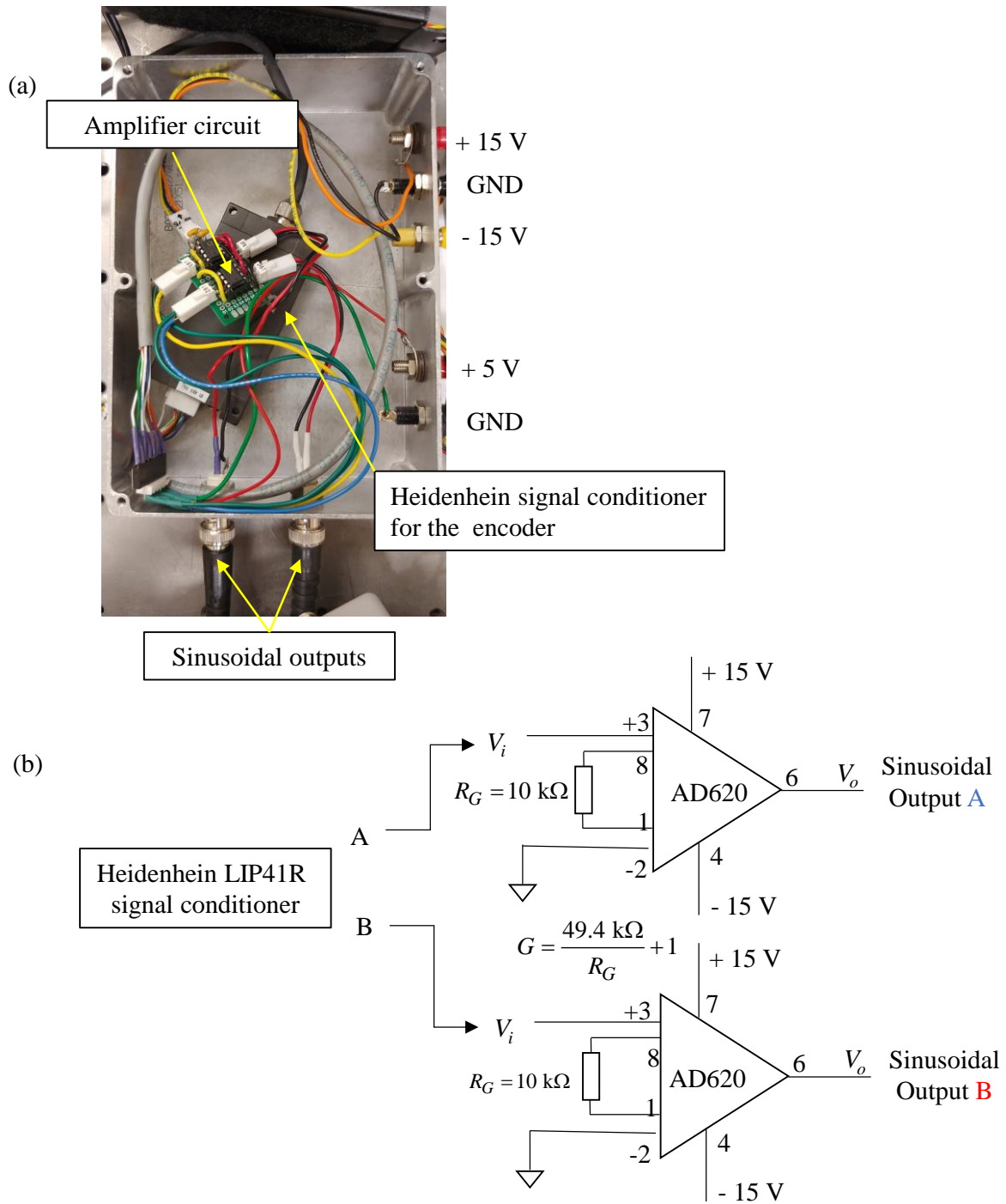


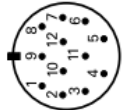


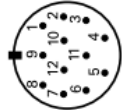
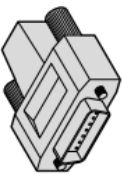
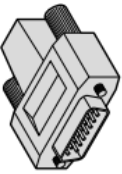
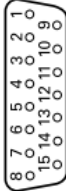


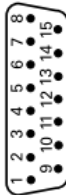









Figure 195: Amplifier circuit for the encoder signals; (a) fabricated circuit (b) circuit diagram

Pin layout												
12-pin coupling, M23				12-pin connector, M23								
												
												
15-pin D-sub connector For HEIDENHAIN controls and IK 220				15-pin D-sub connector For encoders or IK 215								
												
												
Voltage supply				Incremental signals				Other signals				
	12	2	10	11	6	8	1	3	4	9	7	/
	1	9	2	11	4	6	7	10	12	5/8/13/15	14	/
	4	12	2	10	9	3	11	14	7	5/6/8/15	13	/
	U _P	Sensor ¹⁾	0V	Sensor ¹⁾	A+	A-	B+	B-	R+	R-	Vacant	Vacant
												
	Brown/ Green	Blue	White/ Green	White	Brown	Green	Gray	Pink	Red	Black	/	Yellow
<div><div>O</div><div>Br</div><div>BrW</div><div>BI</div><div>BIW</div><div>G</div><div>GW</div></div> (Colors of wires I used)												

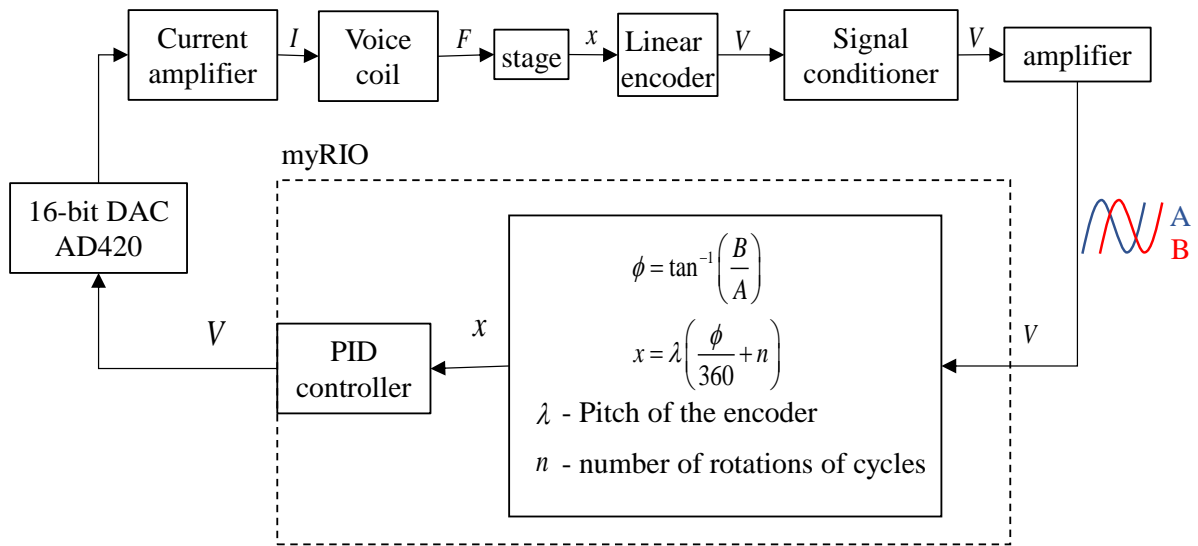


Figure 197: PID Control architecture for the stage

B.9 LabVIEW program to detect peak intensity from the confocal probe and to control the flexure-based scanning stage

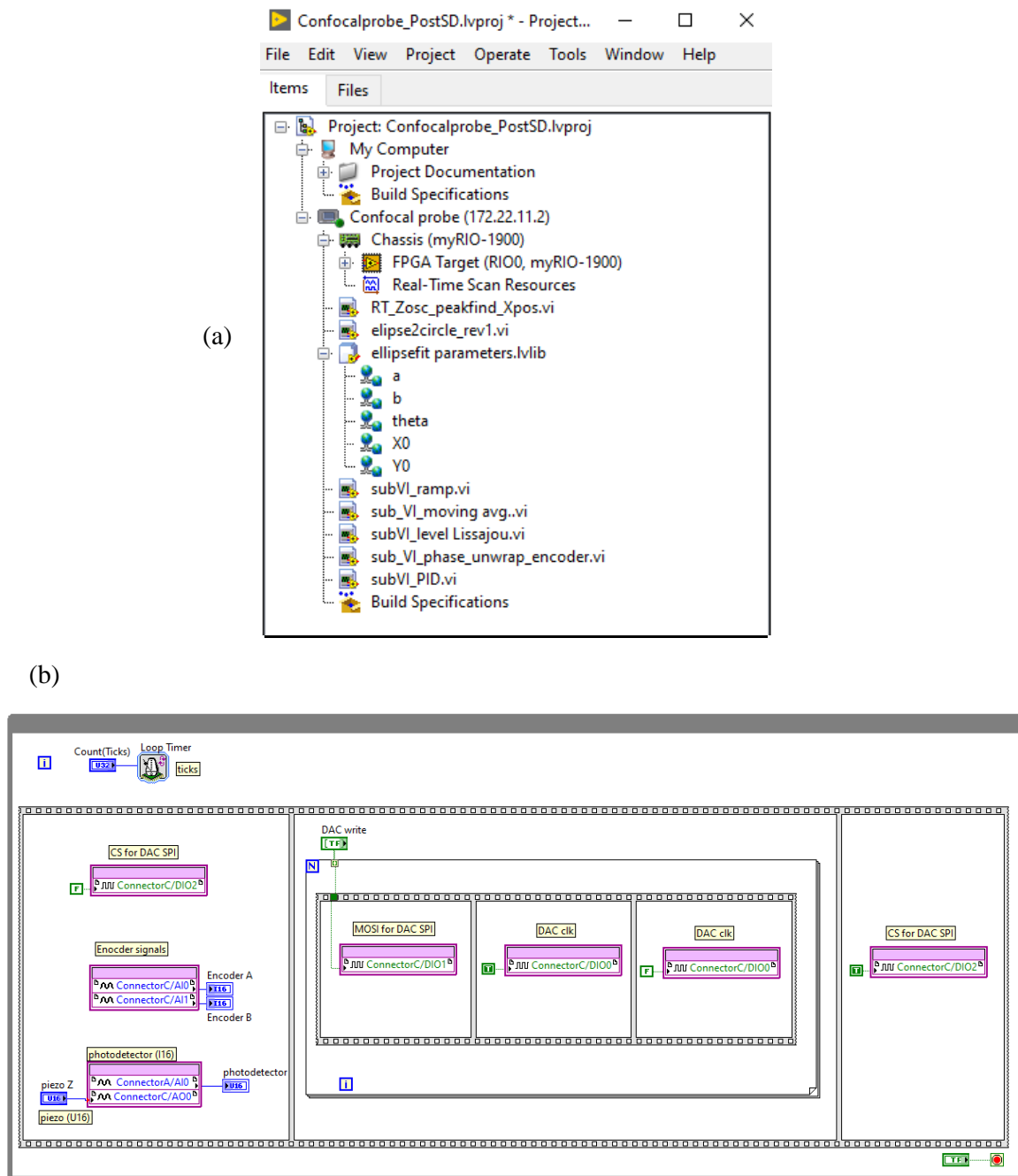


Figure 198: (a) LabVIEW Project explorer window containing the programs to find the intensity peaks detected by the confocal probe, actuate the piezo oscillating the objective lens, and PID controller for the x axis scanning stage (b) FPGA program showing the Analog inputs to read the encoder, photodetector signals, Analog output to the piezo, and Digital input and outputs to control the DAC used to actuate the voice coil of the scanning stage.

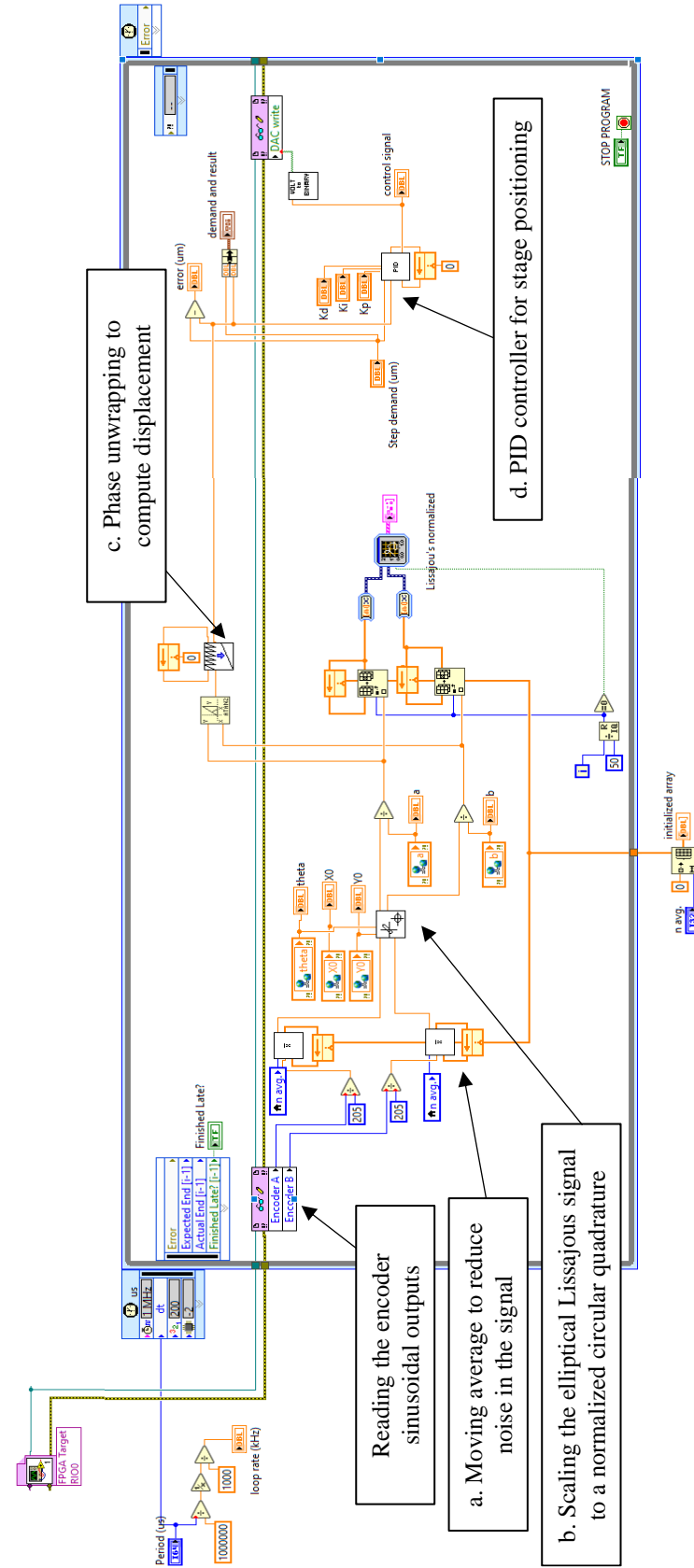
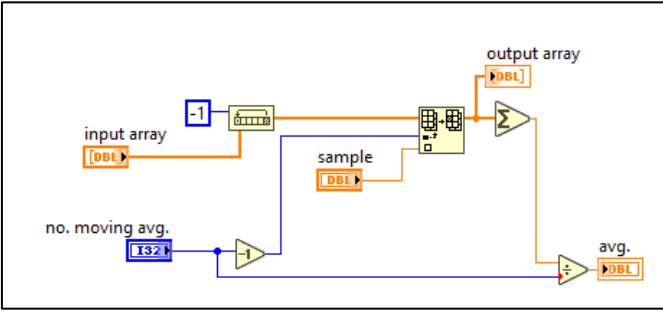
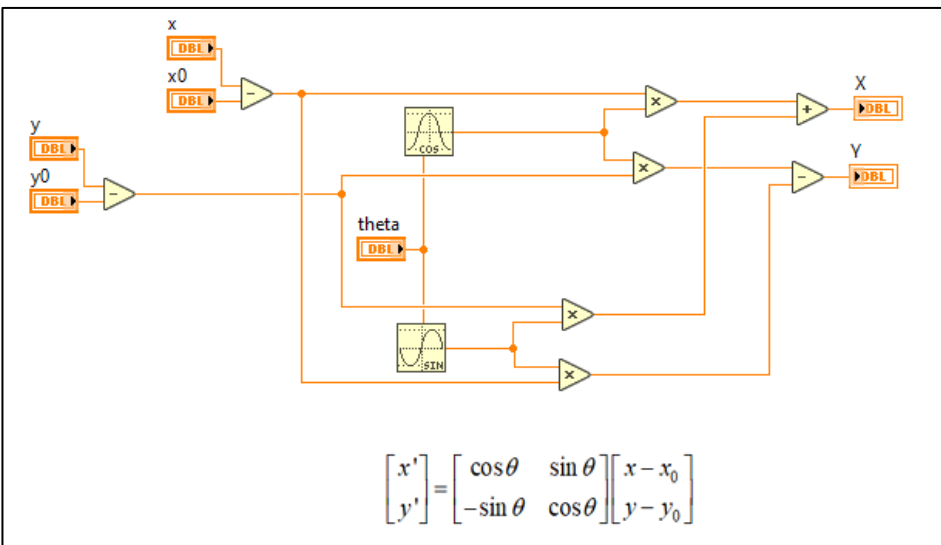


Figure 199: LabVIEW program to control the flexure stage using a PID controller

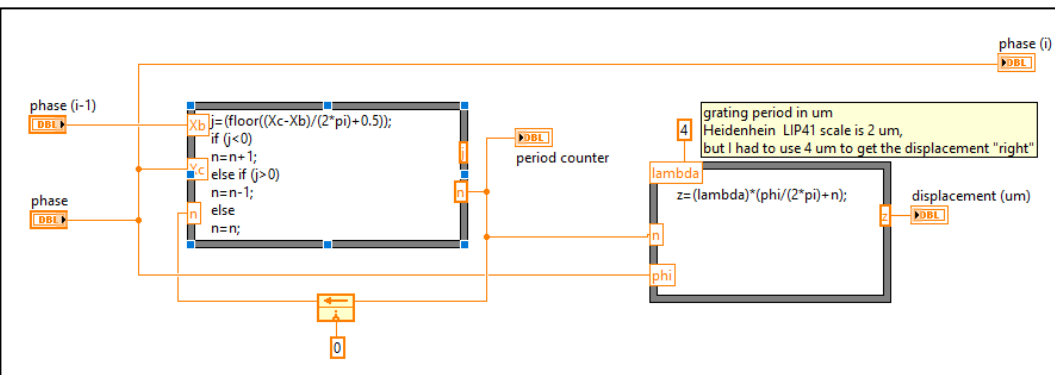
a. Moving average to reduce noise in the signal



b. Scaling the elliptical Lissajous signal to a normalized circular quadrature using the scaling parameters provided by the ellipse2circle.vi



c. Phase unwrapping to compute displacement



d. PID controller for stage positioning

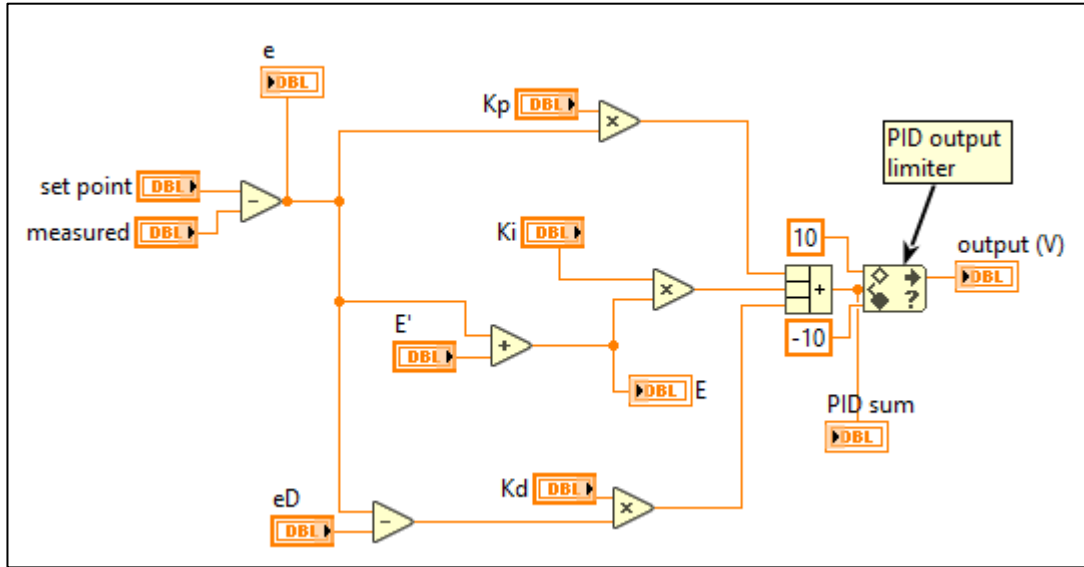


Figure 200: Sub VI's used in the LabVIEW program to control the flexure stage

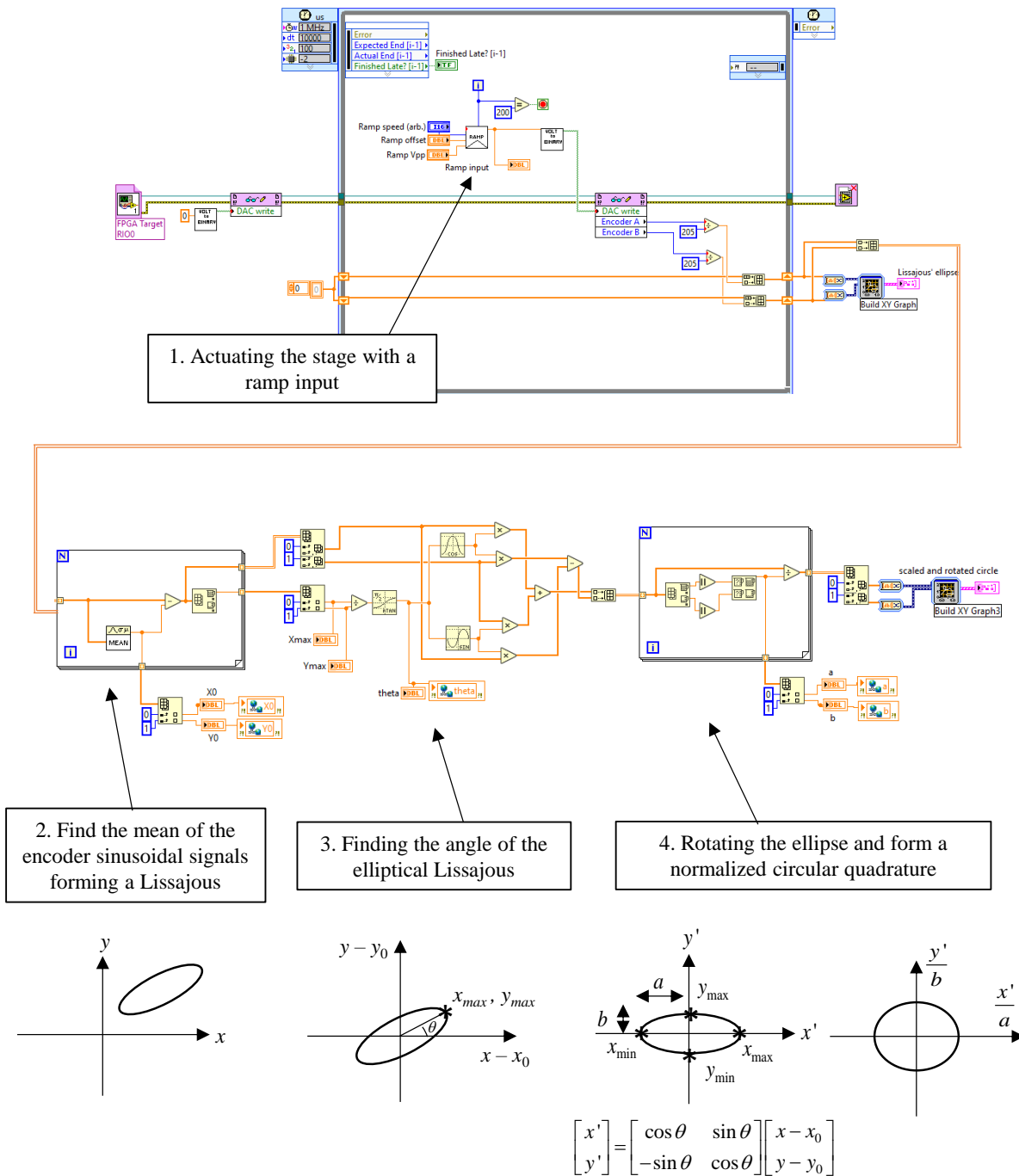


Figure 201: Ellipse2circle.vi providing the parameters to convert the elliptical Lissajous to a normalized circular quadrature. This program must be run before running the PID controller program for the scanning stage to obtain the parameters transferred using the shared variables.

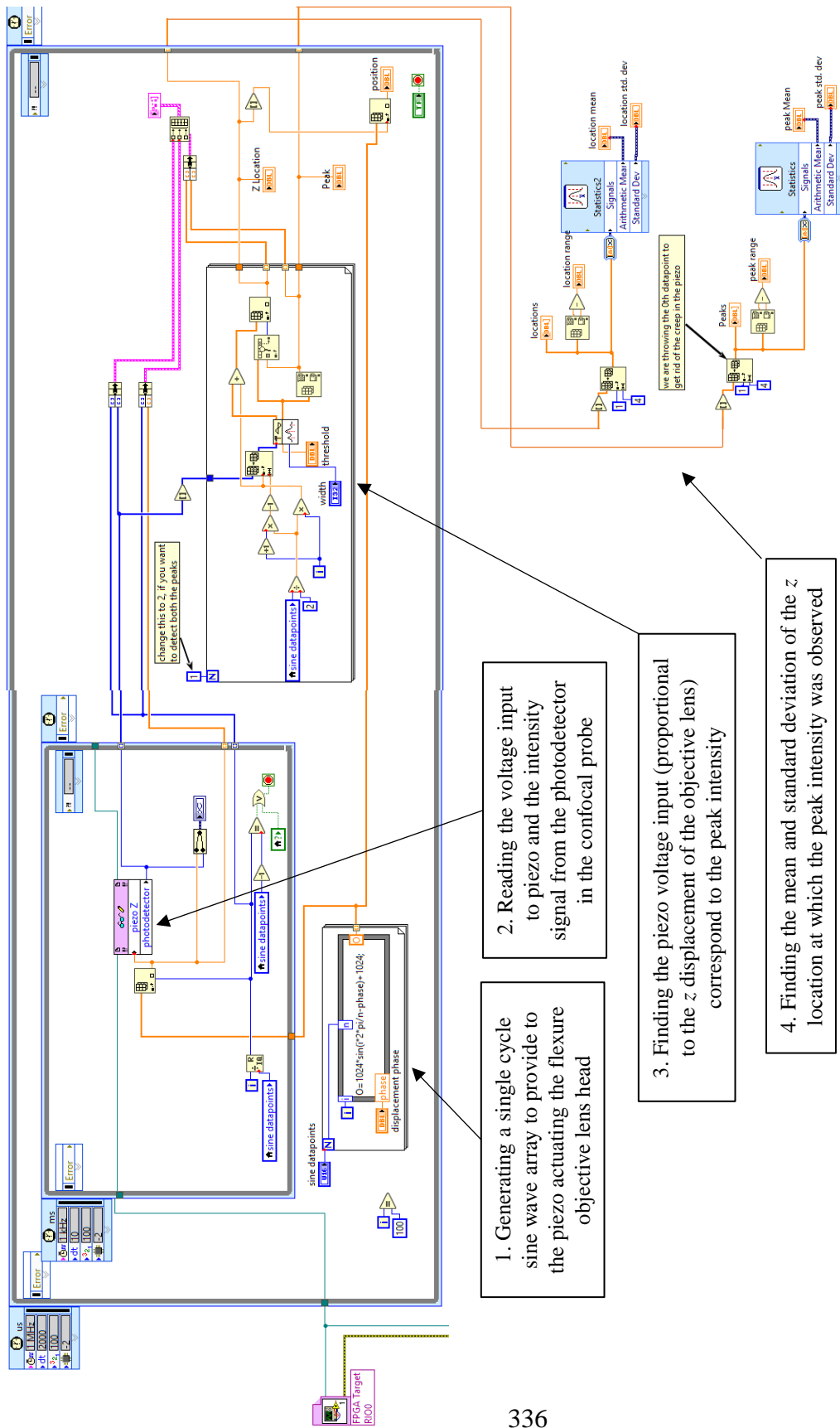


Figure 202: LabVIEW program to detect the intensity peak signal from the confocal probe and relate the peak location to the proportional piezo input voltage

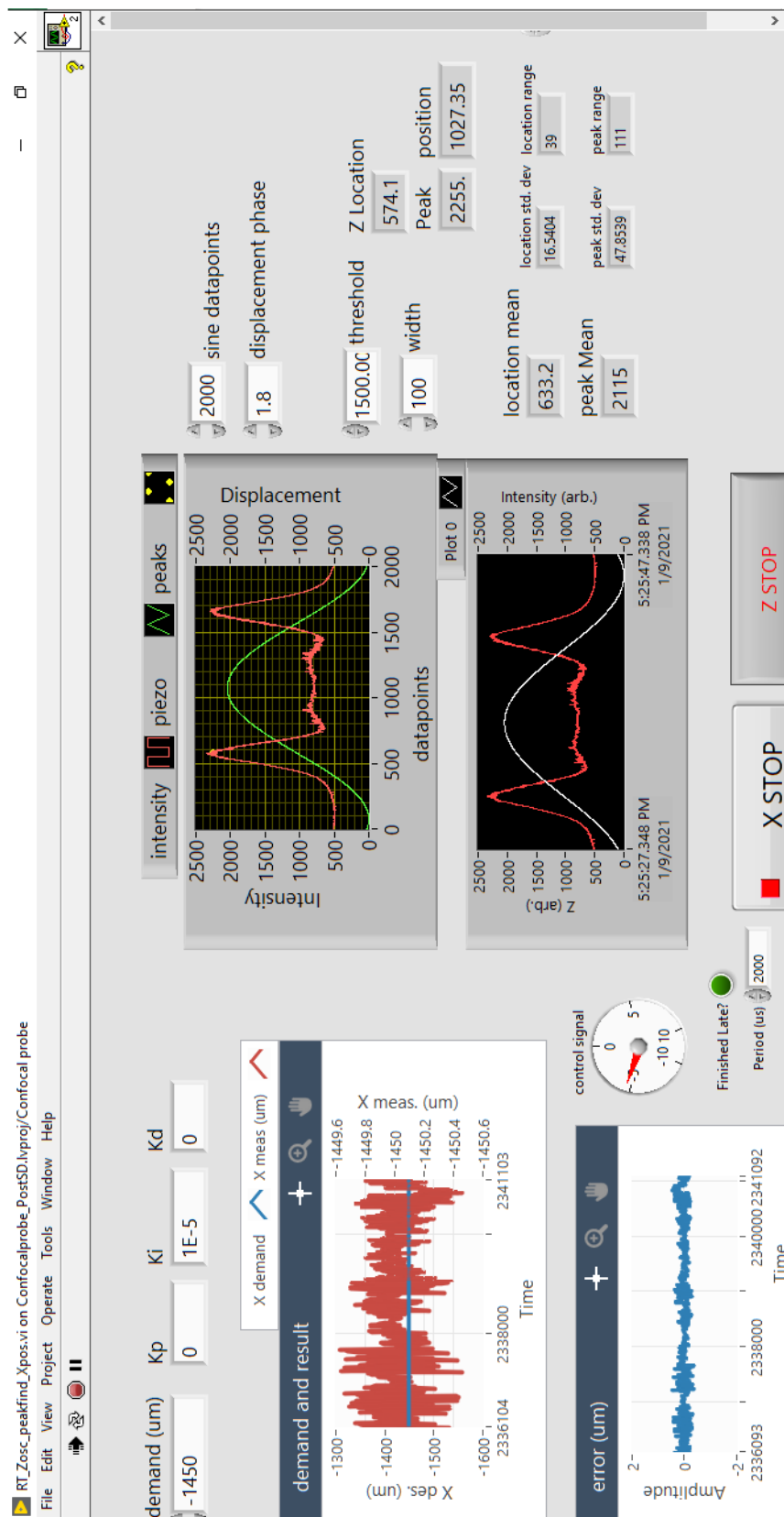



Figure 203: Front panel of the LabVIEW program; Left: Controller and indicators for the scanning stage, Right: Intensity peaks from the confocal probe, and the left peak location related to the piezo displacement in z

APPENDIX C

C.1. Manufacturer specification of carriages and equipment used with the profilometer

C.1.1 Manufacturer specification of the Y carriage

Mechanical Specifications			
Model			ABL1500-200
Travel			200 mm
Accuracy ⁽¹⁾	E1	Calibrated	±0.5 µm
		Standard	±8.0 µm
	E3	Calibrated	±0.4 µm
		Standard	±5.0 µm
Repeatability (Bidirectional) ⁽¹⁾	E1	±0.2 µm	
	E3	±0.1 µm	
Straightness ⁽¹⁾			±0.5 µm
Flatness ⁽¹⁾			±0.5 µm
Pitch			±2 arc sec
Roll			±2 arc sec
Yaw			±2 arc sec
Maximum Speed			2 m/s
Maximum Acceleration			2 g (No Load)
Maximum Force (Continuous)			93.6 N
Maximum Speed			2 m/s
Maximum Acceleration			2 g (No Load)
Maximum Force (Continuous)			93.6 N
Load Capacity ⁽²⁾	Horizontal		35 kg
	Side		25 kg
Operating Pressure			80 psi ±5 psig
Air Consumption			24-30 SLPM @ 551 kPa (0.85-1.06 SCFM @ 5.51 bar)
Moving Mass (No Load)			5.1 kg
Stage Mass		14.7 kg	16.0 kg
Material			Aluminum
MTBF (Mean Time Between Failure)			30,000 Hours

A black, rectangular piezo stage with a blue cable connected to the top left. The front face has the 'ABROTECH' logo and 'ABL1500' printed on it. The top surface is a flat, perforated metal plate.



Specifications are for single-axis systems measured 25 mm above the tabletop. Performance of multi-axis systems is payload and work point dependent.

```

*****
***** HP laser header information *****
; Rotary Calibrator: Linear Error Plot
; Filename: C:\Linear Calibrator\182316-A-1-1-X - 04.8.2016\Accuracy\182316-A-1-1-X\CalData.dat
; Acquisition Date: April 8, 2016 12:01:46 EDT
; Current Date: Apr.08,2016 12:30:39
; Measurement Type: Linear
; Travel Mode: Unidirectional
; Number of Target Positions: 41
; Number of total data pairs: 41
; Number of total data runs: 1
; Expansion Coefficient: 3.25 PPM/°C
; Position Value Units: millimeters
; Error Value Units: micrometers
;
;
; environmental data - MIN MAX AVG
; Air Temp (C) 19.94 19.95 19.94
; Air Prs (mm) 728.49 728.61 728.57
; Air Hmd (%) 31.16 31.73 31.35
; MT1 Temp (C) 19.84 19.85 19.85
;
;
*****
:START 1 SAMPLEDIST=5.000000 POSUNIT=PRIMARY CORUNIT=PRIMARY/1000.000
:START EXPANDCOEFF=3.250000e-006 MATERIALTEMP=20.00
:START SERIALNUMBER="182316-A-1-1"
:START HOMEDIRECTION=CCW HOMEOFFSET=-101.040001

```

Serial no. labeled on Y stage

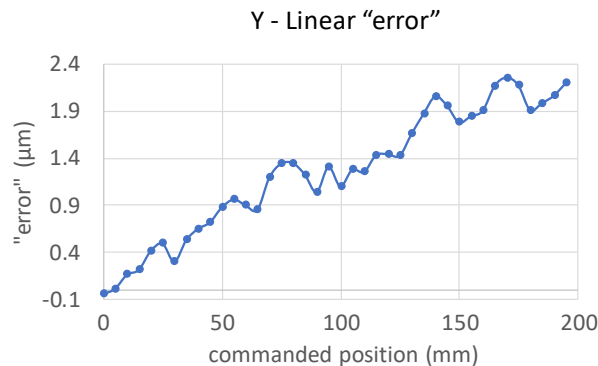


Figure 204: Manufacturer's specification of the Y carriage used in the Profilometer system.

C.1.2 Manufacturer specification of the rotary (C) carriage

Model		ABRS200MP
Width		200 mm
Tabletop Diameter		178.1 mm
Height		90 mm
Aperture		20 mm
Total Travel		
Bus Voltage		340 VDC
Fundamental Encoder Resolution		8192 lines/rev
Max Speed ⁽¹⁾		300 rpm
Accuracy ⁽²⁾		±2 arc sec
Bidirectional Repeatability		<1 arc sec
Max Load ⁽³⁾	Axial	31 kg
	Radial	15 kg
	Tilt	10 N-m
Axial Error Motion (Synchronous)		<100 nm
Radial Error Motion (Synchronous)		<250 nm
Tilt Error Motion (Synchronous)		<3.4 μ rad (<0.7 arc sec)
Axial Error Motion (Asynchronous)		<20 nm
Radial Error Motion (Asynchronous)		<20 nm
Tilt Error Motion (Asynchronous)		<0.3 μ rad (<0.06 arcsec)
Operating Pressure ⁽⁵⁾		80 psig (5.5 bar) + 0 psig (0.0 bar)/-10 psig (0.7 bar)
Air Consumption ⁽⁶⁾		<56.6 SLPM (<2 SCFM)
Inertia	Unloaded	13,800 kg-mm ²
Total Mass		9.1 kg
Material		Aluminum
Finish		Hardcoat (62 Rockwell Hardness)



1. Maximum speed based on stage capability. Maximum application velocity may be limited by system data rate and system resolution.
2. Certified with each stage. Requires the use of an Aerotech controller.
3. Maximum loads are mutually exclusive.
4. All error motion specifications measured at 60 rpm.
5. To protect air bearing against under-pressure an in-line pressure switch tied to the motion controller is recommended.
6. Air supply must be clean, dry to 0°F dew point and filtered to 0.25 μ m or better. Recommend nitrogen at 99.9% purity.

```

*****
;***** HP laserheader information *****
; Rotary Calibrator: Rotational Accuracy Plot
; Filename: C:\Rotary Calibrator\182316-A-1-1-X-U- 04.8.2016\182316-A-1-1-X-U CalData.dat
; Acquisition Date: April 8, 2016 09:30:59 EDT
; Current Date: Apr.08,2016 09:35:23
; Measurement Type: Rotary
; Travel Mode: Unidirectional
; Number of Target Positions: 36
; Number of total data pairs: 36
; Number of total data runs: 1
; Position Value Units: degrees
; Error Value Units: arcsec
;
;
; environmental data - MIN MAX AVG
; Air Temp (C) 19.50 19.70 19.55
;*****
:START 2 SAMPLEDIST=10.000000 POSUNIT=ROTARYCORUNIT=ROTARY/3600.000
:START SERIALNUMBER="182316-A-1-1"
:START HOMEDIRECTION=CCW HOMEOFFSET=1.220000
:START ROLLOVER=33554432

```

Serial no. labeled on rotary stage

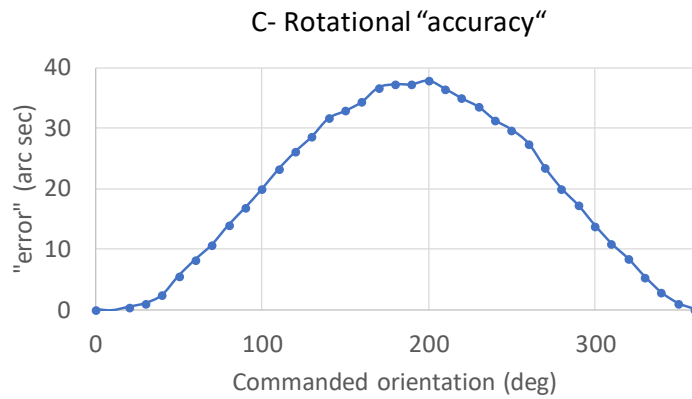


Figure 205: Manufacturer's specification of the Rotary carriage, C used in the Profilometer system.

C.1.3 Manufacturer specification of the indicator used for centering the parts

Millimar EHE-2048

Inductive probe

FEATURES

- Clutch mounted contact swivels through 280° arc for easy positioning
- Involute tip** (normally furnished) automatically corrects for cosine error when finger is at an angle up to 20°. Simplifies "reach over" jobs.

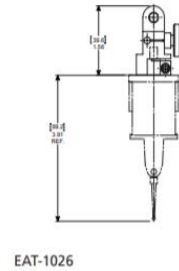


Application:

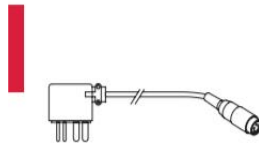
For use on test stands, surface plate work, or where light pressure is needed

TECHNICAL DATA

Order no.	2120417	
Product type	EHE-2048	
Probe type	Post bracket back, (BK-108) tamper-proof mounted	
Measuring range	mm	± 0.25
Measuring range	inch	± .010"
Measuring force	N	0,04 N .14 oz.) in either direction
Increase in measuring force	N/mm	0,001 N / 25µm
Repeatability f ₅₀	µm	0.1
Repeatability f ₅₀	inch	4 µ"
Linearity deviation within +/- 0,250 mm	0.1% (over full range)	
Linearity deviation within +/- .010"	0.1% (over full range)	
Cable length	m	1.2
Compatibility	Federal	



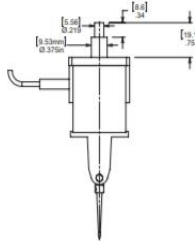
EAT-1026



ECB-1852

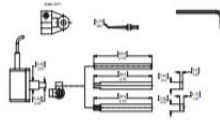
Order no.

2120417



ACCESSORIES

Order no.	Product name	Compatibility	Product type
2216178	Stylus ø 1.6 mm/.062", steel, l = 27.6 mm/1.085", 1:1 ratio	Federal	EPT-1004
2216180	Stylus ø 1.6 mm/.062" involute, steel, l = 27.6 mm/1.085", 1:1 ratio up to 20° involute tip	Federal	EPT-1008
2216179	Stylus ø 0.787 mm/.031", carbide, l = 27.6 mm/1.085", 1:1 ratio	Federal	EPT-1007
2216184	Stylus ø 0.787 mm/.031", steel, l = 27.6 mm/1.085", 1:1 ratio	Federal	EPT-1013
2216217	Stylus ø 1.6 mm/.062", Sapphire, l = 27.6 mm/1.085", 1:1 ratio	Federal	EPT-1059-W1
2185448	Stylus ø 1.6 mm/.062", Sapphire, l = 122.8 mm/4.835", 4:1 ratio	Federal	EPT-1059-W4
2216218	Stylus ø 1.6 mm/.062", Sapphire, l = 59.3 mm/2.335", 2:1 ratio	Federal	EPT-1059-W2
2185449	Stylus ø 1.6 mm/.062", Sapphire, l = 154.6 mm/6.085", 5:1 ratio	Federal	EPT-1059-W5
2216219	Stylus ø 1.6 mm/.062", Sapphire, l = 91.1 mm/3.585", 4:1 ratio	Federal	EPT-1059-W3
2208685	Adaptor to mount EHE-2048 on model 2400 stand		EAM-1071
2208910	Accessories kit for EHE-2048. Includes EAM-1071, CP-116, EPT-1013, two rectangular holding bars and a holding rod		EAS-1333
2210400	Fine adjust attachment for EHE-2048		EAT-1026
2206061	Clamp for mounting EHE-2048 on model 2300 stand		CP-116
2211459	Gagehead adapter cable. Adapts EHE-2XXX and P2XXXF gageheads to older model 432 & 230 amplifiers (5 pin round female to 8 pin square male connector)	Federal	ECB-1852



EAS-1333

C.2. Interferometric measurements of reference objects and data processing

This section discusses the interferometric measurements performed on

1. optical flats made of Fused Silica with diameters, 6 in., 4 in., and 3 in.,
2. optical flats made of Zerodur with diameters, 4 in. and 3 in.,
3. a glass bar coated with Aluminum,
4. a hollow Aluminum bar coated with Silicon Carbide, and
5. two right angled prisms made of Fused Silica

C.2.1 Six inch diameter Fused Silica flat

Figure 206(a) shows the experimental setup to measure the 6 in. Dia. Fused Silica flat. which is applied with Petroleum jelly (Vaseline - Cocoa butter flavor) on its back surface to reduce the internal reflection between the surfaces of the flat, see Figure 206 (b). Refractive index of petroleum jelly is not available in any literature or internet, but it should be close

enough to that of Fused Silica ($n=1.457$, $\lambda=633$ nm) because inter reflections were successfully reduced in various measurements. Also, two fiducials with adhesive surface are stuck on the front surface of the flat, whose locations on the flat are shown in Figure 206 (c).

The diameter of the flat is 6 in. (152.4 mm), whereas the aperture of the interferometer is only 4 in. (101.6 mm). Therefore, to cover the complete diameter of the flat in vertical (y) axis, the flat is measured as two halves. First, capturing the top half as shown in Figure 207(a), and then translating the flat in Y axis to capture the bottom half of the flat as shown in Figure 207(b). Tilt removed interferograms are shown in Figure 207 (c) and (d), read using Zygo Mx. It is noted that both the interferograms contain the two fiducials that were stuck on the surface of the flat. Profile taken across the y axis of the interferograms are shown in Figure 207 (e) and

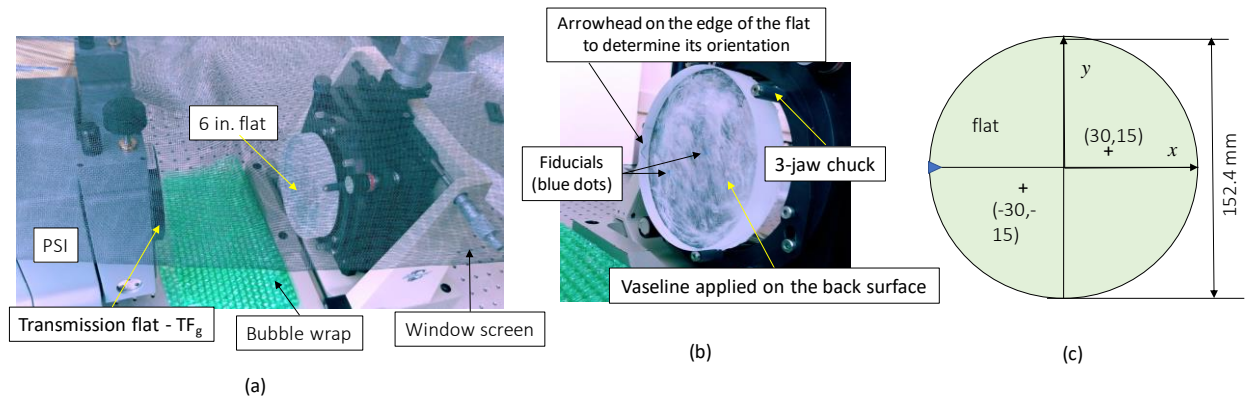


Figure 206: Experimental setup to measure the 6 in. flat; (a) photograph of the setup; (b) Vaseline applied to the back surface of the flat, and the fiducials stuck on the front surface (c) The locations at which the fiducials are placed.

(f) in black, M_1 and M_2 . Shown in blue is the profile of the Transmission flat, TF_g used in the experiment, and this profile was obtained from a 3-flat test. M_1 and M_2 are subtracted from TF_g to obtain nominal profiles of top and bottom halves of the flat. Figure 208 shows the bottom half profile iteratively translated in Y axis (in Matlab) to match the features of top half profile.

Height of this “stitched” nominal profile is 15 nm PV, which is about $\lambda/40$ as opposed to vendor’s specification of $\lambda/10$.

a) Stitching of interferograms using fiducials, and averaging the intersecting regions

This section discussed the utilization of the fiducials to align two interferograms by offsetting one with respect to the other, and the surface height is averaged at the intersecting region. Figure 209(a) and (b) shows the recorded interferograms of top and bottom half of the flat respectively , read using h5read function in Matlab. Planes are fit (see Figure 209(c & d), and subtracted from them and shown in Figure 209 (e & f). The x , y pixel locations of the fiducials are also marked. This data processed using Zygo Mx is shown in Figure 207 (c) and (d).

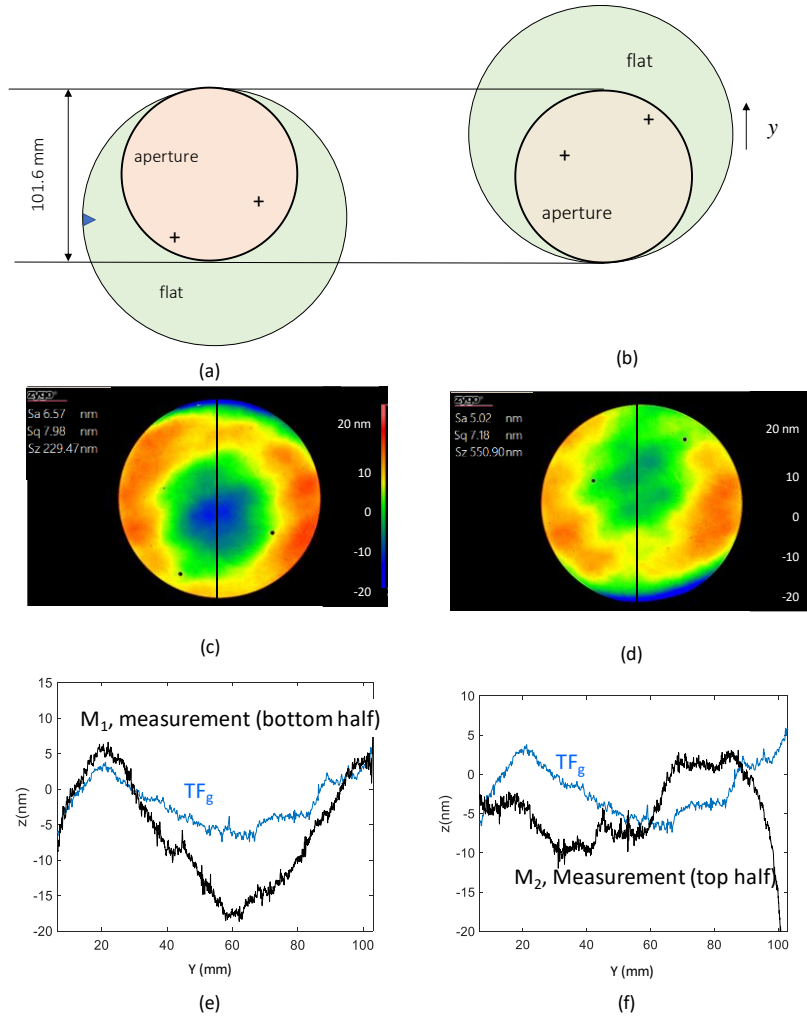


Figure 207: Interferometric measurement results of the flat; (a), (b) Two orientations the flat is located to measure the complete diameter of the flat in Y axis (c), (d) interferograms of the measurement, (e), (f) Profiles taken along the Y axis of the interferograms (black), Profile of the Transmission flat, TF_g obtained from a 3-flat test.

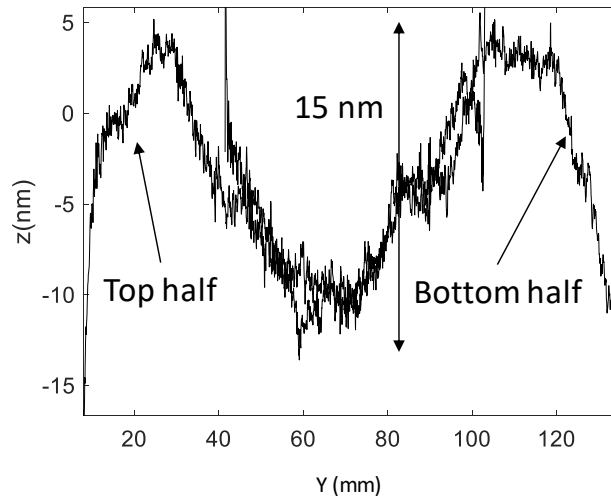


Figure 208: Stitched profile from both the measurements to obtain the nominal profile of the flat along the Y axis, whose profile height is 15 nm PV.

b) Subtract or Rotate?

Figure 210 shows a 2D example of two known ways of removing tilt in a measured data. Figure 210(a) shows, the removal of tilt by subtracting a line from the tilted measurement, which has a disadvantage that the length of the resulted data is less than the original length, l of measurement. Whereas, Figure 210 (b) shows that this length could be conserved if the tilt is removed by rotating the data using a rotation matrix.

Since the tilts in the interferometric measurements are naturally low, I used the first approach to subtract the plane from the measured data because the resulted length is not that different from the length of the measured surface. For example, data shown in Figure 209 (a) is two dimensionally represented in Figure 210, where the length of the line subtracted data is almost as same as the length of the measured surface.

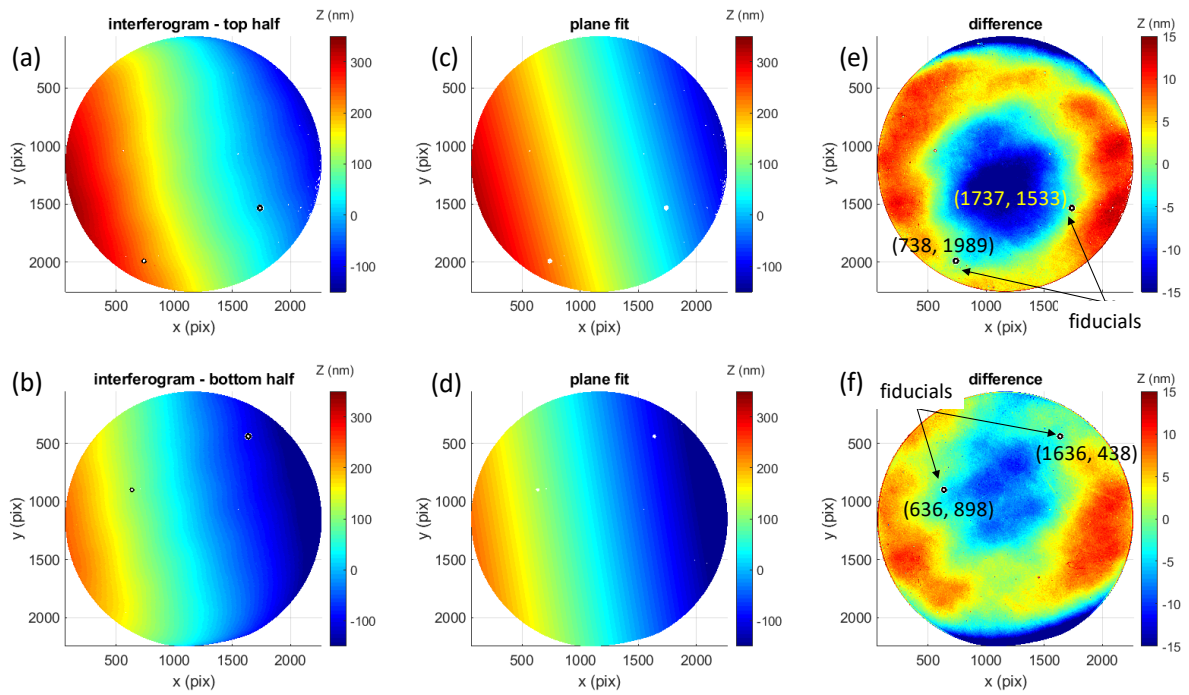


Figure 209: (a), (b) Recorded interferograms of top and bottom half of the flat (c), (d) planes fit to the interferograms (e), (f) planes subtracted from the interferograms shown in (a), (b).

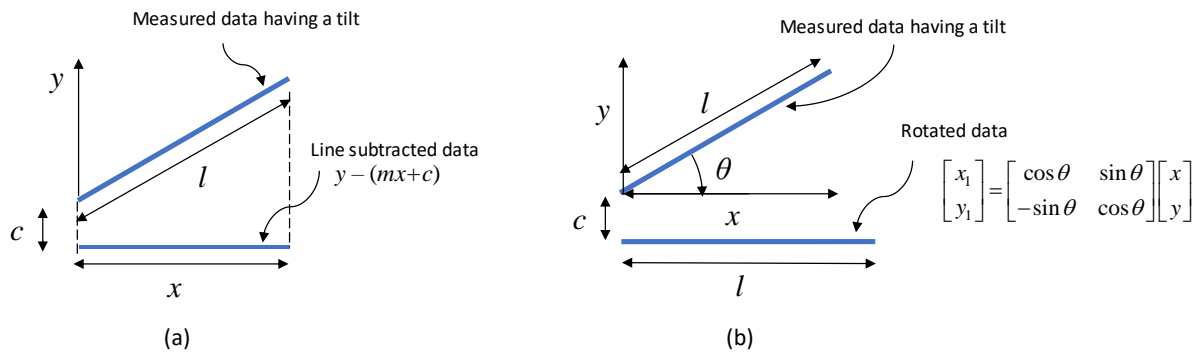


Figure 210: Tilt in the measured data removed by (a) subtracting a line vs. (b) rotating the data.

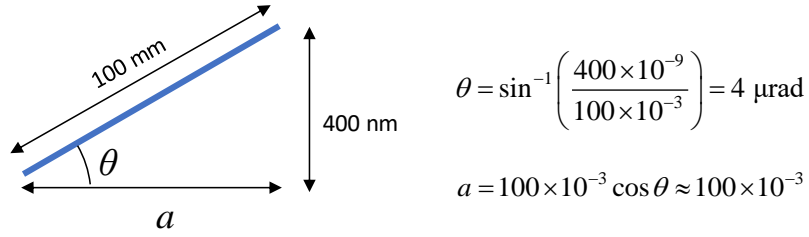


Figure 211: Schematic showing the length of the data after subtracting a line is almost as same as the length of the surface measured.

c) Locating the fiducials, and alignment of interferograms using the fiducials

To stitch the top and bottom half interferograms, pixel locations of the fiducials shown in Figure 209 (e) and (f) are found using the Matlab function `imfindcircles.m`. For example, location of the left fiducial in top and bottom interferograms are (738, 1989) and (636,898), see Figure 209 (e) and (f).

Figure 212(a) shows the empty pixels added to the top interferogram, and Figure 212 (b) shows the bottom interferogram translated in x and y axis to move its left fiducial from (636,898) to (738, 1989). Figure 212 (c) shows the interferograms after getting aligned.

d) Error in alignment

I'm using only the left fiducial in the alignment procedure, assuming the flat does not rotate in its optical axis when translated in Y to measure the bottom half, see Figure 207 (a) and (b). Due to this, there is a difference of 1 pixel in x axis and 4 pixels in Y axis in the translated location of right fiducial, see Figure 212(a) and (b). Since there are about 2204 pixels in 101.6 mm (4 in.) aperture, conversion factor from pixels to mm is, $101.6/2204$, therefore the difference is $46 \text{ } \mu\text{m}$ (1 pixel) in x axis, and $184 \text{ } \mu\text{m}$ (4 pixels) in y axis. It is possible to rotate the right fiducial with respect to the left fiducial, to reduce this error, or translating the bottom interferogram so that the both the fiducials could be aligned to their average x,y locations.

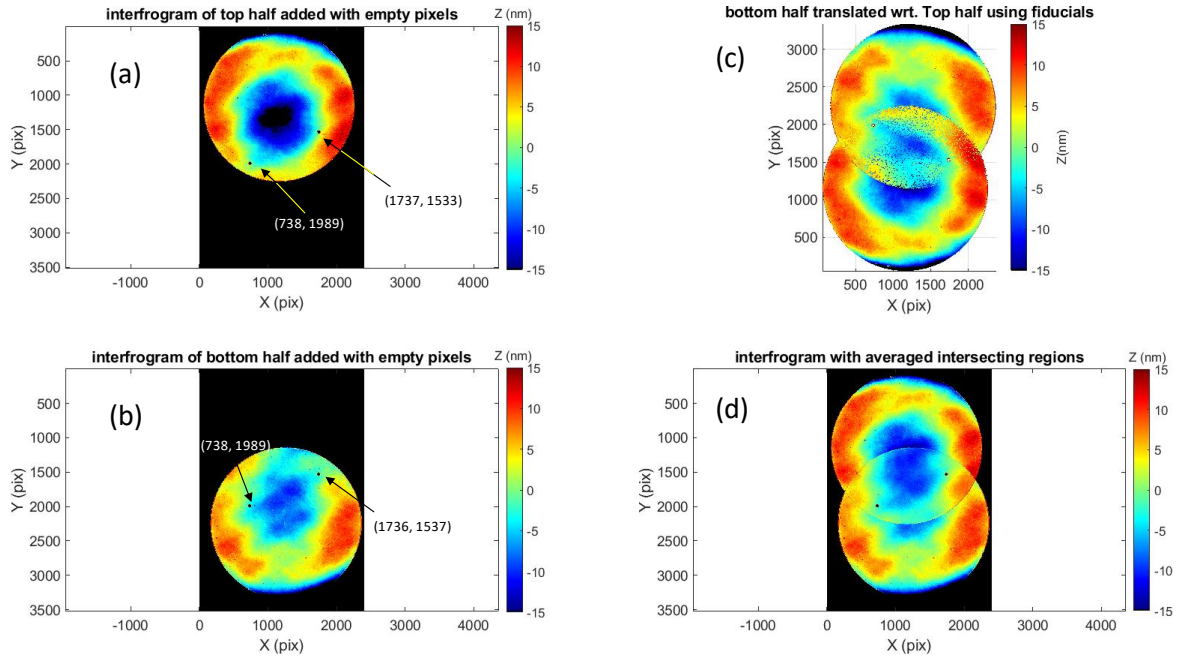


Figure 212: Procedure to stitch the interferograms of the flat; (a) Empty pixels (in black) added to the interferogram of the top half of the flat (b) same for the bottom half (c) bottom half translated wrt the top half using the fiducials (d) intersecting region of the stitched data is averaged.

To estimate the error in the above stitching approach, the object being measured (optical flat), and the transmission flat are considered as a 4th order polynomial, see Figure 213 (a) and (b) respectively. The object has a span of 150 mm and a height of ± 20 nm PV. The transmission flat has a span of 100 mm and a height of ± 5 nm PV (this height was estimated from a 3 flat test. Figure 213(c) shows the resulted measurement of the left and right half of the object, which includes the effect of transmission flat (summation). Figure 213(d) shows the measurement data, with its overlapping region averaged. Figure 213(e) shows this averaged data plotted along with the object, and the difference between them is shown in Figure 213(f), and it is about ± 5 nm PV.

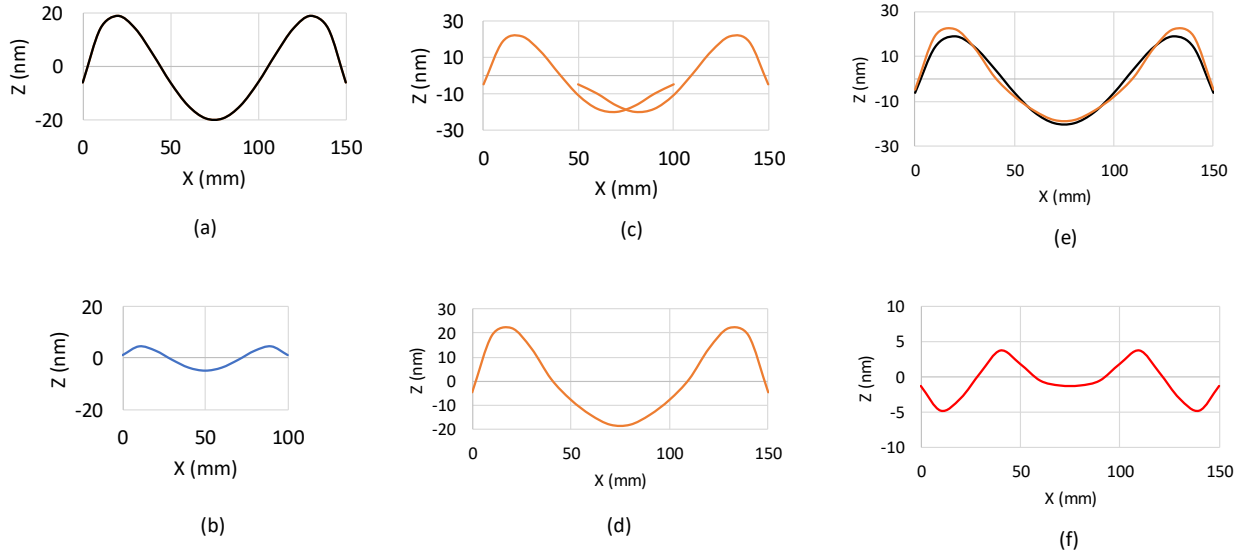


Figure 213: Simulation showing the stitching error; (a) Simulated Measurement object (b) Transmission flat (c) Measurements of left and right half of the object (d) overlapping region of the measurements is averaged (e) averaged measurement plotted with object (f) difference between the averaged result and the object.

e) Stitching of interferograms using fiducials and tilt one with respect to the other

One way to mitigate the error in the above discussed stitching procedure is, once the interferograms are aligned in the xy plane, the bottom interferogram will be first tilted with respect to the top interferogram, making the tilts of the interferograms the same, then this tilt is removed to realize the form of the object. To align the interferograms in the xy plane, pixel locations of the fiducials shown in Figure 214(a and b) are found using the Matlab function `imfindcircles.m`. For example, location of the left fiducial in top and bottom interferograms are (738, 1989) and (636, 898) respectively. Figure 214(d) shows the bottom interferogram translated in x and y axis to move its left fiducial from (636,898) to (738, 1989), therefore aligning it to the top interferogram.

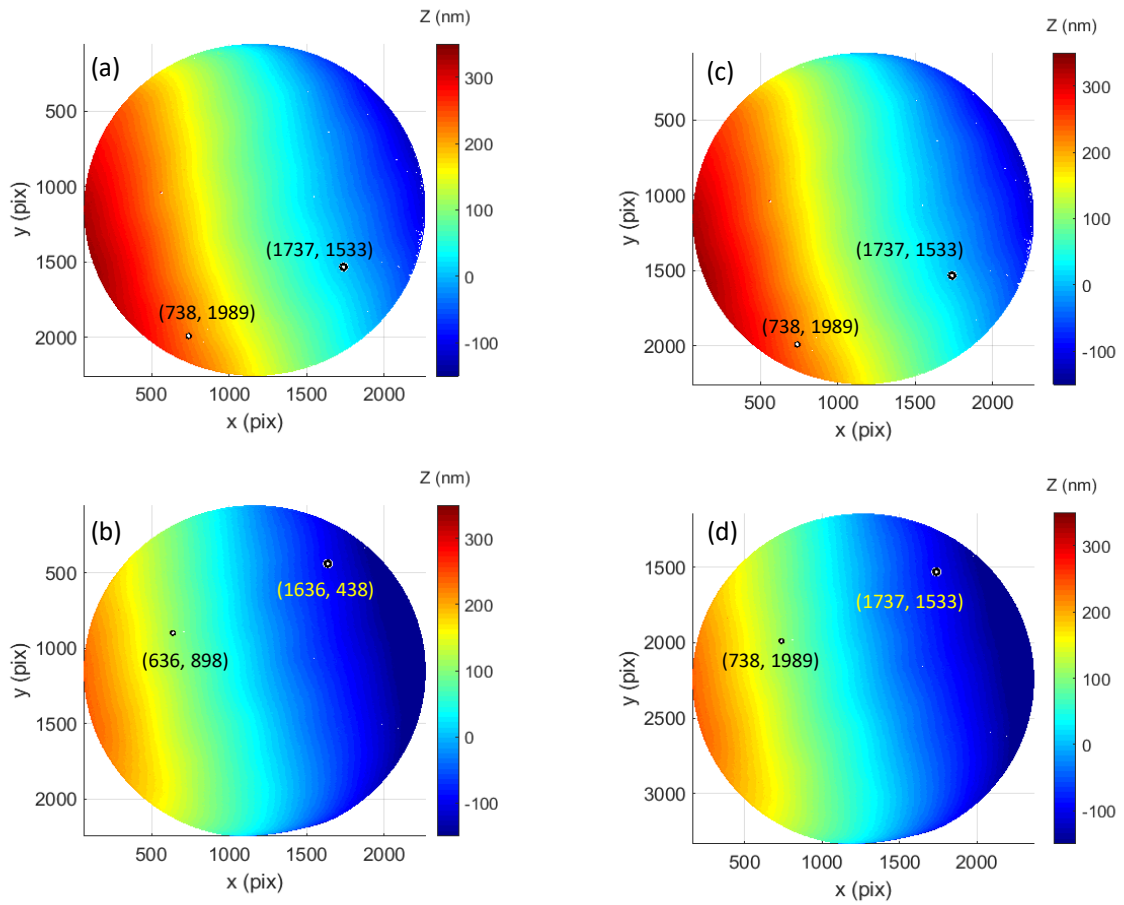


Figure 214: Stitching the interferograms by tilting one interferogram with respect to the other after aligning them in xy plane using the fiducials placed on the measurement surface; (a), (c) Recorded Interferograms of top half of the flat (b) Recorded interferograms of the bottom half of the flat (d) bottom interferogram translated in X and Y by aligning its fiducial with respect to the top interferogram.

The intersecting region of Figure 214(c and d) are shown in Figure 215 and Figure 216(a), it is a coincidence that the intersecting region of bottom half is at the bottom in the figure. Figure 216(b) shows when the bottom intersecting region is tipped, tilted and offset with respect to the top interferogram using the least sum of squares method. The interferograms

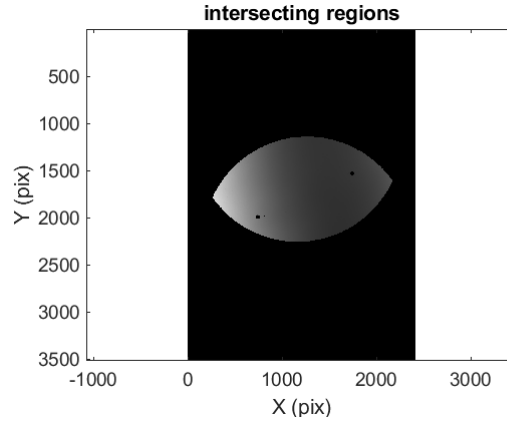


Figure 215: Intersecting region of the interferograms of top and bottom half of the optical flat.

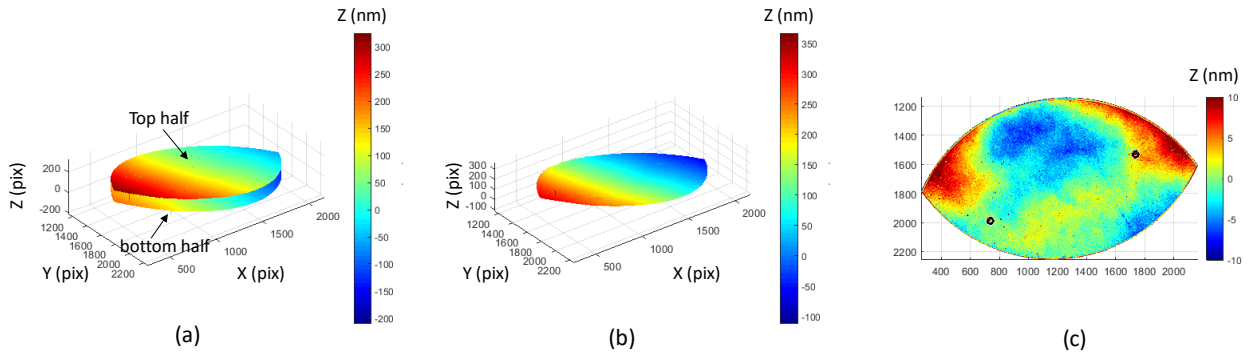


Figure 216: Intersecting region of the interferograms; (a) top and bottom half of the optical flat (b) bottom half aligned with the top half (c) difference of the aligned intersecting areas.

are subtracted from one another and plotted in Figure 216(c) and the difference is about ± 10 nm PV. Figure 217(a) shows the tilt removed data of the top half of the flat, and Figure 217(b) shows the data of the bottom half the flat which was first tilted with respect to the top half and then this tilt was removed and plotted in the same scale as Figure 217 (a), so that the ‘goodness’ of the alignment using least squares method could be seen. Figure 217(c) shows the tilt removed bottom half plotted in full color scale. Figure 217(d) shows the stitched data of top and bottom halves, whose intersecting region is averaged. The same data plotted in millimeters in shown in Figure 218(a), whose slope is removed and plotted in Figure 218(b).

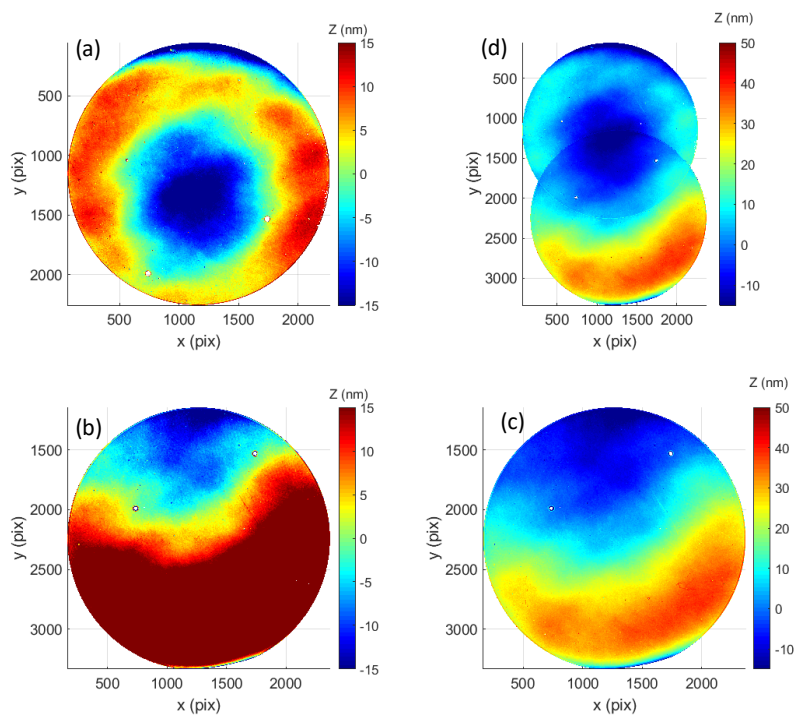


Figure 217: Stitched interferograms; (a) Tilt removed top half of the optical flat (b) tilt removed bottom half of the flat after aligning it with the top half (c) same data as in (b) plotted in its full color scale (d) top and bottom half stitched and its intersecting region averaged.

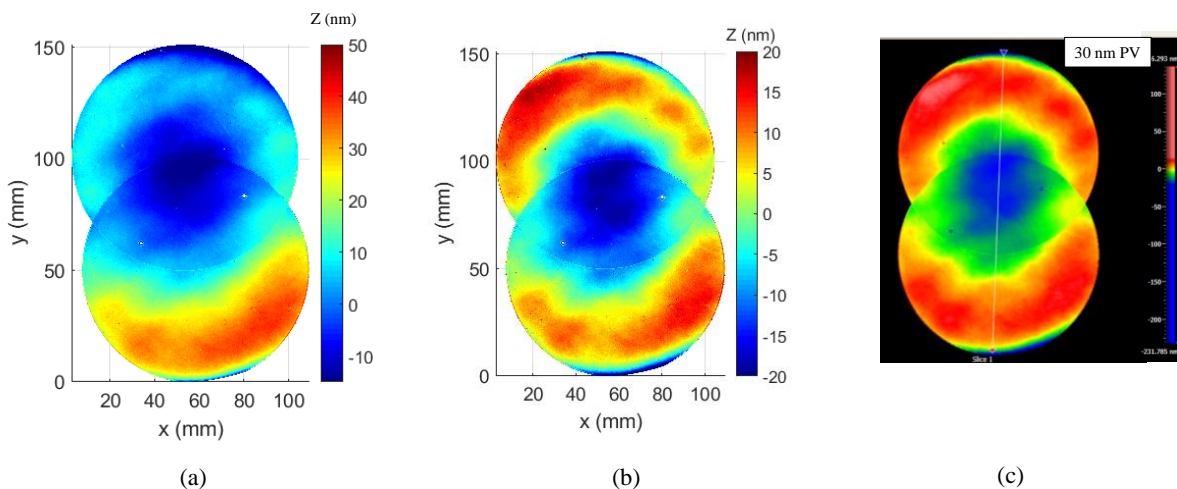


Figure 218: Comparison of the stitched data with the data stitched using the .exe file provided by Zygo; (a) Stitched data plotted in millimeters, (b) tilt removed, (c) stitched using the .exe file provided by Zygo

This stitched data has a height variation of 40 nm PV, which has the influence of transmission flat used in the experiment. The procedure of tilting the bottom half with respect to the top half includes the error due to the presence of the form of transmission flat in the recorded interferograms. Figure 218(c) shows the stitching performed using Zygo stitch.exe file that tilts one of the interferogram in x and y axis and offsets in z axis providing a PV estimate of 30 nm. It is noted that this method does not use the fiducials on the surface of the flat. This .exe file was obtained from an email conversation with Richard Pultar, applications engineer, Zygo and is provided in the flash drive attached at the back cover of the dissertation

C.2.2 Four inch diameter Fused Silica flat

A Fused Silica flat of 4 in. diameter is measured in MST and the measurement result is shown in Figure 219 (a). Frequency tuning settings used in this measurement is shown in Figure 220. Measurement result in a PSI is shown in Figure 219 (b and c). During the first measurement, the back surface of the flat is only coated with Vaseline. During the second measurement, a black cardstock is attached to the Vaseline coated surface. The Dropouts in the interferogram are the places where the cardstock did not adhere to Vaseline properly. The application of Vaseline to the back surface reduced the appearance of fringes in the intensity image, but it is still noticeable in the interferograms shown in Figure 219 (b, c). From the measurement results using MST and PSI, the flatness of the flat is estimated to about 20 nm PV.

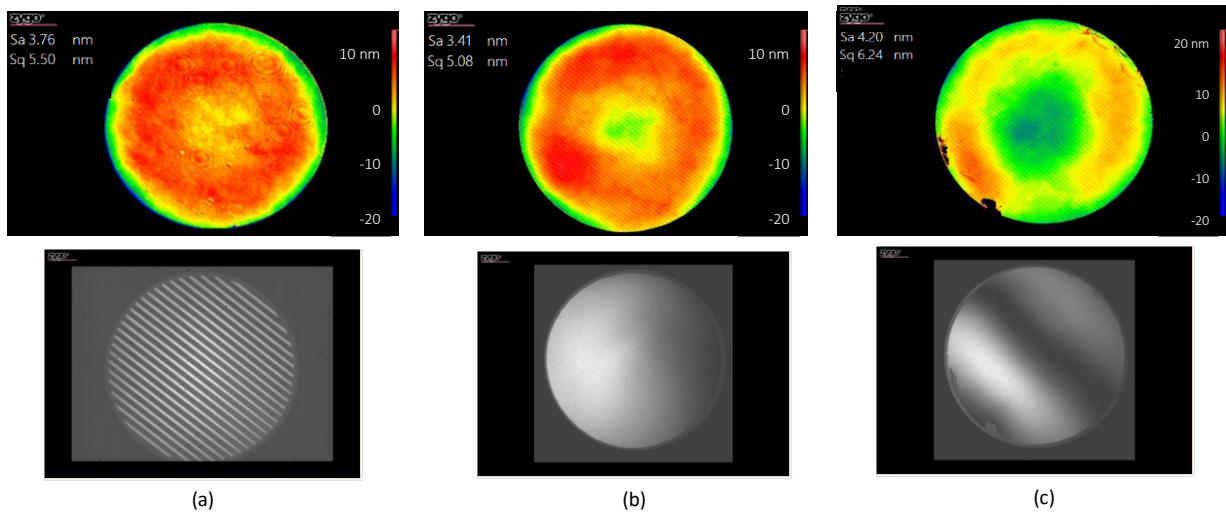


Figure 219: Measurement result of the 4 in. Fused Silica flat; (a) using a MST, Top: interferogram, bottom: intensity image (b) using a PSI Top: interferogram average of 10 measurements on PSI of the flat, whose back surface is coated with Vaseline, bottom: intensity image, (c) Top: interferogram average of 10 measurements using PSI, when a black cardstock is attached on Vaseline coated back surface of the flat, bottom: intensity image.

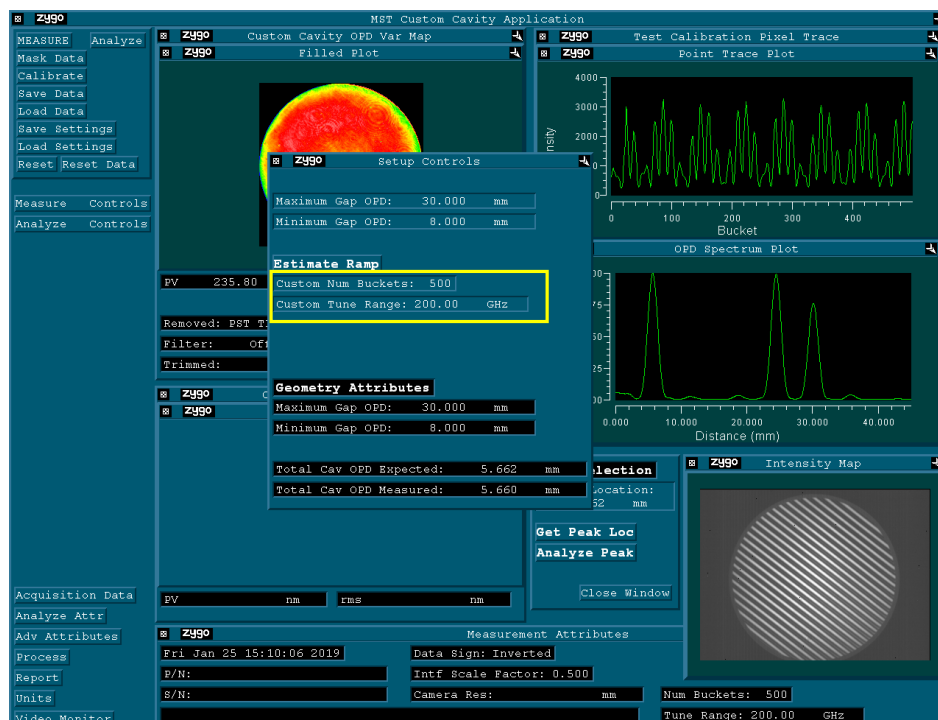


Figure 220: Frequency tuning settings used in the measurement using an MST.

C.2.3 Three inch diameter Fused Silica flat

Figure 221 (a), shows the measurement result of a 3 in. Fused Silica optical flat using MST. Figure 221 (b) shows the measurement result of the flat with Vaseline coated back surface using PSI. Flatness estimate from these measurements is about 30 nm. The difference between the 36 term Zernike polynomial fit to the MST and PSI measurements is shown in Figure 221 (c) and is about 10 nm PV.

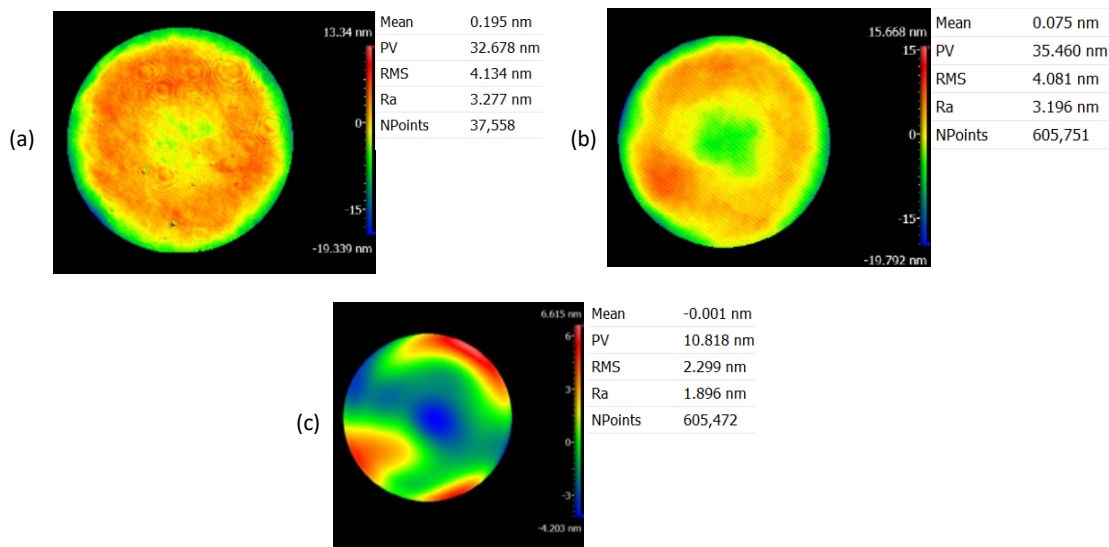


Figure 221: Measurement results of 3 in. Fused Silica optical flat; (a) on MST (b) on PSI (c) difference in the 36 term Zernike polynomials fit to the interferograms.

C.2.4 Four inch diameter Zerodur optical flat

This flat of 3/4 in. thickness, $\lambda/10$ surface flatness (Edmund optics stock #31-392-000) measured interferometrically using

- (i) Phase shifting interferometer (PSI, Zygo Verifire™) with a 1200 X 1200 pixels CCD
- (ii) Wavelength shifting interferometer (Zygo Verifire™ MST, Multi Surface Tester) with a 1000 X 1000 pixels CCD).

The optical flat is tested for two main reasons. one, to verify the specifications provided by the vendor, and two, to realize the ‘true goodness’ of the flat, since it is a practice in optical industries, to deliver a product that is better than the specifications it is supposed to meet. The flat measured using the interferometer could be utilized as a reference object for the measurements on the profilometer (Marsurf LD260).

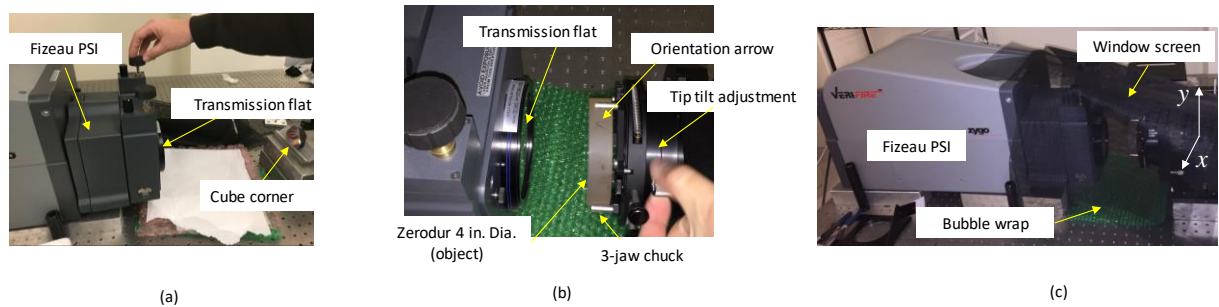


Figure 222: Experimental procedure during the measurement of the flat using a PSI; (a) alignment of transmission flat (b) alignment of object to be measured (c) bubble wrap and window screen to reduce thermal radiation effect in measurements.

Figure 222 shows the experimental setup and the procedure followed during the measurements using PSI. Figure 222 (a) shows the operator aligning the Transmission Flat (TF) of the interferometer using a cube corner (retro reflector) as a reference object. Using the manual controller that comes with the interferometer, turn on to Spot mode, and press View option on the controller. A laser light passing through the TF reflects from the cube corner and passes through TF again and reaches a CCD (Charge Coupled Device) camera housed inside the interferometer case. If the reflected light beam spot observed on the image plane of CCD is offset from the source beam spot, it is typically due to the angular misalignment of the TF, since the beam deviation caused by a cube corner is only few microradians. This angular misalignment of TF is corrected by using the knobs shown in the Figure 222(a), this moves the reflected beam spot close to the source beam spot. Once this coarse alignment is achieved, the

toggle from View to Align option on the controller. Now, one can adjust the TF to fluff the fringes on the CCD to attain about one fringe on the CCD, this is called “nulling”. Nulling is limited by the wavefront error in the retro. Once, nulling is achieved, do not touch the TF alignment knobs again. In the older interferometers, it was possible to align the TF so well that the returning light from the retro would destabilize the laser.

Before placing the measurement object (Zerodur, 4 in. Dia.) on the 3-jaw chuck used in the experiment, it is drag wiped using lens tissue and Methanol, making sure no trace of alcohol droplets are left behind after a couple of minutes. Figure 222(b) shows the alignment of measurement object with respect to the transmission flat. The object has an arrow marked on the top edge to know its orientation during the measurement, this arrow point toward the surface of interest, “front surface”. Use the transmitted and reflected laser spots to achieve coarse alignment, and then null the cavity by fluffing the fringes.

Thermal radiation during the measurement is typically seen as a smoke on the CCD display of the interferometer. Figure 222(c) shows the bubble wrap on the optical table and a window screen covering the transmission flat and object. Window screen reduces the size scale of turbulence cells, due to the averaging of small-scale turbulence. Bubble wrap reduces the effect of varying refractive index in the test cavity. The refractive index variation is due to the turbulence generated from the temperature difference between the surface of the optical table and the atmosphere. Therefore, Window screen and Bubble wrap helps to accomplish a stable measurement.

Measurement on PSI

Figure 223(a) shows the 178 nm PV fringes observed during the measurement of the 4 in. Zerodur flat, due to the internal reflection between the front and back surface of the flat.

This means, the back surface of the flat is not wedged enough to avoid the light reflecting from it. In an attempt to reduce the reflection from the back surface, the flat was tested after spraying Pre-cote #33 Blue on its backside. The fringes due to the internal reflection reduced, but was still present, and is about 40 nm PV, see Figure 224(f).

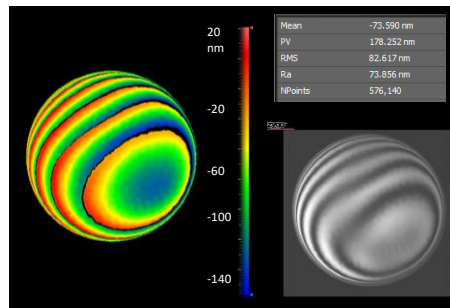


Figure 223: Interferogram of a PSI measurement of 4 in. Zerodur flat.

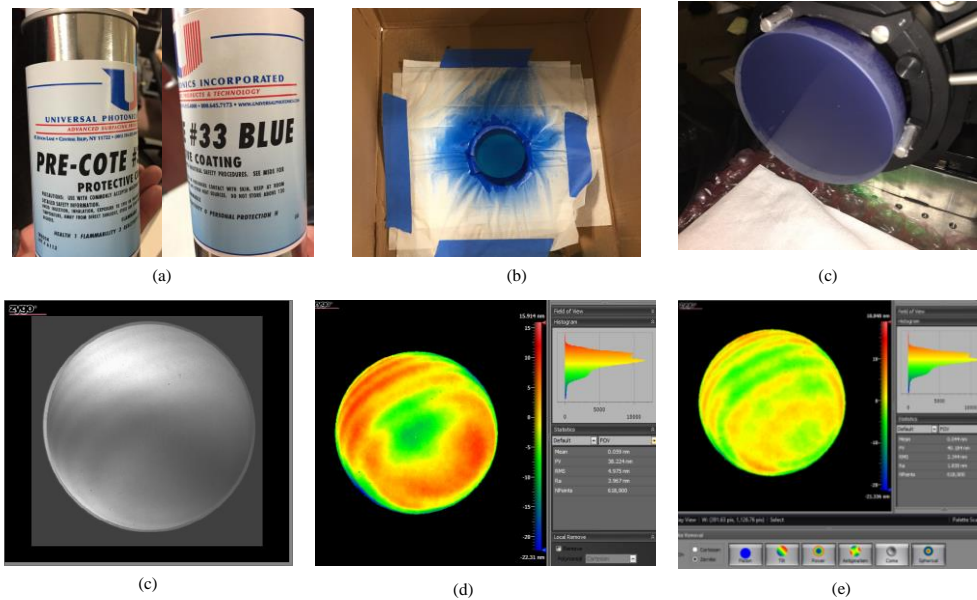


Figure 224: Interferometric measurement results of the 4 in. Zerodur flat when its back surface coated with a blue coating; (a) Product used to coat the back surface of the flat (b) back surface of the flat being spray painted (c) flat with blue coat on the back surface (d) intensity image from the interferometer (e) interferogram showing the presence of fringes due to internal reflection (f) after removing 36 term Zernike polynomials from the interferogram.

Later we learned the refractive index of wintergreen oil (Methyl Salicylate, $n=1.53$, $\lambda=630$ nm) is closer to Zerodur ($n=1.54$, $\lambda=630$ nm). Wintergreen oil is applied to the back

surface, and a black colored cardstock is attached to it. During the measurements, 4% of the interferometer laser source transmitted through the transmission flat would reflect from the front surface of the flat, and 96% of the light would traverse through it. Theoretically, this 96% of the light would transmit through the back surface of the flat, then through wintergreen oil, and then get absorbed by the black card, thereby avoiding internal reflection.

Figure 225(a) shows the interferogram of Zerodur flat measured using the PSI with a transmission flat suitable for measuring glass objects (TF_g , Veeco metrology group, TF-040 S/N:4TF0903-0626). Figure 225(c) shows the measurement with another transmission flat suitable for measuring objects with both metallic and non-metallic surfaces (TF_m Veeco metrology group, TF-040 S/N:4TF0903-0624). The main difference in these flats are form of the flats, and the transmitted wavefronts through the flat and their effect on non-common path errors. Figure 225(c and d) shows a 36 term Zernike fit to the interferograms, and the difference between them is shown in Figure 225(e) and is less than 15 nm PV. This difference is mainly due to the forms of the transmission flats, and the position and orientation of the Zerodur flat in the object plane.

Three flat test

To obtain a single profile of Zerodur flat (along its Y axis, see Figure 222(c) for coordinates) without the effect of transmission flat, a 3-flat test is performed using three different transmission flats TF_g , TF_m , and a reference flat, RF. It is noted that, the back surface of RF is ground to reduce internal reflections. Figure 226(a) shows the flats inside their wooden boxes.

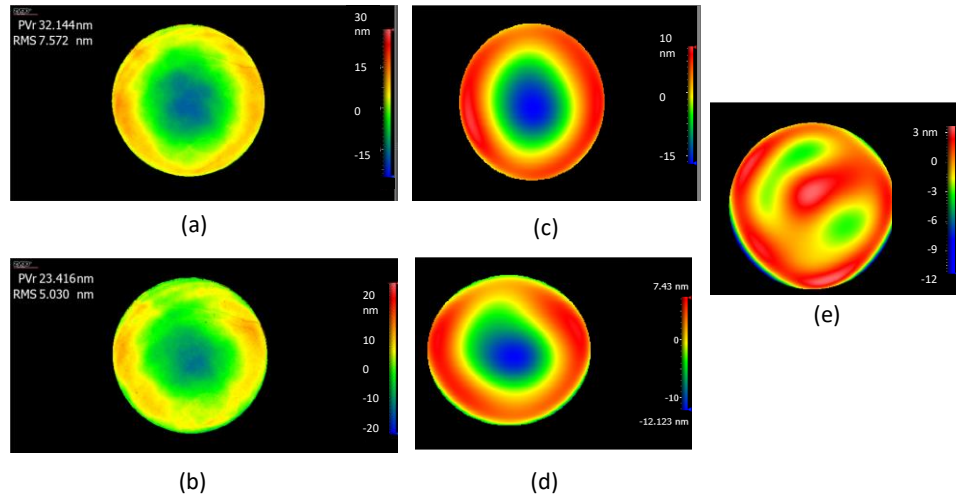


Figure 225: PSI interferograms of the Zerodur flat, whose back surface is coated with wintergreen oil and a black card attached to it; (a) measurement using Transmission flat, Tf_g (b) measurement using Transmission flat, TF_m (c), (d) 36 term Zernike fit to the measurements (e) difference between the fit less than 10 nm PV.

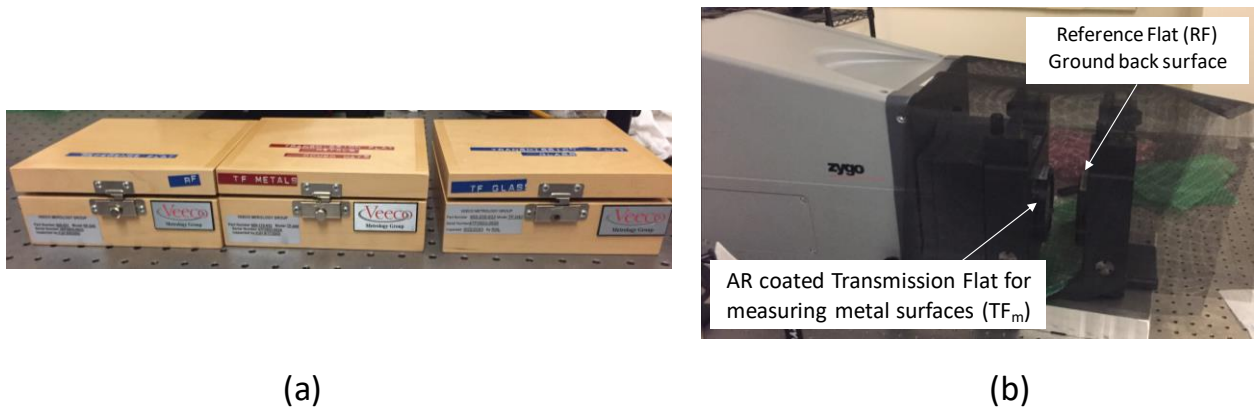


Figure 226: Three flat test - experimental setup; (a) Boxes housing the three flats used in 3-flat test (b) experiment setup with transmission flat TF_m and RF on the object side.

Schematics of the three configurations of 3-flat test is shown in Figure 227(a). Experiment setup of the first configuration using TF_m as transmission flat and RF on the object side is shown in Figure 226(b). The interferograms shown in Figure 227(b) is an average of 5 repeated measurements in each configuration. Figure 227(c) shows the profiles along the y axis

of the interferograms. Uncertainties in the three-flat measurements are discussed in a later section.

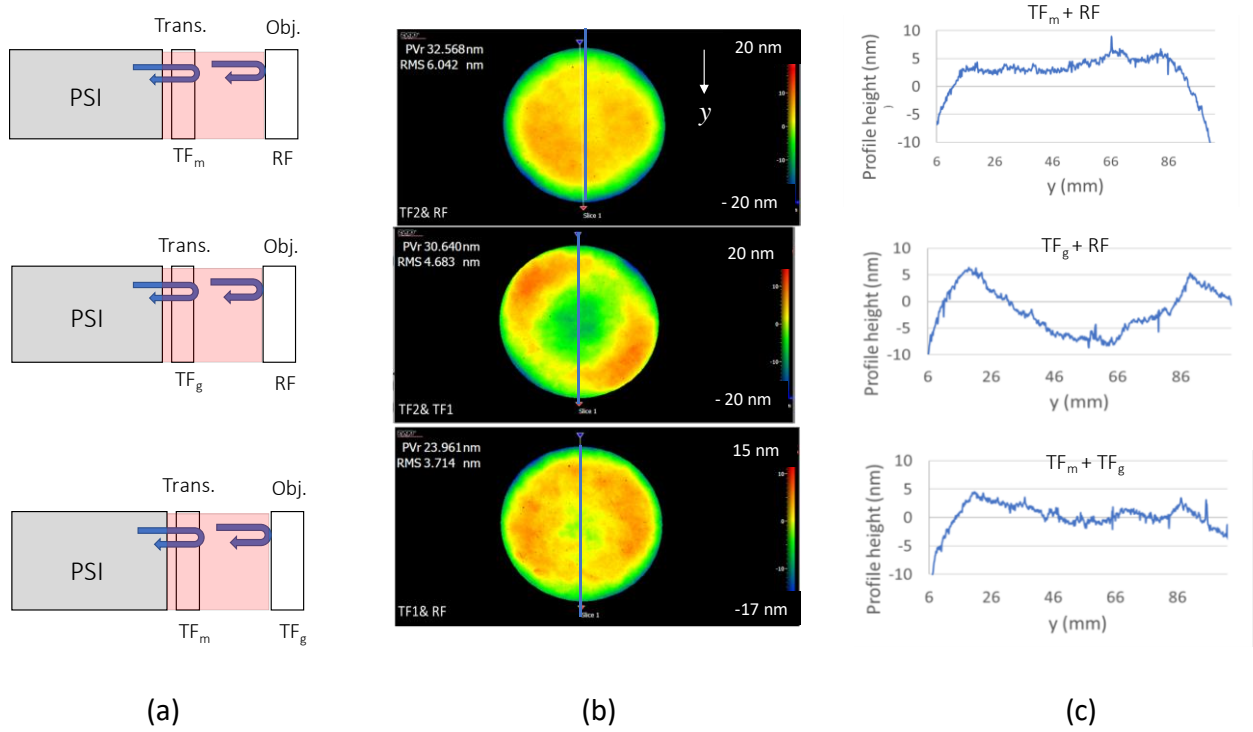


Figure 227: Measurement results of the three flat test; (a) Schematic of the three configurations of 3-flat test (b) interferograms of the measurements, blue line showing a profile taken along the Y axis , and is shown in (c).

To obtain the profiles of the flats used in the above experiments, without the influence of their respective transmission flats, below equations are used. The profiles are plotted in Figure 228. The main contribution to the uncertainty in these estimated profiles is the position of the object flats on the xy plane. A kinematic repeatability in the position of the transmission flat on the interferometer is achieved using a bayonet type mounting on the interferometer.

$$TF_m = \frac{((TF_m + RF) - (TF_g + RF) + (TF_m + TF_g))}{2}$$

$$TF_g = \frac{(-(TF_m + RF) + (TF_g + RF) + (TF_m + TF_g))}{2}$$

$$RF = \frac{((TF_m + RF) + (TF_g + RF) - (TF_m + TF_g))}{2}$$

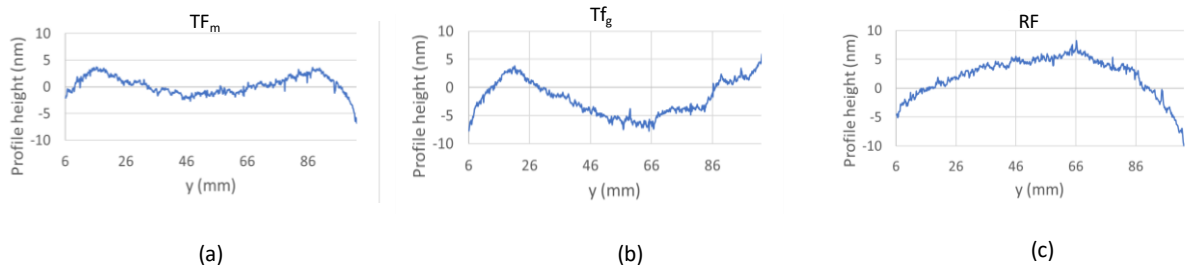


Figure 228: Profiles of the flats along its Y axis obtained from a 3-flat test.

Zerodur flat is once again measured with two transmission flats TF_g and TF_m . But, this time, three fiducials (manufactured by Zygo corp.) with an adhesive back surface are stuck on the surface of the Zerodur flat. Figure 229 (a) shows a fiducial measured on a microscope showing about 2 mm diameter. To avoid any contact on the surface of the optical flat, a cardstock is cut to the diameter of the flat and three holes little larger than 2 mm are drilled, see Figure 229 (b). Fiducials are dropped in these holes using a rubber tip tweezer and pressed gently with the tweezer's tip. Figure 229 (c) shows the flat with fiducials stuck on its surface.

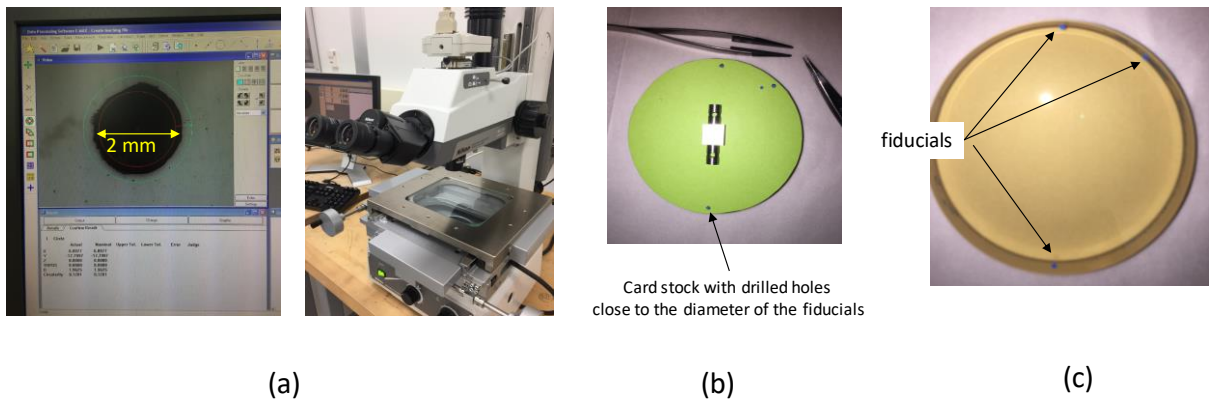


Figure 229: Plastic fiducial with adhesive backing; (a) Fiducial measured using a microscope (b) cardstock used in dropping the fiducials in its location (c) Zerodur flat with fiducials stuck on its surface.

During the measurements, the flat is oriented such that two of the fiducials lined up along the y axis. The interferogram of measurements with transmission flats TF_g and TF_m are shown Figure 230(b and f) respectively. A profile along the fiducials in Y axis is shown in red solid line, see Figure 230(c and g). Also shown in blue and green solid line are the profile of the transmission flats, TF_g and TF_m obtained from 3-flat test (see Figure 228).

A nominal profile of Zerodur flat is obtained by subtracting the red line from the blue and green solid lines, and are shown in Figure 231 (a and b). Difference between the estimated nominal profiles from these two tests is shown in Figure 231(c). Theoretically, this difference should be a straight-line of 0 PV, but the nominal profile estimated is sensitive to the position of object flat on xy plane during the two tests. Nevertheless, from Figure 231 (a, b), the nominal profile along the fiducials is about 15 nm PV and the “uncertainty” in the measurements is 10 nm PV, see Figure 231(c).

Uncertainty in the 3-flat test

Difference between the 1st and 5th measurement in all three configurations of the 3 flat test is shown in Figure 232(a to c) . Time taken for each 5 measurements is about 5 minutes. Figure 233 shows the five continuous interferograms captured in the first configuration (TF_m , RF). Planes fit to the interferograms shows the tilt and piston during the measurements. It is noted that each of these planes are offset in Z axis by 100 nm for visualization. Figure 234 (a) shows the mean of 5 measurements and a profile along the y axis (5 nm PV), omitting 5 mm roll off at the edges. Figure 234 (b) shows the standard deviation in 5 measurements, and is 5 nm PV (Type A uncertainty).

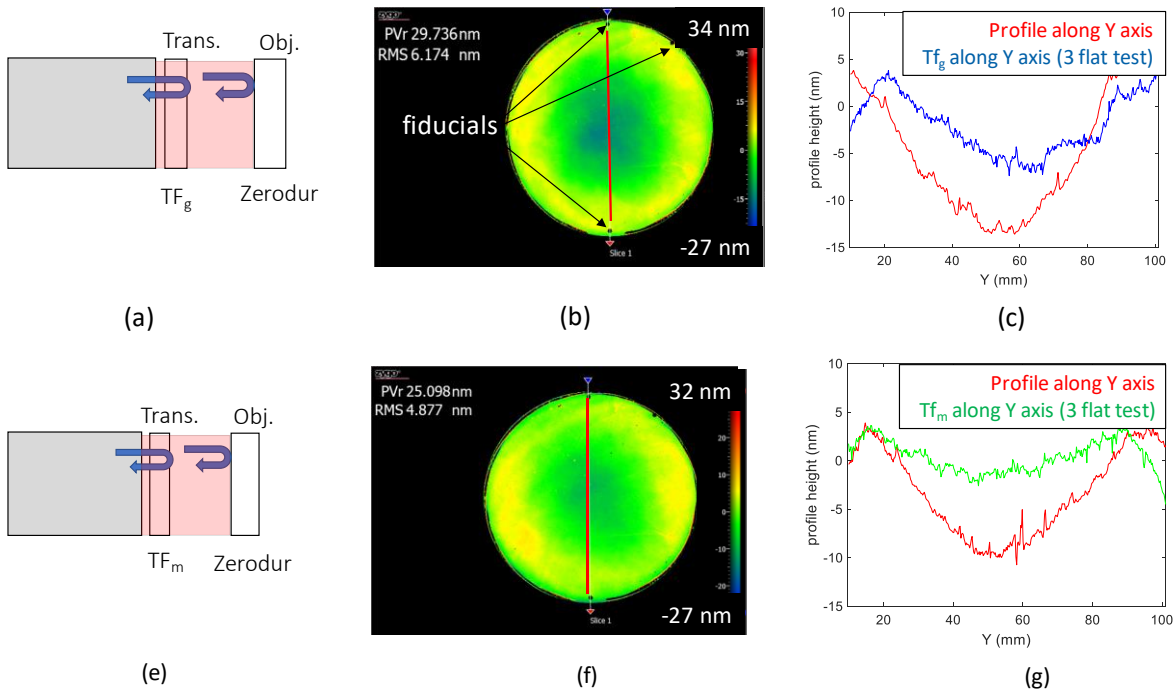


Figure 230: Interferometric measurement profile of the Zerodur flat compared with the profiles of the transmission flat obtained from the three flat test; (a,e) Schematic of the experimental configuration (b,f) interferograms measured (c,e) profile along the y axis of the interferogram shown in red, and transmission flats shown in blue and green.

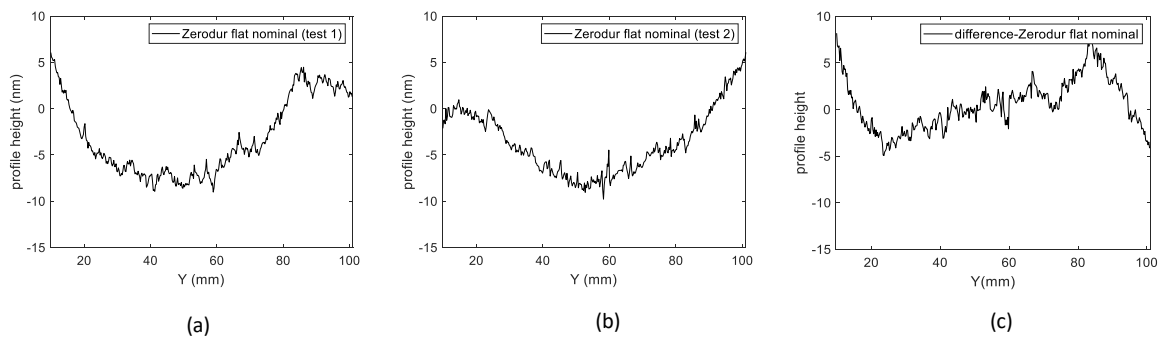


Figure 231: Nominal profile of the Zerodur flat along the fiducials (a) from test 1 with TF_g (b) from test 2 with TF_m (c) difference between the estimated nominal profiles

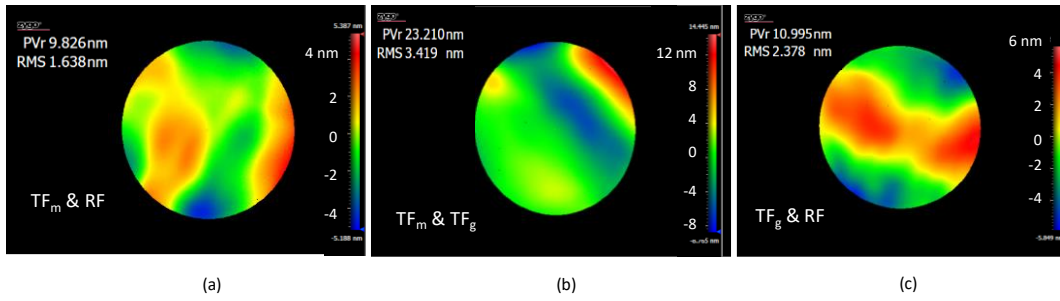


Figure 232: Difference in the interferogram of 1st and 5th measurement in the 3-flat tests using transmission and object flats; (a)TF_m, RF (b) TF_m, TF_g (c) TF_g, RF.

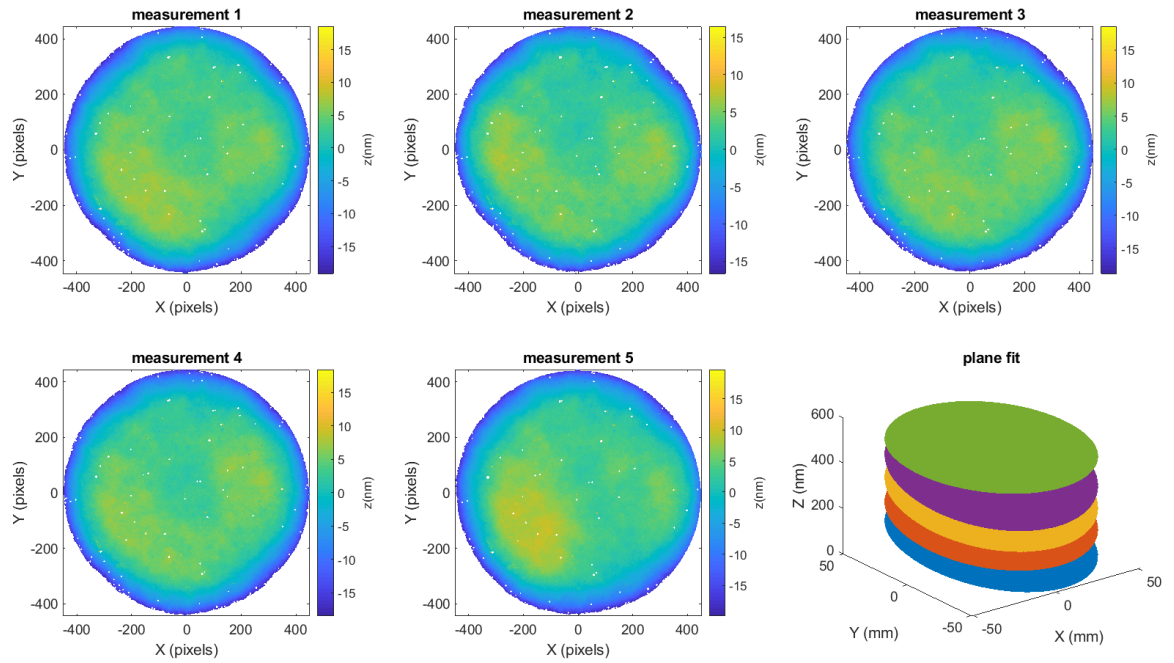


Figure 233: Five continuous measurements with TF_m and RF, and planes fit to the measurements.

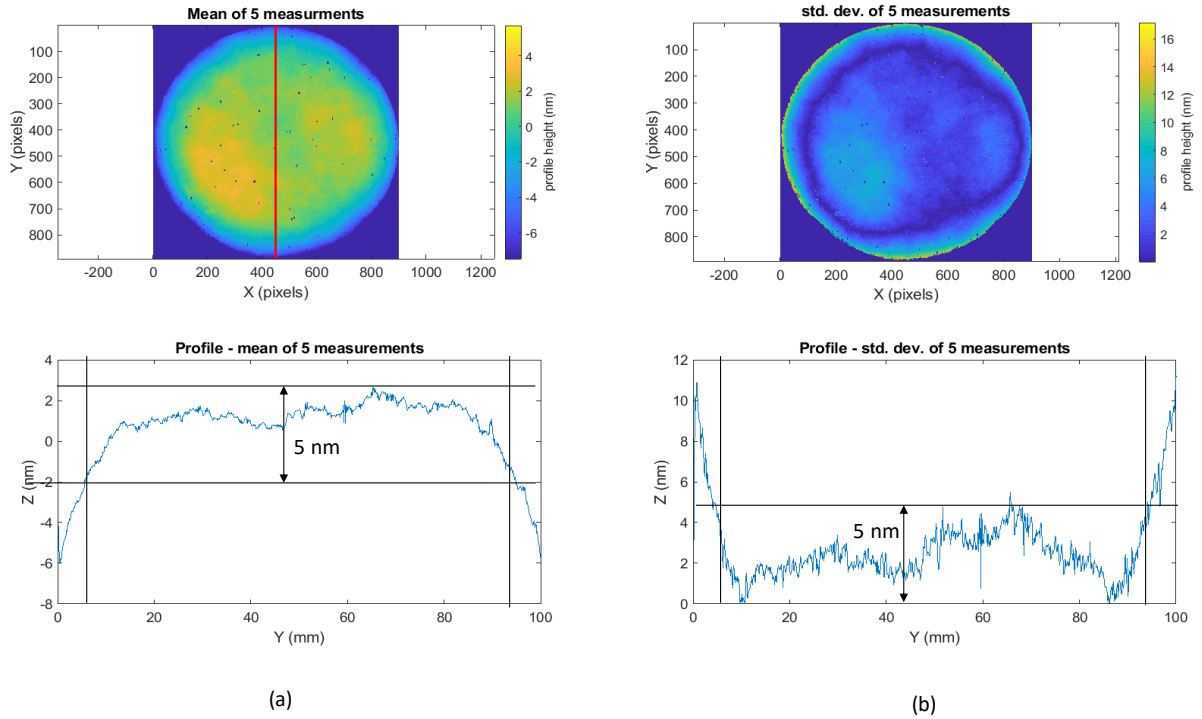


Figure 234: (a) Mean of 5 continuous measurements with TF_m and RF (b) standard deviation of the measurements.

Measurement using MST

MST shown in Figure 235 (a) could measure individual surfaces of the optics by shifting the wavelength of the interferometer laser source. Therefore, the application of refractive index matching liquid on the back surface of the flat is not necessary. The intensity image and the interferogram of the measurement is shown in Figure 235 (b) and (c) respectively. A 36 term Zernike fit to the data, and its difference from the interferogram are shown in Figure 235 (d) and (e) respectively. The transmission flat that used in this experiment is TF_g .

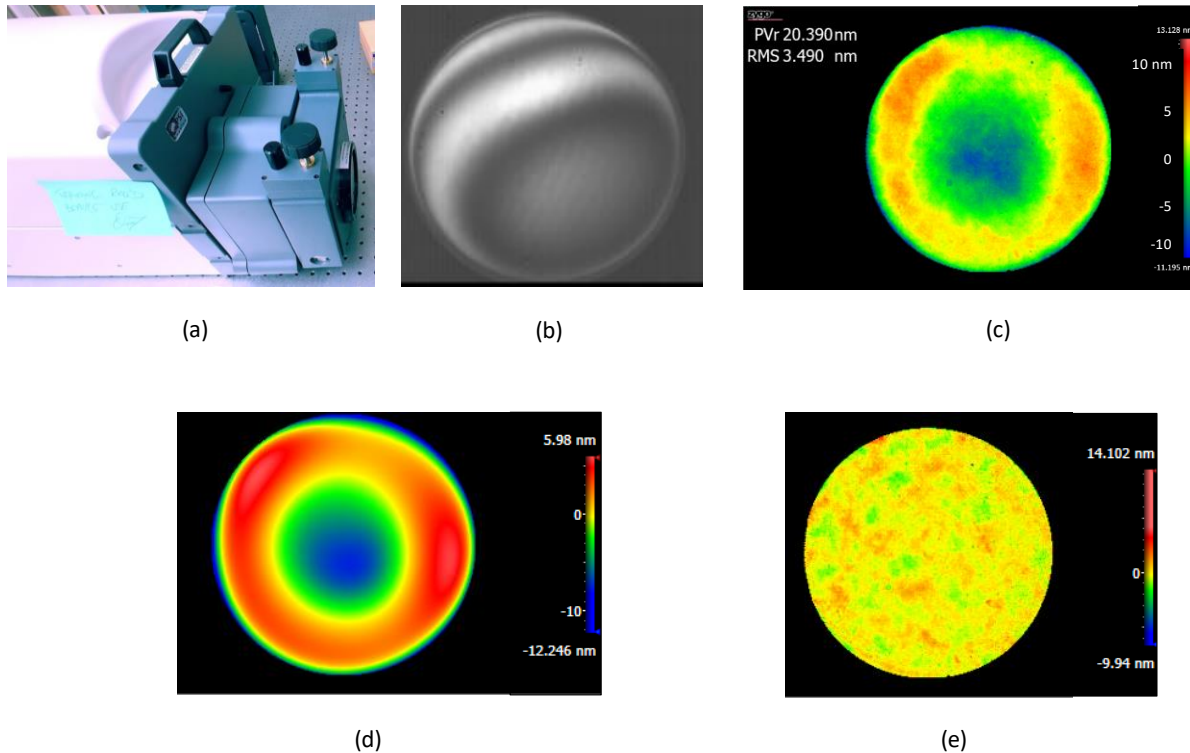


Figure 235: Interferometric measurement of the 4 in. Zerodur flat using the MST; (a) Photograph of MST interferometer (b) intensity image of the measurement (c) interferogram of the measurement (d) 36 term Zernike fit (e) difference between the fit and the interferogram.

Measurement using a PSI in vertical configuration, Zygo Verifire™ XP/D

When a flat is rested on a 3-point contact, the gravitational force would cause it to sag. To know the form of the flat in this orientation, it is measured using a vertically oriented PSI, see Figure 236 (a). The back surface of the flat is coated with wintergreen oil, and a black cardstock is attached to it and rested on the 3-point contact, see Figure 236 (b, c). Figure 237 (a) shows the intensity image of the measurement in the PSI. Figure 237 (b) shows the orientation of flat corresponding to the interferogram shown in Figure 237 (c). By the time the interferogram was captured, it was about 10 minutes after the black card was attached to the surface applied with wintergreen oil. Therefore, air bubble started to seep in, causing the irregularities on the edges of interferogram. A profile taken across the flat is about 6 nm PV,

and is shown in Figure 237 (d). This measurement has an influence of the vertical sag of the transmission flat used in the experiment. But there is no known way of compensating for it. Summary of the above results of 4 in. Zerodur flat measured using three different types of interferometer are listed below.

Equipment	PV (nm)
PSI	15
MST (includes TF)	20
PSI vertical (includes TF)	5

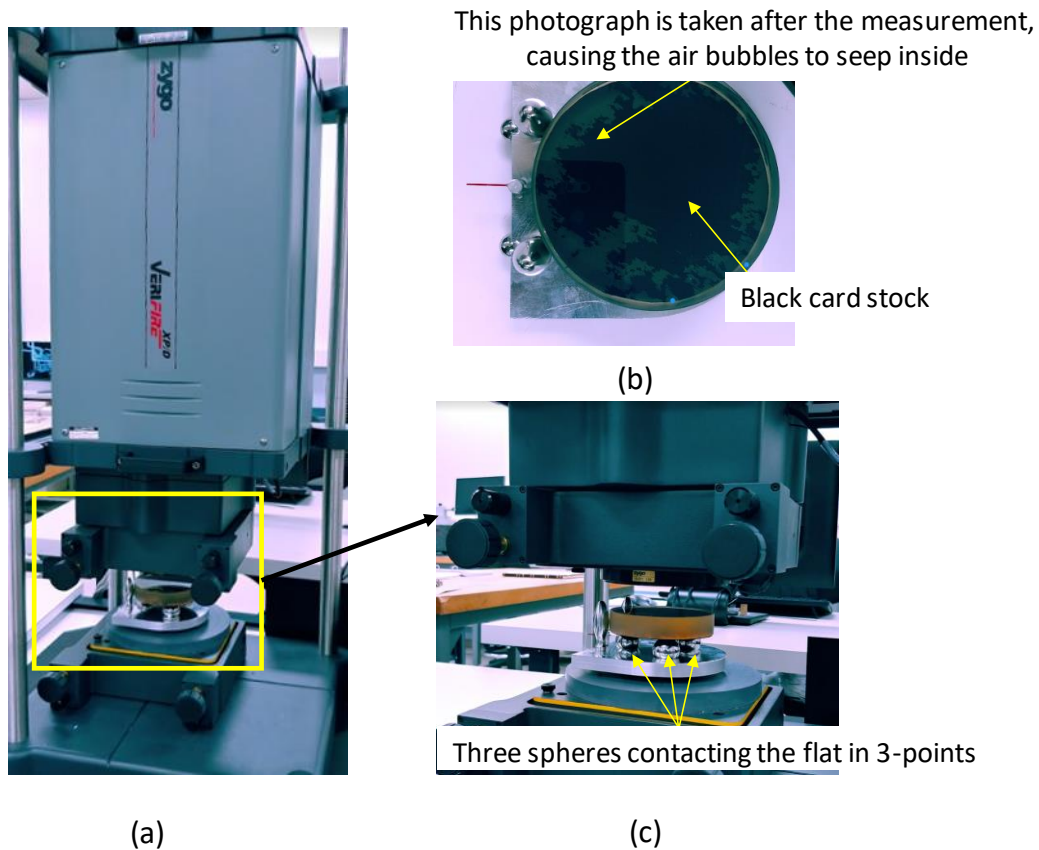
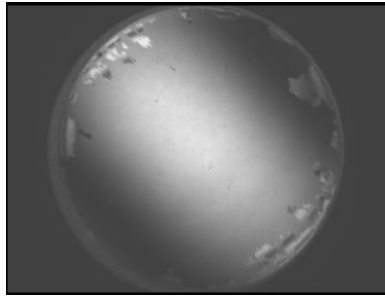
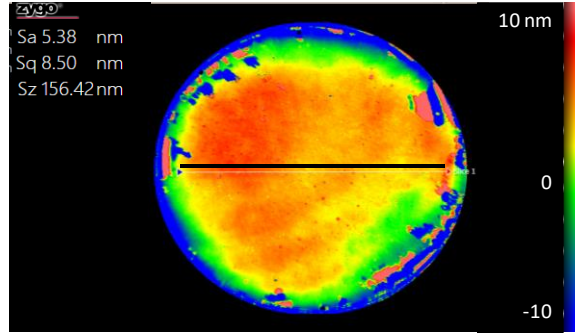


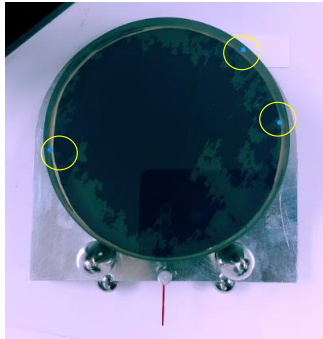
Figure 236: Experimental setup to measure the 4 in. Zerodur flat using a vertically oriented PSI; (a) Photograph of the PSI oriented vertically (b) flat rested on the 3-point kinematic mount (c) photograph showing the flat rested on three spheres.



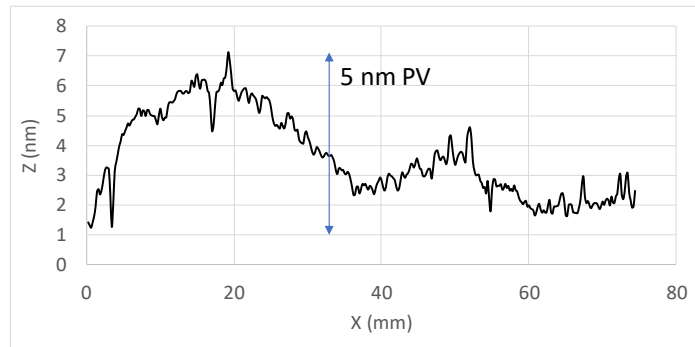
(a)



(c)



(b)



(d)

Figure 237: Measurement result of the 4 in. Zerodur flat measured using a vertically oriented PSI; (a) Intensity image of the measurement (b) orientation of the flat corresponding to the interferogram, yellow circles show the fiducials on the surface of flat, see Figure 229 (c) interferogram of the surface of flat (d) Profile taken across the flat showing 6 nm PV.

C.2.5 Three inch diameter Zerodur optical flat

Another Zerodur flat of 3 in. diameter $\frac{3}{4}$ in. thick is measured on the PSI. Experimental setup, intensity image and the interferogram (45 nm PV) are shown in Figure 238(a, b and c) respectively. and is. The same flat with no coating on backside is measured using the MST, and the interferogram (16 nm PV) is shown in Figure 238 (e). Frequency tuning setting of MST is shown in Appendix C.2.2. The difference between the 36 term Zernike fit to the PSI and MST measurements is shown in Figure 238 (f), and it is about 12 nm PV.

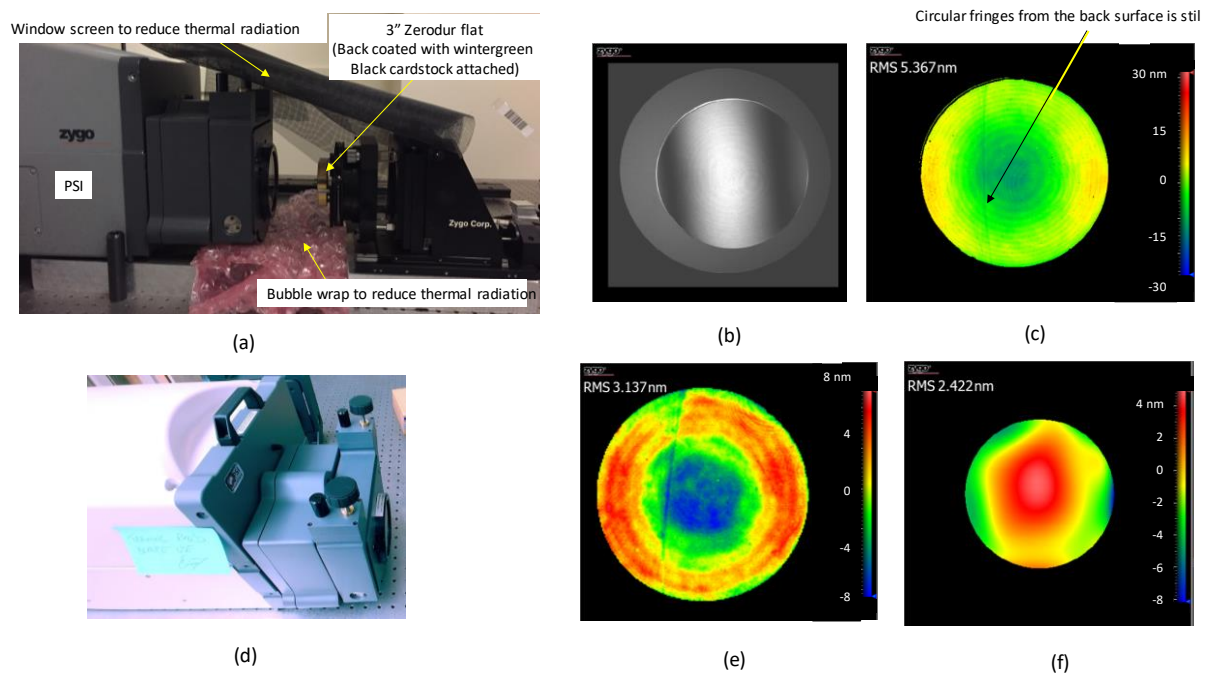


Figure 238: Measurement result of a 3 in. Zerodur flat using the PSI; (a) Experimental setup (b) intensity image of the flat (c) interferogram measured showing 45 nm PV (d) MST used to measure the flat, Zygo mx GUI displaying the experimental settings is given in Appendix C.2.2 (e) interferogram showing 16 nm PV (f) Difference in the Zernike fit to the interferograms measured in PSI and MST.

C.2.6 Aluminum coated glass bar

This section discusses the measurements of a rectangular bar ($320 \times 50 \times 10 \text{ mm}^3$) shown in Figure 239 (a) is coated with Aluminum, and does not have a manufacturer's specification.

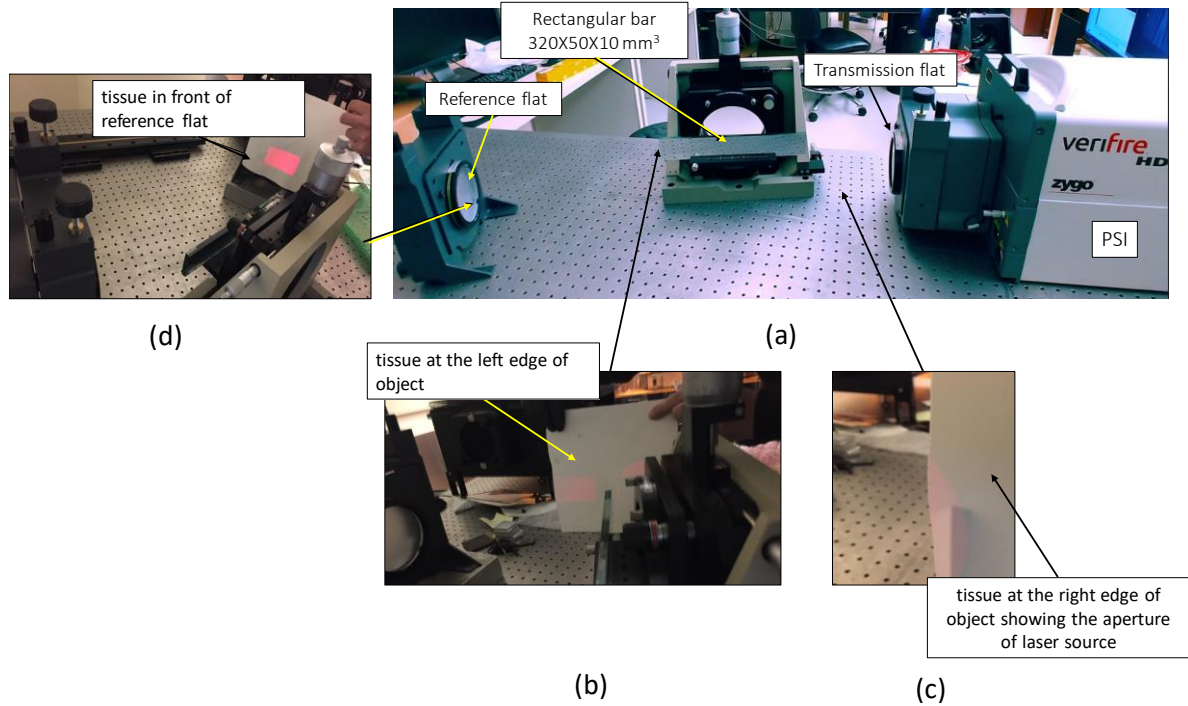
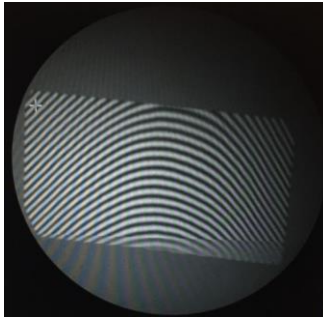


Figure 239: Experimental set up to measure an Aluminum coated rectangular bar using the PSI by following a ‘skip flat’ technique; (a) Photograph showing the transmission flat (TF), object (rectangular bar), and reference flat (RF) used in the measurement (b) using a tissue, operator verifies that the aperture of the laser source covers the right side edge of the bar (c) same is done for the left edge of the bar (d) using the tissue, location of the light beam falling on RF is verified.

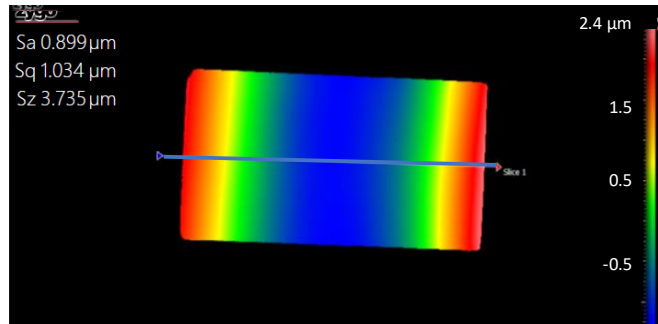
Figure 239 (a) shows the measurement of the rectangular bar using Skip-flat technique used when the length of the measurement object is longer than the aperture of the transmission flat (TF) of the interferometer. In our case, the bar is 320 mm long and the aperture of TF is 100 mm. In a skip flat test, the measurement object is kept in an oblique angle, so that the portion of the aperture of interferometer laser source covers the whole area of the object. This

is verified by looking at the aperture at the right edge of the bar using a tissue, as shown in Figure 239(b). To double check, the tissue is held at the left edge of the bar as well, as shown in Figure 239(c). The reflected light from the bar must reach the reference flat (RF). The position of RF is adjusted by looking at the laser beam using the tissue. The light from RF reflects back to the bar and transmits through the TF to reach the interferometer housing, labeled as PSI in Figure 239 (a). It is noted that, the rectangular bar is drag wiped using lens tissue and Methyl alcohol before setting up the experiment.

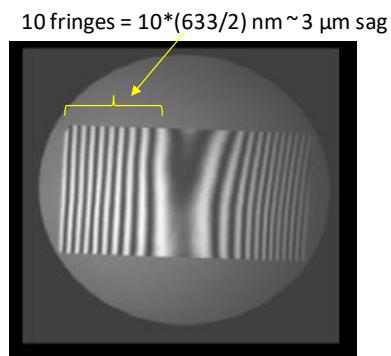
Figure 240 (a) shows the fringes captured by the CCD of the interferometer. As the pitch and yaw of the bar is adjusted, the fringes get ‘fluffed’, and is shown in Figure 240 (b). The experimental setup is left to ‘soak’ (attain thermal equilibrium) for an hour, and the interferogram shown in Figure 240 (c) is recorded. A profile taken across the interferogram has a sag of about 3 μm , and is shown in Figure 240 (d). It is noted that the x axis of the profile shown in Figure 240 (d) is in pixels, this is because of the failure to calibrate the length of the using the 100 mm aperture of the PSI, on its software Zygo, MX. Therefore, the measurement is repeated on Oct 1, 2019. This time, four fiducials (manufactured by Zygo corp.) with adhesive back surface is attached on the bar. These fiducials could be seen in the measurement result shown in Figure 241(b). It is noted that, the rectangular bar is drag wiped using lens tissue and Methyl alcohol before the fiducials were stuck on the bar. Figure 241(b) is an interferogram of an average of 5 continuous measurements. A profile taken along the x axis of the interferogram is shown in Figure 241(c), and it has a sag of about 3 μm . Figure 241(d) shows three profiles taken along the y axis of the interferogram with a profile height of less than 100 nm PV.



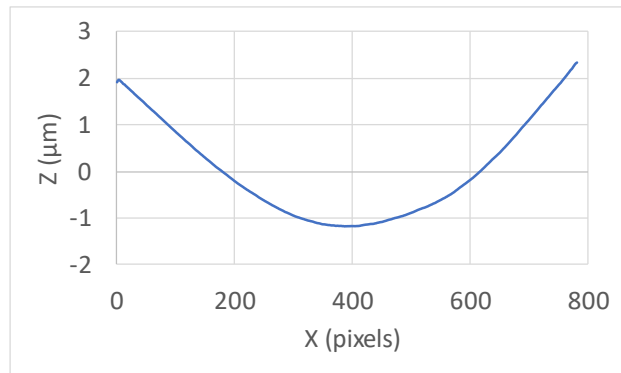
(a)



(c)



(b)



(d)

Figure 240: Experimental results of the skip flat test performed on the rectangular bar.

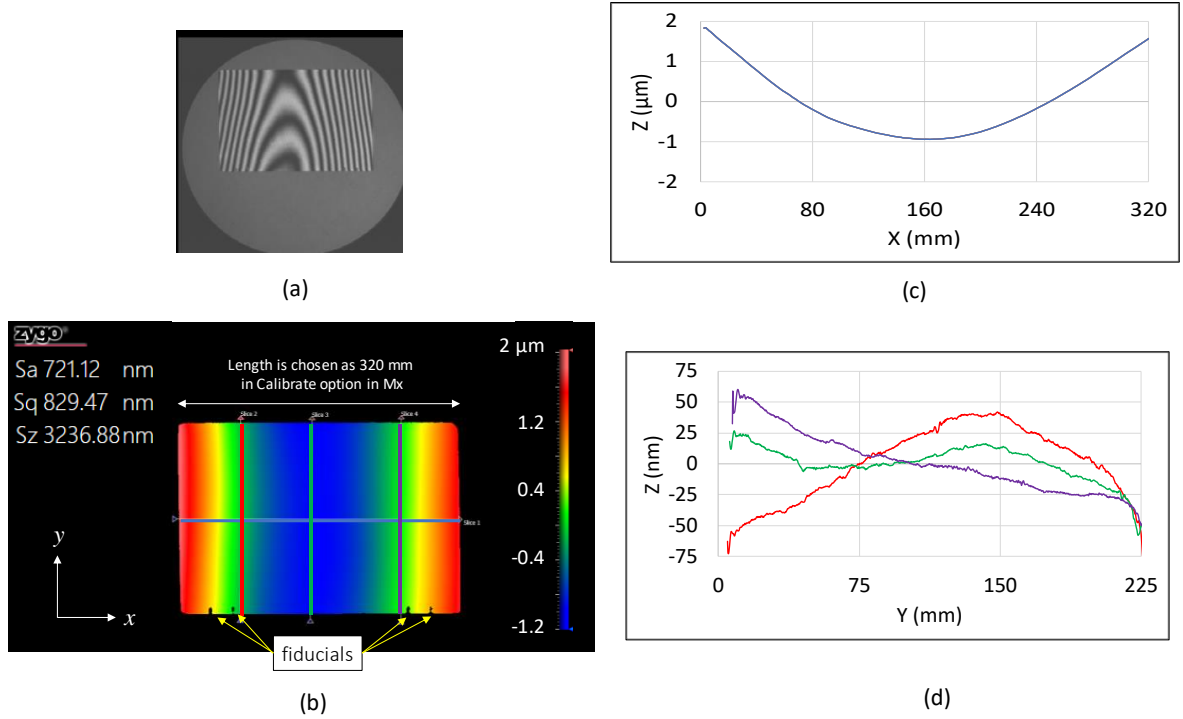


Figure 241: Skip flat measurement results of the remeasurement; (a) fluffed out fringes (b) interferogram whose piston and tilt terms are removed, and fiducials are shown on the bottom (c) profile taken along the X axis of interferogram with 3 μm PV (d) profiles taken along the Y axis of interferogram with less than 100 nm PV.

The optical path length difference (OPD) of an interferometry measurement is given by $2\Delta z \cos \theta$, where Δz is surface height deviation of the object, and θ is the oblique angle at which the object is placed. [Vannoni, 2014]. In a conventional arrangement, when the object is placed parallel to the TF, i.e. $\theta = 0$, making $OPD = 2\Delta z$. But, during the skip flat test θ is not equal to 0, and MX has an option to input the value of θ to correct the measured surface height for this effect. This is not utilized in the above experiment, and must be considered in the future.

Nevertheless, to validate the outcomes of the skip flat test, the bar is measured in a conventional arrangement to cover 100 mm of its length. This test was performed on Feb 22, 2019. Profile taken along the interferogram shown in Figure 242 (c) has an height of 0.6 μm

PV, which is comparable to the 100 mm midsection of the profile from skip flat test shown in Figure 241 (c). This is not expected, because, Δz in skip flat test is not corrected for α . One possibility is that we were lucky during the experiment and the oblique angle was about $\theta = 60^\circ$, making $OPD = \Delta z$. And, if the interferometer software outputs the Δz value corrected for the twice the path length by default, there would still be a factor of 2 error in the two measurements. Therefore, it is not clear how the two results are comparable in the mid 100 mm span.

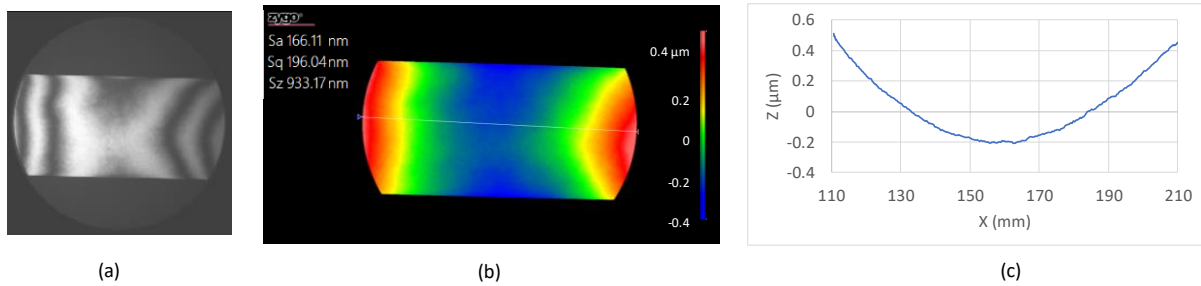
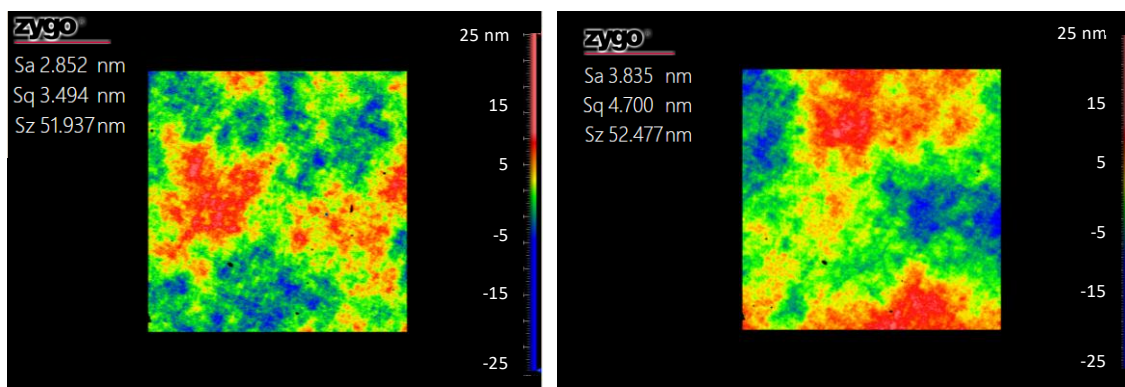


Figure 242: Interferometer measurement of the middle 100 mm portion of the bar; (a) fluffed out fringes (b) resulted interferogram (c) profile along X axis with 0.6 μm PV.

The bar is also measured using a Coherence Scanning interferometer (CSI, Zygo ZeGageTM), and the results of measurement in two locations of the bar is shown in Figure 243(a and b), 50 nm PV and 4 nm RMS. The results are spike clipped to 1σ and edge trimmed to 25 pixels using Zygo MX software.



(a)

(b)

Figure 243: interferograms from the CSI measurements of two locations of the bar showing surface height of about 50 nm PV, and less than 4 nm RMS.

C.2.7 Silicon Carbide coated hollow Aluminum bar

This section discusses the measurements of a hollow aluminum bar coated with Silicon Carbide (SiC), and polished by Dr. Todd Noste. This bar is measured using the PSI in a Skip flat configuration as shown schematically in Figure 244(a). Three fiducials were stuck on the surface of the bar as shown in Figure 244 (b). The resulted interferograms from the measurement contained empty pixels, and it got better when the angle, θ shown in Figure 244 (a) is increased.

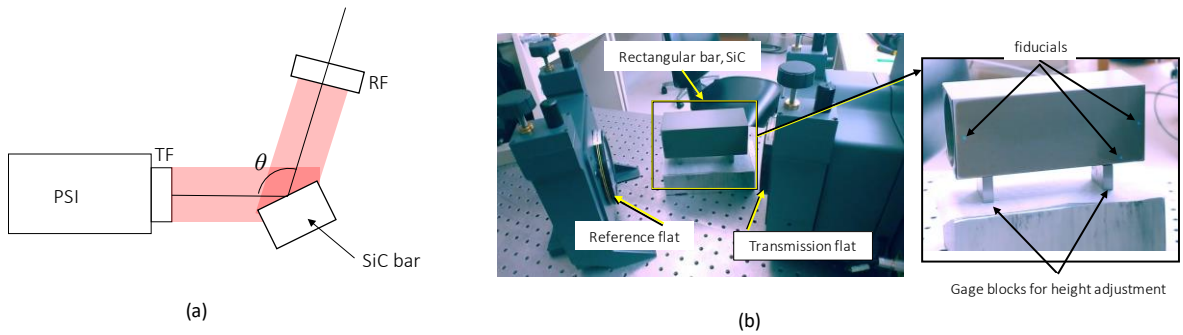


Figure 244: Skip flat test of a Silicon Carbide coated Aluminum hollow bar; (a) schematic, (b) Experimental setup with an inset showing the fiducials on the surface of the bar.

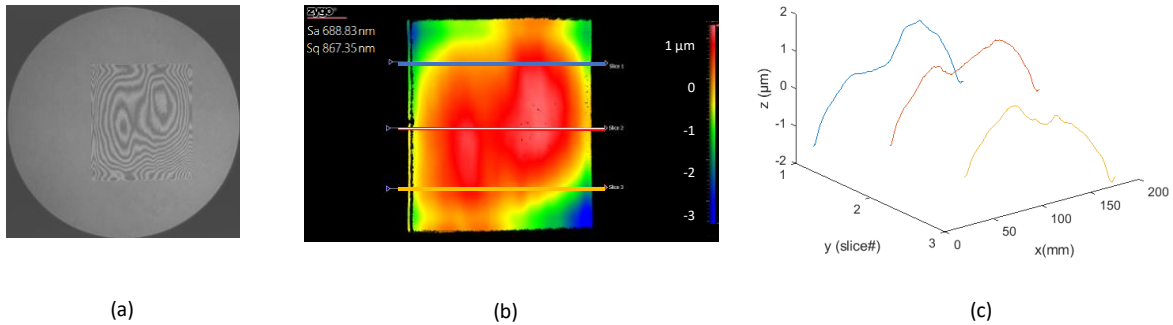


Figure 245: Measurement results of the SiC bar; (a) intensity image (b) interferogram showing the three locations at which the profiles are made (c) profiles with a height of about $4 \mu\text{m}$ PV.

Interferogram of the measurement is shown in Figure 245 (b). Three equally spaced profiles taken across this interferogram is shown in Figure 245 (c). It is not clear why the fiducials on the surface of the SiC bar is not visible in the interferogram. Initially it was thought, it is because of the oblique angle at which the SiC bar is placed. Therefore, another experiment is conducted with the bar facing straight towards the Transmission flat. The aperture of the interferometer covers about 100 mm length of the bar. Interferogram from this measurement is shown in Figure 246, and it does not show the fiducials either. The absence of fiducial in the interferograms could be due to the dark surface of SiC coating.

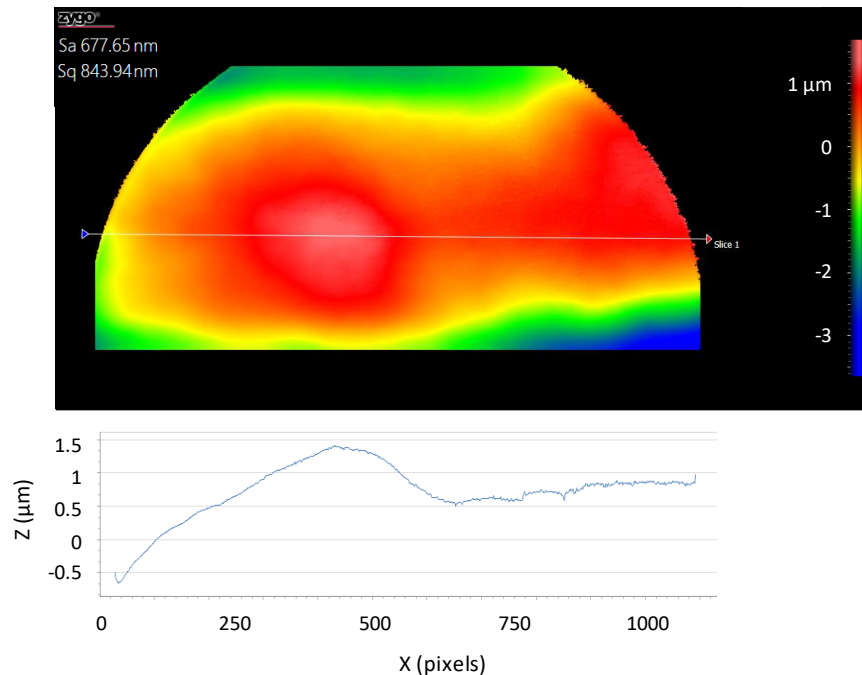


Figure 246: Measurement result of SiC bar when it is facing straight towards the transmission flat used in the interferometer.

Measurement using the profiler

Measurement result of SiC bar using the profiler is shown in Figure 247 (data courtesy: Todd Noste). The fiducials were not present on the surface during the time of this measurement. Although, there exists some similarity in the profiles obtained from

interferometer and profilometer measurements (see Figure 248), the orientation of bar on the profilometer is not clear.

In the future interferometric measurements, efforts must be taken to capture the fiducials in the interferogram. In the future profilometer measurements, data must be collected by running the stylus along these fiducials, so that the data from both the instruments could be reasonably compared. A localized interferogram of the SiC bar surface is captured using a Coherence Scanning Interferometer (CSI), see Figure 249(a). A profile taken across the surface with a variation in height of less 100 nm PV except for the pit, see Figure 249 (b).

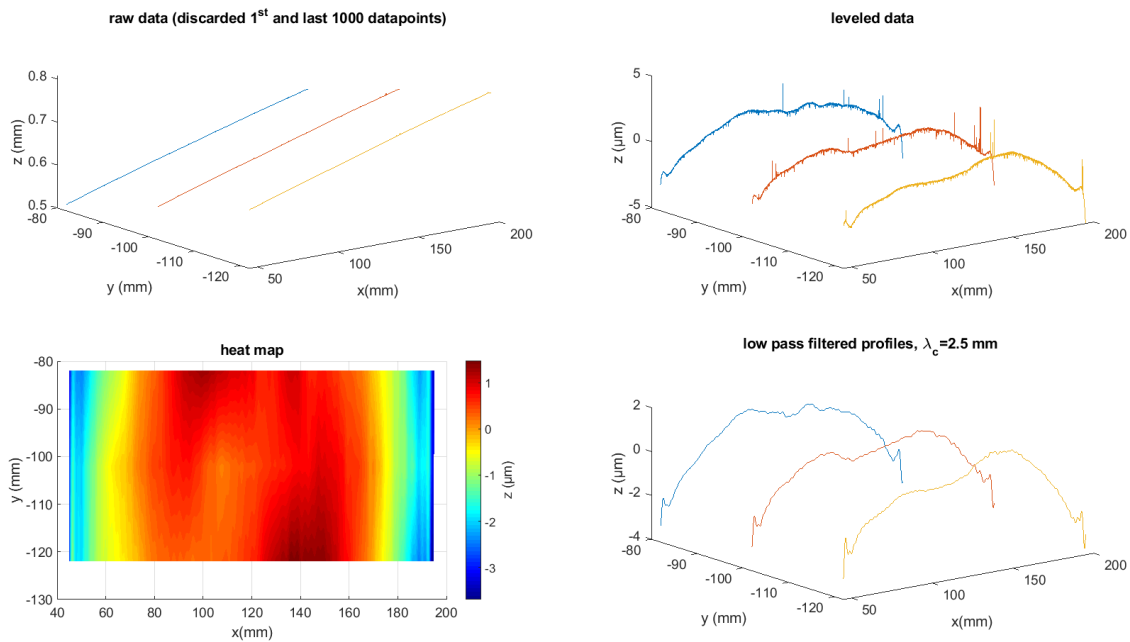


Figure 247: SiC bar measured on the stylus profilometer (Marsurf LD260); (a) raw data (b) leveled data – piston and tilt removed (c) Low pass filtered to 2.5 mm (d) surface heat map of the measurement, Courtesy: Todd Noste.

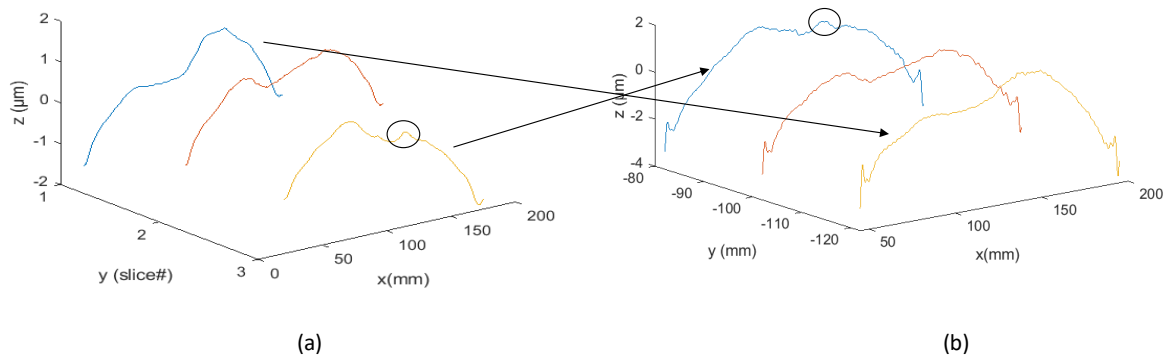


Figure 248 Profiles on the SiC bar from the (a) interferometer measurement, (b) Profilometer measurement.

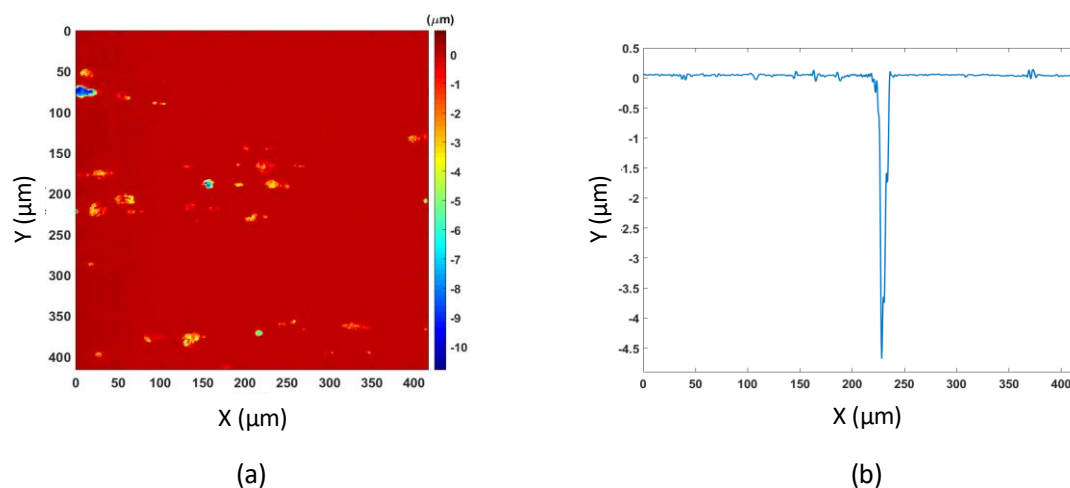


Figure 249: (a) Interferogram of the SiC bar measured using the CSI (b) A profile taken across the surface.

C.2.8 Right-angled prisms

This section discusses the measurements of two Right angled prisms using the PSI and the MST. Both the prisms are made of Fused Silica and have similar dimensions. Figure 250 Shows a schematic of these prisms and a way of identifying the surfaces. Prism ‘E’ has a couple of slanted lines on its back surface which is grounded. Prism F (Edmund optics Stock #47-790) is guaranteed to have a surface flatness of $\lambda/10$. This prism has an alphabet ‘F’ scribed on its front ground surface.

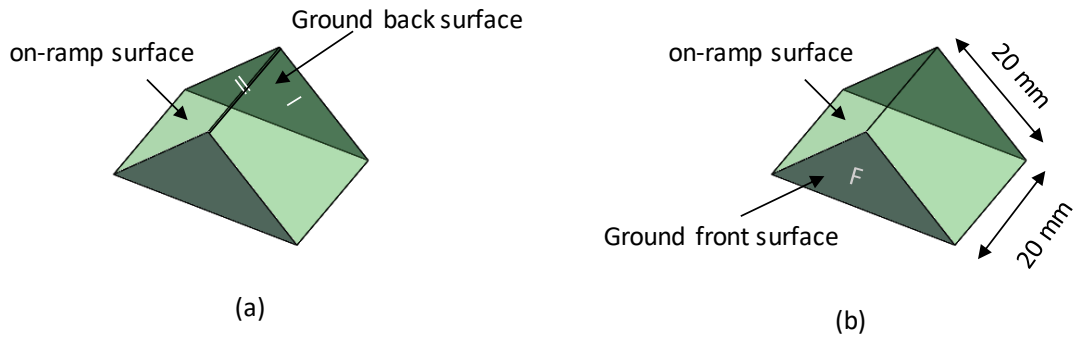


Figure 250: Schematics showing the identification marks on (a) Prism ‘E’ and (b) Prism ‘F’.

Prisms are drag wiped using a lens tissue and Methanol before placing its ground front face contacting the surface of tip tilt stage, see Figure 252. For Prism ‘F’, this is the face on which alphabet ‘F’ is scribed, as shown schematically in the top view in Figure 251 (a). Percentage of light transmitted and reflected during the interactions with surfaces of Transmission flat (TF_g), and the on-ramp surface of prism is shown in Figure 251 (a).

The experimental setup contains two cavities, (i) between the front surface of TF_g and the on-ramp surface of prism, highlighted in blue (ii) inside the prism, highlighted in green. The order in which the transmissions and reflections takes place with the prism is labeled

numerically in Figure 251 (b). To reduce the fringes due to these internal reflections, base of the prism is applied with Vaseline.

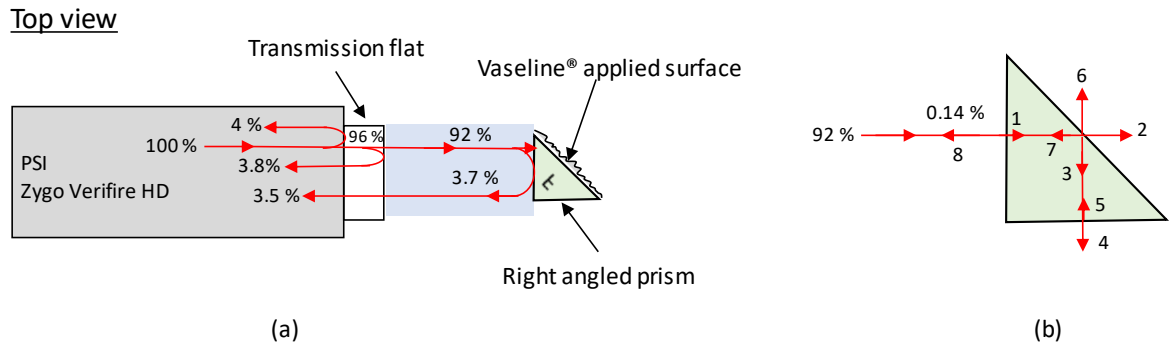


Figure 251: Schematic of the experimental setup of the interferometer measuring the prism; (a) Orientation of the prism during measurement, and the transmissions and reflections surfaces the laser interacts with (b) transmissions and reflections inside the prism cavity.

Upper half of Figure 253 shows (a) intensity image of the on ramp surface of prism ‘E’ (b) interferogram, and (c) a profile across the surface with 40 nm PV. Images in the lower half pertains to the measurement of off ramp of prism ‘F’ with a profile of 20 nm PV. Similarly, upper half of Figure 254 shows (a) intensity image of the on ramp surface of prism ‘F’ (b) interferogram, and (c) a profile across the surface with 10 nm PV. Images in the lower half pertains to the measurement of off ramp of prism ‘F’ with a profile of 20 nm PV. During these measurements, the prism is kept close to the center of the aperture of Transmission flat as shown in Figure 254 (a). Both these measurements have an effect of Transmission flat in its measured flatness. The flatness of Prism ‘E’ is close to the vendor specification of $\lambda/10$ (< 60 nm). However, the flatness of prism ‘F’ is about $\lambda/30$ (< 20 nm).

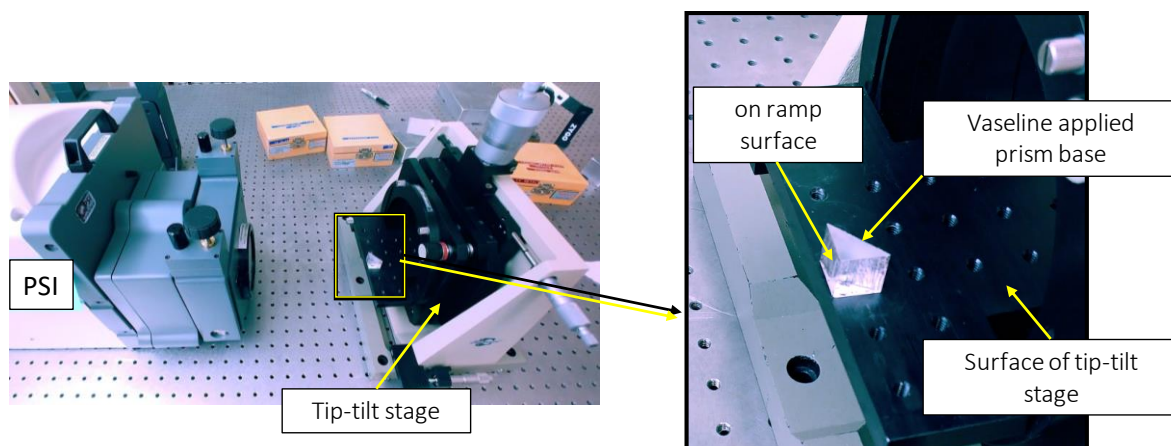


Figure 252: Photograph of the experimental setup measuring the prism

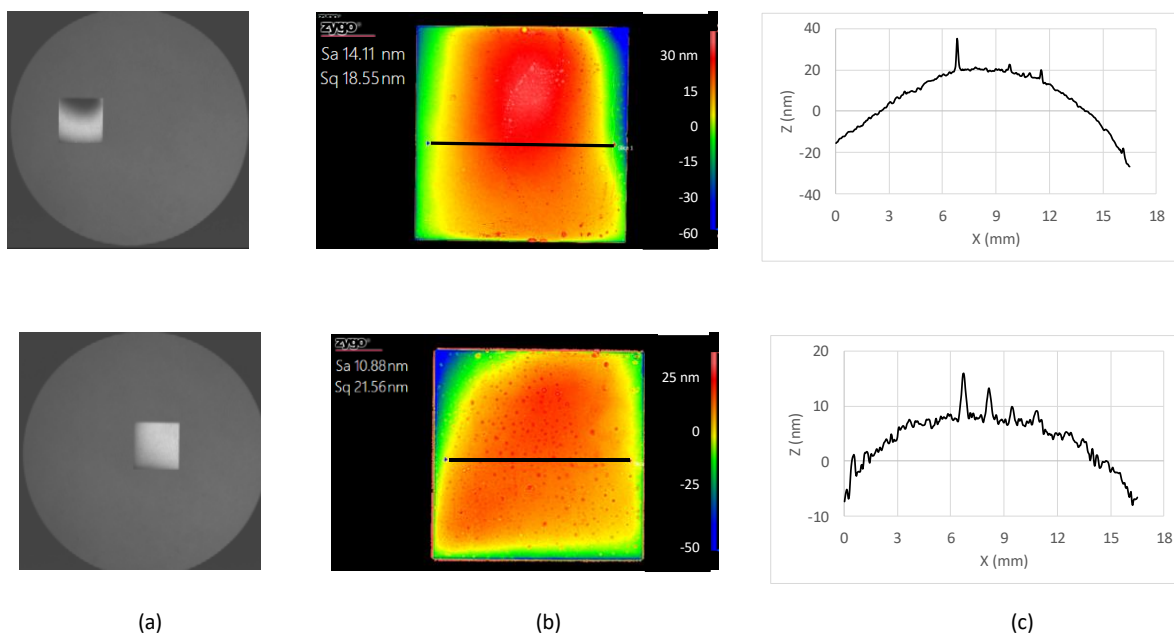


Figure 253: Experimental result of prism 'E'; Top: on-ramp surface Bottom: off-ramp surface (a) intensity image (b) interferogram (c) a profile across the surface

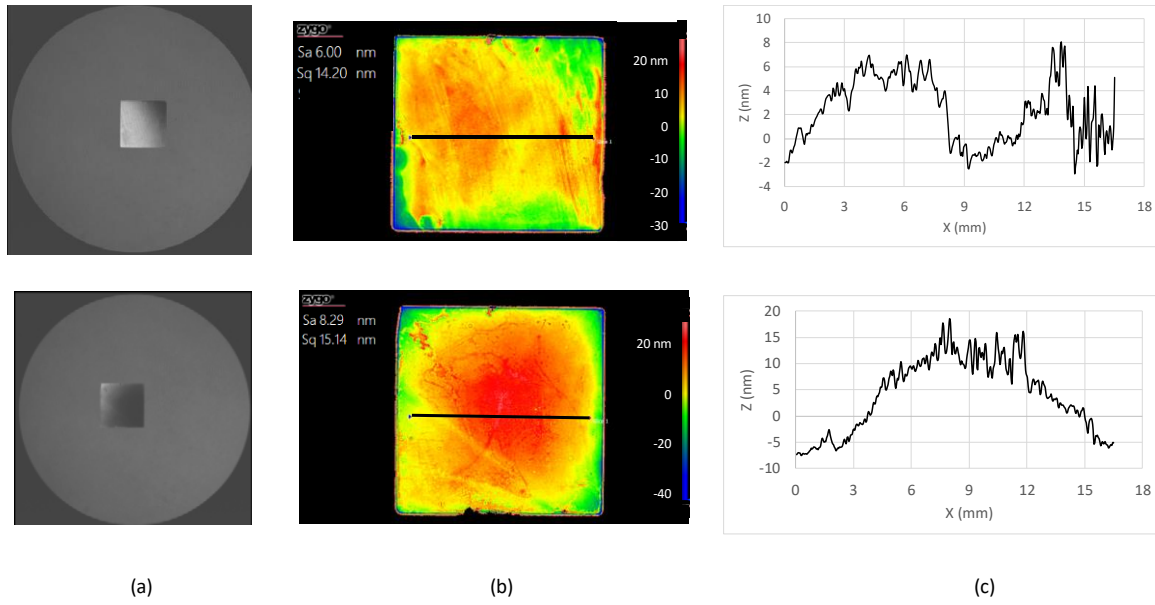


Figure 254: Experimental result of prism 'F'; Top: on-ramp surface Bottom: off-ramp surface
(a) intensity image (b) interferogram (c) a profile across the surface

C.2.9 Measurement of concave mirrors and calibration of the transmission sphere

This section discusses the interferometric measurement of two concave mirrors whose surface is later measured using the profilometer. Since the interferometric measurement uses a transmission sphere as the reference surface, its form errors will affect the measured interferogram of the concave mirror surfaces. Therefore, it will be beneficial to measure its form error (calibrate) and correct for it in the subsequent measurements of concave mirror surfaces. One way of doing this is a ‘Random ball test’ where a ball is setup at the confocal position (see Figure 255(a)), and multiple measurements of different spherical cap areas of the ball are performed using the interferometer when the ball is setup at random angular orientations (pitch, yaw, roll). These measurements are averaged to represent the form of the transmission sphere, because the spherical cap areas measured of the ball are uncorrelated due to its random orientations.

Wavefront error sensitivity to offset of the ball

Figure 255(b) shows the Silicon nitride ball placed on a kinematic seat that constraints its translational degrees of freedom. This seat is held on a 3-axis translation stage using poster tack. Since the measured interferogram of the spherical cap area of the ball is also influenced by the offset in the ball from its confocal position resulting in tilt, coma, astigmatism, defocus, etc., it is necessary to estimate the sensitivity of this effect. When you translate the ball in x using the micrometer knob at the side, it introduces a horizontal tilt in the measured interferogram due to the curvature of the ball surface. Same is true when you translate the ball in y using the knob at the top, introducing a vertical tilt in the measured interferogram. Figure 256 shows the induced horizontal tilt and the resulted horizontal coma (PV normalized Zernike

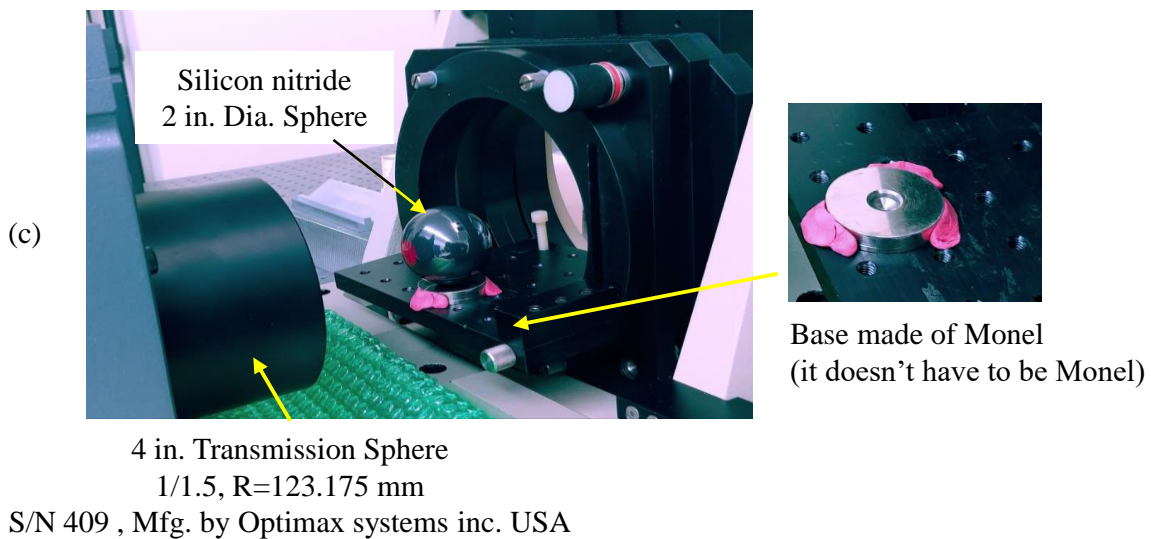
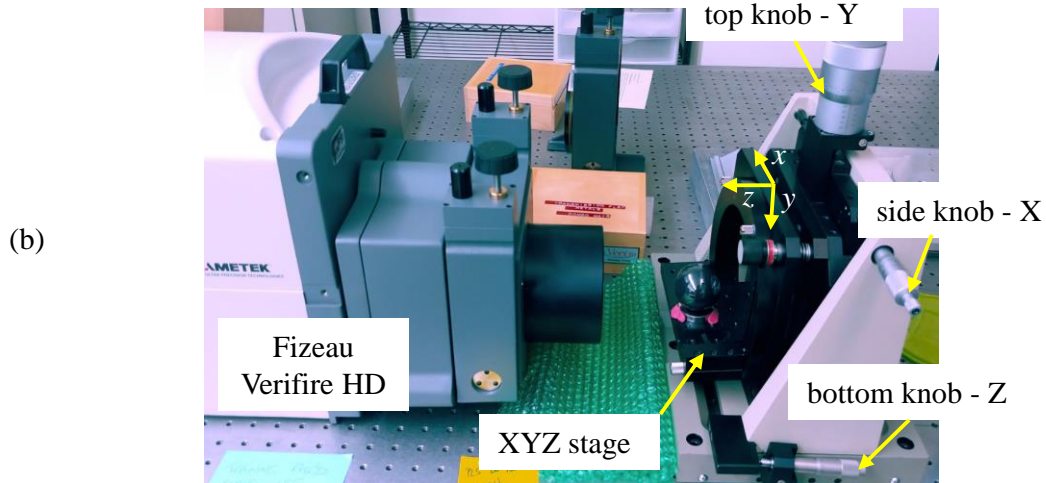
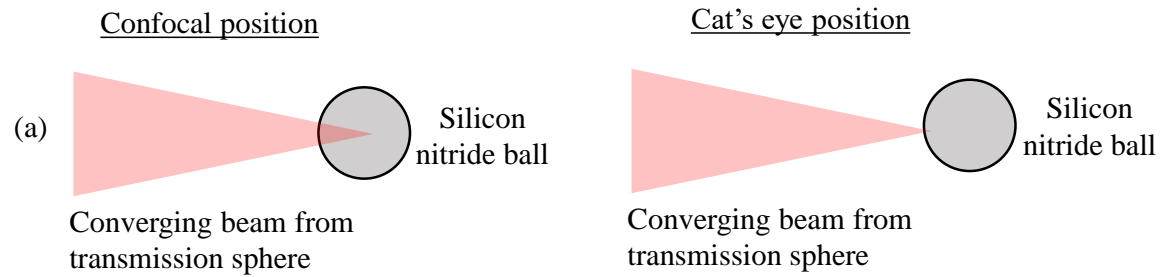


Figure 255: Experimental setup using a Silicon nitride ball to estimate the form of the transmission sphere using the PSI; (a) Schematic showing the confocal and cat's eye position during the measurement (b, c) Silicon nitride ball placed on a 3-axis translation stage to align it to its confocal position.

coefficients) when the ball is translated in x axis in steps of around 0.0005 inches (12.7 μm) for a 0.25 mm range. Also shown is the induced vertical tilt and the resulted vertical coma when the ball is translated in y axis in steps of around 0.00025 inches (6.35 μm) for a 0.13 mm range. Other Zernike terms such as vertical and oblique astigmatisms due to the induced tilts by translating the ball in x and y axis are shown in Figure 257 and Figure 258. Then the ball is translated in z using the knob at the bottom in steps of 20 μm for a range of 0.5 mm, inducing defocus from the confocal position resulting majorly in primary and secondary spherical Zernike terms shown in Figure 259 and Figure 260 respectively.

Among the error terms, primary spherical term is the most sensitive to defocus of the ball (150 nm PV), next term being the vertical astigmatism due to the vertical offset of the ball in y axis (25 nm PV). It is noted that, since the offset of the ball in its kinematic seat is typically repeatable to within a couple of micrometers during random ball tests, the expected wavefront error is minimal.

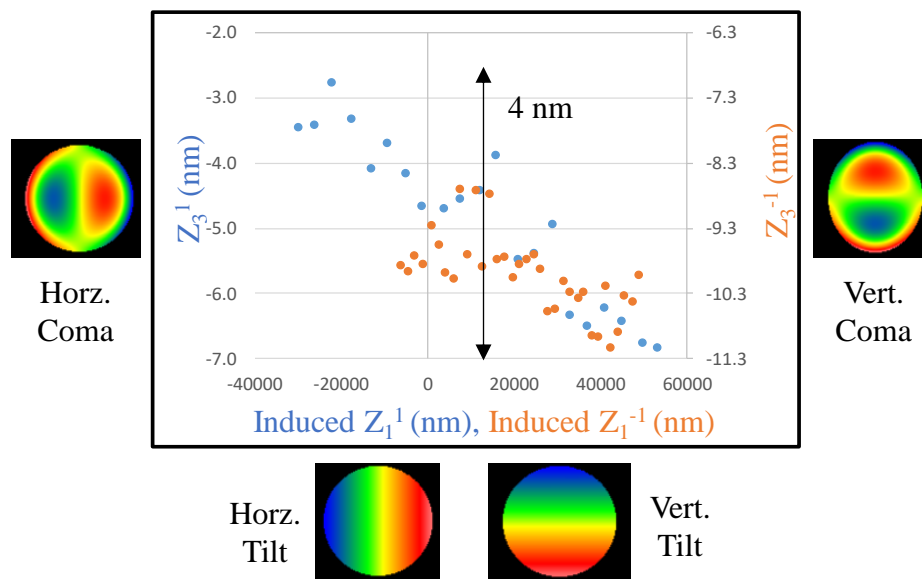


Figure 256: Induced tilt due to the x and y translation of the ball and the resulted coma terms.

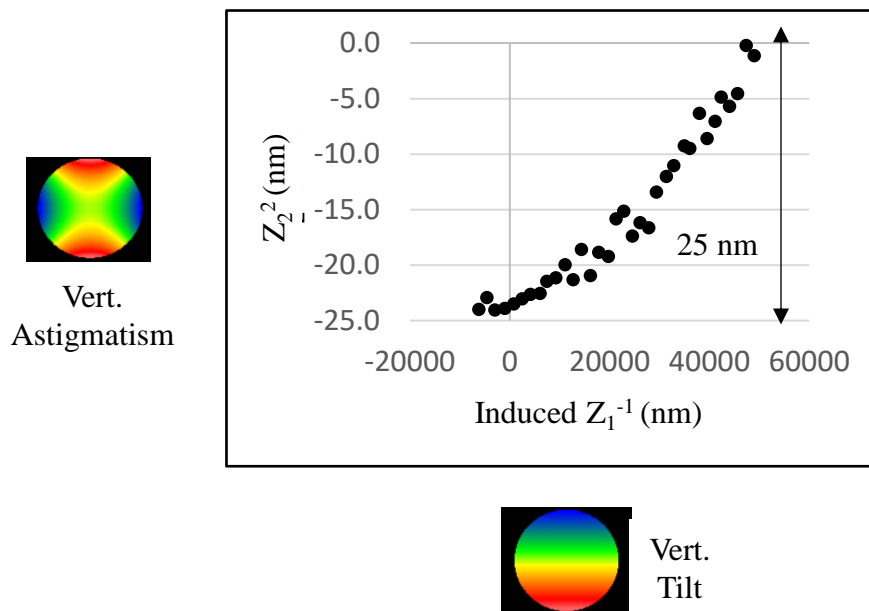


Figure 257: Induced tilt due to y translation of the ball and the resulted vertical astigmatism.

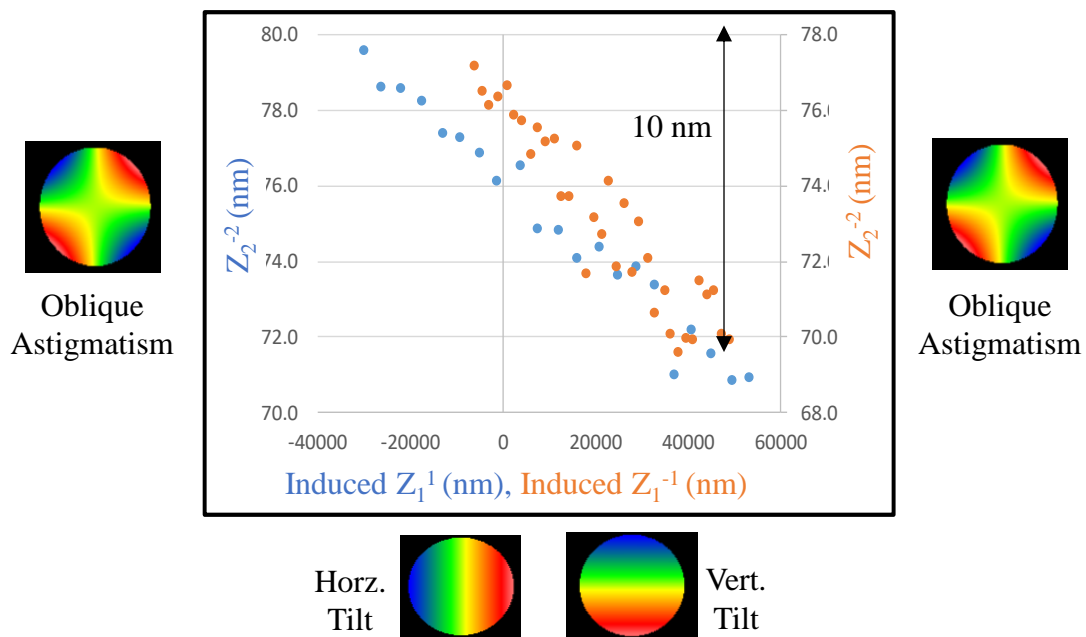


Figure 258: Induced tilt due to the x and y translation of the ball and the resulted oblique astigmatism.

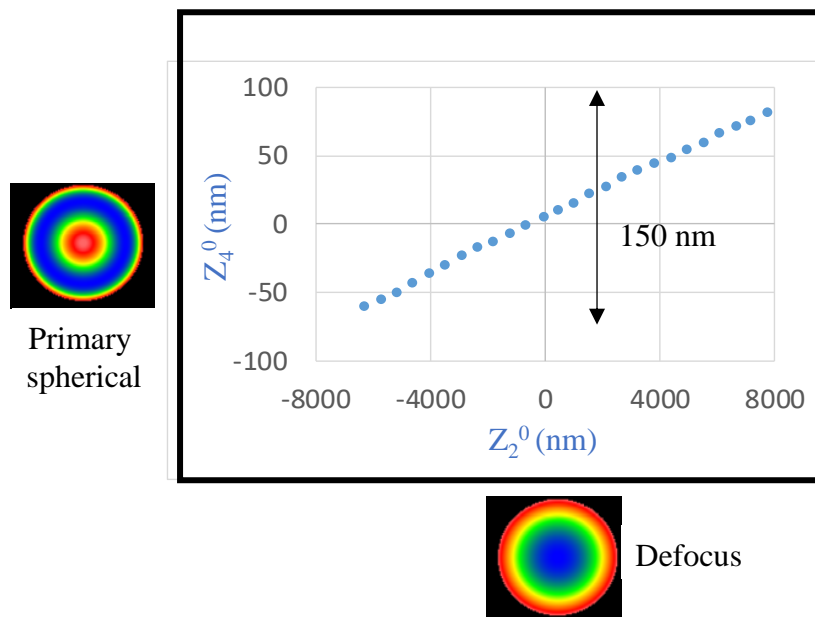


Figure 259: Induced defocus due to the z translation of the ball and the resulted oblique primary spherical error.

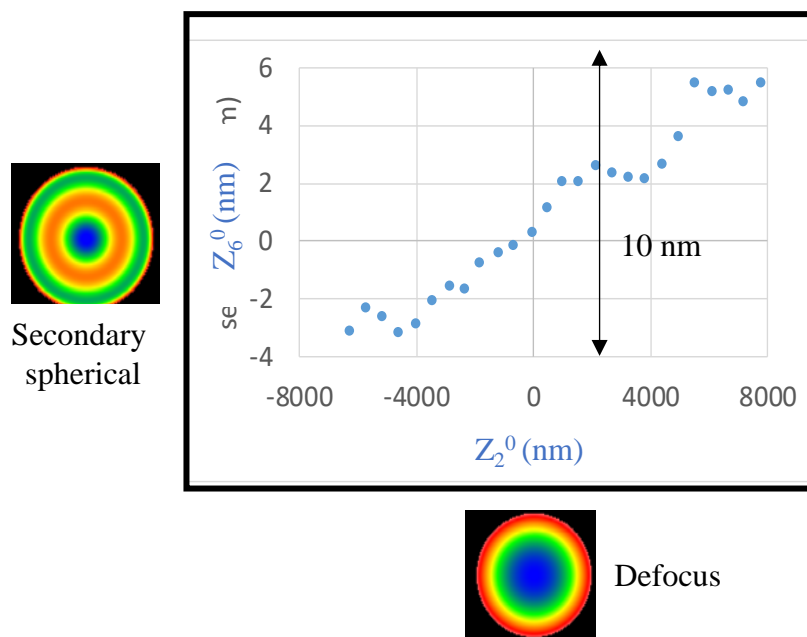


Figure 260: Induced defocus due to the z translation of the ball and the resulted oblique secondary spherical error.

As another method of estimating wavefront errors, the ball is moved in ten steps of 0.001 inches (2.5 μm) in x covering 0.01 inches (25 μm) for every y position varying in ten steps of 0.001 inches covering 0.01 inches, see Table 6. Wavefront error in the interferogram due to the vertical and horizontal tilts induced during the offset of the ball is shown in Figure 261, and from these results, variation in oblique astigmatism and defocus were found to be more sensitive to the offset of the ball.

Table 6: Positions of x and y in measurements to estimate the induced wavefront error in interferogram.

y (in.)	x (in.)
0	0
0	0.001
0	.
0	.
0	0.01
0.001	0
0.001	0.001
0.001	.
0.001	.
0.001	0.01
.	.
.	.
0.01	0.01

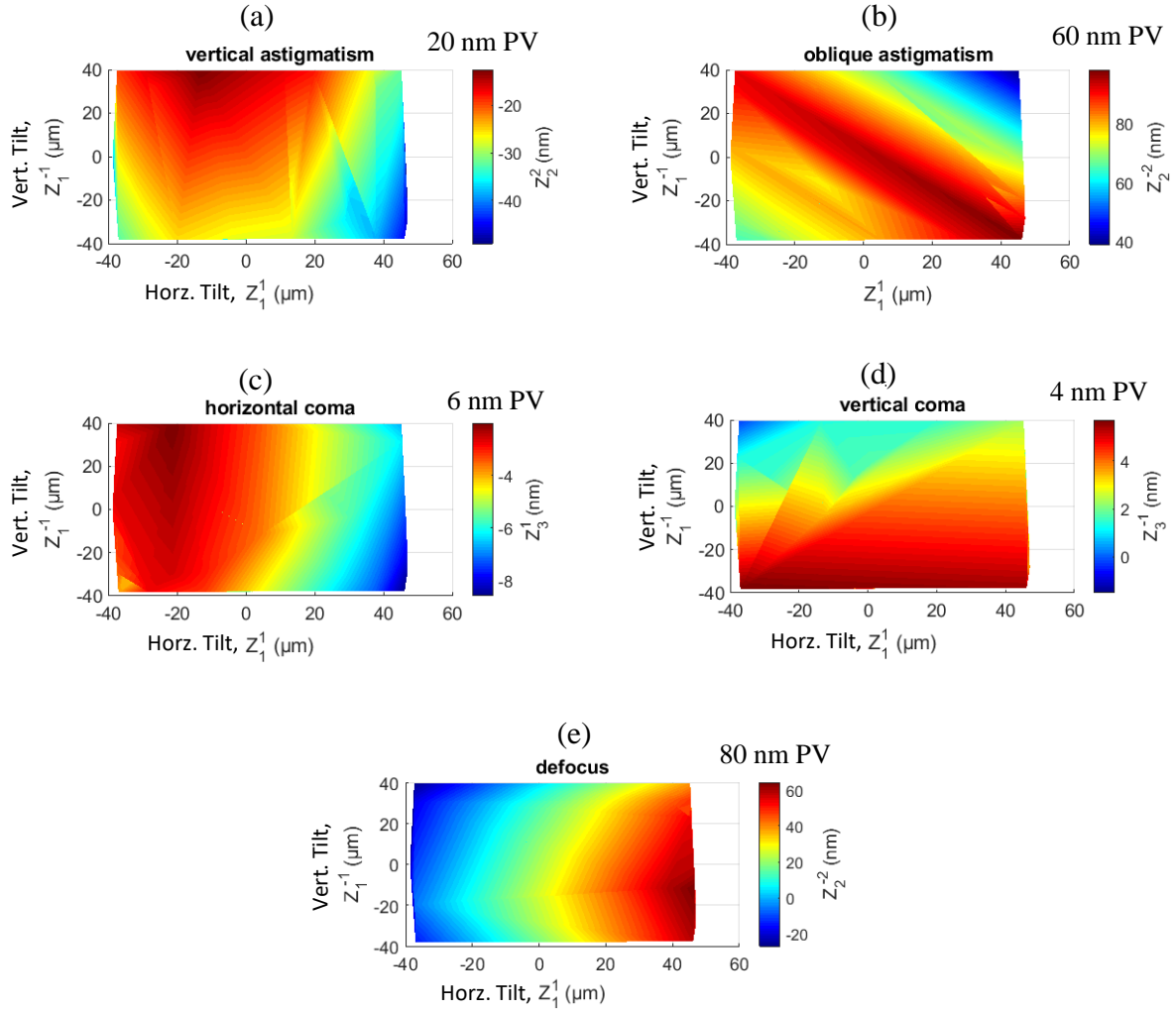


Figure 261: Wavefront errors in the interferograms due to the tilt induced during the offset of the ball in x and y axis.

Random ball test

The ball shown in Figure 255 is oriented in 64 different orientation, and translated in x , y , and z to null the fringes and the interferograms were captured after averaging four times in a QPSI, 16 Ring mode of the interferometer. ‘Rigid body terms’: Piston, tilt, and defocus were removed from the interferograms, and then averaged in the order of first 4, 8, 16, 32, 40, 48, 56, and 64 measurements and shown in Figure 262. A histogram of the values of rigid body

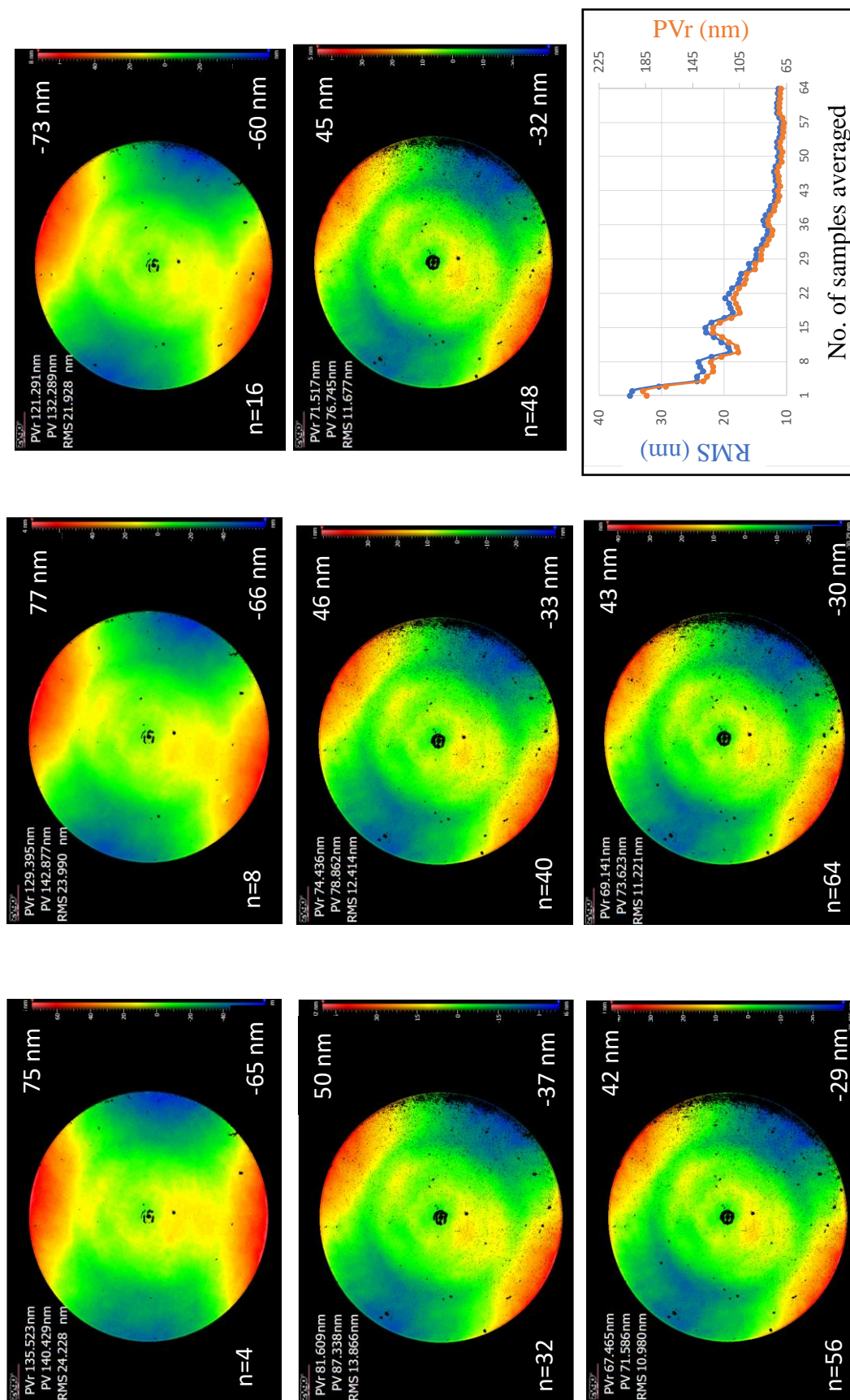


Figure 262: Averages of 64 interferograms in order of four measurements showing the reduction in the RMS and PVr values calculated.

terms removed in each measurement is shown in Figure 263. This information helps us compare the expected variation in the wavefront errors discussed in the previous section. Bottom right of Figure 262 shows the reduction of RMS and PVr of the averaged interferograms as a function of the number of averages.

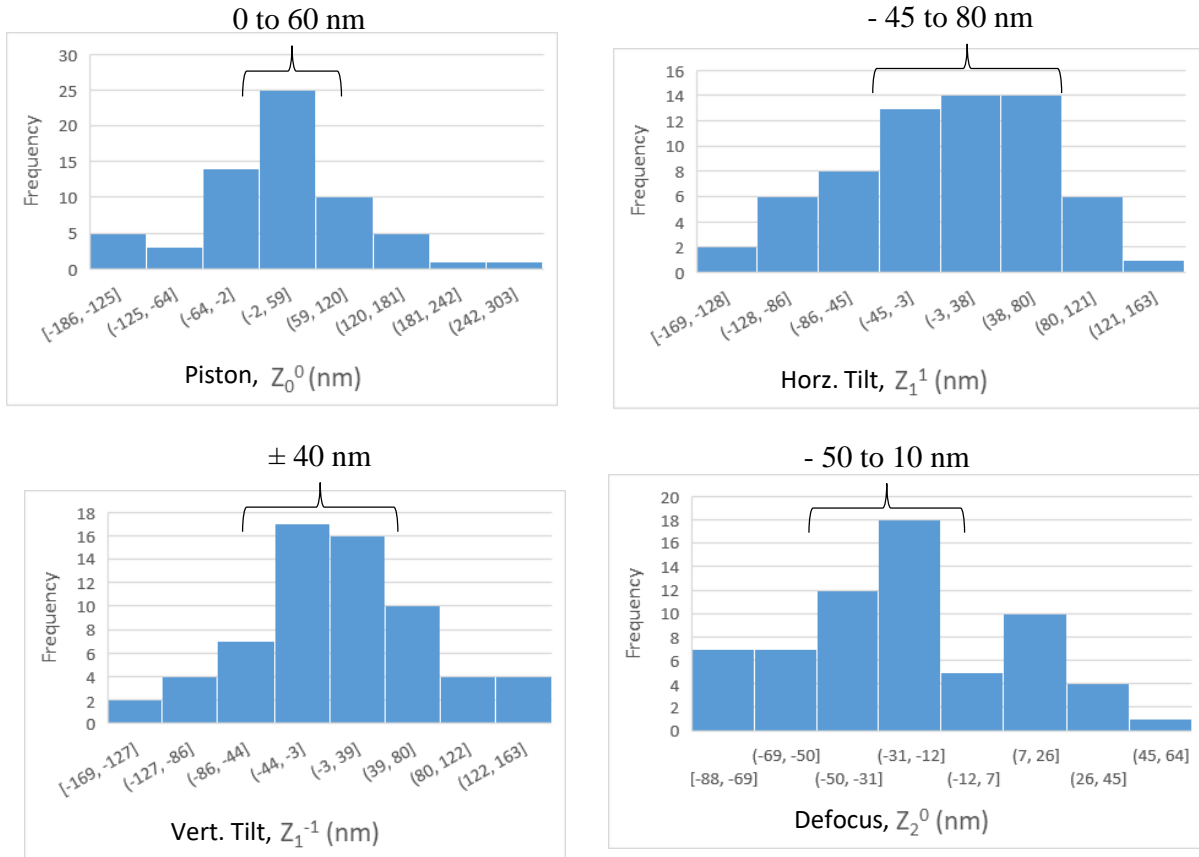


Figure 263: Rigid body terms removed from the interferograms used to estimate the form of transmission sphere.

Figure 264(a) shows the average of the 64 random ball measurements to represent the form of the transmission sphere. Figure 264(b) shows the 32 term Zernike fit to this estimate with a 60% minimum valid percentage, i.e. in the input data, at least 60% of the 64 values in each pixel should be a valid number (not a NaN).

From the Zernike fit, major polynomial terms are: (a) Oblique astigmatism - 22 nm (b) Vertical astigmatism - 12 nm, (c) Primary spherical - 8 nm, (d) Secondary spherical - 5 nm. Uncertainty in the estimated form is given by the standard deviation of the 64 measurements shown in Figure 264(c).

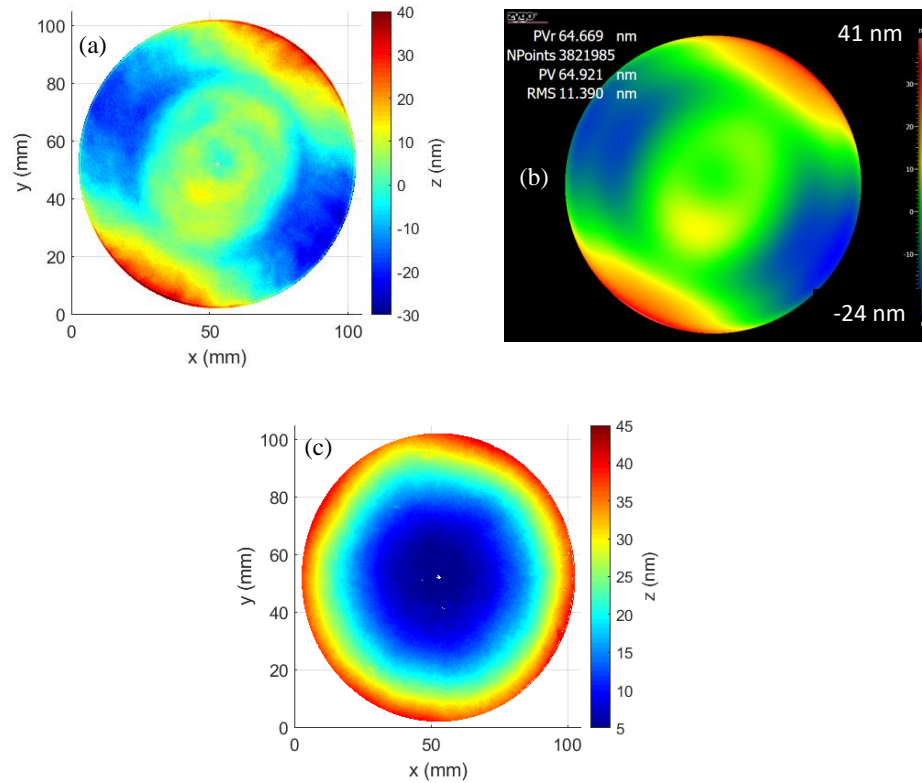


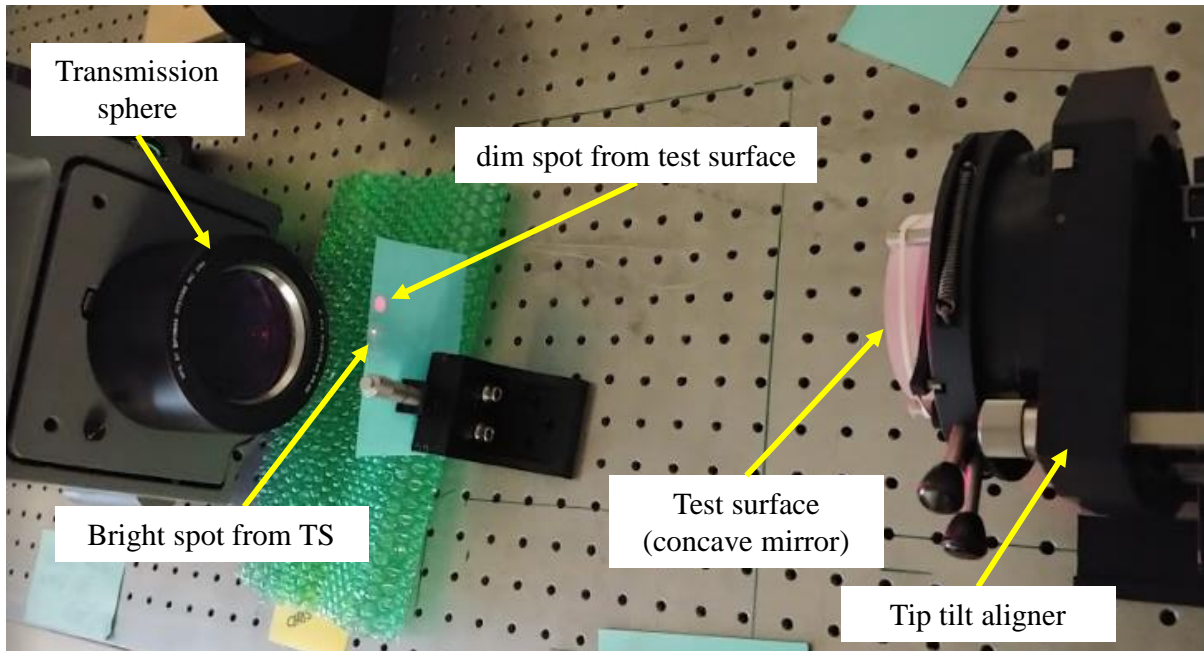
Figure 264: Estimated form of the transmission sphere; (a) Average of 64 random ball tests representing the form of the transmission sphere (b) 32 term Zernike polynomial fit (c) standard deviation representing the uncertainty in the estimated form.

C.2.10 Measurement of concave mirrors

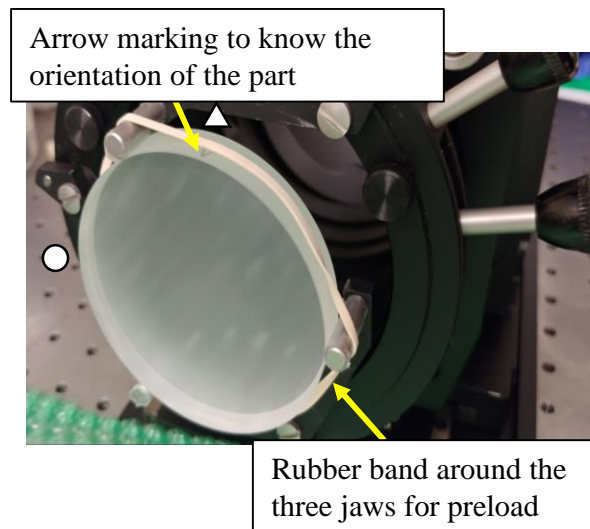
Two concave mirror surfaces (Edmund optics, stock # 32-826) made of Borofloat® of 3 in. Dia. (~75 mm), effective focal length of 152.4 mm are measured using a Fizeau interferometer. The alignment procedure and measurement of these surface are discussed in following sections.

Alignment procedure

Figure 265(a) shows the alignment procedure to interfere the light reflected from the concave mirror with the light beam from the transmission sphere. A cardstock with a small hole of couple of millimeters (‘pinhole’) is placed in front of the transmission sphere near its focal length. The converging light from the transmission sphere passing through the pinhole will illuminate the outer edges of it, termed as ‘Bright spot’ in Figure 265(a). The light passed through the pinhole diverge and illuminate the test surface, and 4% of this light reflects back from it and reaches the cardstock causing a ‘dim spot’. The test surface is moved in x and y to make this dim spot to align with the bright spot, thereby coarsely aligning the test surface with the transmission sphere causing interference. The knobs on the tip tilt aligner is used to fine align the test surface to ‘null’ the fringes before capturing the interferograms. It is noted that the concave test surface is held in the 3-jaw chuck preloaded by a rubber band around it, and an arrow mark on the top edge helps to keep track of the azimuth orientation of the surface around z axis, see Figure 265(b). Figure 266(a) schematically shows the light from the transmission sphere converges at its focal point and proceeds to the test surface diverging. Because of the difference in the focal length of the transmission sphere and the test surface, only a middle portion of the diverging beam illuminates the test surface and about 4% of the light reflects back and converges at the focal point and transmits through the test surface.



(a)



(b)

Figure 265: Experimental setup to measure the concave reference surface using the PSI; (a) alignment of the concave test surface to achieve interference of the light beams (b) Concave mirror held using a 3-jaw chuck preloaded with a rubber band

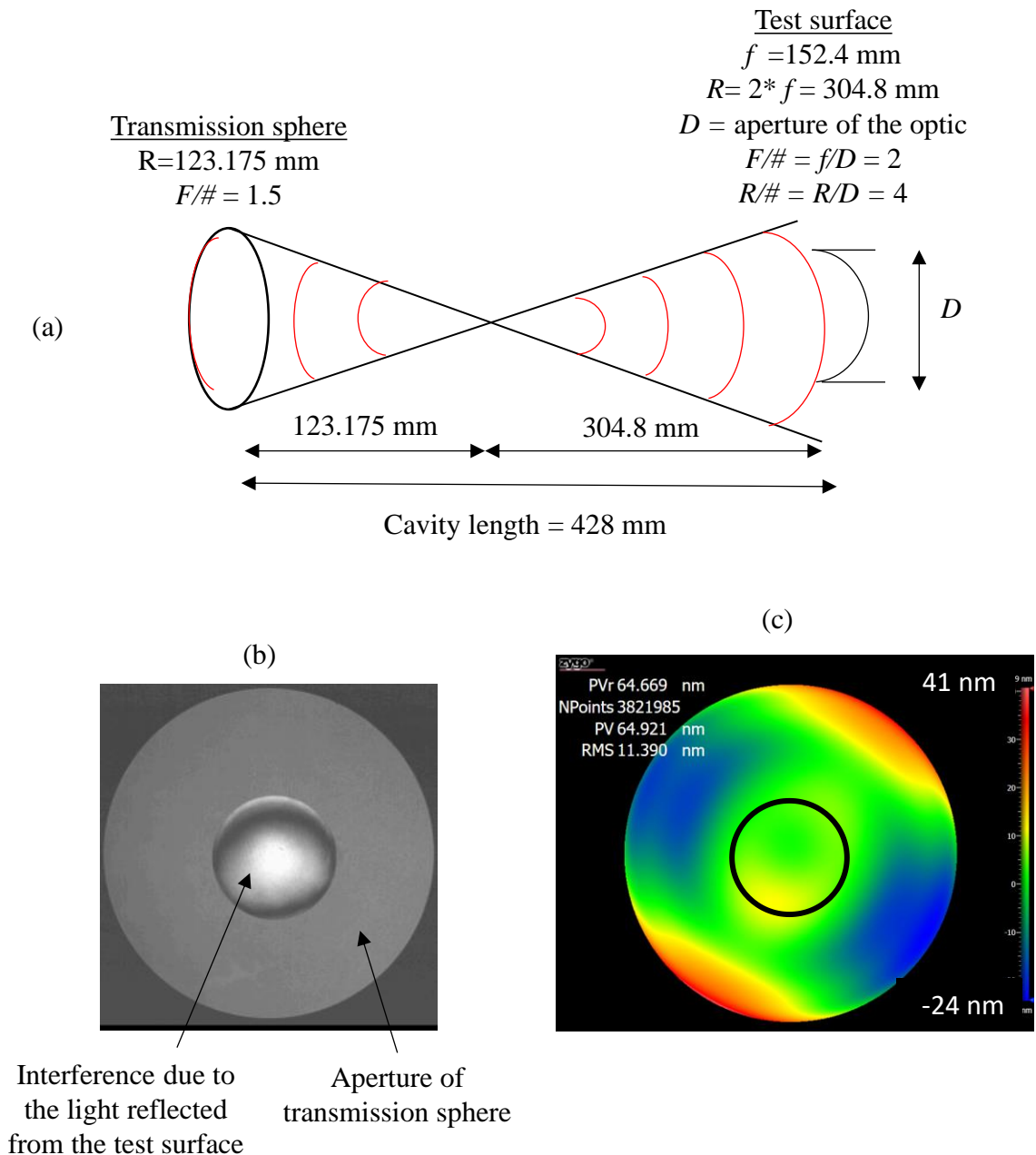


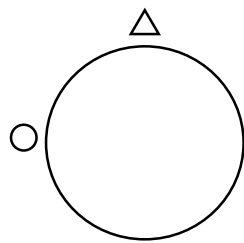
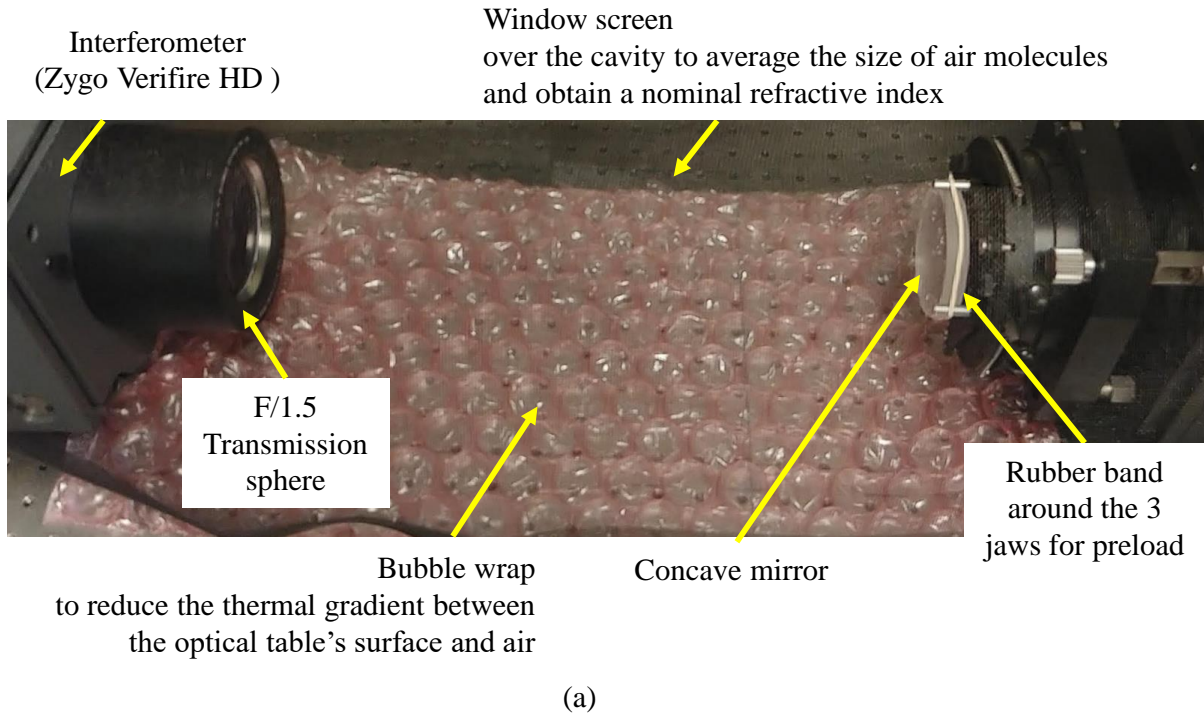
Figure 266: Measurement area of the concave surface with respect to the transmission sphere area; (a) Schematic of the light beam from the transmission sphere illuminating the concave mirror test surface (b) interference fringes after nulling the cavity (c) interference region corresponding to the 36 term Zernike fit to the form of the transmission sphere estimated from a random ball test.

The interference fringes shown in Figure 266(b) corresponds to the central region of the transmission sphere. "The percentage of full-size (of results) can be calculated as the ratio of the $f/\#$ (of the transmission sphere) to $R/\#$ (of the test surface)" - Zygo's Transmission sphere selection guide. In our case, $1.5/4$, therefore, the resulting interferogram would be scaled down to 37.5 % of the aperture of the transmission sphere.

Figure 266(c) shows the interference zone using a black circle, and the form of the transmission sphere represented by the 36 term Zernike fit to the result of the random ball test. The form of the transmission sphere in this zone could be subtracted from the recorded interferograms, thereby correcting for the form of the transmission sphere in the interferogram captured. It is noted that for the central region shown in Figure 266(c), the uncertainty in the estimated form is less than 10 nm , see Figure 264(c).

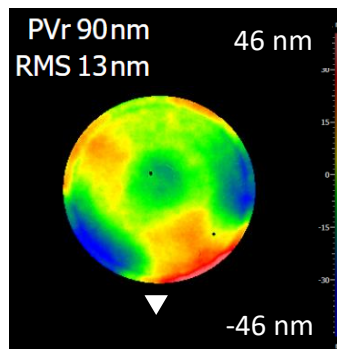
Measurement result

Figure 267(a) shows the experimental setup while capturing the interferograms of concave mirror test surfaces. Figure 267(c and d) shows the interferograms after subtracting the effect of the form of transmission sphere. It is noted that the interferogram captured is upside down and left side right corresponding to the orientation of the test surface, i.e the arrow mark at the top edge of the test surface shown in Figure 265(b), schematically shown in Figure 267(b) corresponds to the bottom of the interferogram. However, during the measurements of these surface using the profiler, the arrow mark will face the operator, therefore making the captured interferogram directly comparable with the profilograms in its measurement coordinates. To ensure that the captures interferograms are due to the form of the surface, and not due to the clamping force of the 3-jaw chuck, the concave mirrors were measured in 4 angular orientations around z axis, and are shown in Figure 268.



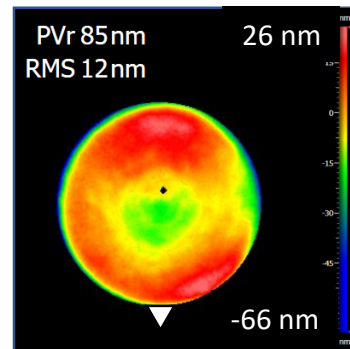
(b)

1



(c)

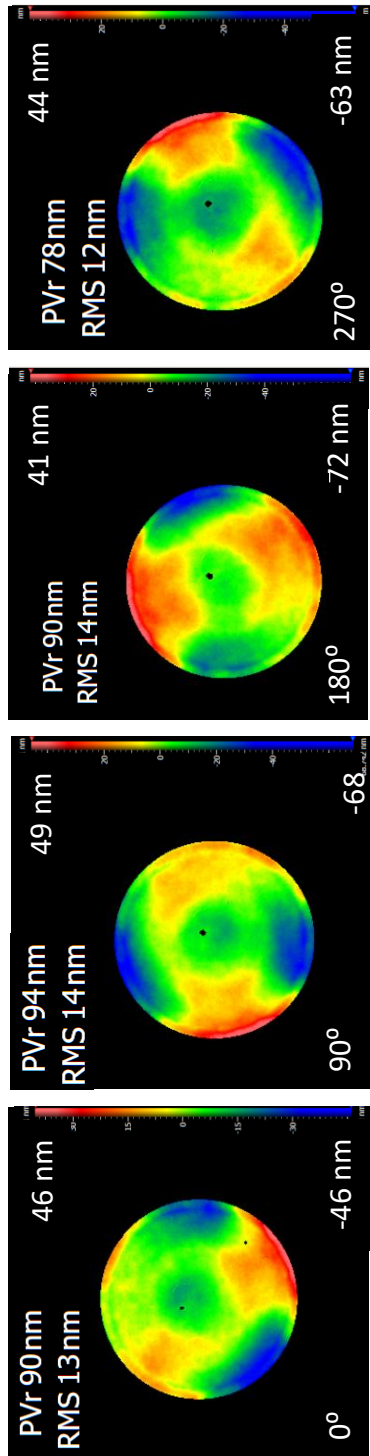
2



(d)

Figure 267: PSI Measurement results of the concave surfaces (a) Experimental setup to reduce the environmental disturbances during the measurements (b) schematic of the orientation of the test surface (c) Resulted interferograms of Concave mirror 1 (d) Concave mirror 2.

1



2

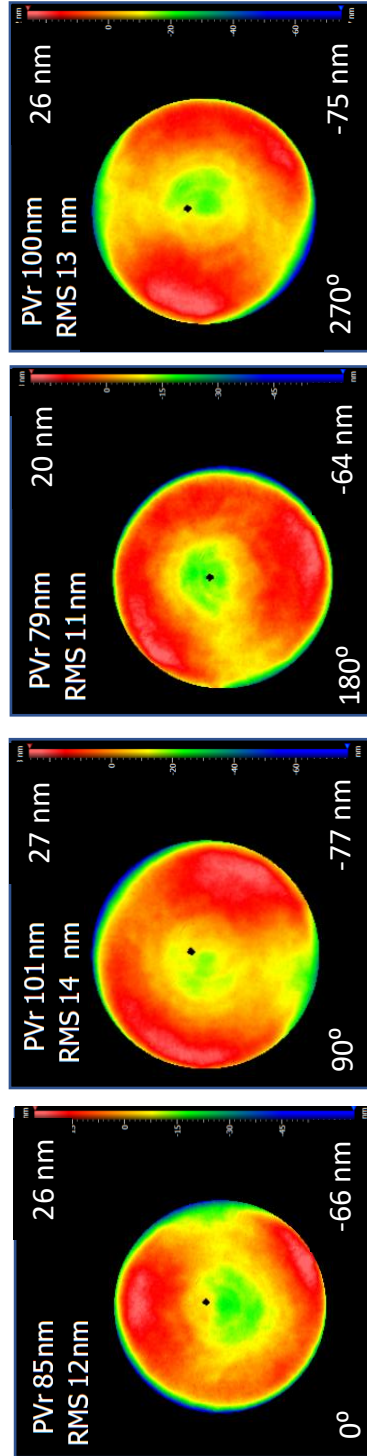


Figure 268: Interferograms of the concave mirrors captured by rotating in steps of 90° clockwise

Variation in Zernike polynomial terms of the fit to the measurement at 0° and 90° could be used to estimate the variation in the measured interferograms due to the clamping force, and other environmental variations. For example, vertical astigmatism in 0° orientation becomes negative vertical astigmatism in 90° orientation, and horizontal coma in 0° becomes negative of vertical coma in 90° , see Figure 269. Zernike coefficients of the fit to the measurements of concave mirror 1 at 0° and 90° orientation and the absolute difference between them are shown in Table 7, where the difference in vertical astigmatism and trefoil terms are larger than 20 nm.

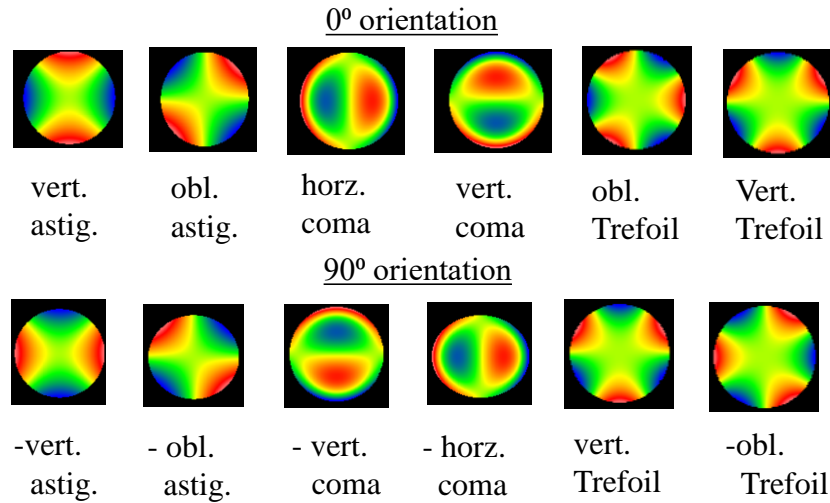


Figure 269: Relatable Zernike polynomials of a surface measured in orthogonal orientations

Table 7: Values of the Zernike fit to the measurements at 0° and 120° orientations and their differences

Zernike polynomial	0°	90°	Difference (nm)
	ZFR (nm)	ZFR (nm)	
vert. Ast.	-13.8	35.0	21
obl. Ast.	-16.3	7.9	8
horz. Coma	5.0	-6.7	2.5
vert. Coma	5.9	-2.5	1
obl. Trefoil	-20.0	-12.1	25
vert. Trefoil	8.9	-4.7	21

Rotationally invariant, and rotationally varying form of the concave mirror

A reversal procedure that uses the measurements at the four angular orientation shown in Figure 270(a), to separate the rotationally invariant, and rotationally varying form of the concave mirror 1 is discussed in this section. Figure 270(b) shows the average of the four measurements representing the rotationally invariant form and the effect of transmission sphere in the measurement. The effect of transmission sphere is removed by subtracting the estimated form of the transmission form in the interference region shown using a black circle in Figure 266(c), and plotted in Figure 270(c).

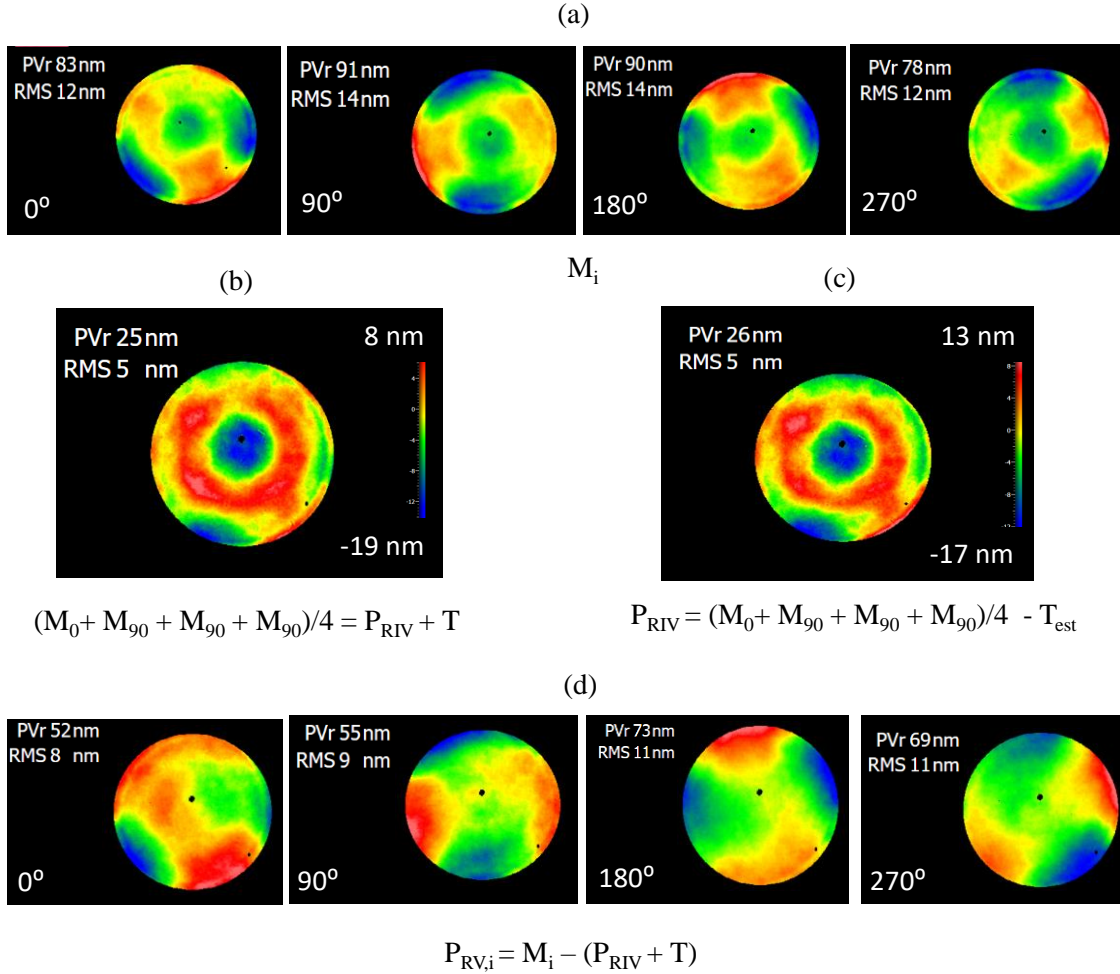


Figure 270: Measurement results of the concave mirror 1 measured at four angular orientations (a) interferograms, (b) average of the interferograms, (c) Rotationally invariant form of the mirror.

Rotationally invariant form at 90° , 180° , 270° angular orientations shown in Figure 270(c), and Figure 271(a) are rotated with respect to the 0° orientation and shown in Figure 271(b). They are overlaid on top of each other, and the common area is averaged to represent the rotationally varying form of the mirror of 40 nm PV with a 10 nm PV uncertainty, see Figure 271(c to d).

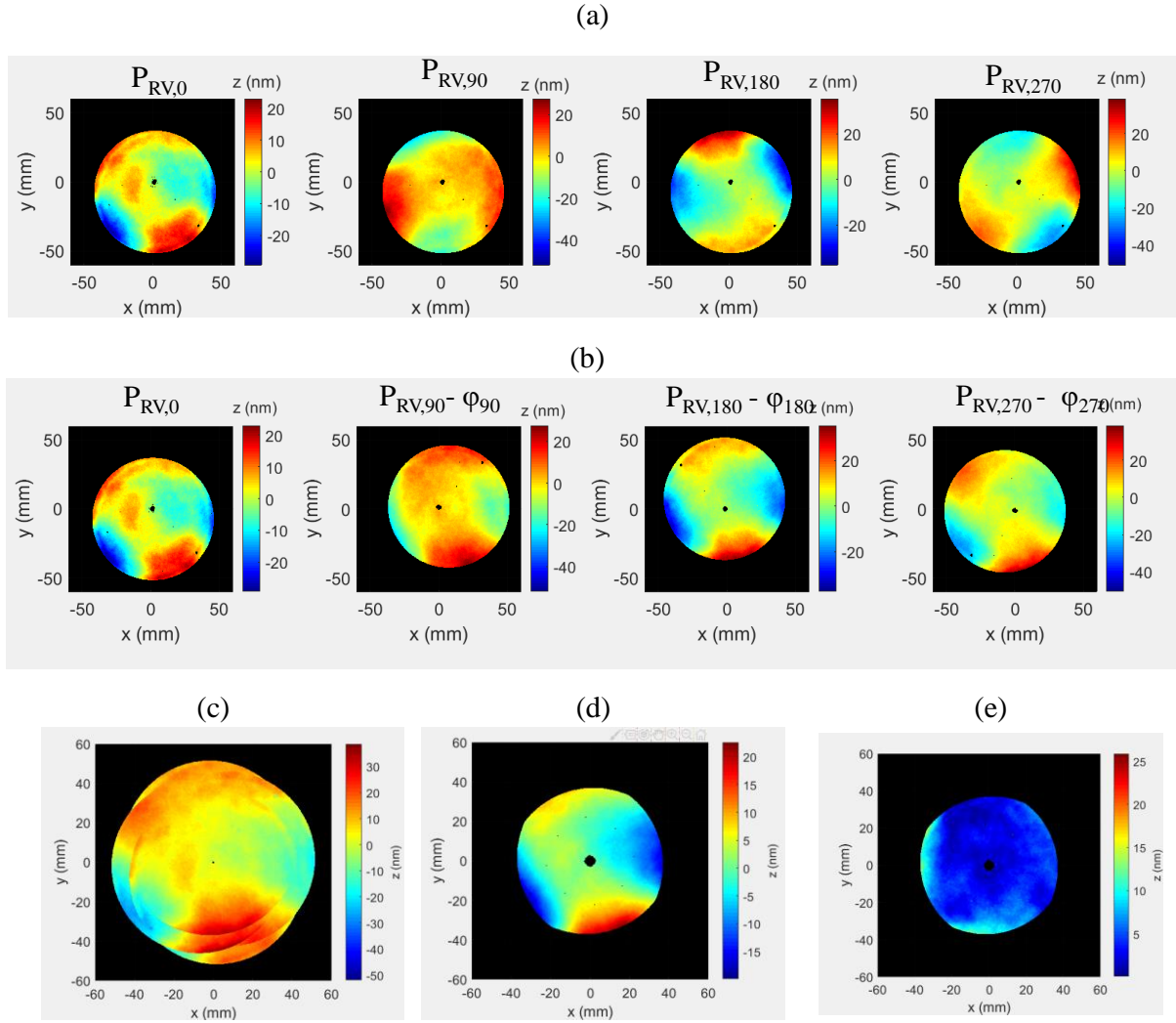


Figure 271: Extraction of the rotationally variant and invariant form of the concave surface;
 (a) Rotationally invariant form of the mirror (b) interferograms at 90°, 180°, 270° rotated with respect to the interferogram at 0°, (c) overlaid on top of one another after rotation (d) average of the four interferograms representing the rotationally varying form of the concave mirror 1 (e) standard deviation

C.3 Calibration of temperature sensors used with the profilometer system

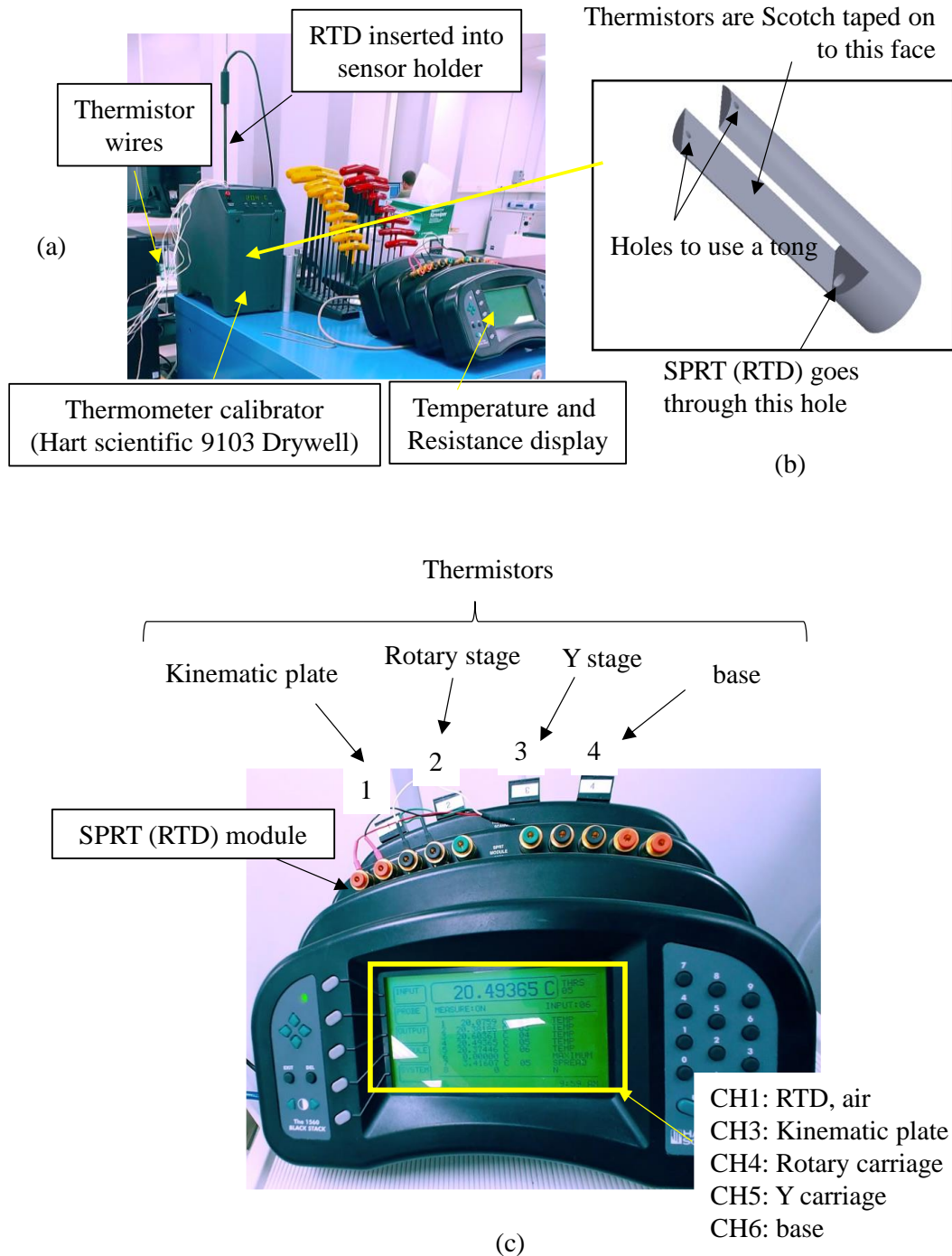


Figure 272: Calibration of the temperature sensors used during the measurement of the drift of the profilometer; (a) Calibration setup, (b) Holder where the sensors are attached to insert it into the calibrator housing, (c) Display for the temperature sensors.

Thermistor,
using 3M double sided tape

Thermistor,
attached using 3M double sided tape

RTD in air

Thermistor on Rotary stage

Thermistor on form

Thermistor on
Rotary stage

Thermistor on
Y stage

409

C.4 Hertzian analysis of a Zerodur flat supported on a 3-point kinematic mount

The equations below are used to perform a Hertzian analysis at the interface of the Zerodur flat contacting one of the steel spheres used in the kinematic mount shown in Figure 81(c). The contact pressure, (P_0) at the interface is estimated to be 192 MPa, and the shear stress (τ) is 58 MPa, which is less than the characteristic strength of optically polished Zerodur, $\sigma = 293$ MPa [Schott, 2004]. The width of contact (w) between the surfaces is 0.12 mm.

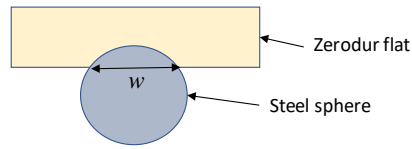


Figure 274: Schematic of a Zerodur flat sitting on a Stainless steel sphere

$$p_0 = \left(\frac{6F\bar{E}}{\pi^3 R^2} \right)^{1/3} = 192 \text{ MPa}; \quad \tau_0 = 0.3 p_0 = 58 \text{ MPa}; \quad w = 2 \left(\frac{3FR}{4\bar{E}} \right)^{1/3} = 0.12 \text{ mm}$$

$$F = \frac{m_{\text{zerodur}}}{3} g$$

$$\frac{1}{\bar{E}} = \frac{(1 - \nu_{\text{zerodur}}^2)}{E_{\text{zerodur}}} + \frac{(1 - \nu_{\text{steel}}^2)}{E_{\text{steel}}}$$

$$\frac{1}{R} = \frac{1}{R_{\text{zerodur}}} + \frac{1}{R_{\text{steel}}}$$

where,

mass of Zerodur flat distributed on each sphere, $m_{\text{zerodur}}/3 = 0.133$ kg

acceleration due to gravity, $g = 9.81 \text{ m.s}^{-1}$

Poisson's ratio of Zerodur and Stainless steel, $\nu_{zerodur} = 0.24$, $\nu_{steel} = 0.3$

Young's modulus of Zerodur and Stainless steel, $E_{zerodur} = 90.3 \text{ GPa}$, $E_{steel} = 200 \text{ GPa}$

radius of Zerodur flat and Stainless steel sphere, $R_{zerodur} = \infty$ $R_{steel} = 12.7 \text{ mm}$

Material properties of Zerodur could be found at [Schott, 2011].

C.5 Hertzian analysis of a Silicon nitride sphere supported on a kinematic 3 point mount

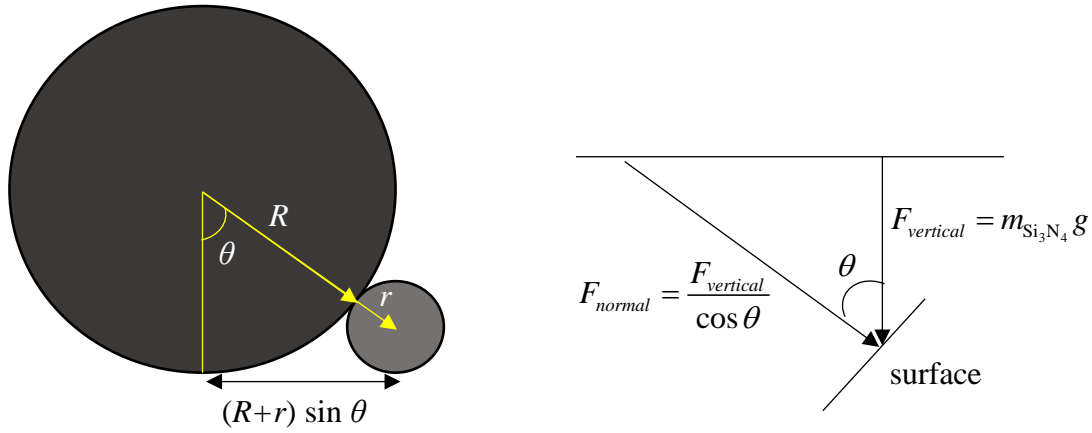


Figure 275: Schematic showing a Silicon nitride sphere in contact with a stainless steel spheres and the normal force on their surfaces

The equations below are used to perform a Hertzian analysis at the interface of the Silicon nitride sphere contacting one of the steel spheres used in the 3-ball kinematic nest discussed in section 4.9.1.1. For the spheres contacting in an angle, θ , the contact pressure (P_0) at the interface for a contact width, $w = 60 \mu\text{m}$ is estimated to be 600 MPa, and the tensile stress is given by $\sigma = 110 \text{ MPa}$.

$$P_0 = \left(\frac{6F\bar{E}}{\pi^3 R^2} \right)^{1/3} = 610 \text{ MPa}; \quad \sigma = \frac{(1 - 2\nu_{\text{SiN}}) P_0}{3} = 110 \text{ Mpa}; \quad w = 2 \left(\frac{3FR}{4\bar{E}} \right)^{1/3} = 60 \mu\text{m}$$

$$F = \frac{m_{\text{SiN}} g}{3 \cos \theta}$$

$$\frac{1}{\bar{E}} = \frac{(1 - \nu_{\text{SiN}}^2)}{E_{\text{SiN}}} + \frac{(1 - \nu_{\text{Steel}}^2)}{E_{\text{Steel}}}$$

$$\frac{1}{R} = \frac{1}{R_{\text{SiN}}} + \frac{1}{R_{\text{Steel}}}$$

where,

mass of Silicon nitride sphere distributed on each steel sphere, $m_{\text{SiN}}/3 = 70 \text{ g}$

acceleration due to gravity, $g = 9.81 \text{ m.s}^{-1}$

Poisson's ratio of Silicon nitride and Stainless steel, $\nu_{\text{SiN}} = 0.23$, $\nu_{\text{steel}} = 0.31$

elastic modulus of Silicon nitride and Stainless steel, $E_{\text{SiN}} = 310 \text{ GPa}$, $E_{\text{steel}} = 200 \text{ GPa}$

radius of Silicon nitride sphere and Stainless steel sphere, $R_{\text{SiN}} = 25.4 \text{ mm}$, $R_{\text{steel}} = 6.35 \text{ mm}$

The Stress intensity factor for a given tensile stress on a crack of $a = 10 \text{ }\mu\text{m}$ on the surface of the Silicon nitride sphere is given by

$$K_I = \gamma \sigma \sqrt{\pi a} = 0.6 \text{ MPa}\sqrt{\text{m}},$$

Where $\gamma = 1$ is the geometric factor for a small crack in infinite solid. The calculated stress intensity factor is ten times smaller than the fracture toughness of Silicon nitride, which is $6.1 \text{ MPa}\sqrt{\text{m}}$ [Hampshire, 2007].